Gas organization in M51

The impact of spiral arm dynamics on Giant Molecular Cloud properties

Dario Colombo
Max-Planck-Institut für Astronomie

Heidelberg 2013

Dissertation in Astronomy
submitted to the
Combined Faculties of the Natural Sciences and Mathematics
of the Ruperto-Carola-University of Heidelberg, Germany,
for the degree of
Doctor of Natural Sciences

Put forward by
M.Sc. *Dario Colombo*
born in Legnano (MI), Italy

Oral examination: 30.10.13

Gas organization in M51

The impact of spiral arm dynamics on Giant Molecular Cloud properties

Dario Colombo
Max-Planck-Institut für Astronomie

Referees: **Prof. Dr. Hans-Walter Rix**
Prof. Dr. Jochen Heidt

Zusammenfassung

Neuere Beobachtungen haben gezeigt, dass Sternentstehung mit der molekularen Phase des interstellaren Mediums in Zusammenhang steht. Das molekulare Gas tendiert dazu, grosse, nahezu selbstgravitierende Einheiten, zu bilden, die so genannten riesigen Molekülwolken (RMW). Diese riesigen Molekülwolken sollten demzufolge die Sternentstehung grundlegend beeinflussen. Allerdings sind ihre physikalischen Eigenschaften, sowie ihre Entstehungs- und Entwicklungsmechanismen nicht sehr gut verstanden - insbesondere in Spiralgalaxien. Die neue Durchmusterung der Whirlpool-Galaxie M51, im Rahmen des PdBI Arcsecond Whirlpool Surveys (PAWS), bietet zum ersten Mal die Möglichkeit, die Verteilung des Molekülgases in einer klassischen Spiralgalaxie zu studieren, die von dynamischen Phänomenen dominiert ist. Das Ziel dieser Doktorarbeit ist es, die Wichtigkeit der galaktischen Umgebung für die Gasorganisation abzuschätzen.

Anhand einer sorgfältigen Analyse der Gaskinematik studiere ich die Struktur des Gravitationspotentials sowie die Strömungsbewegungen der Spiralarme vom M51. Diese Untersuchung zeigt neue Unterschiede zwischen der molekularen und atomaren Phase des interstellaren Mediums auf. Zudem finde ich auch Hinweise auf einen kinematischen $m = 3$ Modus, der die Asymmetrie der Spiralarme erklärt. Um den Einfluss der dynamischen Umgebung auf das Molekülgas zu untersuchen, habe ich den derzeit grössten, extragalaktischen RMW-Katalog mit Hilfe eines automatischen Suchalgorithmuses erstellt. Dieser Algorithmus zieht auch systematische Beobachtungsfehler in Betracht. Die Unterschiede der Wolkeneigenschaften legen nahe, dass die Umgebungen der RMW, und insbesondere ihre dynamischen Eigenschaften, stark die Organisation des Gases in Spiralgalaxien beeinflussen. Sie ermglichen weiterhin, zwischen den verschiedenen Mechanismen zur Wolkenentstehung und -entwicklung, die in der Literatur vorgeschlagen wurden, zu unterscheiden.

Abstract

Recent observations have shown that star formation is correlated with the molecular phase of the interstellar medium. Molecular gas tends to organize itself into large and roughly self-gravitating entities called Giant Molecular Clouds (GMCs). These objects should, therefore, play a key role in controlling star formation and defining its modes. However, their physical properties, formation and evolution mechanisms are still poorly understood - especially in spiral galaxies. The new PdBI Arcsecond Whirlpool Survey (PAWS) offers, for the first time, the possibility to study the molecular gas distribution in a grand-design spiral galaxy dominated by dynamical phenomena. The aim of this thesis is to evaluate the importance of galactic environments for the gas organization.

Via a thorough analysis of the gas kinematics I study the structure of M51's gravitational potential and spiral arm streaming motions. This analysis provides several insights on the differing nature of the molecular and atomic phase of the interstellar medium. I also find evidence for a kinematic $m = 3$ mode that explains the asymmetry of the spiral arms. To investigate the effect of the dynamical environment on the molecular gas I have generated the largest extragalactic GMC catalog to date using an automatic algorithm that accounts for the observational biases. Differences in the cloud properties suggest that environments, and in particular dynamical effects, strongly influence the organization of the gas in spiral galaxies and provide a way to discriminate between the various mechanisms of cloud formation and evolution that have been proposed in the literature.

Alla mia nonna Luigia
che riposa tra le stelle...

Contents

Introduction **1**

0.1 The pivotal role of Giant Molecular Clouds in the star formation cycle . . . 1

0.2 The standard paradigm of the Giant Molecular Clouds 2

0.3 The Giant Molecular Cloud internal structure 6

0.4 Giant Molecular Cloud microphysics: the role of turbulence 9

0.5 The Giant Molecular Cloud life cycle 11

0.5.1 Formation 11

0.5.2 Evolution, destruction and lifetime 13

0.6 Giant Molecular Cloud macrophysics: spiral arm dynamics 15

0.6.1 The density-wave theory: overview 15

0.6.2 Kinematic density-waves 17

0.6.3 Deviations from the QSSS theory 19

1 M51 as seen by the PAWS project **21**

1.1 Introduction 22

1.2 The PdBI+30m Arcsecond Whirpool Survey datasets 25
1.3 ^{12}CO(1-0) emission of M51 at high resolution: the PAWS view 27
1.4 Spatial relation between CO, gas and stellar tracer in M51 29
1.5 Inventory of galactic environments for M51 analysis 33
1.6 Environmental dependence of the molecular gas structure in M51 37
1.7 Dynamical dependence of the star formation in M51 40
1.8 Summary and Conclusions 41

2 Multi-phase cold gas kinematic of M51 **43**

2.1 Introduction 44
2.2 Data 46
2.2.1 Archival THINGS VLA HI data 46
2.2.2 Archival HERACLES IRAM 30m ^{12}CO(2-1) data 47
2.3 The M51 ^{12}CO(1-0) velocity field at high angular resolution 47
2.4 Gas motions in spiral potentials 49
2.4.1 Line-of-sight velocity 50
2.4.2 Kinematic parameter estimation 50
2.4.2.1 Previous M51 kinematic studies 51
2.4.2.2 Tilted-ring analysis 53
2.4.3 Circular motion: gas-derived rotation curve of M51a 56
2.5 Non-circular motions 60
2.5.1 Residual velocity fields 60
2.5.2 Harmonic decomposition of the non-circular velocity component . . . 61
2.5.2.1 Application to residual velocity fields 63
2.5.3 Global Trends 63

2.5.4 RADIAL TRENDS . . . 64

2.5.4.1 Odd velocity modes: the bar and two-armed spiral arms . . . 64

2.5.4.2 Even velocity modes: an additional three-armed spiral structure 65

2.5.4.3 Outer arms . . . 67

2.5.5 THE MAGNITUDE OF STREAMING MOTIONS . . . 67

2.5.5.1 Streaming motions in M51 . . . 69

2.6 DISCUSSION: AN m=3 POTENTIAL PERTURBATION IN M51 . . . 70

2.6.1 ORIGIN AND NATURE OF THE $m = 3$ MODE . . . 72

2.7 DISCUSSION: THE OPTIMAL DATASET FOR KINEMATIC STUDIES . . . 74

2.7.1 RESOLUTION CONSIDERATIONS . . . 74

2.7.2 CHOICE OF TRACER/OBSERVING STRATEGY . . . 75

2.7.2.1 CO versus HI . . . 75

2.7.2.2 Hybrid versus single-dish data . . . 76

2.8 SUMMARY AND CONCLUSIONS . . . 78

3 THE PAWS GIANT MOLECULAR CLOUD CATALOG **83**

3.1 INTRODUCTION . . . 83

3.2 CPROPS DESCRIPTION . . . 85

3.3 GMC CATALOG GENERATION . . . 86

3.3.1 TESTING CPROPS DECOMPOSITION PARAMETERS . . . 87

3.3.2 DEFINITION OF GMC PROPERTIES . . . 91

3.3.2.1 Basic GMC properties . . . 91

3.3.2.2 Derived GMC properties . . . 93

3.4 THE PAWS CLOUD CATALOGS . . . 95

3.4.1 ISLAND CATALOG . . . 96

3.4.2 GMC catalog . . . 96

3.5 Properties of CO emission and GMC Ensemble in different M51 Environments 97

3.6 CPROPS bias correction effects and catalog reliability . . . 100

3.6.0.1 Effect of resolution and sensitivity correction with environment 101

3.6.0.2 GMC extrapolated property reliability . . . 106

3.7 CPROPS corrections and scaling relations . . . 108

3.8 CPROPS corrections and GMC comparative studies . . . 109

3.9 Summary and conclusions . . . 109

4 Environmental dependence of GMC properties in M51 **113**

4.1 Introduction . . . 113

4.2 Statistical variation of M51 GMC properties with environment . . . 119

4.2.1 Basic GMC properties . . . 121

4.2.2 Derived GMC properties . . . 121

4.3 Scaling relations . . . 124

4.3.1 First Larson's law: size-velocity dispersion relation . . . 124

4.3.2 Second Larson's law: virial mass-luminosity relation . . . 125

4.3.3 Third Larson's law: luminosity-size relation . . . 126

4.4 GMC Mass spectra . . . 131

4.4.1 Construction and general properties . . . 131

4.4.2 Slope variations . . . 135

4.4.3 Testing the Shape of the Mass Spectra for Incompleteness Effects . . 136

4.5 X_{CO} in M51 . . . 139

4.6 Discussion . . . 141

4.6.1 The Diversity and Evolution of the GMCs in M51 . . . 141

4.6.2 Larson's laws in M51 147

4.7 Summary and conclusion 148

Summary, future perspective and final considerations **151**

Summary: complex dynamics of M51 as driver of GMC properties 151

Future perspective 152

ALMA capabilities 153

The importance of kinematics 154

GMC segmentation and property calculation 155

Going beyond: atomic gas and simulations 156

Appendix **157**

PAWS M51 GMC catalog 157

PAWS M51 Island catalog 183

PAWS moment maps 189

Datacube masking technique 189

Velocity dispersion map 191

Low-resolution velocity field harmonic decompositions 192

Kolmogorov-Smirnov test matrices 197

Acknowledgements **201**

Bibliography **205**

INTRODUCTION

0.1 THE PIVOTAL ROLE OF GIANT MOLECULAR CLOUDS IN THE STAR FORMATION CYCLE

"Thence we came forth to rebehold the stars." The conclusive words used by Dante Alighieri to end all canticas in his opera omnia, *La Divina Commedia*, well expose the magnificence that humans have always experienced when they turn their gaze at the starry night sky. In addition to being a source of inspiration for generations of poets, the stars are the "atoms" of the galaxies and the objects that astronomers since antiquity have studied to understand the physics and evolution of the Universe. Stars are the dominant source of radiation (together with the cosmic microwave background and the accretion of black holes) and are responsible for the production of all chemical elements heavier than hydrogen, helium and lithium. The dark patches of gas and dust that obscure the stars in the Milky Way when observed on a clear night, are the places in which the stars born. In particular, recent observations (e.g. Bigiel et al. 2008, Schruba et al. 2011, Leroy et al. 2013b) have shown that the star formation is correlated with one particular gaseous phase of the interstellar medium (ISM), the molecular phase.

Molecular gas forms in very cold environments thanks to the catalysis of dust grains and has the tendency to organize itself in massive and roughly self-gravitating objects called Giant Molecular Clouds (GMCs, Sanders et al. 1985). Those clouds are sufficiently cold and dense that small high density clumps within them are able to collapse and form stars. The birth of stars affects the subsequent evolution of the parent cloud, photodissociating, ionizing and dispersing the gas that could return to the ambient medium, reforms molecular clouds and eventually new stars, restarting the cycle. The properties of GMCs, such as turbulence and magnetic field strength, regulate how star formation evolves on local scales (e.g. Larson 1992; McKee 1999; Pudritz 2002), and are intrinsically linked to many of the issues in star formation, such as the time for stellar collapse (e.g. Elmegreen 2007). Understanding how GMCs form and evolve, and how their characteristics depend on the dynamics of galaxies and nature of the ISM, is essential for progress in star formation.

To date, GMC populations have mostly studied in the Milky Way or in nearby low-mass galaxies where atomic gas dominates the neutral ISM. This is because it is difficult to achieve the angular resolution required to identify individual GMCs in any galaxy outside the Local Group with current telescopes. As a result, there are almost no maps of massive star-forming spiral galaxies where individual GMCs can be distinguished (the recent CANON CArma-NObeyama Neaby galaxies CO(1-0) survey of Donovan Meyer et al. 2013 is a notable exception). This is a major lack, because massive star-forming spirals dominate the mass and light budget of blue galaxies and host most of the star formation in the present-day universe (e.g. Schiminovich et al. 2007). Understanding the formation and evolution of GMCs in such systems will help us to understand the physical processes that regulate the bulk of present-day massive star formation, something that studies of HI-dominated, low-mass Local Group galaxies with weak or absent spiral structure cannot do.

The primarily aim of this three years PhD thesis work is to study how dynamical effects contribute to the organization of the molecular gas, namely GMCs, in a grand-design spiral galaxy. To do so, we take advantage of the PdBI+30m Arcsecond Whirlpool Survey (PAWS, Schinnerer et al. 2013) that for the first time imaged M51 at GMC scale. In the following we provide a comprehensive introduction of the GMC topic exploring their basic properties (Section 0.2), structure and microphysics (Section 0.3), formation and evolution (Section 0.5). GMCs observed in a grand-design spiral galaxy are likely to be highly influenced by dynamical effects. Therefore, in Section 0.6.1 we introduce the standard tools to analyze the kinematic of spiral galaxy through the density-wave theory.

0.2 THE STANDARD PARADIGM OF THE GIANT MOLECULAR CLOUDS

Giant Molecular Clouds are the largest molecular structures that can be considered as single objects. The paradigm of GMCs as the basic unit of molecular structure in the Galaxy was established by a number of seminal papers that continue to guide research in this field. Observations by e.g. Scoville & Solomon (1975), Solomon et al. (1979), Solomon & Sanders (1980) showed that a large reservoir of hydrogen within 4 to 8 kpc from the Galactic Center is in molecular form prompted Sanders et al. (1985) to catalog features of the molecular gas distribution that resembled cloud-like structures of various masses. Using their catalog of 315 clouds the authors calculated that in the inner Galaxy ~ 85% of the H_2 mass is within few thousand of clouds larger than 22 pc and with gas masses $M_{H_2} > 10^5$ $M_\odot$ which they define as “Giant” Molecular Clouds. These objects incorporate a total H_2 mass of 3×10^9 $M_\odot$ and constitute the largest mass reservoir of interstellar matter in the inner Galaxy. The authors observed also a close match between cloud distribution and CO emission indicating that is the number of clouds that determines the CO distribution and not variations in the characteristic of their CO emission. Moreover they found that HII regions are always associated with GMCs suggesting that these objects virtually host all star formation in the Galaxy.

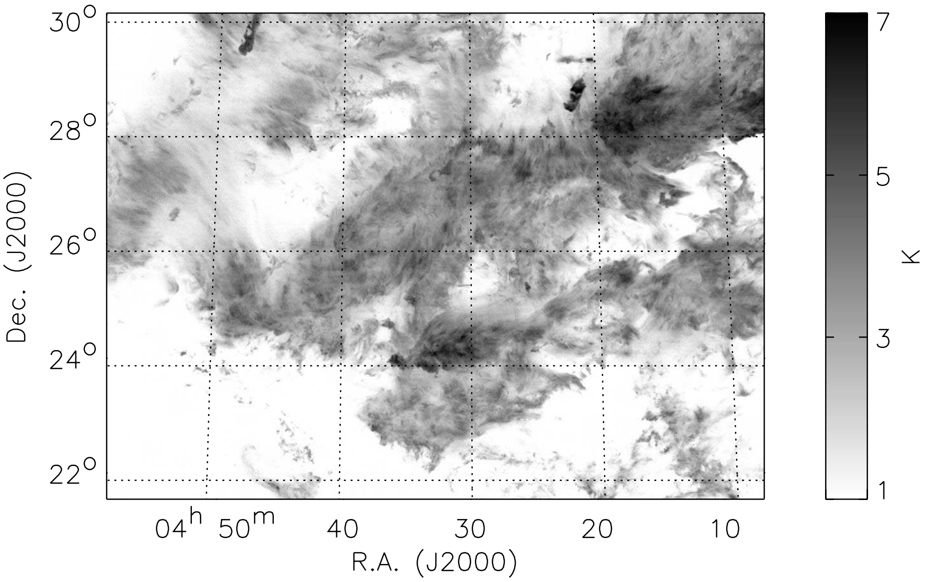

Figure 1: The 100 deg^2 of the Taurus molecular cloud. Maximum antenna temperature of the ^{12}CO(1-0) transition over the velocity range 2-9 km s^{-1}. The scale is shown in the bar on the right. Figure taken from Goldsmith et al. (2008).

Three years before, Larson (1981) using literature data of molecular structures from sub-parsec to few hundred parsec scale defined the basic scaling relations between cloud properties. These relations have become a standard tool to analyze the GMC physics with the name “Larson’s laws” and constitute the grounding point for all subsequent descriptions of interstellar molecular clouds and star formation. The most important “law” measured by Larson describes a relationship between a cloud’s velocity dispersion and its size, which Larson noted has a similar power-law exponent as the scaling predicted by Kolomogorov’s theory for incompressible turbulence. Following this evidence, Larson concluded that GMCs and the features within them are generated by turbulence rather than from a simple gravitational collapse as previously though (e.g. Jeans 1929, Hoyle 1953). He suggested that some of those features are transient, but others become dense enough to attain virial equilibrium and eventually collapse and form stars. This internal superthermal velocities would also be responsible for the apparent self-gravitating state of the clouds.

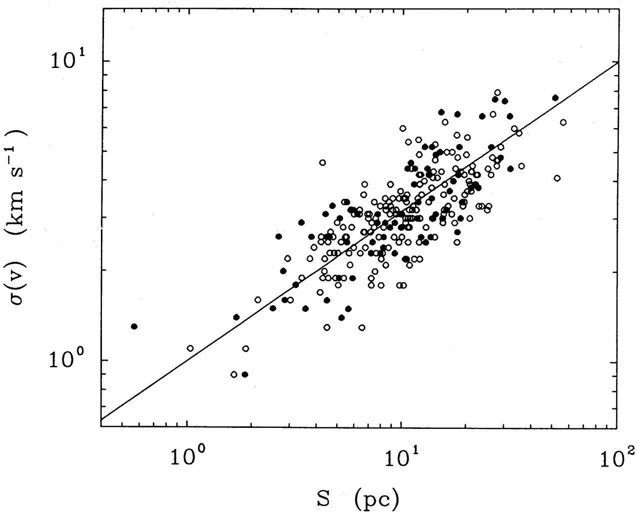

Figure 2: Velocity dispersion σ_v of the 273 GMCs of Solomon et al. (1987) catalog as function of their sizes S. Solid circles indicate clouds with known distance. The solid line is the fit in Eq. 1. Figure taken from Solomon et al. (1987).

However, many of the data used by Larson were collected with the earliest millimeter wave telescopes and included spatially undersampled maps of molecular line emission from a limited number of interstellar clouds with poor sensitivity, compared with currently available data. Indeed, the relations suggested by Larson (1981), assumed the formulation that is used still today after the work of Solomon et al. (1987). Using a sample of 273 clouds cataloged in the first Galactic quadrant, the authors measured a tight correlation between size and velocity dispersion that holds over a factor of 30 in size ("Larson's first law", Fig 2), of the form:

$$\sigma_v[kms^{-1}] = (0.72 \pm 0.07)R[pc]^{0.50\pm0.05}. \tag{1}$$

The authors interpreted this relation as evidence that GMCs are in virial equilibrium ("Larson's second law") rather than a manifestation of ISM turbulence. Solomon et al. (1987) proposed a model of clouds as formed by an ensemble of "droplets" each with thermal internal velocity dispersion. The superposition of their velocity dispersion along the line of sight would mimic a superthermal velocity dispersion of the whole cloud. As natural consequence of the virial equilibrium and the size-linewidth relation the mass surface density of the Galactic clouds is constant and equal to $\Sigma_{H_2} = 170\ \mathrm{M}_\odot\,\mathrm{pc}^2$[1] ("Larson's third law"). Of equal importance they

---

[1] Algebraically the two Larson's laws would provide a $\Sigma_{H_2} = 206\ \mathrm{M}_\odot\,\mathrm{pc}^2$. However this value has been modified

measured also a quasi-liner relation between cloud virial masses and CO luminosity (Fig. 3):

$$M_{vir}[M_{\odot}] = 39 L_{CO}^{0.81\pm0.03} [K\,km\,s^{-1}\,pc^{2}]. \tag{2}$$

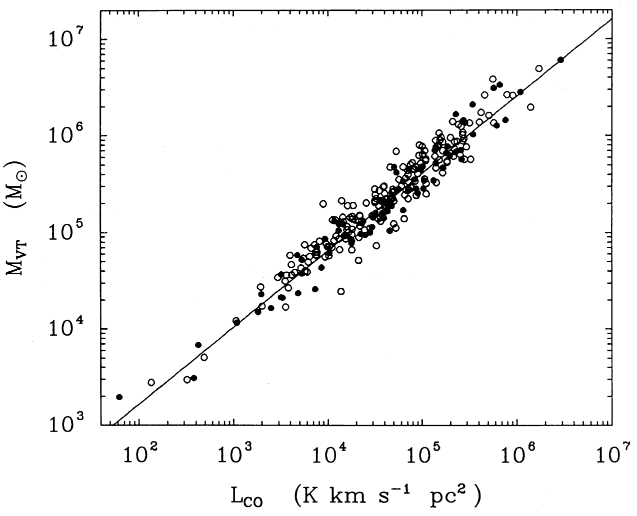

Figure 3: Virial mass M_{VT} of the 273 GMCs of Solomon et al. (1987) catalog as function of their CO luminosity L_{CO}. Solid circles indicate clouds with known distance. The solid line is the fit in Eq. 4.2. Figure taken from Solomon et al. (1987).

The above relation indicates that the CO luminosity is an reliable tracer for the cloud mass. Through this relation the authors measured an I_{CO}–to–N_{H_2} conversion factor or $X_{CO} = 3 \times 10^{20}\,cm^{-2}\,(K\,km\,s^{-1})^{-1}$ very close to other independent measurements in the Galaxy, reinforcing the idea of clouds in virial equilibrium. Finally the large sample of clouds allowed Solomon et al. (1987) to defined a GMCs mass spectrum in the Galaxy:

$$\frac{dN}{dM} \propto M^{-1.5}, \tag{3}$$

confirming the measurements of Sanders et al. (1985) that most of the molecular gas in the Galaxy is in form of GMCs with masses > 10^5 $M_{\odot}$.

The average properties of the GMCs in the Galaxy have been finally summarized by Blitz (1993) as in Table 1.

---

by Solomon et al. (1987) to account for the difference in the values adopted for the galactocentric radius of the Sun (10 kpc vs. 8.5 kpc) that affects the virial mass.

Table 1: Global properties of GMCs in the Solar neighbor

Property	**Averaged value**
Mass	$1-2\times10^5$ $M_\odot$
Mean diameter	40-45 pc
Mass surface density Σ_{H_2}	170 $M_\odot$ pc^2
Mean column surface density N_{H_2}	$3-6\times10^{21}$ cm^{-2}
Projected surface area	2.1×10^3 pc^2
Volume	9.6×10^4 pc^3
Mean separation	$\sim$ 500 pc
Velocity dispersion σ_v	5-10 km s^{-1}

After the advent of new telescopes a large number of surveys have been conducted to determine whether (and how) the GMCs in other galaxies differ from those seen in the solar neighborhood. In 15 years of studies most of the result of the three main seminal works have been confirmed, although several departures from the main paradigm have been seen. An exhaustive description of those observations is reported in the introduction of Chapter 4.

0.3 THE GIANT MOLECULAR CLOUD INTERNAL STRUCTURE

In broad terms, the transition region from ionized to molecular ISM is considered as the external "layer" of the GMCs. In those interface regions, far-UV photons (from the interstellar radiation field (ISRF) or a nearby hot star) dominate the energy balance or chemistry of the gas and both density and UV radiation field are large enough to dissociate molecules. Therefore they are usually called *photodissociation regions* or *PDRs* and encompass most of the interstellar medium where FUV radiation can penetrate (mostly HII regions, Hollenbach & Tielens 1999). PDRs are characterized by a stratified structure where every layer is populated by different atomic and/or molecular species determined by the attenuation of the UV flux by atoms, molecules and dust grains (see Fig. 4). Schematically the most external layer in mainly populated by HII region-ionized hydrogen (H^+), that recombines into atomic hydrogen H and eventually forms H_2 molecules in the innermost region of the PDR (i.e. GMCs). The transition H to H_2 happens at $N_H \approx 1\times10^{21}$ H atom cm^{-2}. Similarly, in the outer part of PDRs C^+ is formed by the recombination of C^{++} with electrons. At a depth of $N_H \approx 2\times10^{21}$ H atom cm^{-2}, C^+ recombines with electrons to give C. Oxygen is everywhere atomic outside the HII region and its abundance decreases when form CO in a region slightly deeper into the cloud than the C dominated zone. A $N_H \approx 4-5\times10^{21}$ H atom cm^{-2} is required to form CO molecules (van Dishoeck & Black 1988). All these transitions are not sharp and various form of hydrogen and carbon coexist over a range of depth. The gap between the hydrogen column density required to form H_2 with respect to CO implies that a fraction of molecular hydrogen is not traced by CO observations. The layer of gas in which the hydrogen is molecular but the carbon is atomic and difficult to observe, has been termed “dark gas” (Grenier et al. 2005).

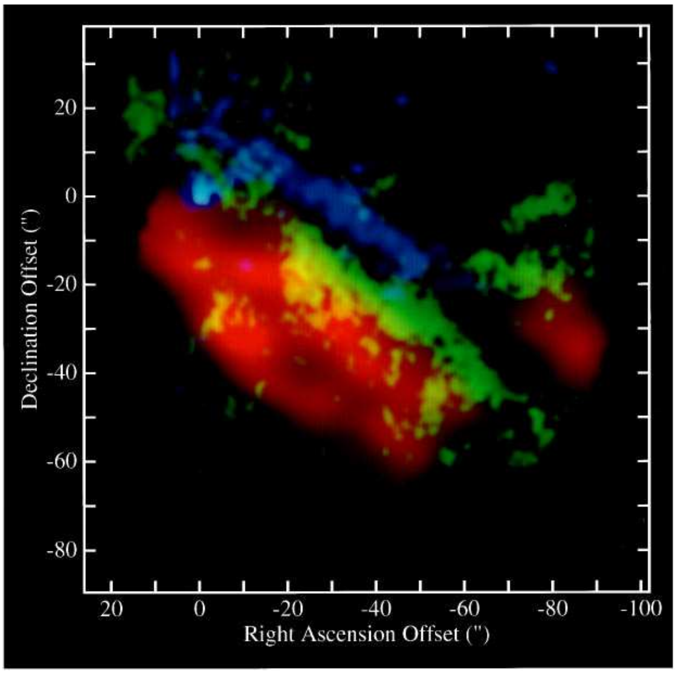

Figure 4: (Color) The Orion Bar region mapped in the 3.3 mm PAH feature (blue), H_2 1-0 emission (yellow), and CO(1-0) emission (red). The illuminating source and the ionized gas are located to the northwest (upper right). The PDR is seen edge on; a separation of ~ 10” is seen between the PAH emission and the H_2 emission, and between the H_2 emission and the CO emission, as predicted by PDR models. Figure adapted from Hollenbach & Tielens (1999).

GMCs are generally considered as the self-gravitating entities within the PDRs that encompass a significant fraction of the molecular gas in the galaxies and have gas masses of $10^5 - 10^6$ $M_\odot$. The inner structure of GMCs is hierarchical down to a very small scale. According to the classical definition by Williams et al. (2000), overdense regions within clouds are called *clumps*. The dynamical state of those clumps appears different from the whole GMCs. ^{13}CO observations have shown that most of the clumps are unbound (e.g. Carr 1987), with a velocity dispersion independent from clump size, i.e. they do not obey to “Larson’s laws”. However most of the cloud mass is concentrated in massive clumps that appear to be self-gravitating Bertoldi & McKee (1992). These structures called “star forming clumps” are the regions where stellar clusters form. Star forming clumps are smaller and have smaller line-widths with respect to quiescent clumps (e.g. Williams et al. 1994) indicating that some kinetic energy has to be dissipated in order to create a gravitationally bound object that collapses and form stars. The unbound clumps are “pressure confined”, in the sense that their internal kinetic pressure, which is primarily turbulent, is comparable to the mean pressure of the intracloud medium (Bertoldi & McKee 1992). Clumps are generally identified from spectral line maps of molecular emission as coherent region in the *ppv* (position–position–velocity) space, which may not necessarily be equivalent to three-dimensional physical objects. Nevertheless in pre-*Herschel* (and pre-ALMA) era, clumps have been useful approximations and tools to study the internal structure of GMCs.

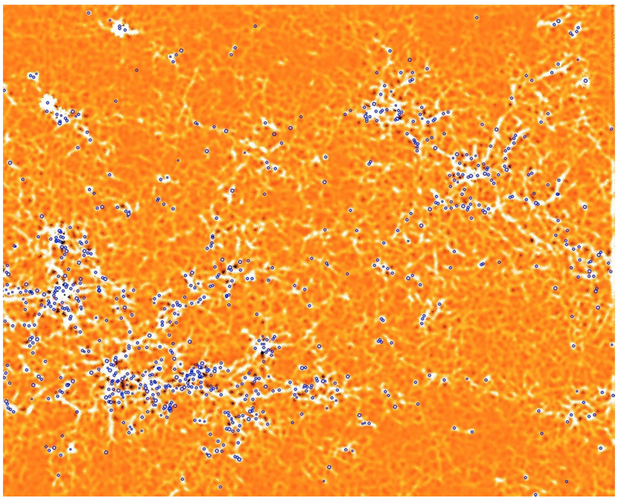

Figure 5: The blue circles represent the compact sources ("cores") detected at 250 μm from the Hi–GAL images. The filamentary structure of the ISM appears at various levels of intensity. The detected compact objects are for the most part distributed only along the brightest filaments. Figure adapted from Molinari et al. (2010).

However, in recent years, surveys with higher sensitivity and better resolution have provided an updated view of the medium within Galactic clouds. Deep, high resolution observations by Goldsmith et al. (2008) of ^{12}CO and ^{13}CO (J=1-0) in the Taurus molecular cloud revealed a complex, highly structured cloud morphology, including filaments, cavities, and rings with on spatial scales between 0.1 to 3 pc (Fig. 1). A similar morphology has been observed in thermal dust emission from other Galactic molecular clouds by the *Herschel* Hi-Gal survey. Images at 70-500 μm of the Aquila rift and the Polaris flare regions (e.g. André et al. 2010, Molinari et al. 2010) have revealed a complex network of thin and long filaments. Moreover, these observations also revealed the presence of compact sources or "cores" detected at 250 μm that are distributed mainly along the filaments. The cores are classically defined as the locum where a single stars is born (Williams et al. 2000), and in Aquila their mass distribution function (CMF) closely resembles the initial mass function (IMF) of the stars in both scale and shape. One interpretation of this result is that these cores form stars on a one-to-one basis with a fixed and high efficiency around 20-40% and that the IMF is determined by pre-collapse cloud fragmentation[2] (e.g. Larson

---

[2] Nevertheless a single core generally forms 2-4 stars (André et al. 2009). For realistic binary fragmentation scenarios, the IMF still follows the CMF at the high-mass end (because the majority of each cores mass can still end up in one stellar component), but may differ substantially from the CMF at the low-mass end.

1985, Padoan & Nordlund 2002, Hennebelle & Chabrier 2008).

This evidence suggests that in order to understand the origin of the IMF, a good knowledge of the prestellar core formation is paramount. However this knowledge is directly linked to the presently poorly known conditions for molecular cloud formation and evolution especially in spiral galaxies.

0.4 GIANT MOLECULAR CLOUD MICROPHYSICS: THE ROLE OF TURBULENCE

The recent observation of extensive filamentary structures on sub-cloud scale appears to be an evidence for the magneto-hydrodynamic turbulence scenario (e.g. Hennebelle et al. 2007) where the exact role of magnetic field, gravity and turbulence from shocks, winds and converging flows is still not completely clear (see e.g. Myers 2009 and reference therein).

In particular, turbulence is observed to be ubiquitous in the ISM suggesting that it is one of the main mechanisms that regulates cloud physics. The first observational evidence supporting this idea is given by the cloud line widths that appear always wider than implied by the excitation temperature of the molecules (except on the scales of isolated prestellar cores). Another significant evidence is provided by the cloud scaling relations. Larson (1981) first attributed the index in the size-velocity dispersion relation to the manifestation of the Kolmogorov's turbulence (see Section 0.2). Solomon et al. (1987) measured an index ~ 0.5 suggesting instead that GMCs are in virial equilibrium. However a similar index for objects between $0.03 - 30\,\mathrm{pc}$ was interpreted by Heyer & Brunt (2004) to be more consistent with the scaling predicted for Burgers' turbulence. GMC masses exceed by orders of magnitude the critical Jeans mass for gravitational stability, computed from their average density and temperature and, if only thermal pressure opposed gravitational attraction, they should be collapsing and very efficiently forming stars on a free-fall timescale ($\sim 10^{10}$ yr, Mac Low & Klessen 2004).

In light of these observations, Mac Low & Klessen (2004) extensively reviewed the role of turbulence for cloud physics and star formation. In their emerging picture of cloud physics, the interstellar turbulence determines the lifetime and fate of molecular clouds, and so their ability to collapse and form stars. The clouds themselves may be the results of various processes (see next Section), but the hierarchical clumpiness within them is considered to be the consequence of supersonic turbulence that fragments the interior of a GMC down to stellar masses and no longer as the product of gravitational instabilities in a region containing a large number of Jeans masses.

Turbulence not only provides an explanation for the internal structure of GMCs, but is also a potential mechanism that supports the cloud against global gravitational collapse. Magnetic fields have long been discussed as a stabilizing agent in molecular clouds. However, magnetic fields with average field strength of 10 μG (Verschuur 1995a, Verschuur 1995b; Troland et al. 1996, Crutcher 1999) cannot stabilize molecular clouds as a whole. The turbulence, instead, works to quickly transfer gravitational (and turbulent) energy to motions of substructures on smaller and smaller scales, and the densest of these small structures (i.e. cores) does the collapsing instead of the whole cloud (e.g. Elmegreen & Scalo 2004). Numerical models demonstrated that although supersonic turbulence can provide global support, it produces density enhancements that allow local collapse (e.g. Klessen et al. 2000). Magnetic fields, however, may be required to remove angular momentum (see next Section).

Recently, Hopkins (2012) developed a model for the formation, structure and time evolution of gas structures (e.g. GMCs, massive clumps/cores, and voids) in the ISM, deriving the conditions for self-gravitating collapse in a turbulent medium applicable on both small scales and large scales. The authors argued that ISM structures are a generic consequence of gravitational collapse in a supersonically turbulent medium with a characteristic scale set by gravitational instability in a gaseous disc. Simple turbulence arguments would explain why simulations including very different physics (e.g. Ostriker 2011, Bournaud et al. 2007, Dobbs 2008, Tasker & Tan 2011) were able to reproduce various expects of cloud observations.

What drives the turbulence, however, is still uncertain. The lack of features in velocity correlations at intermediate scales, and more generally the secular increase in velocity dispersion up to sizes comparable to the entire GMC, indicates that turbulence is driven on large scales by external or internal sources to GMCs (e.g., Ossenkopf & Mac Low 2002, Brunt et al. 2003). Among the possible external mechanisms, supernovae appear to dominate the energy injection in the diffuse ISM (Mac Low & Klessen 2004). On kiloparsec scale instabilities in spiral shocks are expected to make a significant contribution in spiral arm regions (Kim et al. 2006), while swing-amplifier instabilities are expected to be effective in high shear environments, such as inter-arm regions (e.g. Elmegreen & Scalo 2004).

Yorke (1989) have shown that it is difficult, however, for these (or other) external processes to transmit energy from the diffuse ISM into molecular clouds, which are much denser. In fact, the density contrast between molecular clouds and the ambient medium means that energy tends to be reflected from clouds rather than being transmitted into them, such that the kinetic energy of GMCs is primarily limited to the turbulent energy that GMCs inherit during their formation. 3D MHD simulations (Li & Nakamura 2006, Nakamura & Li 2007) show that proto-stellar outflows and winds from newly formed star provide the necessary energy to maintain the surrounding gas in approximate virial equilibrium. Although important for clumps and cores, protostellar outflows are unlikely to be effective for GMCs. On this scale massive stars can inject more momentum into GMCs through HII regions than do the much more numerous low-mass stars through their outflows (Matzner 2002).

0.5 THE GIANT MOLECULAR CLOUD LIFE CYCLE

Turbulence arguments suggest that the physical state of star forming regions within clouds is in general inherited and directly linked to the condition of GMCs themselves. Those conditions are the result of the evolutionary history of the clouds in the galaxies. In the following we review how GMCs may form from the ambient ISM, and which mechanisms regulate their evolution and destruction.

0.5.1 FORMATION

GMCs are mainly constituted by H_2. Therefore, cloud formation is intrinsically connected to the transition between the atomic and the molecular phase of the ISM. The H_2 formation can occur only on dust grains (e.g. Lequeux 2005). Two H atoms stick onto a dust grain, encounter one another and form a H_2 molecule. The new-formed H_2 molecule is not able to efficiently radiate away the energy excess from the process (the reason why the H_2 can not form in the gas phase on interstellar densities) and instead transfers the energy non-radiatively to phonons in the grain. Although conceptual easy, this process is still poorly understood (but see Glover & Clark 2012). The formation of the CO molecules, paramount for the GMC observations, happens mainly in the dense interior of clouds and stars involving a long chain of reactions with H^+ and H_2^+, which are produced by cosmic rays. Formation on dust grains of this molecule is also possible.

Moreover, the H_2 formation is also due to a combination of increased self-shielding (hence a lower H_2 dissociation rate) and increased density (hence increased H_2 formation rate) and happens when the total surface density of the gas is about $\Sigma_{gas} \approx 12\,\mathrm{M}_\odot\,\mathrm{pc}^{-2}$ (Wong & Blitz 2002, Blitz & Rosolowsky 2004) or an atomic surface density of $\Sigma_{HI} \approx 10\,\mathrm{M}_\odot\,\mathrm{pc}^{-2}$ (Krumholz & Matzner 2009) and where the mean mid-plane pressure lies in the range $P/k = 10^4 10^5\,\mathrm{K\,cm}^3$ (Blitz & Rosolowsky 2006). Dobbs (2008) calculated that the transition from atomic to molecular gas occurs on a time scale of few 10 Myr, while Krumholz & Matzner (2009) have shown that it is weakly dependent on metallicity, but it is not generally influenced by the ISRF magnitude.

Early models by Kwan (1979) and Scoville & Hersh (1979) argued that clouds themselves form mainly by bottom-up processes where a self-gravitating GMC is built by random inelastic collisions and coalescence of smaller cold HI clouds. However, these mechanisms appear very slow. Blitz & Shu (1980) found that several times 10^8 years are required in order to form a $\sim 10^5\,\mathrm{M}_\odot$

cloud, more than an order of magnitude greater than their estimate for the average GMC lifetime (10^7 yr, see below).

Thus, other mechanisms appear to be necessary to create GMCs, since coagulation processes alone would not have the time to achieve the high mass objects in which most the molecular mass is actually observed (McKee & Ostriker 2007). Top-down formation scenario involve large-scale instabilities in the diffuse ISM (e.g., Elmegreen 1979, Elmegreen 1994) and generally includes the simple "Jeans instability" due to the self-gravity of the gas and the "Parker instability" (Parker 1966), where a perturbation undulates magnetic field lines and makes the gas slide down along the undulated field lines into magnetic valleys and form clouds. In high shear regions (such as the inter-arm of grand-design spiral arms or the flocculent galaxies), the clouds can grow also via "swing amplification" (see below), while in low shear region another effect called "magneto Jeans instability" can occur, where the growth of condensations is helped by the magnetic field that removes angular momentum from the gas (e.g. Kim et al. 2001). Another recent suggestion is that GMCs form in colliding or turbulent flows (Vazquez-Semadeni et al. 1995, Ballesteros-Paredes et al. 1999, Heitsch et al. 2006, Vázquez-Semadeni et al. 2006).

Since the growth rates for all theoretical mechanisms increase with the gas surface density, clouds are expected to form preferentially in high density environments. Indeed, observations have shown that massive GMCs are exclusively located within spiral arms where the gas is compressed by shocks (see Section 4.1). Thus the above-mentioned mechanisms of cloud formation need to be considered in relation to spiral arm dynamics. Within a spiral potential Jeans instabilities are supposed to be the dominant mechanism of cloud formation (e.g McKee & Ostriker 2007). These instabilities appears to be the fastest mode of structure growth (e.g. Elmegreen 1990), moreover the the spacing between clouds (e.g. Cowie 1980, Elmegreen & Elmegreen 1983, Balbus & Cowie 1985) and the morphology of spiral-arm spurs observed in grand-design spiral galaxies (e.g. La Vigne et al. 2006) are consistent with formation via self-gravity. 3D local magneto-hydrodynamic simulations (Kim et al. 2006) and 2D thick disk global simulations (Shetty & Ostriker 2006), taking into account spiral arms processes, were able to create $1-3\times10^7\,\mathrm{M}_\odot$ condensations within spiral arms and spurs, in agreement with the larger objects observed in the Milky Way and in Local Group galaxies.

Nevertheless, simulations have proved that cloud-cloud interactions could be an important mechanism to aid the growth of massive GMC within spiral arms. Larson (1981) argued that collisional growth of clouds may be adequate if sustained by a kind of systematic motion. He suggested that the required motion should have a scale length of a few hundred parsecs, velocities of $\sim 10\,\mathrm{km\,s^{-1}}$ and time-scales of 10^7 yr. These parameters are in good agreement with the motions induced by spiral arms. Indeed, by including spiral density waves, the time for formation by coalescence is reduced to a few times 10 of Myr (Casoli & Combes 1982, Kwan & Valdes 1987, Roberts & Stewart 1987). Numerical simulations of a disk galaxy by Tasker & Tan (2011) likewise indicate that cloud mergers occur on a timescale of $\sim$ 25 Myr, comparable to the average expected GMC lifetime. Dobbs et al. (2006) have shown that inter-arm spurs can be the results of cold gas clumps forced together by a spiral shock with or without magnetic fields. The gas in their simulations is not self-gravitating and the clouds form mostly through collisions. Dobbs (2008) found that for low surface density gas ($\Sigma_{gas} < 8\,\mathrm{M}_{\odot}\,\mathrm{pc}^{2}$), the structures grow mostly by accumulation, while gravitational instabilities become dominant at higher gas densities ($\Sigma_{gas} \geq 20\,\mathrm{M}_{\odot}\,\mathrm{pc}^{2}$). In the same study, the author observed a difference in the dynamical state of clouds that resulted from the two formation pathways: objects formed via agglomeration of small clumps appears unbound, while the GMCs created by self-gravity are more massive and bound.

Since cloud formation through colliding flows requires a way to create these flows from shocks or supernovae (Koyama & Inutsuka 2000, Bergin et al. 2004), these processes could be also significant within spiral arms. Nevertheless McKee & Ostriker (2007) showed that colliding flows are not able to generate the high surface densities that are present in the spiral arms, but could be important to form some low-mass GMCs especially in inter-arm regions. Other authors (e.g. Lo et al. 1987, Koda et al. 2009), instead, proposed that low-mass inter-arm clouds are just the sheared debris of the massive GMCs formed in the spiral arms.

Finally, Parker instabilities may have limited importance in the formation of GMCs within spiral arms, since the turbulence excited in spiral shocks, together with vertical shear of the horizontal flow, may suppress growth of large-scale Parker modes (Kim et al. 2006).

0.5.2 Evolution, destruction and lifetime

As well as their formation, the physical processes that regulate star formation within GMCs and lead to their destruction also remain a matter of debate. The fraction of molecular gas converted into stars, i.e. the star formation efficiency of GMCs, is very small (between 1-20%, Evans et al. 2009, Murray 2011). However, mechanical and radiative feedback from nascent stars are very important for the subsequent evolution and destruction of GMCs. HII regions from massive star formation or OB associations enclosed within GMCs are a primary source of turbulent energy for the clouds (see Section 0.4). However the same HII regions, that support GMCs against gravitational collapse, also destroy them via photodissociation, which is consider as the dominant cloud evolution and destruction mechanism (e.g. McKee & Ostriker 2007). The photodissociation is less important in small clouds of few $10^{4}\,\mathrm{M}_{\odot}$ gas masses since they do not contain OB associations. These clouds are instead destroyed by nearby expanding HII regions that sweep up more mass than they ionized. This destruction via mechanical feedback is relatively less common for massive ($\sim 10^{6}\,\mathrm{M}_{\odot}$) GMCs.

The presence or the absence of HII regions and young stellar clusters within GMCs can be used as an indication of different cloud evolutionary stages and estimate of their lifetime. Following this idea, Kawamura et al. (2009) grouped the GMCs identified in the LMC into three categories (Fukui et al. 1999): *type I* or starless, i.e. without HII regions associated and corresponding to the newest GMCs; *type II* showing presence of HII regions and *type III* containing both HII regions and young clusters. The latter two categories represent clouds in advanced evolutionary stages, while finding only clusters or supernova remnants means that the hosting clouds have been completely dispersed by stellar feedback. Considerations on the cluster age and on the relative number of the clouds of the different categories allowed the authors to conclude that the GMC lifetime in the LMC is about 20-30 Myr. Gratier et al. (2012) found similar proportions between the categories for the clouds in M33 and Miura et al. (2012) confirmed similar lifetimes comparing CO (J=3-2) observations and stellar clusters in the same galaxy. Therefore in atomic-rich galaxies (where the total mass of HI exceeds the mass of H_2) the GMC lifetimes is few 10^7 Myr and the cloud evolution is mainly driven by stellar feedback.

The same picture was classically applied for the cloud evolution within spiral arms (Koda 2013) and foresaw that GMCs cannot live for more than 30 Myr even in molecular-rich disk galaxies. This prediction relied mostly on the first Galactic observations (e.g. Cohen et al. 1980, Rand & Kulkarni 1990) that found scarce CO emission in inter-arm regions and concluded that clouds are rapidly destroyed by HII regions within the arms. However the most recent surveys changed radically the view of cloud evolution in molecular-rich disk galaxies. A number of interferometric observations that included correction for short-spacing (see Section 1.1) have shown that a large quantity of molecular gas is present within the arms of i.e. M51 and the Milky Way, and that the gas is mostly molecular until the outskirts of the galaxy with low azimuthal variations. This indicates that only a small amount of molecular gas is photodissociated by the massive star formation feedback and that, potentially, clouds could have longer lifetimes than in low mass galaxies ($\gtrsim$ 100 Myr, Koda 2013). However the molecular gas evolves from the arms to the inter-arm regions. Koda et al. (2012) showed that in M51 the ratio between CO (J=2-1) and CO (J=1-0) is larger in spiral arms with respect to the inter-arm region, especially downstream of the molecular arms. This suggests that the molecular gas is arms is denser and/or hotter than in the inter-arm region, probably because of the inner stellar heating (e.g. Louie et al. 2013).

However the clouds in disk galaxies are also subjected to large-scale external processes, such as shear and streaming induced by the stellar potential. Dobbs & Pringle (2013) simulated a spiral potential having the possibility to trace the constituent particles in a given cloud through time. The authors concluded that in disk galaxies the evolution of the GMCs is very complex and they cannot be treated as isolated objects as in atomic-rich galaxies. Larger GMCs appear to be assembled by a mixture of small spiral arm clouds and ambient inter-arm ISM. Then they are dispersed back into smaller clouds and diffuse gas by shear within downstream spurs. Smaller objects are continuously created and/or absorbed by bigger clouds. Because of this complex dynamical interplay, to calculate a cloud lifetime is not straightforward. The clouds in this simulation kept their identity for 4-25 Myr, but the spread in lifetime is very large. Therefore the authors concluded that a reasonable average lifetime for clouds in a spiral potential is around the arm crossing time. They suggested also that shear is the dominant dispersion mechanism on few ten parsec scales, while on smaller scales stellar feedback drives the evolution of the clouds in disk galaxies. A similar dynamical interpretation of cloud evolution is described by Koda et al. (2009) for the evolution of GMCs in M51. In conclusion, the evolution of clouds in disk galaxies does not seem to be only driven by GMC internal processes, i.e. star formation and stellar feedback, but is also strongly influenced by large-scale dynamical effects such shear and spiral arm streaming.

0.6 Giant Molecular Cloud macrophysics: spiral arm dynamics

In the previous Sections we observed that spiral arms appear to have an important influence on the formation, evolution and lifetime of GMCs in disk galaxies. Since the aim of this thesis is to understand how the GMCs organizes themselves in a grand-design spiral galaxy, here we introduce the standard tools generally used to analyze the kinematic features of spiral arms and their dynamical effects, i.e. the density-wave theory.

0.6.1 The density-wave theory: overview

Grand-design spiral galaxies have long, continuous and symmetric spiral arms. This kind of arms is presumably the result of some large-scale global process that involved the whole galaxy. Almost always, the main arms of a grand-design spiral galaxy are two and are approximately symmetric under 180° rotation. Galaxies of this kind have two-fold rotational symmetry. More general, if $I(R;\theta)$, the surface brightness distribution of the disk plane in polar coordinates, is unchanged under a rotation through $2\pi/m$ radians, the galaxy is said to have *$m-$fold rotational symmetry* and m arms ($m > 0$).

Spiral arms can be classified also by their orientation relative to the direction of rotation of the galaxy. A *trailing arm* is one whose outer tip points in the direction opposite to galactic rotation, while the outer tip of a *leading arm* points in the direction of rotation. Most of the spiral galaxies observed have trailing spiral arms. This is caused by a mechanism called *swing amplification* which predicts that any leading spiral is sheared into a trailing spiral by the disk's differential rotation (e.g. Toomre 1981).

Another useful quantity to characterize spiral arms is the *pitch angle*. The pitch angle, i_p, at any galactic radius R is the angle between the tangent to the arm and the circle $R = constant$, by definition $0 < i_p < 90°$. The pitch angle measures how much the spiral arms are tightly wound around the galactic center.

The dynamics of spiral galaxies are generally described through the formalism of the density-wave theory. The basic idea of this theory is due to Lindblad (1963) that recognizes the spiral arms as caused by interactions between the orbits and gravitational forces of the stars in the disk. However Lin & Shu (1964), Lin & Shu (1966) introduced the proper mathematical description to make the density-wave theory a standard tool to study the disk galaxy dynamics. They proposed that spiral structure could be viewed as a quasi-steady density wave, i.e. a periodic compression and rarefaction of the disk surface density that propagates through the disk, analyzable with the mechanic wave formalism. Adopting the hypothesis of Lindblad, the author concluded that the spiral pattern is also *long-lasting*, i.e. its appearance remains stationary over many orbital periods (i.e. $\sim 10^9$ yr). In this scenario, stars, gas, dust, and other components move through the density waves, are compressed, and then move out of them, like cars in a traffic jam.

Various pieces of evidence support the Lin-Shu hypothesis. First, near-infrared images have shown that the distribution of the old stars, responsible for the mass and the gravitational potential of the galaxies (Rix & Rieke 1993), is organized in spiral arms in most of grand-design spiral galaxies (Eskridge et al. 2002). This implies that the whole stellar disk participates to the spiral pattern and it appears like if a wave across has shaped the structures. Second, if spiral arms are stationary density-waves in the stellar density and gravitational potential of the disk they are not subject to the winding problem. Instead if spiral arms were material in nature (i.e. structures always made by the same objects), the differential rotation of the galaxy would wind up the arms in a time short compared to the lifetime of the galaxy. Therefore, nowadays, very few galaxies should show the presence of spiral arms. Indeed, the expected pitch angle of material arms in a spiral galaxy like the Milky Way is only about 0.14° (Binney & Tremaine 1987). However, this pitch angle is far smaller than the ones measured from photographs that range from about 5 degrees for Sa galaxies to 20 degrees for Sc galaxies (Kennicutt 1981), allowing for a density-wave nature of the spiral arms in those galaxies. Third, being collisional in nature, gas should react strongly to the presence of the density-waves. Modern density-wave theories predict a non-linear response of the gas to a density-wave: collisions and shocks are generated above a threshold amplitude perturbation leading to gas accumulations in features narrower than the underlying stellar potential structures as it is actually observed.

According to the Lin-Shu hypothesis some useful quantities can be employed to characterize the spiral arm kinematics. If the spiral structure is a wave pattern that rotates rigidly, we can defined a *spiral arm pattern speed*, Ω_p, to be the angular speed of rotation of the spiral wave as viewed from an inertial frame (e.g. Binney & Tremaine 1987). If the amplitude of the spiral

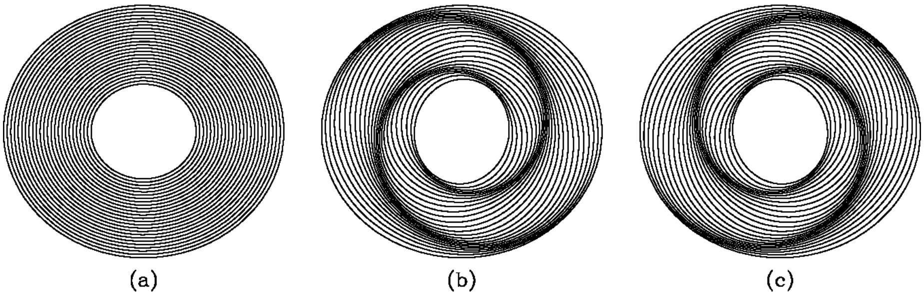

Figure 6: Kinematic wave representation. Arrangement of closed orbits in a galaxy with $\Omega - \kappa/2$ independent of radius, to create bars and spiral patterns. Figure taken from Binney & Tremaine (1987), after Kalnajs (1973).

pattern is small, the material in the galaxy travels in nearly circular orbits at an angular speed that varies with radius, $\Omega(R)$, which we can assume to be positive. The disk is said to be in differential rotation, i.e. $\Omega(R) = dV_c(R)/dR$, where $V_c(R)$ is the circular velocity of the disk. The radius at which $\Omega_p \equiv \Omega(R)$ is called *corotation radius*. At this radius the galactic components such as stars, gas and dust move together with the density-wave. Since the disk angular speed is generally a decreasing function of radius, while Ω_p is, by definition, constant, a spiral pattern at radius R with $\Omega(R) > \Omega_p$ is said to lie *inside corotation*, i.e. the galactic components move more quickly than the pattern. Assuming trailing spirals, gas and stars flow from the concave to convex sides of the arms. Reversely, a pattern with $\Omega(R) < \Omega_p$ is *outside corotation*, then the galactic components move slower than the pattern and flow from the convex to the concave side of the trailing arms.

0.6.2 KINEMATIC DENSITY-WAVES

We can gain intuition about the origin and nature of density-waves by considering a more simplistic picture of "kinematic waves" (Kalnajs 1973) that acts as a starting point for the more exhaustive Lin-Shu density-wave theory. Stars and clouds that move in and out the spiral pattern describe *epicycles*. Consider a star (or a cloud) that approaches the pattern inside the corotation. By definition, the star here has $\Omega_* > \Omega_p$, then entering the spiral pattern it gets slowed down. Therefore the star has to move to larger radii in order to conserve the angular momentum *mvr*, where *m*, *v*, *r* are: its mass, current velocity and radial position, respectively. Under the assumption of angular momentum conservation, the centrifugal force mv^2/r is reduced by r^{-3}, while the gravitational force falls more slowly than r^{-2}. Then the star moves inward and speeds up. The star as seen from a frame that rotates with the angular speed of the disk, would describe a *retrograde* epicycle. Conversely, a mass particle entering the pattern outside corotation is accelerated and, to conserve the angular momentum, has to move inward, describing a *prograde* epicycle.

These motions repeat for each arm. Then for an $m-$fold spiral structure there are m epicycles per orbit, i.e. $2m\pi$ radians of rotation plus an another 2π radians for the galactic rotation. Inside the corotation the rotation of the disk and the epicycles are opposite then there is a total of $2(m-1)\pi$ radians of rotation per orbit, while outside the corotation the disk and the epicycles rotate in the same direction, then the total rotation is $2(m+1)\pi$ radians.

Therefore, inside corotation the azimuthal velocity of the stars (or the gas) is $\propto \sin(m-1)\theta$, while outside it goes as $\sin(m+1)\theta$, where θ is the azimuthal coordinate. In this view, subtracting the disk bulk rotation, a velocity field given solely by the density-wave spiral arms would show an $m-1$ pattern inside corotation and an $m+1$ pattern outside (e.g. Canzian 1993).

Using a simple calculation, Binney & Tremaine (1987) shows that the stellar orbit can be approximate by a small ellipse described which epicyclic frequency κ is given by:

$$\kappa^2(R) = 4\Omega^2\left(1 + \frac{R}{2\Omega}\frac{d\Omega}{dR}\right). \tag{4}$$

In the center of the galaxy, where the rotation velocity rises approximately linearly with the radius, $\kappa \approx 2\Omega$. Elsewhere Ω declines with the radius, but never faster than a Keplerian fall off, i.e. $\Omega \propto R^{\frac{3}{2}}$, and $\kappa \approx \Omega$. Therefore $\Omega \lesssim \kappa \lesssim 2\Omega$. Therefore epicycles are completed before the end of the rotation. Seen from an inertial frame star orbits are not closed and form a rosette.

However in the more proper frame of the spiral arms that rotates with constant angular frequency Ω_p, the galactic rotation appears to be $\Omega' = \Omega - \Omega_p$ and if $\Omega' = \kappa/2$ (as in the case of solid body rotation) the stars described approximately closed elliptical orbit centered at galactic center. The reason is that in this case, during the period of two epicycles the center of rotation of the stars goes around the galactic center once, so that the star goes back to its original location, since the quantity $\Omega - \kappa/2$ does not vary much with the radius[3]. If the elliptical orbits of the stars are concentric and their position angle is aligned (same phase), the density-wave assumes a bar shape. If the phases increase systematically with radius (i.e. the ellipse major axes are rotated according to $\theta = -\alpha\, log$(major axis)+constant) we find a spiral pattern, where the elliptical orbits bunch up (Fig. 6). Density-waves of the type described above are called *kinematic density waves* because they involve only the kinematics of orbits in an axisymmetric potential that is turned in a non-axisymmetric spiral potential by orbit crowding.

Stars move in and out the regions of orbit crowding and the arms are seen to rotate rigidly at the angular frequency Ω_p since they are made always from different stars. However stars and gas

---

[3] If the pattern is faster than the differential rotation of the disk it is still possible to form closed orbits if $\Omega_p = \Omega + \kappa/2$. In this case the orbits make one full revolution in the retrograde sense during two radial periods.

introduce gravitational field and are modified by the presence of the spiral perturbation and react creating new orbits and perturbations. Including the effect of stars self-gravity and considering waves that propagates through a differential rotating disk with the dispersion relation of stars (and the gas), Lin & Shu (1964) calculated that a quasi-stationary state solution (QSSS) for the wave equation that maintains the same epicycles for a long period assumes the form of a logaritmic spiral with constant pitch angle. They found also that density-waves can propagate only between *the inner (ILR) and the outer (OLR) Lindblad resonances* and the waves are absorbed at the ILR. Consistently with the kinematic density-wave theory, these resonances are located at galactic radii where $\Omega_p = \Omega \pm \kappa/m$ for a m armed spiral, i.e. where stars complete exactly 1 epicycle between the passage of each arm that causes an amplification of the epicycle amplitude. According to the QSSS theory, gas is driven inwards to ILR and outwards to ILR.

0.6.3 DEVIATIONS FROM THE QSSS THEORY

Although the QSSS theory is able to account for many galactic features (as streaming motions in the ISM, e.g. Vogel et al. 1993, Rand 1993, Garcia-Burillo et al. 1993b; the downstream location of the stars along the spiral arms, the formation of dust lanes and their close associations with young star forming sites, e.g Visser 1975), it is not clear how often it can be applied (Kormendy & Norman 1979). In some cases, for example, spiral arms (especially $m = 2$ structures) appear to be the result of external or internal phenomena instead of a self-propagating instability of the disk. The grand-design spiral arms are supposed to be generated by tidal interactions from a companion or a satellite galaxy. The M51 system is a clear example (e.g. Toomre & Toomre 1972, Dobbs et al. 2010). Internal mechanism often invoke stellar bars as drivers of spiral structures. This is the natural interpretation of the presence of the spiral arm tips at the end of large bar as for NGC 1300. However, bar pattern speeds are generally much larger than spiral arm ones (Sellwood & Sparke 1988) and it remains an observational challenge to link the two seemingly dynamically independent phenomena (but see, e.g. Masset & Tagger 1997)

For this reason, the basic approximations of the QSSS theory (i.e. the spiral pattern rotates rigidly, is stationary and can be seen as a single short wave) can only be assumed as a working hypothesis. For example the arms in a galaxy are not stationary but are very responsive to temporary disturbances and to steady forcing. Goldreich & Lynden-Bell (1965) found that a gravitational instability in the disk is amplified and grows for a limited time before being sheared by the differential rotation even when the disk is stable. Julian & Toomre (1966) showed that the gravitational field of a mass traveling in a circular orbit within the disk could induces a strong spiral wave in the stars. More recently, D'Onghia et al. (2013) observed that over-dense regions of the spiral arms created through swing amplifiers as the GMCs, act as perturbers of the spiral structure. The response of the disk to these perturbations is highly non-linear, and signicantly modifies the formation and longevity of the resulting patterns. By virtue of these evidences, the pattern is quasi-stationary, since it evolves and is self-sustained by different feedback processes. Moreover, the quantity $\Omega - \kappa/2$ is only approximately constant, thus density-waves could also wind up. Binney & Tremaine (1987) demonstrated that for a Galactic potential an $m = 2$ density-wave spiral would reduce the pitch angle to $\sim 0.8^\circ$ after 10^{10} yr. However, in the same period, a material arm would show a pitch angle of $< 0.2^\circ$. Therefore density-wave spiral do wind up, but resist better than material arms to this phenomenon.

In conclusion, strong spiral arms appear to be the result of a number of phenomena such as tidal forces from companion or satellite galaxies, driving forces from other disk structures as bars, GMCs or substructures in the dark matter halo that argue against the stationary state of spiral arms in galaxies and favor a transitory or an evolving scenario. However a density-wave description of the spiral arms appears highly suitable, since it can account for several observable features in disk galaxies such as patterns in the old stellar distribution, the large pitch angle of spiral arms, gas and dust organization and related dynamics.

1

M51 AS SEEN BY THE PAWS PROJECT[*,†]

CONTENTS

The grand-design double logarithmic spiral of M51 is one of the most well studies object in the sky. In particular, its complex morphology provides the opportunity to study the influence of the spiral arms on the molecular gas distribution. Nevertheless, to date, any observation had the required sensitivity and resolution to detect the basic building-block of the molecular gas in this galaxy, i.e. the GMCs. The PdBI+30m Arcsecond Whirlpool Survey (PAWS) with a resolution of 40 pc and a point mass sensitivity at $5\sigma_{RMS}$ of $1.2{\times}10^5$ $M_\odot$ aimed to access for the first time the GMC scale on a wide range of environments within M51. The molecular gas distribution appears very complex at high resolution. In particular $\sim$ 50% of the flux of the PAWS datacube arises from a diffuse and faint extended component with high velocity dispersion. The CO emission follows faithful the highly structured gravitational potential of the galaxy, however the massive star formation is patchy and mostly located on the convex side of the molecular arms. The complex morphology of the M51 allows to define 7 galactic environments following the gas flowing directions. The probability distribution functions (PDFs) calculated within the environments show deviations from the log-normal shape predicated for a turbulent medium. The deviation is prominent for the spiral arm PDFs where the streaming motions create overpressurized zones that do not allow the cloud collapse on the arm crossing time.

---

[*] This chapter summarizes PAWS papers by Pety et al. (2013), Schinnerer et al. (2013), Hughes et al. (2013).

[†] Based on observations carried out with the IRAM Plateau de Bure Interferometer and 30m telescope. IRAM is operated by INSY/CNRS (France), MPG (Germany) and IGN (Spain).

1.1 Introduction

The Messier 51 (M51) system (Fig. 1.1), was discovered by Charles Messier on October 13th, 1773, in the constellation of Canes Venatici, but not until 1845 NGC 5194 (or M51a) was nicely sketched as a spiral by Lord Rosse (for a recent historical digression on M51's discovery refer to Steinicke 2012). Since then, generations of astronomers have attempted to disentangle the mysteries beyond its astonish spiral structure making the "Whirlpool galaxy" one of the most observed object outside the Local Group across a broad range of wavebands from X-ray to radio.

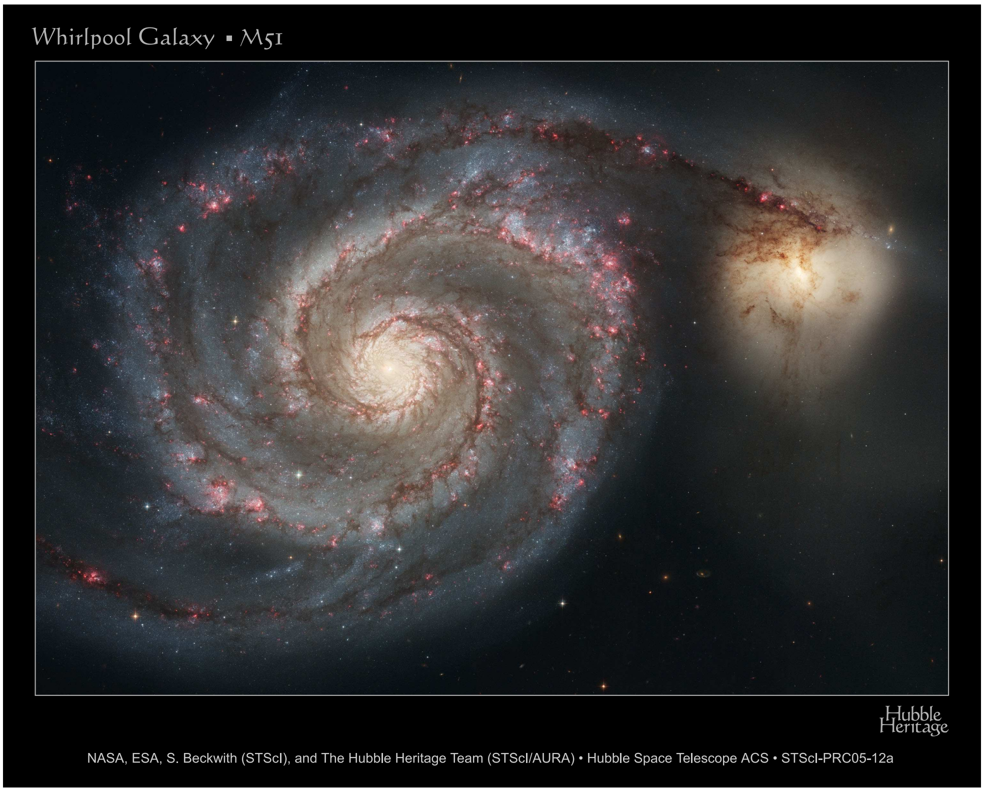

NASA, ESA, S. Beckwith (STScI), and The Hubble Heritage Team (STScI/AURA) • Hubble Space Telescope ACS • STScI-PRC05-12a

Figure 1.1: HST/ACS mosaic image of the NGC 5194/5195 system, taken as part of the Hubble Heritage Project (Mutchler et al. 2005, http://archive.stsci.edu/prepds/m51/). M51a (NGC 5194) is the spiral galaxy on the left. The image spans an area of 430 × 610", which corresponds to 15.8 × 22.5 kpc at the distance of 7.6 Mpc.

M51 is very rich in molecular gas (e.g. Aalto et al. 1999, Shetty et al. 2007, Koda et al. 2009), with molecular gas dominating over atomic gas until the outskirts of the disc (e.g. Garcia-Burillo et al. 1993a, Nakai et al. 1994, Schuster et al. 2007). Because of its importance for star formation, a large number of observations mainly focused on the CO emission have taken place over the years: single-dish maps of the CO(J=10), CO(J=21) and CO(J=3-2) transitions were undertaken by Scoville & Young (1983), Rydbeck et al. (1985), Lord & Young (1990), Garcia-Burillo et al.

(1993b), Garcia-Burillo et al. (1993a), Nakai et al. (1994), Schuster et al. (2007), Leroy et al. (2009), Koda et al. (2009), Koda et al. (2011) and Vlahakis et al. (2013), and aperture synthesis maps have been presented by e.g. Lo et al. (1987), Vogel et al. (1988), Rand & Kulkarni (1990), Tosaki et al. (1991), Adler et al. (1992), Rand (1993), Aalto et al. (1999), Sakamoto et al. (1999), Regan et al. (2001), and Koda et al. (2009), Koda et al. (2011). Other authors have studied tracers such as CO, CI and CII in the central region or at individual positions in the spiral arms (e.g. Israel & Baas 2002, Kramer et al. 2005, Israel et al. 2006, Schinnerer et al. 2010, Egusa et al. 2011). These studies have found that the high surface brightness CO is associated with the dust features at the inner edges of the spiral arms, CO emission is present also in the inter-arm with a relatively large arm-interarm contrast (between 1.5 and 6). M51 thus provides the opportunity to relate the properties of the molecular gas to the physics of the spiral arms.

Several works have attempted to study the properties and the dynamics of the molecular clouds in M51. The first cloud-like structures were recognize by Rand & Kulkarni (1990) as composed by a small number of distinct 10^7 $M_\odot$ components and termed Giant Molecular Cloud Associations (GMAs, Vogel et al. 1988). These objects were interpreted as the results of cloud-cloud collisions or due to the strong arm gravitational instability. Rand & Kulkarni (1990) observed GMAs everywhere in M51, however only spiral arm objects appeared gravitationally bound and stable against tidal forces (Rand 1993). In the same years, Garcia-Burillo et al. (1993a) argued against this picture, suggesting that GMAs are, instead, only an unbound superposition of GMCs. Later, Kuno et al. (1995) studied the separation between GMAs finding consistencies with a GMA's formation mechanism that mainly involved gravitational instability, enhanced by cloud coagulation on the arm crossing time. These objects where actually resolved by Aalto et al. (1999), that cataloged 16 GMAs in the inner part of M51. More recently, Koda et al. (2009) observed that massive clouds are present only within the spiral arms of M51, suggesting that the evolution of the molecular clouds is dynamically driven (as argued also by Lo et al. 1987): leaving the arms GMAs are disrupted by the intense shear. Using a multi-transition analysis, Schinnerer et al. (2010) concluded that clouds in M51 are similar to Milky Way ones when observed at $\sim 120\,\mathrm{pc}$ resolution, with a kinetic temperature of $\sim$ 16 K and a H_2 density of $n(H_2)=240\,\mathrm{cm}^{-3}$. Nevertheless only Egusa et al. (2011) achieved the resolution (and partially the sensitivity) necessary to detect Galactic-size clouds in M51. Studying a small region of the southern arm, they found that the most massive clouds are located downstream the spiral arms and that the GMAs are single and smooth structures. They also proposed an evolutionary scenario where small clouds approaching the arms collide to form GMAs. After forming stars those structures are dissociated by stellar feedback and broken up in smaller clouds.

M51 is also a prototypical example of an interacting system and possesses an exceptional grand-designed spiral structure. This, together with its favorable orientation on the sky, made M51 one of the preferred target to discriminate between different theories of spiral arm formation and evolution. The seminal work on this topic by Tully (1974b) postulated that the high prominence of the spiral arms in M51a is the result of multiple passages of the I0 dwarf companion NGC 5195 or M51b (see also Salo & Laurikainen 2000). In particular the inner spiral arms are consistent with a density-wave (Roberts & Stewart 1987) as supported by the high streaming motion measured along the arms (e.g. Garcia-Burillo et al. 1993b, Aalto et al. 1999) and the oval orbit of the gas streamlines (Kuno & Nakai 1997). The outer arms are instead more compatible with a transient feature generated by a tidal response to the interaction. During the years several authors revealed that M51 has a even more complex morphology and dynamics. For example, in the innermost region a small nuclear bar is present (e.g. Tully 1974b, Garcia-Burillo et al. 1993a, Rix & Rieke 1993), the inner arms are not completely shear-free and support the presence of shocks (e.g. Aalto et al. 1999), possible multiple spiral structures as well as multiple pattern speeds are present (e.g. Elmegreen 1989, Vogel et al. 1993, Henry et al. 2003, Meidt et al. 2008).

The interaction with NGC 5195 had tremendous effects also on the HI morphology. Rots et al. (1990) using high resolution VLA observations found an extremely complicate velocity structure with possible warp and/or oval distortion in the outer disk, a tidal tail and bridges.

Recently, Dobbs et al. (2010) reproduced the present day spiral structure of NGC 5194 and many details of the tidal interaction between NGC 5194 and NGC 5195 in hydrodynamic simulations, finding evidences against a quasi-steady density wave state (e.g. Lin & Shu 1964) of M51a spiral arms as also suggested by e.g. Shetty et al. (2007).

Nevertheless, to date, no observation had the required sensitivity and resolution to detect the basic building-block of the molecular gas in this galaxy, i.e. the GMCs. The PdBI+30m Arcsecond Whirlpool Survey (PAWS) aimed to access for the first time the GMC scale in a wide range of environments.

The survey is especially designed in order to achieve three specific characteristics.
Sensitivity: Sanders et al. (1985) have shown that most of the molecular gas in the Galaxy is localized in clouds with gas masses of $10^5 - 10^6$ M$_\odot$. Hence, PAWS needs to achieve a sensitivity at $5\sigma_{RMS}$ equal to $\sim 10^5$ M$_\odot$ (i.e. a $1\sigma_{RMS}$ point mass sensitivity 2×10^4 $M_\odot$).
Resolution: The typical size of a Milky Way GMCs is 40 pc (Solomon et al. 1987). Thus the survey requires a comparable angular resolution to identify clouds, i.e. 1” considering M51’s distance of 7.6 Mpc (Ciardullo et al. 2002).
Area surveyed: the field-of-view of PAWS is chosen to encompass a substantial area to build up sufficient statistics on M51’s molecular gas and its GMC populations within three distinct environmental regions, the center encompassing the bulge plus the star-bursting ring, the spiral arms and the inter-arm region.

To correctly frame the context of this thesis, a summary of the results from the companion PAWS papers (i.e. Pety et al. 2013, Schinnerer et al. 2013, Hughes et al. 2013 and Meidt et al. 2013) is provided. The PAWS observing strategy and calibrations are exposed in Section 1.2. Then we analyze the appearance of the molecular gas at 1” resolution through the PAWS integrated intensity maps in Section 1.3 and we explain the characteristic of the faint and diffuse extend component that encompasses ~ 50% of the PAWS datacube flux. When observed using different ISM (gas and dust) and stellar tracers (Section 1.4) M51 shows a complex gravitational potential and young massive star formation morphology, allowing for a division of the PAWS field-of-view into seven dynamically-motivated environments as reported in Section 1.5. The study of the molecular gas using probability distribution functions (PDFs) shows that the global distribution of the molecular gas is indeed highly influenced by the presence of the spiral arms on kpc scale as explained in Section 1.6. Finally in Section 1.7 we argue that both complex star formation morphology and deviation from a log-normal PDF are the result of gas in motion across the spiral arms that creates a reduce pressure environment that inhibits the cloud collapse and the ability of GMC to form stars.

1.2 THE PDBI+30M ARCSECOND WHIRPOOL SURVEY DATASETS

PdBI observations dedicated to the PAWS project were achieved with 169 hours of telescope time with 5 antennas in configuration D (19 hours) and 6 antennas in configuration C (18 hours), B (57 hours) and A (75 hours), from August 2009 to March 2010. The two polarizations of the 3mm receivers were tuned at 115.090 GHz, i.e., the ^{12}CO (1-0) rotation rest frequency red-shifted to the LSR velocity (471.7 km s^{-1} Shetty et al. 2007) of M51[1].

The full coverage is achieved by two 30-field mosaics centered such that their combination covers the inner part of M51. The total field of view is approximately 270” × 170” or 10×6 kpc at our adopted M51 distance 7.6 Mpc (Ciardullo et al. 2002). While the two data sets were obtained at different times (and slightly different weather conditions), each point within a mosaic was observed between two calibration cycle ensuring consistent noise properties and uv coverage.

The data, naturally obtained at 3.25 km s^{-1} spectral resolution, were smoothed to a channel resolution of 5 km s^{-1} in order to have lower correlation between adjacent channels and higher signal-to-noise. The final cube contains 120 channels covering a velocity range of [-297.5;+297.5 km s^{-1}] centered at the LSR velocity of M51. Two-thirds of the channels are therefore devoid of signal.

Calibration of the PdBI data was carried out using standard methods implemented in `GILDAS/CLIC` (Pety 2005). The bright (~ $10 Jy$) quasars 0851+202 and 3C279 were used as bandpass calibrators. The amplitude and temporal phase gains were obtained from spline fits through regular measurements of the nearby quasars 1418+546, 1308+326 and J1332+473. The flux scale

---

[1] A detailed description of the observing strategy, calibration and data reduction is presented by Pety et al. (2013).

was determined against PdBI's primary flux calibrator, MWC349, and was found to be accurate within ~ 10%.

Since an interferometer filters out the low spatial frequencies, the extended emission was recovered through the IRAM-30m single dish telescope. The observation run took place on May 18-22, 2010 and provided a ^{12}CO (1-0) map that covers the entire M51 system (60 square arcminute). The angular resolution of the image after calibration and gridding is 22.5" for 5 km s^{-1} channel width.

The `GILDAS/MIRA` software was used to calibrate the temperature scale of the 30m data. "OFF" spectra were built using the default scheme of the software, i.e. averaging the closest (in time) observations together. These spectra were then subtracted from the corresponding on-source spectra. A third-order polynomial was then fit and subtracted from each spectrum. For the baseline fitting, an outlier-resistant approach was used and regions of the spectrum that were known to contain bright emission were excluded. After fitting, we compared the RMS noise about the baseline fit in signal-free regions of each spectrum to the expected theoretical noise. Based on this comparison, we rejected a small number of spectra where the observed noise was much greater than expected.

The final PAWS data cube, used extensively in this thesis, is the result of a joint deconvolution of the PdBI and IRAM-30m data sets. The two data sets were first made consistent (in terms of pixel size, central velocity and channel sampling) and then the single-dish map from the IRAM-30m was used to create the short-spacing visibilities not sampled by the Plateau de Bure interferometer.

This joint deconvolution of interferometric and single-dish data allowed us to achieve the best (pre-ALMA) sensivitivity reachable for such a large mosaic with a median noise of 0.4 K at full resolution, i.e. 1.16" × 0.97".

We also utilize the hybrid data cube gaussian-tapered to a synthesized resolution of 3" and 6" as presented by Pety et al. (2013). Tapering the visibility weights reduces the resolution but increases the surface brightness sensitivity. The typical RMS noise in these cubes is 0.1 K and 0.03 K, respectively. The PAWS datasets at 3" and 6" spans the same range of LSR velocities and have the same field-of-view of the PAWS datasets at 1" and the same channel width of 5 km s^{-1}.

Table 1.1 lists parameters and properties adopted or calculated for M51 by the PAWS papers and by this thesis works.

Table 1.1: Parameters for NGC 5194 or M51a

Parameter	**NGC 5194**	**Notes**	**Reference**
Morphological type	SA(s)bc pec		de Vaucouleurs et al. (1991)
Activity type	Seyfert 2		Véron-Cetty & Véron (2006)
Kinematic center	$13^h29^m52.7087^s; +47°11'42.789''$	$\alpha; \delta(J2000)$	Hagiwara (2007)
	1.80”; 0.81”	Offset from phase center	
Distance	7.6 ± 1 Mpc	1” = 37 ± 5 pc	Ciardullo et al. (2002)
Systemic velocity	471.7 ± 0.3 km s^{-1}	LSR, radio convention	Shetty et al. (2007)
Mean inclination	$22 \pm 5°$		This work
Mean position angle	$173 \pm 3°$		This work
Emitting CO surface	1.9×10^8 pc^2	$I_{CO} \geq 3\sigma_{RMS}$	Pety et al. (2013)
Total CO luminosity	1.4×10^9 K km s^{-1} pc^2	in [LSR-120,LSR+120] km s^{-1}	Pety et al. (2013)
Mean CO brightness	7.6 K km s^{-1}		Pety et al. (2013)
CO velocity dispersion	$5 - 20^a$ km s^{-1}		Pety et al. (2013)
CO scale height	$40 - 250^a$ pc		Pety et al. (2013)
Total H_2 mass	6.2×10^9 $M_\odot$	Helium included	Pety et al. (2013)
Mean H_2 mass surface density	33 $M_\odot$ pc^2		Pety et al. (2013)
I_{CO}–to–N_{H_2} conversion factor	2.0×10^{20} cm^{-2} K^{-1} km^{-1} s		Schinnerer et al. (2010)
Total HI mass	2.5×10^9 $M_\odot$		Walter et al. (2008)
Mean HI surface density	7.7 $M_\odot$ pc^2	$R_{gal} < 11$ kpc	Leroy et al. (2008)
HI velocity dispersion	17.7 km s^{-1}		Tamburro et al. (2009)
Total stellar mass	$\sim 4 \times 10^{10}$ $M_\odot$		Leroy et al. (2008)
Mean star mass surface density	485.0 $M_\odot$ pc^2		Leroy et al. (2008)
SFR	3.125 $M_\odot$ pc^{-2}		Leroy et al. (2008)
Metallicity Z	10.03	Using Kroupa 2001 IMF	Muñoz-Mateos et al. (2011)
Gas to dust ratio	94 ± 17	Constant across M51a	Mentuch Cooper et al. (2012)

[a] Mean values from compact and extended components on PAWS FoV

1.3 ^{12}CO(1-0) EMISSION OF M51 AT HIGH RESOLUTION: THE PAWS VIEW

The high resolution observation performed by PAWS provide an unprecedented view of the molecular gas distribution in the inner zone of M51 (Fig. 1.2). Spiral arms appear as a contiguous flow of CO emission, instead the inter-arm gas is more flocculent, organized into structures stretched along the mid-way point between the concave side of the two arms. On the convex side of the spiral arms, inter-arm structures emerge as spurs, more prominent along the northern arm. The central region contains the brightest zone in CO emission of the galaxy. However in the innermost region the structures appear less compact and with a lower surface brightness with respect to the inner tip of the arms. Only the nucleus is very bright with a surface brightness comparable to the most prominent structures of the arms.

The two spiral arms are also different. The southern spiral appears brighter than the northern one with patches of surface brightness comparable to the inner tips, while the CO intensity of the northern arm is lower and similar to innermost zone. The outermost region of the spiral

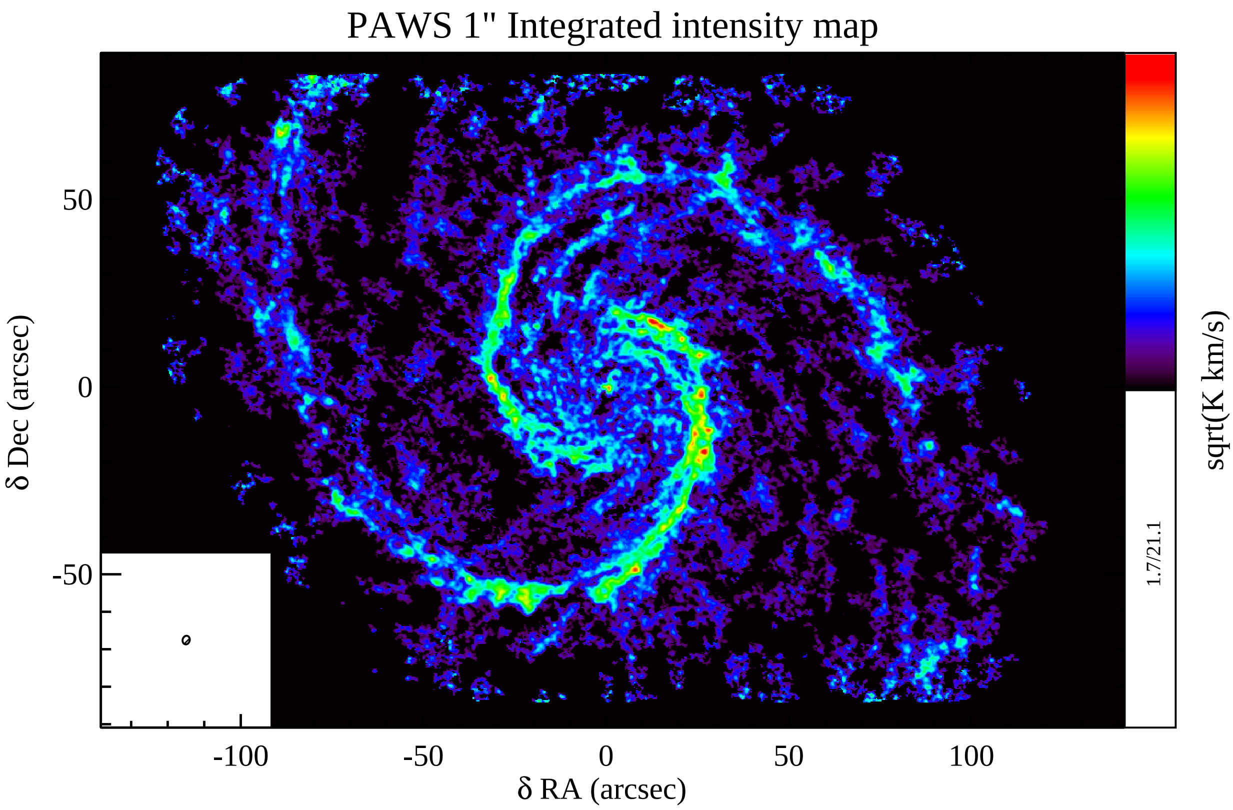

Figure 1.2: The PAWS ^{12}CO(1-0) integrated intensity map at 1” resolution. The surface brightness of the spiral arms and inter-arm is very different: spiral arms appear as a contiguos flow of molecular gas, while the inter-arm region is flocculent. In the bottom left the beam (1” ∼ 40 pc) is shown. The sidebar shows the color scale of the map in $\sqrt{K\,km/s}$ to emphasize the distribution of the faint emission.

arms follow the same behavior especially in the terminal section, where the southern arm is more prominent than the northern one. In general this part of the arms presents a structure morphology and a surface brightness comparable with the inter-arm region.

Some features from the integrated intensity map suggest that the the spiral arm are constituted by more than a single pattern such as the elongated gas feature on the north-eastern side of the nucleus or the bifurcation of the southern arm. Indeed the polar representation (Fig. 4 of Schinnerer et al. 2013) shows three breaks in each arm at ∼ 27”, ∼ 55” and ∼ 90” where the observed pitch angle changes from 40°, to 30° and 10° respectively.

The PAWS integrated intensity map is obtained from emission with high signal-to-noise, generally corresponding to GMCs (for details see Appendix 4.7). However this “compact component” of the CO emission constitutes only a part of the total flux of the PAWS cube. Indeed, one of the most striking and unexpected finding of PAWS is the existence of a faint and extended component of CO emission that accounts for about 50 ± 10% of the hybrid cube's total flux. This component appears to be a real feature of M51 and not a deconvolution artifact (for details about the test made to assess its authenticity refer to Pety et al. 2013). Its flux is distributed on spatial scales larger than 36" (or 1.3 kpc) and covers ∼ 30% of the PAWS area (i.e. it is ∼ 15× larger than the compact components). It is also very faint (it ranges from 0.07 – 1.36 K, with a median brightness temperature ∼ 0.14 K and typical temperatures around 0.75 K in the central region and 0.5 K in the disk) and diffuse (mid-plane density ∼ 1 $H_2\,cm^{-3}$, i.e. ∼ 10× lower than the compact component). Because of its density, this gas does not appear gravitationally bound or prone to form stars. Moreover, it possesses a high velocity dispersion that, following Koyama & Ostriker (2009a), corresponds to a scale height ∼ 200 pc or five time higher than for the compact component. These evidences suggest that part of the molecular gas in M51 is extra-planar as in the Milky Way (Dame & Thaddeus 1994) or in the edge-on galaxy NGC 891 (Garcia-Burillo et al. 1992). The extended component integrated intensity map indicates that this component is generally brighter in correspondence of the spiral arm's convex side. Accordingly, the authors argued that this component could be originated by chimneys or fountains from the massive star formation that has transported some of the molecular material away from the disk (e.g. Putman et al. 2012).

1.4 Spatial relation between CO, gas and stellar tracer in M51

The PAWS field-of-view (FoV) was chosen in order to have a rich and complex environment where to study the molecular gas at GMC scale (∼ 40 pc as inferred from Galactic clouds, Blitz (1993)). In this section we provide an overview of the most important radial and azimuthal variation across the PAWS FoV as seen in both stellar and ISM components that are likely prone to influence the molecular gas. To do this we will make large use of the multi-wavelength analysis reported in Schinnerer et al. (2013).

Several studies (e.g. Bigiel et al. 2008, Schruba et al. 2011, Leroy et al. 2013b) have shown that the molecular gas and the star formation (in term of H_2 mass surface density and surface density of star formation rate) are well correlated on kpc scale. However, on GMC scale, the spatial correlation between CO emission and star formation tracers in M51 is surprisingly complex (Fig. 1.3). The Hα emission (coming from *HII* region and a proxy for stars with ages of a few to 10 Myr, e.g. Whitmore et al. 2011) is coincident with the molecular gas within R_{gal} < 35", while for radii between 35" < R_{gal} < 40" this radiation is basically absent, although the high surface density of the gas. Further the Hα morphology exhibits large and bright *HII* regions corresponding to the gas spurs of the spiral arms. In the last section of the arms (85" < R_{gal})

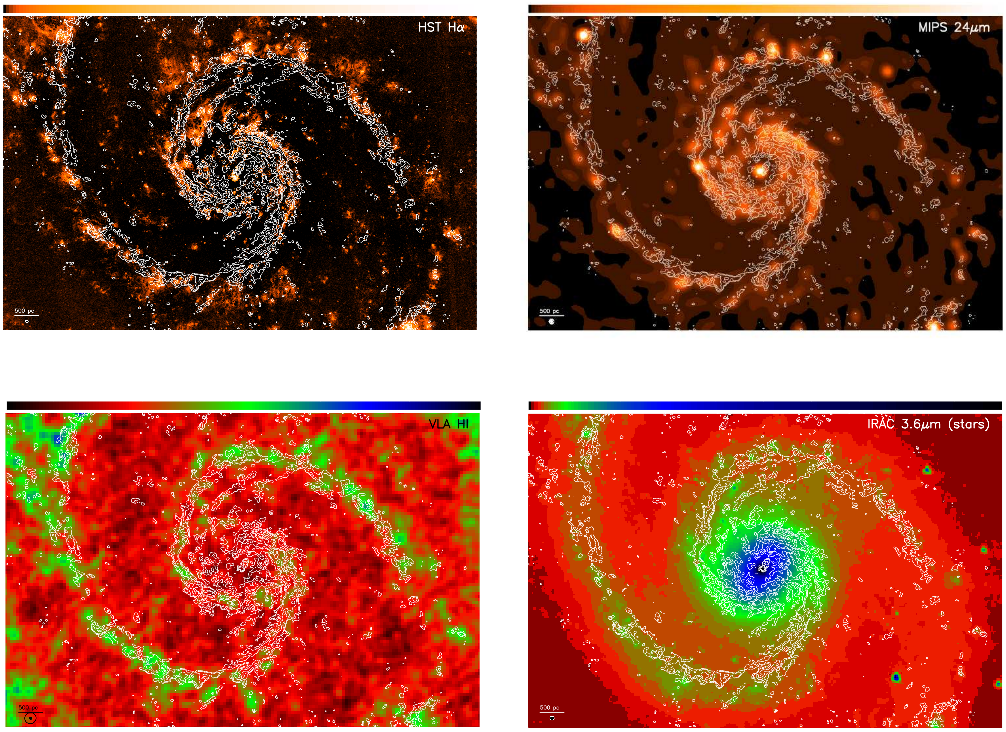

Figure 1.3: HST ACS Heritage Hα emission showing prominent HII regions (top left; GO–10452, PI Beckwith); MIPS HiRes 24 μm image tracing hot dust emission (top right; Kennicutt et al. 2003), THINGS HI robust intensity map tracing the atomic gas (bottom left; Walter et al. 2008) and contamination corrected stellar light at 3.6 μm showing the old stellar distribution (bottom right; Meidt et al. 2012).The PAWS CO intensity map contours (in white at 40, 80, 160 and 320 K km s^{-1}) are overlaid to each map for comparison with the molecular gas emission. Figures adapted from Schinnerer et al. (2013).

young star formation is spatially coincident with the CO emission. This kind of morphology (i.e. coincidence within $R_{gal} \lesssim 35$", then a gap up to $R_{gal} \lesssim 40 - 50$" and a patchy distribution in the convex side of the arms) is also common to other stellar tracers, i.e. thermal radio continuum (indicative for stars a few Myr old), B and V band light from young clusters (with an age of several 10 Myr), and NUV-FUV continuum (a proxy for stars with ages $<$ 100 Myr). Several ISM tracers show a similar spatial correlation with the stellar traces instead of CO radiation. The emission from hot dust at 24 and 70 μm has the same distribution, while the non-thermal synchrotron emission at 6 and 20 cm is likely enhanced along the molecular spurs by massive star formation.

Even the CII and HI radiation does not coincident with the CO emission, but is pronounced at the location of the massive star formation, arguing that it is mostly due to photodissociation of the molecular gas.

Schinnerer et al. (2013) found that along the arms the offset between the sites of ongoing star formation and reservoir of molecular gas is around 300 pc. This would imply that emission from young star does not influence much the properties of the molecular gas. Instead stars and gas are well mixed within the molecular ring and the downstream spurs. Here stellar feedback may have a more important impact on the gas reservoir. However measurements of mid-IR H_2 lines (Brunner et al. 2008) indicate that the gas in the warm and hot molecular phases is only a very small fraction with respect to the cold molecular hydrogen. This, on the other hands, would argue against a strong influence of the massive star formation on the gas properties.

One of the most prominent connection observed by Schinnerer et al. (2013) is between the CO emission and the old stellar population. Indeed the CO gas features show an excellent correlation with the dust-corrected 3.6 μm emission used as a tracer for old red giant stars (Meidt et al. 2012). The old stellar population itself is considered the best tracer of the the underlying stellar potential (Rix & Rieke 1993). From their analysis and the literature, Schinnerer et al. (2013) identified different components of the gravitational potential within the PAWS FoV:

- an accreting super-massive black hole at the very center of the galaxy (e.g. Maddox et al. 2007);
- a bulge that extend up to $R_{gal} < 16$" that contains:
  - a nuclear bar within $R_{gal} < 23$" and first identified by Zaritsky et al. (1993) in near infrared. The bar has a major axis length $r \sim 15" - 17"$ and a $PA \sim 139°$ (Menéndez-Delmestre et al. 2007).
- moreover, the galactic disk contains:

- an oval oriented in north-south direction and likely responsible for the modulation of the 3.6 μm emission between 25” < R_{gal} < 50”.
- a prominent two-folded spiral pattern (within R_{gal} < 85”) consistent with density-waves. Their kinematic features will be broadly examined and discussed in the next chapter. The outer spiral pattern (R_{gal} > 85”) is often considered a material wave (e.g. Tully 1974b).

The molecular gas traces every single component of the potential very well and the CO emission resembles the spiral arm structure at every radius. For example, the inner part of the spiral arms, where the tip of the molecular arms are tightly wound, appears to be reminiscent of a starburst ring and the gas follows the orientation of the nuclear bar. This correlation suggest that the galactic potential plays the major role in the determination of the molecular gas properties in M51. In addition, the old stellar population is the main source of the inter-stellar radiation field (ISRF). Since the ISRF changes from bulge to disk (Muñoz-Mateos et al. 2011), then its influence on the molecular gas properties should do so as well. From the good correlation observed between PAH at 3.6 and 8 μm and CO emissions, Schinnerer et al. (2013) argue that these small grains are located in the external layer of the GMCs and illuminated by the ISRF from the old stellar population.

The effect AGN in the very inner part of the galaxy seems mostly restricted to R_{gal} < 13” where X-ray and radio wave-lengths show a jet-like structure. However if such an influence exists, it would be very localized to the innermost zone of M51, since the AGN jet is likely tilted with respect to the disk and would not affect the gas reservoir on scales larger than $\sim$ 1”.

1.5 Inventory of galactic environments for M51 analysis

In the previous section we observed that the various galactic components as gas, stars and dust show complex relations among themselves. The ongoing star formation is mostly localized in the inner region of the galaxy and along the spurs downstream of the spiral arms. Within the molecular arms, the young stars are basically absent. However the red giant old stars are best correlated with the CO emission. This old stellar population is a good tracer of the underlying galactic potential, that shows a variety of components within the PAWS FoV, and is responsible of the largest contribution to the ISRF. Large-scale dynamical turbulence and variation in the ISRF are likely the main sources of possible differences in molecular gas properties.

In light of these findings, in this section we define seven galactic environments based on dynamical and star formation morphological arguments. These environments will help to obtain a more quantitative view of the molecular ISM through the analysis of the gas distribution (see next Section) and eventually the GMC properties.

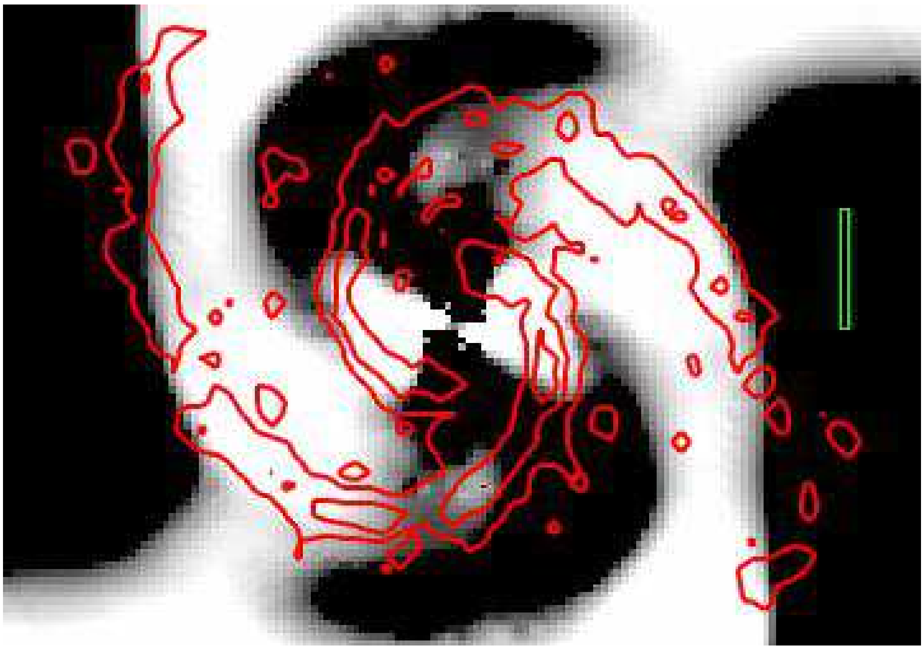

Figure 1.4: Map of torques in the inertial frame $R_{gal} \times \nabla\Phi$, generated from a 3.6 μm map of the old stellar light tracing the stellar potential Φ at galactocentric radius R_{gal} (Meidt et al. 2013). White (black) corresponds to positive (negative) torques that drive motions radially outward (inward). Contours of the CO intensity are overlayed in red. The green bar at right indicates 40”. Figure taken from Meidt et al. (2013).

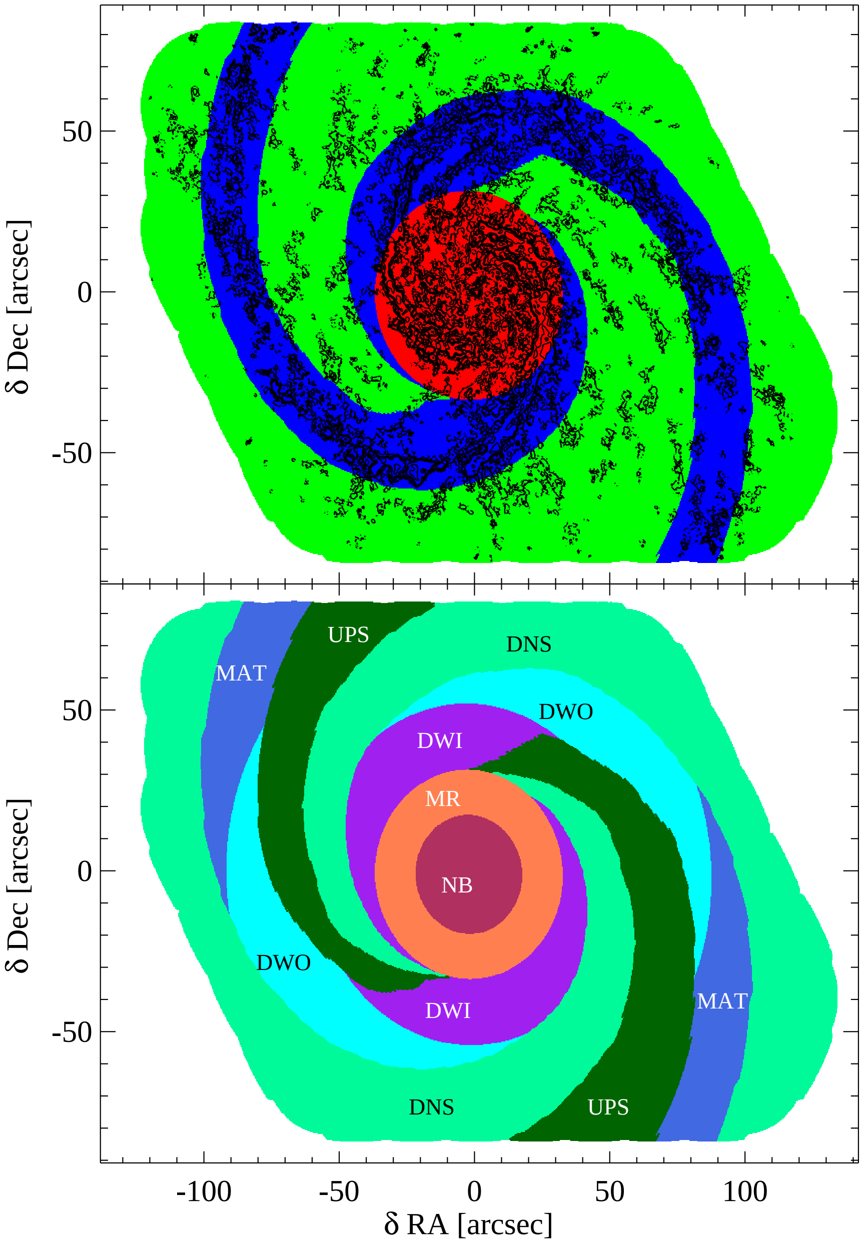

Figure 1.5: Top: the three main regions in which the PAWS field of view is divided: center in red, spiral arm in blue and inter-arm in green. Contours belong to the integrated intensity map of islands. Bottom: M51 environmental mask. Nuclear bar (NB) and molecular ring (MR) are indicated in dark red and orange, respectively. Inner density-wave spiral arms (DWI) are indicated in purple, outer density-wave spiral arms (DWO) in cyan, and material arms (MAT) in light blue. Downstream with respect to the spiral arms (DNS) is marked in light green while upstream in dark green (UPS). These color codes will be kept throughout the thesis.

Within the PAWS field there are three main regions where the molecular gas is likely subject to distinct physical conditions (see Fig. 1.5), i.e. within the strong, nearly symmetric *spiral arms*, the *inter-arm region* situated upstream and downstream of the spiral arms and the *central region*, where the gas is influenced by the presence of a central elliptical concentration of old stars in the form of a nuclear bar (Rix & Rieke 1993). These regions can be further divided into sub-regions, in light of the pattern of star formation (e.g. traced by Hα) and gas flows (according to the profile of present-day torques, Fig. 1.4) within them.

Specifically, the central region is divided in to 2 regions:

- *nuclear bar environment* (NB): $R_{gal} < 23$”, bounded by the bar corotation resonance, inside of which the bar exerts negative torques and drives gas radially inwards
- *molecular ring environment* (MR): 23” $< R_{gal} <$ 35” where the influence of the bar and inner-most portion of the spiral arms overlap, creating a ring-like accumulation of gas. The ring is sitting close to a region of zero torque as the acting forces of the inner bar and the spiral density-wave cancel out. The high gas surface densities reached at this location result the most prominent star formation in M51.

Likewise, we divide the spiral arms region (SA) into three distinct environments according to the direction of gas flows driven in response to the underlying gravitational potential.

- *inner density-wave spiral arm environment* (DWI): 35” $< R_{gal} <$ 55” within which gas is driven radially inward by negative spiral-arm torquing. This portion of the spiral arm is characterized by relatively little star formation as traced by Hα and 24 μm emission (Schinnerer et al. 2013),
- *outer density-wave spiral arm environment* (DWO): 55” $< R_{gal} <$ 85” within which gas is driven radially outward by positive spiral arm torquing. Star formation falls on the convex side of this portion of the spiral arms (Schinnerer et al. 2013),
- *material spiral arm environment* (MAT): $R_{gal} >$ 85” beyond the boundary of positive spiral arm torques associated with the density wave spiral, extending to the edge of the PAWS field (within which there is some indication that the direction of the gas flow is again reversed).

The width of the spiral arm environment (and each of its 3 sub-regions) is defined with respect to observed gas kinematics. We determine the zone of enhanced spiral streaming centered around the arm by measuring the (rotational) auto-correlation of azimuthal streaming velocities in the PAWS field (Meidt et al. 2013). We construct azimuthal profiles of the auto correlation signal in a series of radial bins and take the width of the signal at 95% maximum as our measure of the kinematic arm width. (In testing, we find that the 95% max-width of the CO-brightness auto correlation profile corresponds well with the width estimated by eye from the morphology of CO brightness; Schinnerer et al. 2013). The average kinematic width from along the two arms is centered on the spiral arm ridge located by eye in the PAWS map of CO brightness. Both the location of the ridge and the width are assumed to be symmetric.

This definition of the location and width of the spiral arm ultimately yields the definition of the inter-arm region (IA), which we further divide in to

- *downstream* of the spiral arms (DNS), or the convex side where the majority of star formation realted to the arms is observed in Hα or 24 μm;
- *upstream* of the spiral arms (UPS), or the concave side basically devoid of significant star formation.

These environments are separated at the midpoint of the two spiral arm ridge-lines.

Although inside and outside corotation the gas flowing direction would change and then the definition of the inter-arm regions, M51 is characterized by a non-trivial dynamical structure composed by several patterns (or potential perturbations) with different pattern speeds (e.g Meidt et al. 2013, Meidt et al. 2008, Vogel et al. 1993, Elmegreen 1989, Tully 1974b). Meidt et al. (2013) identified $\Omega_b \sim 200$ km s^{-1} kpc^{-1} at $R_{gal} \sim 20$" corresponding to the nuclear bar corotation, $\Omega_{p,1} \sim 90$ km s^{-1} kpc^{-1} at $R_{gal} \sim 55$" corresponding to the inner spiral arms, $\Omega_{p,2} \sim 55$ km s^{-1} kpc^{-1} at $R_{gal} \sim 85$" the transition between density-wave spiral arms and material arms. This suggests that at any radius (within the PAWS FoV) a pattern is inside a corotation resonance of another and thus the expected reversal gas flow for a single pattern is not observed. This interpretation is supported also by the presence of the massive star formation regions always at one side of the spiral arms. Therefore we consider as downstream all the convex side and upstream all the concave one of the spiral arms, independently by corotation. These environments are separated at the midpoint of the two spiral arm ridge-lines.

1.6 Environmental dependence of the molecular gas structure in M51

Although the main goal of this thesis is to study the properties of the M51 GMC population as function of environment, it is instructive to see whether those differences, if present, are already encoded in the global distribution of the CO emission. With this aim, in the following we summarize the work of Hughes et al. (2013) where the authors analyzed the CO emission in M51 through the shape of the probability distribution functions in M51.

Probability Density Function (PDF) are simple way to represent the density and column density of the ISM (e.g. Kainulainen et al. 2009). The PDFs considered here are simple histograms of (x, y) pixel values within a integrated intensity CO ($I(CO)$) map ($I(CO)$ PDFs) or (x,y,v) pixel values within a spectral line cube measured in brightness temperature (T_{mb} PDFs).

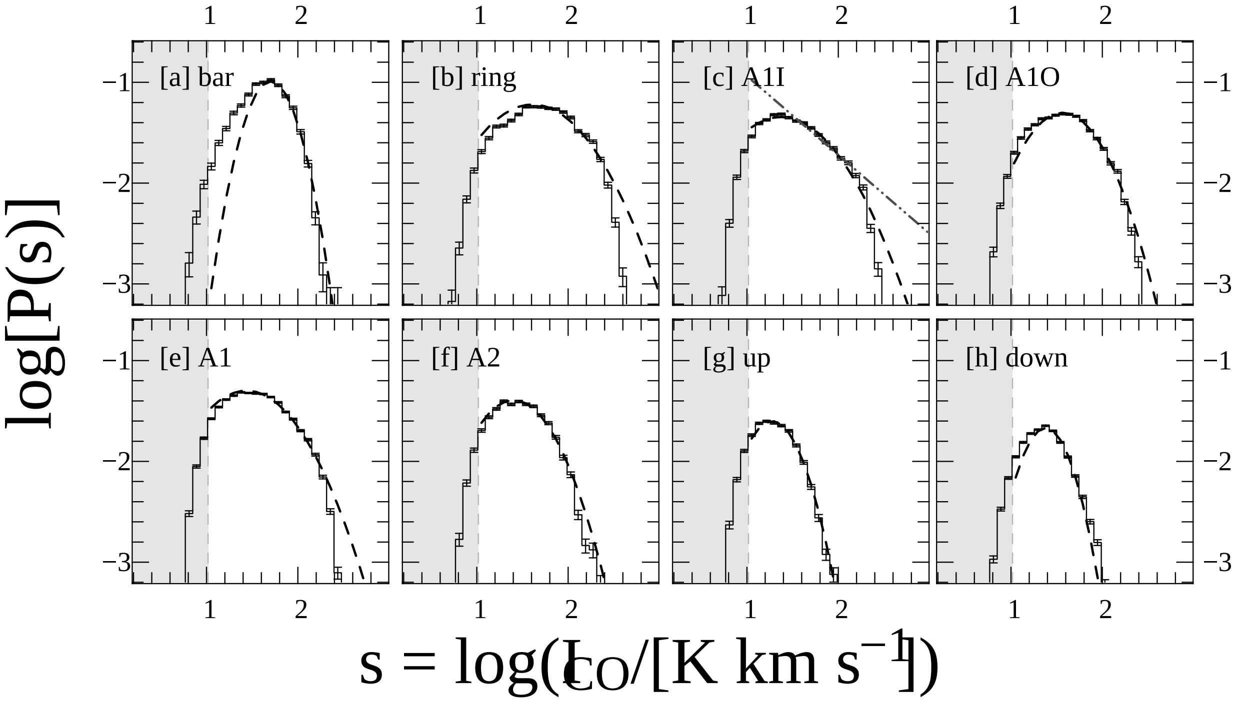

Figure 1.6: The $I(CO)$ PDFs for different environments within the PAWS FoV. The grey shaded area represents values beneath our nominal $3\sigma_{RMS}$ sensitivity limit of 10.5 K km s^{-1}. When a LN (power-law) function provides a good description of the PDF, it is indicated by a dashed (dot–dot–dashed) line. The vertical error bars represent the uncertainty associated with simple counting ($\sqrt(N)$) errors. *Bar* indicates the nuclear bar (NB) environment in our formalism; *ring*, the molecular ring (MR); *A1*, the density-wave spiral arms (DWI+DWO); *AO*, the material arms (MAT); *A1I*, the inner density-wave arms (DWI); *A1O*, the inner density-wave arms (DWO). Figure adapted from Hughes et al. (2013).

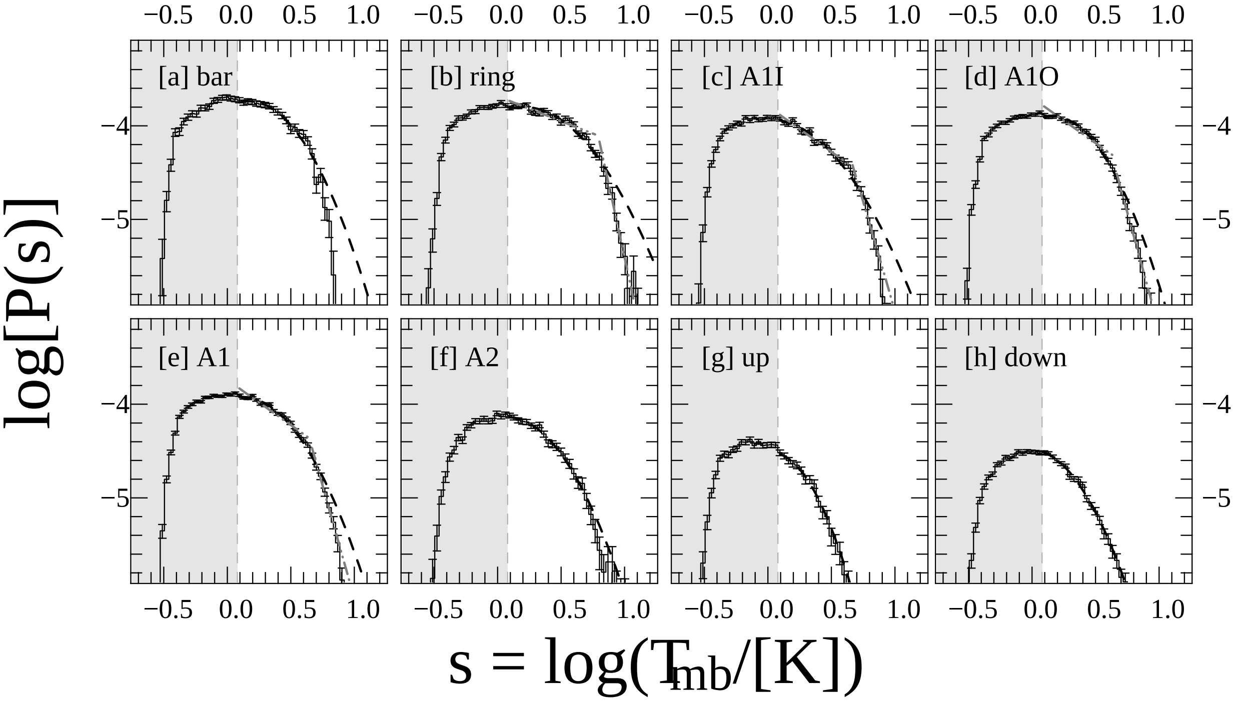

Figure 1.7: *Top*: the $I(CO)$ PDFs for different environments within the PAWS FoV. The grey shaded area represents values beneath our nominal $3\sigma_{RMS}$ sensitivity limit of 10.5 K km s^{-1}. *Bottom:* the PDFs of the CO brightness for different regions within the PAWS field. In each panel, the grey shaded area represents values beneath our nominal $3\sigma_{RMS}$ sensitivity limit of 1.2 K. In both panels, when a LN (power-law) function provides a good description of the PDF, it is indicated by a dashed (dot–dot–dashed) line. The vertical error bars represent the uncertainty associated with simple counting ($\sqrt(N)$) errors. See Figure 1.6 for the description of the environments. Figure adapted from Hughes et al. (2013).

In general PDFs of the ISM are expected to follow a lognormal (LN) distribution since the turbulent nature of it is well represented by a lognormal velocity field (e.g Padoan et al. 1997). However, in some simulations that did not have the required level of thermal and kinetic energy feedback for the modeled galactic disk to reach equilibrium have found deviations from this general shape (Dobbs et al. 2011).

The PDFs for the CO integrated intensity and the brightness temperature are obtained from the PAWS 1” zeroth moment map and PAWS 1” datacube, respectively, masked with the technique described in Appendix. The global $I(CO)$ PDF is well described by a LN function, however it shows evidence for truncation at high intensity values (> 200 K km s^{-1}).

Deviation from a simple LN shape is even more evident when looking at the global brightness temperature distribution that shows fewer high brightness pixels than would be expected from this LN function. Instead it appears to be composed by two flat segments across $1 < T_{mb} < 3$ K and $T_{mb} > 5$ K that can be better represent by a truncated power-law.

The division in environments of the PAWS FoV proposed in Section 1.5 allows for the study of the gas in very different physical conditions. We note first that the projected area of the seven environments is quite large (between 2 and 17 kpc^2) and each contains a statistically significant number of GMCs ($>$ 100, see Section 3.5). Therefore, PDFs of CO emission in these regions are still comparable to the PDFs of simulated galactic disks rather than the PDFs of individual clouds and should, in principle, be described through LN fits.

The PDFs defined for the individual M51 environments (see Section 1.5) differ dramatically and some of them show very large deviation from a general LN shape (Fig. 1.6-1.7). Differences in the environmental PDFs can be summarized by two of their main properties:

- *Width:* the environmental $I(CO)$ PDFs tend to decrease in width from the center to the inter-arm regions. Significant are also the differences between the PDFs of environments that belong to the same region: the nuclear bar PDF has a width $\sim 2\times$ lower than the ring one, and distributions of density-wave spiral arms are wider than material arm ones. These decrements indicate that the fraction of pixels with bright CO emission declines with the overall frequency of CO detection and varies from environment to environment. The T_{mb} PDFs are instead more constant in width.
- *Shape:* LN shape appears to be a good description only of the inter-arm and nuclear bar $I(CO)$ PDFs. Spiral arm and molecular region PDFs show large deviations from this general shape. The inner density-wave spiral arm PDF is more comparable to a truncated power-law, while the molecular ring one is very flat between $20 - 150\,\mathrm{K\,km\,s^{-1}}$. Both distributions shows a steep decline at $I(CO) \sim 300\,\mathrm{K\,km\,s^{-1}}$. A similar departure is observed in the T_{mb} PDFs and only inter-arm and material arm PDFs show shapes comparable with LN functions.

In general it appears that increasing the fraction of bright pixels shifts the shape of the PDFs from generic LN to power-laws or their truncated versions.

The most likely explanation for the PDF feature variations observed within M51's environments is provided by Elmegreen (2011). A certain gas distribution is supposed to generate LN shaped-PDFs when it is dominated by supersonically thermal turbulence with a negligible gravitational support. This might be a reasonable approximation for small galactic regions where the properties of the gas are quite constant. On kpc scale, instead, PDFs are likely the result of the convolution of several local PDFs, each with its own characteristic. Models have shown that such convolution develops power-law tails and truncations in the PDFs that make them deviate from a generic LN shape. Elmegreen (2011) suggests that these deviation reflect large-scale variations in the average density, temperature and/or velocity fluctuations for the molecular gas within different M51 environments.

Such variations can be simultaneous and difficult to disentangle from the shape of the PDFs, however it is interesting to note that in the inter-arm region – where cloud-scale variation are supposed to drive the global gas properties – the PDFs resemble LN distributions as expected for isothermal supersonically turbulent molecular gas, while in the spiral arms – where the gas is highly affected by large-scale non-circular motions and reaches higher densities – we observed larger deviations from a lognormal shape.

1.7 Dynamical dependence of the star formation in M51

Schinnerer et al. (2013) found that some regions of the spiral arms are devoid of young star formation. Meanwhile, Hughes et al. (2013) found that the global molecular gas distribution is highly influenced by the presence of the spiral arms. These two findings have been interpreted together by Meidt et al. (2013), considering the influence of non-axisymmetric stellar structure (i.e. nuclear bar, spiral arms) on gas flows, molecular cloud properties and star formation in the inner disk of M51. Using Hα and 24 μm maps together with the PAWS dataset they define the azimuthally-averaged depletion time profile within the inner part of M51 (Fig. 1.8). The depletion time, τ_{dep}, indicates how much time is needed to consume a certain quantity of molecular gas in star formation and is generally calculated as $\Sigma_{H_2}/\Sigma_{SFR}$. This quantity is the reciprocal of what is referred to as the star formation efficiency (SFE). The section of the spiral arms with anomalously low star formation (35" $< R_{gal} <$ 55") exhibits a long depletion time and strong gas inflow motions. A surprising and clear anticorrelation between the τ_{dep} and the gravitational torque profiles suggests a strong dependence of star formation on dynamics.

In M51, the sections of the spiral arms characterized by gas inflow (negative torque) also exhibit the largest streaming motions, suggesting that the efficiency of star formation efficiency is impacted by gas motions, generally; the depletion time is longer when gas is in motion than when the gas corotates with the galaxy.

In the spiral segment with little star formation, streaming motions are particularly large with respect to the gas velocity dispersion. When the ratio between gas streaming motions and velocity dispersion (which sets the time required for a GMC to reach pressure equilibrium with its surrounding) is high, the cloud moves before it becomes virialized and subsequently collapses and forms stars; the change in environment during the motion leads to a change in the balance between internal and external cloud pressure. This can be viewed as an effective stabilization, quantifiable in term of dynamical pressure that scales as the square of the streaming motion velocity. Clouds are especially sensitive to changes in the balance between internal and external pressure when the two pressures are similar, as for clouds in M51; spiral arm clouds have similar surface densities to the surrounding medium (see Chapter 4). As a consequence of the reduced surface pressure felt by clouds embedded in an ambient medium undergoing large streaming motions, cloud collapse is prevented, leading to a decrease in the star formation efficiency. Applying Bernoulli's principle, which equates an increase in gas velocity with reduced cloud pressure, Meidt et al. (2013) calculated that within the spiral arms, where the streaming motions are high, collapse-unstable clouds need to have a mass 1.5-2 times higher than prescribed by the virial theorem. Any GMCs below this mass would be incapable of collapsing and forming stars, locally reducing the SFE. Meidt et al. (2013) argued that differences in pressure may also play a role in setting up the various shapes exhibited by the molecular gas PDFs in M51 and that those difference may be driven by difference in pressure of the spiral arms with respect to the inter-arm.

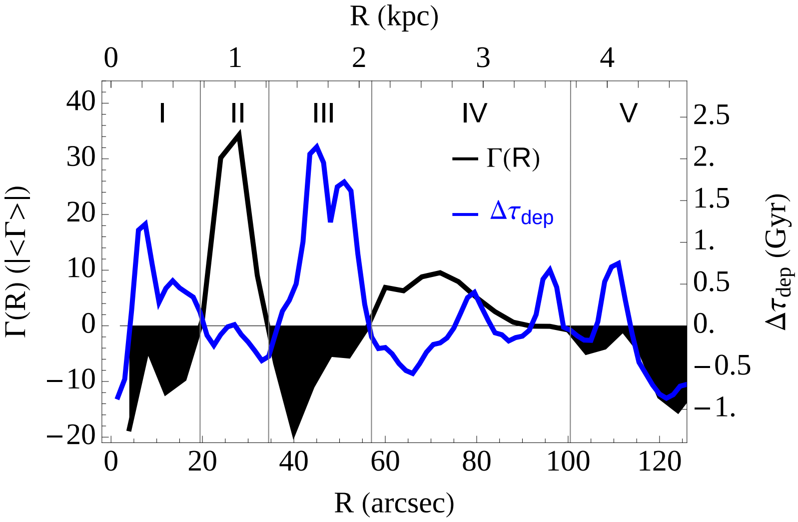

Figure 1.8: Radial profiles of the azimuthally-averaged torque (in units of the absolute magnitude of the average torque across the PAWS field of view |<Γ>|; black and white) and molecular gas depletion time $\Delta\tau_{dep}$=τ_{dep}-<τ_{dep}> (where <τ_{dep}> is the average τ_{dep} across the PAWS field of view; blue) measured in 2.4" radial bins. Each crossing from negative to positive torque corresponds to the location of the corotation radius (CR) of the structure: inside CR material is driven radially inward and outside material moves outward. Figure taken from Meidt et al. (2013)

1.8 SUMMARY AND CONCLUSIONS

In summary, evidence from this series of PAWS papers strongly suggests that the properties of the gas are highly influenced by the presence of the spiral arms (at least over the region of M51 probed by PAWS). When measured in the different M51 environments, CO brightness PDFs show large deviations from the predicted LN distribution. This is especially evident for the PDF in the spiral arms, which reaches higher densities than elsewhere, likely due to the accumulation and organization of gas in the spiral arm. According to the work of Meidt et al. (2013), the difference in the stellar density (potential), streaming motions and gas density in the arm compared to the inter-arm leads to very different cloud pressure in these two zones. Streaming motions in the arm reduce external pressure, so that more massive clouds (reaching higher densities compared to clouds in the inter-arm) can be built before becoming collapse-unstable. At the same time, the increase in the cloud stable mass inhibits the collapse over the arm crossing time. The immediate consequence is the complex pattern of massive star formation observed with a multi-wavelength analysis: regions of the spiral arms where the gas is in motion, even with high gas surface density, are completely devoid of young stars. This is in stark contrast to current models that propose that the surface density of SFR and gas are well-correlated. Dynamical effects appear very likely important for characterizing the GMC organization in M51 and require a detailed study. In the following Chapter we perform a kinematic analysis of the inner M51 region, taking advantage from the high resolution of the PAWS dataset.

2

MULTI-PHASE COLD GAS KINEMATIC OF M51*

CONTENTS

The high kinematic complexity and the favorable position of M51 on the sky make this galaxy an ideal target to test different theories of spiral arm dynamics. Taking advantage of the new high resolution PdBI Arcsecond Whirlpool Survey (PAWS) data, we undertake a detailed kinematic study of M51 to characterize and quantify the origin and nature of the non-circular motions. Using a tilted-ring analysis supported by several other archival datasets we update the estimation of M51's position angle ($PA = (173 \pm 3)^{\circ}$) and inclination ($i = (22 \pm 5)^{\circ}$). The harmonic decomposition of the high resolution ($\sim$ 40 pc) CO velocity field shows the first kinematic evidence of an $m = 3$ wave in the inner disk of M51 with a corotation at $R_{CR,m=3} = 1.1 \pm 0.1$ kpc and a pattern speed of $\Omega_{p,m=3} \approx 150$ km s^{-1} kpc^{-1}. This mode seems to be excited by the nuclear bar, while the beat frequencies generated by the coupling between the $m = 3$ mode and the main spiral structure confirm its density-wave nature. We observe also a genuine signature of an $m = 1$ mode that, together with the $m = 3$, is highly responsible for the lopsidedness of M51 at small and large radii. We provide a simple method to estimate the radial variation of the amplitude of the spiral perturbation (V_{sp}) attributed to the different modes. The main spiral arm structure has $\langle V_{sp} \rangle = 50 - 70$ km s^{-1}, while the streaming velocity associated with the $m = 1$ and $m = 3$ modes is, in general, 2 times lower. The joint analysis of HI and CO velocity fields at low and high resolution reveals that the atomic and molecular gas phases respond differently to the spiral perturbation due to their different vertical distribution and emission morphology.

---

[*] This chapter is adapted from Colombo et al. 2013b, ApJ submitted.

2.1 Introduction

Gas kinematics are key to dissecting how the various components of a galaxy (stars, gas and dust) interact and evolve over time, leading to the variety of morphologies we see in the local universe today. They supply the standard for probing the mass distributions of galaxies through rotation curves and are uniquely sensitive to perturbations to the gravitational potential due to bars and spiral arms (Roberts & Stewart 1987; Vogel et al. 1993; Regan et al. 2001; Dobbs et al. 2010). By providing an instantaneous record of the response of gas to non-axisymmetric (bar and spiral) structures, they supply a unique view of the processes by which these features impact the distribution of gas and stars, from stimulating stellar radial migration (Sellwood & Binney 2002; Minchev et al. 2012) and driving gas inflows (Wong et al. 2004; van de Ven & Fathi 2010) to regulating the conversion of gas into stars (Meidt et al. 2013). Gas kinematics are therefore indispensable for building a firm picture of how bar and spiral structures contribute to the slow, secular evolution of galaxies.

Studying the response of gas to an underlying potential perturbation (in the form of bars or spiral arms) can supply key information about the nature of the perturbation (e.g. Vogel et al. 1993; Wong et al. 2004). Today, spiral structures tend to be described by either one of two opposite theories. In the quasi-stationary spiral structure (QSSS) depiction (Lindblad 1963), spiral arms are a long lasting pattern (Lin & Shu 1964) that slowly evolves and rotates with a single angular speed. This structure is thought to be formed from self-excited and self-regulated standing "density waves" (Bertin et al. 1989a, Bertin et al. 1989b, Bertin & Lin 1996) present in the density and hence gravitational potential. The other theory considers arms to be transient, temporary disturbances generated, i.e., by the tidal interaction with a companion (e.g., Toomre & Toomre 1972) which overwhelms any pre-existing structure (Salo & Laurikainen 2000) or given some an initial seed perturbation (D'Onghia et al. 2013). These structures, which may not obey the Lin-Shu dispersion relation for density waves (Salo & Laurikainen 2000, D'Onghia et al. 2013), are often thought to be winding (with radially decreasing pattern speeds) or to consist of a series of distinct speeds.

Most of the effort to discriminate between these two theories has been centered on M51, which is an ideal target because of its proximity (D=7.6 Mpc, Ciardullo et al. 2002), favorable inclination ($i \sim 22°$, this work), high surface brightness and kinematic complexity. In the classic M51 kinematic study of Tully (1974b), the spiral pattern in the outer disk was argued to be a transient feature stimulated by the interaction between M51a and M51b, while the inner arms were thought to be in a steady state. Indeed, Vogel et al. (1993) find very good agreement between the predictions of density-wave theory and the observed transverse velocities across the inner arms. But more recently, Shetty et al. (2007) argue that the density and velocity profiles are inconsistent with quasi-steady state mass conservation.

At least some part of the ambiguity as to the nature of M51's spiral pattern may stem from the complexity of its structure. Meidt et al. (2008) found evidence for three distinct pattern speeds in M51 using the radial Tremaine-Weinberg (TWR) method, only one of which is similar to the value typically assumed. Their finding that these patterns overlap at resonances would seem to be consistent with the idea that they are physically coupled and not temporary disturbances. But multiple, distinct pattern speeds may also support the D'Onghia et al. (2013) picture wherein a disturbance drives a transient feature that stimulates other transient features, which together give the appearance of long-lived structures.

The disk of M51 may also sustain multiple, spatially coincident patterns. The optical and NIR surface brightness is very clearly lopsided, suggesting an $m = 1$ disturbance in the potential. This lopsidedness persists in tracers of the ISM. Some part of the lopsidedness could be explained by the superposition of the two-armed spiral with a spiral pattern with three-fold symmetry (Henry et al. 2003). The existence of such a pattern in M51 was first suggested between radii of 50" and 100" in blue light optical images by Elmegreen et al. (1992). Rix & Rieke (1993) also find the signature of a three-armed pattern in the K-band, although at a much weaker level than in the V-band.[1] Both studies conclude that the $m = 3$ feature in M51 is a perturbation in the gas and dust only (traced in extinction at optical and NIR wavelengths), rather than a genuine density wave present in the density (traced by the old stellar light) and thus gravitational potential of the system, although this idea was later challenged by Henry et al. (2003).

As pointed out by Elmegreen et al. (1992), simple Fourier transforms of galaxy images often provide misleading results on the nature and number of spiral arms if they are not confirmed by kinematic evidence. The m=3 component, for example, could arise as a beat frequency, modulated by inter-arm star formation or by an intensity gradient from one side of the galaxy to the other (due to extinction or kinematic effects).

In this Chapter we take advantage of the newest high resolution ^{12}CO (1-0) PAWS observations in the central 9 kpc of M51. The high resolution of this data (~ 1") allows us to perform an in-depth study of the gas response to M51's perturbed stellar potential. If the $m = 3$ mode is a genuine perturbation to the potential then our high resolution map of molecular gas motions should reveal it.

We complement our kinematic analysis with lower resolution HI and ^{12}CO (2-1) data from THINGS (Walter et al. 2008) and HERACLES (Schuster et al. 2004, Leroy et al. 2009). The inclusion of observations of various phases of the ISM, at low and high resolution, allows us to assess how uniformly they trace the gravitational potential, and determine which type of observation is optimal for which science goal. The 21 cm and the CO line emission are the common

---

[1] They also found that M51a is lopsided at all radii, as indicated by the high power in the $m = 1$ Fourier component.

tracers of the atomic and the molecular gas phases that are at the basis of star formation. To understand the physics behind empirical laws that relate gas and stars from kpc (e.g. Leroy et al. 2013b, Bigiel et al. 2008 and references therein) to pc scales it is necessary to constrain their characteristics at every level, especially how they are distributed within, and respond to the potential of a given system.

The Chapter is constructed in the following way. In Section 2.2 we present the datasets used for the kinematic analysis. Then we describe the features of the high resolution velocity field from PAWS in Section 2.3. We introduce the formalism to study the line-of-sight velocity (V_{los}) in spiral galaxies in Section 2.4 together with our estimation of the projection parameters of M51 (inclination and position angle) needed for a correct evaluation of the single component of V_{los}. Then we expose the gas-based rotation curves of M51 and we compare their features with the mass derived rotation curve from Meidt et al. (2013). In Section 2.5 we use the harmonic decomposition prescriptions to study residual velocity fields. We propose a method to estimate the amplitude of the perturbation velocity from the spiral arms and we find the first kinematic evidence for a three-fold density-wave in M51. We conclude in Section 2.6 discussing the origin of this structure and highlighting kinematic differences between atomic and molecular gas tracers and low and high resolution data (Section 2.7). We summarize our work and findings in Section 2.8

2.2 DATA

Together with the PAWS datasets (i.e. PAWS at 1”, tapered version at 3”, 6” and PAWS single dish, hereafter 30m) described in Section 1.2, we make use of the archival velocity fields from THINGS and HERACLES reported in the following.

2.2.1 ARCHIVAL THINGS VLA HI DATA

M51 HI data from The HI Nearby Galaxy Survey (THINGS, Walter et al. 2008) was obtained from the dedicated web-page `http://www.mpia-hd.mpg.de/THINGS/Data.html`. M51 was observed between March 2005 and July 2007 using the NRAO Very Large Array (VLA) in B, C and D configuration. The robust weighted THINGS data used here has a spatial resolution of ∼ 6” (i.e. 240 pc at our assumed M51 distance of 7.6 Mpc) and a spectral resolution of ∼ 5 km s^{-1}. The $1\sigma_{RMS}$ noise sensitivity of the survey is homogeneous and ∼ 6 K. We use this data together with the PAWS data to better define the rotation curve of M51, as it covers the entire disk of M51a.

2.2.2 ARCHIVAL HERACLES IRAM 30M ^{12}CO(2-1) DATA

The Heterodyne Receiver Array CO Line Extragalactic Survey (HERACLES, Leroy et al. 2009) re-reduced and mapped the data obtained by Schuster et al. (2004) using the HERA receiver array on the IRAM 30m telescope from January 2006 through March 2008 for M51. The ^{12}CO (2-1) M51 data has a spatial resolution of ~ 13.5” (540 pc in M51) and a spectral one of ~ 2.6 km s^{-1}. The data are sensitive to point sources of $\sim 2 \times 10^6$ M$_\odot$ at $3\sigma_{RMS}$.

2.3 THE M51 ^{12}CO(1-0) VELOCITY FIELD AT HIGH ANGULAR RESOLUTION

The PAWS velocity field shown in Fig 2.1 is obtained by applying the masking procedure described in Appendix and using the task `MOMENTS` of `GIPSY`. The map exhibits only a few sight lines that deviate significantly from the overall pattern. Subtracting our adopted systemic velocity of V_{sys} = 472 km s^{-1} (e.g. Shetty et al. 2007), velocities range from −150 km s^{-1}, on the approaching northern side to 170 km s^{-1} on the receding southern side relative to systemic velocity. The most prominent features of the velocity field (visible in the line-of-nodes) are: strong spiral arm streaming motions, a twist in the central region and the nucleus of M51a itself.

The streaming motions associated with the spiral arms are particularly evident in the southern half of the PAWS FoV, characterized by discontinuities and velocity gradients across the arm. The deviation persists to a much lesser degree in parts of the inter-arm region. The streaming motion appears less strong in the northern with respect to the southern half.

In the central region ($R_{gal} \lesssim 35$”) the iso-velocity contours are strongly twisted by 10 – 15°. A recent torque analysis (Meidt et al. 2013) suggests that the nuclear bar first seen in near-IR images (Zaritsky et al. 1993) is responsible for the observed twisting.

The nuclear gas (see also Scoville et al. 1998, Matsushita et al. 2007) shows a clear out-of-velocity pattern at the very center of the map being redshifted by ≈ 100 km s^{-1} with respect to the systemic velocity.

The technique we used to construct the moment maps allows us to recover the weak inter-arm signal. The velocity field in the inter-arm globally follows the circular motion of the rotating disk. But, especially at the locations of the gas spurs emanating from the arms, we see localized velocity gradients. These are steeper downstream of the spiral arm than upstream and most evident in the spurs along the southern spiral arm.

For comparison in Fig. 2.2 we show the first moment maps from PAWS tapered at 3”, 6”, THINGS at 6” and HERACLES at 13.5”. The prominent streaming motions in the zone of the southern spiral arm and the nucleus are still evident in the PAWS 3” map. In PAWS 6” the redshifted nucleus is smeared out by the beam and the discontinuities of the velocity gradient across the arms are strongly reduced. Those features are completely absent in the THINGS and HERACLES first moment maps. While in the case of HERACLES this absence could be caused by the much lower resolution and the lack of interferometric data, the difference between CO and HI data at the same resolution could be due to a real difference in the nature of the two emission lines. We discuss this possibility in Section 2.7.

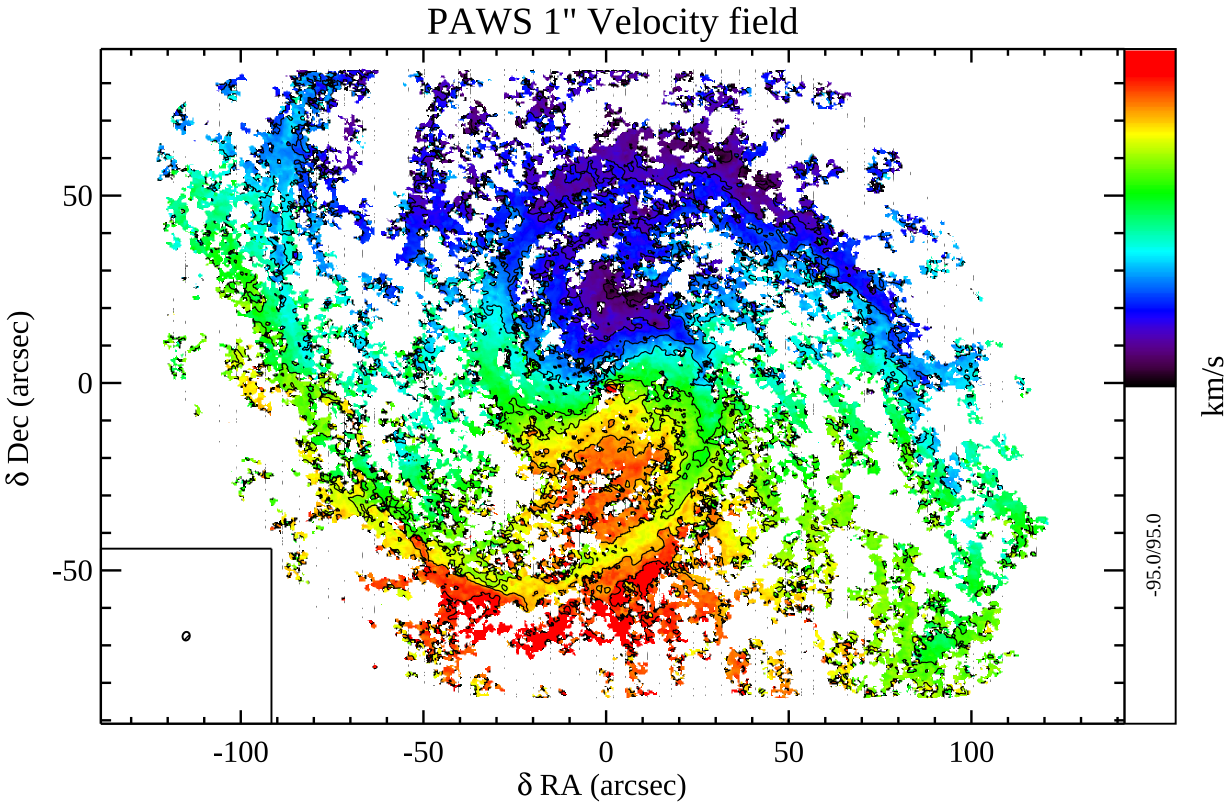

Figure 2.1: The PAWS ^{12}CO(1-0) Velocity field at 1” resolution. Deviations from circular motion are due to streaming motions associated with the spiral arms and the twist in the line-of-nodes is caused by the nuclear stellar bar. M51’s nucleus is redshifted with respect to the systemic velocity of the galaxy. In the bottom left the beam (1” ~ 40 pc) is shown. The sidebar shows the color scale of the map in km/s relative to the systemic velocity of M51, 472 km/s (Shetty et al. 2007).

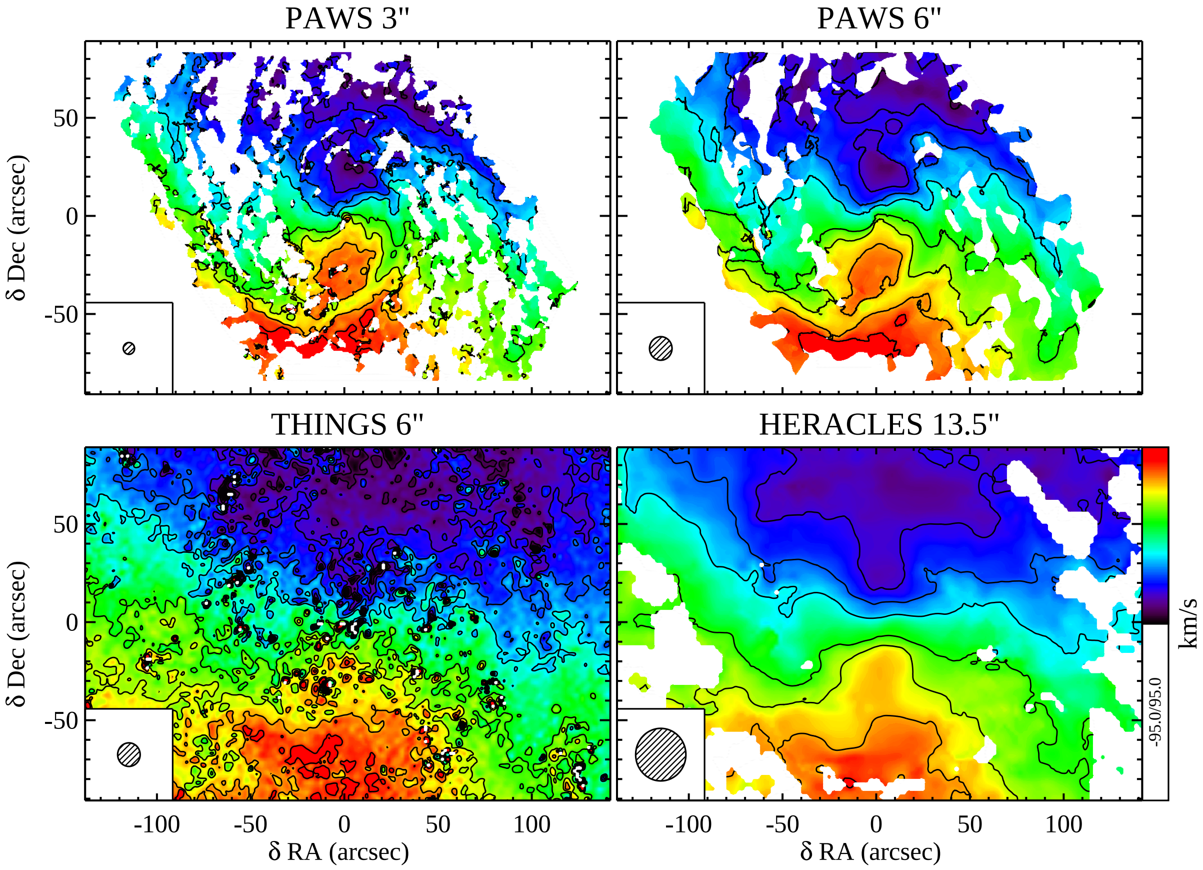

Figure 2.2: Velocity fields from PAWS tapered at 3" and 6", THINGS 6" and HERACLES 13.5" The sidebar shows the color scale of the maps in km/s. In the bottom left of each panel the beam in shown.

2.4 GAS MOTIONS IN SPIRAL POTENTIALS

In this section and the next, we consider the different velocity components that contribute along the line-of-sight in a typical spiral galaxy in the presence of strong non-circular motions. Each component is analyzed in detail in order to gain an optimal view of cold gas kinematics in M51, as well as to explore how this view depends on the resolution at which the gas motions are observed.

2.4.1 LINE-OF-SIGHT VELOCITY

The line-of-sight velocity V_{los} observed at a given location in a galactic disk can be represented as a sum of four parts:

$$V_{los} = V_{sys} + V_{rot} + V_{pec} + V_z \tag{2.1}$$

where V_{sys} is the systemic velocity of the galaxy due to the expansion of the Universe, V_{rot} is the rotational component, V_{pec} represents all peculiar velocities not accounted for the circular motion of the galaxy and V_z is the vertical velocity component (i.e. Canzian & Allen 1997). Studies of face-on grand-design spirals indicate that V_z of the neutral gas is less than 5 km s^{-1} (van der Kruit & Shostak 1982), in which case V_{los} can be well represented by planar motion without considerable vertical motions. Therefore throughout the chapter we assume $V_z \equiv 0$.

The *rotational component* can be expressed as

$$V_{rot} = V_c \cos(\theta) \sin i, \tag{2.2}$$

where V_c is the circular rotation speed, θ is the angle in the plane of the disk from the major-axis receding side, and i represents the inclination of the disk to the plane of the sky. (The inclination i is equal to 0° for an exactly face-on galaxy and $i = 90°$ for a completely edge-on geometry.)

In a grand-design spiral galaxy such as M51, the *peculiar component* is largely due to the gas response to the density wave perturbation, i.e.

$$V_{pec} = (u_\phi \cos\theta + u_r \sin\theta) \sin i \tag{2.3}$$

where u_r and u_ψ are the (non-circular) radial and azimuthal components of streaming motions.

2.4.2 KINEMATIC PARAMETER ESTIMATION

Our main goal in this Chapter is to measure and analyze the streaming motions in the inner disk of M51. To correctly interpret the line-of-sight projections of the circular and peculiar motions (i.e. V_{rot} and V_{pec}) we must therefore first have a good knowledge of the kinematic parameters that describe the projection of the galaxy on the plane of the sky. Several parameters are already well-constrained in the literature and do not require further analysis (Section 2.4.2.1). For others, we provide new estimations – with uncertainties (Section 2.4.2.2) –applying a tilted-ring analysis to the different velocity fields from PAWS 1”, PAWS 3”, THINGS 6”, HERACLES 13.5” and PAWS single dish at 22.5”.

2.4.2.1 Previous M51 kinematic studies

Because of its proximity, favourable inclination and prominent spiral arms, M51 has been the focus of a large number of kinematic studies aimed at testing theories of spiral arm formation and evolution. A summary of those focused on the determination of the kinematic parameters is provided in Tables 2.1-2.2.

In general the systemic velocity of M51 is well-constrained around a value $V_{sys} \approx 472$ km s^{-1}. Therefore, in the following we adopt the literature value for this quantity (e.g. Shetty et al. 2007).

The center of M51, corresponding to the location of the nucleus, has been carefully constrained by measurements of H_2O maser emission and high resolution radio continuum imaging (see Table 2.2 and references therein). Throughout the Chapter we adopt as rotation center the latest measurement of the water maser by Hagiwara (2007), i.e. $(x_0, y_0) = (13^h29^m52^s.71, 47°11'42".79)$. The adopted rotation center almost coincides with the peak of CO emission associated with M51a’s bright core (located at $(x_{core}, y_{core}) = (13^h29^m52^s.62, 47°11'42".58)$), clearly identifiable only by PAWS at 1”.

Estimates for the position angle PA and inclination i span a large range in the literature (see Table 2.1 and references therein), between PA=$165 - 180°$ and i= $15 - 28°$. With the aim of updating these estimates and providing a tighter constraint, in the next section we apply a tilted-ring analysis to the most recent high-resolution gas velocity fields available for M51 from the THINGS, HERACLES and PAWS projects.

Resolution	**Tracer**	V_{sys}	PA	i	**Reference**
2”/4”	Hα/^{12}CO(1-0)	471.7 ± 0.3	175 ± 5	24 ± 3	(1)
4”	^{12}CO(1-0)	469	170 ± 5	...	(2)
5”	Hα	470 ± 2	...	...	(3)
6”	HI	...	...	30	(4)
6”.75	Hα	472 ± 3	170 ± 3	20 ± 5	(5)
16”	^{12}CO(1-0)	469 ± 5	171.6	...	(6)

Table 2.1: M51a (NGC 5194) kinematic parameters measured by previous studies. (1), Shetty et al. (2007); (2), Meidt et al. (2008); (3), Goad et al. (1979); (4), de Blok et al. (2008); (5), Tully (1974a); (6) Kuno & Nakai (1997). In Shetty et al. (2007) and Meidt et al. (2008), 4” refers to the best resolution of the BIMA-SONG data used.

Resolution	**Method**	$\mathbf{x_0, y_0}$	**Reference**
~0”.1	H_2O maser spot	$13^{h}29^{m}52^{s}.71, 47^{\circ}11'42”.79$	(1)
~0”.1	H_2O maser spot	$13^{h}29^{m}52^{s}.71, 47^{\circ}11'42”.80$	(2)
1”	6-20 cm continuum peak	$13^{h}29^{m}52^{s}.70, 47^{\circ}11'42”.60$	(3)
1”.1	6 cm radio continuum peak	$13^{h}29^{m}52^{s}.71, 47^{\circ}11'42”.61$	(4)
~1”.3	6-20 cm continuum peak	$13^{h}29^{m}52^{s}.71, 47^{\circ}11'42”.73$	(5)
...	Optical measurement	$13^{h}29^{m}53^{s}.27, 47^{\circ}11'48”.36$	(6)

Table 2.2: Center of M51a (NGC 5194) as derived from previous studies. (1), Hagiwara (2007); (2), Hagiwara et al. (2001); (3), Ford et al. (1985); (4), Turner & Ho (1994); (5), Maddox et al. (2007); (6), Dressel & Condon (1976). (B1950) coordinates reported by several studies have been converted to (J2000) using NED.

2.4.2.2 Tilted-ring analysis

To quantify the kinematic parameters of M51a we assume that the various quantities of Eq. 2.1 vary only with galactocentric radius R_{gal}. In this case, the first moment of the line-of-side velocity distribution can be studied through a standard tilted ring approach (Rogstad et al. 1974). This assumes that a galaxy disk can be described as a set of concentric rings, each with its own inclination i, line-of-nodes position angle PA, systemic velocity V_{sys}, rotation center (x_0,y_0), and pure circular velocity V_c and expansion or radial velocity V_{exp}, such that

$$V_{los}(R_{gal}) = V_{sys}(R_{gal}) + \Big(V_c(R_{gal})\cos\theta + V_{exp}(R_{gal})\sin\theta\Big)\sin i(R_{gal}), \tag{2.4}$$

The polar coordinates in the galactic plane (R_{gal}, θ) can be related to the observed Cartesian coordinates (x, y) in the plane of the sky by

$$\cos(\theta) = \frac{-(x - x_0)\sin(PA(R_{gal})) + (y - y_0)\cos(PA(R_{gal}))}{R_{gal}}, \tag{2.5}$$

$$\sin(\theta) = \frac{-(x - x_0)\cos(PA(R_{gal})) + (y - y_0)\sin(PA(R_{gal}))}{R\cos(i(R_{gal}))}. \tag{2.6}$$

To perform our least-square tilted-ring fit to the line-of-sight velocity we use the `GIPSY` task `ROTCUR`, sampling the velocity field at one radial bin per synthesized beam width from a starting radius of one half-beam.

We implement a two step procedure to obtain estimates of M51a's kinematic parameters (i, PA):

- First we fix the systemic velocity and rotational center using the literature values discussed in Section 2.4.2.1, i.e. V_{sys} = 472 km s^{-1} and (x_0, y_0)=($13^h29^m52.41^s$, 47°11′42.80”), and V_{rad} = 0 but leaving free inclination i, position angle PA and rotation velocity V_{rot}. We estimate the magnitude of $\langle PA\rangle$ and $\langle i\rangle$ as weighted medians along the radial profile, using the inverse of the squared-errors calculated directly by `ROTCUR` as weights. These errors are typically larger at large galactocentric radius where the data sampling is lower.
- In the second step we set different values of inclination (i.e. 20°, 23°, 25°, 27°, 30°, 33°, 35°, 37°, 40°, 45°) to obtain our final position angle[2]. For every fixed inclination we calculate the weighted median as a function of radius. Then we apply this same procedure

---

[2] V_{sys} and (x_0, y_0) are also kept fixed as in the first step

to obtain the inclination itself, fixing different values of *PA* (i.e. 165°, 167°, 170°, 172°, 173°, 174°, 175°, 177°, 180°, 185°).

Map	**Step**	**⟨i⟩** [*deg*]	**⟨PA⟩** [*deg*]
PAWS 1”	1	48 ± 7	177 ± 4
	2	45 ± 8	177 ± 4
PAWS 3”	1	54 ± 8	176 ± 5
	2	48 ± 10	177 ± 4
THINGS 6”	1	30 ± 12	172 ± 2
	2	22 ± 5	173 ± 3
HERACLES 13.5”	1	30 ± 6	171 ± 4
	2	25 ± 7	172 ± 4
30m 22.5”	1	35 ± 4	174 ± 2
	2	22 ± 3	171 ± 4

Table 2.3: Tilted-ring analysis kinematic parameters. Weighted median and median absolute deviation (MAD) of kinematic parameters (inclination $\langle i \rangle$, position angle $\langle PA \rangle$) derived for each survey following the two steps described in the text.

The final results of the two steps are summarized in Table 2.3. Alongside our analysis of the PAWS velocity field, we perform the tilted ring analysis of the 6” THINGS HI velocity field[3] (Walter et al. 2008), the HERACLES ^{12}CO(2-1) first moment map at 13.5” (Leroy et al. 2009) and the 30m data at 22.5” (Pety et al. 2013). These maps all extend beyond the PAWS field of view and allow us to sample the full disk of M51a. Compared to the hybrid PAWS data, these maps should also be less sensitive to the contribution of non-circular streaming motions, which are progressively smeared out the lower the angular resolution. As described in Section 2.3, strong spiral arm streaming motions cause clear distortions in the iso-velocity contours in the PAWS velocity field at either 1” or 3” (see Figures 2.1-2.2), which influence the estimate of the position angle. Tilted-ring solutions from these independent data sets with a larger field-of-view also provide a much-needed consistency check on estimates from the PAWS data, given that the close to face-on orientation can make it difficult to reliably assess the kinematic parameters.

---

[3] The original 6” velocity field from THINGS has been cut using the GIPSY task BLOT in order to eliminate the warped region of the outer HI disk.

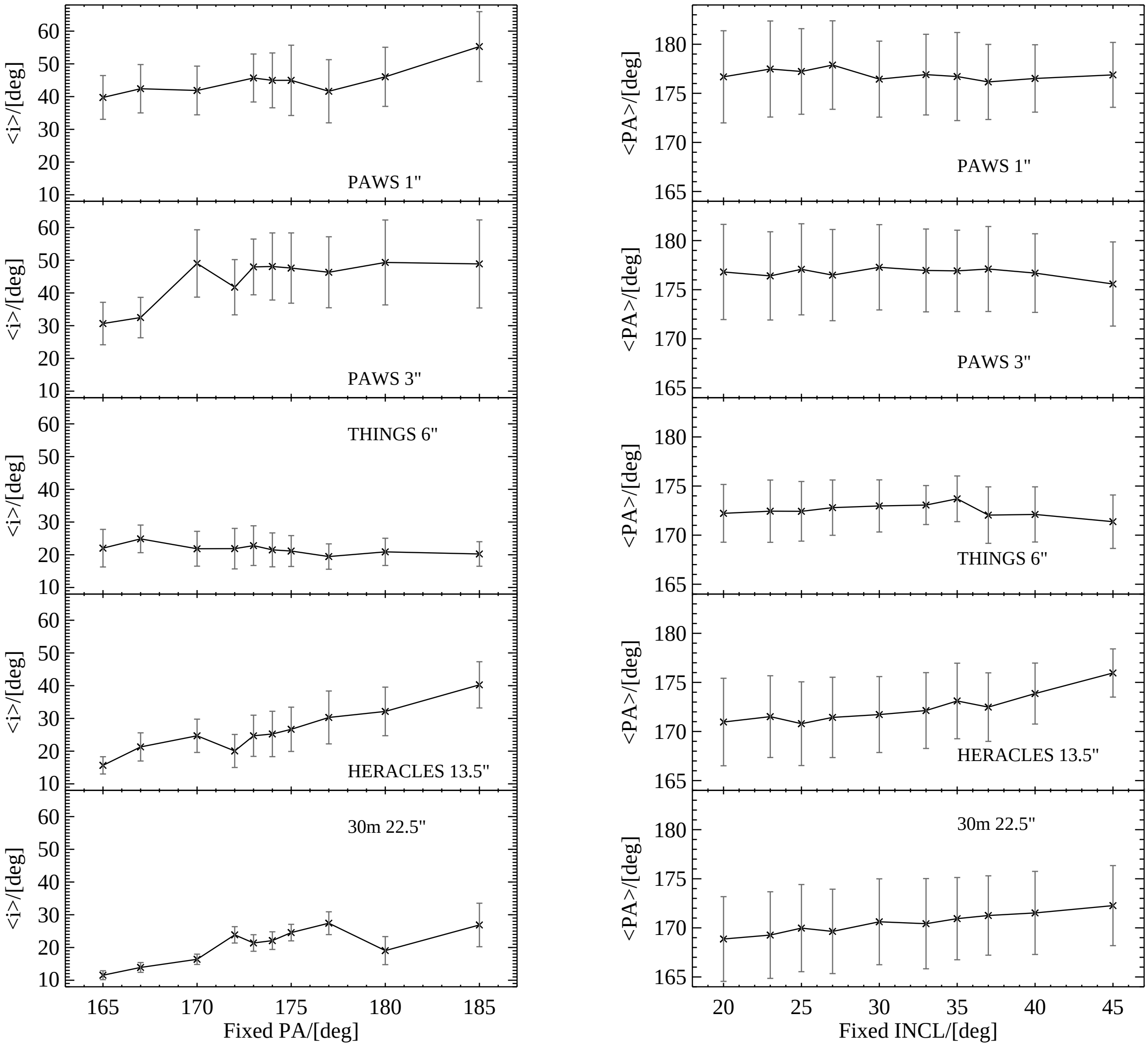

Figure 2.3: Behaviors of weighted median and MAD of inclination $\langle i \rangle$ (position angle $\langle PA \rangle$) along the radial profile with different fixed value of position angle (inclination) as described in the text for Step 2 in the left (right) panel. From top to bottom: results obtained from the hybrid PAWS cube at 1" and 3", THINGS at 6", HERACLES at 13.5" and PAWS single dish observation at 22.5".

In all data sets, we find that the position angle of M51a is fairly robust to changes in the assumed inclination. However the PA is sensitive to the presence of streaming motions. While we find $\langle PA \rangle \sim 170^\circ - 173^\circ$ from the low resolution data where the influence of the streaming motion is reduced, i.e. from 30m, HERACLES or THINGS data, the $\langle PA \rangle$ increases to $\sim 176^\circ$ for the PAWS data at native and 3" resolution.

Streaming motions also influence the inclination estimates, which we find to be additionally sensitive to the assumed position angle (yielding larger error bars). Considering that the strongest streaming motions in M51 appear in the central 5 kpc and weaken at larger galactocentric radius (where the outer spiral pattern is weaker), the FoV of a given survey largely determines the value of the inclination that can be retrieved. For maps with large FoV (30m, HERACLES and THINGS) the inclination is low ($\langle i \rangle \sim 22^\circ - 25^\circ$), while for PAWS at 1" and 3" that cover a smaller FoV, the averaged inclination is higher than 40°. We note that our tilted ring analysis avoids the outer warp in M51 (as obvious in the HI distribution). Since we sample the maps with large FOVs only up to the start of the warp, our inclination and position angles are representative of the disk.

Since the THINGS HI survey has the largest FoV and probes the (outer) part of the disk where we expect the least contribution from streaming motions, we adopt measures from this data as our final best estimation of the kinematic parameters: i.e. $\langle i \rangle = (22 \pm 5)^\circ$ and $\langle PA \rangle = (173 \pm 3)^\circ$. These exhibit the smallest error bars and the most constant behavior for various set values of PA and i, respectively (Step 2). These results are consistent with the most recent measurements of the projection parameters performed by Hu et al. (2013), ($PA = (168.0 \pm 2.5)^\circ$, $i = (20.3 \pm 2.8)^\circ$), using a parametrization of M51's spiral arms imaged in $i-$band by the SDSS (Data Release 9). The more constant behavior of PA and i from HI with respect to other CO datasets might be also given by a true different nature of the gas phases (see Section 2.7).

2.4.3 CIRCULAR MOTION: GAS-DERIVED ROTATION CURVE OF M51A

Using our best estimates of the kinematic parameters obtained in the previous section (i.e. $V_{sys} = 472\ \mathrm{km\,s^{-1}}$, (x_0, y_0)=($13^h29^m52.41^s$, $47^\circ11'42.80''$), $i = 22^\circ$, $PA = 173^\circ$, $V_{exp} = 0$) we again use `ROTCUR` to derive the circular velocity V_c (see Eq. 2.2) or rotation curve. The results, fitting only V_c, are shown in Fig. 2.4.

All curves exhibit bumps and wiggles, and these are strongest at PAWS 1" and 3". These presumably trace a contribution from non-circular streaming motions, not least because the spiral arms dominate the tilted-ring fit; the relatively streaming-free inter-arm region is sampled to a much lesser extent in any given titled ring. Even at larger radii, where the inter-arm covers larger fractional area, the low inter-arm sampling still leads the fit to favor the spiral arm, resulting in the dip between $R_{gal} \sim 100 - 150$" in the PAWS 1" and 3" rotation curves. The appearance of the wiggles reduces with decreasing angular resolution; curves derived from the 30m, HERACLES and THINGS data are much smoother and almost overlap within their error bars. However, especially in the nuclear bar region, all rotation curves show a bump, probably due to the non-circular motion associated with the bar.

Given the difficulty in obtaining a measure of gas circular velocity with a simple tilted-ring analysis in M51, in the following we adopt the total baryonic mass model derived by Meidt et al. (2013) to describe the circular motion in the galaxy.

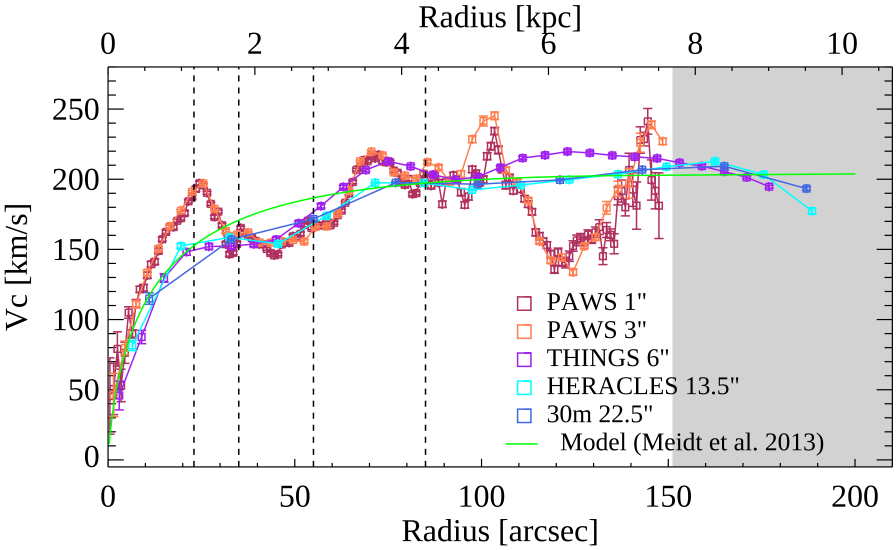

Figure 2.4: M51's rotation curves derived from the different neutral gas surveys and the extrapolated models. Errors on the rotation velocity estimations are calculated directly from the ROTCUR output through a self-generated $1\sigma_{RMS}$ error field. Vertical dashed lines indicate the radial extend of M51's environments as defined in Meidt et al. (2013), while the white area shows the limit of the PAWS FoV.

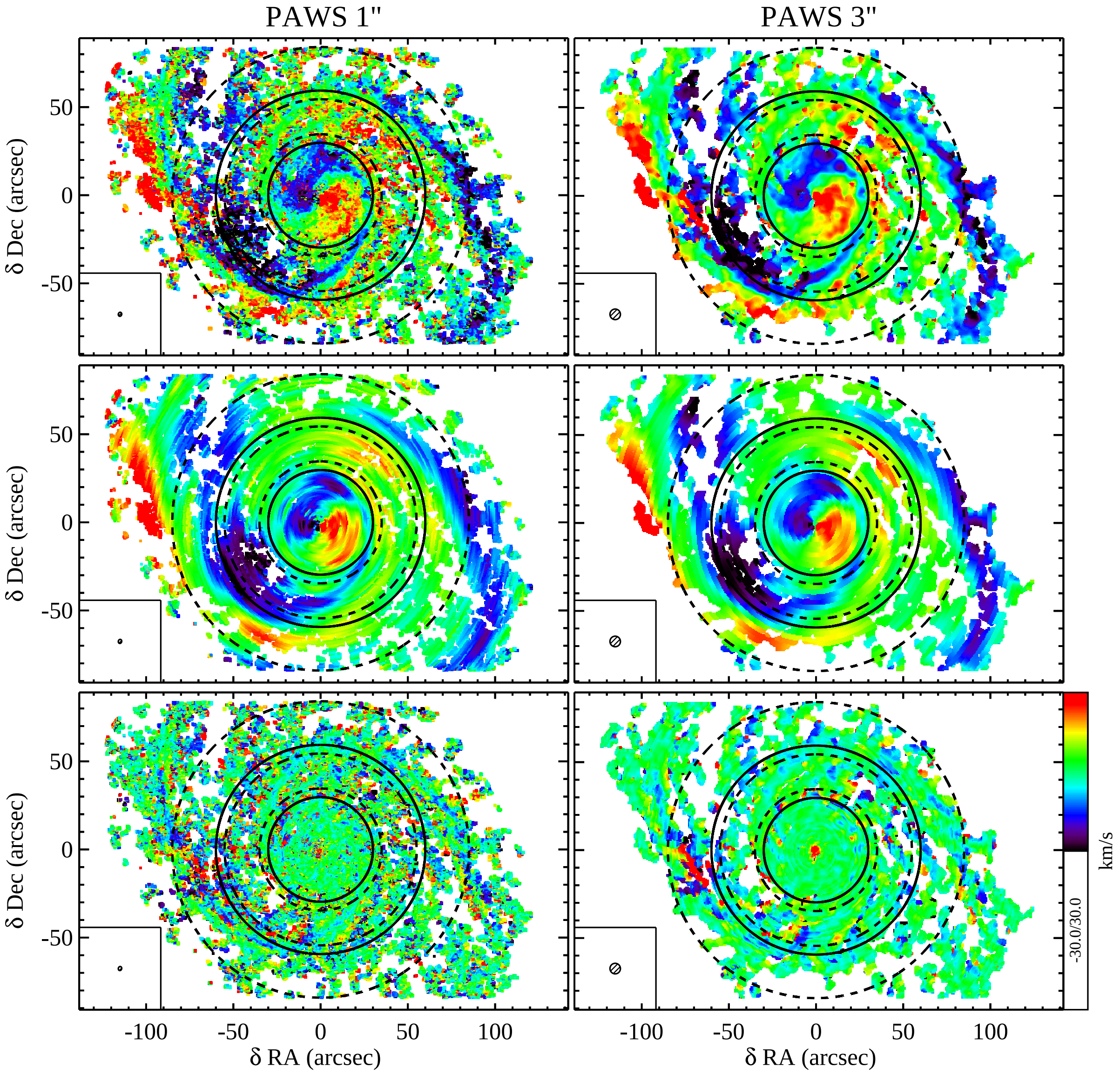

Figure 2.5: *Top*: from left to right, PAWS 1” and PAWS 3” residual velocity fields. The inner dashed black circle indicates the outer boundary of the molecular ring (R_{gal} = 35”). The outer black dashed circles mark the radial location of the first corotation at R_{gal} = 55” and the material arms at R_{gal} = 85” as identified through the present-day torque analysis by Meidt et al. (2013). The solid black circles, instead, indicate the corotation identified with the harmonic decomposition at R_{gal} = 30” and R_{gal} = 60”. Although the residual might shows higher values, we restrict the color bar to values between -25 to 25 km s^{-1}, to highlight the features of the residual velocity fields. *Middle*: harmonic reconstructed residual velocity fields. *Bottom*: difference between residual velocity fields and harmonic reconstructed ones. In the bottom left of each panel the beam is indicated.

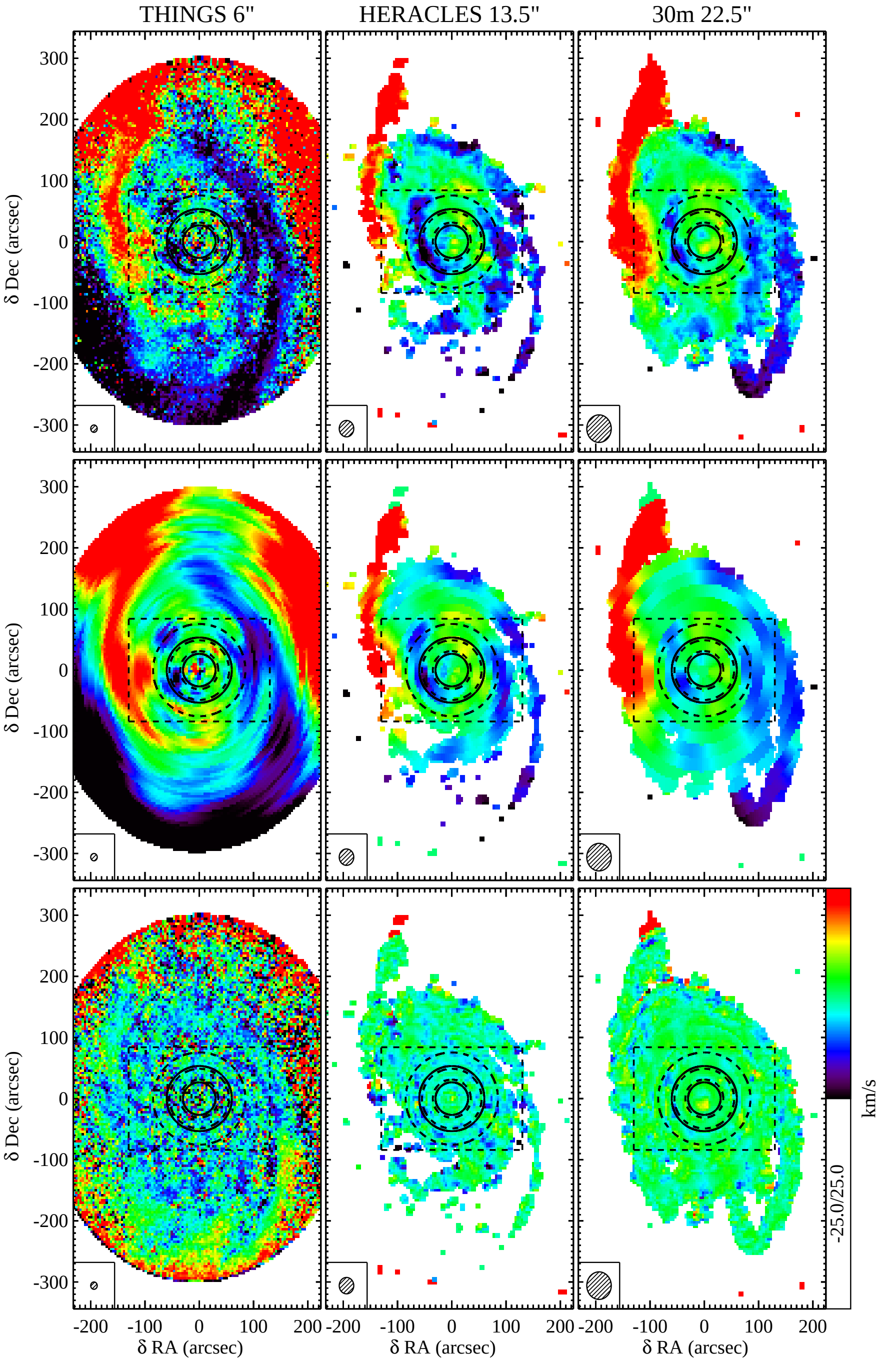

Figure 2.6: *Top*: from left to right, residual velocity fields from THINGS HI, HERACLES ^{12}CO(2-1) and 30m ^{12}CO(1-0). The inner dashed black circle indicates the outer boundary of the molecular ring (R_{gal} = 35”). The outer black dashed circles mark the radial location of the first corotation at R_{gal} = 55” and the material arms at R_{gal} = 85” as identified through the present-day torque analysis by Meidt et al. (2013). The solid black circles, instead, indicate the corotation identified with the harmonic decomposition at R_{gal} = 30” and R_{gal} = 60”. The dashed box delimits the PAWS 1” FoV. Although the residual might shows higher values, we restrict the color bar to values between -25 to 25 km s^{-1}, to highlight the features of the residual velocity fields. *Middle*: harmonic reconstructed residual velocity fields. *Bottom*: difference between residual velocity fields and harmonic reconstructed ones. In the bottom left of each panel the beam is indicated.

2.5 Non-circular motions

As is clear by a simple examination of the PAWS velocity field, gas motions in M51 deviate quite strongly from pure circular motion. The non-axisymmetric stellar bar and spiral arms drive strong radial and azimuthal “streaming” motions, which contribute to the term V_{pec} in Eq. 2.1 and become apparent when removing a circular velocity model from the observed velocity field.

In the following we analyze the peculiar motions that are not described by the model of pure circular motion derived in Section 2.4.3. We start by describing the main features in the residual velocity field, obtained by subtracting a 2D projected model of our best estimate of V_c from the observed velocity field. Then we investigate in detail the features present in the residual velocity field through this harmonic decomposition (Schoenmakers et al. 1997). Finally we use the results of a harmonic decomposition to estimate the amplitude of the spiral arm streaming motions.

2.5.1 Residual velocity fields

Using the rotation curve from Meidt et al. (2013), we generate a 2D model of pure circular motion using the `GIPSY` task `VELFI`. The model is subtracted from the observed velocity fields, giving the residual fields of PAWS 1” and PAWS 3” shown in Fig 2.5 and Fig. 2.6 for the 30m, HERACLES and THINGS velocity fields. In the case of pure circular motion the residuals would be zero everywhere. However here, the residual velocity fields from each of the different surveys exhibit clear signatures of significant non-circular motions, with typical values between -30 and 30 $\mathrm{km\,s^{-1}}$ and extrema reaching values above 90 $\mathrm{km\,s^{-1}}$ (corresponding to the nucleus). In presence of density-wave structures, these non-circular motions would show a particular morphological pattern in the residual velocity field, as realized by Canzian (1993). In the case of a m=2 perturbation to the gravitational potential (introduced by a two-armed stellar spiral or a stellar bar), the residual velocity field exhibits an m=1 pattern (i.e. an approaching-reciding dipole) inside corotation, and this changes to an m=3 morphology outside corotation. This morphology shift is due to the change of sign of the gas streaming motions beyond the corotation circle, affecting only their radial components and is expected to appear at the corotation only if the spiral structure is density-wave based.

Although the pattern predicted by Canzian (1993) can be difficult to distinguish at lower spatial resolution, the residual velocity fields from the PAWS data at 1” and 3” resolution (top of Fig. 2.5) show the signature very clearly, over several radial zones. In the central region (R_{gal} < 35”) the residual velocity field presents a clear m=1 pattern consistent with motions driven by the m=2 stellar nuclear bar. Just outside the molecular ring at R=23” and up until R_{gal} ≈55”, we see another approaching-receding dipole, now introduced by inflow motions driven by the two-armed spiral in this region (especially clear at the location of the southern spiral arm). This is complimented by transition to an $m = 3$ pattern beyond R_{gal} ≈55", although between this radius and $R_{gal} \approx$ 70" the morphology becomes more complex. In the outermost region ($R_{gal} \gtrsim$ 70"), where the density-wave spiral transitions to material spiral arms (Meidt et al. 2013), the PAWS FoV exhibits only a dipole.

2.5.2 HARMONIC DECOMPOSITION OF THE NON-CIRCULAR VELOCITY COMPONENT

In the previous section we identified several kinematic features not associated with pure circular motion.

Here we use a powerful technique first introduced by Schoenmakers et al. (1997) to describe and quantify non-circular motions, namely by expanding the peculiar component of the line-of-sight velocity V_{pec} as the harmonic series

$$V_{pec} = \sum_{j=1}^{N} [c_j \cos(j\theta) + s_j \sin(j\theta)] \sin(i), \tag{2.7}$$

Here N is the number of harmonics considered and c_j and s_j are coefficients that describe the radial and azimuthal components of the non-circular motion, which can be interpreted in terms of the perturbation to the gravitational potential. Canzian (1993) showed that a perturbation of the gravitational potential of m order introduces $j = m - 1$ and $j = m + 1$ patterns in the residual velocity field, each on either side of the pattern's corotation radius (see upcoming section).

We quantify the magnitude or power of each order of the harmonic decomposition j as the quadratically-added amplitude (e.g. Trachternach et al. 2008):

$$A_j = \sqrt{c_j^2 + s_j^2}. \tag{2.8}$$

and write the total power of the non-circular harmonic components as

$$A_r = \sqrt{\Sigma_{j=1}^{N} [c_j^2 + s_j^2]}, \tag{2.9}$$

to get a sense of the total magnitude of non-circular streaming motions. In the next section we inspect radial trends in A_j and A_r for coincidence with morphological features in M51.

Later in Section 2.5.5.1 we use our measurements of A_j to calculate the magnitude of the streaming motions associated with perturbations with *m*-fold symmetry.

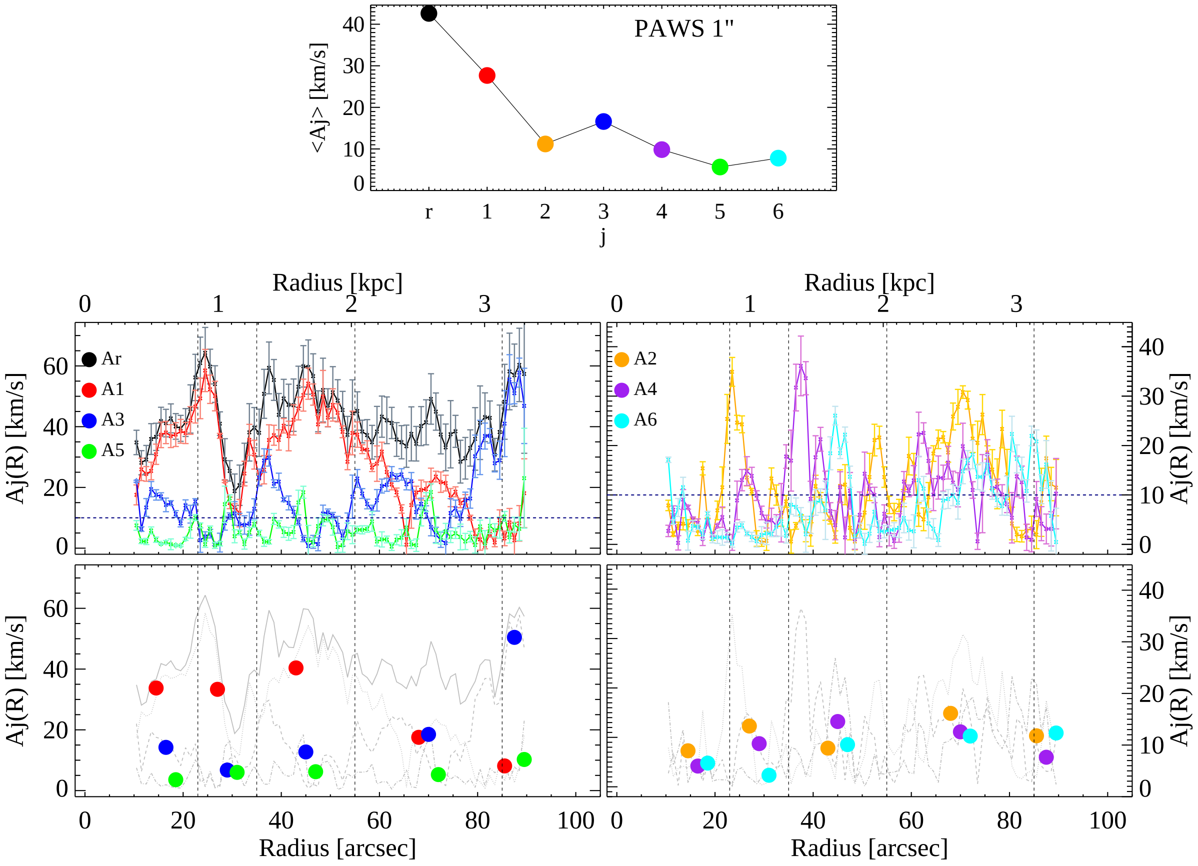

Figure 2.7: *Top plot:* Radial averaged mean of the harmonic component amplitudes A_j from PAWS 1” residual velocity field. *Bottom plot:* Non-circular motion amplitudes from harmonic decomposition: radial trend of the odd components and the total power $A_r(R_{gal})$ (top left) and even components (top right). Horizontal blue dashed straight line indicates the 2× the channel width of the cube, i.e. 5 km s^{-1}. In the bottom row the mean behavior of the odd (left) and even (middle) components in the different M51 environments (dashed vertical lines, as defined in Meidt et al. (2013)) are indicated.

2.5.2.1 APPLICATION TO RESIDUAL VELOCITY FIELDS

We perform the harmonic decomposition of the residual velocity field from PAWS at 1”, PAWS 3”, THINGS, HERACLES, and 30m velocity field up to order $j = 6$ using a modified version of the code first presented in Fathi et al. (2005). The inclination and PA of the best fitting ellipses are fixed to the values derived in Section 2.4.2 ($i = 22°$, $PA = 173°$) and the ring width is set to one beam. Fig 2.5 and Fig 2.6 shows the residual velocity fields reconstructed from the harmonic decomposition (middle row). Since the difference between residual velocity fields and the reconstructed fields is generally close to zero everywhere (Fig 2.5 and Fig 2.6, bottom row) we are confident that the harmonic decomposition using only 6 terms is quite accurate.

In Fig. 2.7 and Fig. 4.13-4.16 we plot the power of the single and total harmonic components as a function of radius (bottom plot, top left and top right columns), the median of those across the M51’s environments defined in Meidt et al. (2013) (top plot, bottom left and bottom right columns) and the median on the FoV (top plot). The error bars shown there are obtained through a bootstrap technique. We generate 100 residual velocity fields, and 100 harmonic decompositions, for a range of PA and i (set to their respective error bars). We take the results determined at our optimal $PA = 173°$ and $i = 22°$ as our final estimate and define the error on that estimate as the median absolute deviation of the bootstrapped amplitudes.

To discriminate between real trends and noisy peaks in the harmonic decompositions, we set a confidence level at 2× the channel width of the survey (i.e. 10 km s^{-1} or in the case of HERACLES 5.2 km s^{-1}). The (azimuthally averaged) harmonic components are highly reliable when they are above this threshold.

2.5.3 GLOBAL TRENDS

As expected, surveys with high spatial resolution reveal larger streaming motions than those with lower resolution. In PAWS 1” and PAWS 3” data the global amplitude of the non-circular components is $\langle A_r \rangle \sim 45$ km s^{-1}, whereas $\langle A_r \rangle \sim 20 - 35$ km s^{-1} for the low resolution surveys, even when restricting the FoV to the PAWS FoV. This difference stems from the fact that contributions from motions induced by the nuclear bar and spiral arms are not well resolved in these other surveys.

However all surveys, independent of resolution, very clearly show the signature of a dominant two-armed pattern. As predicted by Canzian (1993) the expected $j = 1$ and $j = 3$ modes induced by the bar and two-armed spiral in M51 are apparent in all surveys: $j = 1$ is the dominant mode of the residuals ($\langle A_1 \rangle \approx 30$ km s^{-1} for PAWS and $\langle A_1 \rangle \approx 10 - 20$ km s^{-1} for the low resolution surveys, that gets equal to the total power restricting the maps to the PAWS FoV), followed by the $j = 3$ mode ($\langle A_3 \rangle \approx 20$ km s^{-1} for PAWS and $\langle A_3 \rangle \approx 10 - 15$ km s^{-1} for the low resolution surveys). However in all cases, the $j = 2$ mode has a value quite close to the $j = 3$ ($\langle A_2 \rangle \approx 12$ km s^{-1} for PAWS and HERACLES maps and $\langle A_2 \rangle \approx 10$ km s^{-1} for THINGS and PAWS single dish). A non-negligible $j = 2$ velocity term would indicate a possible $m = 1$ or $m = 3$ perturbation to the galactic potential. However this is difficult to confirm from global measurements since, on average, perturbations of order $j > 3$ all have amplitudes < 10 km s^{-1}. Given that individual components may or may not extend as far as the dominant two-armed spiral (that spans the entire field of view), below we explore the evidence for m=1 and m=3 modes by analyzing radial trends.

2.5.4 RADIAL TRENDS

The high resolution of the PAWS data (at either 1" or 3") provides the most accurate depiction of the radial variation in the different harmonic components (at least for radii $R_{gal} < 85"$). We therefore focus on these data in this Section, but note similar trends when present in the lower resolution survey data.

2.5.4.1 ODD VELOCITY MODES: THE BAR AND TWO-ARMED SPIRAL ARMS

The innermost region of M51 ($R_{gal} < 23.5"$) is totally dominated by the peculiar motions driven by the nuclear bar, which introduces an $j = 1$ mode between 2 and 3 times stronger than the other modes in this zone ($\langle A_r^{(R_{gal}<23.5")} \rangle \sim \langle A_1^{(R_{gal}<23.5")} \rangle \sim 35\ \mathrm{km\,s^{-1}}$). Just outside the bar, in the zone of the molecular ring ($23.5" < R_{gal} < 35"$), the peculiar motions are reduced, reaching their lowest values across the FoV ($A_r^{(23.5"<R_{gal}<35")} \sim 20\ \mathrm{km\,s^{-1}}$ and $A_1^{(23.5"<R_{gal}<35")} \sim 10\ \mathrm{km\,s^{-1}}$). However, near R_{gal}=35" the $j = 1$ term begins to increase again ($\langle A_3^{(23.5"<R_{gal}<35")} \rangle \sim 40\ \mathrm{km\,s^{-1}}$). After R_{gal} ~60" the power in the j=3 mode increases again, to a level comparable to that in the j=1 mode.

Here the harmonic expansion confirms the visual impression from the residual velocity field morphology analysis: inside the torque-based estimate of the first spiral arm corotation radius ($R_{CR} = 55"$, Meidt et al. 2013) the residual velocity field appears dominated by a dipole pattern ($\langle A_1^{(35"<R_{gal}<55")} \rangle \sim 40\ \mathrm{km\,s^{-1}}$ and $\langle A_3^{(35"<R_{gal}<55")} \rangle \sim 15\ \mathrm{km\,s^{-1}}$), while beyond the $j = 3$ term is stronger ($\langle A_1^{(55"<R_{gal}<85")} \rangle \sim 10\ \mathrm{km\,s^{-1}}$ and $\langle A_3^{(55"<R_{gal}<85")} \rangle \sim 50\ \mathrm{km\,s^{-1}}$) and they are more less equal to $\sim 10\ \mathrm{km\,s^{-1}}$ in the region ($65" < R_{gal} < 80"$). The switch in dominance from j=1 to j=3 in the PAWS 1" and 3" fields moreover occurs across a zone that is consistent with the expected location of the corotation radius determined from gravitational torques.

The existence of a transition between a j=1 to a j=3 term is also clear at lower resolution, but now the transition occurs slightly further out at R~70” in HERACLES and 30m data. This displacement in the position of the transition with respect to the transitions in PAWS at 1” and PAWS at 3” could be caused by beam smearing that extends the transition radius over a wider region. However this switch in dominance in not well defined in THINGS 6”.

2.5.4.2 EVEN VELOCITY MODES: AN ADDITIONAL THREE-ARMED SPIRAL STRUCTURE

The higher resolution maps also provide valuable information about other, weaker modes that appear over a more limited radial range than those associated with the dominant two-armed pattern. Compared to lower spatial resolution data, we can sample this type of mode in PAWS data at 1” and 3” with many more resolution elements.

Fig 2.7 shows that there is non-negligible power in several of the even harmonic components, over almost the entire PAWS FoV. The j=2 exhibits a strong peak of ~ 35 km s^{-1} at $R_{gal} \approx$ 23”. Between 25” $\lesssim R \lesssim$ 40” the j=2 term weakens and the power in the j=4 term increases, peaking well above our confidence level (~ 35 km s^{-1} at $R_{gal} \approx$ 37”). This switch in dominance between j=2 and j=4 term is most clear in the PAWS 1” velocity field.

Since a perturbation of m order reflects in the residual velocity field as $j = m - 1$ and $j = m + 1$ terms, non-negligible values of j=2 and j=4 constitute the first kinematic evidence of an $m = 3$ wave within R_{gal} ~ 45” (i.e. R ~ 1.7 kpc) in the disk of M51a. According to the transition between these two components, we estimate that the corotation radius of this mode would occur at R_{gal} = (30 ± 3)” (i.e. R_{gal} = 1.1 ± 0.1 kpc[4]).

The PAWS data at 3” show a similar pattern, including a switch in dominance between j=2 and j=4 term at a similar radial distance as in PAWS 1”. But given the lower resolution, the detection of the j=4 in the region between 45” $\lesssim R_{gal} \lesssim$ 50” occurs over only 5 data points, and the signature is also weaker (the maximum is ~ 25 km s^{-1}). Moving to resolution lower than 3”, the behaviors of j=2 and j=4 terms are gradually smeared out and the switch in dominance between the two modes is no longer obvious.

An m=5 perturbation of the potential could also be responsible for the j=4 term. In this case, we would expect the j=6 term to exhibit a substantial value. Considering that only few data points of the j=6 term have values above our confidence level, we conclude that this scenario is improbable, or it is difficult to detect with the present (spatial and spectral) resolution.

---

[4] The corotation radius of the m=3 mode has been fixed to the center of the region where j=2 and j=4 overlap. The uncertainty is given by the width of this zone.

Likewise, since the j=2 component, which becomes dominant again outside R_{gal}~2 kpc, is never accompanied by another transition to a j=4 mode with significant power at larger radii, we argue that this must describe a genuine lopsidedness arising with an m=1 perturbation.

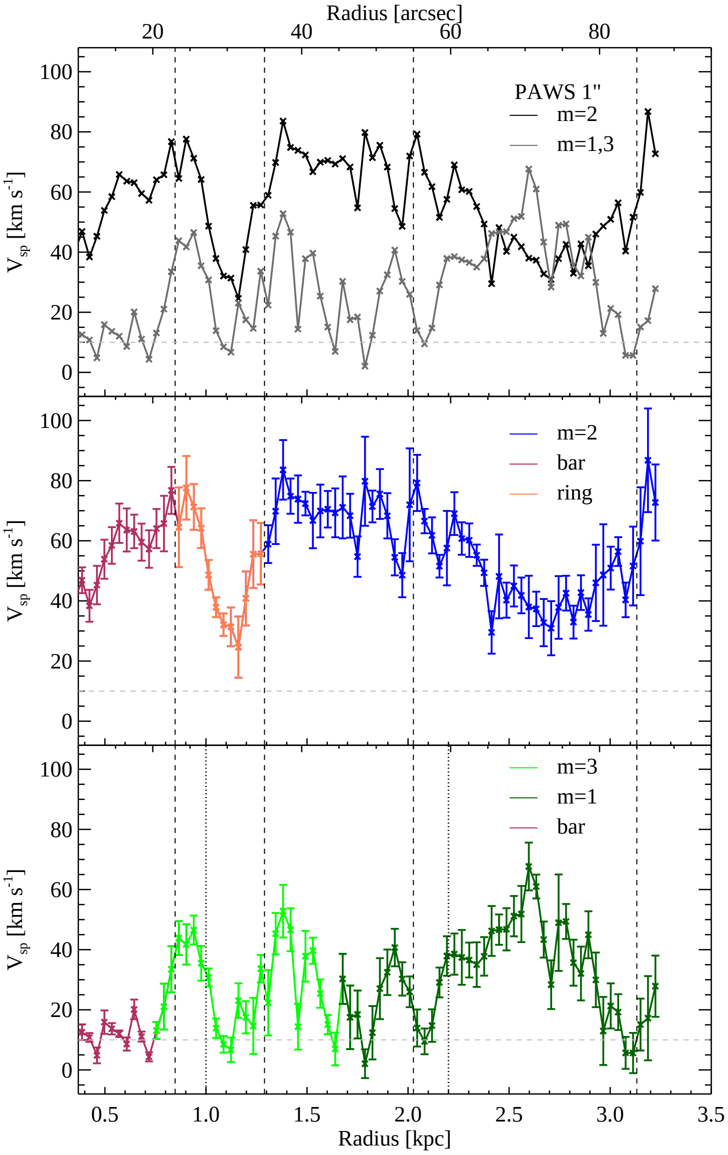

Figure 2.8: Amplitude of the spiral perturbation from PAWS 1”. Main two-fold spiral arms (middle), three-fold structure and m=1 mode (bottom) and merged view (top). In the bottom panel light green indicates the region of a possible m=3 influence. Dotted vertical lines represent the region where Henry et al. (2003) observed a larger deviation from a pure m = 2 symmetry. Vertical dashed lines indicate the M51 environments as defined in Meidt et al. (2013).

2.5.4.3 OUTER ARMS

In the region corresponding to the material arms the PAWS FoV has few data points and the decomposition becomes less accurate. Here it is useful to consider the results from the other lower resolution surveys. The total power of the non-circular components $A_r(R_{gal})$ increases almost monotonically in all harmonic expansions between 10-20 km s^{-1} in the innermost region to $\sim$ 30 km s^{-1} at 140". From HERACLES 13.5" and 30m 22.5" maps the $j = 3$ remains dominant over the whole field with $\langle A_3 \rangle \sim 20 - 30$ km s^{-1}.

2.5.5 THE MAGNITUDE OF STREAMING MOTIONS

In the previous two sections we used measurements of the power in individual components of the harmonic expansion of the residual line-of-sight velocities observed in M51 to characterize the non-circular motions driven by non-axisymmetric structures. In this section we will give these a physical interpretation, which we will then use to understand the nature of M51's patterns.

Similarly to Wong et al. (2004), we express the peculiar velocity component V_{pec} in Eq. 2.10 in terms of the velocities driven in response to a spiral perturbation to the gravitational potential with $m-$fold symmetry, following Canzian & Allen (1997):

$$V_{pec} = V_{sp}\left[\frac{\kappa}{2\Omega}\cos(\theta+\chi)\sin m(\theta-\theta_{sp}) + \nu\sin(\theta+\chi)\cos m(\theta-\theta_{sp})\right]\sin i, \tag{2.10}$$

Here, v_{sp} is the velocity amplitude that depends on the magnitude of the spiral perturbation, θ_{sp} is the spiral phase, χ the spiral arm pitch angle (the angle between the tangent to the arm and a circle with constant radius; by definition $0° < \chi < 90°$) and assuming S-spiral symmetry and trailing spiral arms in the case of M51[5]. The angular frequency $\Omega \equiv (V_c/R_{gal})^{-1}$, with R the galactic radius in kpc, Ω_p is the pattern speed of the spiral arms and the dimensionless frequency ν and epicyclic frequency κ are defined as

$$\nu \equiv \frac{m(\Omega_p - \Omega)}{\kappa}, \quad \kappa^2 \equiv 4\Omega^2 + R_{gal}\frac{d\Omega^2}{dR_{gal}}. \tag{2.11}$$

As shown by Wong et al. (2004), in the case of a single perturbation of mode m, the harmonic decomposition of the peculiar velocities in Eq. 2.10 yield harmonic coefficients of the form:

---

[5] An S-spiral has a shape like the letter "S". This convention refers to the two projections of a (trailing-arm) spiral on the plane of the sky. For details see Canzian & Allen (1997)

$$c_{m-1} = \frac{V_{sp}}{2}\left(\frac{\kappa}{2\Omega} - \nu\right)\sin(m\theta_{sp} - \chi), \tag{2.12}$$

$$s_{m-1} = \frac{V_{sp}}{2}\left(\frac{\kappa}{2\Omega} - \nu\right)\cos(m\theta_{sp} - \chi), \tag{2.13}$$

$$c_{m+1} = \frac{V_{sp}}{2}\left(\frac{\kappa}{2\Omega} + \nu\right)\sin(m\theta_{sp} + \chi), \tag{2.14}$$

$$s_{m+1} = \frac{V_{sp}}{2}\left(\frac{\kappa}{2\Omega} + \nu\right)\cos(m\theta_{sp} + \chi). \tag{2.15}$$

In the general case of more than one mode m, each with its own unique pattern speed $\Omega_{p,m}$, χ_m and $\theta_{sp,m}$, which drives its own streaming motions with amplitude $V_{sp,m}$, we can express the amplitudes of any set of harmonic components as

$$A_{m-1} = \sqrt{c^2_{m-1} + s^2_{m-1}} = \frac{V_{sp,m}}{2}\left(\frac{\kappa}{2\Omega} - \nu_m\right), \tag{2.16}$$

$$A_{m+1} = \sqrt{c^2_{m+1} + s^2_{m+1}} = \frac{V_{sp,m}}{2}\left(\frac{\kappa}{2\Omega} + \nu_m\right). \tag{2.17}$$

Combining A_{m-1}, A_{m+1} with the definition of the dimensionless frequency ν_m in Eq. 2.11 we can obtain the following simple parametrization of the amplitude of velocity perturbation

$$V_{sp,m} = \frac{2\Omega}{\kappa}(A_{m-1} + A_{m+1}). \tag{2.18}$$

The linear combination of j=1 and j=3 amplitudes provides a measure of the streaming motions driven by an m=2 spiral perturbation.

Similarly, the spiral arm pattern speed Ω_p can be expressed as

$$\Omega_{p,m} = \frac{\kappa}{m}\left(\frac{A_{m+1} - A_{m-1}}{v_{sp,m}}\right) + \Omega. \tag{2.19}$$

Note that when $A_{m+1} = A_{m-1}$, $\Omega_p = \Omega$. This is a recasting of the prediction by Canzian (1993) that *corotation* radius (where $\Omega_p = \Omega$) is crossed when the $m - 1$ switches to an $m + 1$ term. However, we emphasize that the pattern speed is likely impossible to estimate reliably in this way, since it depends on κ^2; κ itself can be difficult to accurately constrain with observation and is susceptible to uncertainty as it depends on the derivative of Ω (see Eq. 2.11). For a recent estimation of the radial variation of the spiral arm pattern speed in M51a through the more reliable and model-independent radial Tremaine-Weinberg (TWR) method, we refer the reader to Meidt et al. (2008).

2.5.5.1 Streaming motions in M51

In this section we use the results of the harmonic decomposition and our model of M51's rotation curve to estimate the magnitude of streaming motions (Eq 2.18) driven in response to the bar, dominant two-armed spiral, the three-armed spiral pattern and/or $m = 1$ mode.

We start considering solely the m=2 perturbation of the galactic potential. In this case, the quantity of interest is obtainable from the A_1 and A_3 as:

$$V_{sp,m=2} = \frac{2\Omega}{\kappa}(A_1 + A_3), \tag{2.20}$$

where $\Omega = V_c/R_{gal}$ and κ is given by Eq 2.11.

Fig. 4.17 (Fig. 2.8) shows the amplitude of velocity of the spiral arm perturbation as derived from Eq. 2.20 using the harmonic amplitudes from PAWS 1" residual velocity field as analyzed in Section 2.5.2. In the nuclear bar region ($R_{gal} <$ 23") streaming motions are $\langle V_{sp,m=2}(R_{gal} <$ 23")$\rangle \approx$ 60 km s^{-1}, in the PAWS 1" data set. Further the streaming motions reach the highest values with a median of $\langle V_{sp,m=2}(35 < R_{gal} <$ 60")$\rangle \approx$ 700 km s^{-1} in PAWS 1" than it decreases again to values around $V_{sp,m=2}(60 < R_{gal} <$ 85")$\rangle \approx$ 50 km s^{-1}. However in the lower resolution surveys (i.e. THINGS 6", HERACLES 13.5" and PAWS single dish 22.5"), $\langle V_{sp,m=2}\rangle$ is always below $\sim$ 50 km s^{-1} and reaches a value comparable to that recorded in PAWS only in the region of the material arms ($R_{gal} >$ 85"). This behavior could be due to beam smearing that reduces the observed peak in streaming motions. As discussed in Section 2.7, in the case of HI, this could be also due to an intrinsically different response to the spiral perturbation of the potential. In all cases, the spiral perturbation velocity drops in the molecular ring region reaching the minimum of $V_{sp,m=2} \approx$ 25 km s^{-1} for PAWS 1", as expected from an analysis of the gravitational torques (Meidt et al. 2013).

In Fig. 2.8 we plot also the radial profile of streaming motions that corresponds to the m=3 and

$m = 1$ perturbations, calculated according to:

$$V_{sp,m=1,3} = \frac{2\Omega}{\kappa}(A_2 + A_4), \tag{2.21}$$

As described in the previous section, we expect these motions to be related to the $m = 3$ wave between 20" $< R_{gal} <$ 45" (i.e., 0.8 kpc $< R_{gal} <$ 1.7 kpc), where we observe a peak in the j=2 term switching to a peak in a $j = 4$ term in the residual velocity field. The start of the m=3 mode is taken as the location where the j=2 term increases above our 10 km s^{-1} confidence threshold, while the end of the m=3 mode is set by the decrease in the power of the j=4 term. This zone is consistent with the radial range over which the larger deviation from a pure $m = 2$ mode was identified (1 kpc $< R_{gal} <$ 2.2 kpc, Henry et al. 2003). Across this zone, the m=3 mode drives streaming motions of $V_{sp,m=3} \approx 25 - 30$ km s^{-1} on average with minimum below the confidence limit of 10 km s^{-1} in the ring region. (Note that there is no power in the zone of the bar $\langle V_{sp,m=1,3} \rangle \approx 12$ km s^{-1} only slightly above our confidence limit). At larger radii, the streaming motions arise from a lopsided (m=1) mode (only $j = 2$ appears in the harmonic expansion, i.e. A_4 ~0), with a magnitude of $\langle V_{sp,m=1} \rangle \approx 32$ km s^{-1}.

2.6 DISCUSSION: AN m=3 POTENTIAL PERTURBATION IN M51

In the previous sections we presented kinematic evidence for the existence of an m=3 mode, which supplies confirmation of an m=3 perturbation to M51s gravitational potential first investigated by Elmegreen et al. (1992). This mode is spatially coincident with the inner part of the dominant two-armed spiral. Presumably, the interference of an $m = 3$ wave with the $m = 2$ wave enhances the asymmetry in the velocity field (i.e. increasing the deviation in iso-velocity contours from pure circular motion.) This would seem to support the interpretation of Meidt et al. (2008), who consider the likelihood that their TWR pattern speed estimate calculated using CO(1-0) as a kinematic tracer reflects a combination of that of an m=3 mode with that of the dominant two-armed spiral.

This conclusion moreover supports the finding of Henry et al. (2003), who reconsidered the evidence for an m=3 perturbation in the old stellar light distribution first studied by Rix & Rieke (1993). They claim that the magnitude of the $m = 3$ component in K-band is sufficient to account for the offset between the mirror of one of the two main spiral arms and its counterpart. They also observe patches of molecular gas and star formation in the inter-arm at the location of one of the three arm segments imaged in the K-band.

In the next section we consider the origin of this m=3 mode and its density-wave nature, taking into account our analysis of the gas response.

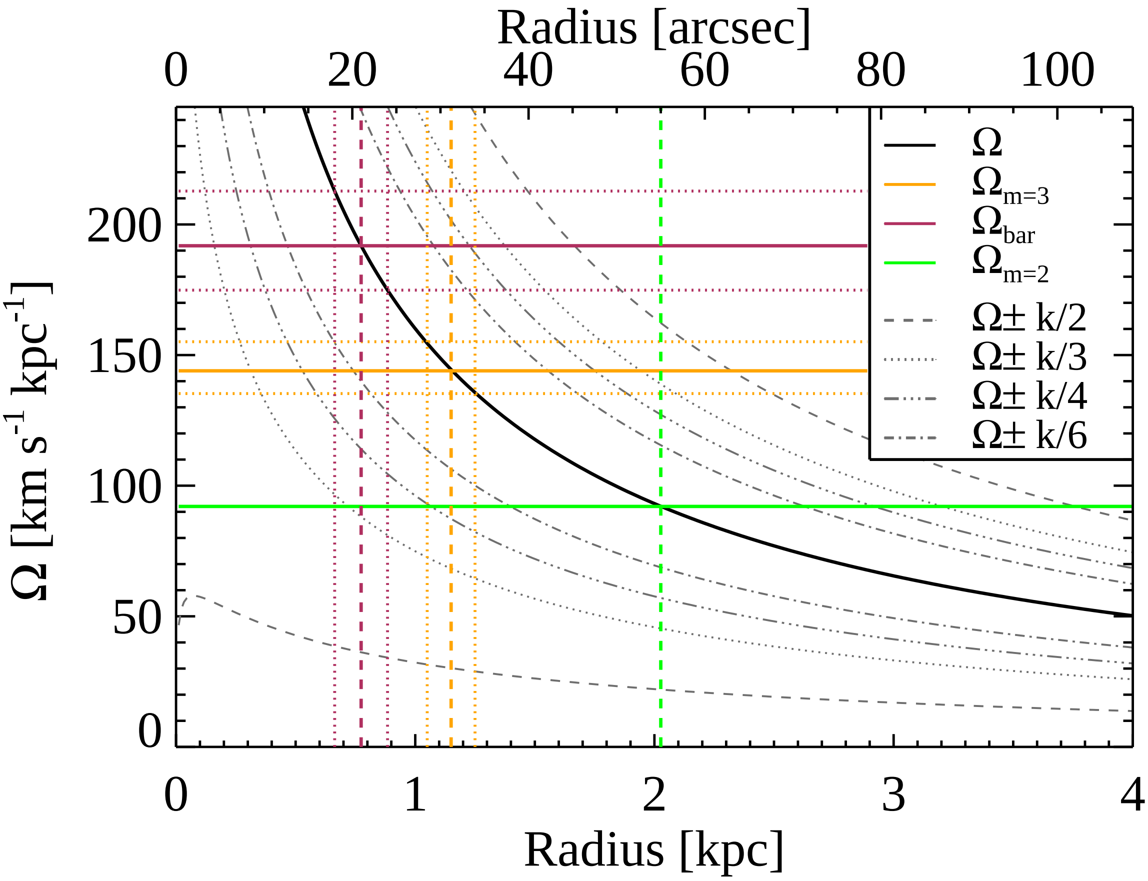

Figure 2.9: Angular frequency curves derived from the gas-based rotation curve of M51: Ω (black solid), $\Omega \pm \kappa/2$ (grey dashed), $\Omega \pm \kappa/3$ (grey dotted), $\Omega \pm \kappa/4$ (grey dashed dotted-dotted-dotted) $\Omega \pm \kappa/6$ (grey dashed-dotted). Pattern speed estimates for the nuclear bar, spiral arms, and m=3 density-wave in M51 are shown in dark red, green and orange (respectively) together with their corotation resonance radii and uncertainties when available.

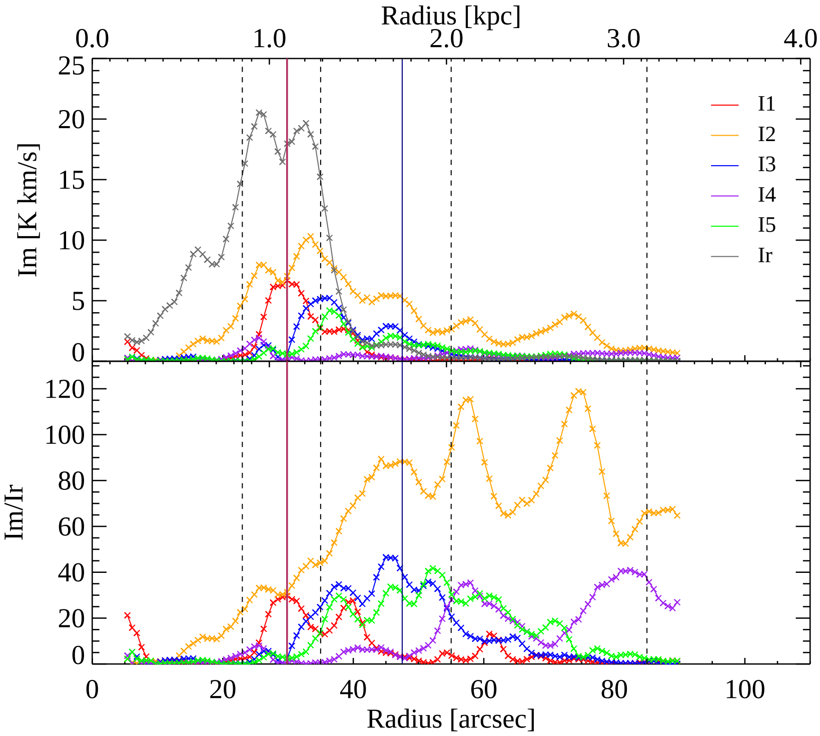

Figure 2.10: Fourier decomposition of the surface brightness from the PAWS 3" zeroth moment map. Power of the Fourier component in K km/s (top). Fourier components normalized by the total power Ir (bottom). The vertical blue line indicates the boundary between $m = 3$ and $m = 1$ dominance estimated in Section 2.5.5.1. The red vertical line represents the $m = 3$ corotation at $R_{gal} \sim 1.1$ kpc. Dashed vertical lines indicates M51's environments as defined in Meidt et al. (2013)

2.6.1 ORIGIN AND NATURE OF THE $m = 3$ MODE

The PAWS 1" residual velocity field shows a clear kinematic signature of a m=3 wave in the central region of M51a. According to Fig. 2.7 we place its corotation radius at $R_{CR,m=3} \approx (30 \pm 3)$" (i.e. $R_{CR,m=3} \approx 1.1 \pm 0.1$ kpc). Together with the angular frequency derived by Meidt et al. (2013), we can define the pattern speed of $\Omega_{m=3} \approx 140 \pm 9$ km s^{-1} kpc^{-1}. The result is shown in Fig. 2.9.

With such a pattern speed, the m=3 density-wave could be driven by the nuclear bar of M51, given the overlap of resonances between the two structures (see Fig. 2.9). Zhang & Buta (2012) derived a corotation radius $R_{CR,b} \approx 0.8 \pm 0.1$ kpc for the nuclear bar of M51 using a potential-density phase shift method (consistent with the estimate of Meidt et al. 2013). This corotation overlaps with the inner ultra harmonic resonance (UHR) of the $\Omega_{p,m=3}$ pattern speed (where

$\Omega_{p,m=3}$=$\Omega - \kappa/6$). Such resonance overlaps have been found before in simulations between bars and two-armed spirals, for which the inner UHR occurs where ($\Omega_{p,m=2}$=$\Omega - \kappa/4$).

Interestingly, the corotation of the dominant two-armed spiral overlaps with the outer Lindblad resonance (OLR) of the $m = 3$ wave (where $\Omega_{p,m=3} = \Omega + \kappa/3$). This may be an instance of non-linear mode coupling, as demonstrated in Fig. 2.10 showing the power in the Fourier decomposition[6] modes of the PAWS CO (1-0) surface brightness at 3". There we see power in m=1 and m=5 modes, in agreement with predictions by Masset & Tagger (1997) (and studied by Rautiainen & Salo 1999) that coupling between $m = 2$ and $m = 3$ modes should generate $m = 1$ and $m = 5$ beat modes. The $m = 1$ and $m = 5$ modes are particularly strong and confined within the region of influence of the $m = 3$ ($R_{gal} < 45$"). Moreover the $m = 1$ mode is peaked exactly at the $m = 3$ corotation of $R = 1.1$ kpc.

The presence of the m=3 mode is therefore arguably responsible for introducing the lopsidedness (m=1) in the CO brightness in the inner portion of the two main spiral arm segments. Perhaps more importantly, the m=3 wave itself appears to provide the link between the bar and two-armed spiral. Consider that the coincidence of the bar CR and m=3 UHR is much tighter than that between the bar CR and two-armed spiral inner Lindbland resonance (ILR), which has been previously suggested as their primary link (Meidt et al. 2013). There is furthermore no other compelling direct link between the bar resonances (CR, OLR) and those of the m=2 spiral (ILR, UHR, CR). Instead, the $m = 3$ wave is associated with several other interesting resonance overlaps, giving us a picture of very specific interaction between waves. The OLR of the m=3 (where $\Omega_{p,m=3} = \Omega + \kappa/3$) overlaps with the corotation radius of the main m=2 spiral pattern, while the CR of the m=3 corresponds to the inner UHR of it (where $\Omega_{p,m=2} = \Omega - \kappa/6$). The $m = 3$ mode itself extends out to $R_{gal} \sim 1.7$ kpc (according to where the amplitude of $j = 4$ is significant/above our confidence threshold), which is very close to the bar's OLR, the outermost extent of its gravitational influence.

Presumably, the particular m=3 structure we find exists in order to couple the bar, which we expect appears as a natural instability of the rotating stellar disk, with the two-armed spiral that extends out to larger radii, and which is presumably independently excited by the interaction with M51b; in the presence of the m=3 wave, energy and angular momentum can be continually transferred radially outward. We therefore interpret this as strong evidence in favor of the density-wave nature of the $m = 3$ mode. The transience or longevity of this feature, on the other hand, cannot be assessed with our observational data, which provides a snapshot of the current state of M51. We note, though, that multiple spiral structure is generally associated with transient, quickly-evolving spiral arms (e.g. Toomre 1981, Fuchs 2001, D'Onghia et al. 2013). Since we

---

[6] The Fourier decomposition of the surface brightness is analog to the harmonic decomposition of the residual velocity fields performed in Section 2.5.2, however the amplitudes of the Fourier modes for $m = 1 - 5$ are given by $I_m = \sqrt{s_m^2 + c_m^2}$.

would argue that the coincidence of a three-fold potential perturbation with that of the main $m = 2$ pattern definitively excludes a single mode in M51 (like Lowe et al. 1994; Henry et al. 2003) our finding may therefore favor theories of multiple, quickly-evolving density wave spirals.

At larger radii, the residual velocity field harmonic decomposition indicates that the m=2 wave may be spatially coincident with an $m = 1$ perturbation to the potential. This perturbation is likely responsible for the lopsidedness in K-band images identified, e.g. by Rix & Rieke (1993). To reliably connect the origin of this feature to the interaction with M51b, new high resolution data beyond the PAWS FoV are necessary.

2.7 DISCUSSION: THE OPTIMAL DATASET FOR KINEMATIC STUDIES

2.7.1 RESOLUTION CONSIDERATIONS

In the previous section we discussed evidence for the existence of an m=3 wave spanning 0.8 kpc $<R_{gal}<$1.7 kpc (i.e. $20 < R_{gal} < 45$”) in the center of M51a. The kinematic signature of such a weak, compact mode is reliable only when analyzing the PAWS residual velocity field at resolution of 1”. At lower spatial resolution (even with equivalent channel widths), the presence of a such weak mode becomes less obvious (see Section 2.5.2). Given that the dominant molecular spiral arm width is around 400 pc (Schinnerer et al. 2013), it is not surprising that high resolution data are needed for an accurate kinematic characterization of the structures traced out in molecular gas. Other small scale kinematic features, such as the bright and high-velocity dispersion core of M51a and the spurs on the downstream side of the spiral arms, also only become clearly visible in high resolution maps.

Data sets at low resolution, which are less sensitive to non-circular motions, on the other hand, are key for obtaining reliable estimates of the kinematic parameters (i.e. position angle and inclination, which describe the projection of the galactic disk on the plane of the sky) as well as the rotation curve itself. When the spiral arm is not well resolved, the gas kinematics are dominated by the bulk rotation of the disk. But in the presence of peculiar kinematic features, such as evident at high resolution, the rotation curve shows prominent wiggles that are hard to interpret (see Section 2.4.3).

2.7.2 CHOICE OF TRACER/OBSERVING STRATEGY

Perhaps more critical to the results of in-depth kinematic analysis than resolution is the nature and distribution of the kinematic tracer. This includes the phase of the tracer and the observing strategy chosen to obtain a given dataset. To understand this we have to consider that in the first moment map the velocity channels are weighted by the signal of the single pixel (Eq. 4.10) and the line-of-sight velocity will tend to the velocity of the channel where the signal is maximum. Accordingly, if we want to characterize the spiral arm gas kinematics we would choose a gas phase that is strongly affected by the mid-plane galactic potential and interferometric observations that are able to resolve them.

2.7.2.1 CO VERSUS HI

In Fig. 2.12 we compare residual velocity fields derived from data cubes smoothed to the same resolution and pixel size. The operations are performed using the `MIRIAD` task `CONVOL` and `REGRID`, respectively. To illustrate the difference between residual velocity fields more quantitatively, we present pixel-by-pixel analysis. The righthand panel shows the pixel-by-pixel comparison of these fields, where the density of the data points is represented by logarithmically spaced contours. Each scatter plot is fit using the `FITEXY` procedure of IDL where all input pixels are attributed an equal, unitary weight.

Consider, first, the top row in Fig. 2.12, showing the kinematic differences between ^{12}CO(1-0) PAWS observations tapered to 6” and THINGS robust weighted data at 6”, with the same pixel scaling and FoV. Despite the fact that these are at the same resolution, the two residual velocity fields look very different. PAWS at 6” appears as a smoothed version of the PAWS 1” residual velocity field, but retains several of the main kinematic features such as the “butterfly” pattern caused by the nuclear bar and the streaming motion from the southern arm. In the THINGS data, though, these features are largely washed out and the map is globally more homogeneous.

The pixel-by-pixel comparison confirms that a large scatter is present between values measured in the two residual velocity fields. Such differences naturally influence the measurement of the velocity associated with the potential perturbation V_{sp} (Fig 2.11), which depends on the amplitude of (non-circular) harmonic components in the residual velocity field (see Eq. 2.18). Whereas the streaming motion magnitude from PAWS 1” and PAWS 6” are basically equal (with the trend from PAWS at 6” appearing as a “smoothed” version of the PAWS 1”), the value derived from THINGS 6” is on average $\sim$ 35 km s^{-1} lower than V_{sp} obtained from PAWS 6” in the region between $R_{gal} \sim 60 - 80$”. Given that the data in this comparison have identical (spatial and spectral) resolution, the reason behind this behavior must be physical.

Indeed, the HI emission is naturally smooth at all spatial scales while the CO radiation is highly clumpy (Leroy et al. 2013a). In addition, the radial and vertical distributions of the two emissions in spiral galaxies could be different. In a recent paper, Schinnerer et al. (2013) analyzed the relationships between the molecular gas, other ISM tracers and stellar populations within the PAWS FoV. While the CO emission correlates very well with the old stellar population traced with the dust-corrected 3.6 μm emission and responsible for the gravitational potential, the CO and HI do not trace each other and the strongest emission in each line originates from different locations within the PAWS FoV. The HI, in particular, appears strongest at the location of recent star formation, which in M51 takes place slightly downstream of the spiral arms, rather than at the minimum of the potential well where the molecular gas traced by CO tends to sit.

The vertical distribution of the two gas phases could also be different. Differences between the scale heights of molecular and atomic hydrogen gas disks are expected, given the difference in the measured velocity dispersion of the two components.[7] Whereas the HI velocity dispersion in M51 is $\sigma \approx 15$ km s^{-1} (Tamburro et al. 2009), the PAWS CO compact emission suggests a much narrower line, $\sigma \sim 5$ km s^{-1} (see Appendix). As a result of the different vertical distributions, these two ISM phases may trace the potential slightly differently. If the atomic gas, for one, sits further away from the mid-plane and thus experiences a slightly weaker potential, this could naturally translate in to a reduction in the magnitude of streaming motions traced by HI observations.

2.7.2.2 HYBRID VERSUS SINGLE-DISH DATA

Single-dish observations are more sensitive to extended, diffuse emission (on the largest spatial scales) than interferometric observations, which tend to reveal emission from compact structures (e.g. Pety et al. 2013). For this reason, the observational strategy may effect the way a given gas phase observation traces motions driven in response to the gravitational potential. Single dish observations, in particular, may be more sensitive to fluffy emission from a more vertically extended component, as was recently discovered in the 30m and hybrid 30m+PdBI observations of M51 by Pety et al. (2013). As discussed at the end of the previous section, this may prevent single-dish observations from revealing the same pattern of streaming motions as obvious with hybrid data even at degraded resolution.

The middle of Figure 2.12 shows this in a little more detail, comparing the PAWS and HERACLES residual velocity fields smoothed to the same 13.5” resolution.[8] Even at 13.5”, the PAWS

---

[7] According to Koyama & Ostriker (2009a) the scale height of the gas is proportional to the vertical velocity dispersion.

[8] To put the two residual velocity field on the same resolution we smoothed PAWS tapered at 6” to the HERACLES resolution of 13.5”.

residual velocity field still exhibits the typical signatures of bar and spiral arm streaming motions. But these departures from circular motion are less clearly visible in the HERACLES residual velocity field. The pixel-by-pixel diagram confirms that the two maps are not the same, as large scatter is present.

The line-width measured from HERACLES IRAM 30m observations is significantly larger than measured from PAWS at 1”. Some part of this could be due to unresolved bulk motions. On the other hand, Caldu-Primo et al. (in preparation), using a sophisticated stacking method, measure similar velocity dispersions for CO from HERACLES and HI from THINGS observations in a sample of 12 galaxies, which would imply that the two phases have similar vertical distributions. They find, for M51 in particular, $\sigma_{HI} \sim \sigma_{CO} \approx 15$ km s^{-1}. This value is comparable to the velocity dispersion of the extended CO component measured by Pety et al. (2013) for M51, rather than the compact CO emission that dominates the PAWS second moment map (see Appendix). This suggests that the single-dish data are dominated by the vertically extended gas than the hybrid data, which mainly traces gas that is more confined to the disk mid-plane, and thus more influenced by the gravitational potential.

We have considered whether the difference between HERACLES and PAWS at 13.5” resolution arises from the fact that the two observations sample two different tracers of the molecular gas; while PAWS traces ^{12}CO(1-0) emission, HERACLES traces ^{12}CO(2-1) that originates from slightly denser and colder regions of molecular clouds. In the last row of Fig 2.11, we compare the residual velocity fields from the PAWS single-dish data with HERACLES observations, smoothed to the same 22.5” resolution. Since both observations have been obtained with the same instrument (IRAM 30m antenna), instrumental effects should be negligible. These maps show only small differences, and the scatter in the pixel-by-pixel comparison is very low. We conclude that, from a kinematic point of view, single-dish observations of ^{12}CO(1-0) and ^{12}CO(2-1) provide similar results.

In summary, the CO emission (at least its brighter part) has a radial and vertical distribution that correlates very well with the location of the spiral potential in M51. The HI, instead, is organized in a thicker disk and its brighter emission does not coincide exactly with the spiral arms. Assuming that M51 is a prototypical grand-design spiral galaxy, we conclude that interferometric observations of molecular gas constitute an optimal choice for kinematic characterization of the galactic potential in spiral galaxies. The atomic gas, which may sit at a slightly different location relative to the potential minimum, can be expected to show a different, perhaps weaker pattern of streaming motions. This is especially true if it also resides in a thicker disk and thus traces the mid-plane stellar potential less directly. Observations of this gas phase should still be considered preferable for measuring the bulk motion of the galaxy (i.e. the rotation curve) and determining other global kinematic parameters.

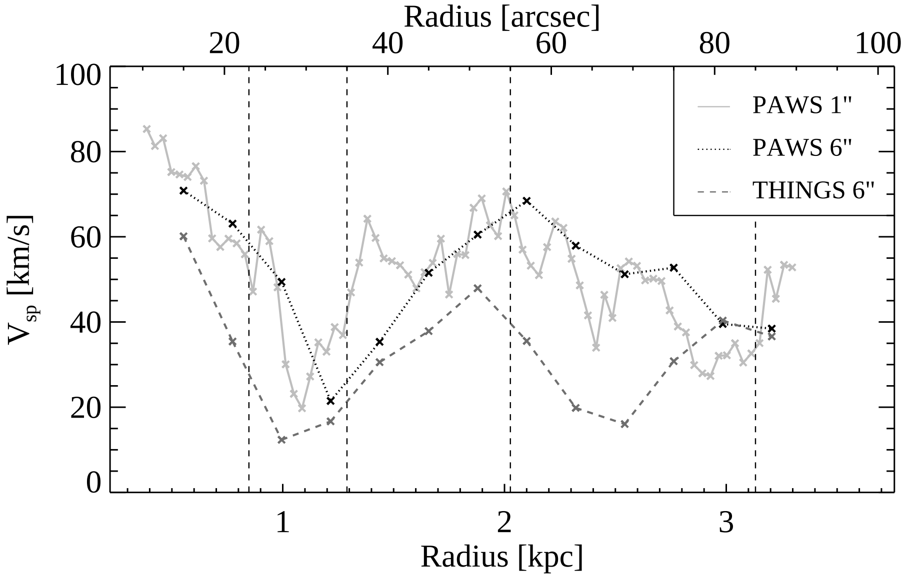

Figure 2.11: Amplitude of the two-armed spiral arm perturbation derived from PAWS 1", PAWS 6" and THINGS 6". Vertical dashed lines represent M51's environments as defined in Meidt et al. (2013)

2.8 SUMMARY AND CONCLUSIONS

In this Chapter we performed a detailed kinematic analysis of the inner disk of M51 with the aim of characterizing and quantifying the non-circular motions driven in response to the bar and spiral patterns present in the disk. Our primary focus is the view of gas motions presented by the high resolution PAWS 1" ^{12}CO(1-0) data set, in addition we support the interpretation of our findings with other lower resolution datasets (PAWS 3" ^{12}CO(1-0), THINGS 6" HI, HERACLES 13.5" ^{12}CO(2-1) and PAWS single dish 22.5" ^{12}CO(1-0)). Our main results are summarized as follows:

- The PAWS 1" velocity field exhibits several unique kinematic features (a highly redshifted core, a bar-induced twist in the line-of-nodes and strong spiral streaming motions) that become progressively smeared out with decreasing spatial resolution.

- By applying a tilted ring analysis on the different velocity fields, we determined updated estimates of projection parameters of M51, namely position angle $PA = (173 \pm 3)^\circ$ and inclination $i = (22 \pm 5)^\circ$. We use these to fit for the circular velocity in each of the data sets. All rotation curves show wiggles caused by the azimuthal contribution of spiral arm streaming motions. Those wiggles are progressively attenuated (but still present) with decreasing spatial resolution.

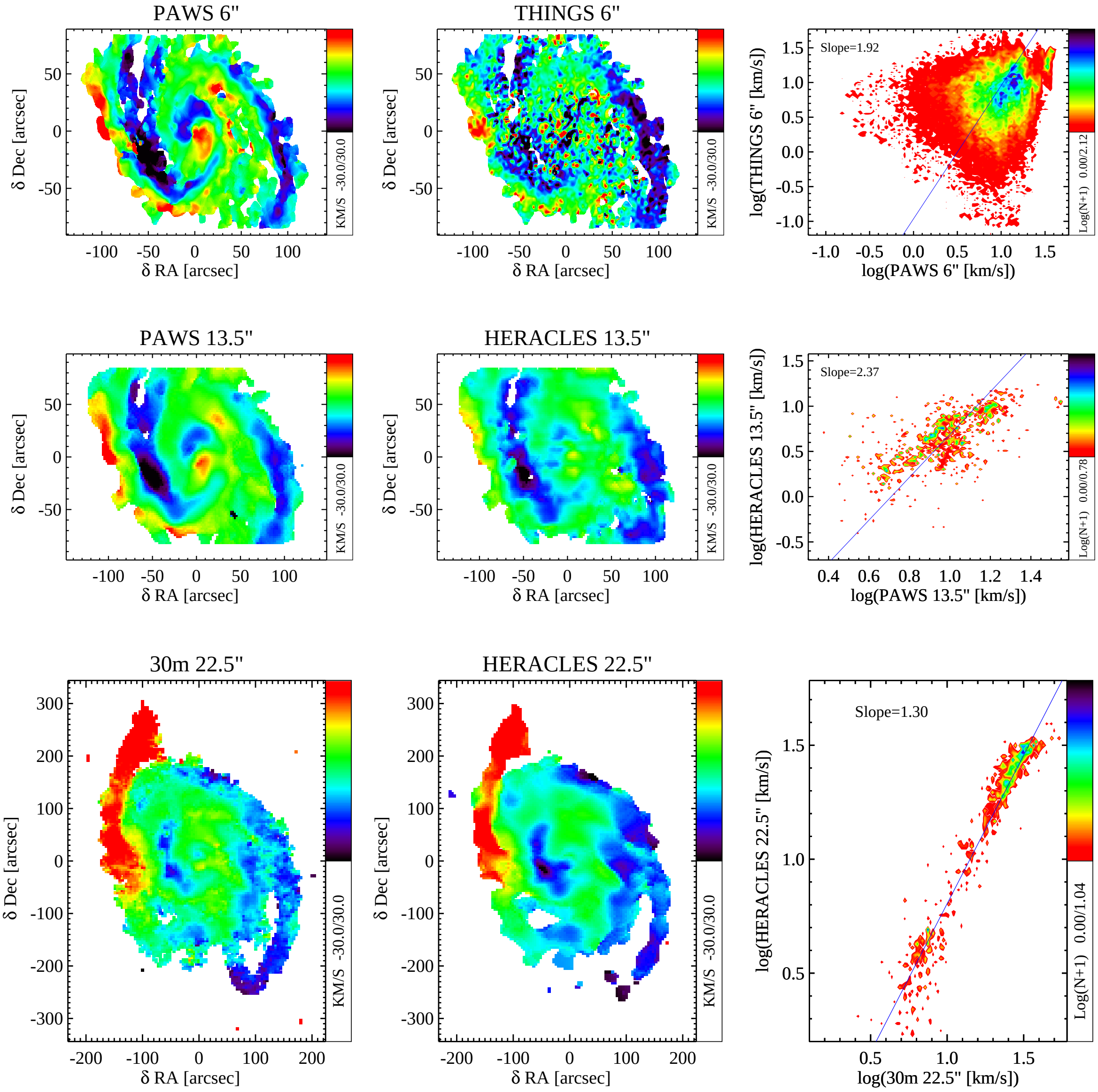

Figure 2.12: Comparison between PAWS 6” and THINGS 6” (top), PAWS 6” smoothed to 13.5” and HERACLES, PAWS single dish and HERACLES smoothed to 22.5” (bottom) residual velocity fields, on the same pixel size and FoV. The right panels show the pixel-by-pixel comparisons of the residual velocity fields in value of the pixels. Number density of the points are in logarithmic scale.

- We perform a harmonic decomposition of the residual velocity fields in order to identify, separate and inspect the contributions of the different modes to the global pattern of non-circular motions in the galaxy. The residual velocity field of M51 is complex, but shows the clear signature of arm-driven inflow (especially along the southern arm) and the butterfly pattern of the inner bar.

  - The dominant $m = 2$ mode is characterized by a corotation radius at $R_{CR,m=2} \approx 2.4$ kpc ($R_{CR,m=2} \approx 60$”), consistent with location of the corotation of the two-armed spiral indicated by the gravitational torque analysis of Meidt et al. (2013).
  - Coincident with this mode, we find the first unequivocal evidence for an $m = 3$ mode in the inner disk of M51, extending out to $R_{gal} \approx 1.7$ kpc ($R_{gal} \approx 45$”). The kinematic signature of this mode allows us to estimate the location of its corotation radius $R_{CR,m=3} \approx 1.1 \pm 0.1$ kpc ($R_{CR,m=3} \approx 30 \pm 3$”).
  - Inspection of the angular frequency curves suggests that the $m = 3$ mode may be coupled to, and stimulated by, the nuclear bar. Evidence for the dynamical coupling between the three-armed spiral and the main two-fold pattern at the overlap of their resonances is suggested by the appearance of $m = 1$ and $m = 5$ components in the CO surface brightness around the overlap. This supports the density-wave nature of the three-armed perturbation to the potential traced by the gas motions. This mode, together with an $m = 1$ evident at large radii may be responsible for the lopsided appearance of M51 that persists from small to large radii.

- Combining the amplitudes of the individual harmonic components, we obtained a simple expression for the streaming motion amplitude of the main modes in M51.

  The streaming motions from the main m=2 mode range from $\langle V_{sp,m=2} \rangle \approx 70$ km s^{-1} in spiral arm region devoid of star formation to $\langle V_{sp,m=2} \rangle \approx 50$ km s^{-1} in the outer density-wave spiral arms, and exhibit a minimum $\langle V_{sp,m=2} \rangle \approx 25$ km s^{-1} in the molecular ring region.

  The streaming motion from the secondary modes ($m = 1, 3$) are $V_{sp,m=3} \lesssim 30$ km s^{-1} in the region influenced by the $m = 3$ mode and $\langle V_{sp,m=1} \rangle \approx 32$ km s^{-1} in the region dominated by the $m = 1$ mode, but no higher than $V_{sp,m=1,3} \approx 20$ km s^{-1} in the bar region.

- The joint analysis of velocity fields obtained from different gas tracers at different resolutions suggests the following guidelines for defining the most appropriate observing strategy to meet a given scientific goal:

  - high resolution CO surveys are particularly well-suited for detailed studies of non-circular motion features, while low resolution observations are equally as important for defining the bulk motion of the galaxies (i.e. rotation curves). In the presence of modes that extend over only a limited radial range, as in M51, and when complex, overlapping structure exists generally, high resolution is key to identifying and characterizing such modes.

- CO and HI can supply independent views of the gravitational potential, as suggested by different natures of the two gas phases; while the atomic gas in M51 has a smooth distribution, is located mostly downstream of the spiral arms and in a thicker disk, the molecular gas is more compact, organized in a thinner disk and mostly confined to the spiral arms. Given the differences in velocity dispersion and morphology, we conclude that CO is optimal for tracing spiral arm streaming motions and, in general, for studying the galactic potential, while HI is more suitable for obtaining the bulk motion and the projection parameters of the galaxies.

3

THE PAWS GIANT MOLECULAR CLOUD CATALOG*

CONTENTS

Using data from the PdBI Arcsecond Whirlpool Survey (PAWS), we have generated the largest extragalactic Giant Molecular Cloud (GMC) catalog to date, containing 1,507 individual objects through an automatic algorithm (`CPROPS`) that corrects for survey biases. GMCs in the inner M51 disk account for only 55% of the total ^{12}CO(1-0) luminosity of the survey, but on average they exhibit physical properties similar to Galactic GMCs. In this Chapter, we underlie some challenges of using existing GMC identification techniques for decomposing the ^{12}CO(1-0) emission in molecule-rich environments, such as M51's inner disk. In particular, using the default emission segmentation of `CPROPS`, several eye-identifiable objects are not decomposed. Therefore, we have made several tests in order to define the most appropriate parameter setup for PAWS. Through the performance requirements of the algorithm we discuss the reliability of the bias corrections. The sensitivity correction of `CPROPS` appears necessary to account for the property differences of GMCs and for the flux within them. Nevertheless this correction introduces a certain amount of scatter in the data. `CPROPS` has the tendency to decompose structures around the resolution limits. This behavior must be taken into account when comparative studies of GMCs are performed.

3.1 INTRODUCTION

One of the major issues faced by all studies of GMCs to date is the cloud identification. Indeed, unlike stars and planets, GMCs do not have a well-defined edge or surface, which makes it non-

---

[*] This chapter is adapted from Colombo et al. 2013a, ApJ submitted.

trivial how to attribute a certain amount of CO flux (preferred tracer of the molecular gas) to a given object. However, the CO emission appears naturally clumpy (e.g. Leroy et al. 2013a) and is organized in cloud-like structures (Sanders et al. 1985). This legitimates the identification of individual entities for the construction of cloud catalogs. To this aim, many techniques have been used by different authors. The earliest studies cataloged clouds simply by eye. The pioneering work of Sanders et al. (1985) utilized contours at 3σ to identify individual objects. Later, Solomon et al. (1987) used appropriate antenna temperature levels as contour criterion for cloud identification. Most of the GMC properties in their catalog were also "extrapolated" to the 1 K level, since it was not possible to separate single objects in crowded environments. But in fact, the "by eye" identification works only as long as the structures are not blended together. In presence of strong blending, it becomes non straightforwards for the eye to divide up the blended emission accurately and correctly describe the clouds. Part of the problem is the difficulty in visualizing a full three-dimensional cube using only two-dimensional slices. Moreover the "by-eye" identification introduces an unavoidable bias due to human subjectivity and is basically unfeasible for large CO dataset.

To overcome these limitations a number of automatic routines has been developed; computer programs can handle large datacubes efficiently and objectively, making possible uniform comparisons of large samples of clouds. The first attempt in this direction was made by Stutzki & Guesten (1990), i.e. the `GAUSSCLUMPS` algorithm that iteratively fits a three dimensional intensity distribution with a series of individual triaxial Gaussian clumps (see also Kramer et al. 1998). The procedure works in a similar way to the CLEAN algorithm, used in interferometric imaging. However, a 3D Gaussian is probably only a rough approximation of the real shape of the molecular clouds likely suitable for extragalactic observation where the beam filling factor is generally lower than the unity. In the Galaxy indeed, real GMCs show a variety of shapes that have little resemblance with Gaussians.

The `CLUMPFIND` algorithm (Williams et al. 1994) uses a friend-to-friend procedure to better reproduce the work of the human eye and decompose the emission within a single cloud. This algorithm contours the data into a finite number of intensity steps, assuming a one-to-one relation between peaks in the intensity profile and clumps. At the "blending level" between two or more clumps, the flux is equally distributed between the clumps. Thus `CLUMPFIND` is flux conservative, i.e. all the flux within the GMCs is assigned to individual clumps. But, in this sense, `CLUMPFIND` is not suitable for decomposing single GMCs in a 3D datacube, since recent observations have shown that a significant amount of CO flux is diffuse (i.e. Sawada et al. 2012, Pety et al. 2013).

The `CLUMPFIND` and `GAUSSCLUMPS` algorithms have been compared by Schneider & Brooks (2004) who used both to analyze the Carina molecular clouds. They found that the properties of the clumps differ significantly when measured by the two procedures and in some cases the results where exactly opposite. This was underlined by Rosolowsky & Leroy (2006), who suggested that differences between the GMCs in the literature could be attributed partially to the methodological approach or to observational biases. To account for the latter, those authors developed a powerful procedure, Cloud PROPS (`CPROPS`) designed especially for extragalactic datasets able to correct for resolution and sensitivity biases. We use this algorithm to generate the PAWS catalogs.

In Section 3.2 we briefly describe the `CPROPS` algorithm. The `CPROPS` tuning parameters have been tested in order to find a recipe suitable for the type of emission recorded within the PAWS data cube. The tests are described in Section 3.3. `CPROPS` provides two catalogs: 1) islands, or connected regions in the *position-position-velocity* (ppv) space and 2) GMCs that better resemble Galactic clouds. The property calculation through moment measurements used by `CPROPS` is described in Section 3.3.2. The PAWS catalogs of islands and GMCs are finally presented in Section 3.4. Using the `CPROPS` performance requirements we discuss the reliability of the catalog in Section 3.6, together with the effects of `CPROPS` bias correction with the galactic environments defined for M51. Finally we explore the degree of scatter introduced by these bias corrections on the "Larsons laws" in Section 3.7.

3.2 CPROPS DESCRIPTION

We used the `CPROPS` package (Rosolowsky & Leroy 2006, herafter RL06) to identify GMCs and measure their physical properties. `CPROPS` has been fully described in RL06. In this Section, we provide a brief summary of `CPROPS` in order to explain the construction of the PAWS GMC and island catalogs.

`CPROPS` begins by identifying a "working area", i.e. regions of significant emission within the data cube. This is done by masking pixels in two consecutive velocity channels in which the signal is above $t\sigma_{RMS}$ (`THRESHOLD` parameter in CPROPS). These regions are then extended to include all adjacent pixels in which the signal is above $e\sigma_{RMS}$ (`EDGE` parameter in `CPROPS`) in at least two consecutive channels. The RMS noise σ_{RMS} is estimated from the median absolute deviation (MAD) of each spectrum.

After defining the working area, `CPROPS` proceeds to generate a catalog of *islands*, emission structures within the working area with a projected area of at least one telescope beam and spanning one or more velocity channels. This kind of approach can be sufficient to catalog discrete molecular structures in irregular and flocculent galaxies, where the emission is typically sparsely distributed within the observed field (e.g. the LMC, Wong et al. 2011). For the PAWS data cube, by contrast, bright CO emission extends throughout the inner spiral arms and across the central region, and is hence identified as a single island. Islands in M51 shows little resemblance with Galactic GMCs and there are not deeply analyzed in this thesis work. The general properties of the island identified within the PAWS FoV are briefly reported in Section 3.4.1 together with the island catalog.

To identify structures that resemble Galactic GMCs, we used a "data-based" decomposition to further segment the islands. These objects are defined using a modified watershed algorithm: local maxima (called "kernels" in `CPROPS`) within a box of 120 pc × 120 pc and 15 $\mathrm{km\,s^{-1}}$ are recognized as independent objects if they lie at least $2\sigma_{RMS}$ above the shared contour (called the "merge level" in `CPROPS`) with any other maximum. By default, `CPROPS` requires that the moments associated with other maxima differ by 100%, otherwise the two maxima are merged into a single cloud. We found that this condition does not work well for the PAWS data, causing `CPROPS` to reject a large number of objects that visual inspection would suggest are GMCs.

Being the first time that `CPROPS` was employed on a crowed dataset as the PAWS one we performed some test on the GMC identification pipeline as described in the next section.

3.3 GMC CATALOG GENERATION

In its fundamental form the `CPROPS` package consists of two sub-pipelines. The first one decomposes all significant emission into smaller substructures. Those substructures are used as starting seeds to derive GMC (or island) properties. The decomposition pipeline can be tuned in a number of ways in order to accommodate the desired analysis or the intrinsic characteristics of the emission in the data cube. The property calculation package treats a decomposed cloud as an isolated object completely separated from the environment in which it has been identified. This second pipeline is practically fixed and depends only on the cloud mask provided by the first pipeline. As a final step, `CPROPS` applies a correction for the biases from instrumental resolution and sensitivity. These processes can significantly alter the property measurements of the initial cloud, but allow for a proper definition of the actual GMC (or island) characteristics. In the following we summarize tests we made in order to ensure an efficient cloud decomposition and to prove the reliability of the catalog given the performance requirements of `CPROPS`.

To obtain the PAWS GMC catalog, `CPROPS` has been set as followed:

- `THRESHOLD` = 4
- `EDGE` = 1.5

- `MINVCHAN` = 1
- `BOOTSTRAP` = 50
- `SIGDISCONT` = 0
- `/NONUNIFORM`

Both decompositions (islands or GMCs) share a similar set of initial parameters. However, for the generation of a the island catalog the connected regions in the *ppv* cube do not need to be decomposed in substructures. Therefore this catalog requires the additional keyword, `/NODECOMPOSITION` to be set. To create the GMC catalog, moreover, `CPROPS` can be tuned in number of different ways (see RL06). `SIGDISCONT` is part of this set of parameters that can be optimized.

Due to the high resolution and large size of the PAWS data cube (935 pixel × 601 pixel × 120 channels), `CPROPS` required a long computational time to analyze the properties of the identified GMCs. To overcome this limitation, the cube was divided in 28 sub-cubes with approximate dimensions of 300 pixel × 300 pixel × 120 channels and every sub-cube was analyzed individually. `CPROPS` decomposition was performed in the central part (200 pixel × 200 pixel × 120 channels) of each sub-cube to avoid edge effects. The splitting scheme was such to ensure enough overlap between sub-cubes so that objects at the edge of the sub-cubes were not lost from the analysis. A procedure to re-build the catalog has been used, taking into account the astrometry of single sub-cubes.

3.3.1 TESTING CPROPS DECOMPOSITION PARAMETERS

In order to test the GMC identification capability of `CPROPS` in different environments, three regions of the PAWS data cube have been used: a part of the southern spiral arm (hereafter: *SA1*), a part of the northern spiral arm (hereafter: *SA2*) and an inter-arm region (hereafter: *IA*). The analysis has been performed in both the final hybrid and the PdBI-only cubes. Since the parameters that control the box to search for a single GMC have been already pushed to the limit (as a result of our velocity and spatial resolution) we concentrated our test on the other decomposition parameters `SIGDISCONT` and `DELTA`. Our aim is to obtain a decomposition recipe that maximizes the flux within GMCs, without loosing obvious eye-identifiable objects.

`SIGDISCONT` is used to distinguish whether merging two kernels significantly affects the property measurement. Numerically it is the maximum logarithmic derivative (i.e. “the percentage jump”) allowed for two kernels to be said to merge seamlessly. A low value of `SIGDISCONT` means that small changes in the radius, line width, or luminosity are registered as discontinuities and force the compared local maxima to remain separate. `DELTA` is a parameter that control the minimum contrast (in unit of σ_{RMS}) between a kernel and the highest shared contour level where it joins with another kernel.

The default `CPROPS` decomposition in terms of GMC identification, is performed by setting `SIGDISCONT`=1 (thus only an 100% variation in the moment measurement results into separating two kernels), and to `DELTA`=2 (i.e. if the uniquely associated emission is not at least $2\sigma_{RMS}$ above the merge level with any other cloud the local maximum is merged with that cloud).

Several tests have been made using the default values for the remaining parameters combined with values of `DELTA` and `SIGDISCONT` (see Tables 3.1-3.3). A value of `DELTA` above the default one causes CPROPS to merge more local maxima together in crowded regions. The final GMCs appear more extended and the flux contained in clouds is higher. However, small and isolated objects are lost when `DELTA`>2. Therefore for generating the catalog we maintained the default value of `DELTA`=2.

A more important cloud loss is observed using the default setting of `SIGDISCONT`. In this case, `CPROPS` rejects bright clouds especially in SA1. However with `SIGDISCONT`≤ 0.8 (i.e. 80% of variation in the moment measurements) these objects are recognized and decomposed. This behavior can be understood considering the morphology of the molecular gas within M51 and the cloud discrimination process that involves `SIGDISCONT` called *derivative decimation*. Through this procedure, `CPROPS` analyzes the measured moment continuity of all local maxima that are in the same island independently of their physical distance. As can be seen from the island decomposition, M51's spiral arms appear as a contiguous region of CO flux, thus kernels in such a region are connected at a very low contour level (above the threshold defined by the working area) although widely separated. If one or more kernels for which a local discontinuity has already been identified exist between two contiguous local maxima, the merging of the kernels is no longer possible and the lower of the two, in terms of peak brightness temperature, is eliminated from the allocated maxima. Fig. 3.2 shows a dendrogram representation of allocated maxima in a given island and the contour relations between them. The double line represents the island, numbers and straight vertical lines indicate the kernels: the length represents their peak brightness temperature. Horizontal dashed lines indicate discontinuities in the measured moments registered by the `SIGDISCONT` analysis, while a continuity between two kernels that would generate a single GMC is shown as a bold line. Kernels 1 and 7 are connected at a very low contour level, but cannot be merged due to the presence of discontinuous maxima between them. Thus the derivative decimation eliminates the kernel with the lower peak temperature (number 7 in this case) even if it is a well defined object. Setting a value of `SIGDISCONT` equal to 0, kernels are considered discontinuous by default. In this way we avoid this control and we force kernels to stay separated. This allows `CPROPS` to allocate kernels normally eliminated by the default decomposition and solves the problem with discarded, but by eye-identifiable GMCs, in the spiral arm region. The PAWS spatial and channel resolution already furnished objects with characteristics of an average GMC by the area and contrast decimation of kernels, therefore the `SIGDISCONT` control is unnecessary for the validation and thus the reliability of the catalog.

In almost all cases, the flux percentage contained in the working area is very high (i.e. 72% of the cube), however at most 30% of it is in discrete structures as in the best case scenario of the inter-arm region. In the spiral arm regions this percentage is always around 20%. The situation for the *PdBI only* cube is similar, but the flux within GMCs with respect to the total is obviously higher (especially in the case of the inter-arm). Fig. 3.1 shows the decomposition results for the default value of `SIGDISCONT` and the value used to build the catalog (`SIGDISCONT`=0) for SA1, SA2 and IA of *PdBI+30m*.

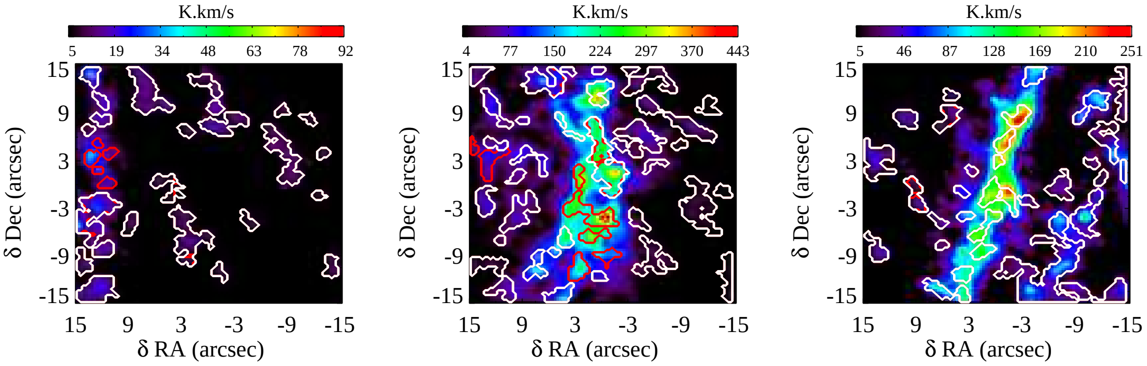

Figure 3.1: From left to right: *IA*, *SA1* and *SA2* subregions of the PdBI+30m cube. Red contours show the additional objects identified using SIGDISCONT=0, white contours objects identified using SIGDISCONT=1 (default value). Although the decomposition for *SA2* and *IA* is quite similar, many objects that can be easily identified by eye are missed in *SA1* because of the unexpected behavior of SIGDISCONT described in the text.

PDBI+30m SA1		*SIGDISCONT*				
		0	0.2	0.5	0.7	1
DELTA	0.5	16	16	16	12	13
	0.7	16	16	16	12	13
	1.0	16	16	16	12	13
	1.2	16	16	16	12	13
	1.5	16	16	16	12	13
	2.0	16	16	16	12	13
	2.5	18	18	18	14	15
	3.0	18	18	18	14	14

PDBI only SA1		*SIGDISCONT*				
		0	0.2	0.5	0.7	1
DELTA	0.5	28	28	28	28	27
	0.7	28	28	28	28	27
	1.0	29	29	29	29	28
	1.2	29	29	29	29	28
	1.5	28	28	28	28	27
	2.0	29	29	29	29	28
	2.5	29	29	29	29	28
	3.0	31	31	31	31	31

Table 3.1: CPROPS test results for the spiral arm test region SA1. Percentage of test cube flux contain in GMCs using different decomposition parameter values.

PDBI+30m SA2		*SIGDISCONT*				
		0	0.2	0.5	0.7	1
DELTA	0.5	19	19	19	19	20
	0.7	19	19	19	19	20
	1.0	19	19	19	19	20
	1.2	19	19	19	19	20
	1.5	18	18	18	19	19
	2.0	19	19	19	19	19
	2.5	19	19	19	19	19
	3.0	18	18	18	19	18

PDBI only SA2		*SIGDISCONT*				
		0	0.2	0.5	0.7	1
DELTA	0.5	34	34	34	34	35
	0.7	34	34	34	34	35
	1.0	34	34	34	34	35
	1.2	33	33	33	33	34
	1.5	33	33	33	33	34
	2.0	32	32	32	32	33
	2.5	32	32	32	32	34
	3.0	35	35	35	35	37

Table 3.2: CPROPS test results for spiral arm test region SA2. Percentage of test cube flux contain in GMCs using different decomposition parameter values.

PDBI+30m IA		*SIGDISCONT*				
		0	0.2	0.5	0.7	1
DELTA	0.5	22	22	22	22	19
	0.7	22	22	22	22	19
	1.0	22	22	22	22	19
	1.2	21	22	22	22	19
	1.5	23	23	23	23	21
	2.0	23	24	24	24	21
	2.5	24	24	24	24	21
	3.0	28	28	28	28	33

PDBI only IA		*SIGDISCONT*				
		0	0.2	0.5	0.7	1
DELTA	0.5	56	58	58	58	49
	0.7	56	58	58	58	49
	1.0	56	58	58	58	49
	1.2	56	58	58	58	49
	1.5	56	58	58	58	49
	2.0	64	66	66	66	57
	2.5	74	76	76	76	67
	3.0	73	75	75	75	67

Table 3.3: CPROPS test results for inter-arm test region IA. Percentage of test cube flux contain in GMCs using different decomposition parameter values.

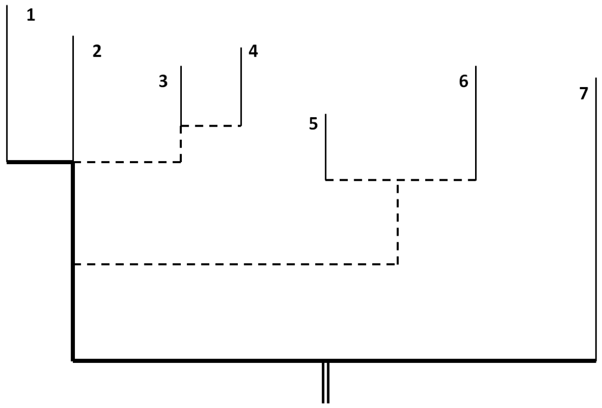

Figure 3.2: Dendrogram illustration of SIGDISCONT's unexpected behavior in the presence of significantly extended islands. Cloud number 7 is eliminated from the catalog since it cannot merge with cloud 1 due to discontinuous maxima between them.

3.3.2 DEFINITION OF GMC PROPERTIES

`CPROPS` uses an extrapolated moment method to measure the physical properties of the clouds that it identifies. To reduce observational bias, `CPROPS` extrapolates the cloud property measurements to values that would be expected in the case of perfect sensitivity by performing a growth-type analysis on the observed emission. `CPROPS` also corrects for finite resolution in the spatial and spectral domain by deconvolving the telescope beam and the width of a spectral channel from the measured cloud size and line width. `CPROPS` estimates the uncertainty in measured cloud properties via bootstrapping of the assigned pixels. We tested that 50 bootstrapping measurements provide a reliable estimate of the uncertainty. This bootstrapping approach captures the dominant uncertainty for bright clouds, but neglects the statistical uncertainty due to noise fluctuations that dominate low S/N clouds. Due to the generally high S/N ratios in our data, we present only the bootstrapping uncertainties. In what follows, we refer to all objects whose properties have been calculated by these procedures as GMCs. We distinguish them from the entities that are initially identified by `CPROPS` (i.e. prior to the application of sensitivity and resolution corrections), which we call “identified objects”. In the rest of this Section, we summarize the cloud property definitions that are used by `CPROPS`.

For clarity, we divide the cataloged properties in two classes, *basic properties* directly measured by the program such as peak brightness temperature, effective radius, velocity dispersion, position angle and cloud orientation; and *derived properties* obtained by combining basic properties and including CO luminosity, cloud mass from the CO luminosity and the virial theorem, H_2 mass surface density, virial parameter and scaling coefficient. A description of the equations used by `CPROPS` for the definition of the properties is provided in the following sections.

3.3.2.1 BASIC GMC PROPERTIES

Peak brightness temperature. The peak brightness temperature of a GMC is the CO brightness at the local maximum within the cloud. It is measured directly from the data, i.e. without extrapolation or deconvolution.

Effective radius. `CPROPS` calculates the major and minor axes of the identified objects using a moment method that takes into account the intensity profile of the emission. In this technique, the cloud root-mean-square (RMS) size, σ_r, is calculated as the geometric mean of the second spatial moment of the intensity distribution along the major ($\sigma_a(0K)$) and minor ($\sigma_b(0K)$) axes extrapolated for perfect sensitivity:

$$\sigma_r = \sqrt{\sigma_a(0K)\sigma_b(0K)}, \tag{3.1}$$

Assuming that the cloud is a sphere, its *effective radius*, R, is related to σ_r through the sphere's density profile, $\rho \propto r^{-\beta}$. `CPROPS` uses a truncated density profile with $\beta = 1$, in which case the object's effective radius is $R = 1.91\sigma_r$. The effective radius is then deconvolved by the beam size θ_{FWHM}:

$$R = 1.91\sqrt{\left(\sigma_a^2(0K) - \left(\frac{\theta_{FWHM}}{\sqrt{8\log(2)}}\right)^2\right)^{1/2}\left(\sigma_b^2(0K) - \left(\frac{\theta_{FWHM}}{\sqrt{8\log(2)}}\right)^2\right)^{1/2}}, \tag{3.2}$$

If one or both axes of the cloud are smaller than the beam ($\theta_{FWHM}/\sqrt{8\log(2)}$), then the deconvolution correction results in an undefined radius. The cloud is not rejected by `CPROPS` since it consists of more pixels than a cylinder with dimensions of one beam area × one channel width. For these objects we define an upper limit to the effective radius:

$$R = 1.91\frac{\theta_{FWHM}}{\sqrt{8\ln(2)}}. \tag{3.3}$$

Approximately $\sim 35\%$ of the GMCs in the PAWS catalog have only an upper limit to their radius. We exclude these clouds from the analysis in this Chapter and in the next.

Velocity dispersion. To estimate the FWHM line width of a GMC, ΔV, `CPROPS` assumes a Gaussian velocity profile. In this case, ΔV is related to the velocity dispersion σ_v as:

$$\Delta V = \sqrt{8\ln(2)}\sigma_v. \tag{3.4}$$

The velocity dispersion σ_v is obtained from its extrapolated value for perfect sensitivity, $\sigma_v(0K)$, deconvolved by the channel width ΔV_{chan}:

$$\sigma_v = \sqrt{\sigma_v^2(0K) - \frac{\Delta V_{chan}^2}{2\pi}}. \tag{3.5}$$

As for the GMC radius, the deconvolution can result in clouds with line widths narrower than a single channel. However, we note that if the initially identified object spans less than two channels, then it is automatically discarded from the catalog.

Axis ratio. The ratio between the major and minor axis is obtained directly from the spatial moments $\sigma_b(0K)$ and $\sigma_a(0K)$ without conversion into their physical quantities. The axis ratio, b/a, parameterises the shape of the cloud: for a round cloud $b/a = 1$, while $b/a < 1$ corresponds to an elongated cloud.

Position angle and orientation. The position angle PA of each cloud's major axis is measured clockwise, i.e. from North through West, with North set to $PA = 0°$. In a spiral galaxy, it is often more instructive to study the position angle of the clouds with respect to the spiral arm frame. Thus we define the cloud orientation ϕ as the angle between the cloud major axis and a double logarithmic spiral with a pitch angle $i_p = 21°$. This pitch angle is conventionally adopted to define M51's spiral arms (e.g. Kuno & Nakai 1997). A GMC population with major axes perfectly aligned with the spiral arms would yield a delta function distribution of ϕ values, centered at $\phi = 0°$.

3.3.2.2 DERIVED GMC PROPERTIES

Cloud mass. `CPROPS` estimates the cloud mass in two ways: from the CO luminosity and from the virial theorem. The CO luminosity of the cloud, L_{CO}, is the integrated flux scaled by the square of the distance D in parsec:

$$L_{CO}[\mathrm{K\ km\ s^{-1}\ pc^2}] = \sum_i T_i \delta_v \delta_x \delta_y \times D^2 \times \left(\frac{\pi}{180 \cdot 3600}\right)^2 , \tag{3.6}$$

where δx and δy are the pixel scale in arcsec, and δv is the channel width in $\mathrm{km\,s^{-1}}$. We use the same formula to calculate the total CO luminosity within the cube (or part thereof). The CO luminosity of each GMC is corrected for finite sensitivity using the standard `CPROPS` procedure to extrapolate L_{CO}.

Assuming that the CO integrated intensity I_{CO} is related to the underlying molecular hydrogen column density N_{H_2} by a constant conversion factor, $X_{CO} = I_{CO}/N_{H_2}$ (e.g. Dickman 1978), the cloud's CO luminosity L_{CO} can be used to estimate its total mass M_{lum}. That is,

$$M_{lum}[M_\odot] = \frac{X_{CO}}{2 \times 10^{20} \mathrm{cm^{-2}\ (K\ km\ s^{-1})^{-1}}} \times 4.4 L_{CO}[\mathrm{K\ km\ s^{-1}\ pc^2}]. \tag{3.7}$$

An appropriate value of X_{CO} is often chosen to bring a cloud population close to virial equilibrium (Hughes et al. 2010, Fukui et al. 2008). By contrast, we calculate M_{lum} using the fiducial `CPROPS` conversion factor $X_{CO} = 2 \times 10^{20}\ \mathrm{cm^{-2}\ (K\ km\ s^{-1})^{-1}}$. We discuss this choice in more detail in Section 4.5.

The virial mass, M_{vir}, depends on the density profile of the cloud. For a cloud with a density profile of $\rho \propto r^{-1}$ the virial mass is:

$$M_{vir}[M_{\odot}] = 1040\sigma_v^2 R, \tag{3.8}$$

where R is the cloud radius in parsec, and σ_v is the velocity dispersion in km s^{-1}.

H_2 mass surface density. The effective radius of the cloud R is defined as the radius of a circle that encompasses an area equivalent to the projected area of the cloud. The molecular gas surface density Σ_{H_2} is then:

$$\Sigma_{H_2} = \frac{M_{lum}}{\pi R^2}. \tag{3.9}$$

Scaling coefficient. The scaling coefficient, c, parameterizes the scaling between size and velocity dispersion of a cloud. It is defined as:

$$c \equiv \frac{\sigma_v}{R^{1/2}}. \tag{3.10}$$

For a cloud in virial equilibrium ($M_{lum} \approx M_{vir}$), the scaling coefficient is related to the cloud surface density as:

$$c = \sqrt{\frac{\pi \Sigma_{H_2}}{1040}}. \tag{3.11}$$

Virial parameter. The dimensionless virial parameter α has a value of order unity and characterizes deviations from the virial theorem applied to a non-magnetized cloud with no external pressure and constant density (see Bertoldi & McKee 1992). This parameter quantifies the ratio of the cloud's kinetic to gravitational energy, i.e.:

$$\alpha = \frac{5\sigma_v^2 R}{G M_{lum}} = \frac{1161\sigma_v^2 R}{M_{lum}}. \tag{3.12}$$

In the literature, clouds with $\alpha \sim 1$ are considered as gravitationally bound and stabilised by internal thermal and turbulent pressure against collapse. Clouds with $\alpha >> 1$ are either externally bound or transient features of the ISM. In general $\alpha = 2$ is regarded as the threshold between gravitationally bound and unbound objects. If long-lived, clouds with $\alpha << 1$ must be supported against collapse by something more than their internal turbulent motions, such as the magnetic field.

3.4 THE PAWS CLOUD CATALOGS

Both PAWS catalogs (island and GMC) provided the following information on the identified structures and are reported fully in the Appendix.

- `Column 1`: *ID*, cloud identification number;
- `Column 2`: *RA (J2000)*, cloud's Right Ascension in sexagesimal format;
- `Column 3`: *Dec (J2000)*, cloud's Declination in sexagesimal format;
- `Column 4`: V_{LSR}, cloud's radial velocity with respect to M51 systemic velocity in the Local Standard of Rest in km s^{-1};
- `Column 5`: T_{max}, cloud's peak temperature in K;
- `Column 6`: S/N, cloud's peak signal-to-noise ratio;
- `Column 7`: R, cloud's deconvolved, extrapolated effective radius in pc including uncertainty;
- `Column 8`: σ_v, cloud's deconvolved, extrapolated velocity dispersion in km s^{-1} including uncertainty;
- `Column 9`: L_{CO}, cloud's integrated and extrapolated CO luminosity in K km s^{-1} pc^2 including uncertainty;
- `Column 10`: M_{vir}, cloud's mass inferred from the virial theorem in $M_\odot$ including uncertainty;
- `Column 11`: α, cloud's virial parameter;
- `Column 12`: *PA*, cloud's position angle in degrees;
- `Column 13`: *b/a*, the cloud's minor-to-major axis ratio;
- `Column 14`: Region where a given GMC has been identified, i.e. center (CR), spiral arms (SA), inter-arm (IA);
- `Column 15`: Flag for radius measurement: 0 = measurement of radius, 1 = upper limit.

The values tabulated for the cloud's location in space and velocity (Column 2 to 4) refer to the weighted mean position within the cloud, which is not necessarily coincident with the location of the brightness temperature peak within the cloud. We consider the catalog to be complete down to a mass equivalent to 3× the survey's $5\sigma_{RMS}$ sensitivity limit. Our adopted mass *completeness limit* is therefore $3.6 \times 10^5\ M_\odot$.

3.4.1 ISLAND CATALOG

Islands are simply connected emission structures inside the working area spanning at least one telescope beam area and one velocity channel. Within the PAWS FoV we cataloged 309 islands. Because of the high sensitivity of the PAWS cube, the Island catalog is highly affected by the presence of a huge central object that encompasses more than 50% of the total flux present in the data cube and more than 70% of the total emission contoured by the CPROPS island identification. It embodies almost the whole central region and a significant portion of the spiral arms. Without this entity, the remaining islands are almost equally shared between spiral arms and inter-arm regions, and only a few objects lie in the central region. This suggest that at PAWS resolution, the central part of M51 appears as a contiguous molecular flow, mainly concentrated in the spiral arms. The next two most massive islands (ID= 45 and ID= 97) contain at most around 50 GMCs (only ~ 6% of the total) and they both lie in the spiral arm region. On the other hand ~ 70% of islands in the catalog embody only one GMC and 55% of those are located in the inter-arm region. Among these, 70% of islands sharing the same number of pixels of GMCs they contain are again detected in the inter-arm region. These undecomposed islands are the clear signature of a flocculent environment in which all the CO emission is located in discrete objects. The full Island catalog is reported in Appendix.

3.4.2 GMC CATALOG

The final GMC catalog of the PAWS project contains 1,507 objects (see Appendix). However, the initial list of objects identified by `CPROPS` includes some objects in regions of the data cube where no CO emission associated with M51 is expected. These detections are likely to be noise peaks that are falsely identified as GMCs. To eliminate obvious false positives from the catalog, we reject 99 objects that lie outside the CLEAN mask that was used in the joint deconvolution of the PAWS cube (Pety et al. 2013). The CLEAN mask includes ~ 50% of the total number of (x,y,v) pixels in the cube, which is large compared to the number of pixels corresponding to identified islands (~ 3%). Objects that fall on the edge of the mask are retained in the catalog if their centers are inside the mask. Fig. 1 presented histograms of the S/N ratio of false positives and the objects identified inside the deconvolution mask. The S/N of the false positives ranges between 4 and 6.5. Since the number of pixels inside and outside the CLEAN mask is roughly equal, we expect ~ 100 of the cataloged GMCs to be spurious. We adopt $S/N = 6.5$ as the threshold for our subsample of 761 "highly reliable" GMCs. Being much larger, island are generally always within the CLEAN mask.

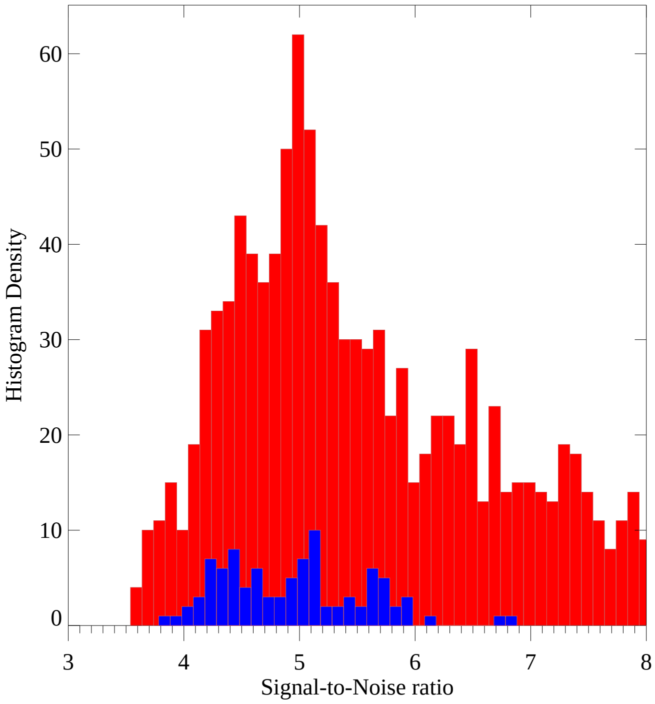

Figure 3.3: Histograms of S/N distribution of cataloged objects (red) and false positives (blue) eliminated via application of the CLEAN mask. The histogram range is restricted to a $S/N = 8$ to emphasize the distribution of the removed false positives.

3.5 Properties of CO emission and GMC Ensemble in different M51 Environments

In Table 3.4, we list several key properties of the CO emission and GMC populations within the different galactic environments. These tabulated properties include the total CO luminosity, the fraction of the CO emission that is relatively bright and hence included within the `CPROPS` "working area", and the total number and number density of GMCs. One obvious difference between the environments is the contribution of high S/N emission to the region's total CO luminosity: emission belonging to the `CPROPS` working area constitutes 80-90% of the CO luminosity present in the spiral arm and central regions, but only $\sim$ 45% of the inter-arm emission. Another way to quantify this is via the average H_2 mass surface density calculated across each region. Assuming a constant conversion factor ($X_{CO} = 2 \times 10^{20}\mathrm{cm}^{-2}$ (K km s^{-1})$^{-1}$), the center of M51 has the highest H_2 mass surface density $\Sigma_{H_2}^{ENV} = 237\,\mathrm{M}_\odot\,\mathrm{pc}^{-2}$, while in the spiral arm and in the inter-arm regions the $\Sigma_{H_2}^{ENV}$ is a factor 2 and 6 lower, respectively. Since the area of the inter-arm relative to the spiral arm increases with galactocentric radius, this decline is consistent with the radial decrease in the molecular mass surface density reported by lower resolution CO studies of M51, e.g. Schuster et al. (2007). The number density of clouds, N_{GMC}, shows a similar trend as $\Sigma_{H_2}^{ENV}$, decreasing from 72 kpc^{-2} in the central region to 45 kpc^{-2} in the spiral arms and 19 kpc^{-2} in the inter-arm region.

Envir.	**Total**				**GMC**					
	$^{(1)}A$ [kpc^2]	$^{(2)}\mathrm{L}_{CO}^{ENV}$ [10^7 K km s^{-1} pc^2]	$^{(3)}\mathrm{L}_{CO}^{WA}$	$^{(4)}\Sigma_{H_2}^{ENV}$ [$\mathrm{M}_\odot$ pc^{-2}]	$^{(5)}\mathrm{L}_{CO}^{NX}$ [10^7 K km s^{-1} pc^2]	$^{(6)}\mathrm{L}_{CO}^{EX}$	$^{(7)}\%^{NX}$	$^{(8)}\%^{EX}$	$^{(9)}\#$	$^{(10)}\mathrm{N}_{GMC}$ [kpc^{-2}]
Cube	47.0	90.83	67.08	84.22	17.81	48.65	20	54	1507	32
CR	4.7	25.47	22.85	237.02	4.71	14.48	18	57	335	72
SA	14.6	39.57	32.39	118.37	8.16	23.22	21	59	657	45
IA	27.7	25.75	11.83	40.44	4.93	10.93	19	42	514	19
NB	1.5	7.48	6.49	213.11	1.43	4.18	19	56	126	82
MR	3.2	17.99	16.35	248.62	3.28	10.30	18	57	209	66
DWI	4.6	13.13	11.23	124.92	2.32	7.23	18	55	204	45
DWO	5.7	18.38	15.73	139.52	3.69	10.72	20	58	274	48
MAT	4.2	8.06	5.44	82.72	2.15	5.27	27	65	179	42
DNS	20.0	17.96	8.54	39.16	3.57	7.66	20	43	350	18
UPS	7.8	7.79	3.28	43.75	1.36	3.27	17	42	164	21

Table 3.4: Global Properties of M51's GMC population: $^{(1)}$ area encompassed by M51's environments; $^{(2)}$ CO luminosity contained in the whole environment area; $^{(3)}$ CO luminosity contained in the environment area within the working area; $^{(4)}$ H_2 mass surface density of the given environment; $^{(5)}$ and $^{(6)}$ CO luminosity associated with identified GMCs, before and after extrapolation, respectively; $^{(7)}$ and $^{(8)}$ percentage CO luminosity contained in GMCs, before and after extrapolation, respectively, with respect to the total CO luminosity of the environment; $^{(9)}$ number of GMCs in a given environment; $^{(10)}$ number density of GMCs in a given environment.

Table 3.4 shows that the flux associated with GMCs (L_{CO}^{EX}) is ~ 55% of the total flux in the PAWS data cube $L_{CO} \approx 91 \times 10^7$ K km s^{-1} pc^2.[1] A significant fraction of the emission of the PAWS cube is thus not decomposed by `CPROPS` into GMCs. The remaining flux could be due to structures smaller than the beam or in the extended component identified by Pety et al. (2013). We note that the CO luminosity contained in the identified objects (L_{CO}^{NX}) is only ~ 20% of the total flux in the cube, i.e. more than half of the combined flux of GMCs is recovered through the extrapolation step of the `CPROPS` decomposition algorithm.

---

[1] In this Chapter we refer to the CO luminosity within the area observed by PAWS as the total CO luminosity. A detailed comparison of the flux measured by PAWS to equivalent measurements by the BIMA SoNG (Helfer et al. 2003) and CARMA-NRO (Koda et al. 2009) surveys is presented in Pety et al. (2013). These authors find that the flux measurements agree within 10%, which is consistent with the uncertainties in absolute flux calibration for millimeter data.

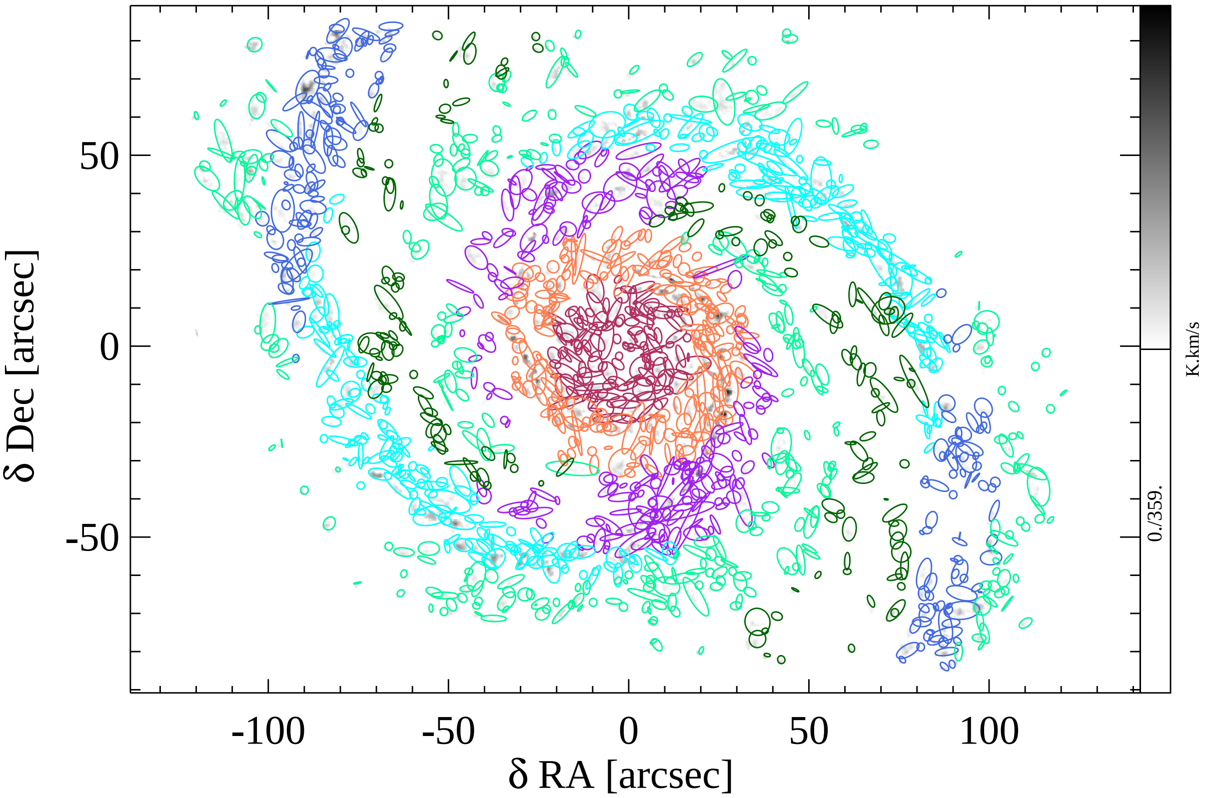

Figure 3.4: The GMC distribution in the PAWS field of M51 superimposed on the integrated identified object CO intensity map (grey-scale). The GMCs are represented as ellipses with the extrapolated and deconvolved major and minor axes, oriented according to the measured position angle. The clouds that appear overlapping are actually separated along the velocity axis. Colors indicate the environment in which a given object has been identified following the color code of Fig. 1.5.

3.6 CPROPS BIAS CORRECTION EFFECTS AND CATALOG RELIABILITY

As noted in Section 3.5, the flux contained in the cataloged GMCs is nearly three times greater than the flux that is directly measured within the objects that are initially identified by `CPROPS`, indicating that bias corrections have a significant impact on the measurements. Here, we assess the reliability of the cloud property measurements in our catalog, paying particular attention to whether the environmental trends that we observe could result from the `CPROPS` extrapolation and deconvolution corrections. A detail statistical investigation of the GMC properties will be perform in the next Chapter.

Envir.	**Sensitivity**			**Resolution**		**Global**	
	R^{ext}/R^{obs}	$\sigma_v^{ext}/\sigma_v^{obs}$	$L_{CO}^{ext}/L_{CO}^{obs}$	R^{dec}/R^{obs}	$\sigma_v^{dec}/\sigma_v^{obs}$	R^{corr}/R^{obs}	$\sigma_v^{corr}/\sigma_v^{obs}$
All	1.6	1.6	2.5	0.7	0.8	1.3	1.5
CR	1.8	1.8	2.8	0.7	0.8	1.5	1.7
SA	1.6	1.7	2.6	0.7	0.9	1.3	1.6
IA	1.4	1.4	2.1	0.7	0.8	1.1	1.3
NB	1.8	1.8	2.8	0.7	0.8	1.4	1.7
MR	1.8	1.7	2.8	0.7	0.8	1.5	1.7
DWI	1.6	1.7	2.6	0.7	0.9	1.4	1.5
DWO	1.7	1.7	2.7	0.7	0.9	1.4	1.6
MAT	1.5	1.6	2.4	0.7	0.8	1.3	1.5
DNS	1.4	1.4	2.0	0.7	0.8	1.1	1.3
UPS	1.4	1.5	2.2	0.7	0.9	1.1	1.4

Table 3.5: Median of the sensitivity, resolution and global corrections applied to the observed values of the GMC properties as a function of region.

3.6.0.1 EFFECT OF RESOLUTION AND SENSITIVITY CORRECTION WITH ENVIRONMENT

Differences in GMC properties as a function of environment only clearly emerge when considering corrected values. These differences are justified and should naturally arise given that the surface brightness of the identified objects much higher in the central and spiral arm region than inter-arm one. In general, the median of the observed object properties do not vary with environments and no significant trends are visible (see Fig. 3.5). Bias corrections applied by `CPROPS` largely increase the value of a given property in the central region, but have lower effects for the inter-arm region. Especially for the CO luminosity the trend tends to disappear if we look at the observed flux alone. Spiral arm trends, however, seem to be present in both corrected and observed properties.

In Table 3.5, we list the median ratio of the corrected and uncorrected cloud properties within the different M51 environments. The properties related to the identified objects are indicated with the superscript *obs*, the superscript *ext* denotes the extrapolated (but not deconvolved) GMC properties, while *dec* stands for deconvolution from the beam or the channel width (without extrapolation). The superscript *corr* denotes cloud properties corrected for both the resolution and the sensitivity bias, and corresponds to the cloud property values listed in the catalog.

The *resolution correction* (i.e. deconvolution for beam or channel width) is approximately constant with environment, decreasing the effective radius and velocity dispersion of GMCs across the PAWS FoV by 20-30% on average. *The sensitivity correction* (i.e. extrapolation), by contrast, varies with environment. Compared to the extrapolated radius R^{ext}, the observed radius R^{obs} is underestimated by $\sim$ 80% in the central region, $\sim$ 60% in the spiral arms and $\sim$ 40% in the inter-arm region. The sensitivity correction yields a similar trend for the velocity dispersion measurements. The CO luminosity is even more dependent on extrapolation than the radius and velocity dispersion measurements. L_{CO}^{ext} is $1.5-2\times$ higher than the observed value in the central and spiral arm regions, while in the inter-arm region, L_{CO}^{ext} is 1.3× higher than L_{CO}^{obs}.

The combined effect of the `CPROPS` corrections on the cloud effective radius and velocity dispersion is summarized in the final two columns of Table 3.5 and illustrated in Fig. 3.6. The correction is higher in the central region and in the density-wave spiral arm where R^{corr} is around $30-50$% higher than R^{obs}. In the inter-arm region, the corrected radius is only $\sim$ 10% higher than the uncorrected one. The `CPROPS` corrections have a larger impact on the velocity dispersion: in the central and spiral arm regions, the corrected σ_v^{corr} is $60-70$% higher than the uncorrected measurement. In the inter-arm region, σ_v^{corr} is $\sim$ 40% higher than σ_v^{obs}.

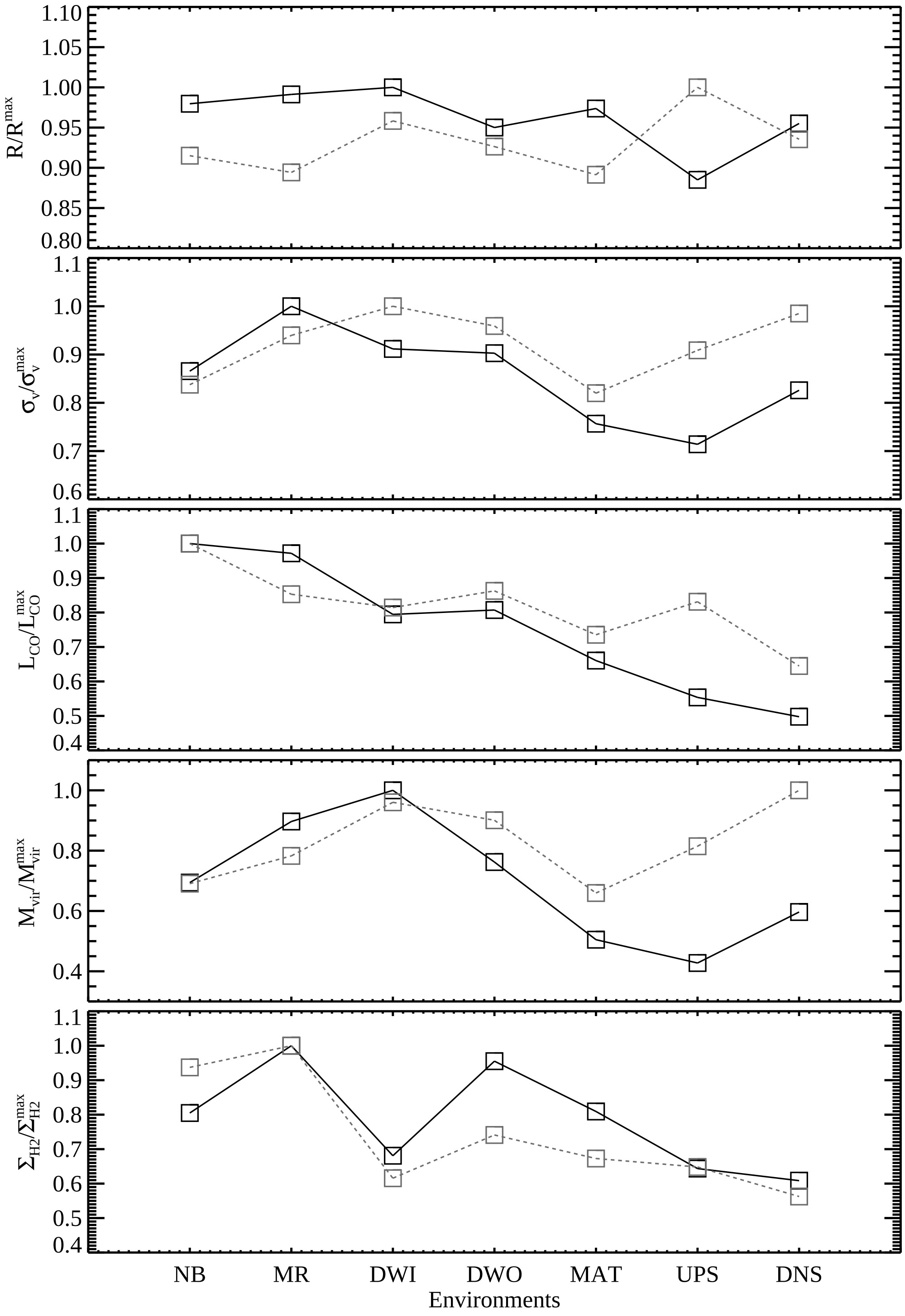

Figure 3.5: Extrapolated (black lines) and observed (dashed grey lines) GMC median properties in the different environments normalized by their maximum value to emphasize the trends.

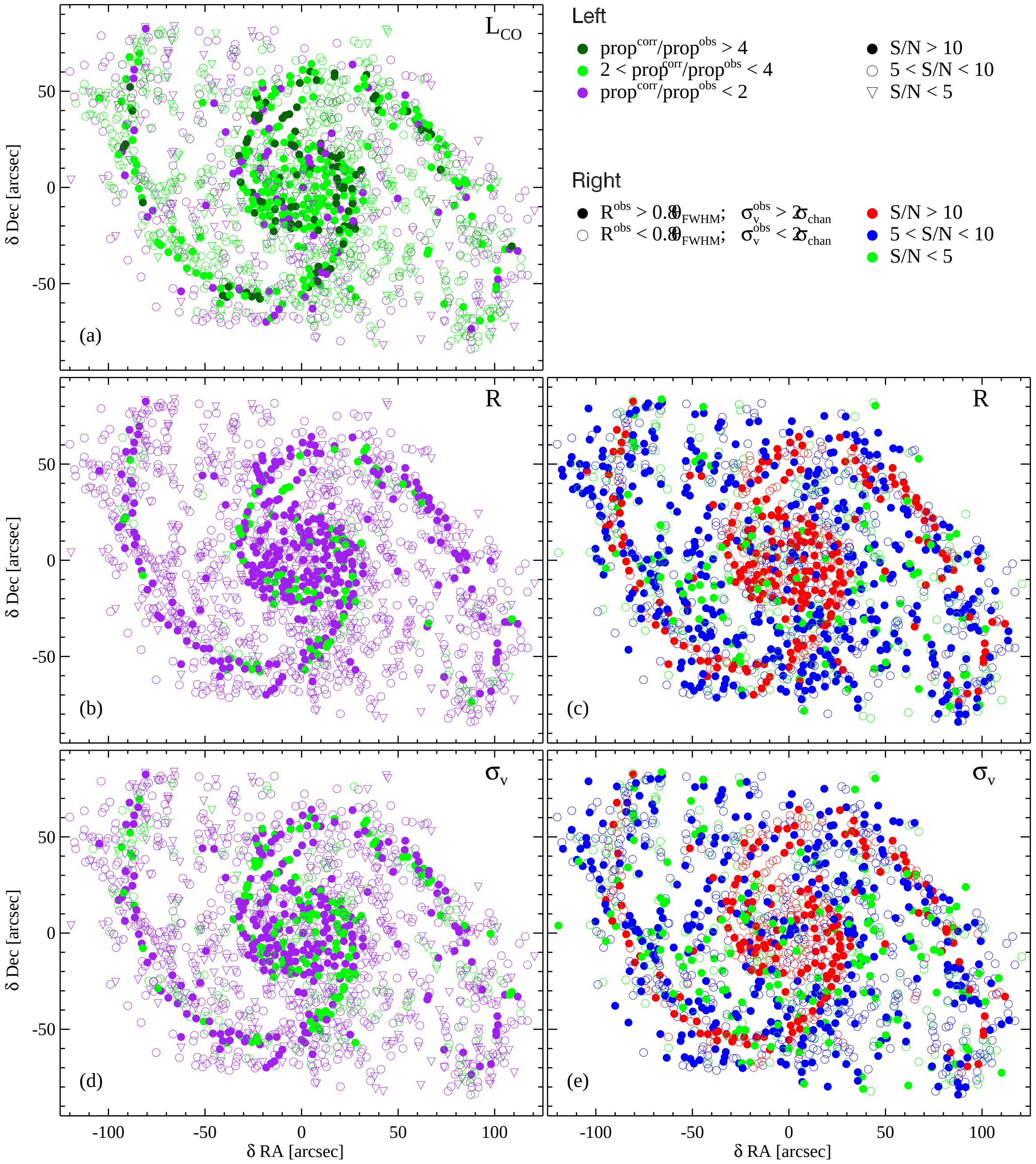

Figure 3.6: *Left:* Spatial illustration of the global correction applied to (a) the CO luminosity, (b) effective radius and (d) velocity dispersion measurements of GMCs as a function of signal-to-noise (S/N). The apex *corr* refers to GMC properties corrected for both sensitivity and resolution biases, while the apex *obs* to the properties of identified objects. *Right:* Spatial illustration of the reliability of (c) the effective radius and (e) velocity dispersion measurement as a function of S/N. A cloud is considered fully resolved by CPROPS if $R^{obs} > 0.8\theta_{FWHM}$ and $\sigma_v^{obs} > 2\sigma_v^{chan}$, where R^{obs} and σ_v^{obs} represent the effective radius and the velocity dispersion of the identified objects, respectively; while θ_{FWHM} and σ_v^{chan} are the beam FWHM and the channel width.

The environmental dependence of the sensitivity correction becomes easy to understand if we consider the method that `CPROPS` uses to perform the extrapolation. An identified object is defined as a set of (x,y,v) pixels with a temperature $T > T_{edge}^{min}$, where T_{edge}^{min} represents the cloud boundary above a certain signal-to-noise level. The unextrapolated properties derived for the identified objects are then a function of the cloud boundary, whereas the estimate of the properties at $T \equiv 0$ K (extrapolation for perfect sensitivity) is performed using a weighted linear – or, for the flux, quadratic – least-squares fit that takes into account the brightness temperature profile within the cloud. Thus the difference between the cloud property values before and after the sensitivity correction (extrapolation) is determined by the magnitude of the brightness temperature gradient within the cloud and consequently by the value of T_{edge}^{min}.

To test whether the cloud brightness temperature gradient varies with environment, we analyzed the full cloud sample in the three main regions (i.e. M51's center, spiral arms, and inter-arm). We fixed 10 T_{edge} levels corresponding to 10% − 20% − ...100% of the peak temperature of a cloud and we calculated the radius, the CO luminosity and CO surface brightness of the object at each level. The radius is estimated as:

$$R = \sqrt{\frac{A}{\pi}}, \tag{3.13}$$

where A is the area of the cloud (in pixels) at a given T_{edge}. Figure 3.7 shows the result as a median of the property distribution at a given T_{edge}/T_{max} value. The cloud radius profiles show similar slopes in all three environments. The CO luminosity profiles, however, appear steeper in the central region. The surface brightness profiles I_{CO} also differ between the three main regions. The central region profile is the steepest, and the inter-arm profile is the most shallow. These differences indicate that the brightness temperature gradient inside the clouds is varying between the different regions, and can explain why the magnitude of the sensitivity correction depends on environment.

The difference between the extrapolated and uncorrected properties is also proportional to the value of T_{edge}^{min}. We can assess the effect of T_{edge}^{min} by examining the brightness temperature distributions of the watershed (i.e. undecomposed emission within the `CPROPS` working area) in the different environments. In the central and spiral arm regions, where the difference between extrapolated and unextrapolated properties is higher, large areas have brightness temperatures > 4 K. In the inter-arm region, where the difference between corrected and uncorrected properties is lower, the watershed mostly has brightness temperatures < 2 K.

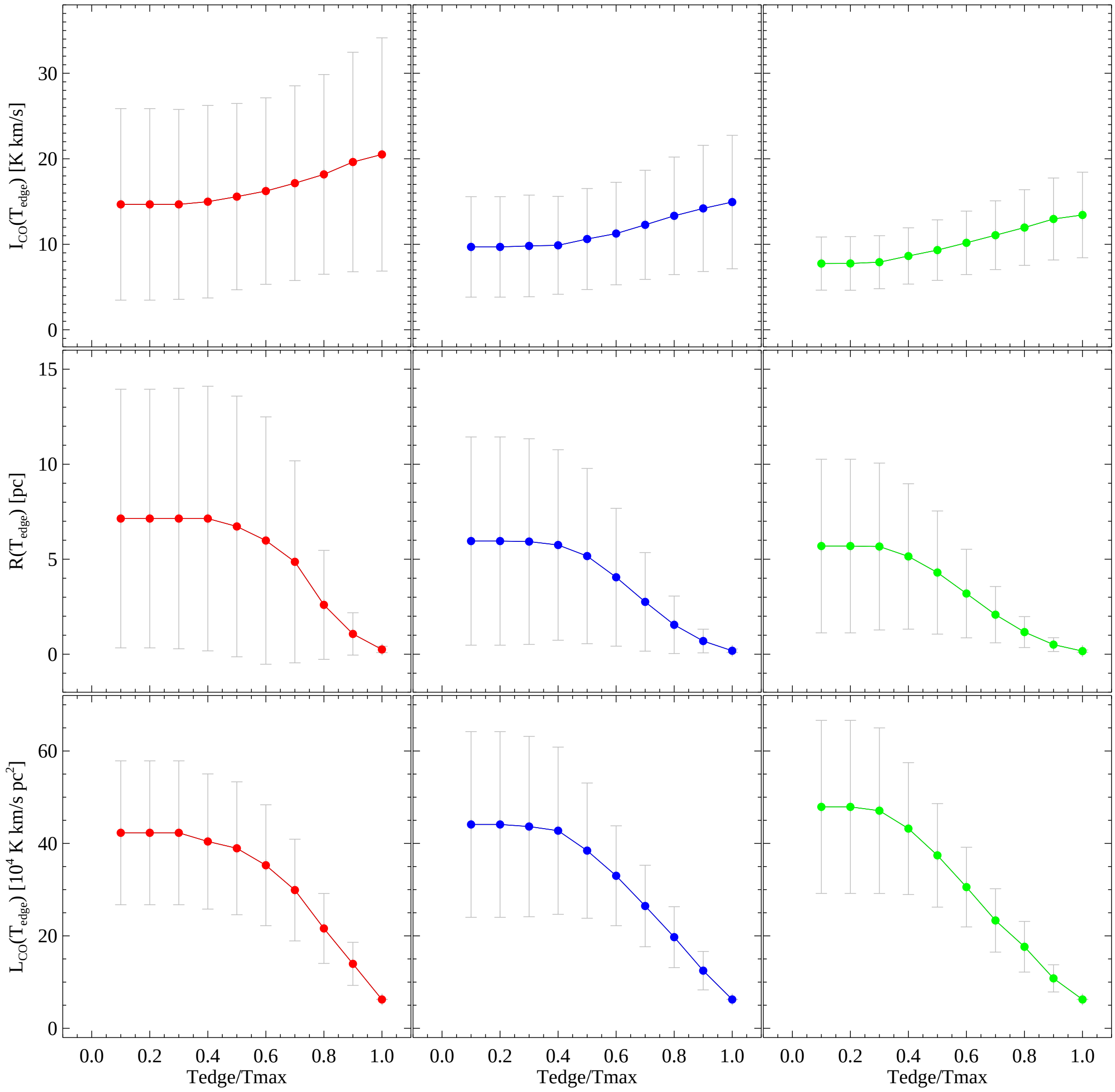

Figure 3.7: Median of cloud profiles relative to surface brightness I_{CO} (top), effective radius R (middle), and CO luminosity L_{CO} (bottom) for the three main region (from left to right: central, spiral arm and inter-arm region). Error bars indicate the median absolute deviation of the distributions.

3.6.0.2 GMC EXTRAPOLATED PROPERTY RELIABILITY

`CPROPS` obtains measurements of GMC properties only if certain requirements on the sensitivity and resolution are satisfied (RL06). Here we examine the properties of the identified objects in order to determine whether the final corrected measurements can be considered reliable.

As discussed by RL06, the sensitivity correction of `CPROPS` will yield the *effective radius* of a cloud with an error below 10% if the signal-to-noise S/N is greater than 10. The algorithm performs well even for barely resolved objects, i.e. for clouds with $R^{obs} > 0.8\theta_{FWHM}$, where θ_{FWHM} is the full width at half maximum size of the beam. For clouds with $5 < S/N < 10$, the measured radius may be underestimated by up to 20%. The accuracy of the corrected radius measurements deteriorates for faint clouds ($S/N < 5$), and when an object is unresolved.

Fig. 3.6 shows the spatial distribution of M51 clouds as a function of the signal-to-noise and the observed radius relative to the beam size. The identified clouds with $S/N > 10$ constitute $\sim$ 25% of the catalog. These clouds are typically located in the ridge line of the spiral arms and in the central region. More than 50% of the objects have a S/N between 5 and 10 and the remaining 25% of clouds have $S/N < 5$. These faint clouds are distributed across the PAWS field. The objects with a peak signal-to-noise above 5 that satisfy the resolution requirement of CPROPS ($R^{obs} > 0.8\theta_{FWHM}$) are 40% of the total, while the objects with an observed radius below this limit that show the same range of S/N are more than $\sim$ 35% of the catalog and could suffer a 10% underestimation of their actual radii. Thus 65% of the clouds have a radius measurement that can be considered reliable. According to Fig. 3.6, the bright clouds with the most reliable radius measurements tend to be located in environments where extrapolation is important for the cloud size determination.

The `CPROPS` performance requirements for the cloud *velocity dispersion* determination are less demanding (RL06). The extrapolation works well – independently of the cloud S/N – if the line width of the identified object is at least twice the channel width. Fig. 3.6 shows a map of the clouds as a function of the velocity dispersion with respect to the channel RMS. The identified clouds with $\sigma_v^{obs}/\sigma_{chan} > 2$ are $\sim$ 40% of the total. Of the remaining objects, $\sim$ 15% have a signal-to-noise peak greater than 10. In this case, according to RL06, the overestimation of the actual velocity dispersion of the cloud is around 20%. The spatial distributions of these two classes of clouds are quite uniform and do not depend on environment. In the PAWS catalog, we therefore have a large number of clouds for which the cloud velocity dispersion may be overestimated. This is especially in the inter-arm, where the signal-to-noise is typically lower. This reinforces our conclusion that GMCs in the spiral arm and the central regions tend to have a higher velocity dispersions than inter-arm GMCs, since the former have higher S/N ratios and hence more accurate velocity dispersion measurements.

The difference between the GMC flux after extrapolation and the flux measured directly within the identified objects is high (Table 3.4). Indeed the average corrected CO luminosity of the GMC is 2.5× greater than the unextrapolated value (Table 3.5). Although this is consistent with the results obtained on IC10 in RL06, it represents a significant addition to the flux of our identified GMCs and therefore merits further examination.

While the original `CPROPS` paper (RL06) provides guidelines for checking whether extrapolated measurements of the cloud radius and velocity dispersion can be considered reliable, this is not the case for extrapolated measurements of the CO luminosity. Nevertheless we can draw some conclusions based on a comparison between the extrapolated and the observed flux within GMCs (see Section 3.5) and the extended component discussed in Pety et al. (2013). Although GMCs are often considered to account for nearly all the CO emission in normal galactic disks (~ 85%, Sanders et al. 1985), roughly half of the CO flux in M51 arises from a diffuse thick disk of molecular gas (see Pety et al. (2013) for a detailed discussion of its properties). The fact that GMCs (after extrapolation) contribute ~ 55% of the total CO flux in the PAWS FoV would seem compatible with the existence of a diffuse, extended component that is resposible for a comparable fraction of the total CO luminosity. If, instead, the CO luminosities of GMCs were closer to their unextrapolated values, ~ 30% of the CO emission within the PAW FoV must be attributed to an ill-defined ”watershed”. Moreover, this undecomposed “watershed” emission reaches temperatures above 4 K, characteristic of compact structures in the Galaxy (Sawada et al. 2012). While this flux could be associated with entities smaller than the beam, it is also possible that the watershed is actually part of the GMCs. Presumably, this part of the emission could not be properly attributed to clouds by the identification algorithm, given the low contrast between cloud and intra-cloud emission.

Overall, our examination of the effects of the sensitivity and resolution corrections on the measured cloud properties highlights the limits of the `CPROPS` method in decomposing physically reliable objects in highly crowded and low contrast environments. We might therefore consider the initially identified objects as “bright cores” of more extended structures that we can access only through an extrapolation technique. Although other methods, like the “patchwork” separation performed by `CLUMPFIND`, are able to attibute all the measured flux to discrete objects, the resulting separation is ambiguous when GMCs do not have well-defined boundaries, as in the case of the cloud population in M51.

3.7 CPROPS CORRECTIONS AND SCALING RELATIONS

The bias corrections partially influence the scaling relations between cloud properties[2]. Considering the uncorrected properties, the identified objects show a lower scatter in the first Larson's law than GMCs (Fig. 3.8). We can assess the degree of correlation and therefore, the scatter between the data through Spearman's correlation rank, r_s (see Section 4.3 for more details). For the first Larson's law, this value is almost 7× higher for GMCs with respect to observed objects. This scatter seems to be mainly introduced by the extrapolation, while beam and channel width deconvolutions have instead a lower effect on the scatter. Considering only extrapolated properties, r_s is 2× lower than in the case of extrapolated and deconvolved GMCs. The CO luminosity is only extrapolated, then we use this value in the second and third Larson's law to compare with the other uncorrected properties. In those scaling relations, the increment of scatter with the correction is not as high as in the first Larson's laws. The Spearman's coefficient decreases by 2-4× from uncorrected to extrapolated only to fully corrected properties. This lower scatter may be due mostly to the intrinsic covariance of the properties considered in these scaling relations.

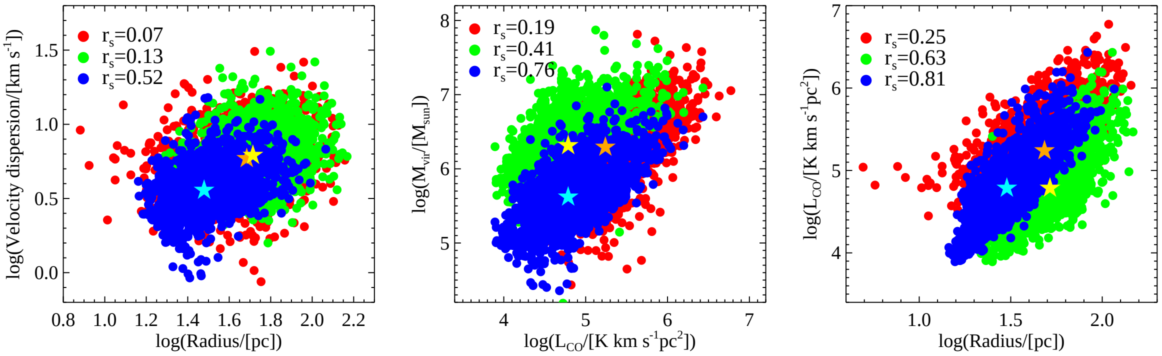

Figure 3.8: Comparison of the Larson's laws for corrected (red), uncorrected (blue) and only extrapolated (green) properties of the full catalog. Spearman's rank correlation coefficients (r_s) of the highly reliable sample are given using the same color code. Orange, cyan and yellow stars indicate the position of the median of the properties of the full samples for corrected, uncorrected and only extrapolated properties, respectively.

---

[2] Scaling relations in the different environments will be presented in the next Chapter.

3.8 CPROPS corrections and GMC comparative studies

Although it is designed to eliminate the observational biases, `CPROPS` has the general tendency to decompose cubes of line emission into structures that are close to the angular and spectral resolution of the input dataset. In a recent PAWS paper, Hughes et al. (submitted) reanalyze with `CPROPS` CO emission datacubes from M51, M33 and LMC. The authors found that the GMCs identified in the native resolution data cubes cluster around the beam size and channel width values in a size-linewidth plot (Fig 3.9). Taken together those measurements give the impression of an apparent extragalactic first Larson's law. When the data cubes are convolved to the same resolution and gridded with the same pixel scale, the observational biases should be identical for all data cubes. Indeed GMCs in M51 are brighter and have larger velocity dispersions than similar size clouds in LMC and M33. However these objects do not show any kind of Larson's law. Surprisingly a strong correlation similar to the canonical size-linewidth relationship for GMCs in the inner Milky Way is apparent when the islands (from both native resolution and smoothed cubes) are used. The authors interpret the islands as cloud associations for which the observed size-linewidth relation could simply reflect more adequate sampling of the inhomeogeneous density and velocity structure of the interstellar medium, rather than virial equilibrium or a turbulent cascade. This analysis shows that care must be taken when comparing clouds identified in different surveys, even when using an algorithm that attempts to correct for observational bias.

3.9 Summary and conclusions

Using the PAWS (PdBI Arcsecond Whirlpool Survey) observations of the ^{12}CO(1-0) line emission in the central 9 kpc of M51, we cataloged a total of 1,507 GMCs and 309 islands using an identification algorithm (`CPROPS`) that partially corrects for survey biases. From the analysis of the fake positives, we consider 761 GMCs with a $S/N > 6.5$ as "highly reliable".

The analysis of the cloud population within a complex and crowded environment, such as the inner region of M51, reveals several challenges for commonly used segmentation algorithms, like `CPROPS`, in identifying and measuring GMCs properties.

- The default setup of `CPROPS` caused a loss of several bright eye-identifiable objects. To avoid this behavior the parameter `SIGDISCONT` needed to be disabled.
- The GMCs contains only 55% of the total survey flux. This is consistent with the CO luminosity within the extended components identified by Pety et al. (2013).

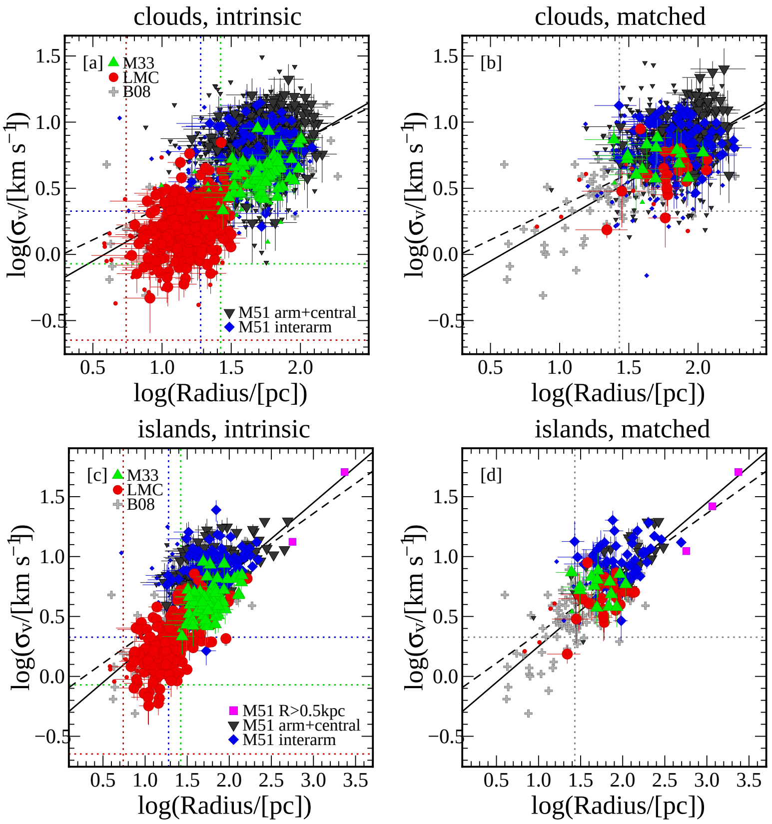

Figure 3.9: A plot of radius versus velocity dispersion for objects identified within the CO datacubes for M51 (PAWS), M33 (Rosolowsky 2007), the LMC (Wong et al. 2011). In panel [a], we plot the relation for clouds identified in the cubes at their intrinsic resolution. The relation for clouds identified in the matched resolution cubes is shown in panel [b]. The relation for island structures are shown in panels [c] and [d] for the decompositions of the original and matched datacubes respectively. Islands with radii greater than 0.5 kpc (i.e. objects that are much larger than GMCs) are indicated by open black squares in panels [c] and [d]. In all panels, the black dashed line indicates the relationship derived from the Solomon et al. (1987) inner Milky Way data, and the black solid line indicates the best-fitting relation for extragalactic GMCs determined by Bolatto et al. (2008) (see next Chapter). The sample of extragalactic GMCs analyzed by Bolatto et al. (2008) is indicated in each panel by black crosses. Figure adapted from Hughes et al., submitted.

- The bias corrections of `CPROPS` have a significant impact on GMC property measurements. However they appear necessary to correctly account for the flux contained in non-isolated clouds and for the intrinsic differences between them.

- Using the performance requirements of `CPROPS` we established that 75% of the clouds have a measurement of the radius that can be considered reliable after the extrapolation process. Especially in the ridge line of the spiral arms and in the center where the extrapolation is significant, clouds (25% of the total) have a S/N higher than 10 that satisfies the more demanding requirement of `CPROPS` to obtain a reliable measurement. However, only 40% of the clouds satisfy the reliability requirement of `CPROPS`, the others, especially those located in the inter-arm region, could have overstimated measurements.

- The extrapolation introduces a significant degree of scatter in the data, as we observed comparing the Larson's laws from GMCs and identified objects. Moreover, `CPROPS` has the general tendency to decompose structures close to the angular and spectral resolutions of the input dataset. This behavior must be taken into account when confronting GMCs from different surveys.

4

ENVIRONMENTAL DEPENDENCE OF GMC PROPERTIES IN M51[*]

CONTENTS

In this Chapter, we analyze whether GMC properties depend on environment. M51's clouds do not show a clear relation between their sizes and velocity dispersions, and a simple virial analysis suggests that a number of GMCs is strongly unbound. The properties of the GMC population have been statistically analyzed as a function of dynamically-motivated galactic environments (within spiral arm, inter-arm and central regions defined in Chapter 1). We find that GMC properties are influenced by galactic environment: objects in the spiral arms and in the central bulge region appear brighter and have higher velocity dispersions and H_2 mass surface densities compared to inter-arm clouds. The shape of the individual GMC mass distributions also depends on environment: it is steeper in inter-arm than in the spiral arms, and exhibits a pronounced truncation at high masses for the innermost zone. From a comparison between the virial mass and the CO luminosity of the GMCs, we obtain an average X_{CO} factor that is similar to the Galactic value, and we argue that this parameter is not responsible for the variation in GMC properties with environment that we observe. We propose that the observed environmental variations in the GMC properties and mass distributions are a consequence of the combined action of large-scale dynamical processes and massive star formation feedback.

4.1 INTRODUCTION

After the seminal works of Larson (1981), Sanders et al. (1985) and Solomon et al. (1987) that established the basic physical properties of GMCs in the inner Milky Way, numerous studies

---

[*] This chapter is adapted from Colombo et al. 2013a, ApJ submitted.

have attempted to determine whether GMCs in other galactic environments have similar physical properties as Galactic clouds. Within the Galaxy, however, distance ambiguities as well as crowding in space and velocity present a serious challenge to empirical studies of GMC properties.

The commissioning of millimeter telescopes such as the NANTEN 4-m telescope and Berkeley Illinois Maryland Association (BIMA) array in the late 1990s provided the opportunity to study individual GMCs in nearby galaxies, circumventing many of the problems confronting Galactic observations, and also opening up a wider range of galactic environments in which GMCs could be studied.

Early observations of low mass galaxies have concluded that the extragalactic GMCs appear very similar to Galactic clouds in term of average properties (e.g Sheth et al. 2000, Fukui et al. 2001, Fukui 2005, Rosolowsky 2007) with no dependency on metallicity (as in the case of IC10, Leroy et al. 2006). However more recent works with improved resolution, sensitivity and field-of-view have reported several departures from the classical picture. Most of these differences are observed in relation to star formation. In the Large Magellanic Cloud (hereafter LMC), $\sim 30\%$ of GMCs are quiescent (Fukui 2005) and appear fainter, with lower line-widths than Galactic clouds and with a mass surface density two times lower (Hughes et al. 2010). Instead star forming GMCs are brighter (Gratier et al. 2012), more massive, with smaller line width and closer to the virial equilibrium than quiescent ones (Hirota et al. 2011). This fact has been interpreted as a lack of heating source (Gratier et al. 2012) or as an evidence that clouds need to dissipate kinetic energy to collapse and form stars (Hirota et al. 2011). Property variations of the clouds have been observed also in relation to their spatial distribution: bigger objects are mostly observed in spiral arms or galaxy centers (Donovan Meyer et al. 2012, Donovan Meyer et al. 2013, Rebolledo et al. 2012) where the density of the gas is higher. Even in the Milky Way, most of massive clouds that contain most of the mass and host the majority of star formation are strongly associated with spiral arms (Solomon et al. 1985, Solomon & Rivolo 1989, Heyer & Terebey 1998, Stark & Lee 2006).

Although most of the observed GMCs seems to follow the "Larson's laws" (e.g. Blitz et al. 2007), some strong departures have been observed. In the outer Galaxy the relation breaks down for very small clouds (< 7 pc) where the velocity dispersion appears constant around 0.8 $\mathrm{km\,s^{-1}}$ (Heyer et al. 2001a). The authors interpreted these objects as pressure supported: i.e. they have an excess of kinetic energy over their gravitational potential energy and, unless they are transient features in the ISM, they must be confined by an external pressure. A dependence of GMC properties on the interstellar gas pressure was also inferred for GMCs in M64. Here a linear size-line width relation was observed (Rosolowsky 2005), and the GMCs shows mass surface densities more than 2 times higher than the Galaxy. These evidences where interpret by the author as caused by the molecule richness of M64 such that M64 GMCs require much higher internal motions to support themselves against the combined effect of the clouds' self-gravity and kinetic pressure of the surrounding ISM.

Another deviation from the classical relations measured by Solomon et al. (1987) was found in the Central Molecular Zone, a small region of the Milky Way ($\sim 400 \times 80$ pc) that contains $\sim 5-10\%$ of the Galactic molecular gas and shows extreme conditions of temperature (typically 30-60 K, though up to 200 K) and turbulence ($\sigma_v \approx 15-50$ km s^{-1}). Although the general properties of the GMCs appears comparable to the inner Galactic ones, the size-velocity dispersion relation shows a similar slope as measured by Solomon et al. (1987) but with a scaling coefficient 3.5-5 times higher (Oka et al. 1998, Miyazaki & Tsuboi 2000, Oka et al. 2001). Using a variety of molecular tracers, Shetty et al. (2012) interpreted this systematic enhancement of turbulent velocities as a combined effect from increased star formation activity, larger densities and higher pressures relative to the local ISM.

One of the most significant work in the field of the extragalactic GMCs was done by Bolatto et al. (2008) that reanalyzed the maps of Milky Way, low mass nearby galaxies together with dwarf galaxies from different surveys (see reference therein). The comparative study defined a new extragalactic standard for the Larson's laws, quite similar to those measured by Solomon et al. (1987):

$$\sigma_v[kms^{-1}] = (0.44^{+0.18}_{-0.13})R[pc]^{0.60\pm0.10}, \tag{4.1}$$

for the size-line width relation and:

$$M_{vir}[M_\odot] = 7.6^{+3.9}_{-2.6}L_{CO}^{1.00\pm0.04}[K\,km\,s^{-1}\,pc^2], \tag{4.2}$$

for the second “Larson's law”, and a CO luminosity-size relation

$$L_{CO}[M_\odot] = 7.8^{+6.9}_{-3.7}R[pc]^{2.54\pm0.20}, \tag{4.3}$$

that allowed them to conclude that extragalactic clouds have similar surface densities as Galactic GMCs. However, again, some significant departures were observed. The authors indicated, for example, that GMCs in dwarf galaxies fall preferentially under the Galactic size-line width relation of Solomon et al. (1987). This happens for most of clouds in the Small Magellanic Cloud (hereafter: SMC), which are significantly inconsistent with the Milky Way ones. Clouds in the dwarf galaxies are also underluminous compared to GMCs of similar size in the Milky Way by a factor of ~ 2. More quantitatively, Bolatto et al. (2008) determined an average mass surface density of $\Sigma_{H_2} \approx 85$ $\mathrm{M}_{\odot}\,\mathrm{pc}^2$ for GMCs in dwarf galaxies instead of the canonical 170 $\mathrm{M}_{\odot}\,\mathrm{pc}^2$. One of the interpretation given by the authors is that clouds in the dwarf galaxies are only transient features in the ISM that dissipate in few Myr.

Recently, the results for Galactic clouds have been questioned by Heyer et al. (2009) that reanalyzed the Solomon et al. (1987) catalog in a more consistent way supported by ^{13}CO Galactic data. They found that the masses measured by Solomon et al. (1987) were overestimated by a factor 5 and, consequently that a more appropriate median mass surface density for the cloud would be $80 - 120\,\mathrm{M}_{\odot}$ (considering abundance variations within the outer envelope of clouds). The authors observed also that the virial parameter $c = \sigma_v/R^{0.5}$ is not constant as required by the Larson's first law, but rather varies with $\Sigma_{H_2}^{0.5}$. They proposed that GMCs are at most self-gravitating (and not in strict virial equilibrium) and that they are sustained by magnetic fields rather than turbulence.

In the most complete extragalactic samples (in M33 and LMC, Gratier et al. 2012, Wong et al. 2011) the size and velocity dispersion measurements exhibit a large scatter, preventing the firm identification of a size-linewidth relation. It remains unclear whether this is a genuine difference in the properties of GMCs in low-mass galaxies, or whether it is a consequence of the different GMC identification and decomposition techniques used to analyze those datasets.

The mass spectrum of the GMCs in the Galaxy has been re-measured by Simon et al. (2001) and Heyer et al. (2001a) finding a constant index $\gamma \sim -1.8$, independent of star formation activity. Most of the nearby galaxies show spectral index close to the Galactic one (Blitz et al. 2007). However, in LMC it appears lower, $\gamma \approx -2.3 \div -2.9$ (depending to the cloud decomposition method, Wong et al. 2011). Fukui et al. (2001) interpreted this steeper spectrum as an evidence of UV flux that progressively dissipate the molecular gas in the LMC, leaving only small mass objects. A similar steeper mass spectrum has been observed in M33, $\gamma \approx -2.6$ (Engargiola et al. 2003). Using a larger field of view, Gratier et al. (2012) observed instead a shallower spectrum in this galaxy $\gamma \approx -2.0$ consistent with the findings of Rosolowsky (2007). Interestingly, the spectral index varies with the galactocentric radius in M33 being shallower within 2 kpc ($\gamma \approx -1.6$) and steeper at large galactocentric radii ($\gamma \approx -2.3$). As noted by the authors, possible explanation for this trend would be a decrease of the N_{H_2}/I_{CO} factor or a real decrease in molecular mass in the outskirts of the galaxy due to the diminishing gas surface density that could result in slower cloud assembly such that star formation stops cloud growth before outer disk clouds reach the masses of inner disk clouds.

Follow the Galactic prescription and assuming the GMCs are well defined objects in virial equilibrium, a number of studies have attempted to measure the I_{CO}–to–N_{H_2} factor comparing cloud

CO luminosity and virial mass. In most of the low mass galaxies of the Local Group the X_{CO} measured through the GMCs is very close to Galactic-like values, i.e. $X_{CO} = 2 - 5 \times 10^{20}$ cm^{-2} (K km s^{-1})$^{-1}$ (e.g. Fukui & Kawamura 2010) with median value around $4{\times}10^{20}$ cm^{-2} (K km s^{-1})$^{-1}$ (Blitz et al. 2007) and no dependency on metallicity (Bolatto et al. 2008). Similar factors have been obtained more recently for nearby spiral galaxies $X_{CO} = 1 - 2 \times 10^{20}$ cm^{-2} (K km s^{-1})$^{-1}$ (Donovan Meyer et al. 2012, Donovan Meyer et al. 2013). By contrast, the X_{CO} in the SMC is much larger: $X_{CO} \approx 13.5 \times 10^{20}$ cm^{-2} (K km s^{-1})$^{-1}$ (e.g. Blitz et al. 2007). Bolatto et al. (2008) explained this discrepancy as an evidence of a large H_2 envelopes that are not traced by CO emission but contain an appreciable mass of molecular gas (see also Israel 1997, Rubio 2004).

Previous observations of M51 have indicated that galactic environment is important for the organization and properties of the molecular gas (see Chapter 1). Recently, for example, Koda et al. 2009 showed that M51's spiral arms contain Giant Molecular Associations (GMAs) with masses between $10^7 - 10^8$ M$_\odot$, while the inter-arm region hosts only smaller clouds with masses less than $\sim 10^6$ M$_\odot$. By virtue of these evidences, in this Chapter we analyze whether GMC properties depend on galactic environment.

Our investigation of environmental trends differs from several previous surveys of molecular gas across the disk of external galaxies, which have tended to analyze the properties of the molecular gas and/or GMCs as function of galactocentric radius (e.g. Hitschfeld et al. 2009, Gratier et al. 2012). In contrast to these CO surveys, PAWS is restricted to the inner disk of M51 ($R_{gal} \lesssim 5$ kpc), and many environmental parameters that could produce a change in the GMC properties show only modest variations. The molecular gas fraction $M_{H_2}/(M_{H_2} + M_{HI})$ is $\sim 80\%$ across the FoV (Leroy et al. 2008, but see also Schuster et al. 2007, Koda et al. 2009), while the dust-to-gas ratio and ambient interstellar radiation field are roughly constant across our FoV (Mentuch Cooper et al. 2012, Muñoz-Mateos et al. 2011). Instead, we use the stellar potential of M51 to divide the PAWS FoV into seven distinct dynamical environments, each of which contains a statistically significant GMC population as exposed in Chapter 1 and 3.

The full analysis of cloud properties, scaling relations and mass spectra in relation to dynamical environment is presented in Sections 4.2 to 4.4. In Section 4.5, we consider whether variations in the X_{CO} factor can account for our results. In Section 4.6.1 we discuss a possible origin for the environmental differences in the GMC properties and mass distributions, and summarize the evidence against the universality of the GMC properties. Our conclusions are presented in Section 4.7.

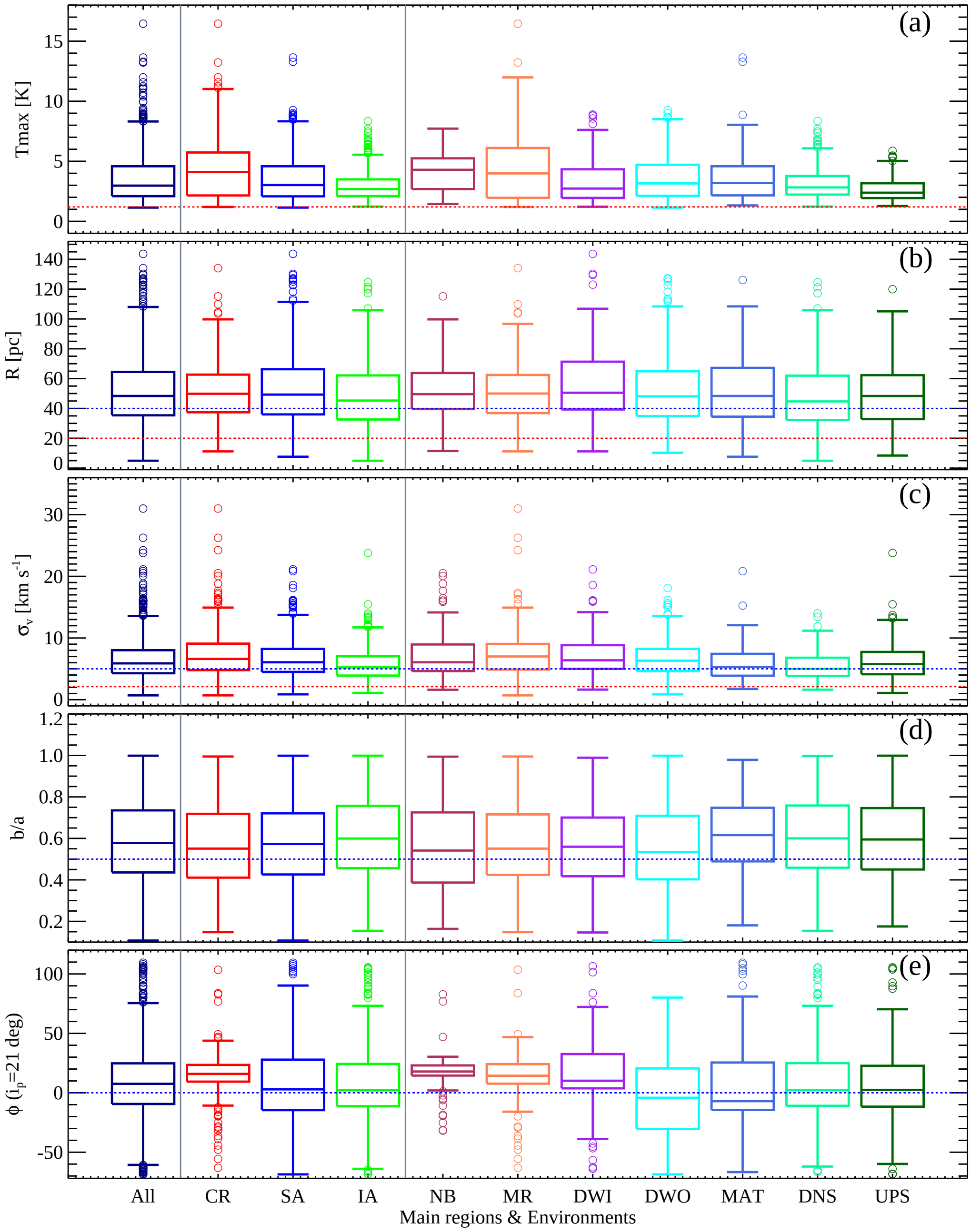

Figure 4.1: Basic GMC properties (from the top to the bottom): (a) peak brightness temperature T_{max}, (b) effective radius R, (c) velocity dispersion σ_v, (d) axis ratio b/a and (e) orientation ϕ shown in a "box and whiskers" representation for different M51's environments (from the left to the right: All -full sample; 3 main regions -center (CR), spiral arm (SA), inter-arm (IA) and 7 environments defined in Fig. 1.5). The box middle band represents the median of the distribution. The box itself contains 50% of the data points. Each whisker that emerges from the box, coinciding with ~ 25% of the data points, corresponds roughly to 3σ of a normal distribution. The median of radius, velocity dispersion and brightness temperature is always higher in the central region (CR and MR, NB) and in the density-wave spiral arms (DWI and DWO), compared to inter-arm environments (DNS, UPS). Straight horizontal red lines indicate the resolution, instrumental or sensitivity limits: 1.2 K for the peak brightness temperature, 20 pc for the radius, 2.12 km s^{-1} for the velocity dispersion. Reference lines at arbitrary values are indicated in blue to help guide the eye.

4.2 STATISTICAL VARIATION OF M51 GMC PROPERTIES WITH ENVIRONMENT

In this section, we examine whether the physical properties of GMCs – such as radius, velocity dispersion and mass – vary with galactic environment. To visualize the GMC property distributions, we use a "box and whiskers" plot (e.g. Tukey 1977) in Figures 4.1 and 4.2. This representation is a useful tool to identify and illustrate differences in the shape of non-Gaussian distributions. The box is delimited by two lines that indicate the lower $Q25$ and upper $Q75$ quartiles of the distribution. The middle band represents the median. For a normal distribution, the interquartile range or distribution spread ($IQR \equiv Q75 - Q25$) corresponds to 1.35σ, where σ is the standard deviation. Therefore, $0.5IQR$ corresponds to 0.6745σ or to the median absolute deviation (MAD). The ends of the whiskers indicate the lowest and the highest data points that lie within $1.5 \times IQR$ of the lower quartile (the bottom whisker, BW) and $1.5 \times IQR$ of the upper quartile (the top whisker, TW). For a normal distribution, the range of values between TW (or BW) and the middle band roughly corresponds to $\pm 3\sigma$. We define "outliers" as data points with values lower or greater than BW or TW, respectively (i.e. outside the 3σ range of a Gaussian distribution), and represent them as circles in the box and whiskers plots. The median and the lower and upper quartiles ($Q25$ and $Q75$, respectively) of the GMC property distributions are listed in Table 4.1.

To test the statistical significance of differences between the GMC property distributions, we use the two-sided Kolmogorov-Smirnov (KS) test (e.g. Eadie et al. 1971) on both the full and the "highly reliable cloud" samples. The two-sided KS statistic quantifies a distance between the empirical distribution functions of two samples assuming as a null hypothesis that the samples are drawn from the same parent distribution. This distance is directly connected to the *p-value*, the probability that two samples descend from the same parent population. Traditionally, the null hypothesis is rejected when the *p-value* is smaller than a certain significance level. We adopt the convention that there is a significant difference between two samples if the *p-value* is lower than 0.001, while *p-values* less than or equal to 0.05 indicate marginally significant differences. We use a modified version of the two-sided KS test that attempts to account for measurement uncertainties (for details see the Appendix).

Envir.	**Cloud Property**									
	T_{max}	R	σ_v	b/a	ϕ	M_{lum}	M_{vir}	Σ_{H_2}	c	α
	[K]	[pc]	[km/s]		[deg]	$[10^5\ M_\odot]$	$[10^5\ M_\odot]$	$[M_\odot pc^{-2}]$	$[km\ s^{-1}\ pc^{-1/2}]$	
All	$3.0^{+4.6}_{-2.1}$	$48.4^{+64.5}_{-35.4}$	$5.9^{+8.0}_{-4.3}$	$0.6^{+0.7}_{-0.4}$	$7.6^{+24.8}_{--9.4}$	$7.6^{+16.5}_{-3.4}$	$19.6^{+40.5}_{-9.4}$	$177.4^{+298.5}_{-110.2}$	$0.9^{+1.3}_{-0.7}$	$1.6^{+3.2}_{-0.9}$
CR	$4.1^{+5.7}_{-2.2}$	$49.8^{+62.7}_{-37.4}$	$6.6^{+9.1}_{-4.8}$	$0.6^{+0.7}_{-0.4}$	$15.9^{+23.5}_{-9.4}$	$10.4^{+24.0}_{-3.9}$	$25.1^{+50.2}_{-12.5}$	$212.4^{+368.2}_{-129.2}$	$1.0^{+1.4}_{-0.7}$	$1.5^{+3.5}_{-0.9}$
SA	$3.0^{+4.6}_{-2.1}$	$49.3^{+66.3}_{-36.0}$	$6.1^{+8.2}_{-4.5}$	$0.6^{+0.7}_{-0.4}$	$2.9^{+27.9}_{--14.6}$	$8.3^{+18.2}_{-3.6}$	$21.7^{+45.1}_{-10.7}$	$185.3^{+304.1}_{-112.4}$	$1.0^{+1.3}_{-0.7}$	$1.7^{+3.0}_{-0.9}$
IA	$2.7^{+3.5}_{-2.1}$	$45.3^{+62.2}_{-32.6}$	$5.2^{+7.0}_{-3.9}$	$0.6^{+0.8}_{-0.5}$	$2.1^{+24.3}_{--11.3}$	$5.8^{+11.0}_{-3.1}$	$14.8^{+31.0}_{-6.9}$	$143.4^{+228.1}_{-94.0}$	$0.8^{+1.2}_{-0.6}$	$1.6^{+3.2}_{-0.8}$
NB	$4.3^{+5.2}_{-2.7}$	$49.6^{+63.8}_{-39.6}$	$6.1^{+9.0}_{-4.6}$	$0.5^{+0.7}_{-0.4}$	$17.9^{+23.0}_{-14.5}$	$10.7^{+19.8}_{-5.7}$	$20.7^{+49.8}_{-11.5}$	$184.3^{+291.1}_{-111.6}$	$0.9^{+1.3}_{-0.6}$	$1.5^{+3.7}_{-0.9}$
MR	$4.0^{+6.1}_{-2.0}$	$50.0^{+62.4}_{-36.9}$	$7.0^{+9.0}_{-4.9}$	$0.6^{+0.7}_{-0.4}$	$14.4^{+24.1}_{-7.7}$	$10.4^{+27.1}_{-3.5}$	$26.8^{+50.2}_{-13.6}$	$227.4^{+387.6}_{-141.8}$	$1.0^{+1.4}_{-0.8}$	$1.6^{+3.4}_{-0.9}$
DWI	$2.7^{+4.3}_{-1.9}$	$50.5^{+71.3}_{-39.3}$	$6.4^{+8.8}_{-5.0}$	$0.6^{+0.7}_{-0.4}$	$10.1^{+32.6}_{-3.8}$	$8.5^{+16.5}_{-3.7}$	$29.9^{+52.0}_{-12.6}$	$155.0^{+251.9}_{-110.2}$	$1.0^{+1.3}_{-0.7}$	$2.1^{+3.6}_{-1.2}$
DWO	$3.2^{+4.7}_{-2.1}$	$48.1^{+65.0}_{-34.8}$	$6.3^{+8.2}_{-4.6}$	$0.5^{+0.7}_{-0.4}$	$-4.2^{+20.5}_{--30.4}$	$8.6^{+22.8}_{-3.8}$	$22.8^{+42.3}_{-11.4}$	$218.7^{+317.3}_{-123.5}$	$1.0^{+1.3}_{-0.8}$	$1.7^{+2.7}_{-1.0}$
MAT	$3.2^{+4.6}_{-2.2}$	$48.3^{+67.2}_{-34.5}$	$5.3^{+7.4}_{-3.9}$	$0.6^{+0.7}_{-0.5}$	$-7.0^{+25.5}_{--14.5}$	$7.1^{+15.0}_{-3.1}$	$15.0^{+31.6}_{-8.7}$	$180.1^{+319.3}_{-92.3}$	$0.8^{+1.3}_{-0.6}$	$1.5^{+2.5}_{-0.8}$
DNS	$2.8^{+3.8}_{-2.2}$	$44.7^{+62.0}_{-32.3}$	$5.0^{+6.8}_{-3.9}$	$0.6^{+0.8}_{-0.5}$	$2.1^{+25.0}_{--10.9}$	$5.9^{+11.9}_{-3.1}$	$12.8^{+27.7}_{-6.7}$	$147.0^{+235.0}_{-94.5}$	$0.8^{+1.1}_{-0.6}$	$1.5^{+2.5}_{-0.8}$
UPS	$2.4^{+3.2}_{-1.9}$	$48.3^{+62.3}_{-32.8}$	$5.8^{+7.7}_{-4.1}$	$0.6^{+0.7}_{-0.5}$	$2.5^{+22.7}_{--11.7}$	$5.3^{+10.3}_{-3.1}$	$17.7^{+37.4}_{-7.5}$	$139.1^{+215.9}_{-92.5}$	$0.9^{+1.3}_{-0.6}$	$1.9^{+4.3}_{-0.8}$

Table 4.1: GMC properties in the different environments of M51. Median, lower quartile ($Q25$) and upper quartile ($Q75$) of the distributions. For Gaussian distributions a quartile corresponds to 0.6745σ or to the median absolute deviation (MAD).

4.2.1 BASIC GMC PROPERTIES

In Fig. 4.1, we plot the distribution of basic GMC properties within each of our environments. The results of the KS tests that were used to assess whether the distributions exhibit significant differences are reported in the Appendix. Fig. 4.1a and Fig. 4.1c show that the distributions of GMC peak brightness temperature T_{max} and velocity dispersion σ_v exhibit the most significant environmental variations: both properties tend to decrease from the center to the spiral arm to the inter-arm region. In the spiral arms and central region, GMCs span a large range of T_{max} and σ_v values, while the inter-arm region lacks GMCs with high T_{max} and σ_v. There is also a subtle difference between the peak brightness of interarm GMCs, such that upstream GMCs tend to have lower T_{max} than downstream clouds.

Galactic environment appears to have at most a modest impact on the size and elongation of GMCs in M51 (Fig. 4.1b and Fig 4.1d). GMCs in M51 are generally elongated with an *axis ratio* b/a around ~ 0.6[1]. However, clouds in the material arm and inter-arm regions have a slightly higher b/a and visually appear more round. By contrast, the *cloud orientation*, ϕ, shows a clear connection to galactic structure in M51. Fig. 4.1e shows that $\langle\phi\rangle$ is generally close to 0° in the spiral arm and inter-arm regions, confirming that the GMC orientation follows the spiral geometry. Clouds in the central region show a larger deviation from the spiral arm model, which is expected since the molecular ring is not a direct extension of the spiral arms. Nevertheless, the width of the ϕ distributions in all environments is fairly large. One possible explanation is that the CO spiral arms are not perfect logarithmic spirals. Although they are well-approximated by a double logarithmic spiral with $i_p = 21° \pm 5°$ for galactocentric radii $1.9 < R_{gal} < 5.5$ kpc (Patrikeev et al. 2006) several breaks are evident in a polar representation (see. Fig. 3 in Schinnerer et al. 2013). Another source of scatter might be due to GMCs located in the spurs that are orthogonal to the spiral arms (especially evident along the northern arm, see Figure 3.4).

4.2.2 DERIVED GMC PROPERTIES

In Figure 4.2, we plot the distributions of GMC mass, as inferred from both the CO luminosity and the virial theorem, H_2 mass surface density, scaling coefficient and virial parameter for each of the M51 environments. The differences in the brightness and velocity dispersion of GMCs that we detected in Figure 4.1 are likely to produce variations in the distributions of cloud properties that are estimated using a combination of these parameters. This is what we observe:

---

[1] It is worth to note that the typical GMC axis ratio (~ 0.5) is significant lower than the beam axis ratio (~ 0.84), i.e. the clouds have a genuine tendency to be elongated rather than round.

Fig. 4.2a shows the GMC mass inferred from the CO luminosity M_{lum} declines from the central and density-wave spiral arm regions to the material arm and inter-arm regions. This is expected since $M_{lum} \propto L_{CO} \propto \langle T \rangle R^2 \sigma_v$.[2] In broad terms, the mass derived from the virial theorem exhibits a similar trend (see Fig. 4.2b), although by definition it is dependent only on σ_v. We note that the average virial mass for GMCs in the PAWS catalog is $\sim 2\times$ greater than the average value of M_{lum}, derived assuming $X_{CO} = 2 \times 10^{20}\mathrm{cm}^{-2}$ (K km s^{-1})$^{-1}$.

Fig. 4.2c shows that the average GMC mass surface density $\langle \Sigma_{H_2} \rangle$ is highest in the central zone (212 $\mathrm{M}_\odot\,\mathrm{pc}^{-2}$), and lower in spiral arm (185 $\mathrm{M}_\odot\,\mathrm{pc}^{-2}$) and the inter-arm region (143 $\mathrm{M}_\odot\,\mathrm{pc}^{-2}$). Across the entire PAWS FoV, the median H_2 mass surface density is $\Sigma_{H_2} \approx 180\ \mathrm{M}_\odot\,\mathrm{pc}^{-2}$, almost twice the average value observed for GMCs in the inner Milky Way ($\sim 100\ \mathrm{M}_\odot\,\mathrm{pc}^{-2}$, Heyer et al. 2009). We note that the PAWS and Galactic values are not strictly comparable: the Galactic structures described by Heyer et al. (2009) are typically smaller than the GMCs in M51, and the filling factor of CO emission within the PAWS beam is likely to be less than unity since the typical peak brightness is only $\mathrm{T}_{max} \approx 4$ K.

Fig. 4.2e shows that the median value of the virial parameter is $\sim$ 1.6 across all M51 environments, with values for individual GMCs ranging between 0 and 8. This suggests that the GMC population in M51 is, on average, self-gravitating, although $\sim$ 30% of the clouds have $\alpha > 2$. The fraction of clouds with $\alpha > 2$ is higher for the upstream subsample than for the downstream subsample of GMCs. Fig. 4.2d shows that the average scaling coefficient $c \approx 0.90$ km s^{-1} pc$^{-1/2}$ of the size-linewidth relation is also roughly constant across the different environments. The median value $\langle c \rangle \approx 0.90$ km s^{-1} pc$^{-1/2}$ is always higher than the Galactic value of 0.72 km s^{-1} pc$^{-1/2}$ (Solomon et al. (1987)). This reflects the fact that GMCs in M51 tend to have higher velocity dispersions than GMCs with comparable size in the Milky Way.

---

[2] A parametric description of the CO luminosity is legitimate, although CPROPS calculates L_{CO} by summing the emission from all pixels that constitute one cloud as described in Section 3.3.2.

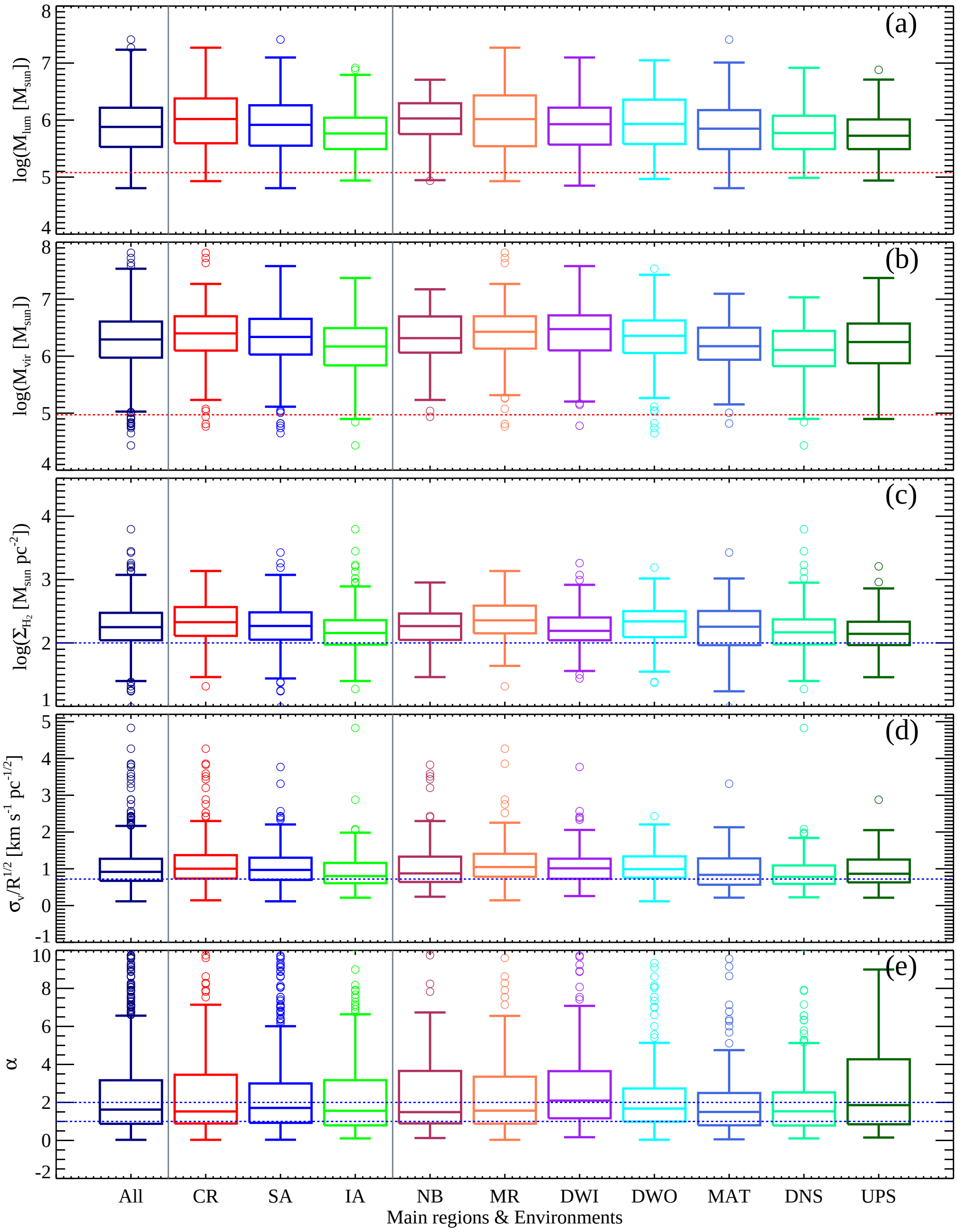

Figure 4.2: Derived GMC properties (from top to bottom): (a) mass derived from CO luminosity M_{lum} and (b) using the virial theorem M_{vir}, (c) H$_2$ surface density Σ_{H_2}, (d) scaling coefficient $\sigma_v/R^{1/2}$ and (e) virial parameter α shown in a "box and whiskers" representation (see Fig. 4.1 for details) for different M51's environments (from the left to the right: All -full sample; 3 main regions -center (CR), spiral arm (SA), inter-arm (IA) and the 7 environments defined in Fig. 1.5). For the box and whiskers representation description refer to Fig 4.1. In general masses, H$_2$ mass surface densities and scaling coefficients are higher in the center and in the spiral arm region than in the inter-arm environments. The cloud population in every environment is, in general, self-gravitating, however a number of objects appears unbound (α > 2). Straight horizontal red lines indicate the sensitivity or resolution limits: 1.2×10^5 $M_\odot$ for the luminosity mass and 10^5 $M_\odot$ for the virial mass. For surface density and scaling coefficient the blue lines show values observed in the Galaxy: 100 M$_\odot$ pc^2 (Heyer et al. 2009) and 0.72 km s^{-1} pc$^{-1/2}$ (Solomon et al. 1987), respectively. Horizontal blue lines in the virial parameter panel indicate the limit between virialized and self-gravitating clouds (α = 1) and unbound objects (α = 2) (see text for details).

4.3 SCALING RELATIONS

Having reviewed the physical properties of GMCs in different regions of M51, we now examine whether the clouds obey the scaling relations commonly referred to as "Larson's laws" (Larson 1981). The first Larson's law, or *size-velocity dispersion relation*, states that $\sigma_v \propto R^{0.5}$ (Solomon et al. (1987)); it is considered to be a manifestation of turbulence inside the cloud or of virial equilibrium (see Kritsuk & Norman 2011). The second Larson's law asserts that GMCs are roughly self-gravitating. The third law describes an inverse correlation between the size of a cloud and its density, implying that all GMCs have approximately constant surface density.

To estimate the degree of correlation between GMC properties we calculate the Spearman's rank correlation coefficient. This coefficient, r_s, assesses how well the relationship between two variables can be described by a monotonic function. If there are no repeated data values, +1 indicates a perfect monotonically increasing function. We consider the properties to be strongly correlated if $r_s \geq 0.8$, and moderately correlated if $0.5 < r_s < 0.8$. For the scaling relations shown in Fig. 4.3 to Fig. 4.6, the corresponding r_s values are indicated in the bottom corner of each panel.

To fit any correlations that we detect, we use the IDL implementation distributed by Erik Rosolowsky of the "BCES" (bivariate, correlated errors with intrinsic scatter) method described by Akritas & Bershady (1996). The BCES bisector estimator takes into account the uncertainty associated with each cloud property measurement. In our estimate for the best-fitting relation, we use only the "highly reliable sample" of clouds of the catalog, i.e. GMCs with $S/N > 6.5$ (see Section **??**), and we assume that the measurement uncertainties are uncorrelated. The parameters for the best-fitting power laws to the correlations in Fig. 4.4 and Fig. 4.6 are summarized in Table 4.2.

4.3.1 FIRST LARSON'S LAW: SIZE-VELOCITY DISPERSION RELATION

The relationship between the size and velocity dispersion of GMCs in the PAWS catalog is shown in Fig. 4.3. For all environments, there is a high degree of scatter and the r_s values indicate that the size and linewidth of the M51 GMCs are, at best, weakly correlated. If we restrict our comparison to GMCs with high signal-to-noise ($S/N > 6.5$), then a linear trend between R and σ_v becomes apparent for some environments, although the correlation is still very weak ($r_s \leq 0.25$). In the bottom row of Fig. 4.3, we use contours to indicate the region of the size-velocity dispersion space occupied by GMCs in different M51 environments. Compared to spiral arm environments, the inter-arm region lacks clouds with high σ_v, while GMCs in the central region seem shifted towards slightly higher values of R and σ_v. It is worth to note also that the majority of the data points lies above the Galactic (Solomon et al. 1987) and extragalactic (Bolatto et al. 2008) fits, in particular in the case of the center and spiral arm samples. This shows that GMCs in M51 have a higher velocity dispersion compared with similar size clouds in the Milky Way or Local Group galaxies.

Envir.	$M_{vir} = (a \pm \delta a) L_{CO}^{(b \pm \delta b)}$		$L_{CO} = (a \pm \delta a) R^{(b \pm \delta b)}$	
	$a \pm \delta a$	$b \pm \delta b$	$a \pm \delta a$	$b \pm \delta b$
All	0.06 ± 0.03	1.35 ± 0.10	233.99 ± 57.27	1.88 ± 1.29
CR	0.14 ± 0.14	1.29 ± 0.17	132.93 ± 68.42	2.06 ± 2.85
SA	0.07 ± 0.06	1.33 ± 0.14	183.97 ± 65.46	1.95 ± 2.00
IA	0.01 ± 0.01	1.47 ± 0.22	887.14 ± 329.13	1.48 ± 1.84
NB	0.04 ± 0.08	1.39 ± 0.35	481.68 ± 272.82	1.68 ± 3.52
MR	0.25 ± 0.33	1.24 ± 0.21	79.97 ± 60.01	2.22 ± 4.08
DWI	0.49 ± 0.57	1.21 ± 0.24	152.94 ± 108.15	1.97 ± 3.67
DWO	0.09 ± 0.11	1.31 ± 0.19	164.88 ± 77.54	2.00 ± 3.02
MAT	0.01 ± 0.02	1.49 ± 0.32	330.35 ± 269.46	1.78 ± 3.72
DNS	0.00 ± 0.00	1.68 ± 0.44	660.50 ± 492.34	1.54 ± 3.52
UPS	0.04 ± 0.05	1.38 ± 0.25	991.33 ± 431.23	1.46 ± 2.17

Table 4.2: Scaling relation fits for the different environments of M51. The errors on the fitting coefficients are the one sigma uncertainties as derived by the BCES procedure using 50 bootstrap iterations.

4.3.2 SECOND LARSON'S LAW: VIRIAL MASS-LUMINOSITY RELATION

In Fig. 4.4, we plot the virial mass of the M51 GMCs as a function of their CO luminosity. We note that both virial mass and CO luminosity depend on a combination of R and σ_v, i.e. $M_{vir} \propto \sigma_v^2 R$ and $L_{CO} \propto \langle T \rangle R^2 \sigma_v$), so a significant degree of correlation between these quantities is expected. Fig. 4.4 shows that GMCs in M51 are scattered around the extragalactic relation obtained by Bolatto et al. (2008) ($M_{vir}(M_\odot) = 7.6 L_{CO}^{1.00} (K\, km/s\, pc^2)$), although the peak-to-peak variations in M_{vir}/L_{CO} span up to ~ 2 orders of magnitude. The best-fitting mass-luminosity relations that we obtain for the different M51 GMC populations are steeper than the Bolatto et al. (2008) relation by ~ 0.2 to 0.5 dex. We note that the slope of the mass-luminosity relation varies with environment, increasing from ~ 1.3 in the spiral arm and central regions to ~ 1.5 in the inter-arm region. This increment is likely driven by differences in luminosity and velocity dispersion observed within the environments. Moreover, the clouds appear roughly distributed around a $X_{CO} = 4 \times 10^{20}$ cm^{-2} (K km s^{-1})$^{-1}$. We provide a more detail derivation of X_{CO} based on cloud measurements in Section 4.5.

The analysis of the distribution of the virial parameter of Section 4.2.2 has shown that clouds in M51 are in general self-gravitating. Here we check if α has some correlation with the cloud mass. In Fig. 4.5, we plot α as function of M_{lum} finding that α tends to decrease for high mass clouds. This behavior is partially expected since we use M_{lum} to the denominator of the virial parameter (but see Wong et al. 2011), but it would indicate that the high mass cloud in M51 are more strongly bound. However a fraction of GMCs with $\alpha > 2$ is present even in between the most massive clouds. Clouds with $\alpha < 1$ are probably due to noise in the virial mass derivation.

4.3.3 THIRD LARSON'S LAW: LUMINOSITY-SIZE RELATION

Fig. 4.6 shows that the size and CO luminosity of M51 GMCs are strongly correlated, with $0.5 < r_s < 0.8$. This is not surprising since $L_{CO} \propto \langle T \rangle R^2 \sigma_v$. The bottom row of Fig. 4.6 shows that the relationship between R and L_{CO} is steeper in the central and spiral arm regions than in the inter-arm region. This is confirmed by the results of a linear regression fit: the slope of the best-fitting power law flattens from 2.4 for GMCs in the molecular ring, to ~ 2 for clouds in the density wave spiral arms, to < 1.5 for the inter-arm environments. The origin of such effect is likely to be the different CO emission properties within the different M51 environments (such as the geometry, CO filling factor and/or density distribution, see also Hughes et al., submitted) but further investigation into its physical significance is required. Nevertheless, the change in slope of the fit appears to be real, given the fact that all environments span a similar range of GMC radii but contain clouds with very different luminosity. Assuming a uniform X_{CO} factor throughout the PAWS field, the linear regression illustrates why the median H_2 mass surface density varies with environment: large GMCs located in molecular ring and density-wave spiral arms contain more high brightness CO emission than clouds of an equivalent size in the inter-arm region.

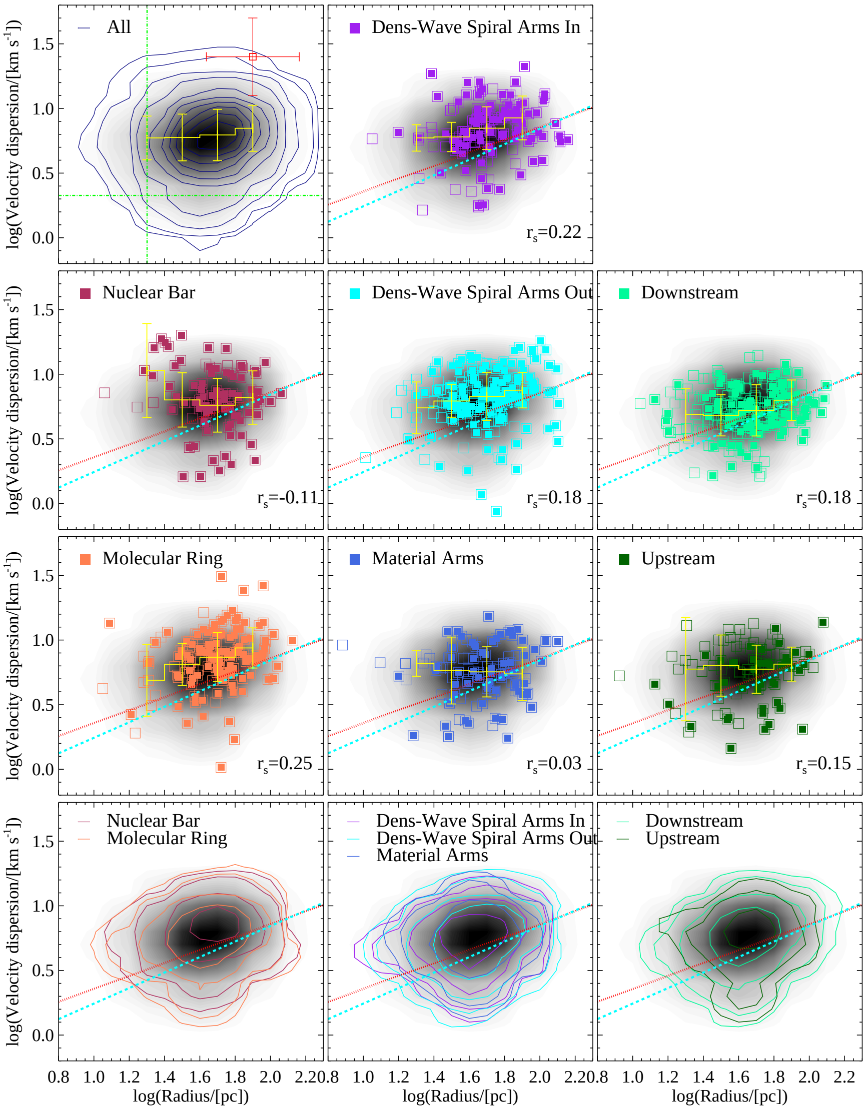

Figure 4.3: Size-velocity dispersion relation ("first Larson's law") for GMCs in M51 within the various environments. Every column refers to a different region (from left to right: spiral arm, inter-arm and central region). Data points corresponding to clouds with $S/N > 6.5$ are highlighted with filled symbols. The shaded area shows the density distribution of the full catalog. Red dotted lines indicate the Galactic fit ($\sigma_v(km/s) = 0.72R(pc)^{0.5}$, Solomon et al. 1987) and cyan dashed lines the extragalactic fit ($\sigma_v(km/s) = 0.44R(pc)^{0.6}$, Bolatto et al. 2008). In the bottom right corner of each panel the Spearman's correlation rank is given. The histogram in yellow illustrates the median and the MAD of $log(\sigma_v/[km/s])$ in bins of 0.2 dex for $log(R/[pc]) \in (1.0-2.0)$. Then bottom row shows a contour representation of all GMCs with $S/N > 6.5$ within the various environments. In the top left panel the contours show the distribution of the full sample of "highly reliable clouds" (with $S/N > 6.5$). Green horizontal and vertical lines indicate the nominal resolution limit: 20 pc (CLEAN beam radius) and 2.12 km/s (channel velocity dispersion). The average error bars are reported in red in the top right corner of the top right panel.

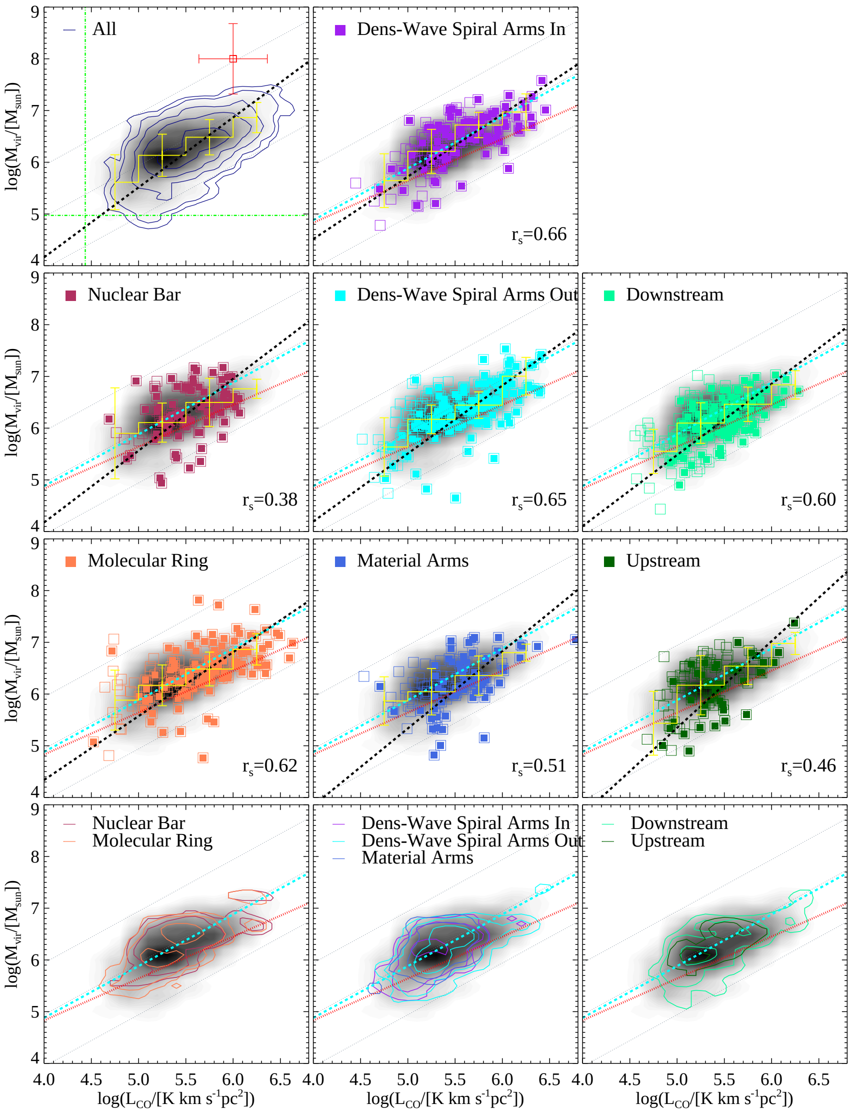

Figure 4.4: Virial mass-luminosity relation ("second Larson's law") for GMCs in M51 for the various environments. Every column refers to a different region (from left to right: spiral arm, inter-arm and central region). Data points corresponding to clouds with $S/N > 6.5$ are highlighted with filled symbols. The shaded area shows the density distribution of the full catalog. Red dotted lines indicate the Galactic fit ($M_{vir}(M_\odot) = 39L_{CO}^{0.81}(K\,km/s\,pc^2)$, Solomon et al. 1987), cyan dashed lines the extragalactic fit ($M_{vir}(M_\odot) = 7.6L_{CO}^{1.00}(K\,km/s\,pc^2)$, Bolatto et al. 2008) and black straight lines the fits for the different environments (see Table 4.2). Dashed grey lines indicate different X_{CO} values, from bottom to top $X_{CO} = 4 \times 10^{19}$, 4×10^{20}, and 4×10^{21} cm^{-2} K^{-1} km^{-1} s. In the bottom right corner of the panels the Spearman's correlation rank is given. The histogram in yellow illustrates the median and the MAD of $log(M_{vir}/[\mathrm{M}_\odot])$ in bins of 0.5 dex for $log(L_{CO}/[\mathrm{K\ km\ s^{-1}\ pc^{-2}}]) \in (4.5 - 6.5)$. The bottom row shows a contour representation of the GMCs with $S/N > 6.5$ within the various environments. In the top left panel the contours show the distribution of the full sample of "high reliable clouds" (with $S/N > 6.5$). Green lines indicate resolution limit: 2.7×10^4 K km s^{-1} pc^{-2} for CO luminosity and 9.3×10^4 $M_\odot$ for the virial mass. The average error bars are reported in red in the top right corner of the top right panel.

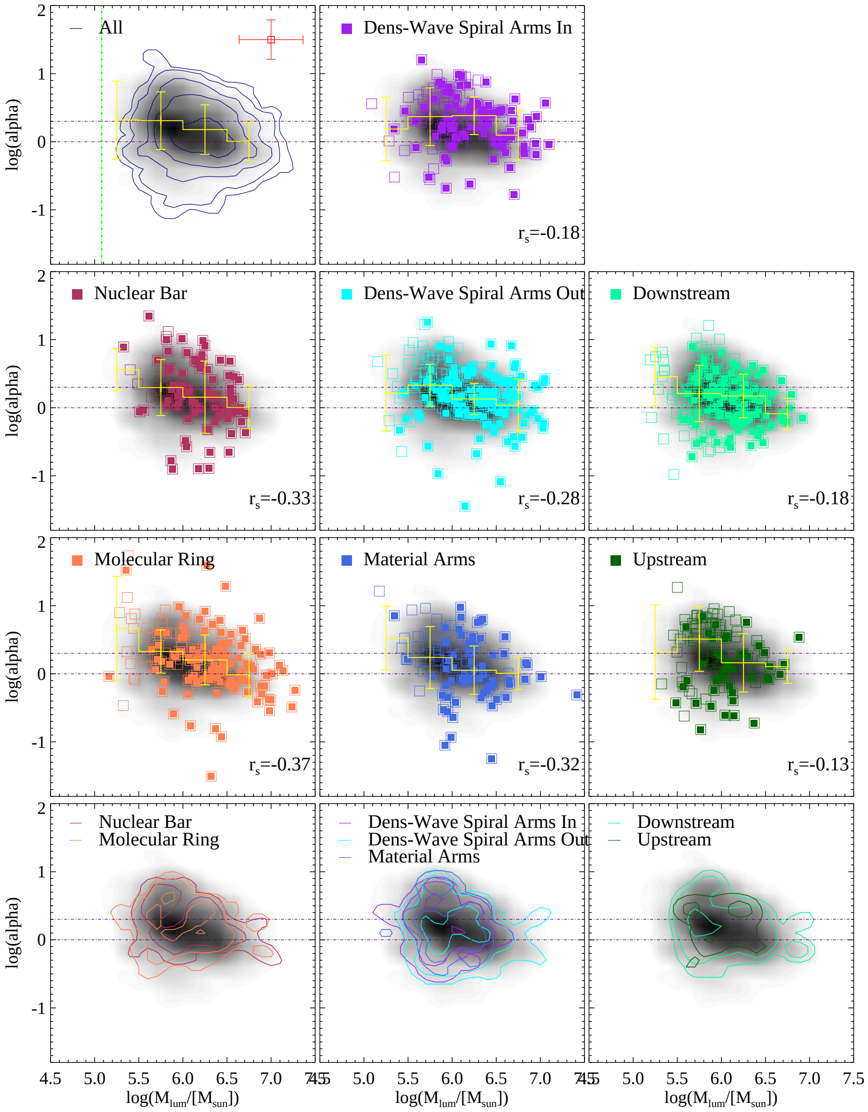

Figure 4.5: Mass-virial parameter relation for GMCs in the various M51 environments. Every column refers to a different region (from left to right: spiral arm, inter-arm and central region). Data points corresponding to clouds with $S/N > 6.5$ are highlighted with filled symbols. The shaded area shows the density distribution of the full catalog. In the bottom right corner of the panels the Spearman's correlation rank is given. The histogram in yellow illustrates the median and the MAD of $log(\alpha)$ in bins of 0.5 dex for $log(M_{lum}/[M_{\odot}] \in (5.0-7.0)$. The bottom row shows a contour representation of the GMCs with $S/N > 6.5$ within the various environments. In the top left panel the contours show the distribution of the full sample of "highly reliable clouds" (with $S/N > 6.5$). Purple horizontal dashed lines indicate the limit between self-gravitating and pressure confined clouds ($\alpha = 1$) and unbound clouds ($\alpha = 2$). Green line indicates our nominal sensitivity limit: 2.7×10^4 K km s^{-1} pc^{-2} for CO luminosity. The average error bars are reported in red in the top right corner.

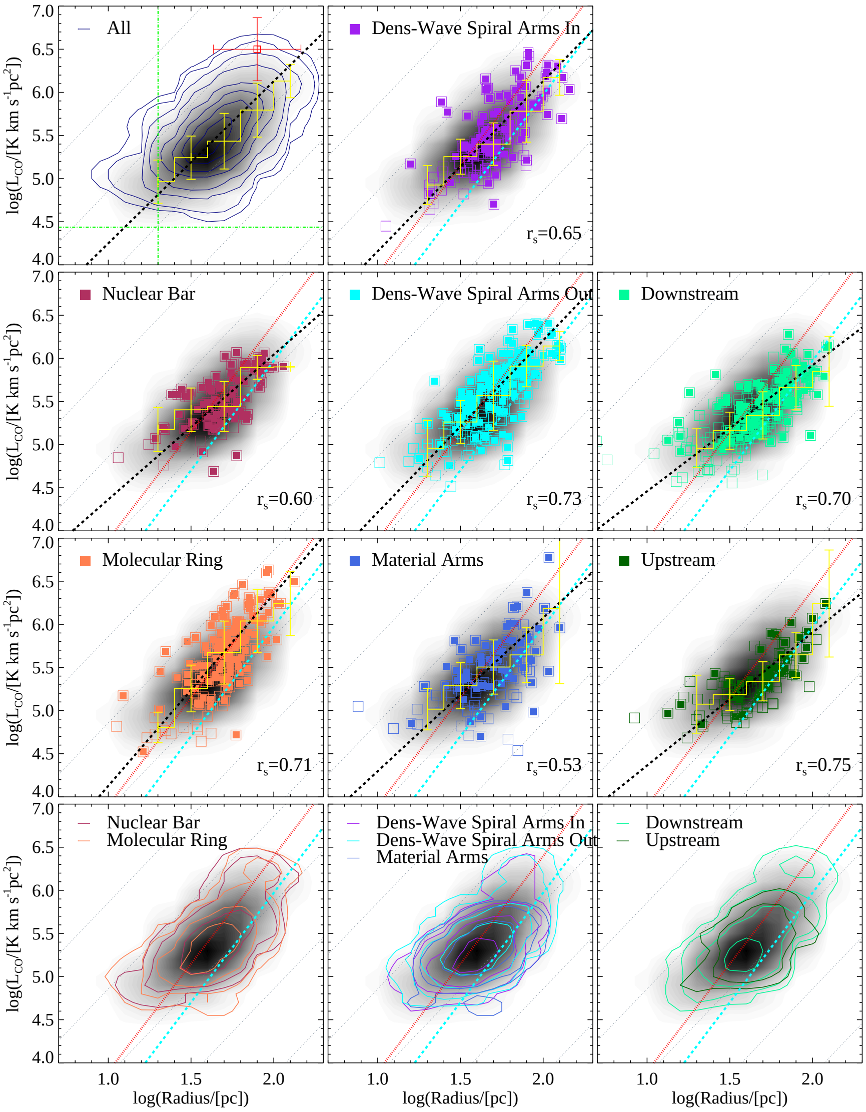

Figure 4.6: Luminosity-size relation (third Larson's law) for GMCs in the various M51 environments. Every column refers to a different region (from left to right: spiral arm, inter-arm and central region). Data points corresponding to clouds with $S/N > 6.5$ are highlighted with filled symbols. The shaded area shows the density distribution of the full catalog. Red dotted lines indicate the Galactic fit ($L_{CO}(K\,km/s\,pc^2) = 25R^5(pc)$, Solomon et al. (1987)), cyan dashed lines the extragalactic fit ($L_{CO}(K\,km/s\,pc^2) = 7.8R^{2.54}(pc)$, Bolatto et al. (2008)) and black straight lines the fits for the different environments (see Table 4.2). Dashed grey lines indicate different H_2 surface density values, from bottom to top $\Sigma_{H_2} = 1$, 10, 100, 10^3, and 10^4 $M_\odot pc^{-2}$. At the bottom of the panels the Spearman's correlation rank is indicated. The histogram in yellow illustrates the median and the MAD of $log(L_{CO}/[\mathrm{K\,km\,s^{-1}\,pc^2}]$ in bins of 0.2 dex for $log(R/[pc]) \in (1.2 - 2.0)$. The bottom row shows a contour representation of the various environments. In the top left panel the contours show the distribution of the full sample of reliable clouds (with $S/N > 6.5$). Green horizontal and vertical lines indicate the nominal sensitivity and resolution limits: 2.7×10^4 K km/s pc^{-2} for CO luminosity and 20 pc for the radius, respectively. The average error bars are reported in red in the top right corner of the top right panel.

4.4 GMC MASS SPECTRA

4.4.1 CONSTRUCTION AND GENERAL PROPERTIES

The GMC *luminosity distribution* depicts how the CO flux is organized into clouds with different luminosity within a galaxy (e.g. Rosolowsky 2005). We convert the CO luminosity to H_2 mass assuming a constant Galactic conversion factor $X_{CO} = 2 \times 10^{20}$ cm^{-2} (K km s^{-1})$^{-1}$, thus $M_{lum} = 4.4 L_{CO}$ (eq. 3.7). In this section, we frame our discussion in terms of the *GMC mass spectrum*, which equivalently describes how molecular gas is organized into cloud structures of different mass throughout a galaxy, assuming that CO emission is a reliable tracer of H_2.

The GMC mass spectrum is usually expressed in differential form and modeled as a power law:

$$f(M) = \frac{dN}{dM} \propto M^{\gamma} \tag{4.4}$$

The integral of this expression yields the *cumulative mass distribution*, i.e. the number of clouds N with masses M greater than a reference mass M_0 as a function of that reference mass:

$$N(M' > M) = \left[\left(\frac{M}{M_0} \right)^{\gamma+1} \right]. \tag{4.5}$$

The index γ describes how the mass is distributed: for values $\gamma > -2$, the gas is preferentially contained in massive structures, while for values $\gamma < -2$, small clouds dominate the molecular mass budget.

Several studies have reported that the mass spectrum steepens at high clouds masses (e.g. Fukui et al. 2001, Rosolowsky 2007, Gratier et al. 2012). In this case, it can be useful to model the mass spectra using a truncated power-law (Williams & McKee 1997):

$$N(M' > M) = N_0 \left[\left(\frac{M}{M_0} \right)^{\gamma+1} - 1 \right], \tag{4.6}$$

where M_0 is the maximum mass in the distribution and N_0 is the number of clouds more massive than $2^{1/(\gamma+1)} M_0$, the mass where the distribution deviates from a power-law.

Fig. 4.7 shows the cumulative M_{lum} distributions for GMCs in different M51 environments. The equivalent values of CO luminosity are indicated on the top y-axis. In the left panel, the distributions are normalized by the projected area (in kpc^2) of the different environments (listed in Table 3.4, and indicated in the top-right corner of the panels in Fig. 4.8). Using this normalization, the vertical offsets between the different mass distributions reflect true variations in the number surface density of GMCs: as noted in Section 3.5, the number density of GMCs is higher in the center than the spiral arms, and higher in the spiral arms than the inter-arm region. The right panel of Fig. 4.7 shows the same GMC mass distributions, this time normalized by the total number of GMCs in each environment to facilitate a comparison of the distribution shapes. Extremely high mass objects ($M_{lum} > 10^7$ M$_\odot$) are only observed in the molecular ring and spiral arms. The inter-arm region (especially the upstream environment) and nuclear bar environment contain very few clouds with masses greater than $10^{6.5}$ M$_\odot$, although the number of GMCs per unit area in the nuclear bar region is much higher than in the inter-arm region.

The GMC mass distributions have a similar overall shape, appearing to steepen with increasing mass in every M51 environment. Across most of the observed mass range, the slope of the mass distribution is shallower in the molecular ring and the density-wave spiral arms than in the inter-arm, while the mass distribution in the material arms has a slope that is intermediate between these extremes. The nuclear bar shows evidence for a strong truncation at $10^{6.5}$ $M_\odot$. Within the inter-arm region, the mass distribution of downstream GMCs is reaches higher cloud masses than the upstream cloud distribution. The mass distribution of upstream and material arm GMCs is the most similar to a pure power-law across the range of cloud masses probed by PAWS.

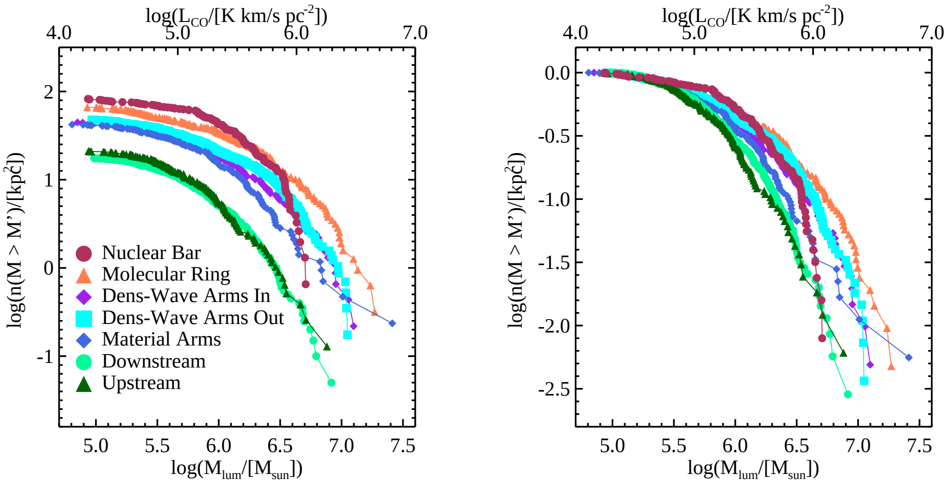

Figure 4.7: Compact view of the cumulative mass spectra for GMCs in the different environments of M51 normalized by the area covered by the environments in *kpc*^{2} (*left*; see Fig. 4.8 for exact area) and to the total number of clouds for each environment (*right*). These representations illustrate clearly a vertical offset (different number density of GMCs), a horizontal offset (maximum mass possible to form in a given environment) and different shape between the spectra. For reference, the top axis provides the equivalent CO luminosity.

Envir.	γ	M_0 $10^6\ M_\odot$	N_0	p-value
All	-2.29 ± 0.09	18.5 ± 3.4	17 ± 7	10^{-4}
NB	-1.33 ± 0.21	5.2 ± 0.3	90 ± 21	1.00
MR	-1.63 ± 0.17	15.0 ± 3.2	26 ± 20	0.72
DWI	-1.75 ± 0.20	12.2 ± 1.8	15 ± 12	1.00
DWO	-1.79 ± 0.09	11.8 ± 0.9	24 ± 9	0.30
MAT	-2.52 ± 0.20	158.6 ± 7.4	0 ± 2	0.92
UPS	-2.44 ± 0.40	9.3 ± 4.0	2 ± 3	1.00
DNS	-2.55 ± 0.23	8.3 ± 1.9	5 ± 4	0.36

Table 4.3: Slopes γ, maximum mass M_0 and number of GMCs at the maximum mass N_0 of the truncated power-law fits to the GMC mass spectra of the different environments in M51. The error are obtained through 50 bootstraps interaction. In the last column the goodness-to-fit tests are given as p-values of the KS tests. Truncated power-law fits to the GMC mass spectra of the M51's environments

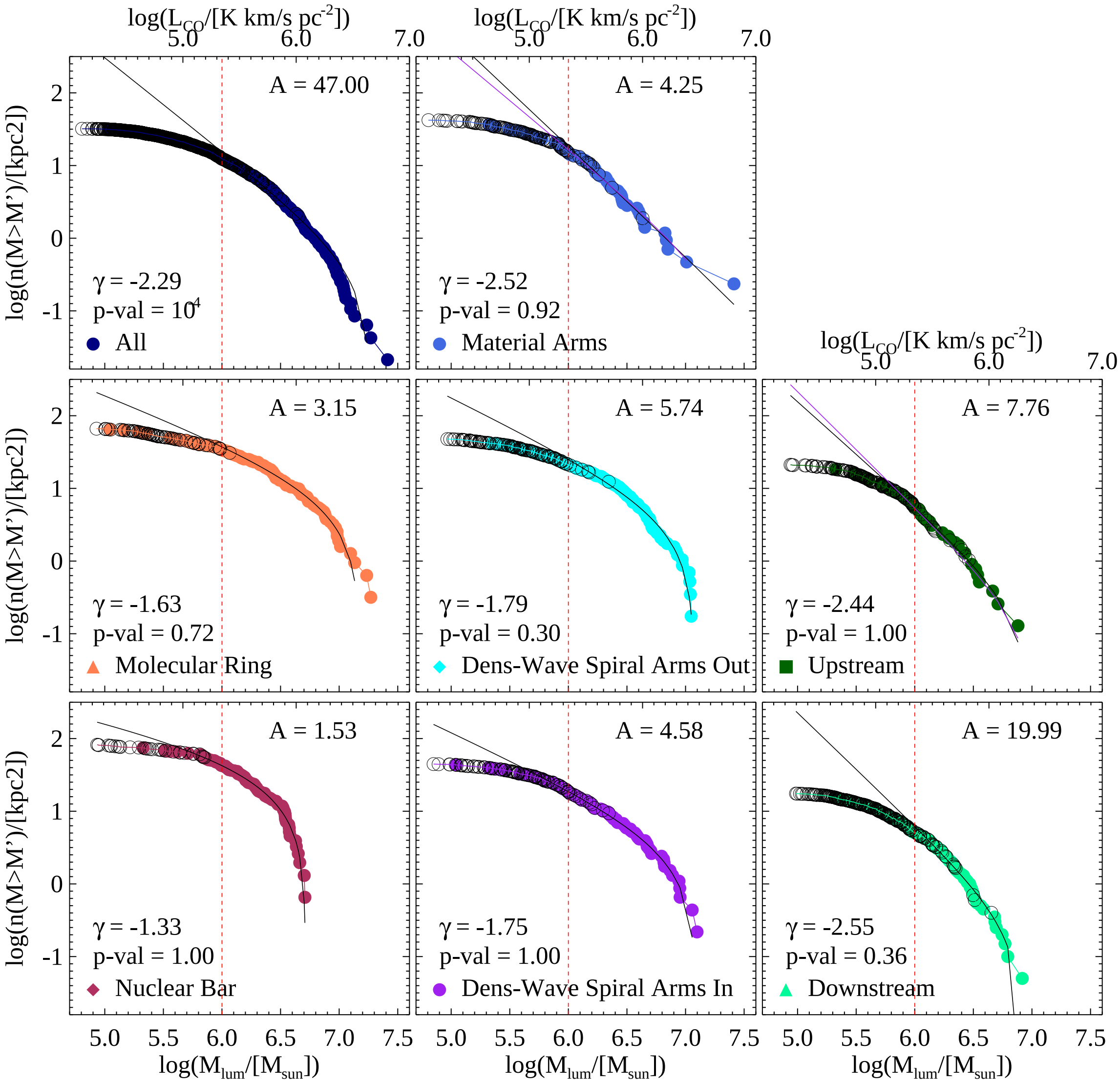

Figure 4.8: Cumulative mass spectra for GMCs in the different environments (from left to right: central, spiral arm, inter-arm regions with the full catalog shown in the top left panel). Colored full circles indicates clouds within the "highly reliable sample", while empty black circles clouds with $S/N < 6.5$. Solid black lines represent the truncated power-law fits while the purple line indicates the power-law fits for distributions that show resemblance with simple power-law. Red vertical dashed line indicates the lower mass limit of the fit (10^6 M⊙). In the top-right corner of each panel the normalization area (in kpc^2) is given, while on the lower-left corner the value of the slope (γ) and of the KS test p-value (p-val) are indicated. For reference, the top axis provides the equivalent CO luminosity.

4.4.2 Slope variations

The shape of the GMC mass distributions in M51 differs from those that have been observed to date in the Milky Way and other galaxies, which tend to be adequately represented by simple or truncated power-laws (e.g. Rosolowsky 2005, Fukui et al. 2008, Fukui & Kawamura 2010, Gratier et al. 2012). In M51, by contrast, the mass distributions appear to steepen continuously with increasing cloud mass, above our adopted sensitivity limit 3.6×10^5 $M_\odot$. This is especially clear in the nuclear bar spectrum where a changes of slope are apparent around 5×10^5 and 3×10^6 $M_\odot$. In part, this may be because our sample of GMCs in M51 is significantly larger than those used by many previous studies and this, in combination with our adoption of the cumulative representation of the mass distribution, allows us to discern subtle changes in the distribution shape that are not well-captured with a small number of objects or a differential formulation (for which clouds must be allocated to mass bins of finite width). The variation in the mass distribution shapes between different M51 environments points toward a physical origin. Here we examine the mass-dependent variations in the mass distribution slope for the different M51 environments in detail; we propose a physical scenario to explain these variations in Section 4.6.1.

To characterize the shape of the GMC mass distributions and facilitate the comparison between M51 and other galaxy results, we fit the spectra with Eq. 4.6 above a fiducial mass of 10^6 $M_\odot$, where the distributions show more resemblance to truncated power-laws. This limit is significantly higher than our adopted catalog completeness limit and roughly corresponds to the lower mass limit of the high reliable sample of clouds. We discuss the reasons for only fitting the mass distributions above this relatively high mass, and the possible effects of incompleteness on the mass distributions in Section 4.4.3. The fit is performed using Erik Rosolowsky's IDL procedure `MSPECFIT`, which implements the maximum likelihood method described in Rosolowsky (2007). As a goodness-of-fit test we use the KS test. The parameters of the fits to the mass distributions are summarized in Table 4.3. The fits are overplotted on the mass distributions in Fig. 4.8.

The GMC mass spectra belonging to the different environments of M51 show different features. The molecular ring and density-wave spiral arm cloud distributions show similar spectral indices ($\gamma \approx -1.8 \div -1.6$) and fitted maximum masses $M_0 > 10^7$ $M_\odot$. The mass distributions from the interarm region, by contrast, have $\gamma \approx -2.5$ and M_0 less than 10^7 $M_\odot$. These results indicate that the molecular gas in the molecular ring and density-wave spiral arms is preferentially distributed in high mass GMCs, whereas smaller clouds are the preferred unit of molecular structure in the inter-arm environments. The mass distribution of the material arms shares features with both the molecular ring/density-wave spiral arm and inter-arm environments: a spectral index $\gamma \approx -2.5$, but with a high maximum mass $M_0 > 10^8$ $M_\odot$, probably biased by the presence of a very massive object (with $M_{lum} \sim 2.5 \times 10^7$ $M_\odot$).

The inter-arm and material arm spectra have N_0 close to the unity, suggesting that a simple power-law is sufficient to describe the mass distributions. We test this possibility finding that upstream and material arm distributions can be well represented by simple power-laws, as shown by the p-values of the corresponding KS tests, which are close to 1. The case of the nuclear bar spectrum is peculiar, since it presents the shallowest slope ($\gamma \approx -1.3$), but the lowest maximum mass ($M_0 \approx 5.5 \times 10^6$ $M_\odot$). Together with a $N_0 \approx 90$, these features prove a sharp truncation in the mass distribution of this environment.

As suggested by the very low value of the KS test ($\sim 10^{-4}$), a single truncated power-law does not provide a good fit for overall M51 distribution. This is not surprising since the distribution for GMCs within the whole PAWS field is composed of the superposition of the mass distributions from the different M51 environments, which have different slopes and different truncation masses.

The mass- and environment-dependent variations in the M51 GMC mass distributions suggest that different mechanisms regulate the formation and destruction of GMCs in different regions of M51's inner disk. The non-power-law shape of the mass distributions, which is most pronounced in the central and density-wave spiral arm environments, is suggestive of processes that promote the formation (and survival) of intermediate mass clouds, without providing an effective formation pathway for extremely high-mass objects. The mass distributions in the inter-arm region (especially upstream) are closer to pure power-laws, suggesting that the mechanism(s) responsible for the curvature in the mass distributions is not as effective in the inter-arm. This provides another possible explanation for why the generic shape of the GMC mass distributions in M51 is distinct from the simple power-law observed for other extragalactic GMC populations, which tend to be from low-mass dwarf galaxies (e.g. the LMC and M33, Wong et al. 2011, Gratier et al. 2012) or regions of galactic disks without strong spiral structure (e.g. the outer Milky Way and an outer arm of M31, Rosolowsky 2005).

4.4.3 TESTING THE SHAPE OF THE MASS SPECTRA FOR INCOMPLETENESS EFFECTS

As we noted in Section 4.4, most extragalactic GMC mass distributions that have been observed to date are adequately represented by a simple power-law. Since we argue that the shape of the mass spectrum yields important clues regarding the physical mechanisms of cloud formation

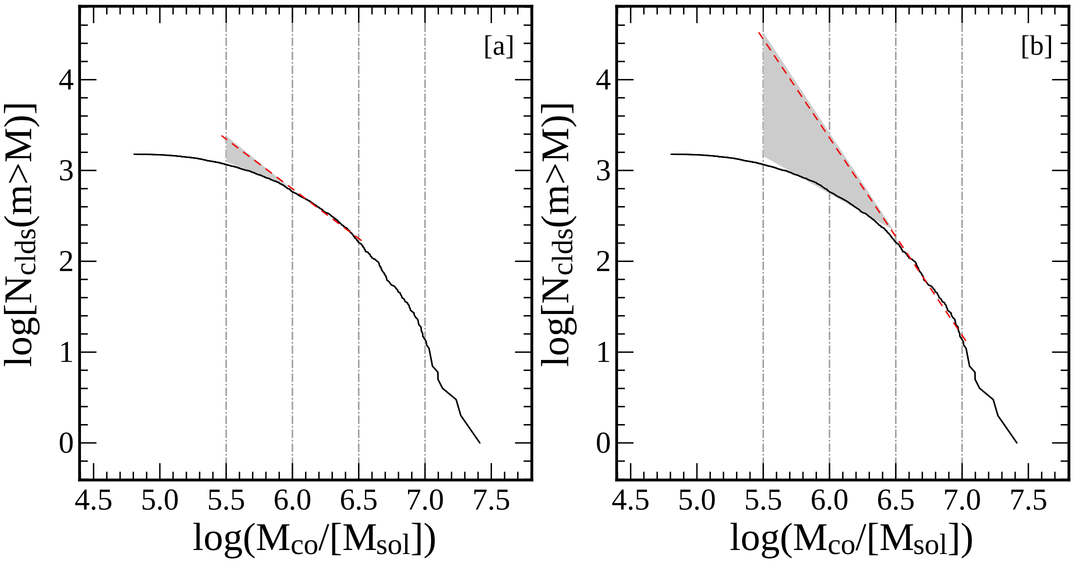

Figure 4.9: Schematic diagram illustrating our test for whether there is a genuine steepening of the GMC mass distributions in M51. We calculate the total number of GMCs under the assumption that the power-law mass distribution observed [a] across the mass range $\log(M) \in [6.0, 6.5]$ (case A) or [b] across the mass range $\log(M) \in [6.5, 7.0]$ continues down to $M > 10^{5.5}\,\mathrm{M}_\odot$. The shape of the distribution at higher GMC masses is assumed to follow the observed distribution. The grey shaded wedge in each panel indicates the difference between the power-law distribution (red dashed line) and observed mass distribution (black solid line) in each case. To test whether the true GMC mass distribution could be consistent with the power-law mass distribution, we examine whether the total CO luminosity corresponding to the power-law mass distribution exceeds the integrated CO flux and working area flux within each M51 environment.

and destruction, it is important to assess whether the mass distributions that we obtain are reliable. In particular, although the mass corresponding to the sensitivity limit of our observations ($\sim 10^5\,\mathrm{M}_\odot$) suggests that our GMC catalog should be reasonably complete above $\sim 5 \times 10^5\,\mathrm{M}_\odot$, CPROPS might still be unable to distinguish clouds above this mass if they are located in a crowded region like the spiral arms, effectively raising the completeness limit.

To test whether the observed GMC mass distributions in M51 could be significantly affected by incompleteness, we estimated the total number of GMCs with masses $M > 10^{5.5}\,\mathrm{M}_\odot$ and their combined CO luminosity that would be expected in each M51 environment if: (i) the true mass distribution followed a simple power-law with the same exponent as in the intermediate mass bin down to $M = 10^{5.5}\,\mathrm{M}_\odot$ (case A); and (ii) the true mass distribution across the mass range followed a simple power-law with the same exponent as in the upper mass bin down to $M = 10^{5.5}\,\mathrm{M}_\odot$ (case B). A schematic explaining the two cases is shown in Figure 4.9, and the results for each M51 environment are presented in Table 4.4.

On one hand, it is clear that there must be a genuine steepening of the GMC mass distribution with increasing mass in all M51 environments. If the mass distributions in the inner spiral arms and molecular ring were simple power-laws with the same exponents that we observe across the mass range $10^{6.5}$ to $10^{7}\,M_{\odot}$ (i.e. case B), then the total number of GMCs with $M > 10^{5.5}\,M_{\odot}$ in each environment would exceed several thousand, and the CO luminosity associated with this mass distribution would be greater than each region's total CO flux (measured via direct integration of the PAWS data cube) by factors between five and ten. A similar – though not identical – situation applies in the material arm and inter-arm regions. The CO luminosity corresponding to a power-law mass distribution for GMCs with $M > 10^{5.5}\,M_{\odot}$ with the same exponent as that in the intermediate mass bin would not exceed (or, in the case of the material arm, would not greatly exceed) the total CO flux of these regions, but it would require that roughly half of the undetected GMCs fall outside the CPROPS 'working area', i.e. the initial mask identifying regions of significant emission. As such, these undetected GMCs would need to be spatially extended, low CO surface brightness structures containing $10^{5.5}$ to $10^{6}\,M_{\odot}$ of CO-emitting molecular gas without an emission peak brighter than $4\sigma_{RMS} = 1.2\,\mathrm{K}$. Since the total CO luminosity associated with this mass distribution is comparable to the total flux of these regions, moreover, it would also entail a strong flattening of the GMC mass distribution for $M < 10^{5.5}\,M_{\odot}$. A more gradual flattening of the GMC mass distribution between $10^{5.0}$ and $10^{6}\,M_{\odot}$ would seem at least as plausible as the possibility that high-mass, low-surface brightness structures are ubiquitous throughout M51's inter-arm and material arm while clouds with $M < 10^{5.5}\,M_{\odot}$ are intrinsically rare.

On the other hand, we cannot use similar arguments to rule out that the slope of the GMC mass distributions between $10^{5.5}$ to $10^{6}\,M_{\odot}$ in the spiral arm and central regions could be due to an algorithmic effect. If the mass distribution in these regions continued with the same exponent that we observe for the intermediate mass bin down to $10^{5.5}\,M_{\odot}$ (or even $10^{5.0}\,M_{\odot}$), then the constraint that the combined CO luminosity should not exceed the observed CO flux is not violated. Indeed, the combined CO luminosity that would be associated with GMCs with $M > 10^{5.0}\,M_{\odot}$ assuming a simple power-law across $10^{5.0}$ to $10^{6.5}\,M_{\odot}$ is less than or comparable to the flux in the working area (i.e. not only the total flux) for these environments.

Nevertheless, moving the completeness limit up to $10^{6}\,M_{\odot}$ does not change our main conclusions about the different physical mechanisms that regulate the formation/disruption of GMCs, which we infer mainly from the intermediate and upper mass bins of the mass spectra. We further note that considering only clouds with $M_{lum} > 10^{6}\,M_{\odot}$ makes the differences in the cloud properties described in Sections 4.2.1-4.2.2 even more pronounced.

Region	**L_{CO} in Envir.**		**Observed Distr.**		**Case A**		**Case B$^{(a)}$**	
	Total	Work. Area	$N_{GMCs}^{(b)}$	$L_{CO}^{(c)}$	$N_{GMCs}^{(b)}$	$L_{CO}^{(c)}$	$N_{GMCs}^{(b)}$	$L_{CO}^{(c)}$
	$[10^7\,\mathrm{K\,km\,s^{-1}\,pc^2}]$			$[10^7\,\mathrm{K\,km\,s^{-1}\,pc^2}]$		$[10^7\,\mathrm{K\,km\,s^{-1}\,pc^2}]$		$[10^7\,\mathrm{K\,km\,s^{-1}\,pc^2}]$
Cube	90.83	67.08	1160	47.05	2207	59.25	27739	407.9
NB	7.48	6.49	116	5.07	270	6.96		
MR	17.99	16.35	160	9.60	315	11.44	5082	79.34
DWI	13.13	11.23	180	7.58	280	8.75	9057	126.39
DWO	18.38	15.73	260	11.73	371	12.76	8290	122.21
MAT	8.06	5.44	148	5.64	537	10.36	825	14.19
DNS	17.96	8.54	156	4.40	566	9.34		
UPS	7.79	3.28	140	3.03	478	7.03		

Table 4.4: Results of GMC Mass Distribution Tests. (a) Only for environments with a maximum GMC mass greater than 10^7 $\mathrm{M}_\odot$; (b) number of GMCs with $M > 10^{5.5}$ $\mathrm{M}_\odot$ in the distribution; (c) combined CO luminosity of GMCs with $M > 10^{5.5}$ $\mathrm{M}_\odot$ (see text for details).

4.5 X_{CO} IN M51

The value of the X_{CO} factor in M51 has been repeatedly investigated. While some works have reported X_{CO} factors 0.25-0.4× the Galactic value (e.g. Garcia-Burillo et al. 1993b, Nakai et al. 1994, Guelin et al. 1995, Israel et al. 2006, Bell et al. 2007), and sometimes even lower values in the inter-arm region, other early studies obtained X_{CO} values close to or above the Galactic one (e.g. Bohlin et al. 1978, Rand & Kulkarni 1990). Galactic-like X_{CO} factors have also been found by more recent studies that benefit from higher spatial and spectral resolution (Schinnerer et al. 2010, Tan et al. 2011).

Measurements of the metallicity and gas-to-dust ratio in M51, moreover, point toward a constant X_{CO} across the PAWS FoV. Bresolin et al. (2004), and Moustakas et al. (2010) both found a metallicity close to solar with only a shallow radial gradient of $-(0.02 \pm 0.01)\,\mathrm{dex\,kpc^{-1}}$. Since X_{CO} shows variations that only become prominent for metallicities below $12 + log(O/H) \sim 8.4 - 8.2$ (e.g. Leroy et al. 2011, 2012), we do not expect metallicity-dependent variations in the conversion factor across the PAWS FoV. A recent analysis of the Herschel FIR continuum (Mentuch Cooper et al. 2012) has likewise shown that the gas-to-dust ratio is roughly constant within the inner 13 kpc of M51. Variations in the X_{CO} factor would lead to corresponding variations in the gas-to-dust ratio, but these are not observed in M51's inner disk.

Envir.	$\mathbf{N_{cl}}$	$\mathbf{X_{CO}}$
All	232	$3.34^{+5.53}_{-1.88}$
CR	68	$3.01^{+7.49}_{-1.75}$
SA	117	$3.54^{+5.18}_{-1.91}$
IA	47	$3.26^{+5.53}_{-2.19}$
NB	22	$5.09^{+8.96}_{-2.45}$
MR	46	$2.49^{+5.89}_{-1.60}$
DWI	38	$4.74^{+6.51}_{-2.55}$
DWO	53	$3.07^{+4.46}_{-1.91}$
MAT	26	$3.54^{+5.30}_{-1.45}$
DNS	34	$3.05^{+5.65}_{-1.87}$
UPS	13	$3.39^{+3.67}_{-2.45}$

Table 4.5: Dynamical Measurements of the X_{CO} conversion factor from M51 GMC populations. I_{CO}-to-N_{H_2} conversion factor X_{CO} derived for the cloud populations in the M51 environments in unit of 10^{20} cm^{-2} (K km s^{-1})$^{-1}$. N_{cl} indicates the number of clouds with $\Delta V_{obs}/\Delta V_{chan} > 2$ and $S/N > 6.5$ used to calculate X_{CO}. Values are indicated as median, lower quartile ($Q25$) and upper quartile ($Q75$) of the distributions.

One widely used technique to calibrate X_{CO} is to assume that GMCs are long-lived structures in dynamical equilibrium ($\langle\alpha\rangle = 1$) and that CO is a faithful tracer of their mass. In this case, an average value of X_{CO} for a GMC population can be obtained from measurements of the clouds' CO luminosity, L_{CO}, and virial mass, M_{vir}. Then for each cloud we get:

$$X_{CO}[\mathrm{cm}^{-2}(\mathrm{K\ km\ s}^{-1})^{-1}] = 4.6 \times 10^{19}\frac{M_{vir}}{L_{CO}}, \tag{4.7}$$

where a factor of 1.36 is included to account for the contribution of helium to the total gas mass.

Here we apply this method to GMCs in M51, restricting our analysis to the “highly reliable sample” of clouds having $S/N > 6.5$. In addition, we require the GMCs to be well-resolved in the spectral domain ($\Delta V_{obs}/\Delta V_{chan} > 2$). These constraints reduce the sample to 232 objects. Our goals are first to verify the consistency of the X_{CO} in M51 with Galactic-like values, and second to check whether X_{CO} varies with environment. For example, a lower X_{CO} factor for GMCs in center or spiral arm region would shift their GMC mass distributions toward lower masses, and also decrease the average H_2 mass surface density to a value more similar to that observed in the inter-arm.

The median X_{CO} factors derived for different M51 environments using the dynamical method are listed in Table 4.5. The X_{CO} factor we calculate in M51 is roughly constant around $3 - 3.5 \times 10^{20}$ cm^{-2} (K km s^{-1})$^{-1}$ across the different M51 environments. There is some indication that X_{CO} could be higher in the nuclear bar and in the inner density-wave spiral arm regions, but the difference is marginal. We note that a higher X_{CO} factor in the central and arm environments would tend to enhance the difference in H_2 mass and surface density between the GMCs in those regions and the clouds in the inter-arm region rather than compensate them.

4.6 DISCUSSION

4.6.1 THE DIVERSITY AND EVOLUTION OF THE GMCS IN M51

Recent studies of GMCs and their associations, i.e GMAs, in nearby disk galaxies have provided evidence that cloud properties are not uniform across the disk and that the galactic environment (such as bulge, disk, nuclear bars, star-forming rings, spiral arms and inter-arm regions) might be the source for the observed differences. Koda et al. (2009), for example, find that GMAs with masses above 10^6 $M_\odot$ are almost exclusively located along the spiral arms of M51. They attribute this observed spatial distribution to large-scale dynamical processes induced by the spiral potential. In a recent sample of five nearby galaxies from the CANON survey, a similar trend for massive GMCs to be associated with strong spiral arms is observed (e.g. Fig. 6 of Donovan Meyer et al. 2013). The differences in M51's GMC properties with galactic environment that we describe in this Chapter are therefore not entirely unexpected. However, our study provides the first quantitative measure of the differences in the cloud properties and also reveals a strong variation in the GMC mass spectra (i.e. slope, normalization and maximum mass; Section 4.4.2). These variations are observational signatures of the mechanisms of cloud formation and evolution acting within different galactic environments. They are evidence for processes that not only change the physical properties of individual clouds, but also influence the ensemble properties of the cloud population.

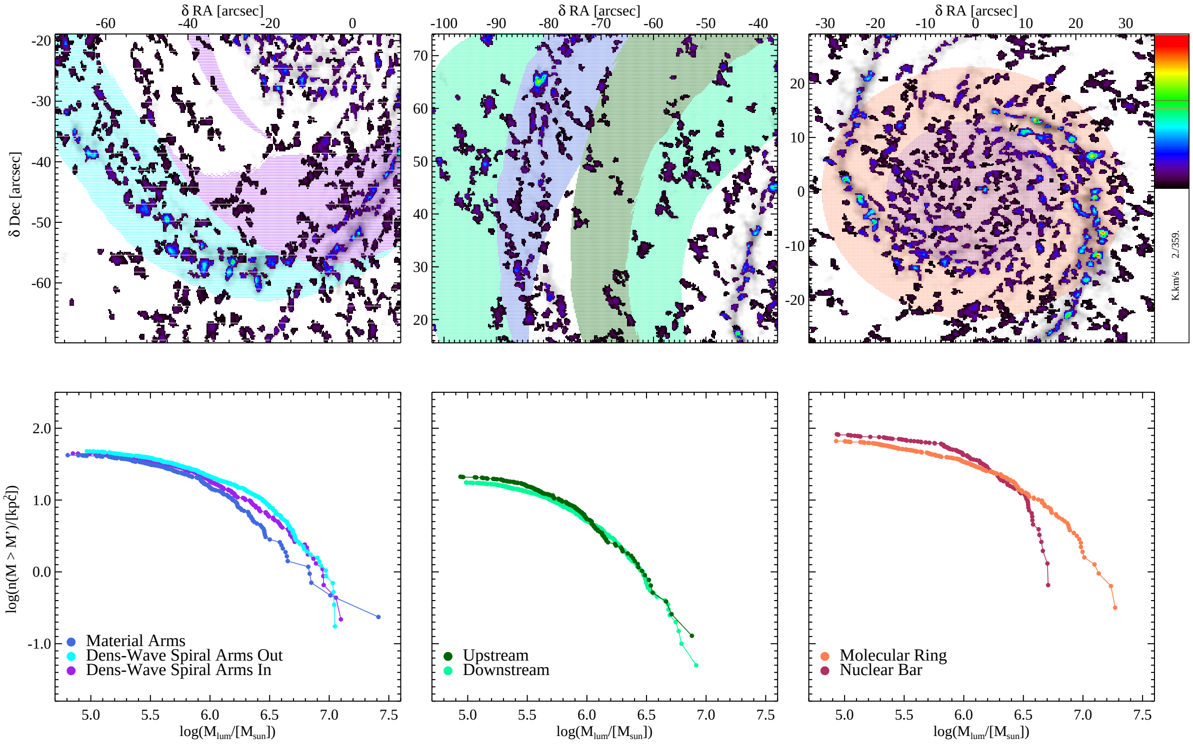

Figure 4.10: Top: part of the southern density-wave spiral arms, inter-arm and material arm, and central region integrated intensity maps of the identified objects. The environments are highlighted with the same color code of the corresponding mass spectra on the bottom. The figure clearly shows different populations of clouds linked to different shapes of mass spectra. This suggests various mechanisms of GMC formation and evolution within the disk and the bulge regions of M51.

The mass spectra of clouds in the inter-arm and density-wave spiral arm are very different. The variation in the slope γ between density-wave spiral arm and upstream mass spectra (Section 4.4.2) implies that spiral arms not only gather GMCs from the upstream inter-arm environment (in this case the slope of the mass distributions would be identical, even though the overall normalization could change), but also affect the nature of the constituent clouds. More precisely, the inter-arm distributions are steep (spectral index $\gamma < -2$) and extend to relatively low masses, characteristic of a population of clouds that is dominated by low-mass objects. The spiral density wave mass spectra, by contrast, are shallower ($\gamma > -2$), with a maximum mass above 10^7 $M_\odot$, consistent with a cloud population mainly constituted by high mass objects. Spiral arms, therefore, must host processes that promote the growth of massive objects, suppressing their destruction. Theoretical studies using simulations of gas in spiral potentials have observed that GMCs increase their mass through collisions, merging of small clouds and agglomeration aided by shocks and converging flows along the streamlines of the spiral potential (Casoli & Combes 1981, Kwan & Valdes 1983, Tomisaka 1986, Dobbs 2008, Tasker & Tan 2009). Mutual gravitational attraction between clouds further promotes coalescence (Cowie 1980, Kwan & Valdes 1987, Dobbs 2008).

Meidt et al. (2013) proposed that streaming motions associated with the spiral potential decrease the external gas pressure leading to increased stable masses (see also Jog 2013 and Chapter 1). Therefore, GMCs exposed to such conditions can become very massive without undergoing significant collapse.

Koda et al. (2009) have argued that GMCs in the inter-arm regions of M51 cannot have formed locally on an inter-arm crossing time-scale, but are rather remnants of GMCs leaving the arms. Therefore, when leaving the spiral arms, the GMCs must undergo a disruptive process (or processes) that preferentially affects the most massive objects. Numerical simulations of the ISM in spiral galaxies (Dobbs et al. 2006, Dobbs & Pringle 2013, see Fig. 4.11) suggest that the prominent “spurs” that emanate downstream from the spiral arms (see La Vigne et al. 2006, Schinnerer et al. 2013) can be interpreted as sheared GMCs or their associations due to large-scale dynamical motions. Recent star formation downstream of the spiral arm – as evidenced by recently formed stellar clusters and enhanced atomic gas (HI, CII) emission at the same location (Schinnerer et al. 2013) – must have consumed and photo-dissociated at least parts of the clouds, but it can not be the primary cause for cloud disruption, as the inner spiral arm segments have no associated star formation (Schinnerer et al. 2013) implying that stellar feed-back is not an effective destruction mechanism in every arm environment. Pety et al. (2013) find an extended, dynamical hot component of the molecular gas in M51 that spatially correlates with the location of star formation in the disk of M51. The authors interpreted this as evidence for galactic fountains or chimneys that transport some of the molecular gas away from the disk (e.g. Putman et al.

2012). This is likely another source of cloud destruction for GMCs leaving the arms.

Subtle differences between the upstream and downstream GMC mass distributions (i.e. the higher number density of low-mass upstream clouds with respect to the downstream ones) suggest that the disruptive events continue to act across the entire inter-arm region. If GMCs (not the molecular gas itself) are indeed "short-living" entities ($\sim$ 30 Myr, Elmegreen 2000), then they are unable to maintain their identity throughout the whole journey from one arm to the other (e.g. Pringle et al. 2001) causing a transformation of the cloud population to include a higher proportion of low mass objects.

The material arms represent an environment with properties between the density-wave spiral arm and inter-arm region. This environments hosts a high number density of clouds (some of them with masses up to 10^7 $M_\odot$), but the GMC population is still dominated by low mass clouds ($\gamma < -2$). Meidt et al. (2013) demonstrated that streaming motions are not completely suppressed in the material arms, but they are strongly reduced relative to the non-circular motions in the density-wave spiral arms. Indeed the clouds are, in average, more round than in the density-wave environments. Therefore gas in the material arms is not simply stretched and/or pulled apart by differential rotation. In addition mechanisms that promote the growth of massive clouds in the density-wave arms (such as converging flows) are likely present in the material arms causing the increase in cloud mass, as otherwise the global population would be similar to the inter-arm one.

In the center, the molecular ring is an environment that is very favorable for cloud formation: the mass distribution in this region is the shallowest one observed in M51 ($\gamma \approx -1.6$) and extends to cloud masses greater than 10^7 $M_\odot$, indicating a cloud population primarily constituted by massive GMCs. The shape, similar to the density-wave one, would appear to suggest that cloud formation mechanisms similar to those in the density wave arms are present. However, the (gas) dynamics in the central region are very different from the disk. The molecular ring is coincident with a zero torque environment caused by the overlap of resonances of the inner bar and the spiral density wave, i.e. the combined action of outflow driven by the nuclear bar and inflow by the spiral wave (Meidt et al. 2013). Thus, the molecular ring zone harbors nearly circular orbits with at most low non-circular motions (Chapter 2) and almost no shear (in analogy to the Galactic ring, Dib et al. 2012). Therefore, converging flows caused by large-scale dynamics can be neglected as a dominant cloud formation mechanism. It seems plausible that gas stalls at the resonance, accumulates and develops high densities. Strong local gravitational instabilities within this large gas reservoir cause the gas in the ring to fragment into massive clouds.

The nuclear bar environment must have very different cloud formation and destruction mechanisms: the mass spectrum in this region has a high number density of low and intermediate mass GMCs, but a sharp mass truncation at around $10^{6.5}$ $M_{\odot}$. This implies that the bar environment either lacks an efficient mechanism to bring small clouds together to form larger structures, or that a very efficient mechanism for the destruction of massive objects is present. The presence of low and intermediate mass GMCs is a consequence of the abundant molecular gas reservoir collected by the nuclear bar dynamics: gas on the leading sides of a bar loses angular momentum and is driven inwards, as a result of negative gravitational torques (e.g. Schwarz 1984). This motion is also expected to generate intense shear in the gas lanes (in analogy with barred galaxies, Athanassoula 1992, Sheth et al. 2002; and as measured by Meidt et al. 2013 for M51), that, in turn, prevents the formation of massive objects or inhibits the density fluctuations that become the seeds of massive GMCs (Hopkins 2012).

Besides the dynamical processes discussed above, other effects could potentially alter the properties of the GMC population in the various environments within M51, such as the variation of the interstellar radiation field (ISRF), the molecular gas fraction and the X_{CO} factor. The ISRF is significantly changing from the bulge to the disk in M51 and, in particular, the intense radiation field of the young massive stars in the star-forming ring and/or the AGN could have a strong impact on cloud properties. However, no radial trend for the ISRF is present in H-band observations for the disk radii probed by PAWS (Muñoz-Mateos et al. 2011), thus we expect no strong effect *except for the one downstream already discussed*. The molecular gas fraction (defined as $M_{mol}/(M_{mol} + M_{HI})$) is very high and does not significantly change radially over the PAWS area (Leroy et al. 2008, Schuster et al. 2007 when correcting for our assumed X_{CO} factor) or azimuthally (see Fig. 2c of Koda et al. 2009). Together with the fact that the metallicity is close to solar with a small radial gradient (e.g. Bresolin et al. 2004) and the gas-to-dust ratio is roughly constant (Mentuch Cooper et al. 2012) (see also Section 4.5), we exclude variations in the X_{CO} factor as the main cause for the global differences in GMC properties observed in M51.

In conclusion, the presence of spiral arms have a dramatic effect on the GMC properties observed in the central 9 kpc of M51. Excluding phenomena such as a varying ISRF, molecular gas fraction and X_{CO} factor that are observed to be roughly constant across the disk, we propose that the formation of high mass objects in the spiral arm region must be attributed to large-scale dynamics driven by the spiral shocks resulting in converging flows along the streamlines. Further, we propose that the variations in the shape of the cloud mass spectra can be interpreted as the evolution of clouds travelling from one side of a spiral arm to the other. A large amount of gas is accumulated by the spiral arm dynamics, and subsequently fragmented by gravitational instabilities and shear. Merging and accretion of small objects contribute to create massive clouds.

Upon leaving the arm, these massive GMCs are destroyed by shear and/or consumed by massive star formation that both influence the ensemble properties of the cloud population.

Lacking strong streaming motions, the presence of high mass objects in the circumnuclear ring can be best explained by gas accumulation and gravitational instabilities in the absence of strong dynamical destructive effects such as shear. Instead, shear appears to be very important to prevent the formation of massive clouds in the nuclear bar region. However, the enhanced ISRF (in the bulge) and the AGN make it difficult to separate their contribution from the large-scale dynamics and more detailed modelling and analyses are needed to clearly identify the main mechanisms for cloud evolution in this region.

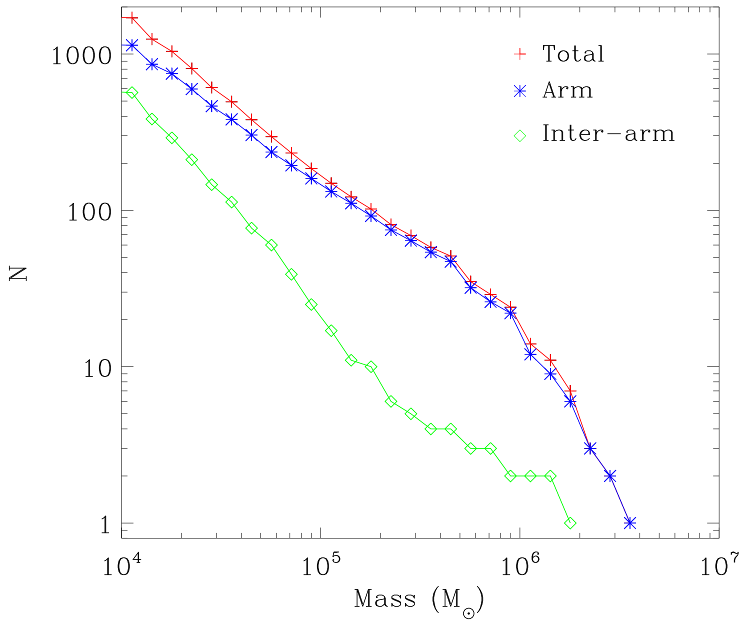

Figure 4.11: The cumulative mass distributions for the arm (blue) and inter-arm (green) regions in a simulation of a two armed spiral galaxy. The simulation is described in Section 7 of Dobbs et al. (2012) and is presented in Dobbs & Pringle (2013). The simulation included a spiral potential, self gravity, heating and cooling of the ISM and stellar feedback, and the mass per particle was 312.5 $M_\odot$. Clouds were identified using a clump-finding algorithm that selects contiguous regions with $> 25\ M_\odot\ \mathrm{pc}^{-2}$, an approach that is not dissimilar to CPROPS.

4.6.2 LARSON'S LAWS IN M51

In addition to the differences in the GMC mass spectra with galactic environment, the scaling relations between cloud properties provide further insight into the processes that regulate their physical properties. From our analysis in Section 4.3, two important features of GMCs in M51 emerge: first, both the size-velocity dispersion and CO luminosity-virial mass relations show a large scatter; and second, the GMC mass surface density varies with environment as seen by the radius-CO luminosity relation. Here, we argue that these results have a common origin, i.e. the different dynamical properties of the environments.

A relation between size and velocity dispersion was identified in the early studies of Milky Way clouds (e.g. Larson 1981). It is often interpreted as evidence for a cloud in virial equilibrium following the work of Solomon et al. (1987), where the authors measured a square-root dependency between velocity dispersion and radius of Galactic GMCs. But unlike the tight size-velocity dispersion relation discovered by Solomon et al. (1987), the corresponding relationship in M51 shows a large scatter. If GMCs are globally unbound then – contrary to clouds that are strongly bound and largely decoupled from their environment – it is likely that they become susceptible to modification and/or disruption by events and conditions in the surrounding interstellar medium. For clouds where $\alpha \gg 1$, external sources of confining pressure, such as ram pressure from inflowing material (e.g. Heitsch et al. 2009) or the (static) weight of the surrounding gas (e.g. Heyer et al. 2001b) become important for their dynamical properties and evolution.

The higher mass surface densities of clouds in the spiral arms compared to the inter-arm region implies that the arm GMCs have higher internal pressures. More precisely, we can estimate the internal pressure P_{int} of a molecular cloud according to:

$$\frac{P_{int}}{k} = \rho_g \sigma_v^2 = 1176 \left(\frac{M}{M_\odot}\right)\left(\frac{R}{pc}\right)^{-3}\left(\frac{\sigma_v}{kms^{-1}}\right)^2, \tag{4.8}$$

where ρ_g is the H_2 volume density. For the cloud populations in the central, inner spiral arm, material arm and inter-arm regions of M51, we find median internal pressures of $\langle P_{int}/k \rangle \sim 8.2\times10^5$, and 6.7×10^5, 5.2×10^5,and 3.5×10^5 respectively. These differences track the variation in the stellar mass surface density between the different M51 environments (Meidt et al. 2013). Since the stellar mass dominates the ambient kinetic pressure of the ISM under the conditions that prevail in the inner disk of M51 (see e.g. estimates for the hydrostatic midplane pressure by Koyama & Ostriker 2009b and Elmegreen 1989), the observed variations in the GMC mass surface density may suggest that the external ISM pressure plays a critical role in regulating the internal pressure (and hence velocity dispersion and density) of molecular clouds in M51 (as suggested by e.g. Rosolowsky & Blitz 2005). This interpretation is discussed in more detail by Hughes et al., submitted, where resolved GMC populations from a small sample of nearby low-mass galaxies are included in the analysis.

4.7 SUMMARY AND CONCLUSION

To investigate possible dependencies of the GMC population on large-scale properties, the PAWS FoV was divided in seven dynamically-motivated galactic environments. GMC properties as a function of these environments have been analyzed in a statistical fashion. We find a distinct dependence of GMCs properties on galactic environment that can be summarized as follows:

1. Clouds in the density-wave spiral arms and the central region of M51 exhibit the highest average values of peak brightness temperature and velocity dispersion. These properties decrease in the material arms, where clouds appear more similar to the inter-arm ones. Inter-arm GMCs have the lowest values of peak brightness temperature, velocity dispersion and size. Most GMCs in M51 shows a preferred orientation in the disk that roughly follows the pattern described by the spiral arms.

2. The analysis of the cloud derived properties suggests that there is a general decrease in H_2 masses and surface density of GMCs from the central to the inter-arm region. Densest and massive clouds are located in the molecular ring and density-wave spiral arm environments. Once again, the lowest density and mass objects are observed in the inter-arm region, clouds within the material arms and nuclear bar environment have intermediate values of H_2 surface density and mass.

3. There is no obvious size-line width relation between the clouds of M51 and large scatter is present. This argues against a global virialized state of the GMCs detected in M51. Instead, a median virial parameter ~ 1.6, broadly constant across the environments, suggest that the cloud population is at most self-gravitating. However, both virial parameter, virial mass-CO luminosity and size-velocity dispersion shows a large scatter, indicating a number of pressure confined or unbound clouds present.

4. Evidences from the scaling relations, indicates that properties of the GMCs in M51 are tightly linked with the properties of the environment in which they form and live, for example high surface density GMCs are likely observed in high gas surface density and

pressure environments.

5. The diverse shapes observed in the GMC cumulative mass spectra can be interpreted with differing mechanisms of GMC formation and evolution within the different M51 environments. Regions in which the conditions of cloud formation are more favorable have higher vertical offsets (number densities of GMCs) and reach toward higher mass clouds (i.e. molecular ring and spiral arms). From the shape of the mass spectra it is possible to identify a common mechanism of cloud formation (local gravitational instabilities), as well as phenomena specific to particular dynamical structures (cloud coalescence and collision in the spiral arms and molecular ring). Beside the downstream environment (where stellar feedback appears more important), the destruction of GMCs is mostly associated with large-scale dynamical effects (i.e. shear and tidal stresses), then local phenomena like stellar feedback. These phenomena prevent also the formation or destroy high mass clouds in certain environments of the M51 such as the nuclear bar region.

6. The dynamical measurement of the conversion factor between CO and H_2 suggests that an environmental variation of X_{CO} is not the likely cause to explain the observed differences between the GMCs properties. This argument is supported by consideration on the solar metallicity of M51 and on the constant gas-to-dust ration across the PAWS FoV. Although the large scatter present in the data, the median X_{CO} obtained is consistent with Galactic-like values.

SUMMARY, FUTURE PERSPECTIVE AND FINAL CONSIDERATIONS

SUMMARY: COMPLEX DYNAMICS OF M51 AS DRIVER OF GMC PROPERTIES

In this thesis I demonstrated the importance of the dynamical effects on the gas organization in a grand-design spiral galaxy taking full advantage of the new PAWS 1” ^{12}CO(1-0) data.

M51 possesses a complex gravitational potential structure that induces strong streaming motions across the spiral arms. However, the atomic and the molecular phases of the ISM responds differently to the presence of the spiral arms in M51. HI appears mostly produced by photodissociation, is located downstream the spiral arm and likely in a thicker disk with respect to the H_2, and its response to the spiral arms is weaker. The molecular gas, instead, is strongly constrained within the arms and is highly influenced by the streaming motion, thus by dynamical phenomena. This fact has several consequences on the global properties of the molecular gas and of its single entities, the GMCs, and, ultimately, on the star formation.

In particular GMC properties exhibit a critical dependence on dynamical environment: spiral arms, where dispersal effects are reduced, are able to collect a large quantity of gas through shocks and converging flows that results in a high density of massive GMCs. Regions with massive star formation and intense shear generally contain a smaller quantity of smaller objects compare to larger clouds.

The dependence of cloud properties on galactic environment argues against the classical picture of GMCs as long-lived, quasi-equilibrium entities, with a constant mass surface density and isolated from their interstellar environment. Instead, prominent dynamical phenomena like spiral arms and bars, are responsible not only for efficiently transporting large quantities of gas, but also for producing cloud structures that are physically different from the GMCs observed in Local Group galaxies where such strong galactic-scale dynamical effects are absent. Instead of isolated clouds, the GMCs identified in high pressure, molecule-dominated environments may be the occasional high density peaks or transient features of a more extended molecular medium that continuously merge, accumulate material and disperse. Therefore, in spiral galaxies large-scale dynamical effects play a larger role in controlling the formation and evolution of GMCs than small-scale phenomena such as star formation feedback (including stellar wind and supernova explosions).

However the same phenomena that promote gas accumulation and create massive GMCs within the spiral arms could, in turn, contribute to inhibit star formation. In fact only specific regions of M51's spiral arms are prone to form stars. In others, generally where the gas is in motion, the star formation efficiencies are extremely low, despite the high surface density of the gas. Therefore star formation may even be seen as a "by-product" that occurs in special places of the galaxy where gas can accumulate and has time to virialize and collapse without being influenced by large scale dynamics, like galactic rings. A corollary of this interpretation that merits further investigation is that only a small fraction of clouds and molecular gas may be associated with star formation in galaxies with a strong spiral potential and Kennicutt-Schmidt-type relations may not hold on cloud-scales in such systems.

These findings suggests a broader new direction for future studies in this field. For example, theoretical works that attempt to reproduce the cloud physics and star formation histories within spiral or bar potentials, must consider effects on the environments for the formation, evolution and lifetime of GMCs. This means also that simulations of single clouds and the star modes within them may not be realistic models or true representations of the molecular ISM of massive star-forming spirals, as our own, that actually dominate the mass and light budget and host most of the star formation in the present-day universe.

FUTURE PERSPECTIVE

When observed as a whole the GMCs in M51 appear very similar to the Galactic ones. However their different properties are revealed only when dividing the sample based on individual dynamical environments. Revealing those differences in M51 made it also possible to disentangle some of the mechanisms proposed for the formation and evolution of GMCs in a grand-design spiral galaxy. Therefore, ideal follow-ups to test the findings of this thesis would require three unavoidable ingredients: 1) a large sample of objects, 2) detailed kinematic information, 3) an efficient algorithm for the cloud identification.

ALMA CAPABILITIES

Most of the uncertainty about the GMC physics is due to the shortage of cloud scale observations of galaxies different from low-mass ones, so far restricted to PAWS and the CANON survey (Donovan Meyer et al. 2013). Moreover, to have a more clear understanding of these objects and the interactions between them, not only sufficient sensitivity and resolution are required, but also a large statistical sample that translates into a large area surveyed allowing for the observation of GMCs in various environments.

New telescope like ALMA (or the future NOEMA mm-interferometer) will give the possibility to explore a large variety of complex systems and will provide a deeper insight into the GMC physics and into the different modes of star formation. For example, at the current ALMA stage (*Cycle 1*), in order to achieve almost the full disk of an M51-like galaxy, such as NGC 628 in ^{12}CO(1-0) with an angular resolution of 1" ($\sim$ 35 pc at a distance of $\sim$ 7 Mpc) and the optimal sensitivity of 0.2 K to obtain a 5σ point mass sensitivity of $2 \times 10^4\ M_\odot$ per 2 km s^{-1}, requires 39 pointing with the 12-m array and 18 pointing with the 7-m array, i.e. approximately 2 hr of observations including overheads[3]. For a galaxy like M51, ALMA would need only one tenth of the time used by PAWS. Ideally in about 100 hr ALMA would be able to scan 50 full galactic disks (considering distances within a factor 2 the distance of M51), or a GMC sample accounting for few ten thousand objects in several environments (considering the amount of clouds observed in the inner disk of M51).

The environmental division proposed for the inner part of M51, spans between 3 regions to 7 dynamically defined environments. If one maps a barred galaxy (the most common morphology in the sky) using an averaged number of 5 environments that would include, for example, bar, two sections of the spiral arms (considering the part of the arms at the tips of the bar and the outer spiral arms that, generally, appear to have different surface brightness) and two inter-arm regions (as for PAWS downstream and upstream), with an approximate number of $\sim$ 1000 clouds identified, we would have samples of $\sim$ 200 objects for environment likely enough for a robust statistic (considering the cloud number densities found for PAWS).

Therefore, the current state of ALMA already constitutes a remarkable step forward in this field in terms of data quantity and quality that could become available in a reasonable amount of time. The future evolution of this telescope (*Cycle 2*) with the possibility to use the full array (66 antennas) will provide higher resolutions and, likely, the opportunity to access the inner structure of extragalactic GMCs.

Some of the early science data are already available. The inner disk of NGC 1068 (one of the biggest galaxy of the Messier catalog) has been observed at GMC scale by an ALMA *Cycle*

---

[3] Information obtained through the ALMA Observing Tool.

0 project (PI Garcia-Burillo) and is ready to be analyzed. Other observations of the *Cycle 0*, that also imaged part of the galaxies, have provided promising results. The GMCs identified in NGC 253 (the nearest southern nuclear star-burst) and the Antennae (the nearest southern major merger) are more luminous and have larger velocity dispersion than any other so far observed cloud (Whitmore et al. in preparation).

Moreover, NGC 628 itself (PI Schinnerer) will be surveyed in the ^{12}CO(2-1) transition by ALMA and will provide a test-bed to confirm the results from PAWS, and NGC 1097 is also scheduled for the Cycle 1 (K. Sheth, private communication)

THE IMPORTANCE OF KINEMATICS

The galactic environments of M51 are drawn mostly from kinematic considerations. Kinematics are therefore critical to obtain a clear understanding of the GMC lifetime especially when dynamical effects are dominant. For example, high quality kinematic information that allows one to resolve the cloud's proper motion can help to distinguish between the different formation mechanisms. In their simulation of a spiral potential, Dobbs et al. (2006) showed that massive clouds created via gravitational instabilities exhibit prograde rotation and are more bound. If one were to find an equal number of prograde and retrograde rotating GMCs, this would mean that those objects are not born from a single gravitational instability but are likely the result of various merger and collisions between small objects with different formation histories.

Kinematics are also important to assess the dynamical state of the clouds themselves. The virialization of GMCs acts as a measure of the autonomy of the clouds and thus the strength of their connection to their environment. Moreover, analysis of cloud virialization is important to understand whether and under what conditions the GMC starts to collapse and forms stars. Or, alternatively, if the virialization condition for GMCs is a necessary prerequisite for the star formation at all. In M51 a large fraction of clouds appear unbound. This conclusion for the objects in the PAWS catalog has been derived through the estimation of their virial parameter. This parameter depends on the correct estimation of the cloud's virial parameter which in turn depends on the value of the CO–to–H_2 conversion factor, X_{CO}. Unfortunately, no measurements of the conversion factor on the scales of GMCs across the galactic disk exist for M51, or any other nearby disk galaxy. Using the capabilities of ALMA, simultaneous observations of different CO isotopes (like ^{12}CO(2-1), ^{13}CO(1-0), C^{18}O(1-0)) are possible and easy to accomplish. This will allow for a good determination of the influence of the CO–to–H_2 conversion factor on the derived GMC properties and provides an independent estimations of the boundedness of the clouds.

Beside these aspects that are closely connected to GMC studies, disentangling the properties of the spiral arms, would help to define their role in the secular evolution of galaxies. In Chapter

2 we found that the CO emission is perfectly suited for the study of the gravitational potential. Moreover, the cloud scale has been critical to reveal an important component of the potential that provides a step forward into understanding the present state of M51 and the origin of its current appearance. This argument is pretty much extensible to many other systems and spiral galaxies that constitute one of the most common galactic morphologies in the sky.

GMC SEGMENTATION AND PROPERTY CALCULATION

One of the major issues associated with the study of GMCs is their identification. GMCs have no well defined edges and their segmentation could be not unique. Indeed, several studies in the past have adopted either a Gaussian decomposition scheme (i.e. `GAUSSCLUMPS`, Stutzki & Guesten 1990) or attempted to define (and separate) clumps following density peaks (`CLUMPFIND` approach, Williams et al. 1994) resulting in no one-to-one correspondence between the identified clouds in either method. Nowadays the community is gradually migrating towards more powerful algorithms such as `CPROPS` that allows for a more homogeneous comparison of GMCs from different observations. However even `CPROPS` is not completely bias-free. Due to its tendency to decompose structures around the resolution limits (e.g. Wong et al. 2011), it is still broadly dependent on the survey design. Moreover the `CPROPS` sensitivity correction introduces a certain amount of scatter in the data and it depends on environment. A similar technique, for example, used by Solomon et al. (1987) for their historical Galactic cloud catalog, was subsequently criticized by Heyer et al. (2009) arguing that extrapolating the data would overestimate the GMC properties. However, in M51 this method appears necessary to correctly account for the flux within GMCs and reveal their property differences. All these issues could have an important impact on the interpretation of GMC characteristics and could bring, sometimes, in misleading results (Hughes et al. submitted, see Chapter 3). An algorithm completely free from biases would provide a correct view of the GMCs and thus allowing for the definition of a global picture of the molecular ISM physics and ultimately of the star formation process itself.

One possible step forward that I plan to take is to implement a clump segmentation algorithm with the aim to correct for these biases and to associate this algorithm to other techniques of the gas emission analysis such as the `DENDROGRAMS` (Rosolowsky et al. 2008).

ALMA has the capability to simultaneous observe different molecular tracers and/or isotopes and will likely provide four-dimensional "hypercubes". Therefore a code capable to analyze a large amount of data in a relatively short period of time will be essential. The version of `CPROPS` used for my analysis of the PAWS datacube was very slow (~ 2 days) and in addition required to split the cube into sub-cubes. The updated and improved version of `CPROPS`, `CPROPStoo` (Leroy et al., in preparation) that I am currently testing is promising, being able to obtain the full PAWS

GMC catalog in less than 1 hour.

GOING BEYOND: ATOMIC GAS AND SIMULATIONS

GMCs are primarily assembled from the atomic phase of the ISM and partially return to it via photodissociation. Thus to completely constrain the GMC formation and evolution a good knowledge of the atomic gas envelope, is needed. In particular high resolution observations achievable through the JVLA will help to create HI cloud catalogs to compare with the existent GMC catalog in order to understand the dynamical interaction between atomic and molecular phases, to discriminate between turbulence models of cloud formation and to establish the role of the atomic gas in the star formation.

Together with this, simulations, that I extensively referred for the interpretation of my results, will be precious to connect observations and theory. Simulations provide a view of the galaxy across the time, something that observations can not do. Moreover they can potentially reach the desired resolution without being affected by instrumental limitations. In principle it would be possible “to downgrade” simulations and transform them into observational FITS datacubes, analyzable with observational tools. This would allow for a more homogeneous comparison between the real and simulated properties of cloud, gas and galaxies.

APPENDIX

THE PAWS M51 GMC CATALOG

ID	**RA (J2000)**	**Dec (J2000)**	**V_{LSR}**	**T_{max}**	**S/N**	**R**	**σ_v**	**L_{CO}**	**M_{vir}**	α	**PA**	**b/a**	**Reg**	**Flag**
	h m s	*d ’ ”*	km/s	K		pc	km/s	10^5 K km/s pc^2	10^5 $M_\odot$		deg			
(1)	(2)	(3)	(4)	(5)	(6)	(7)	(8)	(9)	(10)	(11)	(12)	(13)	(14)	(15)
1	$13^h30^m0.65^s$	47°11′10.58”	−4.3	2.5	5.2	18 ± 19	4 ± 3	0.9 ± 0.3	2.6 ± 5.7	0.71	135	1.0	*IA*	0
2	$13^h30^m0.87^s$	47°10′56.15”	52.8	5.3	7.0	50 ± 8	10 ± 2	4.4 ± 0.7	54.0 ± 25.4	2.82	49	0.9	*IA*	0
3	$13^h30^m1.54^s$	47°11′4.84”	60.5	4.6	5.1	32 ± 0	11 ± 4	2.1 ± 0.8	38.5 ± 31.9	4.29	152	0.6	*IA*	1
4	$13^h29^m58.01^s$	47°11′6.34”	−2.4	1.3	3.8	32 ± 0	5 ± 4	0.7 ± 0.6	8.5 ± 13.0	2.78	179	0.2	*SA*	1
5	$13^h29^m57.79^s$	47°11′7.20”	3.3	2.1	5.8	40 ± 21	10 ± 4	1.6 ± 0.6	38.0 ± 33.7	5.38	8	0.9	*SA*	0
6	$13^h29^m58.14^s$	47°11′6.34”	15.3	2.5	6.7	27 ± 33	2 ± 2	0.6 ± 0.8	1.1 ± 3.2	0.42	116	0.6	*SA*	0
7	$13^h29^m58.76^s$	47°11′9.41”	13.4	2.2	5.8	32 ± 0	3 ± 4	0.3 ± 0.2	3.2 ± 7.3	2.19	11	0.4	*SA*	1
8	$13^h29^m58.36^s$	47°11′10.50”	15.8	2.8	7.8	32 ± 0	11 ± 7	0.5 ± 1.1	40.9 ± 53.3	18.42	158	0.5	*SA*	1
9	$13^h29^m57.72^s$	47°11′2.80”	24.0	4.1	9.9	118 ± 14	7 ± 1	10.8 ± 3.1	65.5 ± 24.8	1.40	163	0.5	*SA*	0
10	$13^h29^m58.24^s$	47°11′9.36”	19.6	5.0	12.0	32 ± 15	8 ± 4	3.8 ± 3.3	21.4 ± 21.7	1.28	133	0.6	*SA*	0
11	$13^h29^m58.34^s$	47°11′6.77”	25.3	1.7	3.8	32 ± 0	5 ± 3	0.4 ± 0.3	7.0 ± 9.2	4.55	176	0.7	*SA*	1
12	$13^h29^m59.00^s$	47°11′10.63”	30.0	2.5	6.3	32 ± 21	5 ± 3	1.8 ± 2.0	6.9 ± 10.0	0.89	37	0.5	*SA*	0
13	$13^h29^m58.03^s$	47°10′59.78”	36.3	3.7	9.6	56 ± 48	6 ± 9	1.3 ± 2.3	18.9 ± 55.1	3.28	150	0.3	*SA*	0
14	$13^h29^m57.47^s$	47°10′59.73”	41.5	1.8	4.5	15 ± 15	5 ± 8	0.6 ± 1.0	4.1 ± 9.7	1.46	51	0.7	*SA*	0
15	$13^h29^m58.95^s$	47°11′5.67”	42.7	5.1	11.9	77 ± 21	7 ± 3	8.6 ± 6.2	35.6 ± 31.2	0.95	137	0.3	*SA*	0
16	$13^h29^m59.53^s$	47°11′9.57”	44.3	9.0	20.6	65 ± 17	9 ± 2	21.6 ± 7.7	58.5 ± 32.9	0.62	168	0.5	*SA*	0
17	$13^h29^m58.39^s$	47°10′59.47”	47.0	3.3	8.1	32 ± 30	12 ± 8	3.2 ± 5.0	44.7 ± 73.6	3.23	173	0.7	*SA*	0
18	$13^h29^m58.55^s$	47°11′4.31”	43.2	3.7	8.9	32 ± 22	6 ± 3	2.1 ± 3.1	10.7 ± 11.6	1.19	81	1.0	*SA*	0
19	$13^h29^m58.69^s$	47°11′6.59”	46.2	2.6	6.4	42 ± 25	6 ± 5	1.8 ± 1.9	15.5 ± 24.5	1.96	162	0.5	*SA*	0
20	$13^h29^m58.50^s$	47°11′1.05”	52.6	4.3	11.2	52 ± 15	7 ± 2	6.3 ± 2.0	25.9 ± 20.4	0.94	62	0.6	*SA*	0
21	$13^h29^m59.99^s$	47°11′6.48”	53.0	2.0	4.0	32 ± 0	6 ± 2	0.9 ± 0.4	11.4 ± 7.0	2.76	84	0.7	*SA*	1
22	$13^h29^m58.94^s$	47°11′9.22”	51.2	2.6	5.9	33 ± 31	7 ± 5	1.1 ± 1.8	14.6 ± 26.0	2.96	31	0.7	*SA*	0
23	$13^h29^m57.69^s$	47°10′57.07”	59.2	3.6	10.7	32 ± 0	6 ± 4	1.6 ± 1.3	10.4 ± 13.9	1.47	160	0.5	*SA*	1
24	$13^h29^m57.99^s$	47°10′59.02”	56.0	6.8	17.7	108 ± 16	15 ± 3	25.6 ± 6.6	267.8 ± 113.2	2.40	12	0.5	*SA*	0
25	$13^h29^m58.59^s$	47°11′8.19”	54.9	2.0	5.2	20 ± 11	9 ± 5	1.0 ± 0.5	17.5 ± 23.1	3.97	135	0.6	*SA*	0
26	$13^h29^m58.95^s$	47°11′10.52”	56.8	1.9	5.2	19 ± 20	5 ± 6	0.5 ± 0.6	6.0 ± 13.7	2.83	83	0.6	*SA*	0

ID	RA (J2000) *h m s*	Dec (J2000) *d ’ ”*	V_{LSR} km/s	T_{max} K	S/N	R pc	σ_v km/s	L_{CO} 10^5 K km/s pc^2	M_{vir} 10^5 $M_\odot$	α	PA deg	b/a	Reg	Flag
(1)	(2)	(3)	(4)	(5)	(6)	(7)	(8)	(9)	(10)	(11)	(12)	(13)	(14)	(15)
27	$13^h29^m58.57^s$	47°11′11.65”	51.9	1.8	5.0	32 ± 0	7 ± 3	1.6 ± 1.3	14.0 ± 12.5	2.03	61	0.6	*SA*	1
28	$13^h29^m57.63^s$	47°10′51.40”	68.4	2.7	7.1	34 ± 29	6 ± 3	2.6 ± 2.8	10.7 ± 18.5	0.95	101	0.6	*SA*	0
29	$13^h29^m58.14^s$	47°11′4.12”	70.9	2.0	4.9	32 ± 0	7 ± 3	0.8 ± 0.3	17.0 ± 16.4	5.03	170	0.3	*SA*	1
30	$13^h29^m57.48^s$	47°10′52.38”	87.8	2.6	8.0	35 ± 30	12 ± 11	1.7 ± 2.1	52.6 ± 97.2	7.22	32	0.5	*SA*	0
31	$13^h29^m57.45^s$	47°11′8.55”	6.0	2.0	5.6	87 ± 12	9 ± 2	5.1 ± 0.9	77.9 ± 40.4	3.51	121	0.5	*SA*	0
32	$13^h29^m58.82^s$	47°10′43.22”	15.7	2.2	4.9	32 ± 0	3 ± 2	0.5 ± 0.2	2.6 ± 4.0	1.13	160	0.6	*IA*	1
33	$13^h29^m58.14^s$	47°10′46.68”	45.0	3.0	6.9	39 ± 9	5 ± 2	2.2 ± 0.3	9.8 ± 7.3	1.02	161	0.4	*IA*	0
34	$13^h29^m57.59^s$	47°10′37.75”	69.5	3.0	6.6	54 ± 10	10 ± 2	3.4 ± 0.6	54.6 ± 23.0	3.68	178	0.4	*IA*	0
35	$13^h29^m57.51^s$	47°10′34.30”	71.4	3.1	6.0	44 ± 9	8 ± 2	3.9 ± 1.1	27.5 ± 12.5	1.60	122	0.8	*IA*	0
36	$13^h29^m58.03^s$	47°10′38.34”	70.2	3.2	6.4	32 ± 0	9 ± 3	2.1 ± 0.4	28.0 ± 17.3	3.06	162	0.4	*IA*	1
37	$13^h29^m58.25^s$	47°10′49.67”	71.7	2.6	6.3	68 ± 10	6 ± 1	3.3 ± 0.4	25.4 ± 14.1	1.76	179	0.7	*IA*	0
38	$13^h29^m59.27^s$	47°10′50.55”	68.5	2.7	5.2	32 ± 0	5 ± 3	0.7 ± 0.2	9.4 ± 8.9	2.92	178	0.8	*IA*	1
39	$13^h29^m58.78^s$	47°10′49.09”	73.2	5.2	11.8	52 ± 9	4 ± 1	3.9 ± 0.3	8.6 ± 3.5	0.50	174	0.5	*IA*	0
40	$13^h29^m58.95^s$	47°10′38.07”	71.8	3.2	5.7	32 ± 0	5 ± 3	0.7 ± 0.2	7.1 ± 8.2	2.25	126	0.7	*IA*	1
41	$13^h30^m0.08^s$	47°10′40.68”	101.1	3.7	5.5	32 ± 0	5 ± 2	0.8 ± 0.3	7.9 ± 8.0	2.13	101	0.8	*IA*	1
42	$13^h29^m58.09^s$	47°10′34.02”	99.9	2.2	5.3	32 ± 0	2 ± 1	0.4 ± 0.2	1.3 ± 1.5	0.74	3	0.8	*IA*	1
43	$13^h29^m57.73^s$	47°10′33.44”	115.7	2.5	6.3	32 ± 0	4 ± 3	0.4 ± 0.1	4.1 ± 8.0	2.13	171	0.8	*IA*	1
44	$13^h29^m55.83^s$	47°11′10.72”	−15.0	1.8	5.2	32 ± 0	9 ± 3	0.7 ± 0.2	25.8 ± 18.1	8.39	155	0.5	*IA*	1
45	$13^h29^m55.47^s$	47°10′50.71”	−0.1	1.9	4.9	36 ± 24	9 ± 7	1.1 ± 1.8	27.7 ± 55.2	5.92	153	0.3	*SA*	0
46	$13^h29^m56.93^s$	47°11′9.85”	12.4	2.7	7.4	51 ± 24	7 ± 4	1.8 ± 1.2	23.4 ± 34.0	2.95	127	0.3	*IA*	0
47	$13^h29^m56.71^s$	47°11′6.24”	15.0	2.1	5.2	32 ± 0	3 ± 4	0.8 ± 1.4	2.7 ± 7.2	0.77	110	0.3	*SA*	1
48	$13^h29^m56.71^s$	47°11′8.63”	16.6	2.1	6.4	58 ± 38	5 ± 6	1.2 ± 2.1	17.6 ± 39.3	3.40	110	0.7	*IA*	0
49	$13^h29^m55.83^s$	47°10′49.56”	28.1	4.4	10.8	42 ± 40	9 ± 10	5.8 ± 9.9	39.0 ± 98.6	1.54	165	0.6	*SA*	0
50	$13^h29^m55.95^s$	47°10′54.47”	25.0	2.0	5.0	32 ± 0	4 ± 5	0.3 ± 0.3	4.7 ± 12.8	3.66	145	0.6	*SA*	1
51	$13^h29^m56.90^s$	47°11′2.68”	26.0	2.3	5.7	37 ± 16	9 ± 3	1.4 ± 0.5	30.1 ± 29.1	4.85	76	0.9	*SA*	0
52	$13^h29^m56.64^s$	47°11′3.19”	30.6	2.1	5.2	61 ± 18	9 ± 3	2.6 ± 1.0	46.1 ± 33.7	4.15	121	1.0	*SA*	0
53	$13^h29^m57.14^s$	47°11′4.73”	23.1	3.2	7.9	66 ± 26	9 ± 6	3.9 ± 1.3	60.2 ± 65.5	3.57	153	0.5	*SA*	0
54	$13^h29^m56.95^s$	47°11′9.34”	31.3	1.4	3.7	32 ± 0	7 ± 5	0.6 ± 0.5	15.2 ± 22.3	6.28	93	0.6	*IA*	1
55	$13^h29^m55.52^s$	47°10′48.56”	39.0	7.7	18.9	90 ± 24	16 ± 7	25.2 ± 14.4	230.0 ± 196.9	2.09	151	0.8	*SA*	0
56	$13^h29^m56.38^s$	47°10′52.01”	32.3	5.6	14.6	32 ± 0	9 ± 6	4.6 ± 4.7	29.2 ± 36.3	1.44	152	0.3	*SA*	1
57	$13^h29^m56.37^s$	47°10′56.13”	36.8	4.0	10.0	47 ± 17	7 ± 3	4.8 ± 1.4	22.3 ± 23.5	1.07	0	0.3	*SA*	0
58	$13^h29^m55.86^s$	47°10′50.75”	44.7	4.9	12.4	39 ± 50	5 ± 9	1.2 ± 1.0	11.0 ± 39.6	2.15	146	0.7	*SA*	0
59	$13^h29^m56.56^s$	47°10′54.08”	38.4	4.0	9.9	25 ± 24	10 ± 9	2.3 ± 5.7	28.2 ± 53.6	2.81	69	0.7	*SA*	0
60	$13^h29^m56.90^s$	47°10′57.66”	44.5	3.3	8.2	49 ± 86	12 ± 11	5.6 ± 20.1	70.9 ± 220.3	2.91	177	0.5	*SA*	0
61	$13^h29^m54.96^s$	47°10′49.03”	46.3	7.7	17.0	32 ± 0	9 ± 6	5.6 ± 6.5	25.4 ± 37.3	1.04	6	0.3	*SA*	1
62	$13^h29^m54.80^s$	47°10′44.63”	54.9	9.3	19.5	95 ± 22	8 ± 4	24.9 ± 24.2	57.3 ± 64.5	0.53	107	0.6	*SA*	0
63	$13^h29^m54.93^s$	47°10′52.55”	51.0	2.1	4.9	39 ± 22	7 ± 3	1.1 ± 1.0	17.4 ± 23.1	3.71	32	0.7	*SA*	0
64	$13^h29^m57.35^s$	47°10′56.75”	53.5	7.0	18.1	95 ± 17	13 ± 2	21.5 ± 3.5	169.2 ± 86.1	1.81	167	0.4	*SA*	0
65	$13^h29^m54.91^s$	47°10′46.66”	57.6	8.5	20.0	62 ± 36	6 ± 6	7.7 ± 11.4	25.7 ± 53.4	0.76	10	0.6	*SA*	0
66	$13^h29^m55.28^s$	47°10′49.17”	58.3	4.0	9.2	91 ± 55	15 ± 15	6.3 ± 19.9	212.2 ± 455.7	7.72	42	0.2	*SA*	0
67	$13^h29^m55.21^s$	47°10′53.46”	63.4	1.9	4.9	32 ± 0	8 ± 6	1.6 ± 1.1	21.3 ± 29.8	3.09	123	0.3	*SA*	1
68	$13^h29^m56.62^s$	47°10′50.31”	62.0	3.1	7.4	32 ± 0	4 ± 6	1.9 ± 2.1	6.1 ± 15.7	0.76	140	0.3	*SA*	1
69	$13^h29^m56.64^s$	47°10′53.13”	64.4	2.0	5.1	32 ± 0	3 ± 4	0.9 ± 1.3	3.6 ± 9.4	0.91	135	0.4	*SA*	1
70	$13^h29^m57.11^s$	47°10′42.11”	71.3	3.1	6.8	13 ± 13	6 ± 6	1.1 ± 1.4	5.6 ± 13.7	1.15	62	0.7	*IA*	0
71	$13^h29^m56.52^s$	47°10′45.94”	68.6	5.3	13.1	42 ± 44	11 ± 11	3.9 ± 8.0	49.3 ± 108.9	2.87	144	0.5	*SA*	0
72	$13^h29^m55.21^s$	47°10′46.01”	68.6	6.0	14.8	56 ± 38	9 ± 5	6.9 ± 8.5	47.2 ± 62.1	1.57	179	0.8	*SA*	0
73	$13^h29^m56.40^s$	47°10′51.49”	61.3	5.2	12.8	22 ± 24	7 ± 18	5.5 ± 7.7	12.1 ± 52.8	0.51	86	0.5	*SA*	0
74	$13^h29^m56.67^s$	47°10′46.28”	76.4	4.9	12.1	32 ± 0	2 ± 0	2.5 ± 1.5	1.5 ± 0.0	0.14	152	0.2	*SA*	1
75	$13^h29^m56.30^s$	47°10′47.70”	76.5	8.6	21.1	82 ± 14	8 ± 1	24.6 ± 5.5	48.0 ± 18.3	0.45	36	0.8	*SA*	0
76	$13^h29^m56.77^s$	47°10′49.77”	74.4	5.9	15.0	70 ± 15	8 ± 2	10.6 ± 3.3	44.8 ± 23.3	0.97	154	0.5	*SA*	0
77	$13^h29^m57.09^s$	47°10′39.34”	76.7	3.8	8.2	37 ± 20	4 ± 2	2.2 ± 2.0	7.2 ± 7.0	0.74	4	0.6	*IA*	0
78	$13^h29^m56.83^s$	47°10′39.21”	75.9	2.6	5.7	32 ± 0	7 ± 6	0.4 ± 0.6	16.9 ± 30.1	9.75	56	0.3	*IA*	1
79	$13^h29^m56.86^s$	47°10′41.96”	79.7	4.4	10.3	92 ± 23	3 ± 2	6.0 ± 1.4	9.1 ± 10.6	0.35	69	0.6	*IA*	0
80	$13^h29^m55.84^s$	47°10′49.25”	79.4	1.6	4.2	32 ± 0	4 ± 3	0.4 ± 0.3	6.7 ± 8.4	3.65	1	1.0	*SA*	1
81	$13^h29^m57.23^s$	47°10′50.96”	74.4	7.5	19.2	62 ± 9	9 ± 1	16.0 ± 1.7	48.4 ± 16.8	0.69	172	0.7	*SA*	0
82	$13^h29^m55.84^s$	47°10′41.62”	84.5	3.0	7.4	61 ± 14	4 ± 2	2.0 ± 0.6	12.5 ± 11.0	1.40	23	0.4	*IA*	0
83	$13^h29^m54.61^s$	47°10′46.05”	81.4	2.5	6.2	32 ± 0	7 ± 8	0.9 ± 0.6	16.6 ± 38.9	4.11	159	0.4	*SA*	1
84	$13^h29^m55.62^s$	47°10′46.43”	80.1	8.3	22.0	48 ± 17	11 ± 4	10.2 ± 6.1	58.0 ± 46.4	1.30	62	0.6	*SA*	0
85	$13^h29^m55.26^s$	47°10′49.23”	86.8	1.8	5.0	37 ± 28	3 ± 4	0.9 ± 0.7	2.8 ± 7.8	0.73	7	0.8	*SA*	0
86	$13^h29^m56.40^s$	47°10′42.25”	89.1	3.1	7.9	53 ± 13	5 ± 2	2.5 ± 0.4	13.7 ± 9.9	1.27	137	0.9	*IA*	0

ID (1)	RA (J2000) *h m s* (2)	Dec (J2000) *d ’ ”* (3)	V_{LSR} km/s (4)	T_{max} K (5)	S/N (6)	R pc (7)	σ_v km/s (8)	L_{CO} 10^5 K km/s pc^2 (9)	M_{vir} 10^5 $M_\odot$ (10)	α (11)	PA deg (12)	b/a (13)	Reg (14)	Flag (15)
87	$13^h29^m55.83^s$	47°10′59.47”	−15.4	1.4	4.3	32 ± 0	4 ± 2	0.2 ± 0.1	4.3 ± 4.9	6.10	145	0.6	*SA*	1
88	$13^h29^m55.71^s$	47°10′59.65”	0.1	1.5	4.1	32 ± 0	7 ± 4	0.7 ± 0.3	16.0 ± 17.5	5.54	177	0.4	*SA*	1
89	$13^h29^m55.91^s$	47°11′0.11”	28.0	3.2	7.8	32 ± 0	6 ± 2	2.8 ± 1.0	10.2 ± 8.3	0.85	11	0.2	*SA*	1
90	$13^h29^m55.24^s$	47°10′58.82”	32.4	2.8	6.6	75 ± 11	7 ± 1	5.5 ± 0.9	36.4 ± 16.3	1.51	9	0.3	*SA*	0
91	$13^h29^m55.46^s$	47°11′0.85”	36.8	2.1	5.1	56 ± 27	9 ± 5	1.7 ± 2.1	42.0 ± 69.0	5.73	170	0.7	*SA*	0
92	$13^h29^m55.33^s$	47°11′2.92”	40.0	3.2	7.4	38 ± 17	3 ± 2	1.9 ± 0.8	4.4 ± 6.1	0.53	63	0.5	*SA*	0
93	$13^h29^m55.05^s$	47°11′4.41”	43.1	2.3	5.3	51 ± 28	4 ± 3	2.2 ± 2.3	8.0 ± 13.0	0.84	155	0.3	*SA*	0
94	$13^h29^m54.64^s$	47°11′2.24”	−6.3	2.1	6.9	32 ± 0	6 ± 3	0.5 ± 0.1	13.4 ± 12.0	5.65	13	0.6	*SA*	1
95	$13^h29^m55.25^s$	47°10′35.15”	−0.0	3.1	5.9	5 ± 11	11 ± 5	1.1 ± 0.2	5.9 ± 14.1	1.24	50	1.0	*IA*	0
96	$13^h29^m54.96^s$	47°10′34.04”	5.1	2.8	5.0	32 ± 0	2 ± 1	0.4 ± 0.2	1.4 ± 2.0	0.78	132	0.8	*IA*	1
97	$13^h29^m56.06^s$	47°10′33.90”	5.4	2.5	5.2	32 ± 0	3 ± 2	0.5 ± 0.2	2.1 ± 2.9	1.04	134	0.8	*IA*	1
98	$13^h29^m56.53^s$	47°11′6.47”	18.6	2.7	6.4	32 ± 0	4 ± 2	0.7 ± 0.3	6.1 ± 4.5	2.14	5	1.0	*IA*	1
99	$13^h29^m54.50^s$	47°11′10.16”	58.1	2.3	5.4	48 ± 24	10 ± 6	2.3 ± 2.3	45.7 ± 67.6	4.65	44	0.4	*IA*	0
100	$13^h29^m55.08^s$	47°11′6.81”	48.7	1.8	4.5	20 ± 22	7 ± 3	0.8 ± 0.3	9.9 ± 12.4	2.90	58	1.0	*IA*	0
101	$13^h29^m56.82^s$	47°10′32.77”	73.9	3.5	5.2	16 ± 12	4 ± 2	1.4 ± 0.6	2.8 ± 3.6	0.47	152	0.7	*IA*	0
102	$13^h29^m56.86^s$	47°10′34.75”	76.6	3.4	6.1	32 ± 0	3 ± 2	0.7 ± 0.4	3.3 ± 4.5	1.05	75	0.7	*IA*	1
103	$13^h29^m56.76^s$	47°10′35.93”	84.1	2.3	4.8	32 ± 0	4 ± 2	0.3 ± 0.2	4.4 ± 5.1	3.38	138	0.7	*IA*	1
104	$13^h29^m54.69^s$	47°10′35.66”	77.3	2.7	4.8	32 ± 0	8 ± 4	0.9 ± 0.7	21.7 ± 20.2	5.29	6	0.6	*IA*	1
105	$13^h29^m54.51^s$	47°10′33.25”	91.4	5.8	11.7	56 ± 27	4 ± 2	3.6 ± 3.4	8.7 ± 11.9	0.56	44	0.3	*IA*	0
106	$13^h29^m55.04^s$	47°10′56.27”	60.7	2.0	4.8	32 ± 0	4 ± 3	0.8 ± 0.3	5.7 ± 8.8	1.66	141	0.5	*SA*	1
107	$13^h29^m56.42^s$	47°10′31.24”	71.6	3.5	5.1	50 ± 14	3 ± 1	1.8 ± 0.5	6.1 ± 6.2	0.76	178	0.4	*IA*	0
108	$13^h29^m55.07^s$	47°10′34.92”	97.0	2.1	5.0	51 ± 12	14 ± 4	1.6 ± 0.5	104.2 ± 75.5	14.54	23	0.6	*IA*	0
109	$13^h29^m57.22^s$	47°10′36.80”	83.4	2.8	6.1	32 ± 0	6 ± 2	1.3 ± 0.3	12.2 ± 7.7	2.22	145	0.6	*IA*	1
110	$13^h29^m56.10^s$	47°10′35.54”	95.8	3.1	7.6	69 ± 11	6 ± 1	4.6 ± 0.5	29.3 ± 9.0	1.47	43	0.6	*IA*	0
111	$13^h29^m55.86^s$	47°10′37.49”	104.4	1.8	5.2	45 ± 33	5 ± 2	1.3 ± 0.5	11.3 ± 16.3	2.04	153	0.8	*IA*	0
112	$13^h29^m57.08^s$	47°10′43.94”	94.6	2.6	6.8	29 ± 12	3 ± 1	0.9 ± 0.2	2.3 ± 2.4	0.60	4	0.9	*IA*	0
113	$13^h29^m55.05^s$	47°10′32.45”	98.4	2.4	5.1	52 ± 15	6 ± 2	1.3 ± 0.4	16.7 ± 13.4	2.97	110	1.2	*IA*	0
114	$13^h29^m55.46^s$	47°10′37.50”	101.9	2.2	6.1	55 ± 21	4 ± 2	1.9 ± 0.9	10.8 ± 10.3	1.33	9	0.9	*IA*	0
115	$13^h29^m55.38^s$	47°10′37.81”	117.3	1.6	5.1	32 ± 0	9 ± 7	0.3 ± 0.4	24.6 ± 41.0	17.69	104	0.4	*IA*	1
116	$13^h29^m52.27^s$	47°10′59.21”	17.7	1.6	4.2	52 ± 15	9 ± 4	2.0 ± 0.9	40.4 ± 38.0	4.75	157	0.4	*SA*	0
117	$13^h29^m53.24^s$	47°10′55.69”	32.2	2.3	5.9	72 ± 26	4 ± 6	3.0 ± 1.8	10.5 ± 34.4	0.81	149	0.4	*SA*	0
118	$13^h29^m53.50^s$	47°10′52.76”	41.0	3.8	8.9	63 ± 35	10 ± 3	4.3 ± 1.3	61.5 ± 50.3	3.25	75	0.5	*SA*	0
119	$13^h29^m53.15^s$	47°10′53.12”	49.3	3.8	9.2	45 ± 39	8 ± 7	2.9 ± 3.5	31.3 ± 63.0	2.51	10	0.4	*SA*	0
120	$13^h29^m52.01^s$	47°10′30.40”	40.4	2.5	3.7	32 ± 0	6 ± 3	1.1 ± 0.7	13.3 ± 12.5	2.81	135	0.4	*IA*	1
121	$13^h29^m54.42^s$	47°10′48.66”	50.0	6.7	14.6	77 ± 24	6 ± 4	7.2 ± 10.7	30.1 ± 36.9	0.96	177	0.8	*SA*	0
122	$13^h29^m52.00^s$	47°10′58.06”	52.4	5.4	13.9	45 ± 59	13 ± 8	14.3 ± 13.3	75.4 ± 170.1	1.21	25	0.9	*SA*	0
123	$13^h29^m53.93^s$	47°10′48.76”	54.2	4.9	11.4	71 ± 33	15 ± 6	11.7 ± 11.0	175.4 ± 146.9	3.45	8	0.5	*SA*	0
124	$13^h29^m52.29^s$	47°10′57.12”	44.0	4.6	10.7	73 ± 35	9 ± 5	4.5 ± 5.3	61.0 ± 73.1	3.13	48	0.5	*SA*	0
125	$13^h29^m51.61^s$	47°11′1.76”	46.9	6.2	14.7	107 ± 45	13 ± 5	20.6 ± 25.2	187.3 ± 156.7	2.08	49	0.2	*SA*	0
126	$13^h29^m51.88^s$	47°11′1.99”	52.8	4.8	11.2	73 ± 49	16 ± 15	11.8 ± 12.7	195.9 ± 345.2	3.82	178	0.6	*SA*	0
127	$13^h29^m52.00^s$	47°11′8.52”	53.6	2.6	6.1	32 ± 0	4 ± 6	0.5 ± 0.6	6.3 ± 18.1	2.68	132	0.8	*SA*	1
128	$13^h29^m52.80^s$	47°10′47.28”	60.1	7.6	17.5	41 ± 17	13 ± 6	12.7 ± 2.8	72.0 ± 77.1	1.30	145	0.4	*SA*	0
129	$13^h29^m51.95^s$	47°10′48.10”	60.4	2.7	6.3	44 ± 28	8 ± 3	3.4 ± 2.7	26.4 ± 27.3	1.79	153	0.3	*SA*	0
130	$13^h29^m51.94^s$	47°10′54.55”	56.5	8.9	20.0	74 ± 74	10 ± 8	2.8 ± 3.5	74.1 ± 174.2	6.04	54	1.0	*SA*	0
131	$13^h29^m52.60^s$	47°10′55.22”	50.5	5.3	12.6	73 ± 24	6 ± 3	8.7 ± 5.6	29.9 ± 29.7	0.79	13	0.4	*SA*	0
132	$13^h29^m52.67^s$	47°10′59.52”	51.5	3.2	7.4	50 ± 31	10 ± 5	3.7 ± 3.0	46.7 ± 74.2	2.93	5	0.3	*SA*	0
133	$13^h29^m52.36^s$	47°10′51.02”	58.7	5.5	12.3	59 ± 74	2 ± 6	3.7 ± 2.7	3.5 ± 15.8	0.22	17	0.5	*SA*	0
134	$13^h29^m53.21^s$	47°10′55.02”	69.3	1.9	5.0	32 ± 0	7 ± 4	0.4 ± 0.3	17.9 ± 21.7	10.31	23	0.6	*SA*	1
135	$13^h29^m51.68^s$	47°10′58.81”	65.7	4.9	12.7	38 ± 44	13 ± 11	1.0 ± 1.0	64.7 ± 132.1	14.33	164	1.2	*SA*	0
136	$13^h29^m52.31^s$	47°11′1.71”	60.6	4.9	11.4	144 ± 39	6 ± 2	10.8 ± 3.5	49.1 ± 41.9	1.04	83	0.7	*SA*	0
137	$13^h29^m52.75^s$	47°11′3.61”	62.5	3.0	6.9	32 ± 0	2 ± 0	0.6 ± 0.5	1.5 ± 0.0	0.59	7	0.2	*SA*	1
138	$13^h29^m52.17^s$	47°11′8.13”	63.0	3.3	7.7	41 ± 19	6 ± 3	3.0 ± 1.4	15.5 ± 18.5	1.19	32	0.3	*SA*	0
139	$13^h29^m52.19^s$	47°10′41.99”	66.3	2.1	4.5	45 ± 35	9 ± 5	1.4 ± 0.8	42.6 ± 60.5	7.09	144	0.5	*IA*	0
140	$13^h29^m51.96^s$	47°10′44.08”	69.5	3.3	7.5	65 ± 18	7 ± 2	4.3 ± 1.2	37.3 ± 22.2	1.98	126	0.3	*IA*	0
141	$13^h29^m52.09^s$	47°10′53.31”	68.5	7.6	20.8	26 ± 37	12 ± 9	5.9 ± 2.4	41.8 ± 105.6	1.63	28	0.6	*SA*	0
142	$13^h29^m53.57^s$	47°10′57.06”	60.5	2.1	5.0	48 ± 25	7 ± 3	1.8 ± 0.9	26.4 ± 34.3	3.28	177	0.5	*SA*	0
143	$13^h29^m52.49^s$	47°11′6.32”	68.6	2.6	6.6	32 ± 0	5 ± 3	0.7 ± 0.5	8.4 ± 11.1	2.88	28	0.6	*SA*	1
144	$13^h29^m51.90^s$	47°11′6.09”	63.9	2.5	6.3	43 ± 20	5 ± 4	2.3 ± 3.5	13.1 ± 21.5	1.32	122	1.1	*SA*	0
145	$13^h29^m53.37^s$	47°11′8.28”	72.9	2.1	5.4	53 ± 30	8 ± 5	2.1 ± 3.9	37.1 ± 55.2	4.14	1	0.9	*SA*	0
146	$13^h29^m52.59^s$	47°11′11.79”	69.1	4.2	10.5	30 ± 12	5 ± 2	2.6 ± 1.4	8.3 ± 6.2	0.72	2	0.6	*CR*	0

ID (1)	**RA (J2000)** *h m s* (2)	**Dec (J2000)** *d ’ ”* (3)	**V_{LSR}** km/s (4)	**T_{max}** K (5)	**S/N** (6)	**R** pc (7)	**σ_v** km/s (8)	**L_{CO}** 10^5 K km/s pc^2 (9)	**M_{vir}** 10^5 $M_\odot$ (10)	α (11)	**PA** deg (12)	**b/a** (13)	**Reg** (14)	**Flag** (15)
147	$13^h29^m52.95^s$	47°11′11.11”	70.6	5.5	13.6	110 ± 16	6 ± 2	17.5 ± 3.8	44.9 ± 26.9	0.59	41	0.8	*CR*	0
148	$13^h29^m51.93^s$	47°10′35.08”	78.3	3.8	8.0	32 ± 0	8 ± 2	1.9 ± 0.5	20.2 ± 10.9	2.46	158	0.4	*IA*	1
149	$13^h29^m53.22^s$	47°10′44.78”	76.2	1.9	5.1	32 ± 0	6 ± 4	0.7 ± 1.1	10.9 ± 15.4	3.52	151	0.4	*SA*	1
150	$13^h29^m52.61^s$	47°10′50.61”	70.5	7.4	17.1	104 ± 40	11 ± 4	16.9 ± 6.9	140.7 ± 155.4	1.91	32	0.3	*SA*	0
151	$13^h29^m52.61^s$	47°11′3.29”	73.3	2.9	8.1	32 ± 0	7 ± 6	1.4 ± 1.7	17.5 ± 30.6	2.84	147	0.7	*SA*	1
152	$13^h29^m52.86^s$	47°11′6.29”	71.1	1.6	4.1	32 ± 0	4 ± 3	0.2 ± 0.3	4.3 ± 8.1	4.47	114	0.6	*SA*	1
153	$13^h29^m51.72^s$	47°11′8.95”	66.5	3.7	8.6	52 ± 20	10 ± 6	3.9 ± 4.3	59.0 ± 78.5	3.46	65	0.2	*SA*	0
154	$13^h29^m51.60^s$	47°10′40.10”	79.4	3.2	7.4	90 ± 54	4 ± 2	4.2 ± 3.6	18.3 ± 22.2	1.00	170	0.7	*IA*	0
155	$13^h29^m51.59^s$	47°10′49.14”	78.9	3.4	9.0	74 ± 101	9 ± 8	2.1 ± 3.5	60.6 ± 152.0	6.57	94	0.7	*SA*	0
156	$13^h29^m52.16^s$	47°10′39.61”	85.3	4.6	11.7	45 ± 21	2 ± 2	2.0 ± 1.2	2.5 ± 3.7	0.28	30	0.8	*IA*	0
157	$13^h29^m52.52^s$	47°10′45.84”	80.7	5.7	14.9	61 ± 49	2 ± 3	0.9 ± 0.6	3.0 ± 7.8	0.73	105	0.8	*SA*	0
158	$13^h29^m54.31^s$	47°10′49.26”	81.4	2.9	7.6	51 ± 33	3 ± 6	1.1 ± 0.7	6.2 ± 20.6	1.27	51	0.5	*SA*	0
159	$13^h29^m51.75^s$	47°10′51.78”	81.4	3.8	10.7	52 ± 108	5 ± 11	1.1 ± 0.8	13.8 ± 59.4	2.88	97	0.6	*SA*	0
160	$13^h29^m51.90^s$	47°10′53.98”	81.6	7.0	18.8	81 ± 64	11 ± 14	28.8 ± 56.5	102.0 ± 286.8	0.81	168	0.9	*SA*	0
161	$13^h29^m52.36^s$	47°11′3.89”	83.9	1.5	4.2	32 ± 0	5 ± 5	0.3 ± 0.3	9.2 ± 17.4	8.29	137	0.6	*SA*	1
162	$13^h29^m53.08^s$	47°11′6.22”	79.6	2.2	6.1	41 ± 13	2 ± 1	1.4 ± 0.5	2.2 ± 2.3	0.36	55	0.7	*SA*	0
163	$13^h29^m52.03^s$	47°10′30.86”	77.4	3.6	6.3	25 ± 11	9 ± 4	3.0 ± 1.1	22.4 ± 19.1	1.74	170	0.7	*IA*	0
164	$13^h29^m52.18^s$	47°10′33.64”	85.1	3.0	5.5	17 ± 26	3 ± 4	0.9 ± 1.9	1.3 ± 4.7	0.35	17	1.3	*IA*	0
165	$13^h29^m52.30^s$	47°10′37.75”	90.3	3.9	9.0	66 ± 29	4 ± 4	1.2 ± 1.0	11.3 ± 20.5	2.13	163	0.2	*IA*	0
166	$13^h29^m52.11^s$	47°10′42.03”	88.2	1.7	4.3	32 ± 0	5 ± 3	0.4 ± 0.4	8.0 ± 10.7	5.15	174	0.6	*IA*	1
167	$13^h29^m51.80^s$	47°10′49.74”	85.5	3.4	9.6	50 ± 52	2 ± 4	0.5 ± 0.9	3.0 ± 13.2	1.38	149	0.5	*SA*	0
168	$13^h29^m52.24^s$	47°10′34.73”	93.0	2.8	5.9	36 ± 22	4 ± 8	1.0 ± 1.7	7.3 ± 23.1	1.68	63	0.7	*IA*	0
169	$13^h29^m52.96^s$	47°10′43.38”	92.6	3.3	9.8	58 ± 23	7 ± 3	2.4 ± 1.0	28.4 ± 28.3	2.68	88	0.5	*SA*	0
170	$13^h29^m52.73^s$	47°10′43.12”	89.7	1.3	3.9	32 ± 0	7 ± 4	0.5 ± 0.5	17.8 ± 19.3	8.42	73	0.7	*IA*	1
171	$13^h29^m53.07^s$	47°10′48.01”	91.7	3.0	9.4	81 ± 27	6 ± 2	5.2 ± 3.2	28.3 ± 22.8	1.24	149	1.1	*SA*	0
172	$13^h29^m54.05^s$	47°10′50.13”	90.7	1.7	4.8	21 ± 31	3 ± 4	0.4 ± 0.5	1.8 ± 4.7	0.92	141	0.8	*SA*	0
173	$13^h29^m53.26^s$	47°10′50.86”	93.0	1.6	5.3	32 ± 0	7 ± 3	0.4 ± 0.2	17.0 ± 15.7	8.99	0	0.7	*SA*	1
174	$13^h29^m53.85^s$	47°10′51.08”	92.9	1.8	5.5	59 ± 12	10 ± 3	1.5 ± 0.5	58.7 ± 37.8	8.71	161	0.8	*SA*	0
175	$13^h29^m53.76^s$	47°10′52.32”	93.9	1.7	5.3	32 ± 0	4 ± 4	0.2 ± 0.1	5.2 ± 9.5	6.61	2	0.7	*SA*	1
176	$13^h29^m53.22^s$	47°11′7.82”	94.1	1.5	4.9	32 ± 0	7 ± 2	0.8 ± 0.3	14.1 ± 9.5	3.80	7	0.5	*SA*	1
177	$13^h29^m52.98^s$	47°10′41.22”	99.1	1.2	4.1	32 ± 0	5 ± 3	0.2 ± 0.3	7.2 ± 9.9	7.27	135	0.5	*IA*	1
178	$13^h29^m52.80^s$	47°10′41.27”	94.6	2.8	7.8	16 ± 18	4 ± 3	0.8 ± 0.7	2.2 ± 4.3	0.59	139	0.9	*IA*	0
179	$13^h29^m52.15^s$	47°10′45.06”	98.6	2.8	9.1	32 ± 0	9 ± 4	1.9 ± 0.6	28.4 ± 22.6	3.52	11	0.4	*IA*	1
180	$13^h29^m52.60^s$	47°10′46.39”	101.8	1.4	5.3	32 ± 0	6 ± 5	0.3 ± 0.3	12.1 ± 19.7	8.36	143	0.6	*SA*	1
181	$13^h29^m54.37^s$	47°10′48.26”	100.3	1.5	5.4	32 ± 0	6 ± 5	0.3 ± 0.6	12.4 ± 21.9	8.31	23	0.7	*SA*	1
182	$13^h29^m54.49^s$	47°10′44.47”	105.5	1.1	3.8	32 ± 0	9 ± 6	0.3 ± 0.3	28.8 ± 36.9	23.46	169	0.6	*SA*	1
183	$13^h29^m51.76^s$	47°10′52.70”	116.6	1.4	4.9	32 ± 0	5 ± 4	0.3 ± 0.2	8.9 ± 12.2	6.62	157	0.7	*SA*	1
184	$13^h29^m52.06^s$	47°11′9.98”	−18.5	1.4	4.1	42 ± 21	16 ± 10	0.5 ± 0.2	115.3 ± 161.7	48.41	144	0.5	*CR*	0
185	$13^h29^m52.13^s$	47°11′9.87”	5.2	1.4	3.7	70 ± 24	5 ± 3	2.3 ± 1.4	17.0 ± 20.8	1.72	125	0.5	*SA*	0
186	$13^h29^m52.70^s$	47°11′9.72”	−26.5	1.7	4.9	32 ± 0	4 ± 2	0.4 ± 0.1	5.5 ± 6.4	3.12	160	0.4	*CR*	1
187	$13^h29^m52.06^s$	47°11′1.89”	−25.6	2.0	6.6	32 ± 0	2 ± 1	0.3 ± 0.1	1.8 ± 1.9	1.64	173	0.7	*SA*	1
188	$13^h29^m54.12^s$	47°11′11.07”	61.5	3.1	7.3	107 ± 45	6 ± 3	3.8 ± 2.8	39.8 ± 46.6	2.42	174	0.3	*IA*	0
189	$13^h29^m53.37^s$	47°11′4.76”	76.7	2.0	5.6	54 ± 9	14 ± 4	3.3 ± 0.5	113.4 ± 69.0	7.98	29	0.5	*SA*	0
190	$13^h29^m53.92^s$	47°10′42.94”	72.3	2.1	5.2	32 ± 0	3 ± 5	0.5 ± 0.4	2.7 ± 9.1	1.31	88	0.6	*SA*	1
191	$13^h29^m54.00^s$	47°10′34.08”	80.5	2.6	5.2	32 ± 0	3 ± 2	0.4 ± 0.3	2.2 ± 3.0	1.18	138	0.8	*IA*	1
192	$13^h29^m53.78^s$	47°10′35.27”	81.5	2.4	5.0	32 ± 0	4 ± 4	0.6 ± 0.5	6.1 ± 11.2	2.54	21	1.0	*IA*	1
193	$13^h29^m54.08^s$	47°10′39.42”	84.9	4.1	9.3	32 ± 0	6 ± 3	0.9 ± 0.4	10.8 ± 12.2	2.68	170	0.7	*IA*	1
194	$13^h29^m53.69^s$	47°10′42.62”	80.1	4.0	10.1	54 ± 24	7 ± 4	5.0 ± 3.1	25.3 ± 26.0	1.17	59	0.4	*SA*	0
195	$13^h29^m54.28^s$	47°10′35.20”	88.8	4.8	10.9	30 ± 24	6 ± 4	3.5 ± 3.9	10.9 ± 14.4	0.70	78	0.9	*IA*	0
196	$13^h29^m54.08^s$	47°10′36.70”	89.0	6.1	14.7	46 ± 15	4 ± 1	5.2 ± 1.8	9.0 ± 5.8	0.40	49	0.6	*IA*	0
197	$13^h29^m53.86^s$	47°10′40.28”	85.7	4.6	10.8	40 ± 14	3 ± 2	2.7 ± 1.6	3.3 ± 5.0	0.27	85	0.7	*IA*	0
198	$13^h29^m53.35^s$	47°10′49.39”	51.5	2.2	4.9	32 ± 0	5 ± 3	0.6 ± 0.2	7.7 ± 8.5	2.91	157	0.7	*SA*	1
199	$13^h29^m52.02^s$	47°10′25.42”	68.3	5.0	5.7	32 ± 0	5 ± 2	1.4 ± 0.6	7.7 ± 5.6	1.25	116	0.8	*IA*	1
200	$13^h29^m53.14^s$	47°10′35.90”	82.9	3.6	7.4	38 ± 8	7 ± 2	2.4 ± 0.4	20.8 ± 14.0	2.00	175	0.5	*IA*	0
201	$13^h29^m52.86^s$	47°10′34.16”	90.8	2.8	6.0	34 ± 10	5 ± 1	1.4 ± 0.3	9.0 ± 6.8	1.44	152	1.0	*IA*	0
202	$13^h29^m51.82^s$	47°10′23.65”	114.7	2.9	4.7	32 ± 0	4 ± 2	1.6 ± 0.4	5.5 ± 5.2	0.78	129	0.4	*IA*	1
203	$13^h29^m53.64^s$	47°10′43.87”	132.5	1.3	4.7	32 ± 0	14 ± 4	0.6 ± 0.3	62.3 ± 39.7	22.16	167	0.7	*SA*	1
204	$13^h29^m51.37^s$	47°11′11.69”	−48.3	2.0	5.5	32 ± 0	8 ± 4	0.9 ± 0.3	22.5 ± 20.2	5.98	5	0.6	*SA*	1
205	$13^h29^m51.09^s$	47°11′11.09”	−30.4	1.8	4.9	32 ± 0	4 ± 4	0.5 ± 0.2	4.3 ± 9.4	1.99	10	0.3	*SA*	1
206	$13^h29^m51.14^s$	47°11′9.45”	−17.0	1.7	5.1	32 ± 0	7 ± 3	0.7 ± 0.3	15.1 ± 14.1	5.30	49	0.3	*SA*	1

ID	**RA (J2000)**	**Dec (J2000)**	**V$_{\rm LSR}$**	**T$_{\rm max}$**	**S/N**	**R**	**$\sigma_{\rm v}$**	**L$_{\rm CO}$**	**M$_{\rm vir}$**	α	**PA**	**b/a**	**Reg**	**Flag**
	h m s	*d ’ ”*	km/s	K		pc	km/s	10^5 K km/s pc^2	10^5 M$_\odot$		deg			
(1)	(2)	(3)	(4)	(5)	(6)	(7)	(8)	(9)	(10)	(11)	(12)	(13)	(14)	(15)
207	$13^h29^m51.15^s$	47°11′9.21”	17.7	2.1	5.5	51 ± 37	3 ± 5	1.4 ± 1.2	4.2 ± 11.6	0.70	85	0.4	*SA*	0
208	$13^h29^m50.15^s$	47°11′7.13”	24.6	1.8	4.3	32 ± 0	10 ± 6	0.8 ± 0.6	34.3 ± 38.9	10.06	113	0.5	*SA*	1
209	$13^h29^m50.73^s$	47°11′10.30”	37.5	8.6	20.3	82 ± 23	21 ± 6	26.1 ± 27.9	380.2 ± 281.1	3.34	39	0.5	*SA*	0
210	$13^h29^m51.16^s$	47°11′5.51”	36.0	6.8	15.8	44 ± 31	8 ± 8	5.3 ± 3.0	26.7 ± 63.7	1.17	45	0.5	*SA*	0
211	$13^h29^m48.92^s$	47°11′0.74”	37.7	2.1	5.0	55 ± 24	6 ± 4	1.7 ± 1.0	21.7 ± 24.6	2.85	171	0.7	*IA*	0
212	$13^h29^m49.32^s$	47°10′55.68”	36.6	2.2	5.1	32 ± 0	8 ± 5	1.3 ± 0.8	21.7 ± 25.1	3.96	170	0.6	*IA*	1
213	$13^h29^m50.89^s$	47°11′3.99”	43.7	4.4	10.0	46 ± 47	6 ± 5	3.3 ± 4.8	15.1 ± 28.1	1.06	108	0.7	*SA*	0
214	$13^h29^m50.99^s$	47°11′7.13”	46.1	7.5	18.8	53 ± 53	11 ± 7	6.0 ± 7.6	61.5 ± 107.7	2.37	58	0.5	*SA*	0
215	$13^h29^m49.16^s$	47°10′58.81”	47.7	3.1	7.3	31 ± 24	8 ± 7	1.4 ± 2.4	23.2 ± 44.7	3.68	178	0.4	*IA*	0
216	$13^h29^m50.12^s$	47°11′6.92”	51.9	2.6	6.6	32 ± 0	10 ± 4	2.1 ± 0.9	36.0 ± 28.9	3.99	16	0.4	*SA*	1
217	$13^h29^m51.06^s$	47°11′9.90”	49.0	5.2	14.4	29 ± 37	6 ± 6	1.8 ± 1.4	12.4 ± 38.6	1.58	8	0.8	*SA*	0
218	$13^h29^m48.97^s$	47°10′58.39”	49.7	3.0	7.6	28 ± 35	2 ± 1	1.1 ± 1.1	0.8 ± 1.8	0.17	94	1.1	*IA*	0
219	$13^h29^m51.27^s$	47°11′0.42”	53.6	6.7	16.7	45 ± 35	9 ± 10	3.7 ± 10.4	36.7 ± 87.4	2.27	8	0.5	*SA*	0
220	$13^h29^m49.51^s$	47°11′3.04”	48.3	3.5	8.0	104 ± 18	4 ± 2	10.3 ± 4.0	16.9 ± 14.7	0.38	108	0.3	*SA*	0
221	$13^h29^m51.14^s$	47°11′2.29”	54.2	4.2	9.6	32 ± 0	16 ± 12	2.1 ± 4.1	83.4 ± 130.0	9.14	9	0.6	*SA*	1
222	$13^h29^m50.57^s$	47°11′7.37”	53.1	3.7	8.5	58 ± 49	8 ± 11	1.9 ± 3.3	40.4 ± 107.3	4.80	120	0.6	*SA*	0
223	$13^h29^m49.67^s$	47°10′40.47”	61.8	3.1	6.7	61 ± 29	4 ± 3	4.1 ± 4.1	10.2 ± 16.8	0.57	110	0.7	*IA*	0
224	$13^h29^m50.15^s$	47°10′48.94”	60.2	4.9	11.2	49 ± 24	5 ± 3	4.5 ± 3.4	11.5 ± 19.2	0.59	117	0.4	*IA*	0
225	$13^h29^m50.80^s$	47°10′53.46”	63.6	2.1	5.5	76 ± 37	6 ± 5	1.8 ± 1.7	32.4 ± 58.0	4.02	176	0.5	*SA*	0
226	$13^h29^m49.21^s$	47°10′54.40”	56.3	2.0	5.2	32 ± 0	4 ± 3	0.3 ± 0.2	5.6 ± 7.9	3.85	8	0.5	*IA*	1
227	$13^h29^m49.48^s$	47°10′57.44”	54.2	3.4	8.5	82 ± 27	6 ± 3	3.9 ± 1.5	31.3 ± 35.6	1.82	59	0.8	*IA*	0
228	$13^h29^m51.42^s$	47°10′59.23”	55.1	5.6	15.4	129 ± 86	6 ± 14	4.9 ± 10.0	50.2 ± 196.6	2.33	10	0.2	*SA*	0
229	$13^h29^m49.81^s$	47°11′3.02”	58.3	3.3	7.9	53 ± 26	5 ± 4	2.6 ± 2.4	11.6 ± 19.8	1.00	157	0.9	*SA*	0
230	$13^h29^m51.50^s$	47°11′10.76”	55.6	3.1	7.4	51 ± 44	7 ± 5	2.1 ± 4.5	25.6 ± 62.3	2.84	5	0.7	*SA*	0
231	$13^h29^m51.30^s$	47°11′11.77”	58.1	4.0	9.5	47 ± 26	3 ± 4	2.0 ± 1.9	4.0 ± 10.0	0.47	26	0.8	*SA*	0
232	$13^h29^m49.62^s$	47°10′42.69”	60.2	2.6	5.7	50 ± 44	3 ± 2	0.4 ± 0.4	3.2 ± 7.3	1.68	3	0.6	*IA*	0
233	$13^h29^m50.80^s$	47°10′48.68”	65.7	1.9	4.6	56 ± 30	2 ± 3	1.1 ± 1.5	2.6 ± 7.1	0.53	156	0.3	*IA*	0
234	$13^h29^m50.59^s$	47°10′51.60”	61.1	2.3	5.4	67 ± 42	7 ± 4	1.6 ± 2.2	33.7 ± 56.8	4.74	4	0.5	*IA*	0
235	$13^h29^m50.84^s$	47°10′56.18”	55.0	1.8	4.9	25 ± 10	6 ± 3	1.2 ± 0.8	10.2 ± 10.1	1.96	33	0.5	*SA*	0
236	$13^h29^m49.68^s$	47°11′6.67”	61.0	2.8	6.9	38 ± 32	7 ± 4	2.0 ± 2.2	17.4 ± 22.8	2.01	75	0.8	*SA*	0
237	$13^h29^m50.04^s$	47°11′10.00”	63.8	1.5	3.7	49 ± 26	7 ± 3	1.2 ± 0.9	25.0 ± 24.8	4.86	11	0.8	*SA*	0
238	$13^h29^m50.20^s$	47°10′43.64”	69.7	3.5	8.3	49 ± 23	4 ± 2	2.2 ± 1.4	6.5 ± 8.4	0.67	28	0.6	*IA*	0
239	$13^h29^m49.93^s$	47°10′45.72”	69.0	5.3	12.2	28 ± 11	7 ± 4	3.1 ± 1.5	15.0 ± 16.6	1.11	156	0.4	*IA*	0
240	$13^h29^m50.24^s$	47°10′46.35”	68.3	2.7	6.6	32 ± 0	9 ± 6	1.8 ± 2.0	23.9 ± 34.2	3.00	146	0.5	*IA*	1
241	$13^h29^m50.49^s$	47°10′48.82”	68.2	2.5	6.2	45 ± 18	3 ± 2	1.4 ± 1.0	5.7 ± 8.7	0.96	117	0.9	*IA*	0
242	$13^h29^m51.44^s$	47°10′57.98”	65.1	5.0	13.4	47 ± 50	4 ± 6	0.9 ± 1.3	6.9 ± 24.9	1.80	40	0.4	*SA*	0
243	$13^h29^m50.80^s$	47°11′4.21”	70.5	2.7	7.1	32 ± 0	11 ± 6	1.3 ± 2.0	38.1 ± 40.1	6.90	159	0.4	*SA*	1
244	$13^h29^m49.87^s$	47°11′7.40”	67.1	3.5	9.5	37 ± 16	7 ± 2	2.2 ± 0.8	17.1 ± 12.8	1.76	85	0.6	*SA*	0
245	$13^h29^m49.69^s$	47°10′36.75”	68.8	2.6	5.0	37 ± 78	3 ± 5	0.9 ± 0.5	2.6 ± 11.5	0.68	78	0.6	*IA*	0
246	$13^h29^m50.22^s$	47°10′41.33”	70.3	2.3	5.0	32 ± 0	4 ± 7	0.6 ± 1.1	5.2 ± 18.4	1.99	133	0.5	*IA*	1
247	$13^h29^m51.27^s$	47°10′41.76”	74.0	3.4	7.7	72 ± 33	7 ± 5	3.0 ± 1.9	37.9 ± 62.3	2.90	10	0.3	*IA*	0
248	$13^h29^m50.50^s$	47°10′43.95”	68.7	1.9	4.2	32 ± 0	6 ± 9	0.5 ± 0.9	12.1 ± 36.7	5.06	53	0.6	*IA*	1
249	$13^h29^m50.85^s$	47°10′43.67”	73.2	3.0	7.6	40 ± 16	5 ± 3	1.6 ± 1.5	9.4 ± 13.0	1.38	7	0.4	*IA*	0
250	$13^h29^m49.91^s$	47°10′43.69”	71.1	3.1	6.9	32 ± 65	9 ± 8	1.4 ± 3.7	28.6 ± 81.5	4.53	27	1.1	*IA*	0
251	$13^h29^m50.68^s$	47°10′46.23”	70.7	1.8	4.5	30 ± 28	9 ± 4	1.2 ± 0.6	28.2 ± 28.7	5.18	97	0.8	*IA*	0
252	$13^h29^m51.40^s$	47°10′47.93”	72.2	2.6	6.3	32 ± 0	7 ± 5	0.7 ± 1.0	16.7 ± 25.4	5.71	137	0.8	*IA*	1
253	$13^h29^m51.12^s$	47°10′56.44”	76.7	3.5	9.2	96 ± 26	9 ± 3	8.0 ± 6.0	85.3 ± 66.6	2.44	61	0.2	*SA*	0
254	$13^h29^m50.94^s$	47°10′38.22”	79.7	4.0	8.7	95 ± 37	5 ± 4	4.7 ± 2.9	29.1 ± 45.1	1.42	123	0.3	*IA*	0
255	$13^h29^m50.38^s$	47°10′39.74”	70.6	3.3	7.1	32 ± 0	11 ± 3	2.0 ± 0.3	41.3 ± 20.7	4.62	3	0.5	*IA*	1
256	$13^h29^m51.49^s$	47°10′43.85”	72.1	2.2	5.1	27 ± 10	3 ± 1	1.6 ± 0.6	2.2 ± 2.2	0.32	103	0.5	*IA*	0
257	$13^h29^m50.24^s$	47°11′8.81”	76.9	2.1	5.7	29 ± 34	5 ± 7	1.0 ± 1.6	7.7 ± 24.1	1.74	132	0.7	*SA*	0
258	$13^h29^m50.53^s$	47°10′54.36”	81.5	1.5	4.3	32 ± 0	6 ± 3	0.4 ± 0.2	10.2 ± 10.5	5.22	14	0.5	*SA*	1
259	$13^h29^m50.68^s$	47°11′2.47”	78.6	2.6	7.1	37 ± 25	4 ± 3	2.3 ± 1.5	7.5 ± 11.0	0.75	45	0.3	*SA*	0
260	$13^h29^m51.48^s$	47°10′51.91”	89.1	2.9	8.7	65 ± 29	8 ± 5	1.7 ± 1.7	48.3 ± 69.4	6.34	68	0.6	*SA*	0
261	$13^h29^m51.43^s$	47°10′48.44”	95.2	1.6	4.8	32 ± 0	5 ± 3	0.3 ± 0.3	7.2 ± 8.5	5.07	145	0.8	*IA*	1
262	$13^h29^m51.52^s$	47°10′48.55”	107.1	1.5	5.0	32 ± 0	5 ± 3	0.3 ± 0.2	7.3 ± 9.8	4.98	145	0.6	*SA*	1
263	$13^h29^m49.45^s$	47°10′38.40”	−26.4	2.0	5.1	32 ± 0	3 ± 2	0.9 ± 0.3	3.9 ± 4.7	0.96	153	0.4	*IA*	1
264	$13^h29^m49.81^s$	47°10′34.62”	13.1	2.6	5.0	32 ± 0	9 ± 6	0.8 ± 0.3	27.7 ± 33.8	7.98	3	0.5	*IA*	1
265	$13^h29^m49.49^s$	47°11′10.41”	48.6	2.8	6.2	48 ± 10	6 ± 1	2.7 ± 0.3	17.4 ± 10.1	1.49	40	0.7	*SA*	0
266	$13^h29^m48.94^s$	47°10′22.05”	55.5	4.9	4.1	18 ± 23	6 ± 3	2.2 ± 1.0	6.7 ± 11.8	0.71	170	0.8	*IA*	0

ID (1)	**RA (J2000)** *h m s* (2)	**Dec (J2000)** *d ’ ”* (3)	$\mathbf{V_{LSR}}$ km/s (4)	$\mathbf{T_{max}}$ K (5)	**S/N** (6)	**R** pc (7)	$\sigma_\mathbf{v}$ km/s (8)	$\mathbf{L_{CO}}$ 10^5 K km/s pc^2 (9)	$\mathbf{M_{vir}}$ 10^5 M$_\odot$ (10)	α (11)	**PA** deg (12)	**b/a** (13)	**Reg** (14)	**Flag** (15)
267	$13^h29^m48.98^s$	47°10′28.13”	67.1	3.3	4.6	25 ± 19	6 ± 5	2.0 ± 1.1	8.4 ± 16.2	0.96	26	0.9	*IA*	0
268	$13^h29^m49.28^s$	47°10′29.70”	66.3	4.1	6.0	105 ± 32	6 ± 2	6.7 ± 2.4	41.0 ± 35.0	1.41	32	1.0	*IA*	0
269	$13^h29^m49.29^s$	47°10′25.56”	66.5	5.3	6.3	68 ± 17	7 ± 2	6.2 ± 1.9	29.9 ± 20.7	1.11	24	1.0	*IA*	0
270	$13^h29^m50.34^s$	47°10′55.47”	58.7	2.7	6.2	40 ± 8	6 ± 1	2.3 ± 0.4	15.9 ± 7.1	1.58	117	0.4	*SA*	0
271	$13^h29^m50.20^s$	47°11′0.79”	62.7	2.3	5.1	33 ± 18	6 ± 3	1.2 ± 0.8	11.8 ± 16.4	2.30	16	0.6	*SA*	0
272	$13^h29^m50.26^s$	47°11′2.11”	70.3	1.6	4.4	32 ± 0	5 ± 6	0.9 ± 1.2	8.4 ± 20.4	2.23	135	0.7	*SA*	1
273	$13^h29^m50.07^s$	47°11′2.20”	76.0	2.4	7.2	32 ± 0	3 ± 2	0.5 ± 0.2	2.3 ± 3.8	1.11	22	0.6	*SA*	1
274	$13^h29^m50.74^s$	47°10′23.16”	71.9	5.9	5.9	32 ± 0	7 ± 5	1.5 ± 0.5	14.7 ± 24.1	2.30	154	0.7	*IA*	1
275	$13^h29^m51.55^s$	47°10′35.38”	79.8	4.5	9.6	49 ± 10	5 ± 1	3.6 ± 0.4	14.8 ± 7.0	0.93	85	0.6	*IA*	0
276	$13^h29^m51.46^s$	47°10′33.79”	102.6	2.3	5.8	32 ± 0	6 ± 3	0.3 ± 0.1	10.5 ± 9.6	7.21	130	0.3	*IA*	1
277	$13^h29^m50.70^s$	47°10′53.90”	99.9	1.4	5.1	32 ± 0	7 ± 3	0.8 ± 0.2	17.9 ± 14.1	5.25	130	0.4	*SA*	1
278	$13^h29^m50.81^s$	47°10′40.08”	100.0	1.8	5.3	32 ± 0	4 ± 2	0.5 ± 0.2	4.4 ± 5.6	2.20	44	0.6	*IA*	1
279	$13^h29^m48.66^s$	47°10′31.99”	110.9	2.1	5.0	32 ± 0	3 ± 2	0.4 ± 0.2	3.3 ± 4.6	1.87	163	0.3	*IA*	1
280	$13^h29^m51.52^s$	47°11′7.54”	111.9	1.2	4.7	11 ± 15	6 ± 4	0.3 ± 0.1	4.0 ± 8.4	3.24	86	0.8	*SA*	0
281	$13^h29^m47.64^s$	47°10′59.31”	−2.7	1.7	4.8	50 ± 23	9 ± 3	1.6 ± 0.4	39.0 ± 28.4	5.66	78	0.5	*IA*	0
282	$13^h29^m48.33^s$	47°11′11.43”	28.2	2.8	7.1	51 ± 32	4 ± 3	1.7 ± 1.0	9.3 ± 20.3	1.26	115	0.5	*IA*	0
283	$13^h29^m48.16^s$	47°11′7.53”	29.4	2.1	5.0	70 ± 20	5 ± 1	2.6 ± 0.8	18.0 ± 11.5	1.62	52	0.5	*IA*	0
284	$13^h29^m48.34^s$	47°11′5.04”	40.0	2.6	6.8	45 ± 26	6 ± 3	2.0 ± 0.7	15.8 ± 14.2	1.77	176	0.4	*IA*	0
285	$13^h29^m48.53^s$	47°11′4.37”	43.0	1.9	5.3	23 ± 17	5 ± 4	0.5 ± 0.4	6.9 ± 11.4	3.07	133	0.5	*IA*	0
286	$13^h29^m48.34^s$	47°11′9.45”	47.1	1.9	5.0	32 ± 0	9 ± 5	0.2 ± 0.1	25.2 ± 31.1	23.26	133	0.6	*IA*	1
287	$13^h29^m47.14^s$	47°11′11.28”	6.5	1.6	4.5	32 ± 0	5 ± 4	0.5 ± 0.5	7.9 ± 13.4	3.67	135	0.6	*IA*	1
288	$13^h29^m47.43^s$	47°11′5.15”	13.1	1.8	4.5	32 ± 0	8 ± 4	0.6 ± 0.5	19.2 ± 19.3	7.90	134	0.3	*IA*	1
289	$13^h29^m47.19^s$	47°11′11.03”	23.7	2.9	7.9	27 ± 21	5 ± 3	1.0 ± 0.8	6.1 ± 9.7	1.45	69	0.9	*IA*	0
290	$13^h29^m47.16^s$	47°11′9.36”	28.9	3.0	7.4	30 ± 22	6 ± 5	1.1 ± 1.7	12.1 ± 26.2	2.43	56	0.6	*IA*	0
291	$13^h29^m47.37^s$	47°11′5.16”	31.2	2.9	7.1	47 ± 30	6 ± 5	1.7 ± 2.6	18.8 ± 26.9	2.58	116	0.7	*IA*	0
292	$13^h29^m47.31^s$	47°11′7.45”	30.2	2.8	6.8	36 ± 22	2 ± 1	1.2 ± 1.6	1.4 ± 2.1	0.26	46	0.8	*IA*	0
293	$13^h29^m47.30^s$	47°11′10.21”	31.0	3.1	7.4	41 ± 32	2 ± 4	1.2 ± 1.4	2.6 ± 8.0	0.50	108	0.6	*IA*	0
294	$13^h29^m47.75^s$	47°10′48.36”	19.5	2.6	6.4	35 ± 9	7 ± 2	1.3 ± 0.2	16.9 ± 14.5	2.92	153	0.4	*IA*	0
295	$13^h29^m46.41^s$	47°11′8.27”	30.9	4.2	11.0	62 ± 74	5 ± 4	3.1 ± 3.3	14.3 ± 28.0	1.07	1	0.6	*IA*	0
296	$13^h29^m46.25^s$	47°11′10.01”	29.5	3.9	10.8	54 ± 41	3 ± 4	1.9 ± 1.3	4.2 ± 10.3	0.51	31	0.4	*IA*	0
297	$13^h29^m46.92^s$	47°10′58.38”	36.4	1.7	5.0	32 ± 0	4 ± 6	0.3 ± 0.3	4.8 ± 14.2	3.27	162	0.6	*IA*	1
298	$13^h29^m47.17^s$	47°10′59.81”	36.6	2.7	7.0	70 ± 14	6 ± 2	3.9 ± 0.6	29.2 ± 15.5	1.70	161	0.6	*IA*	0
299	$13^h29^m47.17^s$	47°10′57.39”	45.2	1.8	4.7	32 ± 0	6 ± 4	0.7 ± 0.6	10.7 ± 16.0	3.44	152	0.4	*IA*	1
300	$13^h29^m47.80^s$	47°10′59.31”	32.4	2.5	6.4	27 ± 12	9 ± 4	2.5 ± 0.9	24.3 ± 21.5	2.19	144	0.5	*IA*	0
301	$13^h29^m48.02^s$	47°10′56.38”	36.3	3.0	7.5	44 ± 17	4 ± 2	1.9 ± 0.7	6.9 ± 6.5	0.85	64	0.7	*IA*	0
302	$13^h29^m47.78^s$	47°10′56.77”	36.6	2.2	5.7	80 ± 26	6 ± 4	2.8 ± 1.4	34.7 ± 49.6	2.87	70	0.4	*IA*	0
303	$13^h29^m46.76^s$	47°10′43.72”	37.1	2.1	4.9	32 ± 0	4 ± 6	0.3 ± 0.2	6.5 ± 16.8	4.84	89	0.5	*IA*	1
304	$13^h29^m46.75^s$	47°10′46.39”	40.8	2.6	6.2	39 ± 15	9 ± 4	1.7 ± 0.5	32.2 ± 37.1	4.29	87	0.5	*IA*	0
305	$13^h29^m48.03^s$	47°10′48.02”	41.7	2.8	7.0	60 ± 19	5 ± 2	3.9 ± 0.9	16.0 ± 12.3	0.94	99	0.4	*IA*	0
306	$13^h29^m48.12^s$	47°10′44.57”	48.3	1.8	4.2	32 ± 0	8 ± 5	0.5 ± 0.6	19.0 ± 26.4	8.42	71	0.7	*IA*	1
307	$13^h29^m48.38^s$	47°10′46.47”	52.1	1.9	4.9	91 ± 18	7 ± 3	3.9 ± 1.6	43.8 ± 46.0	2.60	123	0.6	*IA*	0
308	$13^h29^m48.41^s$	47°10′44.04”	54.4	2.2	5.7	32 ± 0	3 ± 3	0.4 ± 0.5	2.7 ± 6.1	1.42	158	0.8	*IA*	1
309	$13^h29^m46.69^s$	47°10′53.63”	42.7	2.4	6.5	73 ± 10	7 ± 1	4.5 ± 0.6	32.1 ± 11.6	1.63	84	0.7	*IA*	0
310	$13^h29^m48.53^s$	47°10′20.63”	39.1	5.5	4.5	32 ± 0	3 ± 2	1.6 ± 0.8	3.3 ± 4.6	0.49	37	0.7	*IA*	1
311	$13^h29^m46.63^s$	47°10′23.71”	40.3	5.4	4.9	32 ± 0	7 ± 6	1.9 ± 0.6	16.0 ± 26.4	1.93	15	0.7	*IA*	1
312	$13^h29^m46.07^s$	47°10′35.04”	40.8	2.7	4.8	33 ± 13	3 ± 1	1.5 ± 0.4	2.5 ± 2.1	0.38	116	0.6	*IA*	0
313	$13^h29^m48.18^s$	47°10′39.06”	56.3	2.8	6.3	32 ± 0	7 ± 4	0.9 ± 0.2	15.8 ± 16.9	3.98	64	0.8	*IA*	1
314	$13^h29^m47.70^s$	47°10′49.16”	47.4	1.5	4.1	32 ± 12	4 ± 1	0.9 ± 0.5	6.3 ± 4.3	1.57	150	0.5	*IA*	0
315	$13^h29^m47.55^s$	47°10′43.00”	60.4	2.0	5.2	32 ± 0	2 ± 2	0.4 ± 0.2	1.8 ± 3.1	1.09	140	0.7	*IA*	1
316	$13^h29^m44.66^s$	47°11′7.84”	−67.7	1.8	5.7	32 ± 0	5 ± 2	0.5 ± 0.2	7.7 ± 5.3	3.49	154	0.7	*SA*	1
317	$13^h29^m44.37^s$	47°11′6.56”	−39.3	1.8	5.3	32 ± 0	10 ± 6	0.6 ± 0.3	35.3 ± 39.5	12.63	158	0.2	*SA*	1
318	$13^h29^m44.63^s$	47°11′6.74”	−16.9	1.7	4.9	32 ± 0	4 ± 4	0.5 ± 0.4	4.9 ± 9.0	2.07	141	0.6	*SA*	1
319	$13^h29^m43.25^s$	47°11′11.25”	1.8	2.1	5.5	32 ± 0	4 ± 6	0.4 ± 0.6	5.3 ± 16.5	2.96	21	0.6	*SA*	1
320	$13^h29^m43.62^s$	47°11′9.60”	4.7	1.6	4.6	32 ± 0	9 ± 11	0.4 ± 0.3	27.9 ± 64.5	18.26	22	0.5	*SA*	1
321	$13^h29^m42.39^s$	47°10′53.19”	−24.9	1.8	5.1	32 ± 0	3 ± 2	0.3 ± 0.1	3.1 ± 3.8	2.57	44	0.8	*IA*	1
322	$13^h29^m42.77^s$	47°10′58.68”	−4.0	3.9	11.1	49 ± 52	8 ± 5	3.6 ± 5.2	30.1 ± 62.0	1.92	67	0.4	*SA*	0
323	$13^h29^m42.84^s$	47°10′51.89”	2.8	6.0	15.7	45 ± 15	5 ± 2	5.7 ± 2.4	12.4 ± 8.8	0.50	51	0.8	*SA*	0
324	$13^h29^m42.75^s$	47°10′55.22”	3.9	4.0	11.7	50 ± 28	2 ± 2	1.4 ± 1.4	1.9 ± 4.1	0.30	93	0.7	*IA*	0
325	$13^h29^m42.86^s$	47°10′47.39”	7.0	2.5	6.5	70 ± 53	5 ± 8	0.3 ± 0.5	21.9 ± 56.8	14.65	2	0.7	*SA*	0
326	$13^h29^m42.80^s$	47°10′49.48”	11.2	7.7	18.3	26 ± 13	7 ± 2	6.4 ± 2.0	11.9 ± 9.7	0.42	138	0.5	*IA*	0

ID	RA (J2000)	Dec (J2000)	V_{LSR}	T_{max}	S/N	R	σ_v	L_{CO}	M_{vir}	α	PA	b/a	Reg	Flag
	h m s	*d ′ ″*	km/s	K		pc	km/s	10^5 K km/s pc^2	10^5 $M_\odot$		deg			
(1)	(2)	(3)	(4)	(5)	(6)	(7)	(8)	(9)	(10)	(11)	(12)	(13)	(14)	(15)
327	$13^h29^m42.41^s$	47°10′47.07”	21.6	2.6	6.1	27 ± 18	4 ± 4	1.2 ± 0.8	5.4 ± 8.8	1.04	45	0.6	*IA*	0
328	$13^h29^m42.71^s$	47°10′46.57”	25.4	2.0	4.2	32 ± 0	3 ± 3	0.2 ± 0.2	2.1 ± 5.6	2.16	50	0.8	*IA*	1
329	$13^h29^m42.98^s$	47°11′6.14”	−16.9	2.1	6.4	39 ± 20	6 ± 2	1.6 ± 0.6	14.4 ± 14.5	2.04	49	1.2	*SA*	0
330	$13^h29^m42.82^s$	47°11′5.42”	−6.7	1.8	5.1	32 ± 0	3 ± 4	0.2 ± 0.2	3.4 ± 8.9	3.72	82	0.5	*SA*	1
331	$13^h29^m42.70^s$	47°11′7.48”	−2.3	1.6	4.4	39 ± 16	5 ± 3	1.0 ± 0.6	9.3 ± 11.6	2.24	56	1.0	*SA*	0
332	$13^h29^m43.29^s$	47°11′8.53”	−15.5	1.6	5.1	17 ± 6	5 ± 3	0.7 ± 0.2	4.4 ± 4.5	1.45	47	0.6	*SA*	0
333	$13^h29^m42.18^s$	47°11′11.38”	−12.3	2.7	7.0	32 ± 0	5 ± 5	0.7 ± 0.9	8.7 ± 18.1	2.77	2	0.8	*IA*	1
334	$13^h29^m41.73^s$	47°11′9.92”	−0.5	5.4	12.7	70 ± 22	8 ± 2	7.0 ± 8.8	46.7 ± 30.8	1.53	156	0.4	*IA*	0
335	$13^h29^m42.38^s$	47°11′10.73”	−4.0	3.9	10.5	47 ± 17	4 ± 3	3.1 ± 1.9	7.2 ± 10.4	0.53	152	0.6	*IA*	0
336	$13^h29^m42.14^s$	47°11′10.81”	5.9	5.3	13.3	31 ± 42	10 ± 7	1.1 ± 1.2	33.3 ± 42.3	7.05	80	0.8	*IA*	0
337	$13^h29^m41.57^s$	47°11′0.71”	13.6	2.4	5.4	37 ± 17	8 ± 4	1.8 ± 1.0	24.9 ± 36.4	3.13	129	0.4	*IA*	0
338	$13^h29^m41.62^s$	47°11′5.21”	14.1	3.5	7.8	117 ± 37	5 ± 4	6.2 ± 2.9	31.1 ± 47.8	1.14	101	0.6	*IA*	0
339	$13^h29^m42.06^s$	47°10′56.79”	−14.4	3.0	8.3	32 ± 0	4 ± 3	0.5 ± 0.2	5.9 ± 7.3	2.83	175	0.9	*IA*	1
340	$13^h29^m44.00^s$	47°10′33.28”	5.1	4.9	8.5	30 ± 32	2 ± 1	2.2 ± 3.6	1.0 ± 1.9	0.10	47	0.9	*SA*	0
341	$13^h29^m43.64^s$	47°10′33.62”	4.7	5.9	11.4	102 ± 22	7 ± 2	15.3 ± 6.3	49.8 ± 27.3	0.75	4	0.5	*SA*	0
342	$13^h29^m43.26^s$	47°10′39.59”	6.0	2.6	5.7	34 ± 18	6 ± 3	1.6 ± 0.9	11.3 ± 12.6	1.62	30	0.7	*SA*	0
343	$13^h29^m44.09^s$	47°10′29.67”	14.2	6.6	10.5	85 ± 49	4 ± 5	2.1 ± 3.5	12.7 ± 33.4	1.39	100	0.4	*SA*	0
344	$13^h29^m44.22^s$	47°10′34.47”	13.6	2.1	3.8	32 ± 0	6 ± 3	1.2 ± 0.8	11.5 ± 12.5	2.21	50	0.6	*SA*	1
345	$13^h29^m42.96^s$	47°10′38.56”	14.8	1.9	4.4	32 ± 0	3 ± 3	0.3 ± 0.5	3.0 ± 6.4	2.18	125	0.6	*IA*	1
346	$13^h29^m43.02^s$	47°10′40.14”	14.6	2.4	5.2	32 ± 0	2 ± 3	0.8 ± 0.9	1.9 ± 4.4	0.56	10	0.5	*IA*	1
347	$13^h29^m44.12^s$	47°10′24.69”	23.9	6.0	6.5	39 ± 25	5 ± 6	6.5 ± 5.4	8.6 ± 23.5	0.30	139	1.0	*SA*	0
348	$13^h29^m43.77^s$	47°10′25.75”	16.7	6.6	7.7	31 ± 22	3 ± 5	1.8 ± 1.9	3.4 ± 9.6	0.43	137	0.9	*SA*	0
349	$13^h29^m43.94^s$	47°10′30.48”	18.1	6.5	9.6	32 ± 0	6 ± 7	0.7 ± 0.8	11.1 ± 28.6	3.48	6	0.3	*SA*	1
350	$13^h29^m44.69^s$	47°10′38.45”	23.8	4.3	9.1	52 ± 14	5 ± 2	3.9 ± 3.2	12.2 ± 10.1	0.73	91	0.8	*SA*	0
351	$13^h29^m43.75^s$	47°10′21.57”	27.6	7.0	6.8	32 ± 0	5 ± 4	5.4 ± 4.1	6.7 ± 10.9	0.29	88	0.4	*IA*	1
352	$13^h29^m44.31^s$	47°10′25.83”	24.5	8.0	8.9	32 ± 0	8 ± 6	3.9 ± 4.6	20.7 ± 32.0	1.22	18	0.4	*SA*	1
353	$13^h29^m44.53^s$	47°10′28.17”	24.0	3.4	4.6	32 ± 0	5 ± 3	0.5 ± 0.6	7.0 ± 10.6	3.14	84	0.6	*SA*	1
354	$13^h29^m44.69^s$	47°10′30.36”	25.5	4.0	6.4	54 ± 47	2 ± 4	1.9 ± 1.4	2.7 ± 8.4	0.32	0	0.6	*SA*	0
355	$13^h29^m42.89^s$	47°10′35.94”	25.0	4.0	7.3	36 ± 21	3 ± 3	2.9 ± 3.4	3.0 ± 7.6	0.23	144	0.5	*IA*	0
356	$13^h29^m43.15^s$	47°10′38.37”	22.3	2.7	5.4	8 ± 15	9 ± 8	1.1 ± 1.8	6.6 ± 20.4	1.36	173	0.9	*SA*	0
357	$13^h29^m42.75^s$	47°10′39.95”	24.8	3.7	7.6	45 ± 21	4 ± 3	2.2 ± 1.2	7.1 ± 10.5	0.74	145	0.8	*IA*	0
358	$13^h29^m44.08^s$	47°10′27.29”	25.2	6.3	8.5	82 ± 61	8 ± 9	6.6 ± 14.3	48.3 ± 112.3	1.67	14	0.4	*SA*	0
359	$13^h29^m43.14^s$	47°10′31.66”	28.9	4.1	6.4	46 ± 34	6 ± 3	4.2 ± 2.5	16.0 ± 27.1	0.87	97	0.5	*IA*	0
360	$13^h29^m44.70^s$	47°10′34.31”	27.5	3.7	7.8	37 ± 30	2 ± 0	0.7 ± 0.6	1.7 ± 1.4	0.53	148	0.7	*SA*	1
361	$13^h29^m43.17^s$	47°10′34.97”	22.0	6.3	11.3	71 ± 8	8 ± 1	19.0 ± 4.1	52.0 ± 16.7	0.63	149	1.1	*IA*	0
362	$13^h29^m42.42^s$	47°10′35.18”	26.0	3.3	5.4	22 ± 19	7 ± 4	2.0 ± 1.6	10.2 ± 19.4	1.18	51	0.4	*IA*	0
363	$13^h29^m42.63^s$	47°10′38.04”	26.0	3.2	5.9	37 ± 28	7 ± 6	2.4 ± 2.6	20.8 ± 39.9	1.98	28	0.8	*IA*	0
364	$13^h29^m44.48^s$	47°10′41.41”	27.0	4.6	10.3	60 ± 24	5 ± 1	6.7 ± 3.1	18.5 ± 13.1	0.63	67	0.6	*SA*	0
365	$13^h29^m42.43^s$	47°10′41.08”	25.1	3.1	6.0	59 ± 18	6 ± 3	4.3 ± 3.7	22.1 ± 26.1	1.18	73	0.8	*IA*	0
366	$13^h29^m44.63^s$	47°10′43.80”	26.6	3.6	8.9	82 ± 29	5 ± 3	4.1 ± 3.1	17.9 ± 20.5	1.01	74	0.5	*SA*	0
367	$13^h29^m44.98^s$	47°10′28.44”	32.5	3.8	5.2	45 ± 30	6 ± 3	4.2 ± 3.0	14.9 ± 16.3	0.82	54	0.7	*SA*	0
368	$13^h29^m43.89^s$	47°10′19.88”	38.1	7.7	6.5	32 ± 0	4 ± 4	1.5 ± 1.9	4.7 ± 9.8	0.71	21	0.7	*SA*	1
369	$13^h29^m44.58^s$	47°10′27.58”	38.0	3.2	4.5	39 ± 43	7 ± 5	2.3 ± 1.9	22.2 ± 39.8	2.22	55	0.8	*SA*	0
370	$13^h29^m44.62^s$	47°10′33.10”	31.7	4.7	8.6	68 ± 35	12 ± 6	4.4 ± 6.2	98.2 ± 124.5	5.10	51	0.8	*SA*	0
371	$13^h29^m44.54^s$	47°10′37.48”	36.6	2.8	6.5	32 ± 0	4 ± 4	0.5 ± 0.5	5.5 ± 11.7	2.33	123	0.6	*SA*	1
372	$13^h29^m42.19^s$	47°10′42.00”	34.7	2.5	4.7	32 ± 0	3 ± 3	0.4 ± 0.2	3.5 ± 5.9	1.90	7	0.7	*IA*	1
373	$13^h29^m44.11^s$	47°10′19.19”	39.1	6.5	5.4	31 ± 24	7 ± 3	1.9 ± 0.8	16.3 ± 16.6	1.96	138	0.7	*SA*	0
374	$13^h29^m44.09^s$	47°10′22.71”	37.7	8.9	9.0	53 ± 21	5 ± 2	6.2 ± 1.4	16.6 ± 15.7	0.61	8	0.4	*SA*	0
375	$13^h29^m42.50^s$	47°10′38.93”	44.9	2.0	3.9	32 ± 0	4 ± 3	0.3 ± 0.4	4.1 ± 7.1	3.31	49	0.9	*IA*	1
376	$13^h29^m44.27^s$	47°10′34.60”	55.6	1.9	3.9	32 ± 0	4 ± 3	0.7 ± 0.7	4.4 ± 7.5	1.49	16	0.6	*SA*	1
377	$13^h29^m43.60^s$	47°10′41.87”	6.8	1.8	4.4	32 ± 0	5 ± 5	0.2 ± 0.2	7.0 ± 15.8	8.24	15	0.8	*SA*	1
378	$13^h29^m43.87^s$	47°10′43.49”	3.7	1.6	4.2	32 ± 24	5 ± 2	0.7 ± 0.3	8.7 ± 9.6	2.99	151	1.2	*SA*	0
379	$13^h29^m43.71^s$	47°10′43.62”	19.0	2.1	4.8	79 ± 27	4 ± 2	3.0 ± 1.3	11.0 ± 12.7	0.84	68	0.6	*SA*	0
380	$13^h29^m43.73^s$	47°10′46.53”	15.8	1.8	4.1	32 ± 0	5 ± 3	0.6 ± 0.5	7.7 ± 10.7	2.99	142	0.5	*SA*	1
381	$13^h29^m43.85^s$	47°10′46.66”	29.0	2.0	5.0	32 ± 0	4 ± 3	0.4 ± 0.5	4.2 ± 7.0	2.34	76	0.8	*SA*	1
382	$13^h29^m42.71^s$	47°10′43.99”	−4.9	1.8	4.3	32 ± 0	2 ± 1	0.3 ± 0.2	0.9 ± 1.2	0.76	132	0.5	*IA*	1
383	$13^h29^m42.40^s$	47°10′51.93”	4.1	2.1	5.6	32 ± 0	7 ± 3	1.2 ± 0.3	15.1 ± 11.3	2.99	155	0.2	*IA*	1
384	$13^h29^m41.92^s$	47°10′55.66”	2.5	2.5	6.2	32 ± 0	7 ± 3	1.0 ± 0.1	14.9 ± 12.7	3.43	133	0.7	*IA*	1
385	$13^h29^m43.49^s$	47°11′7.07”	10.2	2.1	5.8	23 ± 5	8 ± 2	1.5 ± 0.3	13.9 ± 9.1	2.11	67	0.4	*SA*	0
386	$13^h29^m43.03^s$	47°10′26.90”	5.0	3.5	4.8	52 ± 17	2 ± 1	1.6 ± 0.7	1.4 ± 1.1	0.20	106	0.5	*IA*	0

ID	RA (J2000)	Dec (J2000)	V_{LSR}	T_{max}	S/N	R	σ_v	L_{CO}	M_{vir}	α	PA	b/a	Reg	Flag
	h m s	*d ' "*	km/s	K		pc	km/s	10^5 K km/s pc^2	10^5 $M_\odot$		deg			
(1)	(2)	(3)	(4)	(5)	(6)	(7)	(8)	(9)	(10)	(11)	(12)	(13)	(14)	(15)
387	$13^h29^m45.46^s$	47°10′33.37”	10.3	2.6	4.4	32 ± 0	6 ± 5	0.5 ± 0.3	11.4 ± 19.1	5.20	45	0.7	*IA*	1
388	$13^h29^m45.54^s$	47°10′32.93”	35.6	3.2	5.8	66 ± 8	10 ± 2	5.8 ± 0.7	69.5 ± 26.5	2.75	48	0.5	*IA*	0
389	$13^h29^m43.71^s$	47°10′53.08”	5.5	1.3	3.8	32 ± 0	4 ± 2	0.2 ± 0.2	4.3 ± 5.7	4.89	169	0.7	*SA*	1
390	$13^h29^m43.72^s$	47°10′51.78”	15.8	2.3	5.9	36 ± 12	4 ± 1	1.1 ± 0.2	4.6 ± 4.7	0.98	157	0.5	*SA*	0
391	$13^h29^m44.58^s$	47°10′54.58”	23.2	3.8	9.7	33 ± 24	4 ± 5	1.4 ± 1.3	4.8 ± 14.4	0.82	7	0.8	*SA*	0
392	$13^h29^m44.48^s$	47°10′58.08”	24.4	2.2	6.2	55 ± 23	4 ± 3	1.5 ± 1.4	9.2 ± 13.7	1.37	162	1.4	*SA*	0
393	$13^h29^m44.71^s$	47°10′53.82”	29.7	2.8	7.4	16 ± 33	5 ± 7	0.7 ± 1.2	4.6 ± 15.2	1.47	144	0.9	*SA*	0
394	$13^h29^m45.27^s$	47°10′39.95”	22.2	1.9	4.5	32 ± 0	4 ± 2	0.4 ± 0.3	4.5 ± 5.8	2.28	63	0.6	*IA*	1
395	$13^h29^m45.40^s$	47°10′51.50”	24.8	3.7	9.6	59 ± 22	2 ± 2	3.2 ± 1.9	3.0 ± 4.7	0.22	68	0.8	*IA*	0
396	$13^h29^m45.35^s$	47°10′54.36”	24.6	2.7	6.9	75 ± 46	7 ± 7	2.6 ± 3.7	37.0 ± 79.5	3.23	76	0.9	*IA*	0
397	$13^h29^m45.51^s$	47°10′56.36”	29.8	2.1	4.8	30 ± 17	3 ± 2	1.0 ± 0.6	2.2 ± 3.7	0.50	175	0.7	*IA*	0
398	$13^h29^m45.44^s$	47°10′42.35”	32.3	4.7	10.5	36 ± 29	1 ± 3	1.3 ± 2.4	0.8 ± 2.7	0.14	14	0.5	*IA*	0
399	$13^h29^m45.31^s$	47°10′43.27”	31.9	3.6	8.5	46 ± 64	9 ± 14	1.4 ± 3.5	37.8 ± 127.9	6.17	135	1.0	*IA*	0
400	$13^h29^m45.22^s$	47°10′45.22”	34.9	3.2	7.3	32 ± 0	7 ± 10	1.7 ± 3.6	16.3 ± 45.9	2.23	87	0.2	*IA*	1
401	$13^h29^m45.30^s$	47°10′47.96”	35.3	3.0	8.0	80 ± 40	6 ± 3	2.5 ± 2.7	32.4 ± 44.8	2.95	88	1.0	*IA*	0
402	$13^h29^m41.54^s$	47°10′57.40”	23.0	2.6	5.6	32 ± 0	5 ± 3	0.8 ± 0.3	9.3 ± 9.2	2.54	23	0.6	*IA*	1
403	$13^h29^m45.25^s$	47°10′20.89”	27.4	7.5	6.5	32 ± 0	4 ± 5	1.1 ± 0.6	4.5 ± 12.7	0.94	46	0.6	*SA*	1
404	$13^h29^m44.77^s$	47°10′24.05”	29.1	4.4	4.9	32 ± 0	4 ± 4	0.7 ± 0.9	6.6 ± 11.1	2.27	167	0.6	*SA*	1
405	$13^h29^m45.09^s$	47°10′24.04”	29.9	7.0	8.1	68 ± 13	7 ± 2	10.1 ± 2.5	31.6 ± 18.0	0.72	27	0.5	*SA*	0
406	$13^h29^m43.10^s$	47°10′24.64”	25.6	4.8	5.0	21 ± 22	3 ± 3	2.2 ± 2.2	2.2 ± 5.3	0.23	52	0.7	*IA*	0
407	$13^h29^m43.14^s$	47°10′26.69”	29.3	4.3	5.5	42 ± 28	4 ± 3	3.0 ± 2.3	8.2 ± 13.3	0.62	177	0.7	*IA*	0
408	$13^h29^m43.73^s$	47°10′38.98”	30.2	2.5	5.3	83 ± 18	5 ± 2	2.8 ± 0.5	21.8 ± 16.4	1.76	166	0.5	*SA*	0
409	$13^h29^m41.24^s$	47°10′57.24”	20.2	2.8	5.8	32 ± 0	3 ± 2	0.6 ± 0.3	2.4 ± 2.8	0.92	135	0.8	*IA*	1
410	$13^h29^m45.48^s$	47°11′0.42”	29.8	2.5	6.7	68 ± 24	3 ± 1	3.1 ± 0.6	6.3 ± 6.2	0.47	31	0.4	*IA*	0
411	$13^h29^m45.62^s$	47°11′2.71”	31.5	1.6	4.6	8 ± 12	5 ± 4	0.8 ± 0.5	2.4 ± 3.0	0.68	172	0.9	*IA*	0
412	$13^h29^m41.91^s$	47°10′30.55”	36.9	4.5	4.7	32 ± 0	7 ± 3	1.4 ± 0.4	15.4 ± 13.0	2.60	30	0.4	*IA*	1
413	$13^h29^m43.99^s$	47°10′34.75”	40.4	3.2	5.6	22 ± 11	7 ± 3	1.2 ± 0.3	10.0 ± 9.8	1.87	30	0.8	*SA*	0
414	$13^h29^m43.90^s$	47°11′3.77”	50.2	1.6	5.0	32 ± 0	2 ± 1	0.3 ± 0.1	1.5 ± 1.6	1.32	15	0.8	*SA*	1
415	$13^h29^m43.87^s$	47°11′9.28”	62.0	1.9	5.4	32 ± 0	5 ± 3	0.3 ± 0.1	9.7 ± 10.4	6.42	138	0.9	*SA*	1
416	$13^h30^m2.17^s$	47°11′35.46”	−68.8	2.6	5.6	33 ± 14	3 ± 1	1.0 ± 0.3	3.1 ± 3.3	0.69	144	0.5	*IA*	0
417	$13^h30^m1.76^s$	47°11′39.62”	−51.3	2.3	5.1	32 ± 0	4 ± 2	0.6 ± 0.3	5.0 ± 4.7	1.76	166	0.6	*SA*	1
418	$13^h30^m0.44^s$	47°11′27.67”	12.9	4.2	10.1	58 ± 11	6 ± 1	4.5 ± 0.6	20.8 ± 9.6	1.07	17	0.4	*SA*	0
419	$13^h30^m0.82^s$	47°11′38.03”	25.5	6.0	14.3	92 ± 16	8 ± 4	19.0 ± 6.3	68.0 ± 53.7	0.82	55	0.3	*SA*	0
420	$13^h30^m0.78^s$	47°11′35.03”	30.3	4.4	10.1	38 ± 34	7 ± 7	2.9 ± 6.6	16.8 ± 40.3	1.32	140	0.6	*SA*	0
421	$13^h30^m0.42^s$	47°11′13.25”	44.8	2.4	4.9	10 ± 14	2 ± 3	0.6 ± 0.7	0.5 ± 1.8	0.20	156	0.8	*SA*	0
422	$13^h30^m0.48^s$	47°11′17.92”	47.3	2.5	5.9	56 ± 43	4 ± 5	1.1 ± 2.1	7.5 ± 18.5	1.52	166	0.3	*SA*	0
423	$13^h30^m1.02^s$	47°11′18.60”	24.5	2.5	4.7	32 ± 0	2 ± 2	0.4 ± 0.2	1.6 ± 2.4	0.92	167	0.5	*SA*	1
424	$13^h30^m0.80^s$	47°11′27.98”	31.6	2.4	5.5	32 ± 0	3 ± 2	0.4 ± 0.2	3.3 ± 3.9	1.82	111	0.4	*SA*	1
425	$13^h30^m0.73^s$	47°11′22.74”	44.3	2.1	5.2	54 ± 25	7 ± 2	2.0 ± 0.9	24.1 ± 24.4	2.79	171	0.6	*SA*	0
426	$13^h30^m0.62^s$	47°11′25.54”	40.0	2.7	6.4	55 ± 13	5 ± 2	2.2 ± 0.6	14.4 ± 14.4	1.50	145	0.8	*SA*	0
427	$13^h30^m2.04^s$	47°11′38.79”	52.4	2.4	4.5	39 ± 13	7 ± 3	2.4 ± 0.5	20.2 ± 16.3	1.95	20	0.4	*IA*	0
428	$13^h30^m2.18^s$	47°11′17.27”	40.1	4.3	5.0	32 ± 0	2 ± 2	0.7 ± 0.3	1.7 ± 2.4	0.59	6	0.9	*IA*	1
429	$13^h30^m2.26^s$	47°11′41.64”	50.8	3.9	7.6	71 ± 11	4 ± 1	4.1 ± 0.6	9.5 ± 7.9	0.54	41	0.6	*IA*	0
430	$13^h30^m2.43^s$	47°11′16.32”	95.3	4.4	5.6	32 ± 0	2 ± 2	0.6 ± 0.3	1.8 ± 2.8	0.63	127	0.7	*IA*	1
431	$13^h29^m59.40^s$	47°11′33.56”	−51.7	1.7	4.6	32 ± 0	5 ± 2	0.6 ± 0.3	7.9 ± 6.9	3.02	133	0.5	*IA*	1
432	$13^h29^m59.32^s$	47°11′41.53”	−12.6	2.3	6.2	62 ± 16	11 ± 3	3.3 ± 0.7	79.8 ± 47.0	5.52	103	0.7	*IA*	0
433	$13^h29^m59.03^s$	47°11′41.31”	−12.7	2.3	5.7	45 ± 11	5 ± 1	1.6 ± 0.3	13.3 ± 7.9	1.91	49	0.8	*IA*	0
434	$13^h29^m59.63^s$	47°11′40.98”	6.2	2.6	6.4	32 ± 0	4 ± 3	0.4 ± 0.3	5.0 ± 7.7	2.59	167	0.4	*IA*	1
435	$13^h29^m59.48^s$	47°11′39.75”	10.1	1.9	4.6	17 ± 21	3 ± 3	0.5 ± 0.7	1.3 ± 3.4	0.64	160	0.8	*IA*	0
436	$13^h30^m0.24^s$	47°11′39.91”	−10.5	1.9	4.9	42 ± 16	10 ± 4	2.2 ± 0.8	42.2 ± 33.0	4.36	129	0.5	*SA*	0
437	$13^h30^m0.13^s$	47°11′38.94”	4.9	1.8	4.5	32 ± 0	2 ± 2	0.2 ± 0.3	1.3 ± 2.6	1.25	158	0.8	*SA*	1
438	$13^h30^m0.30^s$	47°11′31.09”	30.9	5.0	12.5	81 ± 16	11 ± 3	10.0 ± 1.3	97.1 ± 54.2	2.23	123	1.0	*SA*	0
439	$13^h30^m0.16^s$	47°11′38.88”	40.9	3.5	8.9	63 ± 17	11 ± 4	8.1 ± 3.7	75.1 ± 61.7	2.12	177	0.5	*SA*	0
440	$13^h30^m0.14^s$	47°11′31.06”	57.5	1.5	4.1	32 ± 0	5 ± 5	0.6 ± 0.2	6.8 ± 15.5	2.75	18	0.3	*SA*	1
441	$13^h29^m57.60^s$	47°11′27.95”	−28.5	1.7	4.6	22 ± 9	10 ± 4	1.4 ± 0.4	22.0 ± 23.0	3.64	117	0.3	*IA*	0
442	$13^h29^m58.17^s$	47°11′24.04”	−17.5	2.6	6.8	53 ± 31	5 ± 4	2.5 ± 1.7	11.5 ± 24.6	1.04	154	0.4	*IA*	0
443	$13^h29^m58.24^s$	47°11′27.14”	−20.5	3.7	9.9	56 ± 25	2 ± 1	2.5 ± 0.6	2.4 ± 2.1	0.22	123	0.5	*IA*	0
444	$13^h29^m57.93^s$	47°11′22.19”	−14.8	2.7	7.2	66 ± 62	3 ± 4	2.8 ± 3.5	7.4 ± 21.3	0.60	49	0.7	*IA*	0
445	$13^h29^m57.66^s$	47°11′21.06”	−7.4	3.2	8.6	33 ± 30	5 ± 7	1.4 ± 1.2	7.7 ± 19.9	1.25	118	0.8	*IA*	0
446	$13^h29^m57.93^s$	47°11′19.47”	−1.7	3.3	8.8	67 ± 49	9 ± 8	6.1 ± 9.8	61.5 ± 136.9	2.30	24	1.2	*IA*	0

ID (1)	**RA (J2000)** *h m s* (2)	**Dec (J2000)** *d ’ ”* (3)	$\mathbf{V_{LSR}}$ km/s (4)	$\mathbf{T_{max}}$ K (5)	**S/N** (6)	**R** pc (7)	σ_v km/s (8)	$\mathbf{L_{CO}}$ 10^5 K km/s pc^2 (9)	$\mathbf{M_{vir}}$ 10^5 $M_\odot$ (10)	α (11)	**PA** deg (12)	**b/a** (13)	**Reg** (14)	**Flag** (15)
447	$13^h29^m57.85^s$	47°11′16.81”	3.1	4.5	12.7	56 ± 23	7 ± 3	7.9 ± 4.1	25.6 ± 23.4	0.74	115	0.6	*IA*	0
448	$13^h29^m57.86^s$	47°11′16.38”	41.1	2.2	5.8	40 ± 17	6 ± 3	1.1 ± 0.4	13.1 ± 14.6	2.72	154	0.5	*IA*	0
449	$13^h29^m58.05^s$	47°11′16.19”	56.8	1.8	4.9	20 ± 17	5 ± 2	0.5 ± 0.3	4.4 ± 4.4	1.84	33	0.7	*SA*	0
450	$13^h29^m59.89^s$	47°11′19.18”	6.9	2.0	5.1	25 ± 27	6 ± 4	1.8 ± 2.3	10.2 ± 19.6	1.34	136	0.8	*SA*	0
451	$13^h29^m59.30^s$	47°11′21.34”	1.5	4.3	11.9	65 ± 14	7 ± 3	9.1 ± 2.8	34.4 ± 29.2	0.87	137	0.5	*SA*	0
452	$13^h29^m58.85^s$	47°11′15.85”	7.6	3.8	10.5	34 ± 23	6 ± 2	2.4 ± 1.5	12.0 ± 13.6	1.12	131	0.5	*SA*	0
453	$13^h30^m0.01^s$	47°11′18.30”	5.9	3.3	7.3	32 ± 0	6 ± 5	0.8 ± 0.8	12.6 ± 21.1	3.80	163	0.4	*SA*	1
454	$13^h29^m59.05^s$	47°11′18.74”	5.4	3.5	8.9	32 ± 0	2 ± 1	1.3 ± 1.5	0.8 ± 0.8	0.14	140	0.3	*SA*	1
455	$13^h30^m0.20^s$	47°11′17.88”	18.6	4.3	9.5	35 ± 13	10 ± 5	3.4 ± 2.6	39.7 ± 45.4	2.66	32	0.4	*SA*	0
456	$13^h29^m59.43^s$	47°11′22.44”	19.0	1.6	4.2	32 ± 0	4 ± 4	0.3 ± 0.4	6.3 ± 12.4	4.20	173	0.5	*SA*	1
457	$13^h29^m59.04^s$	47°11′13.70”	23.9	3.1	7.8	44 ± 35	4 ± 4	1.3 ± 1.5	5.6 ± 12.7	1.01	16	0.8	*SA*	0
458	$13^h29^m59.16^s$	47°11′15.10”	20.4	2.7	6.3	32 ± 0	4 ± 6	1.2 ± 0.6	5.4 ± 17.0	1.07	35	1.5	*SA*	1
459	$13^h29^m58.98^s$	47°11′14.69”	32.8	2.2	5.9	30 ± 35	6 ± 6	0.7 ± 0.5	12.8 ± 32.7	3.98	49	0.5	*SA*	0
460	$13^h29^m59.90^s$	47°11′12.35”	41.6	7.0	16.8	32 ± 0	6 ± 7	3.7 ± 2.0	10.2 ± 27.3	0.64	47	2.3	*SA*	1
461	$13^h29^m60.00^s$	47°11′13.71”	41.4	8.7	19.8	44 ± 24	8 ± 8	6.5 ± 11.8	32.3 ± 67.0	1.14	89	0.3	*SA*	0
462	$13^h30^m0.24^s$	47°11′17.66”	46.0	3.1	7.3	24 ± 30	3 ± 5	1.0 ± 1.5	2.8 ± 8.2	0.64	164	0.9	*SA*	0
463	$13^h29^m58.86^s$	47°11′17.36”	55.5	2.2	5.7	51 ± 21	7 ± 3	1.4 ± 0.4	26.6 ± 28.8	4.45	22	0.6	*SA*	0
464	$13^h30^m0.27^s$	47°11′12.34”	52.0	2.7	5.7	27 ± 15	8 ± 4	2.0 ± 0.8	16.5 ± 23.1	1.88	47	0.7	*SA*	0
465	$13^h29^m59.27^s$	47°11′12.71”	55.7	1.7	4.5	32 ± 0	8 ± 9	0.4 ± 0.6	22.4 ± 47.0	13.61	150	0.3	*SA*	1
466	$13^h29^m59.40^s$	47°11′14.07”	54.2	2.6	6.8	62 ± 42	5 ± 6	1.3 ± 1.8	13.1 ± 35.5	2.40	20	0.4	*SA*	0
467	$13^h29^m59.31^s$	47°11′16.43”	55.6	2.4	6.7	32 ± 0	4 ± 5	1.1 ± 1.7	4.1 ± 12.5	0.86	61	0.3	*SA*	1
468	$13^h29^m59.41^s$	47°11′18.80”	60.6	2.2	5.8	25 ± 17	5 ± 4	0.8 ± 0.5	6.4 ± 14.9	1.76	160	0.7	*SA*	0
469	$13^h29^m57.54^s$	47°11′32.82”	−12.2	4.1	10.8	62 ± 12	10 ± 4	2.3 ± 0.2	58.9 ± 56.0	5.88	107	0.5	*IA*	0
470	$13^h29^m57.83^s$	47°11′32.49”	−13.6	2.0	5.5	17 ± 8	6 ± 2	0.9 ± 0.2	6.5 ± 7.1	1.61	120	0.6	*IA*	0
471	$13^h29^m57.81^s$	47°11′34.64”	−10.1	1.4	3.6	33 ± 13	5 ± 3	1.1 ± 0.7	9.9 ± 12.1	2.04	25	0.4	*IA*	0
472	$13^h29^m59.36^s$	47°11′34.26”	−8.2	3.4	8.9	37 ± 8	7 ± 2	2.0 ± 0.3	16.3 ± 9.2	1.84	112	0.7	*IA*	0
473	$13^h29^m59.86^s$	47°11′33.15”	−7.2	1.6	4.2	42 ± 17	7 ± 2	1.2 ± 0.6	23.5 ± 17.1	4.53	112	0.8	*SA*	0
474	$13^h30^m0.01^s$	47°11′35.67”	3.0	1.3	4.3	32 ± 0	7 ± 4	0.5 ± 0.3	18.0 ± 17.3	9.03	122	0.5	*SA*	1
475	$13^h29^m59.56^s$	47°11′28.92”	4.3	2.1	5.0	32 ± 0	6 ± 2	1.2 ± 0.4	13.5 ± 8.5	2.54	164	0.4	*SA*	1
476	$13^h29^m58.00^s$	47°11′25.30”	8.1	1.8	4.6	40 ± 16	12 ± 5	2.1 ± 0.6	61.0 ± 59.3	6.71	163	0.7	*IA*	0
477	$13^h30^m0.01^s$	47°11′25.20”	12.4	2.2	5.3	50 ± 13	12 ± 2	2.1 ± 0.3	76.4 ± 38.6	8.36	151	0.3	*SA*	0
478	$13^h29^m59.35^s$	47°11′28.78”	48.2	2.1	5.7	32 ± 0	10 ± 7	1.5 ± 2.0	33.6 ± 46.3	5.01	171	0.6	*SA*	1
479	$13^h29^m59.33^s$	47°11′27.23”	51.8	2.6	7.1	32 ± 0	6 ± 5	0.6 ± 0.9	12.0 ± 20.5	4.56	156	0.7	*SA*	1
480	$13^h29^m59.27^s$	47°11′25.78”	58.2	3.4	9.2	32 ± 0	3 ± 4	0.7 ± 0.9	3.9 ± 8.5	1.23	152	0.8	*SA*	1
481	$13^h29^m58.56^s$	47°11′35.04”	55.8	2.0	6.3	32 ± 0	24 ± 6	1.3 ± 0.2	186.5 ± 88.9	32.00	126	0.7	*IA*	1
482	$13^h29^m59.53^s$	47°11′31.88”	66.8	2.4	6.6	64 ± 7	12 ± 3	4.4 ± 0.4	99.5 ± 45.2	5.16	55	0.7	*IA*	0
483	$13^h29^m59.53^s$	47°11′35.01”	50.3	1.8	5.0	32 ± 0	4 ± 6	0.4 ± 0.4	6.0 ± 17.2	3.58	169	0.5	*IA*	1
484	$13^h29^m59.73^s$	47°11′36.73”	49.2	2.4	6.4	32 ± 11	6 ± 3	1.8 ± 0.8	11.4 ± 10.8	1.46	71	0.4	*IA*	0
485	$13^h29^m59.32^s$	47°11′31.58”	45.7	1.5	4.5	32 ± 0	2 ± 2	0.4 ± 0.2	1.9 ± 2.5	1.01	12	0.6	*IA*	1
486	$13^h29^m58.23^s$	47°11′30.33”	76.3	1.5	4.4	32 ± 0	6 ± 2	0.6 ± 0.3	13.1 ± 8.9	4.70	156	0.3	*IA*	1
487	$13^h29^m59.25^s$	47°11′33.77”	81.0	1.6	4.9	50 ± 16	7 ± 2	1.1 ± 0.3	23.1 ± 21.0	4.90	2	0.6	*IA*	0
488	$13^h29^m59.75^s$	47°11′26.51”	90.1	1.6	5.0	32 ± 0	2 ± 1	0.3 ± 0.2	0.9 ± 0.6	0.61	133	0.5	*SA*	1
489	$13^h29^m55.69^s$	47°11′32.32”	−2.1	1.7	5.0	48 ± 12	7 ± 3	2.2 ± 1.0	21.9 ± 17.2	2.26	127	0.4	*CR*	0
490	$13^h29^m54.71^s$	47°11′38.24”	0.2	3.3	8.5	32 ± 0	8 ± 5	2.2 ± 2.3	21.6 ± 25.3	2.25	162	0.5	*CR*	1
491	$13^h29^m55.23^s$	47°11′40.34”	−2.7	4.9	13.2	32 ± 0	13 ± 9	2.9 ± 5.0	52.4 ± 72.0	4.12	125	0.5	*CR*	1
492	$13^h29^m54.75^s$	47°11′40.89”	−2.7	6.2	16.7	56 ± 16	6 ± 1	5.9 ± 3.3	18.0 ± 9.5	0.70	122	0.8	*CR*	0
493	$13^h29^m54.86^s$	47°11′25.92”	9.3	1.9	5.1	32 ± 0	8 ± 4	0.7 ± 0.5	19.0 ± 20.1	6.17	20	0.3	*CR*	1
494	$13^h29^m55.75^s$	47°11′33.71”	14.9	1.8	4.6	21 ± 25	3 ± 3	0.6 ± 0.5	2.1 ± 4.5	0.77	40	0.7	*CR*	0
495	$13^h29^m55.02^s$	47°11′38.20”	9.6	5.0	13.8	47 ± 47	7 ± 7	3.0 ± 3.7	26.6 ± 69.7	2.07	129	0.4	*CR*	0
496	$13^h29^m55.79^s$	47°11′39.20”	9.7	3.2	8.1	32 ± 0	6 ± 3	0.9 ± 0.5	12.8 ± 12.9	3.16	171	0.7	*CR*	1
497	$13^h29^m55.14^s$	47°11′33.76”	25.1	8.9	22.5	83 ± 33	8 ± 5	19.2 ± 25.1	50.2 ± 67.5	0.60	90	0.5	*CR*	0
498	$13^h29^m54.79^s$	47°11′35.53”	18.3	5.0	11.8	30 ± 40	5 ± 5	1.6 ± 3.4	8.9 ± 20.0	1.24	130	0.5	*CR*	0
499	$13^h29^m55.26^s$	47°11′36.32”	18.0	8.9	22.7	74 ± 31	7 ± 3	12.5 ± 4.5	38.0 ± 32.8	0.69	43	0.5	*CR*	0
500	$13^h29^m55.44^s$	47°11′39.87”	15.0	9.1	23.7	71 ± 17	10 ± 4	20.4 ± 22.7	76.0 ± 59.8	0.86	116	0.4	*CR*	0
501	$13^h29^m55.40^s$	47°11′31.59”	21.6	6.6	16.7	60 ± 24	5 ± 2	6.0 ± 4.6	17.9 ± 17.6	0.68	112	0.8	*CR*	0
502	$13^h29^m55.10^s$	47°11′29.83”	27.6	6.1	16.3	51 ± 32	6 ± 4	7.7 ± 11.8	19.9 ± 31.5	0.60	119	0.5	*CR*	0
503	$13^h29^m55.78^s$	47°11′32.32”	27.2	1.9	4.7	32 ± 0	6 ± 3	0.6 ± 0.5	10.0 ± 12.4	4.06	24	0.6	*CR*	1
504	$13^h29^m55.82^s$	47°11′35.22”	25.1	1.6	3.8	32 ± 0	4 ± 4	0.3 ± 0.2	5.1 ± 9.6	3.62	109	0.5	*CR*	1
505	$13^h29^m54.67^s$	47°11′34.94”	22.5	5.2	12.5	26 ± 23	16 ± 13	3.8 ± 6.4	74.1 ± 141.5	4.48	6	0.6	*CR*	0
506	$13^h29^m54.78^s$	47°11′31.79”	31.4	7.2	17.2	54 ± 25	5 ± 3	4.7 ± 7.0	14.9 ± 18.6	0.73	137	0.3	*CR*	0

ID	**RA (J2000)** *h m s*	**Dec (J2000)** *d ′ ″*	**V_{LSR}** km/s	**T_{max}** K	**S/N**	**R** pc	**σ_v** km/s	**L_{CO}** 10^5 K km/s pc^2	**M_{vir}** 10^5 $M_\odot$	α	**PA** deg	**b/a**	**Reg**	**Flag**
(1)	(2)	(3)	(4)	(5)	(6)	(7)	(8)	(9)	(10)	(11)	(12)	(13)	(14)	(15)
507	$13^h29^m54.88^s$	47°11′25.72”	39.7	3.4	9.2	20 ± 24	7 ± 8	1.0 ± 2.5	9.1 ± 26.9	2.05	90	0.5	*CR*	0
508	$13^h29^m54.64^s$	47°11′27.59”	42.6	6.1	15.3	52 ± 36	6 ± 4	4.8 ± 6.9	17.9 ± 15.9	0.86	150	0.6	*CR*	0
509	$13^h29^m54.61^s$	47°11′23.33”	55.2	5.6	14.4	63 ± 16	8 ± 3	6.2 ± 3.6	42.1 ± 30.2	1.56	113	0.4	*CR*	0
510	$13^h29^m54.65^s$	47°11′33.00”	64.5	3.3	8.6	40 ± 23	9 ± 7	4.7 ± 3.8	30.9 ± 50.6	1.51	107	0.5	*CR*	0
511	$13^h29^m54.72^s$	47°11′29.69”	68.0	3.4	9.1	35 ± 45	6 ± 13	1.2 ± 0.6	12.4 ± 54.0	2.35	79	0.8	*CR*	0
512	$13^h29^m54.61^s$	47°11′23.91”	79.4	2.7	7.3	42 ± 18	3 ± 2	1.3 ± 1.2	2.9 ± 4.6	0.49	65	0.9	*CR*	0
513	$13^h29^m54.67^s$	47°11′22.67”	90.9	1.4	4.2	32 ± 0	4 ± 3	0.2 ± 0.2	4.2 ± 7.8	3.91	111	0.5	*CR*	1
514	$13^h29^m57.16^s$	47°11′35.22”	−11.8	2.2	6.1	46 ± 24	13 ± 6	2.2 ± 1.4	86.4 ± 85.5	9.10	176	0.5	*IA*	0
515	$13^h29^m57.28^s$	47°11′36.90”	−3.6	2.1	6.1	31 ± 29	6 ± 7	1.1 ± 1.3	11.5 ± 37.0	2.39	111	0.6	*IA*	0
516	$13^h29^m56.93^s$	47°11′36.40”	−4.9	2.0	6.0	45 ± 19	2 ± 1	1.3 ± 0.9	1.4 ± 1.6	0.25	86	0.4	*SA*	0
517	$13^h29^m57.39^s$	47°11′37.88”	5.2	1.9	5.5	32 ± 0	2 ± 2	0.4 ± 0.2	1.0 ± 1.8	0.58	164	0.5	*IA*	1
518	$13^h29^m57.21^s$	47°11′40.61”	−5.4	2.5	6.9	71 ± 34	4 ± 3	1.8 ± 1.0	13.2 ± 18.9	1.64	164	0.6	*IA*	0
519	$13^h29^m57.32^s$	47°11′12.35”	5.8	1.8	5.0	44 ± 16	11 ± 4	3.5 ± 1.0	56.4 ± 43.8	3.75	1	0.2	*IA*	0
520	$13^h29^m55.92^s$	47°11′13.63”	0.3	1.6	4.3	32 ± 0	10 ± 4	0.8 ± 0.3	36.0 ± 28.5	10.24	120	0.5	*IA*	1
521	$13^h29^m57.10^s$	47°11′21.93”	−2.7	1.8	4.8	39 ± 21	5 ± 2	0.9 ± 0.8	9.0 ± 9.9	2.28	176	0.6	*IA*	0
522	$13^h29^m57.02^s$	47°11′19.26”	−1.3	3.2	8.8	32 ± 0	5 ± 1	2.2 ± 0.4	8.7 ± 4.2	0.91	141	0.2	*IA*	1
523	$13^h29^m56.69^s$	47°11′17.66”	7.1	2.4	6.0	80 ± 23	4 ± 2	2.5 ± 2.3	15.0 ± 14.1	1.35	103	0.4	*IA*	0
524	$13^h29^m56.25^s$	47°11′15.90”	16.2	3.8	9.5	32 ± 0	5 ± 2	3.2 ± 0.9	9.8 ± 6.9	0.71	5	0.3	*IA*	1
525	$13^h29^m56.56^s$	47°11′14.70”	18.1	2.8	7.3	48 ± 34	7 ± 3	1.6 ± 1.0	25.2 ± 39.6	3.53	134	0.6	*IA*	0
526	$13^h29^m56.13^s$	47°11′13.36”	24.9	2.0	5.0	29 ± 15	6 ± 4	2.1 ± 1.0	12.1 ± 17.0	1.32	84	0.4	*IA*	0
527	$13^h29^m56.56^s$	47°11′23.67”	−3.1	1.7	4.9	32 ± 0	4 ± 2	0.6 ± 0.2	4.3 ± 4.1	1.55	130	0.3	*IA*	1
528	$13^h29^m56.56^s$	47°11′29.05”	0.9	1.6	4.6	21 ± 22	6 ± 2	0.8 ± 0.3	7.0 ± 8.1	1.90	54	0.8	*SA*	0
529	$13^h29^m56.08^s$	47°11′23.73”	9.6	1.4	3.8	32 ± 0	5 ± 3	0.6 ± 0.5	9.9 ± 11.6	3.76	86	0.7	*SA*	1
530	$13^h29^m56.01^s$	47°11′22.43”	5.0	1.9	5.1	32 ± 0	2 ± 1	0.3 ± 0.2	1.1 ± 1.2	0.91	154	0.7	*SA*	1
531	$13^h29^m57.23^s$	47°11′29.78”	5.5	1.7	4.7	32 ± 0	4 ± 2	0.5 ± 0.2	4.1 ± 4.0	1.78	140	0.4	*IA*	1
532	$13^h29^m56.48^s$	47°11′32.02”	5.3	1.7	5.2	32 ± 0	2 ± 3	0.4 ± 0.5	2.0 ± 5.1	1.16	157	0.4	*SA*	1
533	$13^h29^m56.23^s$	47°11′30.50”	15.7	3.0	7.0	32 ± 0	4 ± 2	1.3 ± 0.7	4.1 ± 3.8	0.71	159	0.3	*SA*	1
534	$13^h29^m54.51^s$	47°11′13.66”	54.7	1.4	4.3	32 ± 0	2 ± 2	0.5 ± 0.5	1.0 ± 2.0	0.48	114	0.4	*CR*	1
535	$13^h29^m56.81^s$	47°11′39.42”	38.8	1.6	4.2	35 ± 17	6 ± 2	1.2 ± 0.4	13.2 ± 14.8	2.56	10	0.6	*SA*	0
536	$13^h29^m53.81^s$	47°11′41.22”	−15.9	3.0	8.4	27 ± 19	8 ± 5	2.2 ± 2.3	18.1 ± 33.4	1.87	130	0.5	*CR*	0
537	$13^h29^m53.96^s$	47°11′37.90”	1.8	5.1	13.4	42 ± 52	7 ± 6	2.6 ± 2.0	19.2 ± 56.4	1.70	92	0.6	*CR*	0
538	$13^h29^m53.62^s$	47°11′40.20”	−7.1	2.9	7.9	43 ± 41	6 ± 8	0.5 ± 0.4	14.9 ± 56.3	7.01	33	0.7	*CR*	0
539	$13^h29^m54.49^s$	47°11′41.76”	−5.7	4.7	12.0	42 ± 25	4 ± 4	4.3 ± 4.5	8.2 ± 15.7	0.44	64	0.8	*CR*	0
540	$13^h29^m54.16^s$	47°11′34.66”	−3.1	1.6	4.5	22 ± 25	6 ± 4	0.6 ± 0.4	8.2 ± 14.9	3.24	104	0.9	*CR*	0
541	$13^h29^m53.68^s$	47°11′38.02”	0.1	4.0	10.3	62 ± 37	10 ± 5	3.2 ± 1.8	59.5 ± 83.5	4.33	130	0.9	*CR*	0
542	$13^h29^m54.23^s$	47°11′40.59”	−3.0	4.6	12.1	37 ± 23	8 ± 6	4.6 ± 5.3	25.7 ± 39.2	1.29	144	0.3	*CR*	0
543	$13^h29^m53.43^s$	47°11′38.15”	3.8	3.8	9.3	32 ± 0	3 ± 5	2.0 ± 0.9	4.0 ± 11.7	0.45	50	0.4	*CR*	1
544	$13^h29^m53.41^s$	47°11′30.27”	8.9	1.7	4.8	32 ± 0	5 ± 3	0.5 ± 0.3	7.9 ± 9.6	3.62	27	0.6	*CR*	1
545	$13^h29^m54.41^s$	47°11′39.89”	4.7	4.5	11.9	32 ± 19	2 ± 1	1.8 ± 2.0	0.9 ± 1.2	0.11	133	0.5	*CR*	0
546	$13^h29^m52.95^s$	47°11′40.15”	11.4	2.3	5.3	32 ± 0	14 ± 7	1.3 ± 0.4	66.0 ± 61.1	11.56	171	0.5	*CR*	1
547	$13^h29^m53.73^s$	47°11′35.42”	18.6	4.9	11.0	45 ± 43	11 ± 12	3.3 ± 8.1	60.6 ± 142.2	4.23	7	0.4	*CR*	0
548	$13^h29^m54.38^s$	47°11′36.02”	13.8	5.0	12.0	83 ± 20	10 ± 4	7.6 ± 2.6	88.0 ± 84.3	2.65	145	0.4	*CR*	0
549	$13^h29^m52.25^s$	47°11′39.74”	19.1	2.1	5.4	32 ± 0	4 ± 3	0.6 ± 0.3	5.2 ± 7.1	2.17	135	0.7	*CR*	1
550	$13^h29^m54.46^s$	47°11′32.06”	27.3	5.2	12.4	85 ± 43	7 ± 4	8.0 ± 4.2	47.5 ± 69.3	1.36	174	1.1	*CR*	0
551	$13^h29^m53.89^s$	47°11′35.00”	17.4	5.9	12.4	62 ± 49	5 ± 7	3.1 ± 1.5	14.7 ± 43.0	1.07	108	0.9	*CR*	0
552	$13^h29^m53.22^s$	47°11′36.46”	19.7	5.5	12.4	68 ± 22	12 ± 4	8.7 ± 3.9	97.0 ± 88.3	2.54	116	0.7	*CR*	0
553	$13^h29^m52.14^s$	47°11′37.97”	29.5	2.2	4.8	32 ± 0	6 ± 4	1.0 ± 1.0	10.4 ± 13.6	2.38	23	0.6	*CR*	1
554	$13^h29^m52.04^s$	47°11′41.72”	29.7	4.0	9.6	31 ± 27	13 ± 9	3.6 ± 7.2	52.9 ± 94.6	3.40	20	0.3	*CR*	0
555	$13^h29^m51.58^s$	47°11′35.91”	35.0	4.7	10.1	52 ± 27	2 ± 1	3.4 ± 2.3	1.7 ± 2.4	0.11	112	0.5	*CR*	0
556	$13^h29^m53.01^s$	47°11′38.29”	28.3	2.0	4.9	43 ± 40	12 ± 10	1.5 ± 1.3	64.5 ± 142.3	10.00	141	0.7	*CR*	0
557	$13^h29^m53.91^s$	47°11′21.51”	34.9	1.8	3.9	32 ± 0	3 ± 4	0.3 ± 0.2	3.7 ± 8.7	2.57	160	0.5	*CR*	1
558	$13^h29^m54.25^s$	47°11′28.53”	39.6	7.3	17.6	75 ± 26	5 ± 4	7.5 ± 7.0	20.0 ± 31.8	0.62	16	0.2	*CR*	0
559	$13^h29^m54.11^s$	47°11′31.55”	35.7	6.6	15.7	86 ± 56	6 ± 6	9.9 ± 15.6	34.3 ± 71.8	0.80	149	0.3	*CR*	0
560	$13^h29^m53.61^s$	47°11′32.45”	37.8	6.4	15.2	66 ± 29	7 ± 5	5.4 ± 5.4	30.0 ± 50.5	1.28	4	0.2	*CR*	0
561	$13^h29^m52.20^s$	47°11′40.07”	36.0	3.5	8.7	51 ± 28	6 ± 6	2.8 ± 4.7	19.7 ± 40.6	1.63	99	0.4	*CR*	0
562	$13^h29^m51.96^s$	47°11′39.37”	37.5	2.9	6.6	68 ± 44	9 ± 9	3.5 ± 5.4	62.8 ± 159.3	4.14	5	0.6	*CR*	0
563	$13^h29^m51.73^s$	47°11′34.32”	42.2	5.1	12.0	65 ± 52	5 ± 7	2.1 ± 1.2	15.4 ± 42.0	1.68	51	0.9	*CR*	0
564	$13^h29^m51.64^s$	47°11′31.22”	49.6	2.9	6.6	32 ± 0	3 ± 5	0.8 ± 0.4	2.5 ± 8.4	0.75	162	0.6	*CR*	1
565	$13^h29^m53.02^s$	47°11′33.00”	47.5	4.8	12.2	63 ± 56	2 ± 0	2.5 ± 7.3	3.0 ± 2.6	0.28	153	0.6	*CR*	1
566	$13^h29^m51.90^s$	47°11′32.25”	51.5	4.3	10.8	54 ± 81	5 ± 5	2.6 ± 2.8	17.0 ± 56.2	1.51	64	0.5	*CR*	0

ID (1)	**RA (J2000)** *h m s* (2)	**Dec (J2000)** *d ’ ”* (3)	**V$_{\mathrm{LSR}}$** km/s (4)	**T$_{\mathrm{max}}$** K (5)	**S/N** (6)	**R** pc (7)	σ_{v} km/s (8)	**L$_{\mathrm{CO}}$** 10^5 K km/s pc^2 (9)	**M$_{\mathrm{vir}}$** 10^5 M$_\odot$ (10)	α (11)	**PA** deg (12)	**b/a** (13)	**Reg** (14)	**Flag** (15)
567	$13^h29^m52.59^s$	47°11′34.18”	50.2	4.8	10.2	35 ± 16	3 ± 2	2.5 ± 2.2	2.7 ± 5.1	0.24	30	0.4	*CR*	0
568	$13^h29^m52.39^s$	47°11′37.00”	44.8	4.1	10.4	82 ± 53	2 ± 2	4.6 ± 5.9	4.0 ± 8.7	0.20	49	0.8	*CR*	0
569	$13^h29^m51.86^s$	47°11′37.01”	47.6	6.0	14.8	65 ± 21	7 ± 2	8.6 ± 6.2	32.2 ± 23.8	0.86	167	1.4	*CR*	0
570	$13^h29^m54.12^s$	47°11′17.64”	51.3	1.7	5.0	32 ± 0	7 ± 8	0.8 ± 1.2	17.3 ± 38.3	4.96	26	0.9	*CR*	1
571	$13^h29^m54.22^s$	47°11′22.26”	52.1	8.5	21.2	64 ± 20	8 ± 4	10.4 ± 8.9	42.6 ± 49.0	0.94	158	0.6	*CR*	0
572	$13^h29^m54.07^s$	47°11′25.84”	50.0	7.3	18.8	134 ± 33	10 ± 3	31.1 ± 15.2	135.2 ± 65.2	1.00	166	0.7	*CR*	0
573	$13^h29^m53.60^s$	47°11′26.08”	53.0	6.1	17.2	25 ± 38	18 ± 13	0.9 ± 1.6	82.2 ± 154.8	19.97	172	0.6	*CR*	0
574	$13^h29^m51.90^s$	47°11′27.44”	53.7	3.7	9.2	37 ± 28	6 ± 3	2.9 ± 1.9	14.3 ± 19.0	1.12	123	0.8	*CR*	0
575	$13^h29^m53.05^s$	47°11′27.98”	52.5	7.4	17.2	57 ± 35	2 ± 0	2.2 ± 1.3	2.7 ± 1.7	0.27	14	0.6	*CR*	1
576	$13^h29^m53.71^s$	47°11′28.54”	49.9	4.9	11.8	40 ± 28	6 ± 6	2.1 ± 3.2	16.5 ± 29.2	1.78	61	0.4	*CR*	0
577	$13^h29^m53.44^s$	47°11′29.96”	50.6	5.3	14.1	61 ± 21	7 ± 5	5.6 ± 6.2	32.4 ± 43.6	1.32	177	0.3	*CR*	0
578	$13^h29^m53.21^s$	47°11′32.45”	49.6	5.5	12.9	47 ± 29	2 ± 4	4.5 ± 8.2	2.3 ± 6.6	0.12	22	0.8	*CR*	0
579	$13^h29^m52.16^s$	47°11′34.88”	50.7	4.4	11.4	32 ± 0	2 ± 2	1.7 ± 3.6	1.0 ± 2.8	0.13	142	0.3	*CR*	1
580	$13^h29^m51.62^s$	47°11′14.86”	55.5	1.9	4.9	40 ± 28	4 ± 3	0.9 ± 1.1	5.9 ± 13.2	1.57	98	0.4	*CR*	0
581	$13^h29^m53.23^s$	47°11′21.59”	59.3	5.3	15.7	32 ± 0	8 ± 6	2.8 ± 5.7	22.1 ± 33.9	1.78	166	0.4	*CR*	1
582	$13^h29^m51.95^s$	47°11′24.57”	58.4	5.3	11.9	22 ± 23	10 ± 9	4.8 ± 7.6	21.3 ± 44.0	1.01	176	0.4	*CR*	0
583	$13^h29^m52.12^s$	47°11′25.61”	60.1	5.2	12.9	78 ± 22	3 ± 3	7.7 ± 6.0	6.7 ± 12.8	0.20	35	0.3	*CR*	0
584	$13^h29^m53.37^s$	47°11′26.33”	55.0	7.2	17.3	68 ± 50	3 ± 5	2.0 ± 2.5	7.9 ± 24.4	0.92	11	0.9	*CR*	0
585	$13^h29^m52.66^s$	47°11′29.47”	57.3	6.5	15.0	44 ± 31	4 ± 5	1.5 ± 3.7	6.1 ± 14.5	0.94	166	0.6	*CR*	0
586	$13^h29^m52.11^s$	47°11′29.67”	58.1	6.3	15.7	32 ± 0	6 ± 4	4.7 ± 3.1	13.3 ± 17.3	0.65	13	0.2	*CR*	1
587	$13^h29^m54.26^s$	47°11′30.65”	56.6	1.5	4.1	32 ± 0	5 ± 4	0.3 ± 0.3	7.3 ± 13.1	6.43	135	0.3	*CR*	1
588	$13^h29^m52.35^s$	47°11′31.80”	54.3	4.8	11.4	85 ± 30	5 ± 3	5.3 ± 1.4	20.7 ± 24.7	0.90	148	1.0	*CR*	0
589	$13^h29^m52.74^s$	47°11′32.22”	57.5	2.7	6.3	48 ± 50	5 ± 5	1.3 ± 2.5	14.6 ± 29.2	2.56	16	0.4	*CR*	0
590	$13^h29^m53.29^s$	47°11′16.20”	59.1	1.5	4.0	19 ± 20	5 ± 2	0.5 ± 0.4	4.4 ± 7.5	1.89	5	0.7	*CR*	0
591	$13^h29^m51.62^s$	47°11′18.91”	62.3	3.3	8.0	50 ± 55	6 ± 5	4.3 ± 8.2	16.4 ± 30.2	0.87	40	1.1	*CR*	0
592	$13^h29^m54.11^s$	47°11′19.99”	61.4	5.5	14.7	57 ± 40	16 ± 13	6.0 ± 20.5	143.0 ± 247.8	5.44	102	0.2	*CR*	0
593	$13^h29^m53.01^s$	47°11′21.37”	68.3	6.5	18.7	92 ± 31	9 ± 3	13.8 ± 8.7	70.2 ± 52.2	1.17	27	0.6	*CR*	0
594	$13^h29^m53.53^s$	47°11′23.92”	61.5	8.7	23.1	83 ± 35	7 ± 3	10.4 ± 12.5	38.1 ± 42.1	0.84	63	0.8	*CR*	0
595	$13^h29^m53.21^s$	47°11′24.08”	64.8	7.2	17.5	32 ± 0	6 ± 7	6.9 ± 11.5	10.3 ± 25.6	0.34	6	0.2	*CR*	1
596	$13^h29^m52.51^s$	47°11′26.48”	64.4	6.9	18.0	115 ± 61	7 ± 6	8.0 ± 13.9	60.6 ± 115.5	1.75	36	0.5	*CR*	0
597	$13^h29^m52.28^s$	47°11′12.68”	69.6	2.4	6.7	37 ± 13	3 ± 2	1.4 ± 0.6	4.2 ± 4.6	0.69	115	0.7	*CR*	0
598	$13^h29^m52.47^s$	47°11′15.24”	66.7	3.2	9.2	59 ± 72	11 ± 15	0.5 ± 1.0	67.9 ± 178.2	29.93	51	0.5	*CR*	0
599	$13^h29^m52.30^s$	47°11′17.05”	69.0	3.6	9.4	32 ± 0	5 ± 10	3.4 ± 6.8	9.1 ± 35.8	0.61	67	5.6	*CR*	1
600	$13^h29^m52.61^s$	47°11′22.11”	67.3	6.4	17.6	104 ± 45	5 ± 5	6.6 ± 8.8	27.4 ± 55.7	0.95	68	0.3	*CR*	0
601	$13^h29^m52.07^s$	47°11′22.35”	67.2	5.0	12.3	46 ± 34	9 ± 5	5.3 ± 5.9	38.3 ± 44.3	1.67	65	0.7	*CR*	0
602	$13^h29^m51.73^s$	47°11′23.47”	61.3	4.7	11.1	52 ± 94	5 ± 10	1.8 ± 3.5	13.5 ± 62.5	1.68	117	1.0	*CR*	0
603	$13^h29^m52.87^s$	47°11′23.70”	68.4	5.3	15.4	57 ± 53	10 ± 9	4.3 ± 9.6	61.9 ± 129.1	3.28	174	0.4	*CR*	0
604	$13^h29^m53.81^s$	47°11′30.96”	69.0	1.5	3.7	36 ± 13	5 ± 3	1.1 ± 0.9	7.9 ± 11.7	1.64	61	0.4	*CR*	0
605	$13^h29^m52.30^s$	47°11′33.49”	85.7	1.4	4.3	32 ± 0	8 ± 5	0.9 ± 0.4	19.6 ± 26.4	5.10	164	0.3	*CR*	1
606	$13^h29^m52.03^s$	47°11′18.33”	68.6	4.8	12.5	36 ± 16	5 ± 2	3.3 ± 2.3	9.4 ± 11.8	0.65	174	3.4	*CR*	0
607	$13^h29^m51.86^s$	47°11′20.61”	74.0	5.2	11.4	67 ± 40	9 ± 7	6.6 ± 7.3	54.5 ± 73.3	1.91	78	0.5	*CR*	0
608	$13^h29^m52.34^s$	47°11′22.83”	68.8	4.6	13.3	37 ± 29	4 ± 6	2.6 ± 1.6	5.2 ± 15.9	0.45	95	0.6	*CR*	0
609	$13^h29^m52.11^s$	47°11′33.78”	77.0	1.9	4.5	32 ± 0	3 ± 3	0.3 ± 0.1	3.7 ± 7.6	3.29	3	0.6	*CR*	1
610	$13^h29^m53.84^s$	47°11′23.32”	79.6	1.4	4.4	32 ± 0	5 ± 4	0.3 ± 0.3	7.7 ± 14.1	5.25	130	0.5	*CR*	1
611	$13^h29^m54.45^s$	47°11′28.59”	78.0	1.7	4.7	32 ± 0	5 ± 4	1.7 ± 1.4	9.3 ± 13.6	1.22	158	2.0	*CR*	1
612	$13^h29^m53.33^s$	47°11′22.13”	89.8	1.9	6.7	16 ± 26	3 ± 3	0.3 ± 0.3	1.2 ± 2.9	0.82	89	0.9	*CR*	0
613	$13^h29^m53.49^s$	47°11′23.86”	94.9	1.5	5.1	32 ± 0	2 ± 1	0.2 ± 0.1	1.2 ± 1.9	1.23	124	0.7	*CR*	1
614	$13^h29^m54.50^s$	47°11′27.67”	95.2	1.2	4.2	32 ± 0	8 ± 9	0.2 ± 0.4	23.8 ± 51.4	23.39	105	0.7	*CR*	1
615	$13^h29^m52.69^s$	47°11′27.69”	−82.5	1.8	5.0	32 ± 0	4 ± 2	0.8 ± 0.3	4.4 ± 3.9	1.34	179	0.2	*CR*	1
616	$13^h29^m53.36^s$	47°11′20.97”	−74.6	1.2	3.9	32 ± 0	8 ± 3	0.6 ± 0.4	18.8 ± 17.1	7.17	51	0.6	*CR*	1
617	$13^h29^m53.49^s$	47°11′21.23”	−57.9	1.8	5.4	32 ± 0	6 ± 3	0.4 ± 0.1	10.9 ± 10.8	6.80	49	0.7	*CR*	1
618	$13^h29^m53.60^s$	47°11′23.81”	−62.6	1.8	5.5	32 ± 0	6 ± 3	0.6 ± 0.2	12.5 ± 14.2	4.64	21	0.4	*CR*	1
619	$13^h29^m54.31^s$	47°11′14.50”	42.9	2.0	5.1	34 ± 21	7 ± 4	1.2 ± 0.6	17.8 ± 32.6	3.27	123	0.8	*CR*	0
620	$13^h29^m53.68^s$	47°11′12.27”	68.6	3.5	9.4	53 ± 30	5 ± 3	4.7 ± 2.0	16.6 ± 22.7	0.81	86	0.6	*CR*	0
621	$13^h29^m53.72^s$	47°11′15.37”	68.3	1.8	4.8	35 ± 22	9 ± 7	1.3 ± 1.5	28.5 ± 40.6	4.95	19	1.0	*CR*	0
622	$13^h29^m54.47^s$	47°11′13.31”	40.6	2.4	6.7	32 ± 0	3 ± 3	0.3 ± 0.1	2.7 ± 4.9	2.46	157	0.8	*CR*	1
623	$13^h29^m54.20^s$	47°11′17.39”	98.5	1.7	6.3	32 ± 0	6 ± 3	0.5 ± 0.1	11.9 ± 12.5	5.78	100	0.5	*CR*	1
624	$13^h29^m50.13^s$	47°11′40.57”	−6.5	11.3	27.0	49 ± 23	11 ± 6	14.4 ± 18.0	65.5 ± 76.7	1.04	165	0.8	*CR*	0
625	$13^h29^m49.50^s$	47°11′33.67”	−7.0	1.6	4.0	32 ± 0	4 ± 3	0.7 ± 0.4	5.6 ± 7.1	1.98	39	0.4	*SA*	1
626	$13^h29^m49.35^s$	47°11′20.20”	−1.3	2.1	6.1	32 ± 0	6 ± 3	1.0 ± 0.4	10.1 ± 10.0	2.42	128	0.6	*SA*	1

ID (1)	**RA (J2000)** *h m s* (2)	**Dec (J2000)** *d ’ ”* (3)	**V$_{\mathrm{LSR}}$** km/s (4)	**T$_{\mathrm{max}}$** K (5)	**S/N** (6)	**R** pc (7)	**σ_{v}** km/s (8)	**L$_{\mathrm{CO}}$** 10^5 K km/s pc^2 (9)	**M$_{\mathrm{vir}}$** 10^5 M$_\odot$ (10)	**α** (11)	**PA** deg (12)	**b/a** (13)	**Reg** (14)	**Flag** (15)
627	$13^h29^m49.13^s$	47°11′37.03”	−1.8	2.5	6.5	44 ± 18	10 ± 3	2.2 ± 1.4	45.3 ± 35.1	4.76	153	0.4	*SA*	0
628	$13^h29^m51.12^s$	47°11′12.36”	5.0	1.5	3.7	32 ± 0	4 ± 4	0.3 ± 0.3	5.3 ± 11.2	4.40	109	0.7	*SA*	1
629	$13^h29^m50.76^s$	47°11′13.13”	2.1	1.7	4.7	32 ± 0	5 ± 2	0.5 ± 0.4	8.2 ± 7.3	3.73	113	0.6	*SA*	1
630	$13^h29^m49.96^s$	47°11′30.97”	4.5	12.0	31.9	93 ± 12	10 ± 2	42.7 ± 10.2	96.0 ± 41.7	0.52	89	0.5	*CR*	0
631	$13^h29^m50.05^s$	47°11′23.80”	6.3	8.3	21.2	54 ± 45	15 ± 13	8.1 ± 25.9	119.0 ± 282.9	3.39	134	0.8	*CR*	0
632	$13^h29^m50.28^s$	47°11′30.27”	11.5	6.4	13.8	62 ± 43	11 ± 13	2.1 ± 2.4	77.4 ± 201.9	8.60	163	0.9	*CR*	0
633	$13^h29^m50.16^s$	47°11′37.04”	6.6	8.7	22.3	60 ± 27	7 ± 5	10.8 ± 14.0	34.3 ± 47.6	0.73	108	0.3	*CR*	0
634	$13^h29^m49.57^s$	47°11′39.99”	9.2	4.5	11.2	21 ± 14	7 ± 2	2.9 ± 1.1	9.9 ± 9.8	0.80	139	0.7	*CR*	0
635	$13^h29^m49.72^s$	47°11′34.50”	7.4	2.9	7.4	41 ± 28	3 ± 5	1.1 ± 1.5	5.1 ± 15.7	1.03	101	0.6	*CR*	0
636	$13^h29^m51.09^s$	47°11′40.08”	14.4	2.2	5.1	32 ± 0	3 ± 3	0.3 ± 0.3	4.0 ± 5.9	3.08	179	0.6	*CR*	1
637	$13^h29^m50.60^s$	47°11′41.94”	13.4	6.1	13.4	56 ± 50	8 ± 7	3.9 ± 7.0	38.2 ± 60.2	2.22	27	1.2	*CR*	0
638	$13^h29^m49.65^s$	47°11′36.33”	12.9	5.2	11.7	86 ± 18	13 ± 3	11.7 ± 4.1	149.7 ± 94.8	2.94	146	0.5	*CR*	0
639	$13^h29^m49.05^s$	47°11′37.17”	20.7	3.5	8.2	32 ± 0	3 ± 2	3.0 ± 1.9	4.0 ± 4.6	0.31	148	0.2	*SA*	1
640	$13^h29^m51.32^s$	47°11′40.19”	20.3	6.4	15.5	51 ± 25	7 ± 3	10.6 ± 5.5	25.7 ± 20.4	0.56	108	0.4	*CR*	0
641	$13^h29^m51.25^s$	47°11′13.51”	23.1	2.2	5.6	32 ± 0	5 ± 4	0.5 ± 0.2	7.8 ± 12.6	3.68	59	0.6	*CR*	1
642	$13^h29^m50.54^s$	47°11′15.54”	28.6	6.6	15.7	46 ± 32	14 ± 6	11.2 ± 5.8	88.5 ± 90.9	1.82	43	1.5	*SA*	0
643	$13^h29^m50.34^s$	47°11′19.38”	23.4	8.8	21.8	68 ± 22	13 ± 4	17.8 ± 17.7	114.3 ± 78.5	1.48	78	0.6	*SA*	0
644	$13^h29^m50.50^s$	47°11′23.06”	36.3	5.7	14.4	53 ± 43	31 ± 24	7.0 ± 3.3	527.5 ± 950.1	17.24	92	0.6	*CR*	0
645	$13^h29^m50.24^s$	47°11′23.33”	21.4	10.5	25.9	44 ± 31	11 ± 6	12.4 ± 21.1	60.4 ± 66.7	1.12	164	1.0	*CR*	0
646	$13^h29^m50.08^s$	47°11′25.50”	23.2	11.1	28.6	71 ± 22	14 ± 6	15.3 ± 19.3	136.3 ± 99.3	2.04	10	0.6	*CR*	0
647	$13^h29^m50.10^s$	47°11′34.26”	11.3	8.3	20.1	71 ± 44	24 ± 10	17.0 ± 25.2	431.2 ± 550.8	5.83	68	0.5	*CR*	0
648	$13^h29^m51.06^s$	47°11′38.00”	23.3	4.8	11.2	100 ± 34	6 ± 4	7.9 ± 7.2	39.3 ± 49.6	1.14	8	0.5	*CR*	0
649	$13^h29^m50.49^s$	47°11′37.61”	25.9	7.9	18.4	94 ± 32	10 ± 3	23.6 ± 21.8	91.4 ± 74.6	0.89	126	0.3	*CR*	0
650	$13^h29^m50.61^s$	47°11′20.97”	27.5	4.7	12.1	91 ± 45	26 ± 20	4.3 ± 7.3	651.7 ± 1090.1	34.95	98	0.3	*CR*	0
651	$13^h29^m49.51^s$	47°11′20.98”	27.6	2.1	5.1	32 ± 0	10 ± 8	5.1 ± 5.0	33.0 ± 49.7	1.49	107	0.2	*SA*	1
652	$13^h29^m49.99^s$	47°11′21.09”	30.6	7.4	17.9	54 ± 34	8 ± 5	9.0 ± 15.3	38.1 ± 55.5	0.97	18	0.3	*SA*	0
653	$13^h29^m50.39^s$	47°11′27.19”	36.6	8.1	20.2	104 ± 38	11 ± 6	17.3 ± 6.3	131.6 ± 158.9	1.74	41	1.4	*CR*	0
654	$13^h29^m51.33^s$	47°11′32.97”	35.0	4.8	10.8	81 ± 39	7 ± 3	10.3 ± 11.9	40.6 ± 45.2	0.91	61	0.8	*CR*	0
655	$13^h29^m49.22^s$	47°11′35.04”	27.9	1.9	4.4	32 ± 0	6 ± 3	1.0 ± 1.1	10.2 ± 12.6	2.37	11	0.6	*SA*	1
656	$13^h29^m50.86^s$	47°11′27.70”	41.8	3.3	8.0	36 ± 21	5 ± 3	1.2 ± 0.8	7.6 ± 11.2	1.47	102	0.5	*CR*	0
657	$13^h29^m50.34^s$	47°11′30.77”	34.9	7.3	15.6	61 ± 41	17 ± 14	10.9 ± 7.8	185.1 ± 370.0	3.88	95	0.3	*CR*	0
658	$13^h29^m50.95^s$	47°11′33.95”	36.2	5.8	13.8	64 ± 39	12 ± 8	6.2 ± 6.3	98.6 ± 152.5	3.64	42	0.2	*CR*	0
659	$13^h29^m50.60^s$	47°11′13.17”	40.7	7.2	17.5	86 ± 65	6 ± 6	7.2 ± 14.4	27.5 ± 45.8	0.88	72	0.3	*SA*	0
660	$13^h29^m51.14^s$	47°11′14.63”	39.4	2.9	7.3	70 ± 48	4 ± 7	3.1 ± 3.1	11.4 ± 40.6	0.86	57	1.0	*CR*	0
661	$13^h29^m50.75^s$	47°11′32.34”	40.5	5.6	12.8	32 ± 0	4 ± 5	1.2 ± 0.9	6.0 ± 15.3	1.13	94	0.1	*CR*	1
662	$13^h29^m50.27^s$	47°11′12.69”	56.3	1.6	4.2	79 ± 33	6 ± 4	1.4 ± 1.5	34.0 ± 45.2	5.53	151	0.6	*SA*	0
663	$13^h29^m50.12^s$	47°11′18.35”	44.9	3.3	8.6	45 ± 40	2 ± 1	1.2 ± 0.6	1.5 ± 2.7	0.27	3	0.9	*SA*	0
664	$13^h29^m49.67^s$	47°11′19.13”	47.9	2.2	5.6	33 ± 23	2 ± 5	0.7 ± 1.2	1.9 ± 8.6	0.67	147	0.6	*SA*	0
665	$13^h29^m51.26^s$	47°11′19.62”	45.5	1.8	4.5	37 ± 21	11 ± 6	1.4 ± 1.4	48.7 ± 62.2	7.73	173	0.4	*CR*	0
666	$13^h29^m50.82^s$	47°11′18.96”	46.9	4.9	11.5	53 ± 34	11 ± 14	4.1 ± 1.5	68.2 ± 184.8	3.86	1	0.5	*CR*	0
667	$13^h29^m50.79^s$	47°11′21.13”	48.0	4.8	12.2	32 ± 0	14 ± 10	6.2 ± 10.3	61.2 ± 92.0	2.25	68	0.2	*CR*	1
668	$13^h29^m51.39^s$	47°11′27.58”	50.3	5.5	13.2	43 ± 16	8 ± 1	6.6 ± 1.6	28.4 ± 11.7	0.99	99	0.5	*CR*	0
669	$13^h29^m51.02^s$	47°11′31.05”	50.0	4.1	10.4	34 ± 42	2 ± 2	1.8 ± 2.3	1.8 ± 4.9	0.23	57	1.1	*CR*	0
670	$13^h29^m49.22^s$	47°11′32.61”	45.7	1.6	3.9	32 ± 0	4 ± 4	0.3 ± 0.4	4.1 ± 8.5	2.96	20	0.6	*SA*	1
671	$13^h29^m51.17^s$	47°11′16.85”	54.7	3.3	8.6	91 ± 43	8 ± 7	6.5 ± 8.2	57.6 ± 104.5	2.05	170	1.1	*CR*	0
672	$13^h29^m51.03^s$	47°11′26.06”	56.2	6.2	14.7	70 ± 27	8 ± 3	8.0 ± 4.1	43.2 ± 36.5	1.25	76	0.5	*CR*	0
673	$13^h29^m51.28^s$	47°11′35.17”	60.2	2.7	6.5	32 ± 0	7 ± 4	2.5 ± 1.6	18.0 ± 21.3	1.67	165	0.3	*CR*	1
674	$13^h29^m51.32^s$	47°11′14.04”	72.6	1.7	5.2	32 ± 0	8 ± 6	0.9 ± 0.8	21.5 ± 31.6	5.31	92	0.4	*CR*	1
675	$13^h29^m51.21^s$	47°11′23.03”	68.0	3.4	8.6	66 ± 64	9 ± 11	7.1 ± 7.8	51.9 ± 136.4	1.67	67	0.8	*CR*	0
676	$13^h29^m49.79^s$	47°11′41.80”	−90.0	1.6	4.9	32 ± 0	2 ± 1	0.3 ± 0.1	1.1 ± 1.1	0.96	24	0.8	*CR*	1
677	$13^h29^m49.75^s$	47°11′13.74”	−5.5	1.8	5.1	32 ± 0	8 ± 3	0.5 ± 0.2	18.6 ± 15.1	8.85	129	0.5	*SA*	1
678	$13^h29^m48.63^s$	47°11′20.65”	35.6	1.9	4.4	24 ± 31	6 ± 5	0.5 ± 0.4	10.0 ± 21.2	4.55	165	0.9	*IA*	0
679	$13^h29^m48.94^s$	47°11′13.67”	41.9	3.2	7.5	46 ± 29	6 ± 3	2.4 ± 1.5	19.4 ± 25.3	1.88	128	0.6	*SA*	0
680	$13^h29^m48.68^s$	47°11′13.61”	42.3	2.5	6.7	39 ± 33	9 ± 8	1.5 ± 1.8	29.5 ± 67.0	4.63	17	0.5	*IA*	0
681	$13^h29^m48.87^s$	47°11′12.06”	61.9	1.7	4.7	24 ± 15	7 ± 3	1.2 ± 0.5	11.6 ± 12.9	2.21	90	0.7	*IA*	0
682	$13^h29^m49.44^s$	47°11′27.41”	9.3	1.9	4.9	31 ± 10	10 ± 4	1.5 ± 0.3	30.0 ± 30.8	4.58	177	0.8	*SA*	0
683	$13^h29^m49.04^s$	47°11′30.08”	25.0	1.8	4.3	32 ± 0	7 ± 4	1.7 ± 0.6	15.6 ± 18.7	2.13	148	0.3	*SA*	1
684	$13^h29^m49.02^s$	47°11′27.35”	34.4	2.5	6.1	52 ± 12	7 ± 3	3.5 ± 0.8	24.6 ± 22.3	1.62	21	0.7	*SA*	0
685	$13^h29^m48.97^s$	47°11′29.30”	46.4	1.7	4.2	32 ± 0	6 ± 7	0.3 ± 0.3	12.3 ± 28.4	9.62	162	0.9	*SA*	1
686	$13^h29^m48.73^s$	47°11′29.11”	48.8	1.8	4.6	24 ± 11	7 ± 3	0.7 ± 0.3	12.9 ± 14.2	4.03	150	0.7	*SA*	0

ID (1)	RA (J2000) *h m s* (2)	Dec (J2000) *d ′ ”* (3)	V_{LSR} km/s (4)	T_{max} K (5)	S/N (6)	R pc (7)	σ_v km/s (8)	L_{CO} 10^5 K km/s pc^2 (9)	M_{vir} 10^5 $M_\odot$ (10)	α (11)	PA deg (12)	b/a (13)	Reg (14)	Flag (15)
687	$13^h29^m49.08^s$	47°11′25.92”	85.1	1.6	4.5	32 ± 0	6 ± 3	0.4 ± 0.2	11.8 ± 10.1	7.19	153	0.5	*SA*	1
688	$13^h29^m48.89^s$	47°11′39.94”	86.4	1.8	5.5	43 ± 12	6 ± 3	1.0 ± 0.2	18.3 ± 19.8	4.42	103	0.8	*SA*	0
689	$13^h29^m49.69^s$	47°11′25.63”	96.4	1.8	5.9	32 ± 0	6 ± 3	0.9 ± 0.3	12.6 ± 10.4	3.39	122	0.4	*SA*	1
690	$13^h29^m51.21^s$	47°11′19.63”	109.2	1.2	4.4	32 ± 0	3 ± 2	0.2 ± 0.1	2.8 ± 3.5	2.70	72	0.5	*CR*	1
691	$13^h29^m48.04^s$	47°11′41.08”	−7.4	2.8	7.0	79 ± 28	5 ± 3	3.1 ± 1.5	18.6 ± 30.0	1.39	96	0.4	*IA*	0
692	$13^h29^m47.78^s$	47°11′37.05”	−4.9	4.6	12.0	49 ± 13	5 ± 2	4.8 ± 0.9	14.7 ± 9.3	0.71	121	0.5	*IA*	0
693	$13^h29^m47.60^s$	47°11′33.39”	1.2	2.1	5.5	56 ± 38	5 ± 4	2.0 ± 2.4	17.0 ± 31.3	1.94	113	0.4	*IA*	0
694	$13^h29^m47.49^s$	47°11′36.24”	2.5	2.5	6.1	62 ± 31	5 ± 3	3.2 ± 2.9	17.8 ± 23.2	1.27	114	0.6	*IA*	0
695	$13^h29^m47.44^s$	47°11′31.69”	5.3	2.2	5.5	29 ± 22	4 ± 5	1.1 ± 1.4	5.3 ± 10.7	1.08	159	0.6	*IA*	0
696	$13^h29^m46.56^s$	47°11′38.13”	−0.7	2.6	6.4	52 ± 14	6 ± 2	3.2 ± 1.1	17.8 ± 13.5	1.26	116	0.7	*IA*	0
697	$13^h29^m45.86^s$	47°11′30.54”	4.6	3.9	10.1	92 ± 38	2 ± 1	5.4 ± 4.4	4.0 ± 5.4	0.17	129	0.3	*IA*	0
698	$13^h29^m46.10^s$	47°11′36.28”	−1.8	1.8	4.5	53 ± 30	4 ± 5	2.2 ± 1.7	10.9 ± 25.6	1.14	65	0.9	*IA*	0
699	$13^h29^m46.81^s$	47°11′40.45”	2.1	2.1	5.2	48 ± 22	13 ± 5	2.8 ± 1.4	90.0 ± 82.6	7.33	117	0.6	*IA*	0
700	$13^h29^m45.86^s$	47°11′26.70”	8.0	3.3	8.4	38 ± 40	7 ± 9	0.9 ± 1.9	17.4 ± 56.1	4.40	26	0.4	*IA*	0
701	$13^h29^m46.35^s$	47°11′36.15”	2.7	2.0	4.8	51 ± 50	8 ± 6	2.6 ± 1.8	37.6 ± 84.7	3.30	78	0.4	*IA*	0
702	$13^h29^m45.88^s$	47°11′24.45”	15.7	1.8	4.6	32 ± 0	5 ± 4	1.3 ± 0.8	9.1 ± 14.9	1.57	99	0.4	*IA*	1
703	$13^h29^m46.00^s$	47°11′30.46”	33.5	2.0	4.5	32 ± 0	10 ± 5	0.5 ± 0.3	34.4 ± 31.7	17.13	115	0.4	*IA*	1
704	$13^h29^m48.27^s$	47°11′11.99”	3.9	1.9	5.1	32 ± 0	5 ± 2	0.8 ± 0.4	8.3 ± 7.6	2.47	146	0.3	*IA*	1
705	$13^h29^m48.55^s$	47°11′17.24”	29.6	3.3	8.1	106 ± 25	6 ± 2	7.1 ± 2.9	40.2 ± 29.5	1.30	78	0.6	*IA*	0
706	$13^h29^m48.47^s$	47°11′13.22”	34.1	2.8	7.0	70 ± 55	9 ± 8	3.1 ± 1.1	54.5 ± 120.1	4.06	74	0.6	*IA*	0
707	$13^h29^m46.60^s$	47°11′40.82”	−0.6	1.6	4.0	35 ± 19	12 ± 7	0.7 ± 0.4	52.8 ± 72.6	16.66	79	0.6	*IA*	0
708	$13^h29^m46.23^s$	47°11′12.14”	30.7	3.7	9.2	42 ± 18	4 ± 2	2.3 ± 1.4	7.7 ± 10.5	0.78	52	0.8	*IA*	0
709	$13^h29^m47.87^s$	47°11′19.40”	16.3	2.0	5.8	26 ± 11	4 ± 1	0.6 ± 0.2	3.9 ± 3.3	1.37	113	0.7	*IA*	0
710	$13^h29^m47.07^s$	47°11′20.91”	16.0	2.0	4.7	24 ± 15	4 ± 3	0.9 ± 0.6	3.9 ± 5.9	0.95	105	0.8	*IA*	0
711	$13^h29^m47.09^s$	47°11′22.44”	29.9	2.2	5.5	32 ± 0	5 ± 4	0.4 ± 0.3	6.8 ± 10.6	3.63	124	0.8	*IA*	1
712	$13^h29^m47.91^s$	47°11′34.16”	19.4	1.9	4.9	30 ± 13	11 ± 3	1.4 ± 0.4	35.7 ± 22.1	5.68	66	0.8	*IA*	0
713	$13^h29^m46.65^s$	47°11′17.30”	25.1	2.7	7.0	21 ± 12	2 ± 2	0.7 ± 0.7	1.0 ± 2.3	0.33	176	0.6	*IA*	0
714	$13^h29^m46.52^s$	47°11′16.03”	33.1	2.9	7.2	64 ± 53	5 ± 3	2.7 ± 2.7	13.7 ± 31.0	1.16	131	0.5	*IA*	0
715	$13^h29^m46.32^s$	47°11′18.82”	27.8	2.4	5.8	43 ± 21	9 ± 3	1.8 ± 0.4	39.8 ± 30.7	5.02	20	0.6	*IA*	0
716	$13^h29^m48.36^s$	47°11′30.56”	19.4	2.3	5.3	37 ± 11	4 ± 1	1.2 ± 0.3	7.1 ± 6.7	1.31	16	0.7	*IA*	0
717	$13^h29^m44.60^s$	47°11′41.14”	−69.9	1.6	4.4	32 ± 0	3 ± 2	0.3 ± 0.2	2.4 ± 4.0	1.94	39	0.9	*SA*	1
718	$13^h29^m44.59^s$	47°11′38.57”	−32.3	3.7	8.7	32 ± 0	2 ± 4	0.9 ± 1.7	0.9 ± 4.1	0.24	141	0.3	*SA*	1
719	$13^h29^m44.39^s$	47°11′37.67”	−23.1	4.5	10.6	53 ± 11	7 ± 2	7.7 ± 3.3	28.9 ± 14.2	0.86	48	0.7	*SA*	0
720	$13^h29^m44.69^s$	47°11′37.94”	−12.7	3.1	8.3	37 ± 29	7 ± 6	2.3 ± 3.5	20.5 ± 41.3	2.02	38	0.7	*SA*	0
721	$13^h29^m44.44^s$	47°11′40.24”	−2.8	1.7	4.4	32 ± 0	5 ± 3	0.7 ± 0.5	9.0 ± 10.9	3.09	113	0.4	*SA*	1
722	$13^h29^m41.19^s$	47°11′26.17”	−69.0	3.9	5.4	32 ± 0	4 ± 2	0.9 ± 0.3	4.6 ± 5.0	1.18	128	0.7	*IA*	1
723	$13^h29^m40.86^s$	47°11′30.49”	−64.2	4.5	4.7	32 ± 0	4 ± 3	0.8 ± 0.3	4.2 ± 7.4	1.21	129	0.8	*IA*	1
724	$13^h29^m44.32^s$	47°11′22.74”	−26.7	1.6	4.6	32 ± 0	5 ± 8	0.3 ± 0.5	6.7 ± 23.4	5.24	105	0.6	*SA*	1
725	$13^h29^m44.01^s$	47°11′24.39”	−14.5	2.2	5.8	32 ± 0	12 ± 9	2.2 ± 2.0	46.7 ± 68.5	4.89	148	0.4	*SA*	1
726	$13^h29^m44.01^s$	47°11′27.25”	−18.0	4.3	11.5	66 ± 12	11 ± 4	15.7 ± 4.8	89.3 ± 47.9	1.30	165	0.9	*SA*	0
727	$13^h29^m44.39^s$	47°11′23.90”	−6.4	2.0	5.8	32 ± 0	6 ± 5	0.5 ± 0.7	10.2 ± 17.3	5.00	165	0.8	*SA*	1
728	$13^h29^m44.25^s$	47°11′25.77”	−2.2	2.8	7.7	32 ± 0	6 ± 7	2.6 ± 3.2	11.8 ± 28.2	1.03	94	0.3	*SA*	1
729	$13^h29^m44.89^s$	47°11′32.45”	5.8	5.3	13.5	100 ± 12	8 ± 2	11.8 ± 1.3	63.0 ± 30.1	1.23	119	0.2	*IA*	0
730	$13^h29^m44.99^s$	47°11′36.43”	5.6	2.8	7.2	13 ± 14	5 ± 3	0.9 ± 0.8	2.9 ± 5.4	0.71	155	0.8	*IA*	0
731	$13^h29^m44.65^s$	47°11′26.22”	20.8	2.6	6.5	26 ± 16	12 ± 8	2.1 ± 1.6	42.3 ± 62.1	4.56	107	0.5	*SA*	0
732	$13^h29^m44.59^s$	47°11′20.95”	22.6	2.3	6.0	35 ± 27	7 ± 4	0.7 ± 1.0	20.5 ± 27.2	6.30	99	0.5	*SA*	0
733	$13^h29^m45.02^s$	47°11′32.74”	28.4	1.7	4.2	32 ± 0	5 ± 3	0.3 ± 0.3	9.2 ± 11.6	6.38	144	0.7	*IA*	1
734	$13^h29^m44.63^s$	47°11′23.49”	19.8	2.8	6.9	48 ± 15	7 ± 3	3.7 ± 1.8	26.6 ± 23.8	1.66	157	0.5	*SA*	0
735	$13^h29^m44.52^s$	47°11′20.70”	34.9	1.6	4.3	32 ± 0	3 ± 4	0.2 ± 0.3	2.7 ± 6.9	2.59	162	0.6	*SA*	1
736	$13^h29^m43.43^s$	47°11′19.04”	−27.6	2.6	7.2	56 ± 28	4 ± 2	3.0 ± 1.1	9.6 ± 8.9	0.74	156	0.8	*SA*	0
737	$13^h29^m43.27^s$	47°11′14.17”	−23.5	2.7	7.5	26 ± 38	6 ± 5	1.9 ± 2.7	9.1 ± 25.7	1.07	60	0.9	*SA*	0
738	$13^h29^m43.42^s$	47°11′15.66”	−27.1	3.2	8.7	71 ± 33	6 ± 4	3.8 ± 3.5	22.9 ± 32.7	1.38	161	0.5	*SA*	0
739	$13^h29^m43.73^s$	47°11′17.58”	−20.7	2.5	6.5	37 ± 17	4 ± 2	1.0 ± 0.3	5.8 ± 8.3	1.33	155	0.7	*SA*	0
740	$13^h29^m43.61^s$	47°11′13.72”	−18.3	1.9	5.4	32 ± 0	5 ± 4	0.5 ± 0.4	7.6 ± 12.3	3.58	52	0.5	*SA*	1
741	$13^h29^m43.70^s$	47°11′19.75”	0.3	3.2	8.9	34 ± 31	12 ± 9	2.7 ± 4.1	48.0 ± 101.0	4.04	93	0.7	*SA*	0
742	$13^h29^m43.88^s$	47°11′12.72”	5.6	1.6	4.4	32 ± 0	5 ± 2	1.3 ± 0.6	7.0 ± 6.7	1.23	117	0.3	*SA*	1
743	$13^h29^m44.01^s$	47°11′15.66”	5.9	2.0	6.1	39 ± 18	10 ± 6	1.1 ± 0.6	41.0 ± 71.4	8.20	52	0.5	*SA*	0
744	$13^h29^m43.81^s$	47°11′18.31”	3.6	3.2	8.6	43 ± 44	9 ± 7	1.9 ± 2.3	35.8 ± 62.9	4.26	1	0.7	*SA*	0
745	$13^h29^m43.56^s$	47°11′12.66”	9.0	4.3	11.9	93 ± 12	8 ± 3	8.8 ± 0.8	68.2 ± 44.8	1.77	117	0.6	*SA*	0
746	$13^h29^m43.80^s$	47°11′13.83”	16.5	2.0	5.1	32 ± 0	2 ± 3	0.3 ± 0.2	1.9 ± 4.5	1.69	101	0.8	*SA*	1

ID	**RA (J2000)** *h m s*	**Dec (J2000)** *d ’ ”*	$\mathbf{V_{LSR}}$ km/s	$\mathbf{T_{max}}$ K	**S/N**	**R** pc	$\sigma_\mathbf{v}$ km/s	$\mathbf{L_{CO}}$ 10^5 K km/s pc^2	$\mathbf{M_{vir}}$ 10^5 $M_\odot$	α	**PA** deg	**b/a**	**Reg**	**Flag**
(1)	(2)	(3)	(4)	(5)	(6)	(7)	(8)	(9)	(10)	(11)	(12)	(13)	(14)	(15)
747	$13^h29^m43.33^s$	47°11′22.71”	−25.2	2.7	6.7	32 ± 0	2 ± 1	1.4 ± 0.6	1.5 ± 1.8	0.25	119	0.3	*SA*	1
748	$13^h29^m43.14^s$	47°11′21.05”	−15.6	2.2	5.4	32 ± 0	3 ± 2	0.8 ± 0.5	3.9 ± 4.5	1.15	134	0.7	*SA*	1
749	$13^h29^m42.93^s$	47°11′39.21”	−27.6	2.5	5.0	32 ± 0	6 ± 4	0.6 ± 0.5	13.7 ± 16.9	5.00	157	0.7	*IA*	1
750	$13^h29^m42.97^s$	47°11′38.09”	−11.1	2.7	5.2	43 ± 19	5 ± 3	2.6 ± 1.1	10.3 ± 12.7	0.92	74	1.1	*IA*	0
751	$13^h29^m42.01^s$	47°11′12.35”	7.1	5.7	13.2	53 ± 41	3 ± 4	3.5 ± 7.9	6.5 ± 17.2	0.42	49	0.5	*IA*	0
752	$13^h29^m42.27^s$	47°11′19.01”	−5.9	2.6	5.8	32 ± 0	2 ± 2	0.6 ± 0.5	1.6 ± 3.3	0.59	97	0.8	*IA*	1
753	$13^h29^m42.38^s$	47°11′17.06”	−1.7	2.6	6.4	62 ± 15	10 ± 3	3.2 ± 1.6	66.5 ± 40.5	4.71	118	0.5	*IA*	0
754	$13^h29^m42.60^s$	47°11′18.11”	3.6	2.2	5.5	32 ± 0	5 ± 4	0.7 ± 0.8	7.2 ± 12.1	2.34	176	0.5	*IA*	1
755	$13^h29^m42.98^s$	47°11′22.51”	−13.8	2.2	5.6	32 ± 0	8 ± 7	0.6 ± 0.8	19.2 ± 33.3	7.29	106	0.3	*SA*	1
756	$13^h29^m42.95^s$	47°11′25.71”	−9.2	3.3	8.1	73 ± 17	5 ± 2	4.8 ± 1.8	15.6 ± 13.5	0.75	133	0.8	*SA*	0
757	$13^h29^m42.24^s$	47°11′26.97”	−6.5	2.9	5.9	32 ± 0	4 ± 2	1.0 ± 0.3	4.9 ± 5.2	1.18	139	0.5	*IA*	1
758	$13^h29^m42.04^s$	47°11′19.67”	−5.5	1.9	4.4	32 ± 0	8 ± 6	0.7 ± 0.4	23.1 ± 33.3	7.53	40	0.9	*IA*	1
759	$13^h29^m41.36^s$	47°11′40.90”	−4.6	6.5	6.0	32 ± 0	2 ± 1	1.1 ± 0.4	1.5 ± 1.6	0.32	48	0.5	*IA*	1
760	$13^h29^m45.21^s$	47°11′12.05”	7.6	1.9	5.0	32 ± 0	7 ± 2	0.9 ± 0.3	15.4 ± 7.8	3.87	169	0.6	*IA*	1
761	$13^h29^m43.03^s$	47°11′21.99”	15.8	1.9	4.7	32 ± 0	6 ± 3	0.5 ± 0.2	10.4 ± 11.0	4.90	155	0.5	*SA*	1
762	$13^h29^m44.22^s$	47°11′15.89”	22.4	1.9	5.4	73 ± 19	8 ± 2	2.2 ± 0.6	44.0 ± 28.7	4.58	91	0.7	*SA*	0
763	$13^h29^m44.16^s$	47°11′13.88”	30.9	1.7	4.2	32 ± 0	4 ± 4	0.3 ± 0.3	6.6 ± 11.5	5.31	179	0.6	*SA*	1
764	$13^h29^m44.53^s$	47°11′16.01”	36.3	1.9	5.1	32 ± 10	7 ± 2	1.3 ± 0.3	14.4 ± 7.6	2.45	42	0.6	*SA*	0
765	$13^h29^m42.54^s$	47°11′31.07”	50.7	2.5	5.2	32 ± 0	3 ± 2	0.5 ± 0.2	2.3 ± 2.8	1.02	179	0.6	*IA*	1
766	$13^h29^m41.63^s$	47°11′37.22”	75.1	4.1	5.0	32 ± 0	2 ± 1	0.6 ± 0.2	1.2 ± 1.4	0.46	115	0.8	*IA*	1
767	$13^h29^m45.35^s$	47°11′34.00”	111.2	1.4	4.7	22 ± 11	6 ± 2	0.7 ± 0.2	9.5 ± 8.6	3.30	171	0.6	*IA*	0
768	$13^h30^m1.50^s$	47°12′10.69”	−31.7	2.0	4.7	32 ± 0	11 ± 5	2.0 ± 1.0	37.5 ± 37.4	4.27	5	0.3	*SA*	1
769	$13^h30^m1.67^s$	47°12′10.93”	−26.6	2.2	5.2	32 ± 0	5 ± 5	0.8 ± 0.8	7.7 ± 15.3	2.13	166	0.6	*SA*	1
770	$13^h30^m1.40^s$	47°11′57.57”	−38.7	2.0	4.8	32 ± 0	5 ± 4	0.6 ± 0.3	8.3 ± 13.4	3.39	48	0.5	*SA*	1
771	$13^h30^m0.81^s$	47°11′52.14”	−20.2	4.1	9.7	91 ± 17	8 ± 1	9.1 ± 4.1	53.2 ± 22.8	1.35	99	0.5	*SA*	0
772	$13^h30^m1.21^s$	47°11′57.53”	−12.0	4.7	12.0	36 ± 32	13 ± 11	3.9 ± 1.8	62.9 ± 118.4	3.68	137	0.5	*SA*	0
773	$13^h30^m1.26^s$	47°12′2.01”	−12.5	4.0	9.3	66 ± 56	2 ± 0	2.0 ± 1.1	3.1 ± 2.6	0.36	100	1.0	*SA*	1
774	$13^h30^m1.31^s$	47°12′7.60”	−14.9	4.6	10.6	66 ± 17	7 ± 2	5.0 ± 1.2	34.5 ± 24.1	1.57	74	0.8	*SA*	0
775	$13^h30^m0.85^s$	47°11′48.28”	−9.0	2.7	6.7	18 ± 29	3 ± 4	0.7 ± 0.7	1.8 ± 5.3	0.61	124	1.0	*SA*	0
776	$13^h30^m0.65^s$	47°11′48.24”	−9.8	3.5	8.3	26 ± 18	7 ± 4	1.9 ± 1.8	15.3 ± 20.1	1.86	108	1.0	*SA*	0
777	$13^h30^m1.66^s$	47°12′5.16”	−5.4	5.0	11.8	61 ± 66	2 ± 4	2.5 ± 2.7	3.7 ± 11.8	0.34	111	0.4	*SA*	0
778	$13^h30^m1.89^s$	47°12′9.05”	−3.6	1.7	4.1	32 ± 0	4 ± 4	0.5 ± 0.7	5.0 ± 9.2	2.14	96	0.6	*SA*	1
779	$13^h30^m0.72^s$	47°11′46.26”	1.9	3.1	7.4	42 ± 34	9 ± 6	4.7 ± 4.2	34.7 ± 61.0	1.70	114	0.5	*SA*	0
780	$13^h30^m0.98^s$	47°11′47.12”	−1.9	3.7	8.9	31 ± 19	6 ± 4	1.8 ± 2.1	10.4 ± 17.3	1.33	171	0.8	*SA*	0
781	$13^h30^m1.13^s$	47°11′54.99”	−2.9	6.6	16.2	84 ± 28	4 ± 2	11.8 ± 9.7	12.6 ± 15.8	0.24	110	0.5	*SA*	0
782	$13^h30^m1.53^s$	47°11′59.54”	−4.3	2.9	7.0	42 ± 39	4 ± 6	0.9 ± 1.3	7.2 ± 19.4	1.91	54	0.7	*SA*	0
783	$13^h30^m2.18^s$	47°12′5.57”	0.8	2.8	6.7	42 ± 19	7 ± 3	2.0 ± 1.0	22.6 ± 24.7	2.65	174	0.6	*SA*	0
784	$13^h30^m1.22^s$	47°11′50.55”	4.2	4.2	10.2	58 ± 29	4 ± 3	3.8 ± 4.2	11.6 ± 18.4	0.69	44	0.7	*SA*	0
785	$13^h30^m1.81^s$	47°12′1.32”	3.6	6.3	15.0	50 ± 17	4 ± 2	3.2 ± 2.9	9.4 ± 10.8	0.67	135	0.7	*SA*	0
786	$13^h30^m2.02^s$	47°12′3.89”	4.0	2.3	5.2	32 ± 0	5 ± 4	0.9 ± 1.2	9.3 ± 13.2	2.45	165	0.5	*SA*	1
787	$13^h30^m1.73^s$	47°12′3.86”	0.9	4.8	11.0	108 ± 133	10 ± 20	2.9 ± 2.1	106.9 ± 361.2	8.57	45	0.4	*SA*	0
788	$13^h30^m1.15^s$	47°11′46.93”	3.9	3.7	8.7	52 ± 26	5 ± 6	4.6 ± 6.3	13.9 ± 32.7	0.70	126	0.3	*SA*	0
789	$13^h30^m2.04^s$	47°12′1.45”	16.6	5.1	11.0	70 ± 19	11 ± 3	16.2 ± 7.4	85.5 ± 43.8	1.21	100	0.5	*SA*	0
790	$13^h30^m1.43^s$	47°11′46.94”	18.4	2.1	4.6	55 ± 45	9 ± 6	1.5 ± 0.8	42.3 ± 84.5	6.27	20	0.6	*SA*	0
791	$13^h30^m1.79^s$	47°11′54.50”	16.2	3.3	7.3	36 ± 10	11 ± 4	3.9 ± 1.1	43.1 ± 34.5	2.52	7	0.2	*SA*	0
792	$13^h30^m1.45^s$	47°11′56.89”	12.4	2.1	4.8	32 ± 0	6 ± 3	0.8 ± 0.7	12.6 ± 11.7	3.72	163	0.4	*SA*	1
793	$13^h30^m2.27^s$	47°12′9.33”	20.5	3.6	7.9	73 ± 70	4 ± 5	6.1 ± 7.0	15.1 ± 42.5	0.57	111	0.9	*SA*	0
794	$13^h30^m2.79^s$	47°12′11.74”	13.3	2.6	5.7	23 ± 18	4 ± 2	0.6 ± 0.4	3.4 ± 4.7	1.21	147	0.8	*IA*	0
795	$13^h30^m1.65^s$	47°12′4.99”	18.1	2.4	5.4	32 ± 0	4 ± 4	0.5 ± 0.4	5.2 ± 10.9	2.63	179	1.0	*SA*	1
796	$13^h30^m2.29^s$	47°12′6.21”	22.3	3.0	6.4	50 ± 35	6 ± 6	1.3 ± 1.8	20.5 ± 42.4	3.58	166	0.4	*SA*	0
797	$13^h30^m1.02^s$	47°11′42.67”	31.0	4.5	11.1	50 ± 17	7 ± 3	7.2 ± 3.4	28.6 ± 25.4	0.91	142	0.3	*SA*	0
798	$13^h30^m0.93^s$	47°11′47.59”	30.4	2.5	6.2	18 ± 15	3 ± 3	0.8 ± 0.6	1.9 ± 4.4	0.56	170	0.6	*SA*	0
799	$13^h30^m1.96^s$	47°11′57.65”	26.2	4.3	9.3	51 ± 29	15 ± 7	5.1 ± 3.0	124.0 ± 157.5	5.63	158	0.7	*SA*	0
800	$13^h30^m2.35^s$	47°12′2.84”	37.8	1.9	4.1	30 ± 29	7 ± 3	1.1 ± 1.1	16.9 ± 22.4	3.41	110	0.9	*SA*	0
801	$13^h30^m0.40^s$	47°11′44.58”	45.7	1.9	5.0	32 ± 0	6 ± 3	0.9 ± 0.6	10.6 ± 12.5	2.72	11	0.4	*SA*	1
802	$13^h30^m0.64^s$	47°11′44.13”	56.2	1.8	4.6	32 ± 0	5 ± 4	0.2 ± 0.2	7.2 ± 13.0	7.81	138	0.3	*SA*	1
803	$13^h30^m0.50^s$	47°11′44.15”	−14.1	2.1	5.1	26 ± 9	11 ± 4	1.1 ± 0.3	33.4 ± 32.1	7.20	21	0.7	*SA*	0
804	$13^h30^m1.74^s$	47°11′52.71”	−0.3	2.1	4.9	24 ± 19	7 ± 4	0.9 ± 0.5	12.9 ± 18.5	3.14	10	0.7	*SA*	0
805	$13^h30^m1.70^s$	47°11′49.39”	8.9	4.8	11.0	65 ± 10	6 ± 1	6.6 ± 0.4	20.7 ± 8.6	0.72	74	0.6	*SA*	0
806	$13^h30^m4.42^s$	47°11′46.82”	27.7	6.3	4.9	32 ± 0	5 ± 3	1.6 ± 0.5	8.9 ± 9.0	1.27	113	0.4	*SA*	1

ID	**RA (J2000)**	**Dec (J2000)**	**V$_{\mathrm{LSR}}$**	**T$_{\mathrm{max}}$**	**S/N**	**R**	**σ_{v}**	**L$_{\mathrm{CO}}$**	**M$_{\mathrm{vir}}$**	α	**PA**	**b/a**	**Reg**	**Flag**
	h m s	*d ’ ”*	km/s	K		pc	km/s	10^5 K km/s pc^2	10^5 M$_\odot$		deg			
(1)	(2)	(3)	(4)	(5)	(6)	(7)	(8)	(9)	(10)	(11)	(12)	(13)	(14)	(15)
807	$13^h30^m2.59^s$	47°11′50.16”	39.3	3.9	7.4	99 ± 12	6 ± 1	7.2 ± 0.6	42.5 ± 19.9	1.35	85	0.4	*IA*	0
808	$13^h30^m2.82^s$	47°11′47.14”	54.1	2.8	4.9	32 ± 0	3 ± 3	0.3 ± 0.2	2.9 ± 5.0	2.14	175	0.5	*IA*	1
809	$13^h30^m2.48^s$	47°11′43.75”	48.0	2.6	5.2	64 ± 19	8 ± 5	1.5 ± 0.7	42.9 ± 55.0	6.41	33	0.7	*IA*	0
810	$13^h30^m2.41^s$	47°11′42.17”	61.4	1.9	3.5	32 ± 0	4 ± 3	0.6 ± 0.6	5.2 ± 8.8	2.03	8	0.5	*IA*	1
811	$13^h29^m57.80^s$	47°11′44.68”	−58.2	1.7	4.5	32 ± 0	5 ± 3	0.4 ± 0.3	8.4 ± 10.5	4.60	134	0.8	*IA*	1
812	$13^h29^m57.78^s$	47°11′44.75”	−38.5	1.5	3.8	32 ± 0	6 ± 4	0.4 ± 0.3	11.9 ± 17.4	7.03	43	0.5	*IA*	1
813	$13^h29^m57.98^s$	47°11′43.59”	−5.6	1.7	4.4	32 ± 0	6 ± 4	0.3 ± 0.2	10.0 ± 14.4	9.04	108	0.6	*IA*	1
814	$13^h29^m57.97^s$	47°11′45.86”	9.8	2.1	5.6	57 ± 14	8 ± 3	2.7 ± 0.9	42.2 ± 39.9	3.56	39	1.0	*IA*	0
815	$13^h29^m57.81^s$	47°11′44.71”	24.1	1.9	5.1	32 ± 0	9 ± 4	0.5 ± 0.4	23.9 ± 22.1	10.52	139	0.7	*IA*	1
816	$13^h29^m58.47^s$	47°12′8.63”	−59.2	1.8	4.5	32 ± 0	5 ± 5	0.6 ± 0.3	8.5 ± 17.6	3.26	157	0.4	*IA*	1
817	$13^h29^m58.47^s$	47°12′7.01”	−43.4	2.3	5.7	71 ± 12	5 ± 1	3.5 ± 0.9	21.2 ± 10.6	1.39	47	0.7	*IA*	0
818	$13^h29^m58.99^s$	47°12′0.99”	−44.6	2.1	5.4	32 ± 0	3 ± 3	0.7 ± 0.5	2.9 ± 6.0	0.99	171	0.5	*IA*	1
819	$13^h29^m59.21^s$	47°11′59.97”	−26.1	1.7	4.4	61 ± 14	9 ± 5	1.8 ± 0.9	54.9 ± 65.2	6.86	116	0.6	*IA*	0
820	$13^h29^m58.94^s$	47°11′59.90”	−22.9	2.1	4.8	32 ± 0	13 ± 16	1.0 ± 0.7	57.2 ± 138.5	12.90	98	0.5	*IA*	1
821	$13^h29^m59.04^s$	47°11′58.25”	−4.4	1.5	3.9	32 ± 0	9 ± 5	0.5 ± 0.3	25.2 ± 30.9	12.64	98	0.4	*IA*	1
822	$13^h29^m57.46^s$	47°11′52.32”	−26.2	3.8	9.7	38 ± 13	7 ± 3	2.5 ± 0.9	19.6 ± 17.6	1.81	142	0.6	*IA*	0
823	$13^h29^m57.60^s$	47°11′47.43”	−21.1	2.5	6.7	41 ± 19	6 ± 3	1.8 ± 1.8	14.8 ± 15.8	1.87	81	0.7	*IA*	0
824	$13^h29^m57.77^s$	47°11′50.61”	−14.7	2.3	5.6	32 ± 0	4 ± 3	0.5 ± 0.4	4.7 ± 8.2	2.20	6	0.5	*IA*	1
825	$13^h30^m0.33^s$	47°11′43.09”	32.3	2.3	6.2	18 ± 17	8 ± 8	1.5 ± 1.0	12.8 ± 28.6	1.91	84	0.6	*SA*	0
826	$13^h29^m58.72^s$	47°12′10.57”	−42.3	2.4	6.1	32 ± 0	4 ± 2	0.9 ± 0.2	4.5 ± 4.0	1.17	97	0.5	*IA*	1
827	$13^h29^m58.87^s$	47°11′47.98”	−33.7	2.3	6.2	31 ± 21	4 ± 3	0.8 ± 0.5	3.9 ± 7.4	1.11	81	0.8	*IA*	0
828	$13^h29^m58.85^s$	47°11′48.95”	−17.8	2.4	6.0	29 ± 12	4 ± 2	2.5 ± 1.2	6.0 ± 5.5	0.56	127	0.4	*IA*	0
829	$13^h29^m59.36^s$	47°11′54.18”	−21.2	3.6	8.5	93 ± 18	6 ± 2	8.2 ± 1.8	40.5 ± 23.6	1.14	130	0.3	*IA*	0
830	$13^h29^m59.15^s$	47°11′50.75”	−20.6	2.3	5.9	32 ± 0	10 ± 7	0.6 ± 0.5	32.0 ± 43.9	13.24	121	0.5	*IA*	1
831	$13^h29^m59.13^s$	47°11′45.69”	−20.1	1.9	4.6	31 ± 27	10 ± 10	1.5 ± 1.5	32.0 ± 72.0	4.76	133	0.7	*IA*	0
832	$13^h29^m59.65^s$	47°11′43.28”	−12.2	2.0	4.9	96 ± 44	8 ± 3	1.9 ± 2.4	66.5 ± 71.4	8.06	173	0.8	*IA*	0
833	$13^h29^m59.32^s$	47°11′44.65”	−19.0	2.1	5.0	52 ± 37	9 ± 6	2.2 ± 2.5	41.1 ± 56.4	4.29	154	0.4	*IA*	0
834	$13^h29^m59.86^s$	47°11′43.53”	−5.0	1.8	5.1	46 ± 34	6 ± 7	1.1 ± 1.4	14.8 ± 30.3	3.02	64	0.6	*IA*	0
835	$13^h29^m59.11^s$	47°11′43.54”	0.3	1.5	4.2	31 ± 25	8 ± 5	0.9 ± 0.6	21.6 ± 35.8	5.60	93	1.0	*IA*	0
836	$13^h29^m59.31^s$	47°11′45.55”	2.2	2.1	5.1	26 ± 23	9 ± 6	1.2 ± 0.9	21.0 ± 34.0	4.06	161	0.8	*IA*	0
837	$13^h29^m59.30^s$	47°12′0.03”	39.9	1.3	4.0	32 ± 0	2 ± 3	0.2 ± 0.1	1.5 ± 3.7	1.69	106	0.6	*IA*	1
838	$13^h29^m54.93^s$	47°12′11.14”	−112.1	1.4	5.1	32 ± 0	5 ± 3	0.3 ± 0.2	9.8 ± 10.3	7.23	16	0.7	*SA*	1
839	$13^h29^m54.79^s$	47°11′54.58”	−69.1	1.4	3.6	32 ± 0	6 ± 5	0.5 ± 0.4	12.8 ± 18.7	6.41	114	0.7	*CR*	1
840	$13^h29^m54.90^s$	47°11′52.11”	−61.3	1.7	4.7	32 ± 0	6 ± 4	0.4 ± 0.2	11.5 ± 15.5	6.63	165	0.5	*CR*	1
841	$13^h29^m54.59^s$	47°12′11.83”	−59.0	6.1	16.4	32 ± 0	5 ± 4	3.5 ± 2.8	8.4 ± 13.5	0.55	55	0.3	*SA*	1
842	$13^h29^m54.82^s$	47°12′2.99”	−49.3	3.1	7.7	48 ± 11	13 ± 3	3.5 ± 0.6	86.7 ± 45.4	5.65	52	1.1	*CR*	0
843	$13^h29^m54.82^s$	47°11′58.21”	−42.7	5.4	13.8	51 ± 24	7 ± 4	5.7 ± 6.0	27.0 ± 37.9	1.09	82	0.8	*CR*	0
844	$13^h29^m54.67^s$	47°11′55.87”	−35.8	4.0	9.7	30 ± 52	3 ± 5	6.3 ± 12.2	2.9 ± 10.9	0.11	169	0.4	*CR*	0
845	$13^h29^m54.56^s$	47°11′59.00”	−38.6	7.6	19.5	48 ± 15	7 ± 2	8.1 ± 1.1	26.0 ± 19.4	0.74	88	0.7	*CR*	0
846	$13^h29^m54.64^s$	47°11′50.01”	−31.1	3.5	8.7	40 ± 15	5 ± 2	3.1 ± 1.0	11.9 ± 9.2	0.88	152	0.4	*CR*	0
847	$13^h29^m54.77^s$	47°11′53.06”	−34.9	5.0	12.3	49 ± 15	6 ± 2	5.7 ± 3.0	19.2 ± 12.1	0.78	36	0.6	*CR*	0
848	$13^h29^m55.27^s$	47°12′11.82”	−38.6	8.8	22.3	104 ± 23	6 ± 5	15.2 ± 4.5	39.8 ± 67.1	0.60	44	0.6	*SA*	0
849	$13^h29^m55.68^s$	47°11′57.32”	−24.3	5.8	14.7	63 ± 42	2 ± 3	2.8 ± 2.6	1.9 ± 6.1	0.15	26	0.8	*CR*	0
850	$13^h29^m55.39^s$	47°12′1.84”	−28.3	7.8	21.9	65 ± 55	8 ± 5	6.5 ± 2.5	48.8 ± 70.9	1.71	124	1.5	*CR*	0
851	$13^h29^m55.92^s$	47°12′2.52”	−26.6	3.4	9.8	16 ± 13	7 ± 5	1.5 ± 2.5	7.0 ± 12.2	1.09	149	0.5	*SA*	0
852	$13^h29^m55.50^s$	47°12′6.27”	−24.6	7.6	20.0	50 ± 76	9 ± 14	5.6 ± 2.4	44.9 ± 133.2	1.85	72	1.6	*SA*	0
853	$13^h29^m55.47^s$	47°12′8.21”	−26.3	8.1	23.1	45 ± 28	16 ± 9	10.8 ± 18.8	121.0 ± 169.8	2.57	50	0.4	*SA*	0
854	$13^h29^m54.82^s$	47°11′48.76”	−21.7	2.5	6.6	12 ± 16	14 ± 11	1.5 ± 1.8	23.3 ± 48.0	3.60	9	0.6	*CR*	0
855	$13^h29^m54.87^s$	47°11′58.90”	−21.9	2.3	5.9	32 ± 0	8 ± 6	1.0 ± 0.9	21.2 ± 31.0	4.78	1	0.6	*CR*	1
856	$13^h29^m56.43^s$	47°12′3.06”	−25.3	2.5	6.5	32 ± 0	5 ± 6	0.8 ± 0.9	9.4 ± 20.1	2.76	127	0.4	*SA*	1
857	$13^h29^m55.17^s$	47°11′49.19”	−17.2	5.8	14.0	57 ± 34	6 ± 2	8.9 ± 9.2	20.5 ± 19.7	0.53	87	0.6	*CR*	0
858	$13^h29^m56.16^s$	47°11′58.58”	−19.9	3.0	7.3	32 ± 0	9 ± 6	1.4 ± 1.5	26.1 ± 35.9	4.39	140	0.3	*SA*	1
859	$13^h29^m55.56^s$	47°11′59.24”	−20.0	6.9	17.5	46 ± 28	7 ± 6	6.0 ± 2.9	26.0 ± 42.0	1.00	35	0.9	*CR*	0
860	$13^h29^m56.40^s$	47°12′0.82”	−18.6	3.6	8.9	32 ± 0	5 ± 2	1.7 ± 0.5	8.2 ± 6.9	1.09	134	0.6	*SA*	1
861	$13^h29^m55.59^s$	47°12′2.33”	−18.1	8.3	21.9	73 ± 100	7 ± 5	17.8 ± 32.7	35.2 ± 69.6	0.45	66	1.4	*CR*	0
862	$13^h29^m54.54^s$	47°11′44.70”	−13.6	5.3	13.6	29 ± 18	7 ± 3	3.6 ± 2.7	13.6 ± 10.8	0.86	126	0.5	*CR*	0
863	$13^h29^m55.02^s$	47°11′46.83”	−12.5	4.6	11.5	32 ± 0	2 ± 0	0.9 ± 1.6	1.5 ± 0.0	0.38	161	0.3	*CR*	1
864	$13^h29^m55.68^s$	47°11′54.81”	−14.0	6.1	17.4	59 ± 87	6 ± 5	8.0 ± 5.0	24.7 ± 60.7	0.71	25	1.2	*CR*	0
865	$13^h29^m55.87^s$	47°11′59.30”	−12.5	5.6	14.4	63 ± 51	2 ± 0	3.7 ± 7.9	3.0 ± 2.4	0.18	9	0.5	*SA*	1
866	$13^h29^m56.74^s$	47°11′42.98”	−5.2	1.9	4.9	22 ± 18	2 ± 1	0.5 ± 0.3	0.6 ± 1.1	0.27	136	0.8	*SA*	0

ID	**RA (J2000)**	**Dec (J2000)**	$\mathbf{V_{LSR}}$	$\mathbf{T_{max}}$	**S/N**	**R**	σ_v	$\mathbf{L_{CO}}$	$\mathbf{M_{vir}}$	α	**PA**	**b/a**	**Reg**	**Flag**
	h m s	*d ′ ″*	km/s	K		pc	km/s	10^5 K km/s pc^2	10^5 $M_\odot$		deg			
(1)	(2)	(3)	(4)	(5)	(6)	(7)	(8)	(9)	(10)	(11)	(12)	(13)	(14)	(15)
867	$13^h29^m54.93^s$	47° 11′51.22”	−0.3	1.7	4.6	34 ± 27	10 ± 11	1.3 ± 1.3	34.1 ± 101.8	5.87	55	0.3	*CR*	0
868	$13^h29^m56.13^s$	47° 11′55.69”	−7.3	2.8	6.7	27 ± 30	3 ± 6	0.9 ± 1.1	2.9 ± 10.3	0.73	25	0.7	*SA*	0
869	$13^h29^m55.76^s$	47° 11′56.66”	−9.4	7.0	17.0	70 ± 56	5 ± 8	2.2 ± 2.7	18.4 ± 53.5	1.89	0	0.6	*CR*	0
870	$13^h29^m54.65^s$	47° 11′48.48”	−2.3	2.1	5.4	32 ± 0	5 ± 5	0.3 ± 0.3	7.4 ± 16.7	6.08	109	0.6	*CR*	1
871	$13^h29^m56.14^s$	47° 11′49.87”	−0.0	6.6	17.1	32 ± 0	9 ± 5	3.0 ± 3.1	29.6 ± 28.6	2.23	152	0.3	*CR*	1
872	$13^h29^m55.89^s$	47° 11′52.06”	−4.6	5.7	14.3	54 ± 41	5 ± 6	1.9 ± 1.4	13.4 ± 37.5	1.63	25	0.8	*CR*	0
873	$13^h29^m54.73^s$	47° 11′55.11”	−0.0	2.0	4.7	51 ± 32	7 ± 4	1.7 ± 0.8	25.5 ± 39.8	3.52	3	0.6	*CR*	0
874	$13^h29^m55.02^s$	47° 11′56.30”	−3.7	2.1	5.3	32 ± 0	4 ± 3	0.7 ± 0.5	5.1 ± 8.9	1.66	0	0.3	*CR*	1
875	$13^h29^m56.51^s$	47° 11′42.66”	−3.8	2.1	5.1	64 ± 36	12 ± 8	2.9 ± 2.1	99.6 ± 140.4	7.95	136	0.6	*SA*	0
876	$13^h29^m55.16^s$	47° 11′52.57”	3.6	1.8	4.9	32 ± 0	9 ± 5	0.7 ± 0.5	29.4 ± 28.6	9.01	152	0.6	*CR*	1
877	$13^h29^m55.34^s$	47° 11′52.89”	−4.8	1.9	5.0	46 ± 26	8 ± 5	2.2 ± 1.8	33.6 ± 49.0	3.51	73	0.9	*CR*	0
878	$13^h29^m56.11^s$	47° 12′10.82”	2.6	2.0	5.2	32 ± 0	5 ± 5	1.1 ± 0.8	9.7 ± 17.5	1.95	37	0.2	*SA*	1
879	$13^h29^m55.73^s$	47° 11′42.85”	8.7	7.9	21.8	59 ± 57	2 ± 5	5.4 ± 3.3	3.3 ± 12.7	0.14	31	0.9	*CR*	0
880	$13^h29^m56.49^s$	47° 11′45.10”	5.7	1.5	4.3	32 ± 0	4 ± 2	0.4 ± 0.2	4.8 ± 6.2	3.11	84	0.5	*SA*	1
881	$13^h29^m55.16^s$	47° 12′1.12”	10.3	1.7	4.5	32 ± 0	7 ± 2	0.6 ± 0.2	15.8 ± 11.0	6.00	154	0.5	*CR*	1
882	$13^h29^m55.78^s$	47° 11′45.33”	8.1	10.0	28.0	65 ± 23	15 ± 7	28.7 ± 19.2	150.0 ± 137.9	1.20	156	0.7	*CR*	0
883	$13^h29^m54.94^s$	47° 11′49.04”	17.0	2.0	4.8	35 ± 32	7 ± 4	0.9 ± 1.0	16.5 ± 26.6	4.19	31	0.5	*CR*	0
884	$13^h29^m54.64^s$	47° 11′47.44”	22.5	3.4	8.1	46 ± 12	10 ± 2	4.9 ± 0.7	49.8 ± 24.3	2.31	114	0.5	*CR*	0
885	$13^h29^m56.19^s$	47° 11′50.06”	37.4	1.5	3.6	19 ± 10	8 ± 3	0.8 ± 0.6	11.2 ± 11.5	3.11	143	0.5	*CR*	0
886	$13^h29^m55.84^s$	47° 11′46.84”	60.6	1.5	4.1	32 ± 0	5 ± 2	0.6 ± 0.3	9.1 ± 8.2	3.27	171	0.4	*CR*	1
887	$13^h29^m57.24^s$	47° 11′58.10”	−26.9	3.0	7.4	44 ± 12	10 ± 4	2.6 ± 0.5	45.3 ± 45.2	4.06	155	0.3	*SA*	0
888	$13^h29^m56.83^s$	47° 11′54.73”	−18.8	3.8	9.0	38 ± 15	6 ± 2	2.3 ± 0.3	14.2 ± 10.5	1.39	122	0.6	*SA*	0
889	$13^h29^m56.93^s$	47° 12′6.96”	−31.4	2.7	6.9	86 ± 10	9 ± 1	7.0 ± 0.7	74.3 ± 20.4	2.42	135	0.6	*SA*	0
890	$13^h29^m56.83^s$	47° 12′10.07”	−23.5	2.2	5.5	43 ± 13	6 ± 2	2.0 ± 0.6	13.5 ± 11.1	1.58	2	0.4	*SA*	0
891	$13^h29^m56.53^s$	47° 12′11.59”	−33.9	4.4	10.8	33 ± 11	6 ± 1	2.5 ± 0.3	11.2 ± 5.8	1.04	145	0.7	*SA*	0
892	$13^h29^m57.20^s$	47° 11′51.87”	−16.1	2.6	6.5	32 ± 0	5 ± 3	1.5 ± 0.9	8.2 ± 9.7	1.23	18	0.5	*SA*	1
893	$13^h29^m57.45^s$	47° 11′50.20”	−16.3	3.3	8.3	49 ± 21	3 ± 2	2.9 ± 1.6	4.0 ± 5.9	0.32	15	0.5	*IA*	0
894	$13^h29^m57.24^s$	47° 11′46.15”	−9.1	2.3	5.9	22 ± 12	6 ± 2	1.0 ± 0.2	9.5 ± 6.6	2.10	89	0.9	*SA*	0
895	$13^h29^m54.93^s$	47° 11′49.86”	105.2	1.4	4.8	35 ± 15	6 ± 3	0.6 ± 0.3	15.1 ± 20.4	5.79	90	0.9	*CR*	0
896	$13^h29^m54.94^s$	47° 11′51.36”	125.5	1.3	4.9	24 ± 23	11 ± 5	0.5 ± 0.3	27.7 ± 35.6	11.84	174	1.0	*CR*	0
897	$13^h29^m52.00^s$	47° 11′58.60”	−92.9	1.4	4.1	36 ± 26	6 ± 3	0.4 ± 0.2	13.6 ± 23.4	7.08	22	0.6	*CR*	0
898	$13^h29^m52.05^s$	47° 12′5.13”	−83.8	5.9	16.1	62 ± 20	6 ± 3	8.9 ± 5.5	23.3 ± 25.5	0.60	45	0.3	*CR*	0
899	$13^h29^m51.72^s$	47° 12′5.77”	−82.5	4.2	12.4	54 ± 37	2 ± 0	2.3 ± 5.5	2.5 ± 1.8	0.26	57	0.6	*CR*	1
900	$13^h29^m52.57^s$	47° 11′51.26”	−80.1	1.7	4.4	32 ± 0	3 ± 2	0.3 ± 0.1	2.9 ± 4.1	2.12	19	0.6	*CR*	1
901	$13^h29^m52.39^s$	47° 12′2.85”	−77.4	9.4	24.9	47 ± 31	12 ± 6	6.3 ± 5.5	69.8 ± 70.4	2.53	162	0.6	*CR*	0
902	$13^h29^m51.86^s$	47° 12′4.45”	−80.8	4.4	12.5	32 ± 0	4 ± 7	2.1 ± 4.1	4.3 ± 16.5	0.46	7	0.4	*CR*	1
903	$13^h29^m52.87^s$	47° 12′5.89”	−74.9	4.8	11.6	55 ± 31	5 ± 6	3.3 ± 2.2	16.0 ± 34.4	1.11	27	0.3	*CR*	0
904	$13^h29^m52.78^s$	47° 12′9.21”	−78.9	2.8	7.3	35 ± 40	7 ± 6	1.2 ± 2.7	18.7 ± 45.1	3.62	24	0.9	*CR*	0
905	$13^h29^m52.58^s$	47° 12′11.04”	−78.1	3.0	7.3	49 ± 29	9 ± 7	2.3 ± 2.8	44.8 ± 80.9	4.48	38	0.4	*CR*	0
906	$13^h29^m53.00^s$	47° 12′0.09”	−70.3	4.0	9.4	29 ± 26	12 ± 9	1.5 ± 2.6	40.7 ± 76.8	6.03	41	0.8	*CR*	0
907	$13^h29^m51.73^s$	47° 12′4.72”	−70.7	3.9	10.5	32 ± 0	11 ± 9	0.5 ± 0.6	37.0 ± 64.5	18.09	35	0.3	*CR*	1
908	$13^h29^m52.32^s$	47° 12′5.39”	−73.4	3.1	7.2	40 ± 24	8 ± 5	3.4 ± 3.1	27.0 ± 39.0	1.84	136	0.5	*CR*	0
909	$13^h29^m53.03^s$	47° 12′11.78”	−74.3	5.7	15.3	32 ± 0	17 ± 17	2.5 ± 3.3	98.9 ± 193.7	9.01	61	0.3	*CR*	1
910	$13^h29^m52.75^s$	47° 11′57.73”	−69.5	6.3	14.9	40 ± 22	6 ± 4	5.3 ± 4.6	13.0 ± 20.4	0.56	170	0.6	*CR*	0
911	$13^h29^m52.37^s$	47° 11′58.30”	−68.9	7.5	19.2	32 ± 0	7 ± 9	1.9 ± 1.2	17.8 ± 44.9	2.20	18	0.2	*CR*	1
912	$13^h29^m52.77^s$	47° 12′0.70”	−71.1	5.1	13.0	77 ± 72	10 ± 9	7.6 ± 7.3	85.3 ± 205.7	2.58	55	0.4	*CR*	0
913	$13^h29^m51.97^s$	47° 12′1.64”	−68.6	9.9	24.9	32 ± 0	1 ± 3	13.6 ± 6.7	0.5 ± 2.4	0.01	172	0.2	*CR*	1
914	$13^h29^m53.04^s$	47° 12′4.02”	−68.8	4.4	11.4	61 ± 31	4 ± 5	3.3 ± 4.0	9.9 ± 21.6	0.70	85	0.6	*CR*	0
915	$13^h29^m53.20^s$	47° 12′6.42”	−68.3	7.5	17.4	97 ± 28	5 ± 3	22.0 ± 14.6	24.8 ± 28.6	0.26	60	0.3	*CR*	0
916	$13^h29^m53.67^s$	47° 12′6.55”	−62.2	5.9	14.6	53 ± 20	8 ± 5	6.4 ± 5.7	36.2 ± 44.7	1.29	159	0.3	*CR*	0
917	$13^h29^m53.16^s$	47° 12′9.67”	−71.1	7.5	17.8	52 ± 96	1 ± 2	4.8 ± 8.1	0.6 ± 2.6	0.03	37	0.8	*CR*	0
918	$13^h29^m52.35^s$	47° 12′11.44”	−68.4	3.5	8.8	34 ± 56	8 ± 3	3.3 ± 2.4	20.3 ± 35.6	1.43	67	0.7	*CR*	0
919	$13^h29^m53.32^s$	47° 11′53.83”	−59.4	3.4	7.2	40 ± 23	2 ± 1	1.7 ± 2.3	1.1 ± 1.7	0.15	87	0.6	*CR*	0
920	$13^h29^m53.02^s$	47° 11′52.17”	−54.5	4.9	11.1	67 ± 62	4 ± 4	8.1 ± 3.6	13.2 ± 36.1	0.37	62	0.3	*CR*	0
921	$13^h29^m52.59^s$	47° 11′55.07”	−60.6	4.5	10.5	55 ± 30	2 ± 4	2.4 ± 3.6	3.1 ± 9.8	0.29	86	0.4	*CR*	0
922	$13^h29^m52.91^s$	47° 11′56.07”	−61.1	4.0	9.8	58 ± 39	4 ± 6	2.0 ± 1.3	9.1 ± 26.0	1.02	135	0.8	*CR*	0
923	$13^h29^m51.72^s$	47° 11′57.47”	−55.9	11.0	26.0	58 ± 11	8 ± 2	22.7 ± 7.4	36.6 ± 21.5	0.37	8	0.5	*CR*	0
924	$13^h29^m53.52^s$	47° 11′57.38”	−55.3	4.5	10.0	87 ± 34	6 ± 2	11.6 ± 5.9	37.4 ± 27.4	0.74	105	0.6	*CR*	0
925	$13^h29^m54.26^s$	47° 12′10.58”	−59.2	1.9	4.5	17 ± 18	2 ± 2	0.5 ± 0.5	0.6 ± 1.3	0.31	172	0.7	*CR*	0
926	$13^h29^m52.15^s$	47° 12′11.80”	−56.6	4.2	9.8	36 ± 26	9 ± 8	2.4 ± 1.7	31.6 ± 56.0	3.07	85	0.7	*CR*	0

ID	**RA (J2000)**	**Dec (J2000)**	$\mathbf{V_{LSR}}$	$\mathbf{T_{max}}$	**S/N**	**R**	$\sigma_{\mathbf{v}}$	$\mathbf{L_{CO}}$	$\mathbf{M_{vir}}$	α	**PA**	**b/a**	**Reg**	**Flag**
	h m s	*d ’ ”*	km/s	K		pc	km/s	10^5 K km/s pc^2	10^5 $M_\odot$		deg			
(1)	(2)	(3)	(4)	(5)	(6)	(7)	(8)	(9)	(10)	(11)	(12)	(13)	(14)	(15)
927	$13^h29^m52.35^s$	47°11′55.16”	−48.6	5.6	13.8	44 ± 40	5 ± 3	3.4 ± 3.7	13.1 ± 17.6	0.89	32	0.3	*CR*	0
928	$13^h29^m53.74^s$	47°12′0.61”	−50.2	2.2	5.3	32 ± 0	4 ± 3	0.5 ± 0.7	5.4 ± 8.8	2.32	150	0.4	*CR*	1
929	$13^h29^m54.22^s$	47°12′7.12”	−48.1	5.3	12.1	52 ± 82	11 ± 21	2.5 ± 2.4	69.5 ± 301.8	6.40	92	0.2	*CR*	0
930	$13^h29^m54.26^s$	47°11′43.73”	−44.4	1.5	3.9	11 ± 13	7 ± 3	0.7 ± 0.5	6.2 ± 9.9	2.00	95	0.8	*CR*	0
931	$13^h29^m53.44^s$	47°11′50.65”	−51.2	3.7	8.5	60 ± 33	10 ± 4	2.6 ± 2.7	64.5 ± 90.6	5.78	50	0.8	*CR*	0
932	$13^h29^m53.98^s$	47°11′51.38”	−45.4	2.8	6.7	44 ± 44	5 ± 6	2.0 ± 2.8	11.5 ± 32.3	1.33	112	0.5	*CR*	0
933	$13^h29^m52.58^s$	47°11′52.48”	−47.0	4.6	10.5	32 ± 0	10 ± 6	3.7 ± 1.6	34.8 ± 41.9	2.18	65	3.4	*CR*	1
934	$13^h29^m53.61^s$	47°11′53.21”	−47.0	4.7	11.4	83 ± 25	6 ± 2	6.8 ± 2.3	29.4 ± 15.5	1.00	122	0.4	*CR*	0
935	$13^h29^m52.10^s$	47°11′53.85”	−42.9	6.5	16.4	69 ± 45	11 ± 9	2.2 ± 2.4	90.2 ± 138.1	9.23	30	0.7	*CR*	0
936	$13^h29^m54.34^s$	47°12′4.15”	−47.3	1.8	4.4	29 ± 23	6 ± 4	0.6 ± 0.7	11.6 ± 19.0	4.15	54	0.5	*CR*	0
937	$13^h29^m54.06^s$	47°12′5.73”	−47.0	6.7	14.5	76 ± 37	7 ± 6	10.9 ± 17.5	41.3 ± 67.7	0.87	76	0.2	*CR*	0
938	$13^h29^m54.45^s$	47°12′5.96”	−47.8	3.1	7.1	32 ± 0	1 ± 1	0.4 ± 0.3	0.2 ± 0.6	0.08	165	0.7	*CR*	1
939	$13^h29^m53.29^s$	47°11′47.94”	−43.5	3.6	8.5	41 ± 35	8 ± 5	1.7 ± 2.3	24.7 ± 45.3	3.41	22	0.7	*CR*	0
940	$13^h29^m52.96^s$	47°11′49.21”	−42.7	5.0	12.7	41 ± 29	8 ± 6	4.4 ± 4.9	30.8 ± 43.6	1.59	64	0.8	*CR*	0
941	$13^h29^m53.79^s$	47°11′51.65”	−43.3	3.2	7.1	33 ± 43	6 ± 4	1.7 ± 2.0	12.3 ± 24.2	1.65	140	0.9	*CR*	0
942	$13^h29^m52.27^s$	47°11′52.14”	−41.9	6.2	15.3	56 ± 51	16 ± 13	3.9 ± 10.5	146.9 ± 265.4	8.73	142	0.4	*CR*	0
943	$13^h29^m53.87^s$	47°11′58.59”	−47.5	2.6	5.9	39 ± 22	6 ± 4	2.2 ± 1.9	13.9 ± 21.1	1.48	43	0.9	*CR*	0
944	$13^h29^m54.41^s$	47°12′1.73”	−44.3	4.3	10.5	32 ± 0	4 ± 2	1.4 ± 1.2	4.6 ± 5.7	0.73	61	0.6	*CR*	1
945	$13^h29^m53.87^s$	47°11′48.23”	−36.0	4.9	11.4	32 ± 0	10 ± 9	3.6 ± 5.1	34.3 ± 59.7	2.19	152	0.2	*CR*	1
946	$13^h29^m53.50^s$	47°11′47.96”	−33.4	1.8	4.3	32 ± 0	12 ± 7	0.7 ± 1.0	49.0 ± 58.0	17.12	179	0.3	*CR*	1
947	$13^h29^m52.29^s$	47°11′49.80”	−37.2	4.6	11.6	49 ± 24	11 ± 6	3.1 ± 2.6	62.9 ± 89.9	4.66	159	0.4	*CR*	0
948	$13^h29^m54.32^s$	47°12′9.08”	−36.2	1.8	4.2	49 ± 28	3 ± 3	1.1 ± 1.1	5.6 ± 11.1	1.13	163	0.8	*CR*	0
949	$13^h29^m53.79^s$	47°11′45.36”	−34.1	4.4	11.3	59 ± 26	4 ± 4	3.2 ± 2.4	10.4 ± 21.3	0.76	51	0.3	*CR*	0
950	$13^h29^m54.15^s$	47°11′49.55”	−33.9	5.3	13.1	59 ± 48	3 ± 4	2.6 ± 5.0	7.1 ± 16.1	0.61	122	0.5	*CR*	0
951	$13^h29^m51.93^s$	47°11′51.66”	−30.4	6.8	16.6	82 ± 55	11 ± 11	9.7 ± 5.6	99.0 ± 250.9	2.33	162	0.5	*CR*	0
952	$13^h29^m53.29^s$	47°11′43.71”	−23.7	4.2	10.4	93 ± 23	12 ± 2	7.9 ± 2.9	149.0 ± 80.0	4.35	79	0.4	*CR*	0
953	$13^h29^m53.98^s$	47°11′46.09”	−27.7	4.1	11.0	22 ± 18	10 ± 7	1.6 ± 2.6	21.1 ± 37.7	3.08	44	0.6	*CR*	0
954	$13^h29^m54.33^s$	47°11′46.56”	−26.2	5.8	14.9	78 ± 22	8 ± 3	8.6 ± 5.8	46.1 ± 39.1	1.23	162	0.8	*CR*	0
955	$13^h29^m52.44^s$	47°11′46.69”	−23.3	3.1	8.0	45 ± 16	16 ± 5	6.2 ± 2.9	120.0 ± 112.6	4.47	10	0.6	*CR*	0
956	$13^h29^m52.60^s$	47°11′52.05”	−26.3	2.3	5.5	18 ± 24	6 ± 6	1.0 ± 1.0	5.7 ± 16.1	1.29	144	1.0	*CR*	0
957	$13^h29^m54.46^s$	47°12′7.24”	−25.6	1.6	3.9	34 ± 22	7 ± 6	0.7 ± 0.5	19.3 ± 33.2	6.75	58	0.6	*CR*	0
958	$13^h29^m53.89^s$	47°11′43.17”	−24.4	3.5	8.8	37 ± 21	3 ± 3	0.8 ± 0.7	3.0 ± 5.8	0.83	120	0.7	*CR*	0
959	$13^h29^m53.60^s$	47°11′43.77”	−22.8	2.6	6.7	60 ± 23	2 ± 3	0.7 ± 0.7	2.5 ± 7.9	0.78	128	0.6	*CR*	0
960	$13^h29^m52.59^s$	47°11′44.93”	−10.1	3.3	7.7	24 ± 14	19 ± 13	3.8 ± 4.5	88.8 ± 160.7	5.39	129	0.5	*CR*	0
961	$13^h29^m52.61^s$	47°11′49.04”	−22.5	1.8	4.5	32 ± 0	2 ± 0	0.3 ± 0.2	1.5 ± 0.0	1.12	4	0.4	*CR*	1
962	$13^h29^m52.07^s$	47°11′50.25”	−23.9	3.7	8.9	48 ± 45	5 ± 7	1.8 ± 0.6	14.9 ± 44.5	1.93	177	2.2	*CR*	0
963	$13^h29^m54.43^s$	47°12′9.78”	−20.9	2.0	5.0	32 ± 0	4 ± 3	0.4 ± 0.4	5.7 ± 9.1	3.20	159	0.7	*CR*	1
964	$13^h29^m54.08^s$	47°11′42.26”	−10.8	4.9	12.5	32 ± 0	10 ± 5	3.6 ± 1.8	32.6 ± 30.4	2.07	98	0.5	*CR*	1
965	$13^h29^m54.01^s$	47°11′49.76”	−12.8	1.8	3.8	32 ± 0	5 ± 6	0.2 ± 0.2	7.5 ± 17.6	8.49	158	0.3	*CR*	1
966	$13^h29^m52.94^s$	47°11′48.91”	−6.1	2.0	5.4	32 ± 0	6 ± 5	1.6 ± 1.8	12.3 ± 18.3	1.73	140	0.9	*CR*	1
967	$13^h29^m53.02^s$	47°11′44.38”	8.0	1.6	3.9	32 ± 0	21 ± 11	1.6 ± 0.6	138.6 ± 143.7	20.04	106	0.6	*CR*	1
968	$13^h29^m52.13^s$	47°11′45.87”	3.4	3.0	7.0	47 ± 32	7 ± 6	1.6 ± 2.3	23.1 ± 49.2	3.40	132	0.6	*CR*	0
969	$13^h29^m51.89^s$	47°11′46.74”	2.8	4.0	9.7	43 ± 29	4 ± 3	1.5 ± 1.2	7.8 ± 15.2	1.15	101	0.6	*CR*	0
970	$13^h29^m51.60^s$	47°11′43.15”	14.4	6.3	14.6	28 ± 19	5 ± 4	4.4 ± 2.8	8.2 ± 11.6	0.42	18	0.8	*CR*	0
971	$13^h29^m52.36^s$	47°11′45.18”	14.5	2.8	6.5	57 ± 34	12 ± 7	1.6 ± 1.7	80.7 ± 134.5	11.83	87	0.8	*CR*	0
972	$13^h29^m51.97^s$	47°11′43.12”	23.6	4.4	10.9	50 ± 37	7 ± 4	2.3 ± 1.9	28.6 ± 41.3	2.87	127	0.4	*CR*	0
973	$13^h29^m52.67^s$	47°11′42.80”	31.5	4.6	11.3	31 ± 17	20 ± 12	4.1 ± 4.0	131.1 ± 180.5	7.38	168	0.4	*CR*	0
974	$13^h29^m54.37^s$	47°11′44.64”	30.4	1.9	4.5	32 ± 0	2 ± 2	0.4 ± 0.4	1.5 ± 2.9	0.75	160	0.3	*CR*	1
975	$13^h29^m52.63^s$	47°11′42.31”	74.3	3.5	9.4	19 ± 26	11 ± 8	1.2 ± 0.5	23.0 ± 57.7	4.47	95	1.0	*CR*	0
976	$13^h29^m52.35^s$	47°11′42.79”	68.4	1.5	3.7	32 ± 0	6 ± 6	0.4 ± 0.4	11.0 ± 23.8	6.71	38	0.8	*CR*	1
977	$13^h29^m52.80^s$	47°11′42.85”	94.6	1.6	5.9	32 ± 0	6 ± 3	0.5 ± 0.6	11.0 ± 13.2	4.81	25	0.7	*CR*	1
978	$13^h29^m52.63^s$	47°11′42.08”	104.2	2.5	9.0	22 ± 37	16 ± 16	1.5 ± 2.3	58.7 ± 198.2	8.99	89	1.2	*CR*	0
979	$13^h29^m54.08^s$	47°11′42.97”	−59.6	2.2	5.4	32 ± 0	5 ± 3	0.5 ± 0.1	9.4 ± 9.0	4.22	24	0.9	*CR*	1
980	$13^h29^m54.22^s$	47°11′52.24”	−17.2	2.1	5.0	32 ± 0	4 ± 2	0.7 ± 0.2	6.1 ± 5.7	2.06	32	0.4	*CR*	1
981	$13^h29^m53.39^s$	47°12′1.27”	41.0	2.0	4.6	32 ± 0	3 ± 2	0.4 ± 0.2	3.6 ± 4.6	1.87	14	0.9	*CR*	1
982	$13^h29^m52.83^s$	47°12′1.78”	71.0	1.9	5.5	32 ± 0	3 ± 1	0.6 ± 0.1	2.7 ± 2.7	1.08	99	0.4	*CR*	1
983	$13^h29^m49.61^s$	47°11′49.71”	−104.4	2.1	6.5	32 ± 0	7 ± 2	0.8 ± 0.2	17.9 ± 11.4	4.92	160	0.5	*CR*	1
984	$13^h29^m51.07^s$	47°12′1.41”	−97.9	1.5	4.8	32 ± 0	5 ± 5	0.2 ± 0.1	7.8 ± 16.1	9.16	84	0.4	*CR*	1
985	$13^h29^m51.21^s$	47°11′59.00”	−77.2	10.7	28.5	39 ± 41	11 ± 18	5.4 ± 4.6	48.8 ± 157.0	2.09	176	0.4	*CR*	0
986	$13^h29^m51.47^s$	47°12′0.46”	−66.0	16.5	38.6	50 ± 15	7 ± 3	12.4 ± 14.2	26.5 ± 22.3	0.49	160	0.4	*CR*	0

ID (1)	**RA (J2000)** *h m s* (2)	**Dec (J2000)** *d ’ ”* (3)	$\mathbf{V_{LSR}}$ km/s (4)	$\mathbf{T_{max}}$ K (5)	**S/N** (6)	**R** pc (7)	$\sigma_\mathbf{v}$ km/s (8)	$\mathbf{L_{CO}}$ 10^5 K km/s pc^2 (9)	$\mathbf{M_{vir}}$ 10^5 $M_\odot$ (10)	α (11)	**PA** deg (12)	**b/a** (13)	**Reg** (14)	**Flag** (15)
987	$13^h29^m51.56^s$	47°11′51.21”	−62.1	1.6	4.0	32 ± 0	6 ± 5	0.2 ± 0.2	10.1 ± 19.0	11.40	6	1.0	*CR*	1
988	$13^h29^m51.51^s$	47°12′8.71”	−59.5	3.2	7.8	55 ± 20	5 ± 2	2.8 ± 2.6	17.1 ± 18.1	1.40	34	0.4	*CR*	0
989	$13^h29^m50.67^s$	47°11′55.83”	−49.2	11.6	26.1	57 ± 16	8 ± 3	21.3 ± 8.5	35.3 ± 23.3	0.38	138	0.5	*CR*	0
990	$13^h29^m50.91^s$	47°11′58.40”	−52.5	9.3	22.8	34 ± 30	10 ± 6	7.0 ± 9.9	33.6 ± 48.1	1.10	7	0.7	*CR*	0
991	$13^h29^m50.73^s$	47°11′59.47”	−54.7	5.0	12.1	32 ± 0	5 ± 10	2.1 ± 1.1	8.9 ± 34.7	0.95	172	0.4	*CR*	1
992	$13^h29^m51.20^s$	47°12′3.19”	−56.4	2.4	5.8	49 ± 50	9 ± 8	2.7 ± 3.1	45.0 ± 104.1	3.87	139	1.0	*CR*	0
993	$13^h29^m50.40^s$	47°11′45.06”	−56.1	1.8	4.4	32 ± 0	4 ± 3	0.6 ± 0.4	4.2 ± 8.2	1.70	8	0.3	*CR*	1
994	$13^h29^m51.29^s$	47°11′55.92”	−43.9	8.6	20.1	91 ± 19	14 ± 4	22.1 ± 12.2	174.1 ± 109.5	1.81	161	0.6	*CR*	0
995	$13^h29^m50.62^s$	47°12′1.61”	−48.7	2.1	4.6	11 ± 17	4 ± 3	0.7 ± 0.6	2.1 ± 4.3	0.72	145	0.9	*CR*	0
996	$13^h29^m51.15^s$	47°12′11.11”	−45.7	5.8	13.6	36 ± 10	6 ± 1	4.8 ± 0.9	12.8 ± 5.3	0.62	67	0.7	*IA*	0
997	$13^h29^m50.54^s$	47°11′53.71”	−40.1	6.6	16.8	45 ± 39	9 ± 11	2.4 ± 4.0	39.3 ± 111.3	3.78	141	0.5	*CR*	0
998	$13^h29^m50.82^s$	47°12′0.65”	−39.6	4.5	9.8	44 ± 50	6 ± 9	2.6 ± 5.6	17.8 ± 45.5	1.55	61	1.0	*CR*	0
999	$13^h29^m50.17^s$	47°11′51.17”	−31.7	13.2	33.5	90 ± 17	7 ± 1	39.4 ± 8.4	50.2 ± 20.3	0.29	29	0.6	*CR*	0
1000	$13^h29^m50.43^s$	47°11′52.64”	−31.8	7.2	16.5	32 ± 0	9 ± 12	1.2 ± 2.0	28.2 ± 73.3	5.60	139	0.3	*CR*	1
1001	$13^h29^m50.85^s$	47°11′53.56”	−31.2	5.6	14.1	67 ± 54	12 ± 14	5.0 ± 10.0	103.1 ± 267.9	4.75	29	0.5	*CR*	0
1002	$13^h29^m50.67^s$	47°12′2.30”	−30.9	3.7	8.9	61 ± 32	4 ± 5	3.9 ± 4.0	12.6 ± 28.6	0.75	10	0.3	*CR*	0
1003	$13^h29^m50.80^s$	47°12′6.29”	−37.5	2.0	5.4	32 ± 0	7 ± 3	0.8 ± 0.3	14.8 ± 14.2	4.52	31	0.5	*CR*	1
1004	$13^h29^m50.12^s$	47°11′42.23”	−24.9	10.4	27.2	52 ± 21	7 ± 4	16.1 ± 8.6	24.2 ± 30.3	0.35	16	0.4	*CR*	0
1005	$13^h29^m51.10^s$	47°11′53.23”	−25.7	5.4	13.5	77 ± 54	5 ± 11	5.3 ± 14.5	23.1 ± 89.7	1.01	153	0.8	*CR*	0
1006	$13^h29^m50.16^s$	47°11′55.90”	−34.5	2.0	4.8	33 ± 13	6 ± 3	2.0 ± 0.9	10.7 ± 11.7	1.23	136	0.7	*CR*	0
1007	$13^h29^m50.15^s$	47°12′0.01”	−28.2	2.6	6.1	22 ± 18	4 ± 3	0.6 ± 0.8	3.2 ± 7.4	1.26	173	0.7	*CR*	0
1008	$13^h29^m50.28^s$	47°12′3.37”	−26.6	3.1	8.2	67 ± 33	11 ± 8	5.9 ± 7.8	78.2 ± 141.1	3.04	20	0.1	*SA*	0
1009	$13^h29^m51.12^s$	47°11′45.00”	−24.5	2.0	5.3	32 ± 0	5 ± 6	0.2 ± 0.3	6.8 ± 16.8	6.37	28	1.1	*CR*	1
1010	$13^h29^m49.96^s$	47°11′47.16”	−20.5	3.1	7.5	32 ± 0	2 ± 1	0.5 ± 0.1	2.0 ± 2.3	0.99	9	0.8	*CR*	1
1011	$13^h29^m49.94^s$	47°11′49.48”	−21.1	5.0	13.5	31 ± 31	8 ± 6	3.5 ± 4.7	22.5 ± 49.9	1.45	143	0.6	*CR*	0
1012	$13^h29^m51.56^s$	47°11′51.94”	−23.2	7.0	17.9	55 ± 26	7 ± 6	8.5 ± 12.4	28.9 ± 44.0	0.78	178	0.3	*CR*	0
1013	$13^h29^m50.65^s$	47°11′52.96”	−21.9	7.6	17.5	45 ± 25	8 ± 6	4.0 ± 5.9	29.6 ± 53.6	1.69	162	0.4	*CR*	0
1014	$13^h29^m50.42^s$	47°11′59.11”	−21.2	2.8	7.7	32 ± 0	10 ± 7	1.0 ± 1.0	30.0 ± 43.0	6.79	9	0.4	*CR*	1
1015	$13^h29^m49.78^s$	47°11′48.28”	−13.0	3.8	9.7	41 ± 69	8 ± 13	2.2 ± 5.0	29.2 ± 104.3	3.06	144	0.9	*CR*	0
1016	$13^h29^m51.16^s$	47°11′49.94”	−15.8	7.7	19.1	60 ± 32	6 ± 3	11.7 ± 11.1	19.6 ± 23.9	0.38	126	0.5	*CR*	0
1017	$13^h29^m49.88^s$	47°11′59.85”	−16.7	2.7	6.9	62 ± 23	13 ± 6	2.9 ± 1.4	106.1 ± 135.4	8.28	69	0.8	*SA*	0
1018	$13^h29^m50.92^s$	47°11′47.62”	−9.5	6.4	17.6	53 ± 53	14 ± 10	10.4 ± 15.1	105.3 ± 176.8	2.33	1	0.3	*CR*	0
1019	$13^h29^m50.47^s$	47°11′51.02”	−12.2	5.2	14.5	32 ± 0	8 ± 6	2.0 ± 2.0	20.3 ± 32.0	2.34	37	0.8	*CR*	1
1020	$13^h29^m49.69^s$	47°11′51.74”	−13.7	5.1	13.0	32 ± 0	9 ± 7	2.6 ± 2.4	27.2 ± 42.8	2.42	48	0.4	*CR*	1
1021	$13^h29^m50.05^s$	47°11′58.28”	−13.0	2.2	5.6	32 ± 0	7 ± 5	0.8 ± 0.9	16.2 ± 22.7	4.88	29	0.5	*CR*	1
1022	$13^h29^m50.34^s$	47°11′48.08”	−6.3	5.0	12.6	39 ± 38	5 ± 3	5.6 ± 7.2	11.5 ± 22.9	0.47	129	0.6	*CR*	0
1023	$13^h29^m50.59^s$	47°11′47.83”	−6.4	2.8	7.5	30 ± 30	7 ± 6	2.1 ± 1.3	17.4 ± 31.5	1.90	119	0.6	*CR*	0
1024	$13^h29^m51.44^s$	47°11′48.33”	−7.4	4.4	12.0	45 ± 38	5 ± 6	2.2 ± 1.5	12.7 ± 39.5	1.30	138	0.4	*CR*	0
1025	$13^h29^m51.15^s$	47°11′54.14”	−1.4	1.8	4.6	32 ± 0	9 ± 11	0.9 ± 0.5	26.2 ± 65.8	6.85	106	0.2	*CR*	1
1026	$13^h29^m50.83^s$	47°11′46.01”	−4.0	7.4	19.4	50 ± 28	11 ± 7	12.2 ± 11.5	66.2 ± 94.4	1.25	66	0.5	*CR*	0
1027	$13^h29^m50.48^s$	47°11′45.41”	−1.6	4.5	12.1	47 ± 21	7 ± 3	5.2 ± 3.7	26.8 ± 24.1	1.19	111	0.5	*CR*	0
1028	$13^h29^m49.62^s$	47°11′49.46”	−5.2	3.3	8.4	50 ± 45	4 ± 7	1.3 ± 1.6	7.8 ± 25.4	1.37	24	1.2	*CR*	0
1029	$13^h29^m50.56^s$	47°11′52.16”	5.0	2.5	5.5	32 ± 0	2 ± 1	0.4 ± 0.3	1.0 ± 1.3	0.55	169	0.8	*CR*	1
1030	$13^h29^m50.78^s$	47°11′43.14”	8.0	6.6	15.8	42 ± 21	12 ± 8	9.7 ± 6.2	64.3 ± 80.9	1.53	143	0.7	*CR*	0
1031	$13^h29^m50.59^s$	47°11′43.79”	5.8	6.2	14.5	32 ± 0	7 ± 4	3.2 ± 3.8	18.5 ± 18.2	1.35	125	0.2	*CR*	1
1032	$13^h29^m51.42^s$	47°11′45.28”	9.7	6.2	15.7	55 ± 22	6 ± 3	6.6 ± 3.6	23.1 ± 19.9	0.80	30	0.4	*CR*	0
1033	$13^h29^m51.34^s$	47°11′51.49”	19.8	2.5	6.3	32 ± 0	2 ± 3	0.2 ± 0.1	1.6 ± 3.6	1.81	5	0.7	*CR*	1
1034	$13^h29^m50.41^s$	47°11′50.61”	32.9	2.8	6.9	64 ± 15	14 ± 4	4.1 ± 0.9	132.4 ± 86.2	7.42	79	0.8	*CR*	0
1035	$13^h29^m50.86^s$	47°11′42.66”	46.8	1.8	4.4	20 ± 24	5 ± 3	1.0 ± 1.0	5.0 ± 11.1	1.17	104	0.7	*CR*	0
1036	$13^h29^m51.14^s$	47°12′8.72”	−99.8	1.5	5.0	32 ± 0	2 ± 1	0.4 ± 0.2	1.5 ± 2.0	0.92	19	0.4	*CR*	1
1037	$13^h29^m50.22^s$	47°12′11.96”	−53.9	1.8	4.6	32 ± 0	3 ± 3	0.2 ± 0.2	3.7 ± 6.7	4.07	155	0.6	*IA*	1
1038	$13^h29^m49.10^s$	47°11′59.90”	−34.9	3.3	8.1	15 ± 14	4 ± 5	1.8 ± 2.7	3.1 ± 7.2	0.39	159	0.6	*IA*	0
1039	$13^h29^m48.91^s$	47°11′59.66”	−30.8	2.9	7.4	32 ± 0	2 ± 4	1.0 ± 0.5	2.1 ± 6.1	0.47	143	0.3	*IA*	1
1040	$13^h29^m48.82^s$	47°11′57.75”	−27.5	2.9	7.3	56 ± 46	2 ± 0	1.1 ± 2.9	2.6 ± 2.1	0.55	157	0.5	*IA*	1
1041	$13^h29^m48.83^s$	47°12′1.68”	−12.4	1.7	4.6	42 ± 13	6 ± 2	1.4 ± 0.4	15.3 ± 12.0	2.53	166	0.3	*IA*	0
1042	$13^h29^m51.36^s$	47°12′5.56”	−49.8	2.8	6.5	32 ± 0	4 ± 2	1.3 ± 0.3	5.1 ± 5.1	0.88	70	0.5	*CR*	1
1043	$13^h29^m49.18^s$	47°12′5.18”	−46.2	2.1	5.3	32 ± 0	6 ± 4	0.8 ± 0.7	10.8 ± 16.3	3.15	154	0.8	*IA*	1
1044	$13^h29^m50.21^s$	47°12′10.15”	−38.2	3.0	7.5	62 ± 16	7 ± 3	3.2 ± 1.2	31.1 ± 26.2	2.21	4	1.0	*IA*	0
1045	$13^h29^m49.36^s$	47°12′4.16”	−28.7	4.5	11.7	80 ± 16	7 ± 1	7.8 ± 1.4	35.3 ± 13.9	1.05	148	0.5	*IA*	0
1046	$13^h29^m49.72^s$	47°12′5.51”	−34.5	1.8	4.5	20 ± 17	8 ± 6	0.5 ± 0.5	12.5 ± 29.9	5.88	34	0.7	*IA*	0

ID (1)	RA (J2000) h m s (2)	Dec (J2000) d ’ ” (3)	V_{LSR} km/s (4)	T_{max} K (5)	S/N (6)	R pc (7)	σ_v km/s (8)	L_{CO} 10^5 K km/s pc^2 (9)	M_{vir} 10^5 $M_\odot$ (10)	α (11)	PA deg (12)	b/a (13)	Reg (14)	Flag (15)
1047	$13^h29^m50.38^s$	47°12′8.17”	−35.7	2.2	5.1	39 ± 28	3 ± 4	0.7 ± 0.7	4.9 ± 11.6	1.53	149	0.6	*IA*	0
1048	$13^h29^m49.82^s$	47°12′9.22”	−35.9	3.2	7.9	96 ± 17	5 ± 2	6.0 ± 1.0	22.3 ± 19.6	0.85	140	0.5	*IA*	0
1049	$13^h29^m48.99^s$	47°12′4.78”	−28.1	2.5	6.7	32 ± 0	7 ± 3	0.9 ± 0.2	15.0 ± 11.6	3.76	178	0.8	*IA*	1
1050	$13^h29^m49.33^s$	47°12′6.46”	−30.2	2.5	6.2	54 ± 42	9 ± 9	1.2 ± 1.5	49.2 ± 93.3	9.43	155	0.9	*IA*	0
1051	$13^h29^m49.70^s$	47°12′4.26”	−16.9	1.5	3.9	32 ± 0	5 ± 4	0.7 ± 0.6	8.9 ± 12.3	2.74	107	0.6	*IA*	1
1052	$13^h29^m48.65^s$	47°11′48.21”	−18.6	2.7	6.8	63 ± 13	5 ± 1	2.3 ± 0.4	14.9 ± 8.8	1.48	126	0.6	*IA*	0
1053	$13^h29^m49.09^s$	47°12′9.67”	−34.6	2.1	5.3	60 ± 18	8 ± 2	2.2 ± 0.8	37.1 ± 23.1	3.90	76	0.9	*IA*	0
1054	$13^h29^m48.82^s$	47°12′9.96”	−24.7	2.1	5.2	32 ± 0	3 ± 2	0.3 ± 0.2	2.5 ± 3.0	1.75	119	0.8	*IA*	1
1055	$13^h29^m48.84^s$	47°12′11.73”	−19.1	1.6	4.0	32 ± 0	4 ± 3	1.0 ± 0.5	4.6 ± 6.7	1.10	143	0.3	*IA*	1
1056	$13^h29^m49.35^s$	47°11′42.11”	−5.3	2.2	5.4	32 ± 0	10 ± 7	0.6 ± 0.8	33.8 ± 44.3	12.59	153	0.3	*SA*	1
1057	$13^h29^m49.70^s$	47°11′42.70”	2.5	2.8	6.9	26 ± 14	11 ± 4	2.4 ± 0.8	35.8 ± 30.8	3.43	74	0.9	*CR*	0
1058	$13^h29^m49.78^s$	47°11′44.93”	−3.1	2.6	6.8	32 ± 0	7 ± 6	1.2 ± 0.7	16.5 ± 27.8	3.28	132	0.5	*CR*	1
1059	$13^h29^m49.45^s$	47°11′44.07”	5.6	3.1	7.6	77 ± 28	11 ± 3	3.4 ± 1.5	91.7 ± 75.8	6.12	138	0.4	*SA*	0
1060	$13^h29^m49.56^s$	47°11′45.83”	16.6	1.9	5.0	47 ± 28	5 ± 4	1.5 ± 0.6	11.5 ± 18.7	1.80	178	0.4	*CR*	0
1061	$13^h29^m49.69^s$	47°11′47.42”	22.7	1.8	4.4	32 ± 0	8 ± 6	0.3 ± 0.3	21.4 ± 33.4	15.75	69	0.5	*CR*	1
1062	$13^h29^m48.64^s$	47°11′48.22”	12.6	2.0	4.7	49 ± 10	9 ± 4	2.1 ± 0.6	42.0 ± 41.1	4.59	100	0.5	*IA*	0
1063	$13^h29^m48.71^s$	47°11′48.17”	39.9	1.8	4.6	19 ± 12	7 ± 2	1.1 ± 0.4	9.3 ± 6.7	1.99	20	0.7	*IA*	0
1064	$13^h29^m49.80^s$	47°12′10.33”	89.6	1.3	4.3	32 ± 0	3 ± 2	0.3 ± 0.1	2.2 ± 3.9	1.95	149	1.1	*IA*	1
1065	$13^h29^m50.89^s$	47°11′45.80”	125.3	1.5	5.7	32 ± 0	2 ± 2	0.4 ± 0.2	1.9 ± 2.9	1.02	128	0.6	*CR*	1
1066	$13^h29^m46.15^s$	47°12′7.09”	−55.5	3.1	7.3	32 ± 0	6 ± 5	1.4 ± 0.6	10.6 ± 18.2	1.79	174	0.6	*SA*	1
1067	$13^h29^m46.75^s$	47°12′11.57”	−56.5	1.9	4.8	32 ± 0	6 ± 8	0.6 ± 1.1	13.6 ± 35.8	5.23	117	0.4	*SA*	1
1068	$13^h29^m45.79^s$	47°12′8.88”	−54.0	5.3	11.4	61 ± 20	5 ± 4	6.8 ± 5.7	13.9 ± 23.1	0.47	120	0.6	*SA*	0
1069	$13^h29^m46.16^s$	47°12′10.46”	−54.0	5.6	12.9	64 ± 23	6 ± 4	9.1 ± 7.3	27.8 ± 41.4	0.70	154	0.3	*SA*	0
1070	$13^h29^m46.72^s$	47°12′8.20”	−37.5	2.3	5.1	56 ± 13	5 ± 2	1.9 ± 0.6	15.5 ± 11.4	1.87	117	0.7	*SA*	0
1071	$13^h29^m47.52^s$	47°12′10.37”	−29.2	3.5	8.2	55 ± 20	3 ± 2	3.1 ± 1.2	4.9 ± 7.8	0.36	162	0.6	*IA*	0
1072	$13^h29^m46.25^s$	47°12′8.73”	−25.3	5.2	10.5	32 ± 18	8 ± 4	4.1 ± 3.0	22.8 ± 25.4	1.28	172	0.5	*SA*	0
1073	$13^h29^m46.43^s$	47°11′54.29”	−18.3	1.9	4.5	32 ± 0	3 ± 5	0.5 ± 0.2	4.0 ± 11.3	1.77	64	0.8	*IA*	1
1074	$13^h29^m45.79^s$	47°11′59.05”	−22.2	2.3	5.9	32 ± 0	7 ± 3	0.8 ± 0.2	16.7 ± 15.8	4.99	93	0.9	*SA*	1
1075	$13^h29^m45.89^s$	47°12′4.18”	−24.1	5.2	12.4	112 ± 19	4 ± 2	11.3 ± 2.6	16.6 ± 14.8	0.34	123	0.3	*SA*	0
1076	$13^h29^m46.54^s$	47°12′9.14”	−23.1	3.5	8.5	32 ± 0	3 ± 6	2.1 ± 4.5	2.6 ± 11.5	0.29	144	0.2	*SA*	1
1077	$13^h29^m46.96^s$	47°12′9.80”	−20.4	2.3	5.8	77 ± 13	7 ± 2	3.0 ± 0.6	34.4 ± 18.0	2.64	165	0.4	*SA*	0
1078	$13^h29^m46.01^s$	47°11′52.40”	−11.2	4.3	10.5	74 ± 22	7 ± 2	10.6 ± 3.1	40.7 ± 25.9	0.88	128	0.2	*IA*	0
1079	$13^h29^m45.70^s$	47°11′55.12”	−9.4	2.1	4.8	57 ± 31	8 ± 6	1.2 ± 0.9	34.4 ± 60.1	6.53	68	0.7	*IA*	0
1080	$13^h29^m45.77^s$	47°11′49.01”	1.3	2.5	6.6	32 ± 0	1 ± 2	0.5 ± 0.4	0.4 ± 1.7	0.18	108	0.3	*IA*	1
1081	$13^h29^m47.69^s$	47°11′52.39”	−93.0	2.5	7.4	32 ± 0	4 ± 2	0.6 ± 0.1	6.0 ± 5.0	2.35	123	0.7	*IA*	1
1082	$13^h29^m46.55^s$	47°12′6.57”	−63.6	2.5	6.1	25 ± 10	6 ± 2	1.4 ± 0.3	9.9 ± 7.8	1.58	6	0.8	*SA*	0
1083	$13^h29^m48.33^s$	47°12′2.35”	−33.5	2.3	6.1	32 ± 0	5 ± 2	0.7 ± 0.2	7.1 ± 7.6	2.42	166	0.4	*IA*	1
1084	$13^h29^m48.50^s$	47°12′1.66”	−19.7	1.6	4.2	32 ± 0	4 ± 4	0.7 ± 0.5	6.0 ± 12.0	1.99	84	0.7	*IA*	1
1085	$13^h29^m48.34^s$	47°11′51.87”	−11.1	2.4	5.7	49 ± 28	7 ± 3	2.5 ± 1.1	23.7 ± 22.2	2.19	101	0.5	*IA*	0
1086	$13^h29^m48.47^s$	47°11′54.31”	0.4	2.3	5.7	32 ± 0	6 ± 3	0.5 ± 0.1	10.9 ± 12.8	5.07	67	0.8	*IA*	1
1087	$13^h29^m48.06^s$	47°11′43.24”	−35.3	1.4	3.7	32 ± 0	4 ± 3	0.5 ± 0.5	6.7 ± 9.1	3.18	163	0.6	*IA*	1
1088	$13^h29^m48.16^s$	47°11′43.36”	−23.1	1.7	4.6	32 ± 0	5 ± 6	0.4 ± 0.2	7.1 ± 18.8	4.25	138	1.1	*IA*	1
1089	$13^h29^m48.38^s$	47°11′45.03”	−21.3	2.1	5.2	32 ± 0	4 ± 3	1.0 ± 0.8	4.1 ± 5.9	0.98	156	0.5	*IA*	1
1090	$13^h29^m48.31^s$	47°11′44.06”	−12.8	2.0	4.8	32 ± 19	4 ± 7	0.5 ± 0.6	5.5 ± 17.0	2.56	61	0.5	*IA*	0
1091	$13^h29^m48.18^s$	47°11′46.00”	−5.9	1.7	4.7	35 ± 25	3 ± 3	0.7 ± 0.6	2.3 ± 5.4	0.75	92	0.6	*IA*	0
1092	$13^h29^m48.42^s$	47°11′44.43”	−1.9	1.5	3.8	16 ± 27	7 ± 4	0.4 ± 0.4	9.0 ± 16.8	5.03	130	0.9	*IA*	0
1093	$13^h29^m48.51^s$	47°11′57.73”	−33.4	2.1	4.9	32 ± 0	4 ± 3	0.5 ± 0.3	6.6 ± 7.4	3.19	145	0.8	*IA*	1
1094	$13^h29^m48.44^s$	47°12′6.10”	−29.8	2.2	5.9	32 ± 0	6 ± 3	0.6 ± 0.3	11.0 ± 11.8	3.92	168	0.6	*IA*	1
1095	$13^h29^m47.03^s$	47°11′50.35”	−25.2	2.4	6.6	32 ± 0	3 ± 4	0.7 ± 0.5	3.1 ± 7.2	0.99	109	0.5	*IA*	1
1096	$13^h29^m47.09^s$	47°11′49.16”	−10.9	2.1	5.2	32 ± 0	6 ± 3	0.8 ± 0.3	10.5 ± 11.8	2.85	81	0.3	*IA*	1
1097	$13^h29^m47.41^s$	47°11′52.55”	−16.2	2.8	6.8	84 ± 20	8 ± 2	7.0 ± 1.2	56.2 ± 35.7	1.84	145	0.4	*IA*	0
1098	$13^h29^m46.61^s$	47°11′55.78”	−11.7	2.9	7.1	54 ± 13	8 ± 2	2.0 ± 0.3	40.0 ± 21.2	4.67	89	0.4	*IA*	0
1099	$13^h29^m44.54^s$	47°12′0.44”	−100.2	1.9	5.2	26 ± 17	11 ± 4	0.8 ± 0.3	29.5 ± 32.6	8.15	152	1.0	*SA*	0
1100	$13^h29^m44.44^s$	47°11′46.27”	−75.9	1.4	3.8	32 ± 0	4 ± 6	0.4 ± 0.4	6.1 ± 16.0	3.84	104	0.7	*SA*	1
1101	$13^h29^m44.55^s$	47°11′50.02”	−69.6	1.9	4.7	32 ± 0	6 ± 5	0.3 ± 0.4	12.1 ± 20.6	9.56	9	0.6	*SA*	1
1102	$13^h29^m45.05^s$	47°12′3.48”	−63.2	2.6	6.3	20 ± 20	4 ± 5	0.9 ± 1.2	3.8 ± 10.0	0.95	13	0.6	*SA*	0
1103	$13^h29^m45.46^s$	47°12′4.96”	−52.3	4.5	11.2	88 ± 38	9 ± 4	8.9 ± 9.7	82.0 ± 66.8	2.11	148	0.3	*SA*	0
1104	$13^h29^m44.09^s$	47°11′43.05”	−41.3	2.4	5.1	39 ± 17	8 ± 3	1.2 ± 1.3	27.1 ± 28.0	4.99	118	0.4	*SA*	0
1105	$13^h29^m45.03^s$	47°11′47.40”	−43.9	2.0	4.6	32 ± 0	5 ± 2	0.3 ± 0.1	6.7 ± 6.5	5.06	21	1.0	*SA*	1
1106	$13^h29^m44.70^s$	47°11′47.70”	−44.3	3.1	6.6	39 ± 24	5 ± 4	1.8 ± 1.0	9.9 ± 15.4	1.24	143	0.7	*SA*	0

ID	**RA (J2000)** *h m s*	**Dec (J2000)** *d ′ ″*	$\mathbf{V_{LSR}}$ km/s	$\mathbf{T_{max}}$ K	**S/N**	**R** pc	$\sigma_\mathbf{v}$ km/s	$\mathbf{L_{CO}}$ 10^5 K km/s pc^2	$\mathbf{M_{vir}}$ 10^5 $M_\odot$	α	**PA** deg	**b/a**	**Reg**	**Flag**
(1)	(2)	(3)	(4)	(5)	(6)	(7)	(8)	(9)	(10)	(11)	(12)	(13)	(14)	(15)
1107	$13^h29^m45.59^s$	47°11′59.70”	−43.7	3.6	8.7	32 ± 0	8 ± 7	1.2 ± 3.1	23.4 ± 36.7	4.33	18	0.5	*SA*	1
1108	$13^h29^m45.60^s$	47°12′11.32”	−40.1	3.7	8.3	41 ± 25	6 ± 5	1.8 ± 1.6	13.6 ± 26.2	1.70	170	0.8	*SA*	0
1109	$13^h29^m44.32^s$	47°11′45.38”	−39.9	4.8	12.7	32 ± 0	2 ± 2	2.2 ± 2.3	1.0 ± 1.9	0.11	135	0.2	*SA*	1
1110	$13^h29^m45.46^s$	47°11′52.58”	−34.1	5.0	12.1	120 ± 54	14 ± 6	17.4 ± 13.2	235.2 ± 243.4	3.09	19	0.7	*IA*	0
1111	$13^h29^m45.11^s$	47°11′54.13”	−38.6	4.3	9.9	57 ± 38	8 ± 4	6.2 ± 3.4	34.2 ± 42.8	1.27	159	1.1	*SA*	0
1112	$13^h29^m44.84^s$	47°11′55.20”	−38.3	3.9	9.9	55 ± 33	8 ± 7	2.4 ± 4.9	36.6 ± 78.8	3.48	37	0.3	*SA*	0
1113	$13^h29^m45.36^s$	47°11′56.38”	−36.2	3.7	8.8	30 ± 25	6 ± 7	1.4 ± 1.1	11.2 ± 34.4	1.83	2	0.3	*SA*	0
1114	$13^h29^m44.43^s$	47°11′46.97”	−33.9	5.2	12.0	30 ± 31	8 ± 10	2.0 ± 1.0	20.8 ± 52.3	2.33	131	0.6	*SA*	0
1115	$13^h29^m43.27^s$	47°11′48.28”	−30.5	2.8	5.0	32 ± 0	8 ± 5	0.9 ± 0.6	19.9 ± 23.4	4.92	1	0.6	*IA*	1
1116	$13^h29^m45.15^s$	47°11′48.81”	−29.9	2.7	5.9	46 ± 25	12 ± 7	1.1 ± 1.5	72.9 ± 136.8	14.98	159	0.3	*SA*	0
1117	$13^h29^m45.50^s$	47°12′2.48”	−34.7	4.2	8.8	41 ± 24	14 ± 6	9.4 ± 5.2	82.2 ± 113.0	2.01	101	0.7	*SA*	0
1118	$13^h29^m43.71^s$	47°11′46.41”	−30.4	3.1	5.9	72 ± 55	4 ± 4	3.7 ± 3.2	12.3 ± 33.5	0.76	132	1.6	*SA*	0
1119	$13^h29^m43.06^s$	47°11′47.46”	−27.7	3.4	5.2	45 ± 28	5 ± 4	1.2 ± 1.2	12.5 ± 21.7	2.42	146	1.0	*IA*	0
1120	$13^h29^m42.91^s$	47°11′49.32”	−28.9	4.6	6.5	95 ± 39	4 ± 3	6.4 ± 2.0	12.4 ± 17.8	0.44	3	0.8	*IA*	0
1121	$13^h29^m45.28^s$	47°11′59.33”	−29.7	6.2	13.9	113 ± 21	12 ± 3	19.6 ± 7.8	162.1 ± 85.4	1.90	92	0.7	*SA*	0
1122	$13^h29^m43.11^s$	47°11′43.01”	−22.6	6.3	11.1	58 ± 17	6 ± 2	7.3 ± 2.6	21.8 ± 13.4	0.68	31	0.8	*IA*	0
1123	$13^h29^m42.89^s$	47°11′45.09”	−22.5	4.8	7.9	44 ± 28	2 ± 0	1.3 ± 2.3	2.1 ± 1.3	0.36	95	0.6	*IA*	1
1124	$13^h29^m44.67^s$	47°11′42.77”	−20.7	5.6	13.3	77 ± 20	16 ± 3	12.1 ± 11.4	208.1 ± 137.7	3.96	114	0.5	*SA*	0
1125	$13^h29^m44.81^s$	47°11′45.31”	−23.7	4.7	11.5	48 ± 44	7 ± 9	2.7 ± 4.8	23.5 ± 72.1	1.99	164	0.3	*SA*	0
1126	$13^h29^m45.32^s$	47°11′47.75”	−14.2	3.2	8.4	32 ± 0	12 ± 7	2.1 ± 2.9	45.8 ± 51.4	5.00	48	0.2	*IA*	1
1127	$13^h29^m43.78^s$	47°11′42.22”	−13.9	1.6	3.6	32 ± 0	4 ± 3	0.4 ± 0.4	6.4 ± 9.1	3.87	142	0.6	*SA*	1
1128	$13^h29^m44.01^s$	47°11′44.64”	−14.0	1.9	4.1	32 ± 0	4 ± 3	0.1 ± 0.1	6.4 ± 9.0	10.05	151	0.7	*SA*	1
1129	$13^h29^m42.78^s$	47°11′45.44”	−5.9	2.7	4.3	6 ± 11	2 ± 3	0.7 ± 0.5	0.3 ± 1.0	0.09	4	1.0	*IA*	0
1130	$13^h29^m45.37^s$	47°11′51.77”	−5.9	3.9	9.7	76 ± 59	9 ± 6	6.1 ± 8.8	70.9 ± 88.3	2.68	120	0.5	*SA*	0
1131	$13^h29^m44.97^s$	47°11′46.77”	−5.9	4.3	10.8	74 ± 58	3 ± 4	4.7 ± 1.7	6.4 ± 19.0	0.31	139	0.5	*SA*	0
1132	$13^h29^m45.58^s$	47°11′51.79”	3.7	3.4	8.8	32 ± 29	7 ± 6	2.2 ± 2.5	15.9 ± 34.0	1.63	4	0.8	*IA*	0
1133	$13^h29^m45.46^s$	47°11′51.82”	25.5	1.9	4.8	49 ± 20	5 ± 3	1.4 ± 0.6	12.6 ± 16.8	2.06	78	0.7	*IA*	0
1134	$13^h29^m44.14^s$	47°11′57.15”	−61.4	2.2	4.5	32 ± 0	9 ± 3	1.2 ± 0.4	27.3 ± 17.6	5.37	22	0.6	*SA*	1
1135	$13^h29^m44.53^s$	47°11′55.24”	−49.0	1.9	4.4	36 ± 11	6 ± 2	1.7 ± 0.6	13.7 ± 10.7	1.80	38	0.5	*SA*	0
1136	$13^h29^m44.76^s$	47°12′1.37”	−34.2	3.5	7.4	67 ± 16	6 ± 2	3.7 ± 0.4	26.2 ± 14.7	1.64	152	0.3	*SA*	0
1137	$13^h29^m43.73^s$	47°12′6.78”	7.2	3.4	4.9	32 ± 0	5 ± 2	0.8 ± 0.4	8.8 ± 8.0	2.63	126	0.8	*IA*	1
1138	$13^h29^m45.60^s$	47°12′5.97”	38.2	2.4	6.2	16 ± 7	8 ± 4	0.9 ± 0.2	9.6 ± 12.8	2.45	91	0.8	*SA*	0
1139	$13^h29^m43.15^s$	47°11′53.50”	43.2	3.4	5.1	32 ± 0	5 ± 2	1.0 ± 0.4	8.0 ± 6.7	1.87	177	0.9	*IA*	1
1140	$13^h30^m0.57^s$	47°12′42.05”	−74.0	1.7	4.3	17 ± 10	7 ± 3	1.0 ± 0.4	7.8 ± 10.9	1.73	149	0.6	*SA*	0
1141	$13^h30^m0.55^s$	47°12′41.98”	−48.0	1.7	4.1	32 ± 0	6 ± 2	0.9 ± 0.4	11.5 ± 7.4	2.98	149	0.6	*SA*	1
1142	$13^h30^m1.40^s$	47°12′47.36”	−58.8	2.0	4.2	32 ± 0	5 ± 3	0.4 ± 0.4	7.4 ± 10.6	3.91	153	0.7	*SA*	1
1143	$13^h30^m0.62^s$	47°12′58.07”	−63.4	3.6	4.7	37 ± 16	7 ± 2	3.4 ± 1.6	20.0 ± 16.4	1.36	164	0.6	*SA*	0
1144	$13^h30^m1.29^s$	47°12′59.95”	−51.0	4.0	4.7	32 ± 0	4 ± 2	1.0 ± 0.7	5.1 ± 6.1	1.16	163	0.7	*SA*	1
1145	$13^h30^m0.80^s$	47°12′33.23”	−45.9	2.9	7.1	56 ± 26	10 ± 5	4.8 ± 2.3	62.7 ± 72.0	2.98	104	0.6	*SA*	0
1146	$13^h30^m1.83^s$	47°12′35.09”	−44.9	1.5	4.0	32 ± 0	7 ± 6	0.3 ± 0.3	17.3 ± 26.7	14.28	160	0.8	*SA*	1
1147	$13^h30^m0.78^s$	47°12′37.91”	−47.5	2.4	5.9	61 ± 48	2 ± 0	0.5 ± 0.3	2.9 ± 2.2	1.41	128	0.8	*SA*	1
1148	$13^h30^m0.66^s$	47°12′44.53”	−49.3	2.0	4.6	47 ± 24	7 ± 5	0.8 ± 0.9	27.1 ± 46.1	7.75	178	0.7	*SA*	0
1149	$13^h30^m1.15^s$	47°12′58.47”	−43.0	4.0	4.4	32 ± 0	4 ± 4	1.2 ± 0.8	4.1 ± 10.1	0.76	111	0.3	*SA*	1
1150	$13^h30^m0.66^s$	47°12′36.04”	−41.9	2.2	5.2	69 ± 30	5 ± 4	1.4 ± 1.1	16.0 ± 32.8	2.61	164	0.6	*SA*	0
1151	$13^h30^m0.90^s$	47°12′36.13”	−43.5	2.6	6.3	67 ± 34	7 ± 5	1.5 ± 2.6	38.2 ± 66.0	5.70	88	0.4	*SA*	0
1152	$13^h30^m0.96^s$	47°12′45.62”	−42.9	3.9	9.0	60 ± 47	11 ± 6	2.9 ± 5.1	76.2 ± 118.2	6.08	120	0.4	*SA*	0
1153	$13^h30^m0.91^s$	47°12′50.54”	−38.8	3.3	5.9	27 ± 21	6 ± 4	1.6 ± 1.4	10.2 ± 16.6	1.43	43	0.8	*SA*	0
1154	$13^h30^m0.40^s$	47°13′2.31”	−47.9	6.3	6.5	76 ± 17	7 ± 2	9.9 ± 3.7	39.1 ± 22.1	0.91	61	0.9	*SA*	0
1155	$13^h30^m2.28^s$	47°12′40.39”	−32.5	3.6	7.3	62 ± 12	8 ± 2	5.5 ± 0.8	41.8 ± 23.6	1.73	144	0.4	*IA*	0
1156	$13^h30^m1.25^s$	47°12′43.85”	−35.4	5.0	10.9	90 ± 28	3 ± 2	4.9 ± 5.1	8.5 ± 9.1	0.40	147	0.4	*SA*	0
1157	$13^h30^m1.01^s$	47°12′47.69”	−38.3	7.1	14.3	60 ± 14	5 ± 2	9.4 ± 4.3	16.5 ± 15.7	0.40	123	0.7	*SA*	0
1158	$13^h30^m1.42^s$	47°12′50.45”	−34.7	13.3	23.1	108 ± 12	10 ± 1	59.4 ± 6.3	113.2 ± 29.0	0.44	62	0.6	*SA*	0
1159	$13^h30^m1.53^s$	47°12′15.84”	−32.5	4.0	9.1	60 ± 41	2 ± 0	1.1 ± 1.8	2.8 ± 1.9	0.57	57	0.6	*SA*	1
1160	$13^h30^m1.84^s$	47°12′46.51”	−34.9	3.6	7.2	32 ± 0	9 ± 6	1.8 ± 3.7	25.7 ± 36.9	3.33	33	0.2	*SA*	1
1161	$13^h30^m0.72^s$	47°12′58.95”	−34.6	5.8	6.8	80 ± 32	4 ± 2	7.3 ± 5.1	11.9 ± 16.3	0.38	170	0.5	*SA*	0
1162	$13^h30^m0.63^s$	47°13′4.54”	−37.3	13.6	10.0	80 ± 10	10 ± 1	23.5 ± 1.7	83.2 ± 26.6	0.81	46	0.5	*SA*	0
1163	$13^h30^m1.67^s$	47°12′23.83”	−29.4	2.0	4.9	32 ± 0	5 ± 5	0.5 ± 0.6	7.5 ± 16.9	3.35	166	0.5	*SA*	1
1164	$13^h30^m1.84^s$	47°12′27.71”	−28.9	5.5	12.7	53 ± 21	6 ± 3	5.2 ± 2.8	19.8 ± 18.4	0.87	167	0.7	*SA*	0
1165	$13^h30^m1.83^s$	47°12′30.57”	−24.9	3.6	8.8	29 ± 46	2 ± 2	6.4 ± 11.2	1.4 ± 3.8	0.05	83	0.6	*SA*	0
1166	$13^h30^m0.58^s$	47°12′31.02”	−21.5	2.0	4.7	32 ± 0	21 ± 9	1.9 ± 1.1	143.2 ± 129.9	17.35	138	0.4	*SA*	1

ID	**RA (J2000)**	**Dec (J2000)**	$\mathbf{V_{LSR}}$	$\mathbf{T_{max}}$	**S/N**	**R**	$\sigma_\mathbf{v}$	$\mathbf{L_{CO}}$	$\mathbf{M_{vir}}$	α	**PA**	**b/a**	**Reg**	**Flag**
	h m s	*d ’ ”*	km/s	K		pc	km/s	10^5 K km/s pc^2	10^5 M$_\odot$		deg			
(1)	(2)	(3)	(4)	(5)	(6)	(7)	(8)	(9)	(10)	(11)	(12)	(13)	(14)	(15)
1167	$13^h30^m2.08^s$	47°12′35.31”	−24.3	4.2	9.8	86 ± 60	4 ± 3	3.8 ± 3.8	13.4 ± 25.9	0.82	147	0.5	*SA*	0
1168	$13^h30^m1.40^s$	47°12′34.74”	−26.6	6.3	13.4	54 ± 34	10 ± 9	3.9 ± 8.6	53.2 ± 120.2	3.14	118	0.9	*SA*	0
1169	$13^h30^m1.62^s$	47°12′40.24”	−29.4	5.1	10.9	62 ± 15	7 ± 1	10.3 ± 2.8	28.3 ± 13.0	0.63	89	0.3	*SA*	0
1170	$13^h30^m0.97^s$	47°12′40.36”	−27.5	2.4	5.9	36 ± 36	2 ± 0	0.5 ± 0.9	1.7 ± 1.7	0.74	130	0.7	*SA*	1
1171	$13^h30^m1.31^s$	47°12′39.01”	−29.7	6.3	15.0	51 ± 34	5 ± 3	5.2 ± 3.4	10.8 ± 12.9	0.47	78	0.2	*SA*	0
1172	$13^h30^m1.00^s$	47°12′52.53”	−30.0	5.4	10.1	32 ± 0	9 ± 11	2.3 ± 2.2	26.8 ± 67.9	2.68	179	0.2	*SA*	1
1173	$13^h30^m1.02^s$	47°12′54.23”	−30.2	4.4	6.9	39 ± 29	2 ± 2	1.8 ± 3.5	2.1 ± 4.6	0.27	0	0.9	*SA*	0
1174	$13^h30^m0.91^s$	47°12′55.61”	−28.7	5.7	7.5	26 ± 20	6 ± 4	3.3 ± 2.2	10.6 ± 14.9	0.74	173	0.5	*SA*	0
1175	$13^h30^m1.07^s$	47°12′56.66”	−29.8	4.8	5.6	32 ± 0	6 ± 7	1.4 ± 1.9	11.2 ± 26.1	1.83	117	0.5	*SA*	1
1176	$13^h30^m0.66^s$	47°13′1.02”	−30.0	6.5	7.2	19 ± 20	2 ± 2	1.9 ± 2.1	0.7 ± 1.6	0.08	154	0.9	*SA*	0
1177	$13^h30^m1.34^s$	47°12′15.01”	−22.2	2.9	6.5	44 ± 47	3 ± 3	2.1 ± 2.6	4.3 ± 7.9	0.47	68	0.6	*SA*	0
1178	$13^h30^m1.40^s$	47°12′24.40”	−20.2	5.3	12.5	42 ± 19	10 ± 4	4.2 ± 4.4	40.3 ± 35.8	2.19	49	0.7	*SA*	0
1179	$13^h30^m1.28^s$	47°12′31.59”	−22.5	3.8	9.2	87 ± 60	2 ± 0	1.0 ± 0.6	4.1 ± 2.8	0.97	127	0.5	*SA*	1
1180	$13^h30^m1.72^s$	47°12′35.41”	−21.5	3.6	8.8	42 ± 28	6 ± 6	0.5 ± 0.3	14.1 ± 37.0	6.39	82	0.9	*SA*	0
1181	$13^h30^m0.67^s$	47°12′44.63”	−24.7	2.2	5.1	32 ± 0	3 ± 4	0.3 ± 0.3	2.9 ± 7.1	2.06	150	0.6	*SA*	1
1182	$13^h30^m1.61^s$	47°12′15.94”	−20.5	3.8	8.8	32 ± 0	9 ± 8	0.5 ± 0.7	28.8 ± 50.7	13.75	130	0.3	*SA*	1
1183	$13^h30^m1.31^s$	47°12′18.60”	−19.1	3.5	7.8	75 ± 19	12 ± 3	4.9 ± 3.3	114.2 ± 70.7	5.38	170	0.5	*SA*	0
1184	$13^h30^m1.33^s$	47°12′22.74”	−19.4	4.6	10.4	31 ± 27	7 ± 9	2.4 ± 5.2	17.7 ± 44.5	1.70	176	0.8	*SA*	0
1185	$13^h30^m2.03^s$	47°12′25.19”	−19.0	1.9	4.2	12 ± 23	7 ± 6	0.6 ± 1.1	5.8 ± 11.0	2.14	165	0.9	*SA*	0
1186	$13^h30^m1.32^s$	47°12′26.12”	−14.7	4.4	10.0	56 ± 41	2 ± 5	2.0 ± 1.7	3.6 ± 12.6	0.40	111	0.7	*SA*	0
1187	$13^h30^m1.34^s$	47°12′29.52”	−20.3	2.9	7.3	30 ± 35	12 ± 10	2.9 ± 2.7	42.1 ± 82.9	3.28	43	0.7	*SA*	0
1188	$13^h30^m1.25^s$	47°12′12.72”	−14.9	4.0	10.1	38 ± 11	2 ± 1	2.0 ± 0.7	2.2 ± 3.0	0.25	32	0.6	*SA*	0
1189	$13^h30^m2.11^s$	47°12′18.98”	−10.8	3.6	7.8	126 ± 32	10 ± 2	9.1 ± 2.3	124.4 ± 68.7	3.13	87	0.6	*SA*	0
1190	$13^h30^m1.96^s$	47°12′24.15”	−13.4	2.7	5.4	28 ± 32	6 ± 7	1.5 ± 2.0	10.9 ± 28.6	1.70	25	0.6	*SA*	0
1191	$13^h30^m2.20^s$	47°12′31.87”	−8.7	3.2	7.2	76 ± 22	4 ± 3	3.2 ± 2.5	12.8 ± 20.6	0.93	162	0.7	*SA*	0
1192	$13^h30^m2.57^s$	47°12′32.04”	−11.3	3.8	7.0	32 ± 0	5 ± 3	1.5 ± 0.7	8.2 ± 10.8	1.21	19	0.5	*IA*	1
1193	$13^h30^m1.69^s$	47°12′15.02”	−6.3	4.2	10.7	47 ± 23	3 ± 4	1.9 ± 1.4	5.1 ± 11.7	0.61	175	0.4	*SA*	0
1194	$13^h30^m1.21^s$	47°12′21.17”	−8.8	3.0	7.5	35 ± 29	6 ± 4	2.4 ± 2.4	11.4 ± 18.5	1.10	7	0.6	*SA*	0
1195	$13^h30^m1.18^s$	47°12′24.92”	−7.5	3.2	8.2	42 ± 25	2 ± 0	0.9 ± 1.5	2.0 ± 1.2	0.53	31	0.5	*SA*	1
1196	$13^h30^m2.67^s$	47°12′30.50”	−5.9	2.1	4.9	32 ± 0	4 ± 6	0.7 ± 1.1	6.4 ± 16.9	2.10	117	0.4	*IA*	1
1197	$13^h30^m1.41^s$	47°12′38.29”	−5.1	1.9	4.4	32 ± 0	4 ± 3	0.2 ± 0.1	5.1 ± 8.6	6.46	8	0.7	*SA*	1
1198	$13^h30^m2.02^s$	47°12′19.83”	−0.0	2.2	5.2	32 ± 0	2 ± 2	0.7 ± 0.4	1.6 ± 2.3	0.50	118	0.5	*SA*	1
1199	$13^h30^m1.73^s$	47°12′29.29”	−4.0	1.4	3.7	32 ± 0	6 ± 5	0.3 ± 0.4	10.7 ± 19.5	7.33	105	0.4	*SA*	1
1200	$13^h30^m1.44^s$	47°12′59.12”	−69.1	4.2	5.6	32 ± 0	11 ± 3	1.1 ± 0.2	38.5 ± 20.5	7.89	163	0.6	*SA*	1
1201	$13^h30^m0.71^s$	47°13′5.91”	−65.8	6.4	4.9	32 ± 0	3 ± 3	1.2 ± 0.5	2.7 ± 5.3	0.50	172	0.2	*SA*	1
1202	$13^h30^m2.91^s$	47°13′1.73”	−40.0	6.8	5.8	58 ± 9	10 ± 2	10.3 ± 2.0	56.6 ± 29.6	1.26	21	0.9	*IA*	0
1203	$13^h30^m3.75^s$	47°12′46.43”	−60.2	4.8	6.1	32 ± 0	2 ± 2	0.7 ± 0.3	1.8 ± 2.3	0.58	134	0.7	*IA*	1
1204	$13^h30^m2.43^s$	47°12′50.99”	−44.1	3.4	5.6	16 ± 5	4 ± 1	1.4 ± 0.4	2.1 ± 1.6	0.36	132	0.5	*IA*	0
1205	$13^h30^m2.92^s$	47°12′18.77”	6.2	3.7	6.9	72 ± 38	5 ± 4	3.2 ± 2.7	18.5 ± 31.6	1.34	126	0.5	*IA*	0
1206	$13^h30^m2.73^s$	47°12′19.91”	8.0	4.3	8.0	18 ± 9	8 ± 5	4.0 ± 2.1	12.9 ± 18.5	0.74	142	0.4	*IA*	0
1207	$13^h30^m2.45^s$	47°12′12.89”	16.1	4.0	7.9	33 ± 18	5 ± 2	2.3 ± 1.3	7.0 ± 7.0	0.71	133	0.8	*SA*	0
1208	$13^h30^m2.63^s$	47°12′15.78”	15.9	3.3	6.4	56 ± 51	6 ± 5	3.3 ± 4.5	20.2 ± 42.1	1.41	128	0.9	*SA*	0
1209	$13^h30^m0.42^s$	47°12′12.74”	−16.8	2.0	4.7	32 ± 0	6 ± 3	0.3 ± 0.1	11.2 ± 12.1	8.50	88	0.9	*IA*	1
1210	$13^h30^m2.87^s$	47°12′44.60”	−25.7	4.6	7.7	79 ± 8	8 ± 1	8.9 ± 0.6	56.2 ± 14.2	1.45	83	0.7	*IA*	0
1211	$13^h30^m0.63^s$	47°12′21.47”	−38.8	2.1	5.3	32 ± 0	4 ± 2	0.8 ± 0.2	5.3 ± 5.2	1.61	21	0.4	*SA*	1
1212	$13^h30^m0.95^s$	47°12′16.08”	−21.6	1.7	4.3	32 ± 0	7 ± 3	1.0 ± 0.3	16.8 ± 13.1	3.82	70	0.4	*SA*	1
1213	$13^h30^m2.69^s$	47°12′26.01”	−10.5	2.2	4.4	32 ± 0	5 ± 4	0.3 ± 0.3	8.0 ± 11.7	5.47	13	0.6	*IA*	1
1214	$13^h30^m2.97^s$	47°12′28.89”	−6.5	6.7	11.9	69 ± 13	7 ± 1	12.8 ± 2.6	31.4 ± 16.2	0.56	74	0.5	*IA*	0
1215	$13^h30^m3.03^s$	47°12′32.41”	−9.9	3.6	6.7	71 ± 25	9 ± 4	4.4 ± 4.2	55.3 ± 53.7	2.91	11	0.6	*IA*	0
1216	$13^h30^m3.39^s$	47°12′33.16”	−11.8	3.6	5.7	36 ± 17	5 ± 2	3.3 ± 1.9	8.4 ± 7.9	0.58	6	0.6	*IA*	0
1217	$13^h30^m3.67^s$	47°12′36.78”	−7.8	5.7	7.6	94 ± 17	5 ± 1	11.1 ± 2.5	28.0 ± 13.8	0.58	108	0.3	*IA*	0
1218	$13^h30^m3.32^s$	47°12′26.45”	−1.8	4.6	7.0	86 ± 31	10 ± 4	6.8 ± 3.8	94.6 ± 100.9	3.19	87	0.3	*IA*	0
1219	$13^h30^m3.73^s$	47°12′32.90”	−1.1	3.9	5.4	43 ± 24	4 ± 3	1.7 ± 1.5	6.0 ± 9.0	0.78	160	0.3	*IA*	0
1220	$13^h30^m3.19^s$	47°12′30.69”	7.2	3.1	5.2	22 ± 33	2 ± 4	0.5 ± 0.8	0.7 ± 3.0	0.31	164	0.8	*IA*	0
1221	$13^h30^m3.52^s$	47°12′32.00”	13.7	2.7	4.2	32 ± 0	5 ± 3	0.4 ± 0.3	7.6 ± 9.1	4.25	152	0.7	*IA*	1
1222	$13^h30^m4.47^s$	47°12′43.13”	−16.3	7.4	6.3	32 ± 0	3 ± 2	1.4 ± 0.4	3.4 ± 4.7	0.56	16	0.9	*IA*	1
1223	$13^h30^m4.25^s$	47°12′29.90”	−4.6	8.3	7.7	41 ± 14	4 ± 2	5.0 ± 1.2	5.4 ± 4.9	0.25	146	0.9	*IA*	0
1224	$13^h30^m4.15^s$	47°12′26.38”	0.2	5.5	5.8	90 ± 29	8 ± 4	7.2 ± 4.0	65.9 ± 57.5	2.09	139	0.6	*IA*	0
1225	$13^h30^m3.46^s$	47°12′21.09”	7.3	4.6	6.7	74 ± 34	10 ± 4	5.1 ± 2.5	83.9 ± 102.8	3.74	42	0.7	*IA*	0
1226	$13^h30^m3.68^s$	47°12′19.29”	5.2	5.9	7.4	69 ± 20	3 ± 1	6.8 ± 1.5	8.1 ± 9.2	0.27	135	0.3	*IA*	0

ID (1)	**RA (J2000)** *h m s* (2)	**Dec (J2000)** *d ’ ”* (3)	$\mathbf{V_{LSR}}$ km/s (4)	$\mathbf{T_{max}}$ K (5)	**S/N** (6)	**R** pc (7)	$\sigma_\mathbf{v}$ km/s (8)	$\mathbf{L_{CO}}$ 10^5 K km/s pc^2 (9)	$\mathbf{M_{vir}}$ 10^5 $M_\odot$ (10)	α (11)	**PA** deg (12)	**b/a** (13)	**Reg** (14)	**Flag** (15)
1227	$13^h30^m3.19^s$	47°12′16.52”	15.5	5.2	8.9	68 ± 10	6 ± 3	5.4 ± 0.6	27.9 ± 21.9	1.18	100	0.6	*IA*	0
1228	$13^h30^m3.41^s$	47°12′19.26”	12.3	3.5	5.0	20 ± 28	4 ± 4	1.1 ± 0.6	3.0 ± 9.2	0.61	79	0.6	*IA*	0
1229	$13^h30^m0.78^s$	47°12′46.36”	4.3	2.4	4.7	32 ± 0	4 ± 3	0.7 ± 0.5	4.1 ± 6.4	1.33	122	0.9	*SA*	1
1230	$13^h30^m0.64^s$	47°12′47.75”	5.6	2.3	5.1	35 ± 16	2 ± 2	1.0 ± 0.8	2.1 ± 3.4	0.50	156	0.8	*SA*	0
1231	$13^h30^m2.72^s$	47°12′47.78”	5.9	2.9	5.7	32 ± 0	3 ± 2	0.5 ± 0.2	3.0 ± 4.1	1.34	142	0.4	*IA*	1
1232	$13^h30^m1.54^s$	47°12′14.82”	14.5	1.7	4.3	32 ± 0	2 ± 2	0.4 ± 0.2	1.9 ± 2.6	1.16	58	0.7	*SA*	1
1233	$13^h30^m2.97^s$	47°12′29.15”	42.7	2.7	5.0	32 ± 0	7 ± 3	0.6 ± 0.2	17.4 ± 12.2	6.41	8	0.5	*IA*	1
1234	$13^h29^m57.93^s$	47°13′4.41”	−120.8	4.9	5.0	32 ± 0	5 ± 3	1.2 ± 0.4	7.5 ± 10.3	1.42	154	0.6	*IA*	1
1235	$13^h30^m0.26^s$	47°12′54.21”	−109.9	2.6	5.3	32 ± 0	8 ± 3	0.9 ± 0.2	21.1 ± 16.7	5.21	136	0.6	*SA*	1
1236	$13^h30^m0.07^s$	47°13′2.28”	−56.2	3.6	4.1	32 ± 0	4 ± 4	0.9 ± 1.0	6.0 ± 11.2	1.53	92	1.1	*SA*	1
1237	$13^h29^m59.76^s$	47°13′3.38”	−62.6	5.8	5.7	28 ± 27	4 ± 3	2.0 ± 2.7	4.1 ± 9.3	0.48	68	0.8	*SA*	0
1238	$13^h29^m59.79^s$	47°13′4.31”	−48.4	6.9	5.5	58 ± 34	6 ± 3	5.4 ± 4.6	23.3 ± 23.3	0.99	159	0.3	*SA*	0
1239	$13^h29^m59.96^s$	47°13′2.46”	−40.7	6.8	6.1	53 ± 30	4 ± 4	2.6 ± 2.1	8.0 ± 14.0	0.71	55	0.5	*SA*	0
1240	$13^h29^m59.93^s$	47°13′2.37”	−17.9	6.0	5.0	32 ± 0	5 ± 6	1.0 ± 0.9	8.0 ± 19.3	1.88	26	0.5	*SA*	1
1241	$13^h29^m58.84^s$	47°12′19.63”	−81.7	1.6	4.8	32 ± 0	4 ± 4	0.3 ± 0.1	5.6 ± 10.9	4.74	172	0.7	*IA*	1
1242	$13^h29^m59.50^s$	47°12′39.75”	−65.8	1.9	4.1	32 ± 0	5 ± 4	0.4 ± 0.4	7.3 ± 11.1	3.71	138	0.7	*IA*	1
1243	$13^h30^m0.04^s$	47°12′43.03”	−68.6	2.6	5.8	45 ± 22	5 ± 3	2.0 ± 1.4	13.8 ± 13.1	1.55	123	0.3	*SA*	0
1244	$13^h29^m59.93^s$	47°12′28.20”	−60.7	1.3	4.0	32 ± 0	5 ± 2	0.2 ± 0.2	7.6 ± 6.7	8.69	25	0.4	*IA*	1
1245	$13^h29^m59.69^s$	47°12′40.35”	−65.2	2.2	5.6	32 ± 0	6 ± 4	0.6 ± 0.4	10.2 ± 14.8	4.10	0	0.5	*IA*	1
1246	$13^h29^m59.61^s$	47°12′41.63”	−64.3	2.3	5.5	32 ± 0	6 ± 3	0.8 ± 0.9	10.9 ± 11.5	3.22	145	0.8	*IA*	1
1247	$13^h29^m59.99^s$	47°12′39.64”	−60.0	2.8	6.5	66 ± 28	2 ± 1	2.3 ± 1.9	2.1 ± 2.1	0.20	58	0.7	*SA*	0
1248	$13^h30^m0.35^s$	47°12′40.15”	−57.3	2.9	6.8	42 ± 21	9 ± 5	3.5 ± 1.5	38.3 ± 46.5	2.51	148	0.4	*SA*	0
1249	$13^h29^m59.78^s$	47°12′29.24”	−51.2	3.5	9.1	16 ± 7	3 ± 1	1.2 ± 0.2	1.7 ± 1.3	0.33	163	0.6	*IA*	0
1250	$13^h30^m0.01^s$	47°12′32.94”	−45.2	3.3	7.9	35 ± 32	2 ± 3	1.7 ± 3.1	2.3 ± 6.5	0.30	104	0.6	*IA*	0
1251	$13^h30^m0.01^s$	47°12′28.21”	−39.7	3.2	8.2	32 ± 0	7 ± 2	2.4 ± 0.3	17.6 ± 8.0	1.67	158	0.5	*IA*	1
1252	$13^h30^m0.01^s$	47°12′30.72”	−41.3	3.4	8.6	30 ± 16	4 ± 3	2.0 ± 1.6	6.1 ± 7.9	0.71	105	0.9	*IA*	0
1253	$13^h29^m59.58^s$	47°12′46.08”	−75.1	2.3	5.0	36 ± 18	10 ± 2	1.5 ± 0.4	40.6 ± 28.5	6.05	68	0.5	*IA*	0
1254	$13^h29^m59.44^s$	47°12′52.56”	−79.1	2.4	4.1	32 ± 0	4 ± 3	0.5 ± 0.4	4.5 ± 6.5	2.03	157	0.8	*SA*	1
1255	$13^h29^m59.65^s$	47°12′49.38”	−72.3	3.9	8.1	47 ± 8	8 ± 3	3.9 ± 0.8	31.2 ± 20.3	1.82	65	0.7	*SA*	0
1256	$13^h29^m59.53^s$	47°12′51.99”	−69.8	2.4	4.3	32 ± 0	3 ± 3	0.4 ± 0.4	2.4 ± 6.1	1.53	135	0.8	*SA*	1
1257	$13^h29^m59.51^s$	47°12′53.67”	−69.0	2.9	4.6	32 ± 0	4 ± 3	0.4 ± 0.3	5.8 ± 8.2	3.71	92	0.7	*SA*	1
1258	$13^h29^m57.86^s$	47°12′31.52”	−61.7	2.8	6.9	42 ± 25	5 ± 5	1.6 ± 1.8	10.5 ± 23.4	1.52	79	0.9	*IA*	0
1259	$13^h29^m58.00^s$	47°12′25.84”	−58.7	1.9	5.3	32 ± 0	5 ± 4	0.5 ± 1.0	9.0 ± 13.8	3.87	127	0.4	*IA*	1
1260	$13^h29^m57.74^s$	47°12′27.02”	−55.8	4.1	11.0	121 ± 19	6 ± 2	13.5 ± 4.7	52.2 ± 28.2	0.89	100	0.7	*IA*	0
1261	$13^h29^m57.80^s$	47°12′34.21”	−59.0	2.0	5.2	32 ± 0	4 ± 3	1.6 ± 1.0	5.5 ± 8.5	0.80	168	0.4	*IA*	1
1262	$13^h29^m57.49^s$	47°12′34.65”	−57.5	2.0	5.0	36 ± 18	6 ± 2	1.1 ± 0.5	12.5 ± 10.6	2.49	89	0.8	*IA*	0
1263	$13^h29^m57.55^s$	47°12′41.76”	−63.1	2.8	6.7	26 ± 15	8 ± 4	2.7 ± 1.7	15.3 ± 18.6	1.30	170	0.5	*IA*	0
1264	$13^h29^m57.64^s$	47°12′44.79”	−57.2	2.5	5.5	40 ± 20	6 ± 4	1.0 ± 0.5	13.5 ± 15.5	3.25	10	0.8	*IA*	0
1265	$13^h29^m57.97^s$	47°12′17.54”	−48.4	3.8	9.8	79 ± 24	5 ± 2	3.2 ± 3.6	19.5 ± 21.8	1.39	18	0.7	*IA*	0
1266	$13^h29^m57.83^s$	47°12′42.81”	−55.2	2.6	5.5	21 ± 16	2 ± 2	0.9 ± 0.9	0.8 ± 2.0	0.21	176	0.7	*IA*	0
1267	$13^h29^m57.89^s$	47°12′20.46”	−47.5	3.2	8.4	97 ± 41	2 ± 0	1.3 ± 1.1	4.6 ± 1.9	0.82	103	0.5	*IA*	1
1268	$13^h29^m57.67^s$	47°12′16.01”	−36.7	3.2	8.0	89 ± 51	4 ± 8	5.8 ± 6.2	17.7 ± 67.3	0.70	146	0.3	*IA*	0
1269	$13^h29^m59.16^s$	47°13′4.63”	−56.3	8.0	6.7	32 ± 13	9 ± 2	5.1 ± 1.1	25.9 ± 21.2	1.17	16	0.5	*SA*	0
1270	$13^h29^m59.29^s$	47°13′5.92”	−61.3	5.5	4.2	32 ± 0	6 ± 3	3.5 ± 2.6	12.5 ± 13.0	0.82	3	0.3	*SA*	1
1271	$13^h29^m59.34^s$	47°13′3.04”	−65.2	6.1	5.7	34 ± 12	12 ± 4	3.5 ± 0.9	46.8 ± 41.8	3.04	24	0.6	*SA*	0
1272	$13^h29^m57.64^s$	47°12′51.57”	−67.2	2.5	4.4	32 ± 0	7 ± 4	0.8 ± 0.3	14.1 ± 15.1	4.16	3	0.5	*IA*	1
1273	$13^h29^m59.37^s$	47°12′25.84”	−64.5	1.9	5.0	32 ± 0	2 ± 2	0.6 ± 1.2	1.3 ± 2.6	0.51	8	0.7	*IA*	1
1274	$13^h29^m59.17^s$	47°12′22.56”	−47.7	2.4	5.7	76 ± 31	5 ± 2	2.9 ± 2.0	22.4 ± 16.2	1.74	83	0.4	*IA*	0
1275	$13^h29^m59.21^s$	47°12′25.02”	−43.7	2.4	5.7	32 ± 0	5 ± 4	0.7 ± 1.1	8.2 ± 12.5	2.70	97	0.4	*IA*	1
1276	$13^h29^m59.22^s$	47°13′0.78”	−60.7	5.2	5.4	32 ± 0	4 ± 3	1.9 ± 1.9	5.3 ± 8.7	0.64	3	0.5	*SA*	1
1277	$13^h29^m59.29^s$	47°12′59.01”	−57.6	3.9	4.6	32 ± 0	8 ± 5	2.2 ± 2.4	19.1 ± 26.9	1.95	49	0.4	*SA*	1
1278	$13^h29^m59.26^s$	47°12′30.28”	−55.4	2.0	5.0	32 ± 0	3 ± 2	0.3 ± 0.1	2.2 ± 3.4	1.64	23	0.9	*IA*	1
1279	$13^h30^m0.31^s$	47°12′14.96”	−32.6	3.7	8.9	88 ± 10	6 ± 1	4.0 ± 0.4	31.0 ± 15.4	1.77	116	0.5	*IA*	0
1280	$13^h29^m57.46^s$	47°12′58.34”	−4.6	4.6	5.6	17 ± 11	7 ± 3	1.4 ± 0.4	9.8 ± 9.8	1.56	51	0.5	*IA*	0
1281	$13^h29^m55.19^s$	47°13′1.07”	−113.3	3.5	4.8	32 ± 0	5 ± 2	1.2 ± 0.6	8.2 ± 6.8	1.54	161	0.5	*IA*	1
1282	$13^h29^m55.49^s$	47°12′31.13”	−84.8	1.7	5.1	32 ± 0	5 ± 4	0.4 ± 0.2	9.8 ± 16.0	5.61	146	0.3	*SA*	1
1283	$13^h29^m55.35^s$	47°12′18.18”	−77.2	1.6	4.5	32 ± 0	8 ± 6	0.8 ± 0.5	19.2 ± 29.0	5.81	115	0.8	*SA*	1
1284	$13^h29^m55.50^s$	47°12′32.54”	−73.6	1.9	4.8	23 ± 14	5 ± 2	0.7 ± 0.4	5.6 ± 7.0	1.76	155	0.6	*IA*	0
1285	$13^h29^m54.67^s$	47°12′34.81”	−59.1	5.5	12.0	47 ± 27	1 ± 2	1.6 ± 1.6	0.7 ± 2.4	0.10	94	0.7	*SA*	0
1286	$13^h29^m54.70^s$	47°12′37.06”	−62.2	6.1	12.8	40 ± 25	8 ± 3	4.5 ± 3.7	26.0 ± 25.1	1.33	171	0.8	*IA*	0

ID (1)	RA (J2000) *h m s* (2)	Dec (J2000) *d ' "* (3)	$\mathbf{V_{LSR}}$ km/s (4)	$\mathbf{T_{max}}$ K (5)	S/N (6)	R pc (7)	σ_v km/s (8)	$\mathbf{L_{CO}}$ 10^5 K km/s pc^2 (9)	$\mathbf{M_{vir}}$ 10^5 $M_\odot$ (10)	α (11)	PA deg (12)	b/a (13)	Reg (14)	Flag (15)
1287	$13^h29^m55.89^s$	47°12′25.98”	−57.9	2.5	6.5	21 ± 23	6 ± 7	0.7 ± 1.1	7.5 ± 21.4	2.54	148	0.7	*SA*	0
1288	$13^h29^m54.75^s$	47°12′23.26”	−50.4	6.8	16.3	79 ± 18	8 ± 2	20.5 ± 10.2	51.4 ± 28.7	0.58	19	0.8	*SA*	0
1289	$13^h29^m55.59^s$	47°12′26.10”	−49.8	4.1	9.5	92 ± 14	4 ± 1	6.7 ± 2.0	14.6 ± 11.2	0.50	47	0.7	*SA*	0
1290	$13^h29^m54.60^s$	47°12′27.35”	−57.6	4.3	10.3	24 ± 19	19 ± 16	7.8 ± 11.3	87.5 ± 206.1	2.58	144	0.4	*SA*	0
1291	$13^h29^m54.87^s$	47°12′27.90”	−54.2	4.9	10.8	33 ± 19	5 ± 3	2.3 ± 1.6	7.7 ± 10.8	0.78	142	0.5	*SA*	0
1292	$13^h29^m55.28^s$	47°12′33.14”	−54.5	3.4	7.9	32 ± 0	5 ± 3	1.8 ± 1.1	8.0 ± 9.3	1.01	155	0.4	*IA*	1
1293	$13^h29^m54.85^s$	47°12′20.34”	−46.2	5.1	12.9	48 ± 39	8 ± 9	2.5 ± 5.4	33.4 ± 66.6	3.06	56	0.9	*SA*	0
1294	$13^h29^m55.06^s$	47°12′21.22”	−47.8	5.6	12.1	77 ± 54	8 ± 8	6.0 ± 9.4	57.1 ± 128.1	2.17	66	0.3	*SA*	0
1295	$13^h29^m55.02^s$	47°12′29.66”	−45.5	5.2	12.5	39 ± 38	16 ± 10	2.7 ± 3.2	102.5 ± 184.8	8.65	2	0.4	*SA*	0
1296	$13^h29^m55.03^s$	47°12′31.82”	−48.5	5.7	12.0	36 ± 32	6 ± 6	3.3 ± 5.6	12.1 ± 24.2	0.84	71	0.8	*SA*	0
1297	$13^h29^m55.01^s$	47°12′36.00”	−45.6	2.1	4.8	15 ± 25	3 ± 3	0.4 ± 0.5	1.0 ± 3.0	0.65	164	0.7	*IA*	0
1298	$13^h29^m54.79^s$	47°12′43.19”	−51.0	2.9	5.9	32 ± 0	8 ± 4	0.7 ± 0.5	19.9 ± 23.0	6.09	97	0.4	*IA*	1
1299	$13^h29^m55.10^s$	47°12′17.28”	−46.4	4.9	11.2	79 ± 45	8 ± 7	1.6 ± 1.7	47.4 ± 109.3	6.64	45	0.5	*SA*	0
1300	$13^h29^m54.88^s$	47°12′18.51”	−41.4	5.1	12.0	35 ± 32	11 ± 7	5.3 ± 4.4	45.5 ± 83.8	1.96	159	0.7	*SA*	0
1301	$13^h29^m54.81^s$	47°12′25.37”	−46.2	4.2	11.3	38 ± 63	5 ± 8	1.8 ± 0.8	10.4 ± 37.3	1.33	25	0.6	*SA*	0
1302	$13^h29^m55.54^s$	47°12′33.26”	−42.6	2.3	5.4	33 ± 31	5 ± 5	0.4 ± 0.4	7.1 ± 16.0	4.53	169	0.7	*IA*	0
1303	$13^h29^m55.39^s$	47°12′22.34”	−38.8	3.3	7.9	51 ± 21	5 ± 3	2.2 ± 2.1	13.3 ± 14.7	1.38	152	0.7	*SA*	0
1304	$13^h29^m55.83^s$	47°12′22.52”	−35.0	2.5	6.1	73 ± 22	14 ± 4	4.5 ± 1.2	142.6 ± 87.6	7.23	88	0.4	*SA*	0
1305	$13^h29^m55.40^s$	47°12′29.64”	−25.1	1.8	4.6	32 ± 0	5 ± 5	0.3 ± 0.5	6.9 ± 14.7	6.35	119	0.8	*SA*	1
1306	$13^h29^m56.03^s$	47°12′12.73”	−3.9	1.8	4.5	40 ± 25	6 ± 3	1.4 ± 0.6	17.1 ± 18.2	2.74	167	0.7	*SA*	0
1307	$13^h29^m54.68^s$	47°12′23.39”	−102.0	1.8	5.7	36 ± 14	7 ± 2	1.3 ± 0.2	16.5 ± 10.7	3.02	124	0.5	*SA*	0
1308	$13^h29^m56.14^s$	47°12′49.89”	−99.8	1.8	4.4	32 ± 0	2 ± 2	0.4 ± 0.3	1.6 ± 3.4	0.85	143	0.4	*IA*	1
1309	$13^h29^m56.32^s$	47°12′51.23”	−80.6	4.9	9.7	68 ± 11	6 ± 2	3.8 ± 1.3	24.7 ± 20.1	1.49	92	0.9	*IA*	0
1310	$13^h29^m56.21^s$	47°12′54.38”	−73.3	5.0	7.9	49 ± 20	6 ± 2	5.1 ± 1.5	17.9 ± 12.8	0.81	94	0.8	*IA*	0
1311	$13^h29^m56.21^s$	47°12′50.37”	−65.3	2.8	5.6	32 ± 0	5 ± 4	0.6 ± 0.3	8.9 ± 14.2	3.69	14	0.5	*IA*	1
1312	$13^h29^m56.03^s$	47°12′53.58”	−67.8	4.4	6.8	36 ± 22	8 ± 6	2.5 ± 1.9	25.9 ± 39.7	2.38	57	0.7	*IA*	0
1313	$13^h29^m56.09^s$	47°12′57.25”	−82.2	3.5	5.0	32 ± 0	5 ± 3	0.9 ± 0.3	8.8 ± 9.4	2.12	142	0.5	*IA*	1
1314	$13^h29^m56.79^s$	47°12′23.39”	−81.4	1.6	4.3	32 ± 0	6 ± 4	0.3 ± 0.3	10.1 ± 14.8	7.67	165	1.1	*IA*	1
1315	$13^h29^m57.25^s$	47°12′30.03”	−54.0	2.5	6.2	55 ± 22	5 ± 3	1.8 ± 0.6	12.6 ± 14.5	1.63	30	0.6	*IA*	0
1316	$13^h29^m57.28^s$	47°12′35.55”	−57.2	2.2	5.0	66 ± 25	7 ± 3	2.0 ± 0.7	36.3 ± 44.5	4.11	127	0.5	*IA*	0
1317	$13^h29^m57.14^s$	47°12′26.09”	−53.7	4.7	11.4	88 ± 15	4 ± 1	8.4 ± 2.0	17.8 ± 7.9	0.49	36	1.0	*IA*	0
1318	$13^h29^m56.63^s$	47°12′23.28”	−49.1	3.4	8.4	35 ± 33	4 ± 5	1.6 ± 2.4	5.8 ± 15.2	0.82	175	1.0	*IA*	0
1319	$13^h29^m56.75^s$	47°12′24.95”	−46.2	3.4	7.4	46 ± 30	6 ± 4	1.3 ± 1.5	16.5 ± 27.0	2.91	154	0.3	*IA*	0
1320	$13^h29^m57.19^s$	47°12′32.94”	−49.5	2.5	5.3	36 ± 33	6 ± 3	1.6 ± 0.6	13.4 ± 23.1	1.96	64	1.1	*IA*	0
1321	$13^h29^m57.27^s$	47°12′34.68”	−35.8	1.8	4.1	32 ± 0	4 ± 2	0.2 ± 0.2	4.8 ± 5.6	4.58	146	0.4	*IA*	1
1322	$13^h29^m56.47^s$	47°12′28.53”	−61.0	3.9	9.2	66 ± 8	10 ± 2	6.0 ± 0.4	70.6 ± 24.7	2.71	156	0.7	*IA*	0
1323	$13^h29^m54.63^s$	47°12′54.91”	−64.5	5.8	7.6	73 ± 19	12 ± 4	11.0 ± 7.6	107.5 ± 84.8	2.24	61	0.3	*IA*	0
1324	$13^h29^m56.70^s$	47°12′31.64”	−70.1	1.8	4.4	25 ± 13	4 ± 3	0.9 ± 0.6	3.3 ± 4.3	0.84	53	0.4	*IA*	0
1325	$13^h29^m56.49^s$	47°12′32.44”	−65.5	3.0	7.0	39 ± 14	8 ± 2	2.0 ± 0.4	28.4 ± 20.7	3.33	33	0.6	*IA*	0
1326	$13^h29^m56.31^s$	47°12′37.03”	−69.7	3.3	7.3	32 ± 14	3 ± 2	1.1 ± 0.5	2.8 ± 3.3	0.60	18	0.8	*IA*	0
1327	$13^h29^m56.28^s$	47°12′39.62”	−66.2	1.9	4.3	34 ± 33	5 ± 3	0.5 ± 0.6	7.2 ± 13.6	3.17	117	0.9	*IA*	0
1328	$13^h29^m57.43^s$	47°12′39.25”	−63.6	3.4	8.3	36 ± 10	5 ± 2	2.0 ± 0.6	8.0 ± 5.9	0.93	91	0.6	*IA*	0
1329	$13^h29^m57.08^s$	47°12′58.75”	−59.5	5.0	5.5	63 ± 12	6 ± 2	4.6 ± 0.9	20.2 ± 15.1	1.01	75	0.6	*IA*	0
1330	$13^h29^m57.20^s$	47°13′1.38”	−65.4	4.7	4.6	45 ± 14	6 ± 3	5.6 ± 1.6	16.3 ± 15.4	0.67	55	0.4	*IA*	0
1331	$13^h29^m55.41^s$	47°12′43.72”	−53.4	2.9	6.0	44 ± 9	8 ± 2	1.6 ± 0.2	27.1 ± 19.2	3.89	31	0.6	*IA*	0
1332	$13^h29^m56.06^s$	47°12′19.87”	−46.0	3.0	7.1	75 ± 11	9 ± 1	5.1 ± 0.4	59.6 ± 23.0	2.68	100	0.4	*SA*	0
1333	$13^h29^m55.95^s$	47°12′32.48”	−53.9	2.5	5.3	11 ± 16	6 ± 3	0.8 ± 0.3	4.1 ± 9.4	1.19	20	0.9	*IA*	0
1334	$13^h29^m55.24^s$	47°13′4.05”	−58.9	5.9	4.6	32 ± 0	3 ± 2	1.2 ± 0.7	3.0 ± 4.7	0.58	173	0.8	*IA*	1
1335	$13^h29^m54.86^s$	47°13′1.42”	−50.2	5.5	5.1	32 ± 0	5 ± 2	1.8 ± 0.7	8.0 ± 7.9	1.05	122	0.5	*IA*	1
1336	$13^h29^m56.02^s$	47°12′45.88”	−49.7	2.9	5.9	32 ± 0	3 ± 1	0.5 ± 0.1	2.3 ± 2.5	1.14	65	0.8	*IA*	1
1337	$13^h29^m57.06^s$	47°12′37.24”	−37.9	2.3	5.0	32 ± 0	7 ± 2	1.1 ± 0.4	16.8 ± 10.3	3.55	2	0.4	*IA*	1
1338	$13^h29^m57.31^s$	47°12′46.60”	−17.8	1.9	4.0	41 ± 26	9 ± 5	1.2 ± 1.4	30.7 ± 40.8	5.84	15	0.5	*IA*	0
1339	$13^h29^m56.19^s$	47°12′54.61”	15.1	3.4	5.3	33 ± 13	10 ± 3	1.2 ± 0.4	33.6 ± 29.1	6.31	29	0.5	*IA*	0
1340	$13^h29^m53.38^s$	47°12′33.36”	−106.9	1.5	5.2	32 ± 0	4 ± 3	0.2 ± 0.1	5.7 ± 7.9	5.84	153	0.5	*SA*	1
1341	$13^h29^m51.66^s$	47°12′42.44”	−97.4	1.7	4.5	32 ± 0	6 ± 4	0.4 ± 0.2	13.9 ± 19.1	8.02	156	0.8	*SA*	1
1342	$13^h29^m51.93^s$	47°12′28.29”	−94.6	1.6	5.0	32 ± 0	2 ± 1	0.4 ± 0.2	1.4 ± 2.0	0.87	141	0.5	*SA*	1
1343	$13^h29^m51.64^s$	47°12′28.51”	−79.8	3.0	7.1	32 ± 0	3 ± 3	1.4 ± 0.7	2.4 ± 4.5	0.38	141	0.3	*SA*	1
1344	$13^h29^m54.10^s$	47°12′38.88”	−88.6	1.8	5.1	32 ± 0	9 ± 8	0.8 ± 0.4	28.7 ± 50.2	8.21	168	0.4	*SA*	1
1345	$13^h29^m52.15^s$	47°12′25.28”	−67.0	2.0	4.7	32 ± 0	12 ± 11	0.8 ± 0.9	43.8 ± 84.8	13.19	124	0.5	*SA*	1
1346	$13^h29^m53.30^s$	47°12′36.47”	−71.7	5.4	12.0	59 ± 37	11 ± 6	7.4 ± 6.3	81.5 ± 97.1	2.52	59	0.6	*SA*	0

ID	RA (J2000) *h m s*	Dec (J2000) *d ’ ”*	V_{LSR} km/s	T_{max} K	S/N	R pc	σ_v km/s	L_{CO} 10^5 K km/s pc^2	M_{vir} 10^5 $M_\odot$	α	PA deg	b/a	Reg	Flag
(1)	(2)	(3)	(4)	(5)	(6)	(7)	(8)	(9)	(10)	(11)	(12)	(13)	(14)	(15)
1347	$13^h29^m51.77^s$	47°12′37.85”	−69.4	4.8	10.7	35 ± 51	5 ± 9	2.8 ± 4.8	8.8 ± 33.3	0.72	57	0.8	*SA*	0
1348	$13^h29^m52.26^s$	47°12′43.13”	−72.1	8.5	17.0	32 ± 0	10 ± 7	10.2 ± 11.7	33.1 ± 47.2	0.74	176	0.3	*SA*	1
1349	$13^h29^m52.25^s$	47°12′46.42”	−70.1	7.5	14.2	75 ± 17	7 ± 2	11.4 ± 3.9	36.2 ± 23.0	0.73	36	0.4	*IA*	0
1350	$13^h29^m51.58^s$	47°12′49.25”	−73.9	3.0	5.8	40 ± 19	4 ± 3	3.5 ± 2.2	6.5 ± 8.5	0.42	53	1.4	*IA*	0
1351	$13^h29^m51.77^s$	47°12′50.25”	−73.7	2.9	5.3	32 ± 0	5 ± 4	1.1 ± 0.7	7.5 ± 13.2	1.55	19	0.7	*IA*	1
1352	$13^h29^m54.10^s$	47°12′33.92”	−65.8	5.7	13.1	72 ± 26	7 ± 4	6.7 ± 3.9	36.1 ± 48.2	1.24	32	0.5	*SA*	0
1353	$13^h29^m53.70^s$	47°12′34.61”	−68.9	5.3	11.8	73 ± 36	6 ± 3	6.8 ± 8.4	25.7 ± 25.4	0.87	28	0.5	*SA*	0
1354	$13^h29^m53.96^s$	47°12′37.06”	−71.5	4.0	8.1	61 ± 50	6 ± 9	4.9 ± 9.6	21.3 ± 69.3	1.00	43	0.7	*SA*	0
1355	$13^h29^m52.92^s$	47°12′39.17”	−65.4	3.0	6.5	28 ± 33	5 ± 5	0.3 ± 0.3	6.1 ± 12.8	4.27	122	0.7	*SA*	0
1356	$13^h29^m53.24^s$	47°12′40.73”	−63.6	5.9	12.2	123 ± 32	4 ± 2	14.1 ± 6.1	20.3 ± 23.2	0.33	12	0.7	*SA*	0
1357	$13^h29^m52.04^s$	47°12′42.67”	−67.0	8.2	17.8	59 ± 22	5 ± 3	7.9 ± 4.8	17.9 ± 20.0	0.52	115	0.6	*SA*	0
1358	$13^h29^m52.66^s$	47°12′43.98”	−67.3	6.2	12.8	60 ± 20	4 ± 2	6.9 ± 3.2	11.8 ± 8.0	0.40	127	0.8	*SA*	0
1359	$13^h29^m53.82^s$	47°12′16.01”	−60.2	5.0	10.7	32 ± 0	2 ± 2	5.1 ± 2.8	1.4 ± 2.9	0.07	94	1.5	*SA*	1
1360	$13^h29^m52.24^s$	47°12′17.53”	−60.5	2.7	6.3	47 ± 21	4 ± 3	1.7 ± 1.4	6.0 ± 9.2	0.81	146	0.8	*SA*	0
1361	$13^h29^m53.53^s$	47°12′20.25”	−61.7	5.8	13.5	106 ± 82	12 ± 12	5.5 ± 13.0	162.5 ± 348.7	6.76	3	0.6	*SA*	0
1362	$13^h29^m53.30^s$	47°12′21.37”	−61.2	5.6	13.2	47 ± 50	14 ± 11	8.5 ± 20.7	98.1 ± 201.1	2.66	58	0.4	*SA*	0
1363	$13^h29^m52.61^s$	47°12′26.26”	−61.8	4.3	9.3	32 ± 0	9 ± 15	1.1 ± 1.3	27.7 ± 90.1	5.64	155	0.2	*SA*	1
1364	$13^h29^m51.76^s$	47°12′25.45”	−61.9	3.8	8.9	61 ± 41	6 ± 5	9.3 ± 4.8	25.3 ± 46.3	0.63	106	0.4	*SA*	0
1365	$13^h29^m54.46^s$	47°12′27.84”	−64.2	3.8	8.1	62 ± 41	6 ± 7	3.8 ± 7.4	23.9 ± 55.6	1.46	136	0.4	*SA*	0
1366	$13^h29^m52.15^s$	47°12′29.68”	−61.9	5.4	12.6	68 ± 25	9 ± 5	10.6 ± 8.6	58.7 ± 65.0	1.27	40	0.3	*SA*	0
1367	$13^h29^m54.02^s$	47°12′32.16”	−62.5	5.6	11.6	48 ± 28	2 ± 5	2.0 ± 2.6	1.6 ± 7.6	0.19	48	0.9	*SA*	0
1368	$13^h29^m52.78^s$	47°12′37.18”	−63.6	5.8	13.5	62 ± 44	12 ± 9	11.3 ± 16.5	101.2 ± 190.0	2.05	2	0.5	*SA*	0
1369	$13^h29^m54.40^s$	47°12′13.90”	−55.7	7.2	15.9	61 ± 25	9 ± 3	5.2 ± 4.9	48.2 ± 45.5	2.14	161	0.8	*SA*	0
1370	$13^h29^m53.99^s$	47°12′13.54”	−59.6	6.0	12.9	42 ± 40	8 ± 7	4.5 ± 7.2	27.9 ± 67.2	1.41	66	0.4	*SA*	0
1371	$13^h29^m52.01^s$	47°12′15.16”	−57.8	3.1	6.7	51 ± 23	4 ± 3	2.5 ± 1.6	9.1 ± 11.7	0.83	26	0.7	*IA*	0
1372	$13^h29^m53.69^s$	47°12′18.84”	−60.2	6.0	13.6	78 ± 72	3 ± 5	11.6 ± 36.7	7.6 ± 24.4	0.15	56	0.4	*SA*	0
1373	$13^h29^m51.85^s$	47°12′19.79”	−55.2	4.0	8.6	130 ± 32	6 ± 1	14.9 ± 6.0	41.3 ± 21.2	0.64	110	0.8	*SA*	0
1374	$13^h29^m52.88^s$	47°12′24.18”	−62.8	5.6	13.0	123 ± 22	8 ± 3	20.2 ± 10.6	74.6 ± 57.6	0.85	24	0.8	*SA*	0
1375	$13^h29^m54.27^s$	47°12′30.29”	−59.8	4.6	10.8	44 ± 24	9 ± 4	3.5 ± 1.7	38.7 ± 49.2	2.53	171	0.8	*SA*	0
1376	$13^h29^m52.11^s$	47°12′34.95”	−56.9	4.2	8.7	31 ± 14	6 ± 4	3.0 ± 1.9	12.6 ± 16.3	0.96	172	0.8	*SA*	0
1377	$13^h29^m52.38^s$	47°12′38.85”	−58.7	7.5	16.3	111 ± 34	7 ± 4	18.3 ± 14.6	60.7 ± 75.4	0.76	22	0.3	*SA*	0
1378	$13^h29^m51.87^s$	47°12′38.95”	−61.3	6.3	13.3	32 ± 0	11 ± 10	8.2 ± 13.8	42.3 ± 74.8	1.19	35	0.7	*SA*	1
1379	$13^h29^m53.98^s$	47°12′39.64”	−58.9	3.2	6.6	32 ± 0	2 ± 2	1.4 ± 0.5	1.9 ± 3.6	0.30	29	0.2	*SA*	1
1380	$13^h29^m52.64^s$	47°12′41.06”	−57.7	3.4	7.0	20 ± 14	7 ± 3	1.8 ± 1.2	9.9 ± 14.1	1.29	25	0.4	*SA*	0
1381	$13^h29^m54.34^s$	47°12′24.94”	−53.4	6.0	13.5	62 ± 41	6 ± 4	7.8 ± 9.3	26.3 ± 45.3	0.78	176	0.7	*SA*	0
1382	$13^h29^m52.67^s$	47°12′28.45”	−56.6	7.5	15.8	73 ± 20	8 ± 3	15.0 ± 4.4	50.6 ± 38.3	0.77	151	0.7	*SA*	0
1383	$13^h29^m52.64^s$	47°12′33.18”	−56.2	4.2	9.1	90 ± 38	6 ± 2	7.0 ± 2.3	32.0 ± 21.3	1.05	15	0.3	*SA*	0
1384	$13^h29^m51.56^s$	47°12′19.96”	−49.9	3.3	7.1	35 ± 27	5 ± 5	1.7 ± 2.4	10.4 ± 21.3	1.40	4	0.8	*SA*	0
1385	$13^h29^m52.44^s$	47°12′22.23”	−49.5	2.0	4.2	25 ± 29	5 ± 4	1.4 ± 1.2	6.6 ± 13.3	1.11	166	0.6	*SA*	0
1386	$13^h29^m52.30^s$	47°12′16.74”	−45.2	2.3	5.0	32 ± 0	7 ± 9	2.0 ± 1.7	17.7 ± 42.1	2.01	128	0.4	*SA*	1
1387	$13^h29^m53.93^s$	47°12′27.26”	−48.1	3.0	6.5	51 ± 17	10 ± 4	2.1 ± 2.1	52.6 ± 47.2	5.74	65	0.9	*SA*	0
1388	$13^h29^m53.40^s$	47°12′32.67”	−41.0	2.6	6.2	32 ± 0	7 ± 3	1.2 ± 0.5	14.7 ± 12.2	2.80	52	0.3	*SA*	1
1389	$13^h29^m51.58^s$	47°12′18.22”	−32.5	1.6	3.9	32 ± 0	6 ± 3	0.7 ± 0.5	13.2 ± 14.1	4.05	165	0.5	*IA*	1
1390	$13^h29^m52.97^s$	47°12′48.90”	−91.6	2.5	5.1	32 ± 0	6 ± 5	0.5 ± 0.4	13.2 ± 20.3	6.63	174	0.8	*IA*	1
1391	$13^h29^m52.72^s$	47°12′49.36”	−80.2	5.2	9.1	27 ± 5	5 ± 2	2.8 ± 0.6	8.2 ± 7.5	0.68	5	0.4	*IA*	0
1392	$13^h29^m54.11^s$	47°13′4.38”	−96.1	5.5	5.1	32 ± 0	4 ± 2	1.4 ± 0.3	6.3 ± 6.4	1.07	166	0.6	*IA*	1
1393	$13^h29^m52.60^s$	47°12′54.70”	−81.6	4.5	6.3	30 ± 8	4 ± 1	1.8 ± 0.4	5.3 ± 5.2	0.67	40	0.7	*IA*	0
1394	$13^h29^m54.26^s$	47°12′55.07”	−66.4	5.3	7.0	35 ± 16	5 ± 3	2.0 ± 0.6	8.1 ± 10.7	0.94	130	0.5	*IA*	0
1395	$13^h29^m54.45^s$	47°12′57.19”	−68.2	5.7	7.2	32 ± 0	4 ± 7	1.4 ± 2.0	5.7 ± 19.8	0.91	76	0.5	*IA*	1
1396	$13^h29^m54.45^s$	47°12′59.38”	−67.9	6.4	6.4	30 ± 21	5 ± 5	1.2 ± 1.8	7.2 ± 14.8	1.32	114	0.6	*IA*	0
1397	$13^h29^m53.91^s$	47°12′44.78”	−60.4	3.1	6.2	47 ± 12	4 ± 1	1.9 ± 0.3	7.1 ± 5.9	0.85	157	0.4	*IA*	0
1398	$13^h29^m49.69^s$	47°12′48.14”	−111.1	1.8	5.0	40 ± 13	6 ± 3	1.0 ± 0.3	15.3 ± 16.6	3.37	17	0.4	*IA*	0
1399	$13^h29^m49.05^s$	47°12′39.48”	−83.5	2.3	5.7	42 ± 23	5 ± 4	2.4 ± 0.7	11.7 ± 18.3	1.13	163	0.4	*SA*	0
1400	$13^h29^m51.21^s$	47°12′37.82”	−79.9	2.2	5.6	22 ± 34	2 ± 2	0.4 ± 0.9	1.1 ± 3.6	0.58	3	0.8	*SA*	0
1401	$13^h29^m49.46^s$	47°12′47.38”	−83.6	3.2	7.4	16 ± 22	5 ± 3	1.3 ± 0.9	4.1 ± 7.2	0.76	19	0.8	*IA*	0
1402	$13^h29^m51.30^s$	47°12′19.10”	−79.0	1.8	4.4	32 ± 0	8 ± 4	0.6 ± 0.3	19.3 ± 18.1	7.39	168	0.6	*IA*	1
1403	$13^h29^m48.92^s$	47°12′34.85”	−76.0	4.0	9.7	33 ± 23	7 ± 4	2.0 ± 1.8	16.1 ± 17.4	1.83	52	0.7	*SA*	0
1404	$13^h29^m48.66^s$	47°12′35.32”	−79.1	1.9	5.1	32 ± 0	5 ± 4	0.4 ± 0.5	9.3 ± 14.8	5.37	18	0.8	*SA*	1
1405	$13^h29^m49.41^s$	47°12′41.32”	−76.9	8.3	18.3	78 ± 36	12 ± 9	11.8 ± 15.0	118.0 ± 168.4	2.29	158	0.6	*SA*	0
1406	$13^h29^m51.11^s$	47°12′44.42”	−72.9	4.5	8.9	38 ± 25	6 ± 3	2.3 ± 2.1	12.8 ± 17.1	1.28	145	0.8	*SA*	0

ID	RA (J2000) *h m s*	Dec (J2000) *d ’ ”*	V_{LSR} km/s	T_{max} K	S/N	R pc	σ_v km/s	L_{CO} 10^5 K km/s pc^2	M_{vir} 10^5 $M_\odot$	α	PA deg	b/a	Reg	Flag
(1)	(2)	(3)	(4)	(5)	(6)	(7)	(8)	(9)	(10)	(11)	(12)	(13)	(14)	(15)
1407	$13^h29^m50.70^s$	47°12′46.45”	−79.3	3.8	7.7	85 ± 12	7 ± 1	6.8 ± 0.9	42.3 ± 12.0	1.44	174	0.6	*IA*	0
1408	$13^h29^m48.64^s$	47°12′26.49”	−68.7	1.7	4.2	28 ± 25	6 ± 8	1.1 ± 1.1	10.7 ± 31.8	2.21	20	0.6	*SA*	0
1409	$13^h29^m49.54^s$	47°12′39.55”	−71.7	7.8	16.9	48 ± 39	7 ± 7	4.5 ± 8.8	22.7 ± 47.1	1.16	35	1.0	*SA*	0
1410	$13^h29^m51.00^s$	47°12′42.18”	−72.2	6.2	12.9	52 ± 29	7 ± 7	7.2 ± 8.0	27.7 ± 55.4	0.88	170	0.2	*SA*	0
1411	$13^h29^m50.13^s$	47°12′48.14”	−74.7	5.3	10.1	125 ± 8	8 ± 1	14.3 ± 0.9	87.3 ± 16.2	1.40	101	0.5	*IA*	0
1412	$13^h29^m49.32^s$	47°12′48.29”	−70.2	3.4	6.3	53 ± 37	2 ± 1	1.7 ± 0.7	1.6 ± 2.0	0.22	38	1.1	*IA*	0
1413	$13^h29^m51.08^s$	47°12′18.39”	−69.3	2.5	5.9	32 ± 0	4 ± 2	0.9 ± 0.4	6.3 ± 4.8	1.60	113	0.4	*IA*	1
1414	$13^h29^m48.69^s$	47°12′29.53”	−70.7	4.2	10.4	50 ± 28	4 ± 5	2.7 ± 3.3	8.6 ± 18.6	0.73	141	0.5	*SA*	0
1415	$13^h29^m51.20^s$	47°12′30.42”	−59.8	2.3	5.2	44 ± 13	8 ± 2	3.8 ± 0.9	30.6 ± 22.6	1.83	126	0.6	*SA*	0
1416	$13^h29^m50.66^s$	47°12′32.83”	−61.9	2.6	5.6	32 ± 0	10 ± 6	0.8 ± 0.4	33.0 ± 37.9	10.01	143	0.8	*SA*	1
1417	$13^h29^m49.30^s$	47°12′33.98”	−66.5	5.7	13.5	69 ± 29	12 ± 6	6.5 ± 9.3	104.7 ± 117.8	3.70	59	0.5	*SA*	0
1418	$13^h29^m48.78^s$	47°12′33.81”	−71.9	3.5	8.6	32 ± 0	8 ± 8	2.3 ± 4.3	18.7 ± 41.4	1.89	162	0.1	*SA*	1
1419	$13^h29^m51.00^s$	47°12′40.69”	−65.1	6.0	12.5	74 ± 37	2 ± 2	8.1 ± 17.7	2.6 ± 5.0	0.07	43	0.4	*SA*	0
1420	$13^h29^m49.19^s$	47°12′44.83”	−66.0	3.4	6.7	45 ± 26	5 ± 3	2.1 ± 1.4	13.3 ± 18.8	1.44	14	0.3	*IA*	0
1421	$13^h29^m49.12^s$	47°12′49.89”	−66.1	3.2	5.6	32 ± 0	4 ± 3	0.7 ± 0.5	6.4 ± 10.0	2.20	143	0.5	*IA*	1
1422	$13^h29^m49.15^s$	47°12′25.78”	−61.7	3.0	7.0	30 ± 18	6 ± 3	1.5 ± 1.3	10.7 ± 13.8	1.63	178	0.6	*SA*	0
1423	$13^h29^m49.87^s$	47°12′27.16”	−64.3	2.0	4.9	32 ± 0	3 ± 3	0.2 ± 0.2	3.9 ± 6.8	3.94	171	0.9	*SA*	1
1424	$13^h29^m51.44^s$	47°12′26.70”	−58.2	3.7	8.9	99 ± 36	6 ± 2	8.8 ± 3.8	43.2 ± 31.2	1.12	36	0.3	*SA*	0
1425	$13^h29^m49.03^s$	47°12′30.43”	−60.4	5.6	12.5	100 ± 38	18 ± 11	10.7 ± 11.2	342.0 ± 524.7	7.30	160	0.2	*SA*	0
1426	$13^h29^m50.40^s$	47°12′39.69”	−62.6	3.7	7.7	39 ± 35	5 ± 6	3.4 ± 7.6	10.4 ± 30.0	0.69	64	1.3	*SA*	0
1427	$13^h29^m51.51^s$	47°12′16.81”	−57.4	2.7	6.2	32 ± 0	8 ± 3	1.0 ± 0.8	19.9 ± 16.3	4.69	167	0.6	*IA*	1
1428	$13^h29^m51.11^s$	47°12′26.92”	−57.1	3.1	6.8	53 ± 33	7 ± 10	1.4 ± 2.7	23.7 ± 75.8	3.78	161	0.4	*SA*	0
1429	$13^h29^m49.85^s$	47°12′34.24”	−52.1	5.2	11.6	127 ± 38	6 ± 4	13.1 ± 19.1	47.1 ± 57.0	0.82	18	0.3	*SA*	0
1430	$13^h29^m49.47^s$	47°12′25.66”	−47.3	2.8	6.5	72 ± 16	6 ± 2	8.1 ± 4.8	31.0 ± 23.2	0.87	178	0.3	*SA*	0
1431	$13^h29^m50.91^s$	47°12′27.59”	−51.4	2.7	6.3	32 ± 44	10 ± 11	2.4 ± 4.0	34.0 ± 105.9	3.28	173	0.5	*SA*	0
1432	$13^h29^m49.48^s$	47°12′36.56”	−58.3	6.2	15.0	32 ± 0	10 ± 9	3.1 ± 2.4	30.1 ± 58.3	2.22	117	0.5	*SA*	1
1433	$13^h29^m50.64^s$	47°12′38.63”	−57.8	3.9	8.7	64 ± 38	7 ± 5	7.1 ± 8.8	37.2 ± 62.2	1.20	25	1.2	*SA*	0
1434	$13^h29^m51.32^s$	47°12′17.03”	−49.0	2.3	5.0	39 ± 40	4 ± 4	0.7 ± 0.5	5.9 ± 13.3	1.87	14	0.4	*IA*	0
1435	$13^h29^m51.31^s$	47°12′23.20”	−44.1	2.3	5.5	65 ± 17	10 ± 3	3.6 ± 1.4	72.9 ± 47.6	4.61	17	0.6	*SA*	0
1436	$13^h29^m48.79^s$	47°12′26.97”	−46.3	5.4	13.5	45 ± 19	5 ± 2	5.9 ± 3.0	13.3 ± 10.4	0.52	144	0.4	*SA*	0
1437	$13^h29^m49.84^s$	47°12′28.00”	−49.7	3.3	7.5	32 ± 19	4 ± 2	1.9 ± 0.8	6.3 ± 8.1	0.75	145	0.6	*SA*	0
1438	$13^h29^m50.75^s$	47°12′28.61”	−48.2	4.3	9.5	32 ± 0	10 ± 7	3.4 ± 4.0	34.1 ± 44.9	2.33	33	0.5	*SA*	1
1439	$13^h29^m49.08^s$	47°12′29.32”	−48.7	5.4	10.8	32 ± 24	6 ± 5	1.8 ± 3.7	12.2 ± 26.1	1.53	123	0.6	*SA*	0
1440	$13^h29^m50.48^s$	47°12′29.43”	−45.3	4.1	9.8	36 ± 28	8 ± 4	5.4 ± 4.2	24.1 ± 31.9	1.02	14	0.4	*SA*	0
1441	$13^h29^m51.28^s$	47°12′35.18”	−51.7	2.5	5.7	48 ± 33	6 ± 5	1.0 ± 0.9	19.3 ± 39.2	4.60	3	0.5	*SA*	0
1442	$13^h29^m49.19^s$	47°12′35.41”	−48.1	2.3	5.5	32 ± 0	5 ± 2	0.9 ± 0.6	6.8 ± 7.4	1.69	14	0.4	*SA*	1
1443	$13^h29^m50.91^s$	47°12′13.58”	−40.8	3.4	7.9	32 ± 0	4 ± 3	2.6 ± 1.6	6.6 ± 9.2	0.58	46	0.3	*IA*	1
1444	$13^h29^m51.17^s$	47°12′18.56”	−44.6	2.2	5.3	20 ± 36	13 ± 8	1.4 ± 1.7	35.2 ± 73.9	5.95	148	0.9	*IA*	0
1445	$13^h29^m51.32^s$	47°12′20.54”	−39.3	1.9	4.4	32 ± 0	5 ± 4	0.7 ± 0.4	7.3 ± 11.8	2.39	154	0.4	*IA*	1
1446	$13^h29^m48.80^s$	47°12′23.30”	−40.9	4.8	11.2	125 ± 50	11 ± 5	13.9 ± 13.5	157.0 ± 162.4	2.59	179	0.2	*SA*	0
1447	$13^h29^m49.68^s$	47°12′29.25”	−46.6	2.4	5.2	32 ± 0	7 ± 5	1.4 ± 0.6	16.5 ± 24.7	2.79	172	0.6	*SA*	1
1448	$13^h29^m50.84^s$	47°12′37.43”	−45.3	3.1	6.6	39 ± 20	2 ± 2	1.2 ± 1.3	1.3 ± 2.8	0.25	21	0.7	*SA*	0
1449	$13^h29^m50.90^s$	47°12′19.09”	−40.7	2.7	6.3	72 ± 24	8 ± 5	3.4 ± 2.5	45.3 ± 68.6	3.10	6	0.4	*IA*	0
1450	$13^h29^m49.12^s$	47°12′20.92”	−39.4	2.0	4.7	40 ± 30	2 ± 3	1.1 ± 1.2	2.1 ± 4.3	0.46	165	1.1	*IA*	0
1451	$13^h29^m50.96^s$	47°12′25.31”	−34.0	1.6	4.1	32 ± 0	5 ± 3	0.7 ± 0.5	7.6 ± 10.4	2.46	23	0.3	*SA*	1
1452	$13^h29^m49.59^s$	47°12′34.35”	−26.5	2.2	5.0	32 ± 0	5 ± 5	0.7 ± 0.7	6.8 ± 15.4	2.23	126	0.5	*SA*	1
1453	$13^h29^m49.79^s$	47°12′56.90”	−66.1	5.0	6.3	60 ± 28	5 ± 3	7.4 ± 4.6	16.3 ± 21.8	0.50	41	0.3	*IA*	0
1454	$13^h29^m49.98^s$	47°12′58.86”	−60.0	6.6	7.0	30 ± 21	5 ± 3	3.1 ± 2.6	8.7 ± 15.0	0.65	143	0.6	*IA*	0
1455	$13^h29^m49.38^s$	47°12′58.12”	−52.1	4.2	4.3	32 ± 0	9 ± 5	2.8 ± 1.9	25.4 ± 26.5	2.09	159	0.6	*IA*	1
1456	$13^h29^m49.95^s$	47°12′12.78”	−55.9	2.7	6.4	32 ± 0	15 ± 4	2.3 ± 0.3	78.9 ± 42.5	7.88	10	0.3	*IA*	1
1457	$13^h29^m50.86^s$	47°12′58.09”	−61.2	5.4	5.5	50 ± 11	7 ± 3	5.0 ± 0.9	22.4 ± 16.5	1.03	38	0.6	*IA*	0
1458	$13^h29^m48.71^s$	47°12′44.36”	−50.4	2.7	5.1	87 ± 13	6 ± 1	5.1 ± 1.0	29.1 ± 11.9	1.30	19	0.5	*IA*	0
1459	$13^h29^m49.12^s$	47°12′17.18”	−32.3	2.4	5.4	32 ± 0	9 ± 2	1.6 ± 0.4	24.9 ± 13.7	3.52	152	0.5	*IA*	1
1460	$13^h29^m48.82^s$	47°12′16.10”	−28.3	1.7	4.3	32 ± 0	12 ± 8	0.8 ± 0.5	45.3 ± 63.0	12.32	156	0.7	*IA*	1
1461	$13^h29^m48.86^s$	47°12′17.31”	−1.9	2.1	5.7	32 ± 0	8 ± 3	1.0 ± 0.3	22.2 ± 18.3	5.28	155	0.5	*IA*	1
1462	$13^h29^m49.51^s$	47°12′22.49”	−36.5	2.1	4.9	32 ± 0	4 ± 2	0.8 ± 0.2	5.1 ± 4.0	1.43	159	0.6	*IA*	1
1463	$13^h29^m50.17^s$	47°12′24.23”	4.5	2.0	5.3	32 ± 0	3 ± 1	0.5 ± 0.2	2.1 ± 1.9	1.05	165	0.8	*IA*	1
1464	$13^h29^m46.81^s$	47°12′13.45”	−115.3	1.7	5.3	32 ± 0	2 ± 1	0.3 ± 0.1	1.8 ± 2.3	1.60	56	0.7	*SA*	1
1465	$13^h29^m48.25^s$	47°12′36.26”	−97.6	1.9	5.6	32 ± 0	5 ± 5	0.4 ± 0.3	7.2 ± 14.7	4.09	119	0.9	*SA*	1
1466	$13^h29^m46.26^s$	47°12′13.51”	−89.7	1.5	3.8	32 ± 0	6 ± 6	0.5 ± 0.4	13.6 ± 24.6	6.39	155	0.6	*SA*	1

ID (1)	**RA (J2000)** *h m s* (2)	**Dec (J2000)** *d ′ ”* (3)	$\mathbf{V_{LSR}}$ km/s (4)	$\mathbf{T_{max}}$ K (5)	**S/N** (6)	**R** pc (7)	$\sigma_\mathbf{v}$ km/s (8)	$\mathbf{L_{CO}}$ 10^5 K km/s pc^2 (9)	$\mathbf{M_{vir}}$ 10^5 $M_\odot$ (10)	α (11)	**PA** deg (12)	**b/a** (13)	**Reg** (14)	**Flag** (15)
1467	$13^h29^m47.24^s$	47°12′25.19”	−89.2	1.6	3.9	32 ± 0	5 ± 3	0.5 ± 0.5	9.9 ± 11.1	4.62	159	0.5	*SA*	1
1468	$13^h29^m48.51^s$	47°12′37.28”	−83.3	2.5	6.5	72 ± 57	4 ± 3	3.4 ± 3.0	11.8 ± 18.4	0.78	174	0.8	*SA*	0
1469	$13^h29^m48.04^s$	47°12′26.33”	−69.7	2.0	5.0	32 ± 0	7 ± 4	0.8 ± 0.4	15.5 ± 17.5	4.50	133	0.7	*SA*	1
1470	$13^h29^m48.24^s$	47°12′36.93”	−75.6	3.5	8.6	90 ± 20	9 ± 4	6.7 ± 1.5	71.1 ± 82.6	2.42	70	0.4	*SA*	0
1471	$13^h29^m48.38^s$	47°12′30.92”	−71.3	4.5	10.6	78 ± 30	6 ± 3	7.8 ± 4.9	29.7 ± 26.4	0.88	140	0.2	*SA*	0
1472	$13^h29^m46.94^s$	47°12′18.23”	−59.3	4.8	11.3	53 ± 27	7 ± 7	2.6 ± 5.1	24.4 ± 52.2	2.17	151	0.3	*SA*	0
1473	$13^h29^m47.63^s$	47°12′20.65”	−62.5	4.1	9.4	43 ± 27	7 ± 4	4.5 ± 3.6	23.5 ± 29.2	1.20	33	0.9	*SA*	0
1474	$13^h29^m48.05^s$	47°12′32.08”	−67.5	2.5	5.9	27 ± 12	9 ± 3	1.7 ± 0.3	21.7 ± 17.1	2.89	86	0.9	*SA*	0
1475	$13^h29^m46.28^s$	47°12′13.32”	−56.2	7.2	15.3	65 ± 25	7 ± 3	14.9 ± 7.1	34.5 ± 29.4	0.53	140	0.4	*SA*	0
1476	$13^h29^m46.68^s$	47°12′20.16”	−56.2	5.4	11.8	47 ± 16	6 ± 2	5.2 ± 1.6	14.8 ± 11.2	0.66	9	0.5	*SA*	0
1477	$13^h29^m46.90^s$	47°12′23.10”	−59.1	5.3	12.4	58 ± 21	7 ± 2	5.9 ± 2.0	25.9 ± 19.7	1.01	23	0.5	*SA*	0
1478	$13^h29^m47.51^s$	47°12′25.64”	−61.1	4.7	12.1	127 ± 64	3 ± 3	9.7 ± 3.0	12.0 ± 20.1	0.28	92	0.5	*SA*	0
1479	$13^h29^m46.94^s$	47°12′26.91”	−59.2	2.2	5.3	32 ± 0	4 ± 2	0.4 ± 0.2	4.4 ± 4.2	2.68	176	0.5	*SA*	1
1480	$13^h29^m46.53^s$	47°12′16.59”	−53.8	4.5	11.0	46 ± 25	6 ± 4	2.8 ± 2.8	15.7 ± 19.8	1.28	105	1.1	*SA*	0
1481	$13^h29^m47.32^s$	47°12′22.73”	−54.5	5.7	13.2	75 ± 43	9 ± 7	10.4 ± 11.9	69.6 ± 134.6	1.53	28	0.5	*SA*	0
1482	$13^h29^m47.87^s$	47°12′24.51”	−58.1	2.1	5.1	44 ± 71	4 ± 6	2.0 ± 2.3	9.2 ± 31.3	1.05	42	0.9	*SA*	0
1483	$13^h29^m48.47^s$	47°12′24.53”	−52.5	4.1	9.9	80 ± 38	2 ± 0	3.8 ± 3.1	3.8 ± 1.8	0.23	157	0.3	*SA*	1
1484	$13^h29^m46.23^s$	47°12′15.87”	−49.4	7.1	15.6	51 ± 27	3 ± 3	4.3 ± 4.0	3.6 ± 6.5	0.19	112	0.4	*SA*	0
1485	$13^h29^m47.84^s$	47°12′19.45”	−46.6	2.6	6.3	40 ± 28	5 ± 4	0.9 ± 0.9	8.9 ± 17.4	2.30	124	0.8	*SA*	0
1486	$13^h29^m47.82^s$	47°12′16.46”	−42.0	2.0	4.5	33 ± 18	6 ± 3	1.3 ± 1.6	10.8 ± 11.0	1.92	168	0.5	*SA*	0
1487	$13^h29^m48.58^s$	47°12′21.68”	−41.2	5.4	12.4	65 ± 32	6 ± 3	6.3 ± 6.3	24.2 ± 21.9	0.89	175	0.4	*SA*	0
1488	$13^h29^m46.73^s$	47°12′15.11”	−35.8	7.1	16.3	57 ± 15	11 ± 3	11.4 ± 11.0	72.5 ± 37.9	1.47	134	0.6	*SA*	0
1489	$13^h29^m48.17^s$	47°12′15.57”	−39.2	2.8	6.8	34 ± 28	2 ± 4	0.8 ± 0.8	2.1 ± 6.4	0.58	11	1.1	*IA*	0
1490	$13^h29^m48.28^s$	47°12′19.75”	−42.0	3.9	8.8	57 ± 35	1 ± 1	3.2 ± 3.3	0.4 ± 1.6	0.03	104	0.2	*SA*	0
1491	$13^h29^m47.85^s$	47°12′20.62”	−38.2	2.7	6.3	59 ± 23	2 ± 3	0.6 ± 0.3	3.2 ± 10.5	1.24	11	0.6	*SA*	0
1492	$13^h29^m48.08^s$	47°12′22.20”	−40.2	3.5	7.6	61 ± 40	3 ± 3	0.7 ± 0.7	4.3 ± 9.3	1.50	93	1.0	*SA*	0
1493	$13^h29^m47.53^s$	47°12′22.25”	−40.6	4.5	10.6	45 ± 54	14 ± 14	1.2 ± 2.3	85.3 ± 207.8	16.22	147	0.5	*SA*	0
1494	$13^h29^m46.62^s$	47°12′12.86”	−28.0	5.5	13.6	32 ± 0	15 ± 14	4.4 ± 8.8	74.1 ± 138.6	3.88	127	0.4	*SA*	1
1495	$13^h29^m48.04^s$	47°12′14.47”	−29.4	4.6	11.4	60 ± 16	6 ± 2	7.6 ± 2.8	25.8 ± 20.0	0.78	154	1.1	*IA*	0
1496	$13^h29^m47.22^s$	47°12′16.57”	−31.1	2.3	5.4	54 ± 35	12 ± 9	2.7 ± 3.3	78.7 ± 159.2	6.76	7	0.3	*SA*	0
1497	$13^h29^m46.65^s$	47°12′13.37”	2.7	1.7	4.3	32 ± 0	8 ± 8	0.9 ± 0.5	19.7 ± 39.3	4.89	131	0.3	*SA*	1
1498	$13^h29^m47.37^s$	47°12′30.80”	−67.6	4.4	10.1	38 ± 10	5 ± 1	2.7 ± 0.2	10.5 ± 7.2	0.89	175	0.5	*SA*	0
1499	$13^h29^m47.52^s$	47°12′40.82”	−64.8	3.4	7.5	40 ± 12	8 ± 2	2.0 ± 0.3	26.6 ± 15.0	3.07	173	0.6	*IA*	0
1500	$13^h29^m47.07^s$	47°12′39.60”	−66.1	2.4	5.2	40 ± 11	5 ± 1	1.3 ± 0.4	9.5 ± 5.4	1.65	98	0.6	*IA*	0
1501	$13^h29^m48.10^s$	47°12′49.25”	−61.7	3.6	6.3	61 ± 11	8 ± 2	5.0 ± 0.7	38.8 ± 21.2	1.77	38	0.3	*IA*	0
1502	$13^h29^m48.30^s$	47°13′3.07”	−53.0	5.3	4.5	32 ± 0	11 ± 5	4.9 ± 2.3	40.1 ± 38.9	1.88	3	0.4	*IA*	1
1503	$13^h29^m48.42^s$	47°13′4.80”	−52.6	5.5	4.4	32 ± 0	6 ± 2	2.0 ± 1.2	11.5 ± 8.7	1.29	28	0.6	*IA*	1
1504	$13^h29^m46.63^s$	47°12′38.61”	−51.8	2.4	4.5	36 ± 19	5 ± 3	1.0 ± 1.1	7.7 ± 14.1	1.71	17	0.4	*IA*	0
1505	$13^h29^m46.49^s$	47°12′39.66”	−57.1	2.8	5.1	32 ± 0	4 ± 2	0.6 ± 0.3	6.4 ± 6.7	2.44	178	0.3	*IA*	1
1506	$13^h29^m46.05^s$	47°12′35.80”	−15.4	2.7	4.6	32 ± 0	3 ± 2	1.0 ± 0.3	2.8 ± 3.5	0.64	3	0.3	*IA*	1
1507	$13^h29^m46.33^s$	47°12′40.28”	−0.4	2.9	5.6	32 ± 0	10 ± 4	0.8 ± 0.2	33.7 ± 23.4	9.16	148	0.6	*IA*	1

Table 4.6: (1) island identification number (*ID*), (2) Right Ascension (*RA (J2000)*), (3) Declination (*Dec (J2000)*), (4) Velocity with respect to the systematic velocity of the galaxy (V_{LSR} = 472 km/s, Shetty et al. (2007)), (5) Peak brightness temperature (T_{max}), (6) Peak signal-to-noise ratio (S/N), (7) Radius (R), (8) Velocity dispersion (σ_v), (9) CO luminosity (L_{CO}), (10) Mass from virial theorem (M_{vir}), (11) Virial parameter (α), (12) Position angle of island major axis, measured from North through West (*PA*), (13) Ratio between minor axis and major axis (b/a), (14) Region of M51 where a given island has been identified, i.e. center (*CR*), spiral arms (*SA*), inter-arm (*IA*), (15) Flag= 0 indicates an actual measurement of the island radius, Flag= 1 indicates that the radius is an upper limit.

THE PAWS M51 ISLAND CATALOG

ID (1)	RA (J2000) *h m s* (2)	Dec (J2000) *d ’ ”* (3)	V_{LSR} km/s (4)	T_{max} K (5)	S/N (6)	R pc (7)	σ_v km/s (8)	L_{CO} 10^5 K km/s pc^2 (9)	M_{vir} 10^5 $M_\odot$ (10)	α (11)	PA deg (12)	b/a (13)	Reg (14)	Flag (15)
1	$13^h29^m48.60^s$	47°12′8.20”	−125.1	1.3	4.4	14 ± 26	4 ± 3	0.3 ± 0.2	2.5 ± 6.3	1.71	95	1.0	*IA*	0
2	$13^h29^m57.93^s$	47°13′4.42”	−120.7	4.9	5.0	33 ± 0	5 ± 3	1.3 ± 0.6	8.1 ± 10.2	1.40	155	0.6	*IA*	1
3	$13^h29^m46.81^s$	47°12′13.44”	−115.5	1.7	5.3	33 ± 0	2 ± 2	0.3 ± 0.1	1.9 ± 2.5	1.50	56	0.8	*SA*	1
4	$13^h29^m49.69^s$	47°12′48.13”	−111.1	1.8	5.1	42 ± 13	6 ± 3	1.1 ± 0.3	16.0 ± 16.2	3.35	18	0.4	*IA*	0
5	$13^h29^m55.19^s$	47°13′1.08”	−113.3	3.5	4.8	33 ± 0	5 ± 2	1.2 ± 0.5	8.3 ± 7.7	1.60	163	0.5	*IA*	1
6	$13^h29^m49.61^s$	47°11′49.70”	−104.4	2.1	6.5	33 ± 0	7 ± 2	0.9 ± 0.2	17.8 ± 11.8	4.59	158	0.5	*CR*	1
7	$13^h29^m53.21^s$	47°11′54.42”	−110.4	1.7	5.3	22 ± 10	7 ± 3	0.6 ± 0.2	12.3 ± 9.5	4.86	37	0.5	*CR*	0
8	$13^h29^m52.22^s$	47°11′40.99”	0.8	16.5	41.6	2346 ± 7	51 ± 0	6446.7 ± 24.1	62661.8 ± 825.9	2.23	52	0.7	*CR*	0
9	$13^h29^m54.93^s$	47°12′11.14”	−112.1	1.4	5.2	33 ± 0	5 ± 3	0.3 ± 0.2	9.8 ± 11.9	6.65	15	0.7	*SA*	1
10	$13^h30^m0.26^s$	47°12′54.19”	−110.0	2.6	5.4	33 ± 0	8 ± 4	1.0 ± 0.3	21.7 ± 19.7	5.07	132	0.6	*SA*	1
11	$13^h29^m44.53^s$	47°12′0.38”	−100.3	1.9	5.3	31 ± 11	10 ± 3	1.0 ± 0.2	31.2 ± 28.6	6.91	148	0.6	*SA*	0
12	$13^h29^m46.96^s$	47°12′10.80”	−105.2	1.8	6.1	33 ± 0	5 ± 3	0.4 ± 0.2	7.5 ± 9.2	4.55	139	0.5	*SA*	1
13	$13^h29^m54.68^s$	47°12′23.40”	−102.0	1.8	5.9	37 ± 10	7 ± 2	1.3 ± 0.3	17.5 ± 11.3	3.01	124	0.5	*SA*	0
14	$13^h29^m56.21^s$	47°12′52.77”	−74.3	5.0	9.2	115 ± 5	10 ± 1	13.4 ± 0.8	114.5 ± 35.8	1.95	55	0.6	*IA*	0
15	$13^h29^m54.48^s$	47°12′56.16”	−64.8	6.4	9.2	175 ± 8	12 ± 1	34.6 ± 1.4	249.5 ± 51.9	1.66	76	0.7	*IA*	0
16	$13^h29^m59.88^s$	47°13′3.25”	−46.7	6.9	6.3	94 ± 8	18 ± 3	24.5 ± 2.3	303.2 ± 117.1	2.84	30	0.5	*SA*	0
17	$13^h29^m49.02^s$	47°11′39.53”	−93.1	2.0	6.4	33 ± 0	7 ± 2	0.9 ± 0.2	14.4 ± 8.6	3.81	174	0.2	*SA*	1
18	$13^h29^m51.14^s$	47°12′8.72”	−99.8	1.5	5.0	33 ± 0	2 ± 2	0.4 ± 0.2	1.5 ± 2.3	0.90	19	0.4	*CR*	1
19	$13^h29^m52.75^s$	47°12′49.36”	−81.2	5.2	10.1	30 ± 5	7 ± 2	3.3 ± 0.3	17.1 ± 13.4	1.18	9	0.3	*IA*	0
20	$13^h29^m54.11^s$	47°13′4.38”	−96.1	5.5	5.2	33 ± 0	5 ± 2	1.4 ± 0.4	6.9 ± 6.9	1.12	166	0.6	*IA*	1
21	$13^h29^m47.07^s$	47°11′39.32”	−89.1	1.6	4.7	33 ± 0	5 ± 3	0.4 ± 0.2	8.4 ± 10.8	4.30	153	0.6	*IA*	1
22	$13^h29^m49.79^s$	47°11′41.80”	−90.0	1.6	5.0	33 ± 0	2 ± 1	0.3 ± 0.2	1.1 ± 1.4	0.94	24	0.8	*CR*	1
23	$13^h29^m49.30^s$	47°11′46.49”	−83.8	1.9	5.2	33 ± 0	12 ± 3	0.8 ± 0.2	48.6 ± 25.2	14.30	151	0.6	*SA*	1
24	$13^h29^m47.69^s$	47°11′52.39”	−93.0	2.5	7.5	33 ± 0	4 ± 1	0.6 ± 0.1	6.7 ± 4.0	2.49	123	0.7	*IA*	1
25	$13^h29^m56.09^s$	47°12′57.24”	−82.2	3.5	5.3	33 ± 0	5 ± 3	1.0 ± 0.3	9.1 ± 10.8	2.02	143	0.5	*IA*	1
26	$13^h29^m50.74^s$	47°13′4.50”	−71.0	5.9	5.0	33 ± 0	13 ± 3	5.7 ± 1.0	56.8 ± 26.7	2.28	29	0.4	*IA*	1
27	$13^h29^m52.80^s$	47°13′5.96”	−72.2	7.9	5.8	33 ± 0	11 ± 4	2.1 ± 0.8	43.2 ± 28.5	4.80	144	0.7	*IA*	1
28	$13^h29^m52.69^s$	47°11′27.69”	−82.5	1.8	5.0	33 ± 0	4 ± 2	0.8 ± 0.2	4.5 ± 5.2	1.31	179	0.2	*CR*	1
29	$13^h29^m58.85^s$	47°12′19.64”	−81.2	1.6	4.8	33 ± 0	4 ± 4	0.3 ± 0.1	4.4 ± 10.9	3.70	174	0.7	*IA*	1
30	$13^h30^m0.06^s$	47°12′36.69”	−54.6	3.5	8.3	279 ± 13	12 ± 1	21.7 ± 0.7	396.6 ± 68.4	4.19	97	0.4	*SA*	0
31	$13^h29^m59.58^s$	47°12′46.08”	−75.1	2.3	5.0	37 ± 16	11 ± 2	1.6 ± 0.6	42.1 ± 24.7	5.95	68	0.5	*IA*	0
32	$13^h29^m59.62^s$	47°12′50.16”	−73.5	3.9	7.6	83 ± 11	8 ± 1	6.5 ± 0.6	54.5 ± 22.1	1.93	63	0.4	*SA*	0
33	$13^h30^m2.17^s$	47°11′35.54”	−72.5	2.6	5.4	31 ± 14	8 ± 3	1.4 ± 0.3	19.0 ± 16.3	3.05	141	0.6	*IA*	0
34	$13^h29^m57.55^s$	47°12′24.41”	−51.4	4.7	12.1	336 ± 6	10 ± 1	76.3 ± 1.6	371.9 ± 43.5	1.12	63	0.6	*IA*	0
35	$13^h29^m56.46^s$	47°12′28.56”	−61.0	3.9	10.0	68 ± 7	10 ± 1	6.6 ± 0.4	73.8 ± 22.4	2.58	155	0.8	*IA*	0
36	$13^h29^m47.50^s$	47°12′40.62”	−67.0	3.4	8.2	61 ± 13	11 ± 2	2.7 ± 0.2	75.7 ± 46.7	6.50	147	0.5	*IA*	0
37	$13^h29^m56.99^s$	47°12′41.96”	−76.5	2.1	5.6	33 ± 0	5 ± 3	0.7 ± 0.2	8.4 ± 8.9	2.58	7	0.3	*IA*	1
38	$13^h29^m52.55^s$	47°12′54.82”	−80.1	4.5	6.8	49 ± 11	5 ± 1	3.0 ± 0.5	14.4 ± 7.3	1.11	18	0.3	*IA*	0
39	$13^h29^m59.22^s$	47°13′5.28”	−59.0	8.0	6.5	66 ± 17	9 ± 2	9.6 ± 1.8	53.4 ± 32.8	1.27	166	0.5	*SA*	0
40	$13^h29^m49.90^s$	47°12′13.26”	−59.6	2.7	7.1	77 ± 13	15 ± 3	4.8 ± 0.4	178.7 ± 84.4	8.63	29	0.4	*IA*	0
41	$13^h29^m47.37^s$	47°12′30.80”	−67.6	4.4	11.1	40 ± 8	5 ± 1	2.9 ± 0.3	11.4 ± 6.1	0.89	175	0.5	*SA*	0
42	$13^h29^m56.53^s$	47°12′32.35”	−65.6	3.0	7.7	63 ± 9	11 ± 3	3.8 ± 0.3	83.5 ± 56.2	5.00	29	0.3	*IA*	0
43	$13^h29^m56.30^s$	47°12′37.94”	−68.2	3.3	7.9	71 ± 10	5 ± 1	2.8 ± 0.2	15.6 ± 9.2	1.27	89	0.4	*IA*	0
44	$13^h29^m49.71^s$	47°12′57.82”	−62.4	6.6	8.6	124 ± 11	9 ± 1	16.0 ± 1.2	94.1 ± 30.0	1.35	2	0.5	*IA*	0
45	$13^h30^m1.31^s$	47°12′41.81”	−30.1	13.6	30.7	563 ± 9	13 ± 0	363.1 ± 4.4	1029.1 ± 52.6	0.65	78	0.3	*SA*	0
46	$13^h30^m1.44^s$	47°12′59.11”	−69.3	4.2	5.5	33 ± 0	11 ± 3	1.1 ± 0.3	39.0 ± 22.3	7.87	161	0.7	*SA*	1
47	$13^h29^m50.40^s$	47°12′59.18”	−57.3	6.1	6.5	70 ± 9	10 ± 2	9.0 ± 1.7	75.8 ± 36.9	1.93	39	0.4	*IA*	0
48	$13^h29^m59.34^s$	47°13′3.04”	−65.2	6.1	5.7	34 ± 14	12 ± 3	3.7 ± 1.2	48.5 ± 46.1	2.98	24	0.6	*SA*	0
49	$13^h29^m41.20^s$	47°11′26.16”	−68.9	3.9	5.1	33 ± 0	4 ± 2	0.9 ± 0.4	4.6 ± 4.7	1.23	128	0.6	*IA*	1
50	$13^h29^m44.14^s$	47°11′57.14”	−61.4	2.2	4.6	33 ± 0	9 ± 3	1.2 ± 0.5	27.4 ± 15.4	5.25	22	0.5	*SA*	1
51	$13^h29^m46.56^s$	47°12′6.57”	−63.6	2.5	6.4	26 ± 11	6 ± 2	1.5 ± 0.2	10.1 ± 8.4	1.52	8	0.8	*SA*	0

ID	**RA (J2000)**	**Dec (J2000)**	**V_{LSR}**	**T_{max}**	**S/N**	**R**	**σ_v**	**L_{CO}**	**M_{vir}**	α	**PA**	**b/a**	**Reg**	**Flag**
	h m s	*d ’ ”*	km/s	K		pc	km/s	10^5 K km/s pc^2	10^5 $M_\odot$		deg			
(1)	(2)	(3)	(4)	(5)	(6)	(7)	(8)	(9)	(10)	(11)	(12)	(13)	(14)	(15)
52	$13^h29^m55.96^s$	47°12′32.48”	−56.4	2.5	5.9	33 ± 0	12 ± 4	1.0 ± 0.3	50.8 ± 34.3	11.95	5	0.8	*IA*	1
53	$13^h29^m57.59^s$	47°12′39.92”	−59.3	3.4	8.3	179 ± 12	10 ± 1	17.5 ± 0.9	193.6 ± 54.9	2.53	74	0.5	*IA*	0
54	$13^h29^m47.07^s$	47°12′39.59”	−66.1	2.4	5.6	42 ± 10	5 ± 2	1.5 ± 0.3	10.3 ± 8.3	1.56	96	0.6	*IA*	0
55	$13^h29^m46.56^s$	47°12′39.19”	−55.3	2.8	5.5	43 ± 11	6 ± 2	2.5 ± 0.4	15.2 ± 11.2	1.37	26	0.4	*IA*	0
56	$13^h29^m57.64^s$	47°12′51.57”	−67.2	2.5	4.4	33 ± 0	7 ± 4	0.8 ± 0.4	14.5 ± 16.3	4.05	3	0.5	*IA*	1
57	$13^h29^m49.25^s$	47°13′1.03”	−72.2	4.1	4.6	33 ± 0	4 ± 2	1.0 ± 0.5	6.0 ± 5.4	1.36	154	0.7	*IA*	1
58	$13^h29^m57.08^s$	47°13′0.05”	−60.1	5.0	5.6	113 ± 10	9 ± 2	13.2 ± 2.0	98.4 ± 32.5	1.71	140	0.9	*IA*	0
59	$13^h29^m44.66^s$	47°11′7.83”	−67.7	1.8	5.4	33 ± 0	6 ± 2	0.6 ± 0.3	11.4 ± 7.3	4.57	156	0.7	*SA*	1
60	$13^h29^m55.41^s$	47°12′43.75”	−53.5	2.9	6.5	46 ± 10	8 ± 3	2.0 ± 0.3	31.4 ± 20.1	3.63	27	0.6	*IA*	0
61	$13^h29^m53.82^s$	47°12′44.88”	−56.5	3.1	7.0	92 ± 16	9 ± 2	4.5 ± 0.4	77.1 ± 38.1	3.96	179	0.3	*IA*	0
62	$13^h29^m48.09^s$	47°12′49.31”	−61.6	3.6	6.7	69 ± 12	8 ± 2	5.6 ± 0.8	48.0 ± 25.5	1.96	38	0.3	*IA*	0
63	$13^h29^m50.85^s$	47°12′58.12”	−60.7	5.4	6.3	54 ± 10	7 ± 2	5.8 ± 0.8	29.4 ± 16.5	1.16	38	0.6	*IA*	0
64	$13^h29^m55.39^s$	47°12′59.58”	−70.1	4.2	4.5	33 ± 0	2 ± 1	0.7 ± 0.4	0.9 ± 0.8	0.30	179	0.9	*IA*	1
65	$13^h29^m48.33^s$	47°13′3.57”	−52.8	5.5	5.1	59 ± 11	9 ± 3	7.4 ± 1.6	54.0 ± 30.9	1.68	132	0.7	*IA*	0
66	$13^h29^m53.28^s$	47°13′2.36”	−57.9	6.2	5.4	52 ± 13	8 ± 2	5.9 ± 1.0	38.7 ± 25.5	1.52	143	0.5	*IA*	0
67	$13^h30^m0.71^s$	47°13′5.91”	−65.8	6.4	4.7	33 ± 0	3 ± 3	1.3 ± 0.6	2.7 ± 5.3	0.49	172	0.2	*SA*	1
68	$13^h29^m54.08^s$	47°11′42.95”	−59.7	2.2	5.8	33 ± 0	5 ± 2	0.6 ± 0.1	9.5 ± 8.8	3.91	35	0.9	*CR*	1
69	$13^h29^m59.22^s$	47°12′23.79”	−49.8	2.4	6.0	99 ± 11	6 ± 1	5.6 ± 0.5	37.0 ± 17.9	1.51	106	0.5	*IA*	0
70	$13^h29^m45.45^s$	47°12′34.43”	−52.4	3.5	5.3	59 ± 21	11 ± 3	3.4 ± 0.7	72.6 ± 49.0	4.94	7	0.5	*IA*	0
71	$13^h29^m48.71^s$	47°12′44.33”	−50.3	2.7	5.8	91 ± 11	6 ± 1	5.8 ± 0.7	31.3 ± 12.3	1.24	20	0.5	*IA*	0
72	$13^h29^m55.02^s$	47°12′46.69”	−61.1	2.8	5.7	33 ± 0	4 ± 2	0.7 ± 0.2	5.5 ± 6.7	1.92	118	0.5	*IA*	1
73	$13^h29^m54.32^s$	47°12′47.59”	−56.2	2.5	5.2	25 ± 10	6 ± 3	2.3 ± 0.5	11.0 ± 9.5	1.10	41	0.5	*IA*	0
74	$13^h29^m59.25^s$	47°12′59.99”	−59.4	5.2	5.6	35 ± 13	4 ± 2	2.7 ± 0.7	6.2 ± 6.3	0.53	60	0.4	*SA*	0
75	$13^h29^m57.92^s$	47°11′45.13”	−3.0	2.1	5.6	70 ± 9	25 ± 4	7.0 ± 0.7	435.3 ± 149.9	14.24	153	0.7	*IA*	0
76	$13^h29^m44.53^s$	47°11′55.25”	−49.1	1.9	4.5	37 ± 9	6 ± 2	1.9 ± 0.5	13.7 ± 9.1	1.67	38	0.5	*SA*	0
77	$13^h29^m58.46^s$	47°12′7.15”	−43.9	2.3	5.7	78 ± 11	9 ± 2	4.8 ± 0.7	68.7 ± 36.2	3.27	47	0.7	*IA*	0
78	$13^h29^m56.06^s$	47°12′19.88”	−45.9	3.0	7.7	78 ± 8	9 ± 1	5.5 ± 0.4	62.5 ± 20.4	2.61	100	0.4	*SA*	0
79	$13^h29^m43.99^s$	47°12′22.79”	−39.2	5.3	5.2	61 ± 11	14 ± 2	6.1 ± 1.2	122.2 ± 54.2	4.63	158	0.4	*IA*	0
80	$13^h30^m3.75^s$	47°12′46.43”	−60.2	4.8	5.9	33 ± 0	2 ± 2	0.7 ± 0.3	1.8 ± 2.6	0.57	134	0.7	*IA*	1
81	$13^h30^m2.91^s$	47°13′1.72”	−39.7	6.8	5.8	60 ± 11	10 ± 2	10.9 ± 1.8	58.1 ± 35.8	1.22	19	0.9	*IA*	0
82	$13^h29^m55.23^s$	47°13′4.03”	−58.6	5.9	5.1	33 ± 0	3 ± 2	1.4 ± 0.7	3.9 ± 4.9	0.62	171	0.7	*IA*	1
83	$13^h29^m48.71^s$	47°11′57.77”	−22.9	3.3	8.3	211 ± 18	13 ± 2	14.9 ± 0.8	382.7 ± 123.1	5.88	126	0.5	*IA*	0
84	$13^h29^m57.04^s$	47°11′56.52”	−22.1	3.8	9.1	90 ± 9	10 ± 2	5.8 ± 0.4	99.3 ± 39.1	3.94	145	0.2	*SA*	0
85	$13^h29^m51.36^s$	47°12′5.58”	−49.9	2.8	6.8	17 ± 5	4 ± 2	1.5 ± 0.2	2.8 ± 2.9	0.43	68	0.5	*CR*	0
86	$13^h29^m56.92^s$	47°12′7.45”	−29.6	2.7	6.8	107 ± 7	11 ± 1	10.5 ± 0.7	143.4 ± 36.8	3.13	101	0.7	*SA*	0
87	$13^h29^m54.86^s$	47°13′1.36”	−50.5	5.5	5.6	33 ± 0	5 ± 3	2.1 ± 0.7	8.2 ± 9.3	0.91	121	0.5	*IA*	1
88	$13^h29^m44.51^s$	47°11′6.73”	−28.2	1.8	4.9	32 ± 12	11 ± 4	1.3 ± 0.4	41.9 ± 33.1	7.36	173	0.4	*SA*	0
89	$13^h29^m59.10^s$	47°12′0.03”	−27.1	2.1	5.4	82 ± 11	11 ± 2	4.3 ± 0.7	95.3 ± 48.2	5.04	167	0.8	*IA*	0
90	$13^h29^m49.69^s$	47°12′7.07”	−33.6	4.5	11.4	188 ± 9	8 ± 1	25.0 ± 0.8	133.3 ± 21.8	1.22	149	0.3	*IA*	0
91	$13^h29^m56.53^s$	47°12′11.59”	−33.9	4.4	10.8	34 ± 10	6 ± 1	2.6 ± 0.3	11.7 ± 6.7	1.04	145	0.7	*SA*	0
92	$13^h29^m56.43^s$	47°12′15.64”	−43.5	3.2	8.2	45 ± 8	5 ± 1	2.3 ± 0.3	12.9 ± 5.7	1.27	15	0.4	*SA*	0
93	$13^h29^m57.06^s$	47°12′37.25”	−38.4	2.3	5.4	33 ± 0	8 ± 2	1.3 ± 0.4	19.4 ± 10.1	3.44	2	0.4	*IA*	1
94	$13^h29^m56.02^s$	47°12′45.89”	−49.6	2.9	6.5	33 ± 0	3 ± 1	0.6 ± 0.2	2.5 ± 2.4	1.02	38	0.8	*IA*	1
95	$13^h29^m43.61^s$	47°11′15.74”	−5.1	4.3	11.6	194 ± 7	16 ± 1	32.9 ± 1.3	523.1 ± 47.7	3.65	106	0.6	*SA*	0
96	$13^h29^m57.51^s$	47°11′50.22”	−20.2	3.8	9.7	148 ± 7	7 ± 1	14.8 ± 0.8	79.7 ± 18.4	1.24	60	0.7	*IA*	0
97	$13^h30^m1.28^s$	47°11′53.77”	8.0	6.6	15.9	495 ± 8	20 ± 0	292.9 ± 2.9	2016.3 ± 78.7	1.58	117	0.2	*SA*	0
98	$13^h29^m44.76^s$	47°12′1.37”	−34.2	3.5	7.7	68 ± 13	6 ± 1	3.9 ± 0.4	25.8 ± 11.9	1.53	152	0.3	*SA*	0
99	$13^h29^m58.72^s$	47°12′10.54”	−42.3	2.4	6.0	33 ± 0	4 ± 1	0.9 ± 0.2	4.7 ± 3.7	1.17	98	0.5	*IA*	1
100	$13^h30^m0.32^s$	47°12′14.84”	−31.7	3.7	9.3	97 ± 9	7 ± 2	4.6 ± 0.4	50.6 ± 29.5	2.53	111	0.6	*IA*	0
101	$13^h29^m49.12^s$	47°12′17.19”	−32.5	2.4	5.9	33 ± 0	9 ± 2	1.8 ± 0.4	26.3 ± 13.7	3.36	154	0.5	*IA*	1
102	$13^h30^m2.88^s$	47°12′44.58”	−25.6	4.6	8.1	83 ± 7	8 ± 1	9.7 ± 0.7	58.4 ± 15.8	1.39	85	0.7	*IA*	0
103	$13^h30^m2.43^s$	47°12′51.00”	−44.0	3.4	5.4	18 ± 6	4 ± 1	1.4 ± 0.4	2.4 ± 2.2	0.39	132	0.5	*IA*	0
104	$13^h29^m44.43^s$	47°11′27.77”	−2.4	5.3	13.6	263 ± 6	20 ± 1	53.5 ± 1.2	1058.9 ± 75.7	4.54	138	0.6	*SA*	0
105	$13^h29^m48.26^s$	47°11′44.24”	−13.7	2.8	7.1	142 ± 13	12 ± 1	13.6 ± 0.8	219.4 ± 42.0	3.69	131	0.4	*IA*	0
106	$13^h29^m58.90^s$	47°11′48.96”	−20.6	2.4	6.2	104 ± 15	15 ± 3	6.1 ± 0.6	230.9 ± 101.7	8.66	12	0.6	*IA*	0
107	$13^h29^m59.34^s$	47°11′54.28”	−20.5	3.6	8.8	114 ± 9	7 ± 1	10.4 ± 0.7	64.0 ± 17.8	1.42	122	0.5	*IA*	0
108	$13^h29^m48.51^s$	47°11′57.73”	−33.4	2.1	5.2	33 ± 0	4 ± 2	0.5 ± 0.2	6.8 ± 7.3	3.11	145	0.8	*IA*	1
109	$13^h29^m48.03^s$	47°12′4.13”	−30.3	2.2	5.9	33 ± 0	6 ± 3	1.0 ± 0.3	14.0 ± 11.3	3.32	143	0.4	*IA*	1
110	$13^h29^m49.01^s$	47°12′10.21”	−29.7	2.1	5.5	91 ± 12	9 ± 2	3.8 ± 0.5	78.0 ± 36.1	4.70	34	0.6	*IA*	0
111	$13^h29^m48.84^s$	47°12′16.67”	−15.1	2.1	5.7	34 ± 13	16 ± 3	2.1 ± 0.4	91.1 ± 45.0	9.91	121	0.6	*IA*	0

ID (1)	**RA (J2000)** *h m s* (2)	**Dec (J2000)** *d ’ ”* (3)	**V_{LSR}** km/s (4)	**T_{max}** K (5)	**S/N** (6)	**R** pc (7)	**σ_v** km/s (8)	**L_{CO}** 10^5 K km/s pc^2 (9)	**M_{vir}** 10^5 $M_\odot$ (10)	α (11)	**PA** deg (12)	**b/a** (13)	**Reg** (14)	**Flag** (15)
112	$13^h30^m0.62^s$	47°12′21.47”	−38.5	2.1	5.4	33 ± 0	4 ± 2	0.8 ± 0.2	6.3 ± 6.5	1.79	21	0.4	*SA*	1
113	$13^h29^m49.51^s$	47°12′22.48”	−36.5	2.1	5.4	33 ± 0	4 ± 2	0.9 ± 0.2	5.1 ± 4.7	1.36	159	0.6	*IA*	1
114	$13^h29^m47.31^s$	47°12′41.68”	−33.2	2.0	4.8	33 ± 0	4 ± 3	0.6 ± 0.2	5.9 ± 8.4	2.37	5	0.6	*IA*	1
115	$13^h30^m4.15^s$	47°12′51.13”	−33.8	5.0	4.4	27 ± 11	4 ± 2	3.0 ± 1.2	4.8 ± 5.6	0.37	123	0.4	*IA*	0
116	$13^h29^m59.39^s$	47°11′43.24”	−9.3	2.6	6.7	165 ± 9	12 ± 2	18.9 ± 1.0	244.0 ± 66.1	2.96	7	0.8	*IA*	0
117	$13^h29^m47.34^s$	47°11′52.00”	−17.2	2.8	7.2	103 ± 11	9 ± 1	8.7 ± 0.7	91.2 ± 25.4	2.40	144	0.4	*IA*	0
118	$13^h29^m52.66^s$	47°12′3.88”	−33.7	1.9	5.1	33 ± 0	4 ± 3	0.4 ± 0.2	6.2 ± 8.5	3.55	2	0.4	*CR*	1
119	$13^h29^m48.44^s$	47°12′6.10”	−29.8	2.2	6.2	33 ± 0	6 ± 3	0.7 ± 0.3	11.5 ± 11.2	3.88	168	0.6	*IA*	1
120	$13^h29^m49.45^s$	47°10′38.40”	−26.5	2.0	4.7	33 ± 0	4 ± 3	0.9 ± 0.4	4.8 ± 7.0	1.21	151	0.4	*IA*	1
121	$13^h29^m57.92^s$	47°11′20.25”	−1.4	4.5	12.3	191 ± 8	17 ± 2	39.5 ± 1.0	561.5 ± 108.0	3.26	111	0.5	*IA*	0
122	$13^h29^m43.28^s$	47°11′22.30”	−22.7	2.7	6.4	22 ± 6	6 ± 2	1.9 ± 0.3	7.8 ± 6.8	0.95	133	0.3	*SA*	0
123	$13^h29^m57.11^s$	47°11′35.85”	−5.6	2.2	6.2	128 ± 11	10 ± 1	10.0 ± 0.8	133.5 ± 42.1	3.07	144	0.7	*IA*	0
124	$13^h29^m47.65^s$	47°11′35.88”	0.3	4.6	11.8	138 ± 7	10 ± 1	13.0 ± 0.6	131.5 ± 38.1	2.33	127	0.5	*IA*	0
125	$13^h29^m42.95^s$	47°11′38.50”	−10.2	2.7	5.2	52 ± 11	15 ± 4	4.4 ± 0.9	122.3 ± 62.1	6.31	64	0.6	*IA*	0
126	$13^h30^m0.37^s$	47°11′51.77”	−12.5	1.9	4.7	40 ± 11	8 ± 2	2.0 ± 0.4	25.9 ± 13.6	2.97	157	0.4	*IA*	0
127	$13^h30^m0.95^s$	47°12′16.04”	−21.4	1.7	4.6	33 ± 0	6 ± 2	1.1 ± 0.3	13.8 ± 8.3	2.90	71	0.4	*SA*	1
128	$13^h29^m59.36^s$	47°12′27.14”	−27.9	1.5	3.8	33 ± 0	4 ± 2	0.6 ± 0.4	5.0 ± 4.9	1.96	153	0.4	*IA*	1
129	$13^h30^m3.28^s$	47°12′31.24”	−5.4	6.7	11.1	235 ± 11	9 ± 1	60.4 ± 2.3	205.1 ± 24.0	0.78	124	0.5	*IA*	0
130	$13^h29^m57.44^s$	47°12′58.34”	−8.6	4.6	5.7	31 ± 12	14 ± 5	1.9 ± 0.7	64.9 ± 58.4	7.87	15	0.5	*IA*	0
131	$13^h29^m42.78^s$	47°10′52.69”	5.3	7.7	19.4	166 ± 9	11 ± 1	26.8 ± 1.1	193.4 ± 36.6	1.65	92	0.3	*IA*	0
132	$13^h29^m42.99^s$	47°11′6.11”	−16.8	2.1	6.0	39 ± 11	6 ± 2	1.6 ± 0.2	16.1 ± 9.5	2.30	53	1.0	*SA*	0
133	$13^h29^m52.12^s$	47°11′9.89”	4.0	1.4	3.9	70 ± 18	7 ± 3	2.6 ± 1.2	39.7 ± 46.1	3.51	127	0.6	*CR*	0
134	$13^h29^m57.54^s$	47°11′32.81”	−11.9	4.1	11.1	65 ± 13	10 ± 4	2.5 ± 0.2	69.5 ± 63.2	6.45	107	0.6	*IA*	0
135	$13^h29^m49.61^s$	47°11′44.01”	7.1	3.1	7.7	122 ± 8	16 ± 2	13.3 ± 0.8	321.0 ± 109.0	5.56	157	0.6	*CR*	0
136	$13^h30^m0.50^s$	47°11′44.16”	−14.2	2.1	5.4	28 ± 12	11 ± 5	1.1 ± 0.3	35.9 ± 34.9	7.25	29	0.8	*SA*	0
137	$13^h29^m54.22^s$	47°11′52.24”	−17.2	2.1	5.0	33 ± 0	4 ± 2	0.7 ± 0.2	6.3 ± 7.3	2.01	32	0.4	*CR*	1
138	$13^h29^m46.61^s$	47°11′55.80”	−11.9	2.9	7.3	55 ± 9	8 ± 2	2.1 ± 0.3	41.1 ± 22.5	4.55	89	0.4	*IA*	0
139	$13^h29^m56.24^s$	47°12′19.89”	−22.2	1.8	5.1	33 ± 0	5 ± 1	0.6 ± 0.2	7.0 ± 4.3	2.81	134	0.8	*SA*	1
140	$13^h29^m46.05^s$	47°12′35.79”	−15.5	2.7	4.9	33 ± 0	3 ± 2	1.1 ± 0.4	3.6 ± 4.8	0.75	3	0.3	*IA*	1
141	$13^h30^m4.47^s$	47°12′43.13”	−16.1	7.4	6.7	33 ± 0	3 ± 2	1.7 ± 0.3	3.9 ± 4.8	0.53	9	0.8	*IA*	1
142	$13^h29^m57.42^s$	47°12′46.07”	−17.6	3.3	7.0	69 ± 15	5 ± 1	2.6 ± 0.4	15.2 ± 11.0	1.35	29	0.6	*IA*	0
143	$13^h29^m47.64^s$	47°10′59.32”	−2.5	1.7	4.8	51 ± 23	9 ± 3	1.7 ± 0.3	39.8 ± 22.1	5.47	78	0.5	*IA*	0
144	$13^h29^m42.40^s$	47°11′17.72”	−2.2	2.6	6.2	88 ± 9	9 ± 1	7.2 ± 0.5	82.1 ± 25.1	2.61	138	0.7	*IA*	0
145	$13^h29^m42.93^s$	47°11′25.42”	−8.5	3.3	7.8	91 ± 11	6 ± 1	6.1 ± 0.6	33.2 ± 12.9	1.25	98	0.7	*SA*	0
146	$13^h29^m42.24^s$	47°11′26.98”	−6.5	2.9	5.9	33 ± 0	4 ± 2	1.0 ± 0.3	4.9 ± 4.8	1.12	140	0.5	*IA*	1
147	$13^h29^m42.72^s$	47°11′32.87”	−2.4	2.3	4.5	33 ± 0	10 ± 6	0.7 ± 0.4	30.7 ± 41.0	10.03	126	0.5	*IA*	1
148	$13^h29^m57.82^s$	47°11′33.75”	−11.6	2.0	5.5	72 ± 15	6 ± 2	2.5 ± 0.6	30.4 ± 21.4	2.81	79	0.6	*IA*	0
149	$13^h29^m59.36^s$	47°11′34.26”	−8.2	3.4	9.2	38 ± 7	7 ± 2	2.1 ± 0.2	16.6 ± 8.7	1.79	112	0.7	*IA*	0
150	$13^h29^m57.22^s$	47°11′40.76”	−5.6	2.5	6.8	60 ± 10	8 ± 2	2.8 ± 0.5	35.8 ± 19.4	2.95	163	0.7	*IA*	0
151	$13^h29^m57.24^s$	47°11′46.16”	−9.0	2.3	5.9	23 ± 12	6 ± 2	1.1 ± 0.3	9.6 ± 8.1	2.00	86	0.9	*SA*	0
152	$13^h30^m4.30^s$	47°12′19.37”	−12.5	5.2	4.9	27 ± 8	5 ± 2	2.6 ± 0.9	7.7 ± 7.1	0.69	178	0.6	*IA*	0
153	$13^h29^m42.06^s$	47°10′56.79”	−14.4	3.0	7.8	33 ± 0	4 ± 3	0.5 ± 0.2	6.7 ± 9.4	3.04	175	0.9	*IA*	1
154	$13^h29^m54.64^s$	47°11′2.23”	−5.9	2.1	6.7	33 ± 0	7 ± 3	0.6 ± 0.1	14.6 ± 12.9	5.98	9	0.6	*SA*	1
155	$13^h29^m41.84^s$	47°11′8.93”	5.4	5.7	13.1	210 ± 7	10 ± 0	42.4 ± 1.2	201.2 ± 23.3	1.09	132	0.5	*IA*	0
156	$13^h29^m49.75^s$	47°11′13.74”	−5.0	1.8	5.0	33 ± 0	8 ± 4	0.5 ± 0.2	19.4 ± 20.3	9.25	127	0.5	*SA*	1
157	$13^h29^m42.04^s$	47°11′19.65”	−5.1	1.9	4.4	13 ± 16	8 ± 5	0.7 ± 0.5	8.3 ± 20.2	2.61	16	1.0	*IA*	0
158	$13^h29^m56.58^s$	47°11′16.96”	10.0	3.8	9.9	170 ± 10	12 ± 1	14.5 ± 0.6	234.5 ± 46.3	3.71	146	0.2	*IA*	0
159	$13^h29^m46.10^s$	47°11′32.30”	5.0	3.9	9.7	222 ± 14	9 ± 1	30.5 ± 1.1	205.6 ± 44.2	1.55	126	0.3	*IA*	0
160	$13^h29^m59.89^s$	47°11′33.66”	−5.0	1.6	4.5	52 ± 16	8 ± 2	1.7 ± 0.6	38.9 ± 29.8	5.39	120	0.3	*SA*	0
161	$13^h30^m1.71^s$	47°11′49.79”	7.9	4.8	11.1	84 ± 9	7 ± 1	8.3 ± 0.4	48.6 ± 19.6	1.35	91	0.5	*SA*	0
162	$13^h29^m59.97^s$	47°12′10.02”	−5.4	1.4	3.7	33 ± 18	12 ± 5	0.8 ± 0.4	51.3 ± 64.4	14.91	113	0.6	*IA*	0
163	$13^h30^m4.17^s$	47°12′28.45”	−1.9	8.3	8.8	127 ± 11	7 ± 1	18.6 ± 1.2	64.0 ± 20.9	0.79	107	0.5	*IA*	0
164	$13^h29^m43.92^s$	47°10′31.83”	22.4	8.9	15.3	454 ± 10	11 ± 0	185.5 ± 3.3	618.6 ± 30.5	0.77	30	0.8	*SA*	0
165	$13^h30^m0.65^s$	47°11′10.56”	−4.4	2.5	5.1	18 ± 15	4 ± 2	0.9 ± 0.3	2.5 ± 4.5	0.67	135	1.0	*IA*	0
166	$13^h29^m57.40^s$	47°11′9.94”	6.4	2.0	5.6	131 ± 11	10 ± 1	9.6 ± 0.8	139.2 ± 33.6	3.32	77	0.6	*SA*	0
167	$13^h29^m59.56^s$	47°11′28.91”	4.3	2.1	5.2	33 ± 0	6 ± 2	1.3 ± 0.4	13.8 ± 9.6	2.44	164	0.4	*SA*	1
168	$13^h29^m55.25^s$	47°10′35.15”	−0.0	3.1	5.8	5 ± 8	11 ± 5	1.2 ± 0.3	5.9 ± 14.5	1.17	50	1.0	*IA*	0
169	$13^h29^m43.74^s$	47°10′43.93”	17.3	2.1	4.8	94 ± 13	8 ± 2	5.6 ± 0.9	65.5 ± 26.9	2.70	99	0.6	*SA*	0
170	$13^h29^m41.92^s$	47°10′55.65”	2.7	2.5	6.1	14 ± 9	7 ± 2	1.0 ± 0.2	6.3 ± 6.8	1.38	135	0.7	*IA*	0
171	$13^h29^m43.49^s$	47°11′7.08”	10.1	2.1	5.8	22 ± 6	8 ± 2	1.5 ± 0.4	13.5 ± 10.0	2.02	67	0.4	*SA*	0

ID	RA (J2000) h m s	Dec (J2000) d ′ ”	V_{LSR} km/s	T_{max} K	S/N	R pc	σ_v km/s	L_{CO} 10^5 K km/s pc^2	M_{vir} 10^5 $M_\odot$	α	PA deg	b/a	Reg	Flag
(1)	(2)	(3)	(4)	(5)	(6)	(7)	(8)	(9)	(10)	(11)	(12)	(13)	(14)	(15)
172	$13^h29^m47.25^s$	47°11′7.28”	30.6	3.1	8.0	153 ± 8	10 ± 1	14.9 ± 0.6	152.2 ± 38.4	2.34	86	0.5	*IA*	0
173	$13^h29^m48.51^s$	47°11′13.51”	32.9	3.3	8.5	224 ± 10	14 ± 1	39.0 ± 1.2	437.3 ± 61.0	2.58	106	0.5	*IA*	0
174	$13^h29^m56.56^s$	47°11′23.67”	−3.1	1.7	4.9	33 ± 0	4 ± 1	0.7 ± 0.2	4.4 ± 3.6	1.51	130	0.3	*IA*	1
175	$13^h29^m49.44^s$	47°11′27.41”	9.3	1.9	5.0	32 ± 12	10 ± 4	1.6 ± 0.4	30.2 ± 28.4	4.39	177	0.8	*SA*	0
176	$13^h29^m56.56^s$	47°11′29.05”	0.9	1.6	4.6	21 ± 19	6 ± 2	0.9 ± 0.4	7.1 ± 9.1	1.85	54	0.8	*SA*	0
177	$13^h29^m41.36^s$	47°11′40.90”	−4.6	6.5	6.0	33 ± 0	2 ± 1	1.2 ± 0.4	1.6 ± 1.9	0.31	48	0.5	*IA*	1
178	$13^h29^m46.60^s$	47°11′40.81”	−0.5	1.6	4.1	35 ± 19	12 ± 8	0.8 ± 0.4	53.7 ± 94.9	15.23	78	0.6	*IA*	0
179	$13^h29^m48.64^s$	47°11′48.18”	12.8	2.0	4.8	56 ± 12	9 ± 3	2.5 ± 0.6	46.9 ± 34.2	4.36	100	0.6	*IA*	0
180	$13^h30^m3.43^s$	47°12′18.85”	9.6	5.9	8.5	143 ± 9	8 ± 1	20.2 ± 1.3	85.9 ± 16.9	0.97	136	0.6	*IA*	0
181	$13^h29^m46.33^s$	47°12′40.28”	−0.2	2.9	5.8	33 ± 0	10 ± 3	0.9 ± 0.3	34.1 ± 19.0	8.56	146	0.6	*IA*	1
182	$13^h29^m43.03^s$	47°10′26.92”	5.0	3.5	4.8	53 ± 20	2 ± 1	1.7 ± 0.7	1.5 ± 1.0	0.20	103	0.5	*IA*	0
183	$13^h29^m54.96^s$	47°10′34.04”	5.1	2.8	5.1	33 ± 0	2 ± 2	0.4 ± 0.2	1.9 ± 3.0	0.96	132	0.8	*IA*	1
184	$13^h29^m49.81^s$	47°10′34.61”	13.3	2.6	5.2	33 ± 0	9 ± 6	0.8 ± 0.3	24.5 ± 31.9	7.13	1	0.5	*IA*	1
185	$13^h29^m45.21^s$	47°11′12.05”	7.6	1.9	4.9	33 ± 0	7 ± 2	1.0 ± 0.3	16.2 ± 8.7	3.85	169	0.6	*IA*	1
186	$13^h29^m56.06^s$	47°11′23.20”	7.7	1.9	5.2	23 ± 11	7 ± 2	1.1 ± 0.3	10.3 ± 8.9	2.16	114	0.5	*SA*	0
187	$13^h30^m0.01^s$	47°11′25.19”	12.6	2.2	5.5	52 ± 14	12 ± 2	2.2 ± 0.4	77.5 ± 38.1	8.07	152	0.3	*SA*	0
188	$13^h29^m50.17^s$	47°12′24.23”	4.5	2.0	5.4	33 ± 0	3 ± 2	0.5 ± 0.2	2.1 ± 2.7	1.02	165	0.8	*IA*	1
189	$13^h29^m56.06^s$	47°10′33.90”	5.4	2.5	5.4	33 ± 0	3 ± 3	0.5 ± 0.3	2.2 ± 4.8	1.02	134	0.8	*IA*	1
190	$13^h29^m43.71^s$	47°10′52.03”	13.9	2.3	5.9	47 ± 16	7 ± 3	1.4 ± 0.3	21.5 ± 17.8	3.58	125	0.8	*SA*	0
191	$13^h29^m44.62^s$	47°10′55.23”	26.9	3.8	10.3	137 ± 8	10 ± 1	12.1 ± 0.7	136.8 ± 43.4	2.60	68	0.7	*SA*	0
192	$13^h29^m46.38^s$	47°11′8.74”	30.6	4.2	11.1	133 ± 7	7 ± 1	22.6 ± 0.8	73.7 ± 10.5	0.75	53	0.6	*IA*	0
193	$13^h29^m56.29^s$	47°11′30.90”	12.9	3.0	7.7	51 ± 13	6 ± 2	2.2 ± 0.2	18.5 ± 14.2	1.97	149	0.3	*SA*	0
194	$13^h29^m49.01^s$	47°11′27.37”	33.6	2.5	6.2	114 ± 12	11 ± 2	8.7 ± 0.7	134.7 ± 58.8	3.55	99	0.4	*SA*	0
195	$13^h30^m0.69^s$	47°12′47.32”	5.3	2.4	5.1	47 ± 12	2 ± 1	1.4 ± 0.4	2.9 ± 2.9	0.47	44	0.6	*SA*	0
196	$13^h29^m56.19^s$	47°12′54.61”	15.1	3.4	5.4	33 ± 17	10 ± 5	1.3 ± 0.4	34.9 ± 46.9	6.21	29	0.5	*IA*	0
197	$13^h29^m47.75^s$	47°10′48.37”	19.6	2.6	6.6	36 ± 8	7 ± 2	1.4 ± 0.2	17.4 ± 11.4	2.80	153	0.4	*IA*	0
198	$13^h29^m56.16^s$	47°11′19.50”	17.2	2.6	6.7	33 ± 0	7 ± 2	1.5 ± 0.2	15.8 ± 7.2	2.39	33	0.5	*IA*	1
199	$13^h29^m47.87^s$	47°11′19.40”	16.4	2.0	6.0	26 ± 12	4 ± 2	0.7 ± 0.2	4.5 ± 4.3	1.51	112	0.7	*IA*	0
200	$13^h29^m47.08^s$	47°11′21.38”	20.5	2.2	5.5	33 ± 0	8 ± 2	1.7 ± 0.3	22.0 ± 10.6	3.06	98	0.4	*IA*	1
201	$13^h29^m43.03^s$	47°11′21.99”	15.9	1.9	4.6	33 ± 0	6 ± 3	0.5 ± 0.3	11.0 ± 10.6	4.67	154	0.5	*SA*	1
202	$13^h29^m47.91^s$	47°11′34.17”	19.1	1.9	5.0	35 ± 16	11 ± 4	1.6 ± 0.4	40.6 ± 25.4	5.72	74	0.9	*IA*	0
203	$13^h29^m58.87^s$	47°11′47.79”	17.5	1.9	4.9	33 ± 0	5 ± 2	0.5 ± 0.2	7.4 ± 5.7	3.20	173	0.9	*IA*	1
204	$13^h30^m1.54^s$	47°12′14.82”	14.4	1.7	4.2	33 ± 0	2 ± 2	0.4 ± 0.2	2.1 ± 2.7	1.26	58	0.7	*SA*	1
205	$13^h29^m58.82^s$	47°10′43.58”	23.4	2.2	5.1	25 ± 13	13 ± 4	1.3 ± 0.4	41.6 ± 41.1	7.50	82	0.8	*IA*	0
206	$13^h29^m45.34^s$	47°10′47.61”	30.5	4.7	11.1	161 ± 9	7 ± 1	22.8 ± 1.2	84.1 ± 11.7	0.85	92	0.2	*IA*	0
207	$13^h29^m47.15^s$	47°10′59.26”	36.8	2.7	7.1	97 ± 11	9 ± 2	5.6 ± 0.5	76.3 ± 35.9	3.13	140	0.7	*IA*	0
208	$13^h29^m49.89^s$	47°11′11.63”	40.6	2.4	6.2	82 ± 11	17 ± 3	6.4 ± 0.8	258.5 ± 74.1	9.21	94	0.7	*SA*	0
209	$13^h29^m44.21^s$	47°11′15.63”	22.9	1.9	5.3	68 ± 11	7 ± 1	2.2 ± 0.4	32.1 ± 15.9	3.39	98	0.7	*SA*	0
210	$13^h29^m46.57^s$	47°11′16.48”	29.1	2.9	7.5	62 ± 10	6 ± 1	4.1 ± 0.3	20.6 ± 9.0	1.17	134	0.6	*IA*	0
211	$13^h29^m46.32^s$	47°11′18.81”	27.8	2.4	6.0	44 ± 15	10 ± 2	1.9 ± 0.4	41.9 ± 27.3	5.08	20	0.6	*IA*	0
212	$13^h29^m59.19^s$	47°11′24.74”	26.2	1.8	4.7	30 ± 15	10 ± 4	0.8 ± 0.4	31.8 ± 36.3	9.45	139	0.6	*SA*	0
213	$13^h29^m48.37^s$	47°11′30.55”	19.1	2.3	5.4	44 ± 18	4 ± 2	1.5 ± 0.3	8.6 ± 7.1	1.33	9	0.5	*IA*	0
214	$13^h30^m4.42^s$	47°11′46.82”	27.6	6.3	4.9	33 ± 0	5 ± 3	1.5 ± 0.7	9.2 ± 10.5	1.36	113	0.4	*IA*	1
215	$13^h29^m45.08^s$	47°10′23.59”	32.5	7.5	8.3	93 ± 9	12 ± 2	17.0 ± 1.6	131.1 ± 43.8	1.77	49	0.6	*SA*	0
216	$13^h29^m43.12^s$	47°10′25.81”	27.7	4.8	5.5	65 ± 10	5 ± 2	5.9 ± 1.0	15.5 ± 10.2	0.61	112	0.5	*IA*	0
217	$13^h29^m45.53^s$	47°10′32.99”	35.3	3.2	5.5	66 ± 11	10 ± 2	5.7 ± 0.8	68.3 ± 30.9	2.75	48	0.5	*IA*	0
218	$13^h29^m43.76^s$	47°10′38.99”	29.6	2.5	5.2	85 ± 24	5 ± 2	2.7 ± 0.6	22.8 ± 15.1	1.91	161	0.6	*SA*	0
219	$13^h29^m41.24^s$	47°10′57.24”	20.2	2.8	5.7	33 ± 0	3 ± 1	0.6 ± 0.3	2.9 ± 2.9	1.06	135	0.8	*IA*	1
220	$13^h29^m41.53^s$	47°10′57.46”	24.0	2.6	5.5	33 ± 0	4 ± 2	0.7 ± 0.3	4.5 ± 5.3	1.39	168	0.8	*IA*	1
221	$13^h29^m47.87^s$	47°10′57.25”	36.3	3.0	7.7	97 ± 10	8 ± 2	8.1 ± 0.6	68.1 ± 24.2	1.93	70	0.6	*IA*	0
222	$13^h29^m45.52^s$	47°11′0.99”	30.1	2.5	6.7	94 ± 14	4 ± 1	3.9 ± 0.6	17.3 ± 9.8	1.03	144	0.9	*IA*	0
223	$13^h30^m1.02^s$	47°11′18.58”	24.5	2.5	4.8	33 ± 0	2 ± 2	0.5 ± 0.2	1.7 ± 3.3	0.83	165	0.5	*SA*	1
224	$13^h29^m58.56^s$	47°11′35.04”	54.7	2.0	6.3	33 ± 0	25 ± 5	1.4 ± 0.2	211.5 ± 80.1	35.80	121	0.6	*IA*	1
225	$13^h29^m53.66^s$	47°10′57.65”	29.9	2.3	6.1	33 ± 0	3 ± 2	0.3 ± 0.1	3.2 ± 4.4	2.11	4	0.7	*SA*	1
226	$13^h29^m54.08^s$	47°11′11.82”	61.3	3.5	9.3	180 ± 8	12 ± 1	18.9 ± 0.8	276.3 ± 48.5	3.36	13	0.5	*CR*	0
227	$13^h29^m59.32^s$	47°11′27.58”	50.6	3.4	8.9	40 ± 8	11 ± 3	3.0 ± 0.3	50.7 ± 33.8	3.93	103	0.3	*SA*	0
228	$13^h30^m2.60^s$	47°11′50.05”	39.9	3.9	7.1	105 ± 12	7 ± 1	7.9 ± 0.5	55.4 ± 24.9	1.61	80	0.5	*IA*	0
229	$13^h29^m45.60^s$	47°12′5.98”	38.4	2.4	6.0	17 ± 10	7 ± 5	0.9 ± 0.2	9.4 ± 13.5	2.32	94	0.8	*SA*	0
230	$13^h29^m46.75^s$	47°10′45.89”	39.8	2.6	6.2	42 ± 10	8 ± 2	2.2 ± 0.3	27.5 ± 22.3	2.85	87	0.3	*IA*	0
231	$13^h29^m48.20^s$	47°10′46.78”	47.5	2.8	7.0	123 ± 12	8 ± 1	9.1 ± 1.0	87.6 ± 29.0	2.21	39	0.6	*IA*	0

ID (1)	**RA (J2000)** *h m s* (2)	**Dec (J2000)** *d ' "* (3)	$\mathbf{V_{LSR}}$ km/s (4)	$\mathbf{T_{max}}$ K (5)	**S/N** (6)	**R** pc (7)	$\sigma_\mathbf{v}$ km/s (8)	$\mathbf{L_{CO}}$ 10^5 K km/s pc^2 (9)	$\mathbf{M_{vir}}$ 10^5 $M_\odot$ (10)	α (11)	**PA** deg (12)	**b/a** (13)	**Reg** (14)	**Flag** (15)
232	$13^h29^m46.69^s$	47°10′53.61”	42.7	2.4	6.5	75 ± 8	6 ± 1	4.8 ± 0.7	33.0 ± 14.9	1.57	83	0.6	*IA*	0
233	$13^h29^m55.74^s$	47°10′57.76”	36.1	1.9	4.7	33 ± 0	6 ± 3	0.9 ± 0.4	12.1 ± 12.0	3.07	172	0.5	*SA*	1
234	$13^h29^m44.53^s$	47°11′16.02”	36.1	1.9	4.9	33 ± 10	7 ± 2	1.4 ± 0.5	15.3 ± 10.3	2.52	41	0.6	*SA*	0
235	$13^h30^m0.68^s$	47°11′24.72”	40.8	2.7	6.3	92 ± 16	7 ± 1	4.8 ± 0.6	42.3 ± 19.9	2.00	89	0.5	*SA*	0
236	$13^h29^m56.81^s$	47°11′39.42”	38.8	1.6	4.3	36 ± 16	6 ± 3	1.2 ± 0.4	13.6 ± 11.8	2.51	10	0.6	*SA*	0
237	$13^h29^m48.71^s$	47°11′48.17”	39.9	1.8	4.6	19 ± 14	7 ± 2	1.1 ± 0.4	9.7 ± 8.9	1.96	20	0.7	*IA*	0
238	$13^h29^m48.53^s$	47°10′20.62”	38.9	5.5	4.5	33 ± 0	3 ± 2	1.8 ± 0.7	4.0 ± 4.8	0.52	40	0.7	*IA*	1
239	$13^h29^m52.64^s$	47°10′21.00”	54.0	5.7	5.2	68 ± 15	10 ± 3	6.3 ± 1.5	69.0 ± 45.4	2.53	78	0.4	*IA*	0
240	$13^h29^m46.62^s$	47°10′24.44”	43.1	5.4	5.5	49 ± 13	7 ± 2	4.1 ± 0.8	25.7 ± 13.7	1.43	86	0.7	*IA*	0
241	$13^h29^m43.99^s$	47°10′34.73”	40.1	3.2	5.2	21 ± 12	7 ± 3	1.4 ± 0.3	9.8 ± 10.5	1.66	16	0.8	*SA*	0
242	$13^h29^m56.90^s$	47°10′34.47”	44.6	3.6	6.4	33 ± 0	8 ± 2	2.2 ± 0.5	20.0 ± 12.4	2.08	95	0.5	*IA*	1
243	$13^h29^m58.14^s$	47°10′46.68”	44.9	3.0	7.3	41 ± 10	5 ± 1	2.3 ± 0.3	10.4 ± 7.3	1.04	161	0.4	*IA*	0
244	$13^h29^m49.47^s$	47°11′10.52”	48.7	2.8	6.9	61 ± 14	6 ± 2	3.2 ± 0.4	21.5 ± 15.5	1.52	33	0.5	*SA*	0
245	$13^h29^m59.53^s$	47°11′31.88”	67.0	2.4	6.5	66 ± 8	12 ± 3	4.6 ± 0.4	101.9 ± 45.2	5.09	54	0.7	*IA*	0
246	$13^h29^m59.68^s$	47°11′36.28”	50.3	2.4	6.6	65 ± 12	7 ± 2	3.1 ± 0.4	33.2 ± 18.0	2.46	135	0.5	*IA*	0
247	$13^h30^m2.04^s$	47°11′38.78”	52.6	2.4	4.4	40 ± 17	7 ± 3	2.5 ± 0.8	21.6 ± 20.3	2.01	20	0.4	*IA*	0
248	$13^h30^m2.98^s$	47°12′29.14”	41.9	2.7	4.8	33 ± 0	7 ± 4	0.6 ± 0.2	15.3 ± 16.3	5.79	12	0.5	*IA*	1
249	$13^h29^m57.27^s$	47°10′24.66”	43.5	4.4	5.2	33 ± 0	4 ± 2	1.4 ± 0.4	5.4 ± 5.8	0.88	113	0.5	*IA*	1
250	$13^h29^m46.07^s$	47°10′35.07”	40.6	2.7	4.9	32 ± 12	3 ± 1	1.6 ± 0.4	2.3 ± 1.9	0.33	118	0.6	*IA*	0
251	$13^h30^m0.87^s$	47°10′56.16”	52.7	5.3	6.9	51 ± 10	10 ± 2	4.6 ± 0.9	56.1 ± 26.5	2.82	53	0.9	*IA*	0
252	$13^h29^m48.73^s$	47°11′29.11”	48.8	1.8	4.6	25 ± 11	7 ± 3	0.8 ± 0.3	13.0 ± 14.6	3.86	150	0.7	*SA*	0
253	$13^h30^m2.28^s$	47°11′41.91”	50.7	3.9	7.4	90 ± 10	5 ± 1	5.2 ± 0.6	21.4 ± 11.2	0.94	114	0.7	*IA*	0
254	$13^h29^m53.39^s$	47°12′1.27”	41.0	2.0	4.7	33 ± 0	3 ± 2	0.5 ± 0.3	3.7 ± 4.9	1.82	14	0.9	*CR*	1
255	$13^h29^m48.94^s$	47°10′21.99”	54.8	4.9	4.4	26 ± 16	7 ± 3	2.6 ± 0.8	14.9 ± 14.2	1.30	20	0.9	*IA*	0
256	$13^h29^m56.80^s$	47°10′33.58”	73.9	3.5	6.1	66 ± 11	11 ± 4	3.9 ± 0.5	81.7 ± 48.9	4.83	99	0.7	*IA*	0
257	$13^h29^m48.18^s$	47°10′39.06”	56.2	2.8	6.2	33 ± 0	7 ± 3	1.0 ± 0.2	16.5 ± 16.3	3.89	62	0.8	*IA*	1
258	$13^h29^m47.70^s$	47°10′49.17”	47.3	1.5	4.0	30 ± 10	4 ± 2	0.9 ± 0.6	5.9 ± 4.9	1.45	150	0.5	*IA*	0
259	$13^h29^m53.91^s$	47°11′3.36”	51.5	1.7	4.8	33 ± 0	5 ± 3	0.4 ± 0.3	7.8 ± 8.5	4.02	21	0.6	*SA*	1
260	$13^h29^m53.37^s$	47°11′4.79”	75.2	2.0	6.0	62 ± 9	15 ± 3	4.2 ± 0.5	151.2 ± 64.6	8.33	30	0.5	*SA*	0
261	$13^h29^m59.32^s$	47°11′31.58”	45.7	1.5	4.4	33 ± 0	2 ± 2	0.5 ± 0.2	2.0 ± 2.5	0.98	12	0.6	*IA*	1
262	$13^h29^m49.22^s$	47°10′27.61”	67.9	5.3	7.9	137 ± 10	7 ± 1	17.4 ± 1.3	71.5 ± 17.6	0.94	75	0.8	*IA*	0
263	$13^h29^m57.64^s$	47°10′36.13”	71.9	3.2	6.7	151 ± 11	11 ± 1	11.0 ± 0.8	172.9 ± 47.0	3.62	138	0.7	*IA*	0
264	$13^h29^m54.15^s$	47°10′37.28”	86.0	6.1	14.7	206 ± 8	11 ± 1	48.3 ± 1.3	264.6 ± 43.5	1.26	45	0.3	*IA*	0
265	$13^h29^m50.34^s$	47°10′55.48”	58.7	2.7	6.8	43 ± 9	6 ± 2	2.5 ± 0.5	16.6 ± 10.1	1.55	117	0.4	*SA*	0
266	$13^h29^m53.68^s$	47°11′4.97”	55.0	1.5	4.3	33 ± 0	8 ± 4	0.7 ± 0.3	20.1 ± 22.2	7.03	134	1.2	*SA*	1
267	$13^h29^m51.90^s$	47°10′25.34”	69.2	5.8	7.1	85 ± 7	6 ± 2	7.1 ± 0.8	28.0 ± 16.1	0.90	46	1.0	*IA*	0
268	$13^h29^m55.04^s$	47°10′56.66”	60.6	2.0	5.3	45 ± 13	5 ± 3	1.4 ± 0.3	13.1 ± 12.8	2.13	101	0.5	*SA*	0
269	$13^h29^m50.20^s$	47°11′1.46”	67.9	2.4	6.6	77 ± 13	7 ± 2	3.1 ± 0.4	42.4 ± 20.6	3.19	124	0.7	*SA*	0
270	$13^h29^m52.10^s$	47°10′19.88”	68.1	5.5	4.6	37 ± 14	8 ± 3	3.4 ± 0.9	24.3 ± 20.1	1.64	108	0.5	*IA*	0
271	$13^h29^m56.87^s$	47°10′25.18”	70.3	5.5	6.8	86 ± 14	7 ± 1	7.2 ± 1.1	44.5 ± 21.6	1.41	75	0.8	*IA*	0
272	$13^h29^m50.02^s$	47°10′34.69”	72.7	2.3	4.6	33 ± 0	7 ± 3	1.3 ± 0.5	18.5 ± 14.8	3.27	115	0.3	*IA*	1
273	$13^h29^m47.55^s$	47°10′43.00”	60.4	2.0	5.0	33 ± 0	2 ± 2	0.4 ± 0.2	1.9 ± 3.0	1.17	133	0.7	*IA*	1
274	$13^h29^m58.56^s$	47°10′49.33”	72.6	5.2	12.7	106 ± 11	5 ± 1	7.6 ± 0.4	30.2 ± 8.1	0.91	5	0.2	*IA*	0
275	$13^h30^m0.29^s$	47°10′49.53”	72.2	3.4	4.5	29 ± 11	8 ± 4	1.3 ± 0.6	18.9 ± 23.1	3.31	70	0.6	*IA*	0
276	$13^h29^m59.27^s$	47°10′50.55”	68.5	2.7	5.3	33 ± 0	5 ± 2	0.8 ± 0.2	9.6 ± 8.9	2.85	178	0.8	*IA*	1
277	$13^h29^m50.74^s$	47°10′23.16”	72.0	5.9	6.2	33 ± 0	7 ± 6	1.7 ± 0.4	16.3 ± 27.3	2.21	162	0.7	*IA*	1
278	$13^h29^m56.42^s$	47°10′31.22”	71.6	3.5	5.6	50 ± 13	4 ± 1	2.1 ± 0.5	6.5 ± 4.2	0.70	179	0.4	*IA*	0
279	$13^h29^m53.03^s$	47°10′35.23”	85.9	3.6	7.9	66 ± 7	8 ± 2	4.2 ± 0.4	40.9 ± 20.6	2.23	153	0.3	*IA*	0
280	$13^h29^m54.74^s$	47°10′24.41”	78.2	3.2	4.3	33 ± 0	6 ± 6	0.8 ± 0.4	11.6 ± 22.0	3.51	39	0.6	*IA*	1
281	$13^h29^m58.95^s$	47°10′38.12”	72.3	3.2	5.9	33 ± 0	5 ± 3	0.8 ± 0.1	9.8 ± 10.6	2.78	128	0.6	*IA*	1
282	$13^h29^m58.23^s$	47°11′30.35”	76.5	1.5	4.4	33 ± 0	6 ± 2	0.7 ± 0.3	14.0 ± 9.7	4.75	156	0.3	*IA*	1
283	$13^h29^m52.83^s$	47°12′1.78”	71.0	1.9	5.4	33 ± 0	3 ± 1	0.6 ± 0.2	3.0 ± 2.2	1.17	99	0.4	*CR*	1
284	$13^h29^m51.55^s$	47°10′35.27”	81.5	4.5	10.1	53 ± 9	8 ± 2	3.8 ± 0.4	39.6 ± 19.8	2.37	96	0.6	*IA*	0
285	$13^h29^m55.06^s$	47°10′33.86”	97.3	2.4	5.6	81 ± 11	12 ± 3	3.4 ± 0.6	115.4 ± 63.5	7.87	94	0.8	*IA*	0
286	$13^h29^m57.22^s$	47°10′36.79”	83.5	2.8	6.7	20 ± 9	6 ± 2	1.4 ± 0.3	7.6 ± 5.8	1.26	147	0.6	*IA*	0
287	$13^h29^m49.08^s$	47°11′25.93”	85.2	1.6	4.5	33 ± 0	6 ± 2	0.4 ± 0.2	11.5 ± 9.9	6.62	154	0.5	*SA*	1
288	$13^h29^m59.25^s$	47°11′33.76”	81.1	1.6	5.0	51 ± 15	7 ± 2	1.1 ± 0.3	23.6 ± 21.6	4.82	2	0.6	*IA*	0
289	$13^h29^m41.63^s$	47°11′37.24”	75.2	4.1	4.7	33 ± 0	2 ± 1	0.6 ± 0.4	1.1 ± 1.3	0.43	119	0.8	*IA*	1
290	$13^h29^m48.89^s$	47°11′39.94”	86.4	1.8	5.4	44 ± 12	6 ± 3	1.0 ± 0.2	19.3 ± 15.6	4.40	103	0.8	*SA*	0
291	$13^h29^m56.06^s$	47°10′35.86”	97.3	3.1	8.2	91 ± 11	7 ± 1	6.4 ± 0.4	48.6 ± 14.7	1.75	39	0.4	*IA*	0

ID	**RA (J2000)** *h m s*	**Dec (J2000)** *d ' "*	$\mathbf{V_{LSR}}$ km/s	$\mathbf{T_{max}}$ K	**S/N**	**R** pc	σ_v km/s	$\mathbf{L_{CO}}$ 10^5 K km/s pc^2	$\mathbf{M_{vir}}$ 10^5 M$_\odot$	α	**PA** deg	**b/a**	**Reg**	**Flag**
(1)	(2)	(3)	(4)	(5)	(6)	(7)	(8)	(9)	(10)	(11)	(12)	(13)	(14)	(15)
292	$13^h29^m49.80^s$	47°12′10.33”	89.6	1.3	4.2	33 ± 0	3 ± 3	0.3 ± 0.1	2.3 ± 5.0	1.90	149	1.1	*IA*	1
293	$13^h29^m49.69^s$	47°11′25.63”	96.4	1.8	5.9	33 ± 0	6 ± 3	0.9 ± 0.2	13.6 ± 11.0	3.48	122	0.4	*SA*	1
294	$13^h29^m59.75^s$	47°11′26.51”	90.1	1.6	5.0	33 ± 0	2 ± 1	0.4 ± 0.2	0.9 ± 0.8	0.60	133	0.5	*SA*	1
295	$13^h29^m54.94^s$	47°11′50.54”	113.6	1.4	5.0	32 ± 10	12 ± 3	1.1 ± 0.4	44.3 ± 17.4	9.02	91	0.6	*CR*	0
296	$13^h29^m55.45^s$	47°10′37.47”	103.3	2.2	6.2	54 ± 10	8 ± 2	3.1 ± 0.3	36.3 ± 16.5	2.67	7	0.7	*IA*	0
297	$13^h30^m0.08^s$	47°10′40.68”	101.2	3.7	5.6	33 ± 0	5 ± 3	0.9 ± 0.3	7.9 ± 8.5	1.99	107	0.8	*IA*	1
298	$13^h30^m2.43^s$	47°11′16.32”	95.3	4.4	5.5	33 ± 0	2 ± 2	0.7 ± 0.3	2.1 ± 3.3	0.70	127	0.7	*IA*	1
299	$13^h29^m54.20^s$	47°11′17.39”	98.5	1.7	6.4	33 ± 0	6 ± 3	0.5 ± 0.2	12.3 ± 13.0	5.66	100	0.5	*CR*	1
300	$13^h29^m58.09^s$	47°10′34.02”	99.9	2.2	5.3	33 ± 0	2 ± 1	0.4 ± 0.2	1.3 ± 1.7	0.72	3	0.8	*IA*	1
301	$13^h29^m50.81^s$	47°10′40.08”	100.0	1.8	5.3	33 ± 0	4 ± 3	0.5 ± 0.2	5.1 ± 8.0	2.45	44	0.6	*IA*	1
302	$13^h29^m51.21^s$	47°11′19.62”	109.2	1.2	4.5	33 ± 0	3 ± 2	0.2 ± 0.2	2.9 ± 3.3	2.66	73	0.5	*CR*	1
303	$13^h29^m45.35^s$	47°11′33.99”	111.3	1.4	4.8	21 ± 12	6 ± 2	0.7 ± 0.2	9.1 ± 8.9	3.00	170	0.6	*IA*	0
304	$13^h29^m51.82^s$	47°10′23.65”	114.7	2.9	4.7	33 ± 0	4 ± 2	1.7 ± 0.5	5.7 ± 4.7	0.76	129	0.4	*IA*	1
305	$13^h29^m48.66^s$	47°10′31.97”	110.8	2.1	5.1	33 ± 0	3 ± 3	0.5 ± 0.1	3.4 ± 5.8	1.75	163	0.4	*IA*	1
306	$13^h29^m57.72^s$	47°10′33.45”	115.8	2.5	6.3	33 ± 0	4 ± 4	0.5 ± 0.1	4.4 ± 9.4	2.20	161	0.9	*IA*	1
307	$13^h29^m51.52^s$	47°11′7.54”	111.9	1.2	4.7	12 ± 13	6 ± 5	0.3 ± 0.1	4.1 ± 8.7	3.14	86	0.8	*SA*	0
308	$13^h29^m53.64^s$	47°10′43.88”	132.6	1.3	4.7	33 ± 0	13 ± 6	0.7 ± 0.3	61.3 ± 58.7	20.04	168	0.7	*SA*	1
309	$13^h29^m50.89^s$	47°11′45.80”	125.3	1.5	5.7	33 ± 0	2 ± 1	0.4 ± 0.1	2.1 ± 2.5	1.10	128	0.6	*CR*	1

Table 4.7: (1) Island identification number (*ID*), (2) Right Ascension (*RA (J2000)*), (3) Declination (*Dec (J2000)*), (4) Velocity with respect to the systematic velocity of the galaxy (V_{LSR} = 472 km/s, Shetty et al. (2007)), (5) Peak brightness temperature (T_{max}), (6) Peak signal-to-noise ratio (S/N), (7) Radius (R), (8) Velocity dispersion (σ_v), (9) CO luminosity (L_{CO}), (10) Mass from virial theorem (M_{vir}), (11) Virial parameter (α), (12) Position angle of island major axis, measured from North through West (*PA*), (13) Ratio between minor axis and major axis (b/a), (14) Region of M51 where a given island has been identified, i.e. center (*CR*), spiral arms (*SA*), inter-arm (*IA*), (15) Flag= 0 indicates an actual measurement of the island radius, Flag= 1 indicates that the radius is an upper limit.

PAWS MOMENT MAPS

In this section we provide a brief description of the main features of the PAWS second moment map, not directly used in the text. To start we illustrate the dedicated masking technique widely used for all PAWS works to preserve low S/N data while eliminating noisy peaks from the datacubes.

DATACUBE MASKING TECHNIQUE

The dynamics in M51 is dominated by prominent spiral arms which strongly influence the global velocity field causing deviation from the pure circular motion of the rotating galactic disk (see Section 1.1). The inter-arm region should not be highly affected by spiral arm streaming motion and, hence, is the best location to obtain information about the rotation curve and the other kinematic parameters of the galaxy. Unfortunately, the atomic and molecular line emission in the inter-arm is not very strong, and only detected at low S/N (average below 1 and maximum ~ 3) in our data.

Therefore, a direct integration over a set velocity range produces a velocity field in which noise pixels are indistinguishable from genuine emission associate with structures in the inter-arm region.

A relative simple way to avoid the inclusion of noise peaks is the *sigma clipping method*, whereby pixels below a certain signal-to-noise level are masked. Moment maps are then built using unmasked pixels only. The classical clipping threshold of $3\sigma_{RMS}$, where σ_{RMS} is the standard deviation of the noise fluctuation, produces a clean map, although significant emission in the inter-arm region is lost.

Thus in order to obtain the moment maps of the PAWS data set used here (i.e. hybrid data cube, single dish data cube and hybrid data cubes at 3" and 6") we adopted a more sophisticated technique that involves a modified version of the sigma clipping method and comparison with the *HI* data. A 3D mask is generated using a sigma clipping level equal to $t = 4\sigma_{RMS}$. The deviation standard of the noise fluctuation σ_{RMS} is calculated from 30 emission-free channels for each line-of-sight. Then a second 3D mask with a lower clipping level, $e = 1\sigma_{RMS}$, is superimposed onto the previous mask and only regions of the second low level mask that contain regions of the high level mask are retained. We call the final product a *dilated mask* in analogy to the homonym CPROPS procedure (Rosolowsky & Leroy 2006). Nevertheless, the velocity field map generated using the dilated mask still contains several noise peaks which can be identified via their large velocity offset. To eliminate those regions, we compare this map to the *HI* velocity field. Such a comparison is supported by the evidence that CO emission in nearby galaxies is mostly associated with high brightness HI emission (e.g. Schruba et al. 2011). As a template we use the 6” robust weighted first moment map of the entire disk of the M51 obtained by the THINGS project (Walter et al. 2008) and regridded to the same pixel scale as the PAWS cube. Based on the comparison we eliminate all regions of the CO velocity field that deviate more than 30 km s^{-1}. The resulting 2D mask is used to further filter the 3-dimensional dilated mask previously created. As this filtered dilated mask removes perfectly valid lines-of-sight especially in the center of M51 ($R_{gal} \sim 30$”), we generated a second dilate mask using more restrictive sigma clipping levels: $t = 10\sigma_{RMS}$ and $e = 1.5\sigma_{RMS}$. Finally we merged the two dilated masks to obtain our final 3D mask.

All moment maps (intensity map, velocity field and velocity dispersion map) are generated from the masked cubes using the Groningen Image Processing System `GIPSY` task `MOMENTS` in `WINDOW` mode. This setting integrates the only channels connected and adjacent to the channel with the maximum signal along a given velocity profile.

Each line-of-sight in the integrated intensity map is obtained by:

$$I(CO)_{los} = \sum S_i \Delta V_{chan}, \tag{4.9}$$

where S_i is the value of the $i-$esim pixel and ΔV_{chan} is the channel width.

The line-of-sight velocities V_{los} of the first moment map are defined as:

$$V_{los} = \langle v_i \rangle = \frac{\sum S_i v_i}{\sum S_i}, \tag{4.10}$$

where v_i is the channel velocity.

Finally, the velocity dispersion at the pixel i through the second moment map is given by:

$$\sigma_{los} = \sqrt{\frac{\sum S_i (v_i - \langle v_i \rangle)^2}{\sum S_i}}, \tag{4.11}$$

VELOCITY DISPERSION MAP

The velocity dispersion map obtained with the technique described above and the task `MOMENTS` of `GIPSY` is shown in Fig 4.12. The velocity dispersion σ_v ranges from $\sigma_v \approx 2 - 40$ km s^{-1}. Regions with a velocity dispersion above 30 km s^{-1}, however, are exclusively associated with the nucleus. The global average value is around 5.5 km s^{-1}. Regions of higher velocity dispersion are the molecular ring ($\langle\sigma_v\rangle \sim 7.5$ km s^{-1}), the central region inside it ($\langle\sigma_v\rangle \sim 6.8$ km s^{-1}) and the spiral arms connecting to the ring ($\langle\sigma_v\rangle \sim 6.2$ km s^{-1}). The high velocity dispersion observed in the spiral arms could potentially be caused by unresolved streaming motion (i.e. Pety et al. 2013). Outer spiral arm and inter-arm environments are regions where significantly less streaming motion is observed. They exhibit also lower values of velocity dispersion ($\langle\sigma_v\rangle \sim 4 - 5$ km s^{-1}).

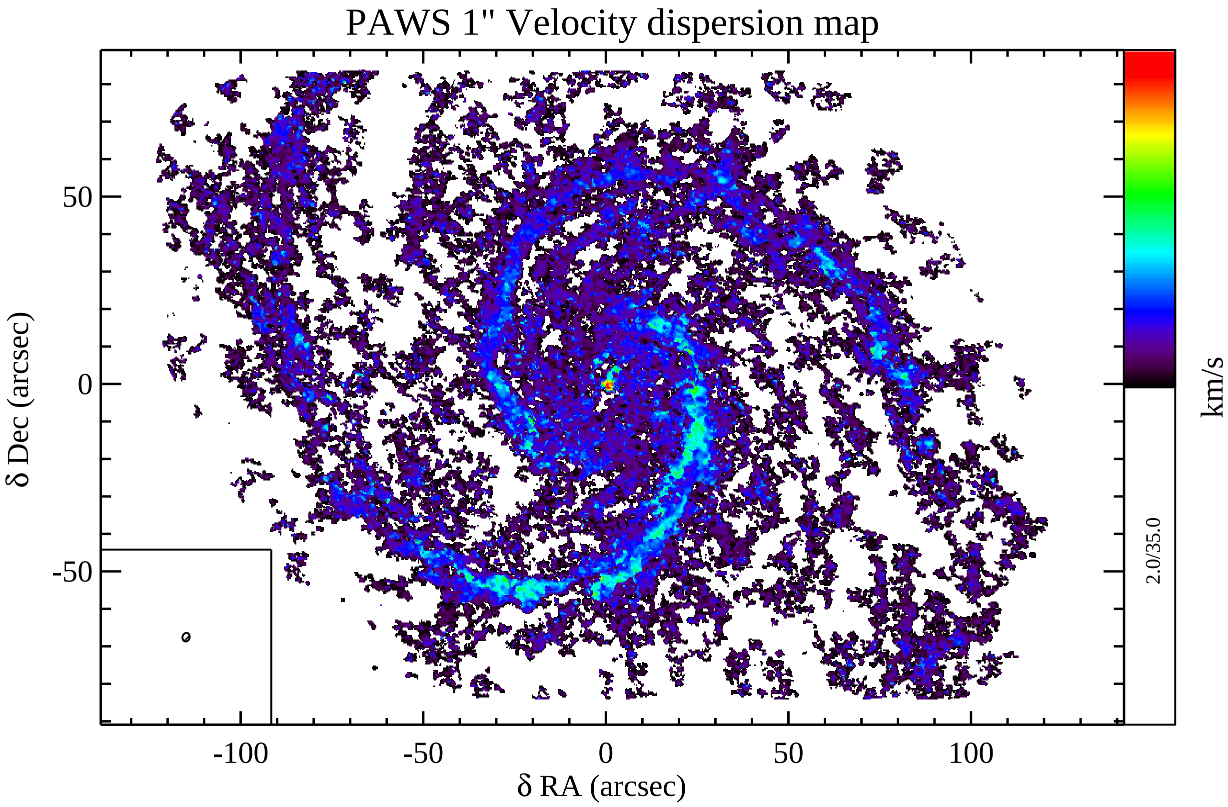

Figure 4.12: The PAWS ^{12}CO(1-0) Velocity dispersion map at 1” resolution. Nucleus and spiral arms are regions of higher velocity dispersion. In the bottom left the beam (1” ~ 40 pc) is shown. The sidebar shows the color scale of the map in km/s.

LOW-RESOLUTION VELOCITY FIELD HARMONIC DECOMPOSITIONS

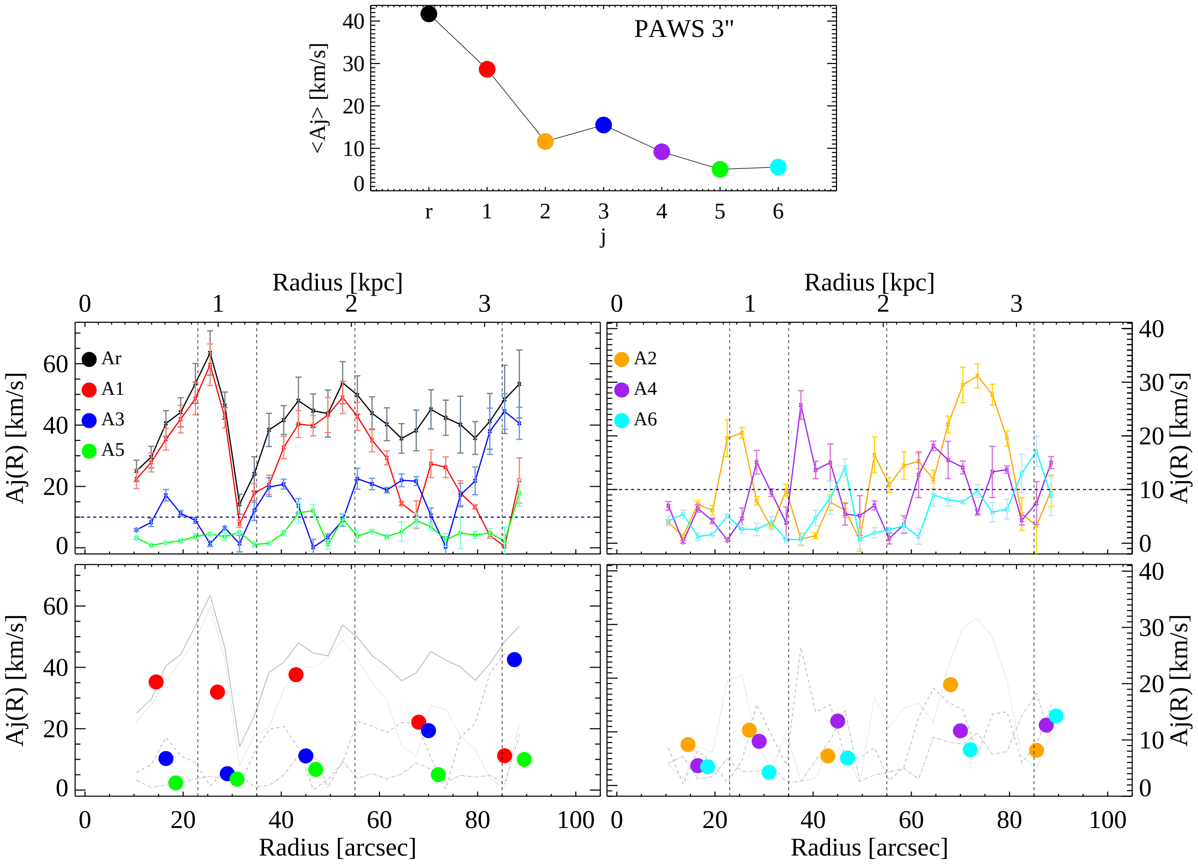

Figure 4.13: *Top plot:* Radial averaged mean of the harmonic component amplitudes from PAWS 3" residual velocity field. *Bottom plot:* Non-circular motion amplitudes from harmonic decomposition: radial trend of the odd components and the total power $A_r(R)$ (top left) and even components (top right). Blue dashed straight line indicates the 2× the channel width of the cube equal to 5 km s^{-1}. In the bottom row the mean behavior of the odd (left) and even (middle) components in the different M51 environments (as defined in Meidt et al. 2013) are indicated.

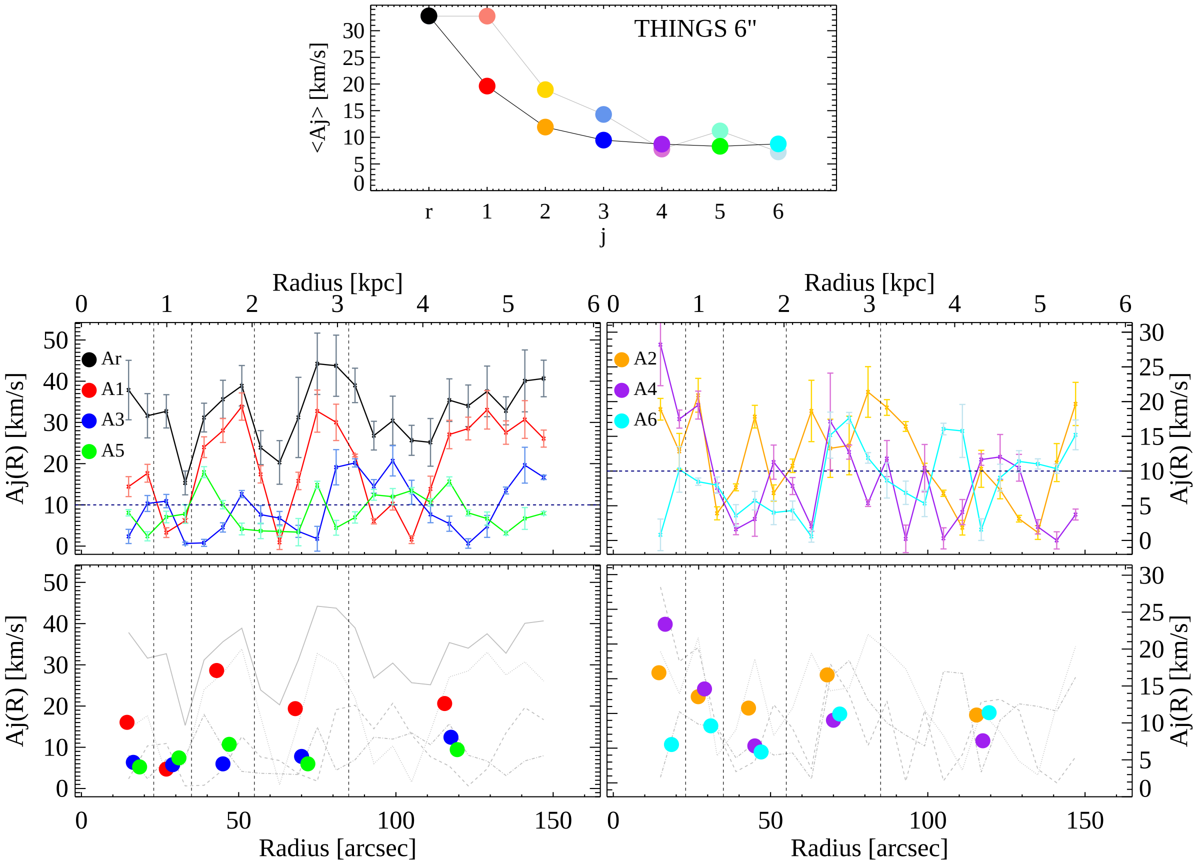

Figure 4.14: *Top plot:* Radial averaged mean of the harmonic component amplitudes from THINGS 6” residual velocity field. The fainter dots indicate the measurements restricted on PAWS FoV. *Bottom plot:* Non-circular motion amplitudes from harmonic decomposition: radial trend of the odd components and the total power $A_r(R)$ (top left) and even components (top right). Blue dashed straight line indicates the 2× the channel width of the cube equal to 5 km s^{-1}. In the bottom row the mean behavior of the odd (left) and even (middle) components in the different M51 environments (as defined in Meidt et al. 2013) are indicated.

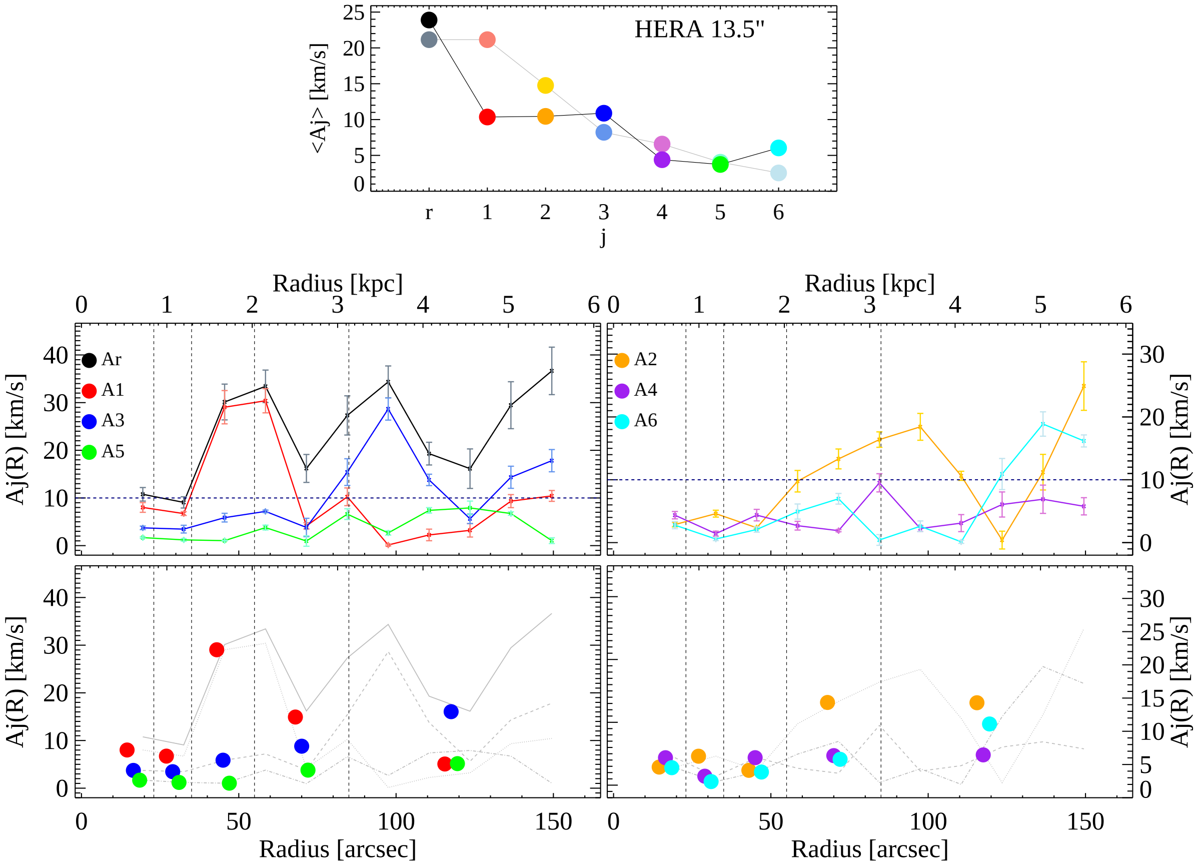

Figure 4.15: *Top plot:* Radial averaged mean of the harmonic component amplitudes from HERACLES 13.5” residual velocity field. The fainter dots indicate the measurements restricted on PAWS FoV. *Bottom plot:* Non-circular motion amplitudes from harmonic decomposition: radial trend of the odd components and the total power $A_r(R)$ (top left) and even components (top right). Blue dashed straight line indicates the 2× the channel width of the cube equal to 2.6 km s^{-1}. In the bottom row the mean behavior of the odd (left) and even (middle) components in the different M51 environments (as defined in Meidt et al. 2013) are indicated.

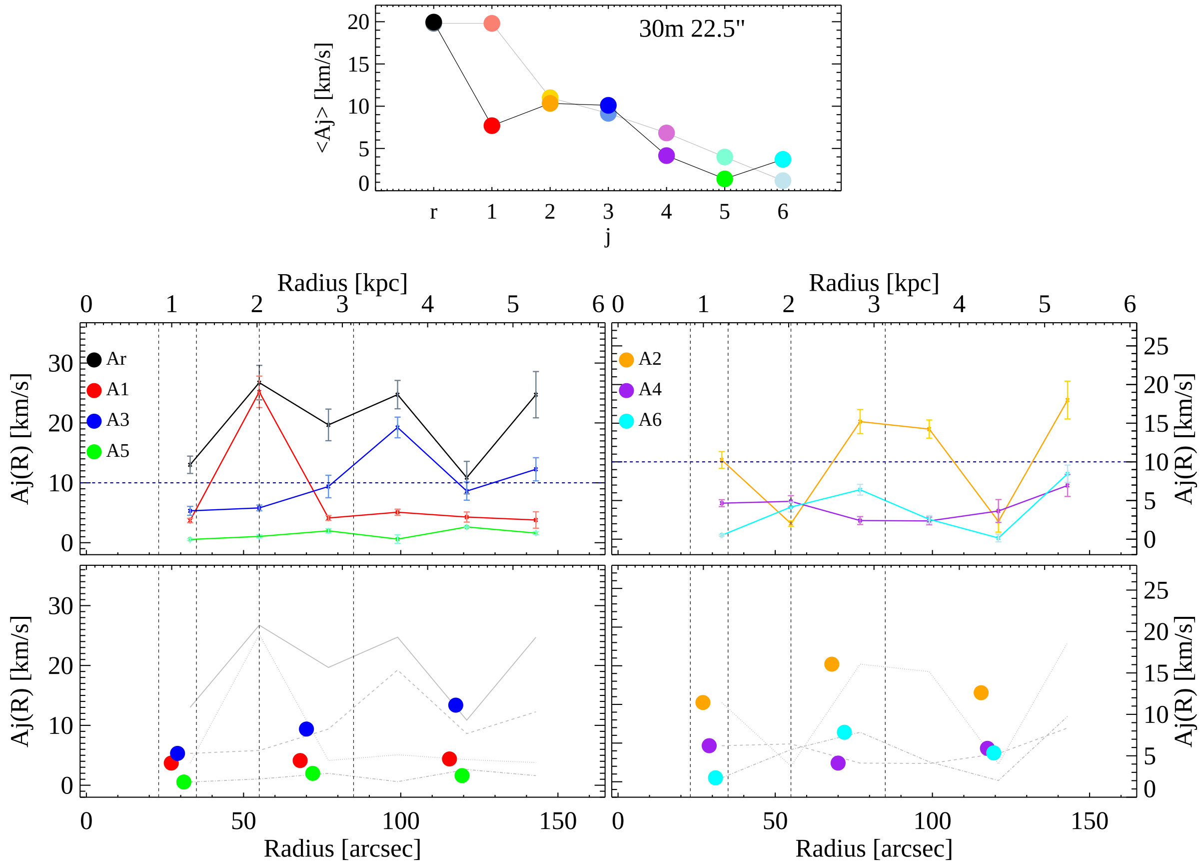

Figure 4.16: *Top plot:* Radial averaged mean of the harmonic component amplitudes from 30m 22.5” residual velocity field. The fainter dots indicate the measurements restricted on PAWS FoV. *Bottom plot:* Non-circular motion amplitudes from harmonic decomposition: radial trend of the odd components and the total power $A_r(R)$ (top left) and even components (top right). Blue dashed straight line indicates the 2× the channel width of the cube equal to 5 km s^{-1}. In the bottom row the mean behavior of the odd (left) and even (middle) components in the different M51 environments (as defined in Meidt et al. 2013) are indicated.

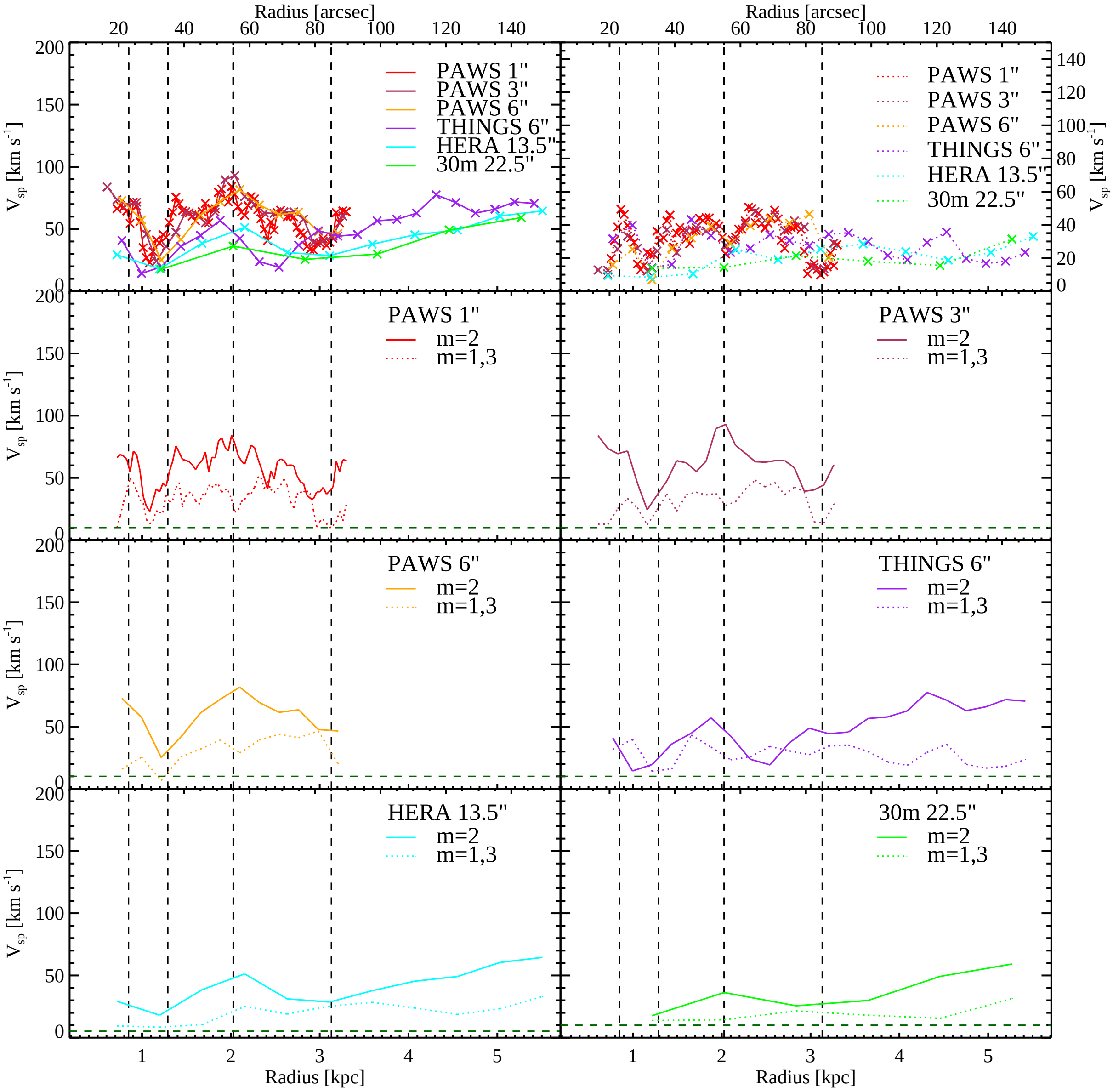

Figure 4.17: Amplitude of the spiral perturbation from PAWS 1" (top right), PAWS 3" (middle left), THINGS 6" (middle right), HERACLES 13" (bottom left), 30m 22.5" (bottom right). The blue solid lines the median on the different radial zones. The top left panel gives the compact view of the pattern speed derived from the different residual maps.

KOLMOGOROV-SMIRNOV TEST MATRICES

The tables presented here list the results of the two-sided Kolmogorov-Smirnov (KS) test carried out for the measured properties of GMCs in different environments. To account for their errors, we generated random values of a given property within the errors and we performed the test using the KSTWO procedure of the IDL astrolibrary. The results listed in the tables are median and median absolute deviation of p-values obtained through 100 bootstrap iterations. P-values lower than 0.01 show that the cumulative distribution function of the two statistical samples are significantly different and are indicated in bold. Values lower than 0.001 are substitute with <0.001. Moderate statistical significance (up to 0.05) is indicated in italic. Upper triangular matrix consider the high reliable objects (with $S/N > 6.5$), while the lower one the full sample of clouds. CPROPS does not provide uncertainties on the peak brightness temperature measurements. We generate those considering the σ_{RMS} along the line-of-sight where a given GMC peak temperature has been measured.

Table 4.8: Kolmogorov-Smirnov test for *Peak brightness temperature*

T$_{\text{max}}$	→	**High reliable** ($S/N > 6.5$)						
↓	**Envir.**	*NB*	*MR*	*DWI*	*DWO*	*MAT*	*DNS*	*UPS*
Full sample	*NB*	x	**0.007** ± **0.002**	**0.009** ± **0.004**	0.126 ± 0.021	*0.049 ± 0.007*	< **0.001**	< **0.001**
	MR	0.066 ± 0.007	x	< **0.001**	< **0.001**	**0.002** ± **0.001**	< **0.001**	< **0.001**
	DWI	< **0.001**	< **0.001**	x	0.093 ± 0.026	0.382 ± 0.000	*0.027 ± 0.014*	< **0.001**
	DWO	**0.002** ± **0.001**	< **0.001**	0.072 ± 0.008	x	0.819 ± 0.024	< **0.001**	< **0.001**
	MAT	< **0.001**	< **0.001**	0.171 ± 0.107	0.857 ± 0.124	x	**0.006** ± **0.002**	< **0.001**
	DNS	< **0.001**	< **0.001**	*0.015 ± 0.007*	< **0.001**	**0.003** ± **0.001**	x	**0.008** ± **0.006**
	UPS	< **0.001**	< **0.001**	**0.001** ± **0.001**	< **0.001**	< **0.001**	< **0.001**	x

Table 4.9: Kolmogorov-Smirnov test for *Radius*

R	→	**High reliable** ($S/N > 6.5$)						
↓	**Envir.**	*NB*	*MR*	*DWI*	*DWO*	*MAT*	*DNS*	*UPS*
Full sample	*NB*	x	0.600 ± 0.098	0.296 ± 0.149	0.586 ± 0.558	0.455 ± 0.427	*0.038 ± 0.056*	0.581 ± 0.459
	MR	0.797 ± 0.187	x	0.603 ± 0.313	0.333 ± 0.291	0.287 ± 0.226	**0.005** ± **0.007**	0.457 ± 0.315
	DWI	0.672 ± 0.322	0.357 ± 0.433	x	0.295 ± 0.308	0.384 ± 0.469	**0.002** ± **0.003**	0.357 ± 0.384
	DWO	0.202 ± 0.197	0.215 ± 0.184	0.272 ± 0.156	x	0.885 ± 0.114	0.125 ± 0.181	0.945 ± 0.054
	MAT	0.279 ± 0.309	0.296 ± 0.167	0.283 ± 0.198	0.983 ± 0.019	x	0.535 ± 0.479	0.934 ± 0.057
	DNS	**0.001** ± **0.002**	**0.002** ± **0.002**	**0.006** ± **0.009**	0.082 ± 0.119	0.071 ± 0.093	x	0.274 ± 0.202
	UPS	0.089 ± 0.130	0.083 ± 0.120	0.106 ± 0.130	0.402 ± 0.348	0.432 ± 0.228	0.643 ± 0.225	x

Table 4.10: Kolmogorov-Smirnov test for *Velocity dispersion*

$\sigma_{\mathbf{v}}$	→	**High reliable** ($S/N > 6.5$)						
↓	**Envir.**	*NB*	*MR*	*DWI*	*DWO*	*MAT*	*DNS*	*UPS*
	NB	x	0.071 ± 0.056	0.173 ± 0.065	0.734 ± 0.279	0.128 ± 0.109	< **0.001**	0.060 ± 0.084
	MR	0.231 ± 0.126	x	0.545 ± 0.202	0.107 ± 0.102	**0.007 ± 0.009**	< **0.001**	< **0.001**
Full	*DWI*	0.486 ± 0.547	0.188 ± 0.102	x	0.395 ± 0.195	0.050 ± 0.045	< **0.001**	**0.002 ± 0.002**
	DWO	0.595 ± 0.196	0.115 ± 0.114	0.700 ± 0.135	x	0.052 ± 0.053	< **0.001**	**0.008 ± 0.011**
sample	*MAT*	**0.007 ± 0.010**	< **0.001**	**0.002 ± 0.003**	< **0.001**	x	*0.018 ± 0.024*	0.154 ± 0.161
	DNS	< **0.001**	< **0.001**	< **0.001**	< **0.001**	0.069 ± 0.100	x	0.175 ± 0.232
	UPS	*0.017 ± 0.026*	< **0.001**	*0.024 ± 0.025*	**0.004 ± 0.005**	0.247 ± 0.255	*0.022 ± 0.018*	x

Table 4.11: Kolmogorov-Smirnov test for *Axis ratio*

b/a	→	**High reliable** ($S/N > 6.5$)						
↓	**Envir.**	*NB*	*MR*	*DWI*	*DWO*	*MAT*	*DNS*	*UPS*
	NB	x	0.503 ± 0.133	0.981 ± 0.008	0.965 ± 0.026	0.129 ± 0.029	0.227 ± 0.075	0.634 ± 0.069
	MR	0.606 ± 0.306	x	0.382 ± 0.031	0.127 ± 0.044	0.300 ± 0.092	0.503 ± 0.249	0.988 ± 0.011
Full	*DWI*	0.808 ± 0.103	0.596 ± 0.096	x	0.847 ± 0.129	0.106 ± 0.073	0.191 ± 0.027	0.537 ± 0.003
	DWO	0.889 ± 0.066	0.576 ± 0.100	0.903 ± 0.088	x	*0.037 ± 0.018*	0.071 ± 0.023	0.263 ± 0.045
sample	*MAT*	**0.009 ± 0.004**	*0.012 ± 0.013*	**0.005 ± 0.002**	< **0.001**	x	0.841 ± 0.103	0.764 ± 0.160
	DNS	*0.025 ± 0.017*	0.108 ± 0.038	*0.037 ± 0.014*	*0.013 ± 0.004*	0.409 ± 0.119	x	0.973 ± 0.028
	UPS	0.130 ± 0.100	0.307 ± 0.245	0.158 ± 0.153	*0.039 ± 0.045*	0.495 ± 0.078	0.971 ± 0.032	x

Table 4.12: Kolmogorov-Smirnov test for *Orientation*

ϕ	→	**High reliable** ($S/N > 6.5$)						
↓	**Envir.**	*NB*	*MR*	*DWI*	*DWO*	*MAT*	*DNS*	*UPS*
	NB	x	< **0.001**	< **0.001**	< **0.001**	< **0.001**	< **0.001**	< **0.001**
	MR	< **0.001**	x	< **0.001**	< **0.001**	< **0.001**	< **0.001**	< **0.001**
Full	*DWI*	< **0.001**	**0.001 ± 0.000**	x	< **0.001**	< **0.001**	< **0.001**	< **0.001**
	DWO	< **0.001**	< **0.001**	< **0.001**	x	**0.008 ± 0.000**	**0.003 ± 0.000**	**0.006 ± 0.000**
sample	*MAT*	< **0.001**	< **0.001**	< **0.001**	< **0.001**	x	**0.001 ± 0.000**	0.060 ± 0.000
	DNS	< **0.001**	< **0.001**	< **0.001**	< **0.001**	< **0.001**	x	0.863 ± 0.000
	UPS	< **0.001**	< **0.001**	< **0.001**	< **0.001**	**0.010 ± 0.000**	0.547 ± 0.000	x

Table 4.13: Kolmogorov-Smirnov test for *Luminosity mass*

$\mathbf{M_{lum}}$	→	**High reliable** ($S/N > 6.5$)						
↓	**Envir.**	*NB*	*MR*	*DWI*	*DWO*	*MAT*	*DNS*	*UPS*
Full sample	*NB*	x	*0.040 ± 0.042*	0.286 ± 0.154	0.055 ± 0.033	0.484 ± 0.387	< **0.001**	**0.004 ± 0.006**
	MR	0.196 ± 0.126	x	0.097 ± 0.106	0.564 ± 0.211	**0.002 ± 0.002**	< **0.001**	< **0.001**
	DWI	*0.024 ± 0.032*	*0.017 ± 0.018*	x	0.237 ± 0.136	0.238 ± 0.261	**0.001 ± 0.002**	*0.017 ± 0.021*
	DWO	*0.044 ± 0.057*	0.233 ± 0.089	0.257 ± 0.139	x	*0.029 ± 0.031*	< **0.001**	< **0.001**
	MAT	**0.002 ± 0.002**	< **0.001**	0.256 ± 0.153	*0.037 ± 0.043*	x	*0.011 ± 0.015*	*0.031 ± 0.040*
	DNS	< **0.001**	< **0.001**	< **0.001**	< **0.001**	**0.008 ± 0.011**	x	0.364 ± 0.181
	UPS	< **0.001**	< **0.001**	< **0.001**	< **0.001**	*0.011 ± 0.015*	0.547 ± 0.230	x

Table 4.14: Kolmogorov-Smirnov test for *Virial mass*

$\mathbf{M_{vir}}$	→	**High reliable** ($S/N > 6.5$)						
↓	**Envir.**	*NB*	*MR*	*DWI*	*DWO*	*MAT*	*DNS*	*UPS*
Full sample	*NB*	x	0.165 ± 0.125	*0.026 ± 0.033*	0.548 ± 0.518	0.072 ± 0.105	< **0.001**	*0.036 ± 0.054*
	MR	0.397 ± 0.140	x	0.418 ± 0.337	0.086 ± 0.087	< **0.001**	< **0.001**	< **0.001**
	DWI	0.142 ± 0.076	0.442 ± 0.206	x	*0.019 ± 0.022*	< **0.001**	< **0.001**	< **0.001**
	DWO	0.415 ± 0.397	*0.021 ± 0.030*	0.089 ± 0.120	x	0.069 ± 0.053	< **0.001**	*0.025 ± 0.014*
	MAT	**0.004 ± 0.006**	< **0.001**	< **0.001**	*0.013 ± 0.014*	x	0.109 ± 0.064	0.343 ± 0.136
	DNS	< **0.001**	< **0.001**	< **0.001**	< **0.001**	0.150 ± 0.140	x	0.281 ± 0.196
	UPS	0.052 ± 0.076	**0.004 ± 0.006**	**0.003 ± 0.004**	0.095 ± 0.080	0.548 ± 0.140	*0.031 ± 0.032*	x

Table 4.15: Kolmogorov-Smirnov test for *Surface density*

$\mathbf{\Sigma_{H2}}$	→	**High reliable** ($S/N > 6.5$)						
↓	**Envir.**	*NB*	*MR*	*DWI*	*DWO*	*MAT*	*DNS*	*UPS*
Full sample	*NB*	x	*0.050 ± 0.073*	0.746 ± 0.288	0.063 ± 0.081	0.623 ± 0.277	0.125 ± 0.146	0.075 ± 0.099
	MR	0.122 ± 0.166	x	**0.003 ± 0.004**	0.115 ± 0.098	*0.049 ± 0.034*	< **0.001**	< **0.001**
	DWI	0.296 ± 0.318	< **0.001**	x	*0.018 ± 0.026*	0.485 ± 0.225	0.168 ± 0.115	0.073 ± 0.033
	DWO	0.355 ± 0.252	0.161 ± 0.089	**0.005 ± 0.007**	x	0.192 ± 0.248	< **0.001**	< **0.001**
	MAT	0.523 ± 0.306	*0.026 ± 0.019*	0.149 ± 0.095	0.109 ± 0.139	x	*0.025 ± 0.018*	*0.042 ± 0.029*
	DNS	*0.041 ± 0.061*	< **0.001**	0.363 ± 0.323	< **0.001**	0.074 ± 0.071	x	0.387 ± 0.100
	UPS	0.086 ± 0.127	< **0.001**	0.086 ± 0.116	< **0.001**	0.055 ± 0.064	0.501 ± 0.285	x

Table 4.16: Kolmogorov-Smirnov test for *Scaling parameter*

c	→	**High reliable** ($S/N > 6.5$)						
↓	**Envir.**	*NB*	*MR*	*DWI*	*DWO*	*MAT*	*DNS*	*UPS*
Full sample	*NB*	x	0.172 ± 0.114	0.265 ± 0.205	0.360 ± 0.120	0.495 ± 0.471	*0.013 ± 0.019*	0.107 ± 0.133
	MR	0.140 ± 0.136	x	0.684 ± 0.215	0.331 ± 0.185	**0.006 ± 0.008**	< **0.001**	< **0.001**
	DWI	0.265 ± 0.121	0.365 ± 0.235	x	0.511 ± 0.174	*0.023 ± 0.030*	< **0.001**	< **0.001**
	DWO	0.304 ± 0.152	0.411 ± 0.232	0.909 ± 0.105	x	*0.029 ± 0.033*	< **0.001**	**0.009 ± 0.014**
	MAT	0.424 ± 0.520	**0.004 ± 0.005**	**0.009 ± 0.013**	*0.014 ± 0.020*	x	0.202 ± 0.115	0.311 ± 0.119
	DNS	*0.023 ± 0.033*	< **0.001**	< **0.001**	< **0.001**	0.158 ± 0.118	x	0.497 ± 0.510
	UPS	0.447 ± 0.182	*0.015 ± 0.015*	*0.029 ± 0.032*	0.080 ± 0.112	0.676 ± 0.149	0.103 ± 0.088	x

Table 4.17: Kolmogorov-Smirnov test for *Virial parameter*

α	→	**High reliable** ($S/N > 6.5$)						
↓	**Envir.**	*NB*	*MR*	*DWI*	*DWO*	*MAT*	*DNS*	*UPS*
Full sample	*NB*	x	0.411 ± 0.122	0.362 ± 0.249	0.079 ± 0.079	0.137 ± 0.077	0.070 ± 0.023	0.430 ± 0.128
	MR	0.791 ± 0.186	x	*0.049 ± 0.039*	0.284 ± 0.205	0.245 ± 0.266	0.304 ± 0.248	0.648 ± 0.426
	DWI	0.196 ± 0.166	*0.025 ± 0.022*	x	*0.023 ± 0.026*	*0.018 ± 0.022*	*0.018 ± 0.017*	0.080 ± 0.088
	DWO	0.578 ± 0.138	0.360 ± 0.133	*0.044 ± 0.031*	x	0.063 ± 0.084	0.170 ± 0.196	0.258 ± 0.224
	MAT	0.372 ± 0.132	0.396 ± 0.309	*0.013 ± 0.013*	0.127 ± 0.128	x	0.648 ± 0.252	0.752 ± 0.291
	DNS	0.178 ± 0.228	0.217 ± 0.215	**0.005 ± 0.005**	0.339 ± 0.427	0.677 ± 0.237	x	0.777 ± 0.212
	UPS	0.456 ± 0.262	0.172 ± 0.089	0.425 ± 0.286	*0.026 ± 0.025*	*0.039 ± 0.036*	**0.009 ± 0.006**	x

ACKNOWLEDGEMENTS

Me and the English language are not best friends. Rather, English was one of the biggest “enemy” I had to defeat when I first arrived in Heidelberg, more than 3 years ago. So I hope that the people listed in this acknowledgment will apologize me for the paucity of my English here. However I wish to write these few pages with my heart more that with my mind and I will take the freedom of the case even with the language.

My first, biggest and honest thanks is for Eva Schinnerer. And this is not because it is due. This is because I really feel it. She believed in me during my stutterer interview, giving me this job and the opportunity to work on a great project. She introduced me in this fantastic field. She was always, always available for comments, suggestions and hints, although as busy as she was. She initiated me in this career, wisely guiding me in this world, changing my life. She was not only a supervisor for me, but a real master. And even this is not enough for all she did during for these years I want just to say thanks for everything you taught me, Eva. I truly hope we will have the possibility to work together again in the future.

There are other two people I want and I need to acknowledge, without which this thesis would have never seen the light. Sharon Meidt and Annie Hughes. They are just GREAT! Great people and scientists! And I feel extremely lucky to have had the opportunity to work with them. I really believe they will be great leaders in the future. Thanks for all the help and support.

I want to thank also the member of the PAWS team, an exceptional selection of people with exceptional talents that truly help me to improve the quality of my papers (and my thesis). In alphabetic order: Adam Leroy, Carsten Kramer, Clare Dobbs, Gaelle Dumas, Jerome Pety, Karl Schuster, Santiago Garcia-Burillo and Todd Thompson.

Between them I would like to thank Adam Leroy in particular for the help, support (and the rides) during my staying at NRAO.

Thanks also to all other old (Alexander Karim, Mark Sargent, Tessel van der Laan) and current (Brent Groves, Emer Brady, Fatemeh Tabatabaei, Kathryn Kreckel, Mark Norris, Maria Kapala, Miguel Querejeta, Paolo Bianchini) members of Eva's group that welcomed me within them as a family and were always available with comments and suggestions about my research or simply for the life at MPIA and in Heidelberg.

I want to acknowledge my referees, Prof. Dr. Hans-Walter Rix and Prof. Dr. Jochen Heidt, that, I hope, have enjoyed the journey and Prof. Dr. Ralf Klessen and Prof. Dr. Luca Amendola that accepted to be part of my defense committee.

I thank my future boss, Erik Rosolowsky, not only for offering me a post-doc, but also for his extremely useful IDL library that I used a lot during this work.

However my stay in Heidelberg would not be so extraordinary without the friends from all around the world that share with me happiness and sorrow, fun and hard work, or in one word, these three years life (ok, maybe four words).

Thanks to all my international friends and in particular: Alberto, Fabrizio, Gabriele (my coffee fellows), Bala, Dading (my gym partners), Somayeh, Yu-Yen, Rahul, Ronald, Jayanta, Sladjana, Cami, Tito and Anja (also my neighbors).

My D&D fellows: Fredrik (the master), Maria (the faithful Aryenne), Maren (the strong Sariel/Xeeliah), Laszlo (the wise Peikka/Drax), Karsten (the small Corrin) and Tobias (the mysterious Sarghon). Which glorious battles we fought together in our minds! Thanks!

My fellow actors: Salvo, Matthieu, Nikolay. Which great play we performed! Thank you!

Thanks to all the people that have sit on the office 224 desks that bear me for most of days: Anahi, Dima, Maria (thanks again for checking the abstract!), Matthias, Quang, Simona.

I hope we will stay in touch in the future!

I want also to acknowledge all the employer of MPIA (scientists and not) that contribute to make this institute a wonderful place to work!

Thanks to all my friends that I had to leave to come here and I cannot frequent as I wish and that I miss a lot... Thanks again Ri, Ca, Giose, W, Je, Mara, Sax, Gippo, Laura, Gas, Carmine, Chiaretta, Fabio, Dani, Angy, Vale e Marco.

I will never be so thankful to my parents, Marinella and Valerio, that patiently wait for my return in Italy. I cannot describe how much I miss you and how much I love you, but I ask you to be patient once again, because my journey around the world apparently is not over yet.

Probably three years ago I would have never though to be here, writing thanks to my girlfriend, Vessy. Thank you a lot my darling. Thanks for your love, your support, your presence, your laugh, your kindness, our discussions, our travels, our adventures, the cakes and the pancakes and everything else that have made to be a better man day by day. Thanks.

My last thanks, however, goes to the person to which this thesis is dedicated and that I lost last year. Farewell Nonna Luigia, I hope you fell well where you are now. I wish one day to see you again and I hope you will always guide me with your love from the stars...

BIBLIOGRAPHY

Aalto, S., Hüttemeister, S., Scoville, N. Z., & Thaddeus, P. 1999, ApJ, 522, 165

Adler, D. S., Lo, K. Y., Wright, M. C. H., Rydbeck, G., Plante, R. L., & Allen, R. J. 1992, ApJ, 392, 497

Akritas, M. G., & Bershady, M. A. 1996, ApJ, 470, 706

André, P., Basu, S., & Inutsuka, S. 2009, The formation and evolution of prestellar cores, ed. G. Chabrier (Cambridge University Press), 254

André, P., et al. 2010, A&A, 518, L102

Athanassoula, E. 1992, MNRAS, 259, 345

Balbus, S. A., & Cowie, L. L. 1985, ApJ, 297, 61

Ballesteros-Paredes, J., Hartmann, L., & Vázquez-Semadeni, E. 1999, ApJ, 527, 285

Bell, T. A., Viti, S., & Williams, D. A. 2007, MNRAS, 378, 983

Bergin, E. A., Hartmann, L. W., Raymond, J. C., & Ballesteros-Paredes, J. 2004, ApJ, 612, 921

Bertin, G., & Lin, C. C. 1996, Spiral structure in galaxies a density wave theory

Bertin, G., Lin, C. C., Lowe, S. A., & Thurstans, R. P. 1989a, ApJ, 338, 78

—. 1989b, ApJ, 338, 104

Bertoldi, F., & McKee, C. F. 1992, ApJ, 395, 140

Bigiel, F., Leroy, A., Walter, F., Brinks, E., de Blok, W. J. G., Madore, B., & Thornley, M. D. 2008, AJ, 136, 2846

Binney, J., & Tremaine, S. 1987, Galactic dynamics

Blitz, L. 1993, in Protostars and Planets III, ed. E. H. Levy & J. I. Lunine, 125–161

Blitz, L., Fukui, Y., Kawamura, A., Leroy, A., Mizuno, N., & Rosolowsky, E. 2007, Protostars and Planets V, 81

Blitz, L., & Rosolowsky, E. 2004, in Astronomical Society of the Pacific Conference Series, Vol.

323, Star Formation in the Interstellar Medium: In Honor of David Hollenbach, ed. D. Johnstone, F. C. Adams, D. N. C. Lin, D. A. Neufeeld, & E. C. Ostriker, 89

Blitz, L., & Shu, F. H. 1980, ApJ, 238, 148

Bohlin, R. C., Savage, B. D., & Drake, J. F. 1978, ApJ, 224, 132

Bolatto, A. D., Leroy, A. K., Rosolowsky, E., Walter, F., & Blitz, L. 2008, ApJ, 686, 948

Bournaud, F., Elmegreen, B. G., & Elmegreen, D. M. 2007, ApJ, 670, 237

Bresolin, F., Garnett, D. R., & Kennicutt, Jr., R. C. 2004, ApJ, 615, 228

Brunner, G., et al. 2008, ApJ, 675, 316

Brunt, C. M., Heyer, M. H., Vázquez-Semadeni, E., & Pichardo, B. 2003, ApJ, 595, 824

Canzian, B. 1993, ApJ, 414, 487

Canzian, B., & Allen, R. J. 1997, ApJ, 479, 723

Carr, J. S. 1987, ApJ, 323, 170

Casoli, F., & Combes, F. 1981, Academie des Sciences Paris Comptes Rendus Serie B Sciences Physiques, 293, 761

—. 1982, A&A, 110, 287

Ciardullo, R., Feldmeier, J. J., Jacoby, G. H., Kuzio de Naray, R., Laychak, M. B., & Durrell, P. R. 2002, ApJ, 577, 31

Cohen, R. S., Cong, H., Dame, T. M., & Thaddeus, P. 1980, ApJ, 239, L53

Cowie, L. L. 1980, ApJ, 236, 868

Crutcher, R. M. 1999, ApJ, 520, 706

Dame, T. M., & Thaddeus, P. 1994, ApJ, 436, L173

de Blok, W. J. G., Walter, F., Brinks, E., Trachternach, C., Oh, S.-H., & Kennicutt, Jr., R. C. 2008, AJ, 136, 2648

de Vaucouleurs, G., de Vaucouleurs, A., Corwin, Jr., H. G., Buta, R. J., Paturel, G., & Fouqué, P. 1991, Third Reference Catalogue of Bright Galaxies. Volume I: Explanations and references. Volume II: Data for galaxies between 0^h and 12^h. Volume III: Data for galaxies between 12^h and 24^h.

Dib, S., Helou, G., Moore, T. J. T., Urquhart, J. S., & Dariush, A. 2012, ApJ, 758, 125

Dickman, R. L. 1978, ApJS, 37, 407

Dobbs, C. L. 2008, MNRAS, 391, 844

Dobbs, C. L., Bonnell, I. A., & Pringle, J. E. 2006, MNRAS, 371, 1663

Dobbs, C. L., Burkert, A., & Pringle, J. E. 2011, MNRAS, 413, 2935

Dobbs, C. L., & Pringle, J. E. 2013, MNRAS, 432, 653

Dobbs, C. L., Pringle, J. E., & Burkert, A. 2012, MNRAS, 425, 2157

Dobbs, C. L., Theis, C., Pringle, J. E., & Bate, M. R. 2010, MNRAS, 403, 625

D'Onghia, E., Vogelsberger, M., & Hernquist, L. 2013, ApJ, 766, 34

Donovan Meyer, J., et al. 2012, ApJ, 744, 42

—. 2013, ApJ, 772, 107

Dressel, L. L., & Condon, J. J. 1976, ApJS, 31, 187

Eadie, W. T., Drijard, D., & James, F. E. 1971, Statistical methods in experimental physics

Egusa, F., Koda, J., & Scoville, N. 2011, ApJ, 726, 85

Elmegreen, B. G. 1979, ApJ, 231, 372

—. 1989, ApJ, 338, 178

—. 1990, ApJ, 357, 125

—. 1994, ApJ, 433, 39

—. 2000, ApJ, 530, 277

—. 2007, ApJ, 668, 1064

—. 2011, ApJ, 731, 61

Elmegreen, B. G., & Elmegreen, D. M. 1983, MNRAS, 203, 31

Elmegreen, B. G., Elmegreen, D. M., & Montenegro, L. 1992, ApJS, 79, 37

Elmegreen, B. G., & Scalo, J. 2004, ARA&A, 42, 211

Engargiola, G., Plambeck, R. L., Rosolowsky, E., & Blitz, L. 2003, ApJS, 149, 343

Eskridge, P. B., et al. 2002, ApJS, 143, 73

Evans, II, N. J., et al. 2009, ApJS, 181, 321

Fathi, K., van de Ven, G., Peletier, R. F., Emsellem, E., Falcón-Barroso, J., Cappellari, M., & de Zeeuw, T. 2005, MNRAS, 364, 773

Ford, H. C., Crane, P. C., Jacoby, G. H., Lawrie, D. G., & van der Hulst, J. M. 1985, ApJ, 293, 132

Fuchs, B. 2001, A&A, 368, 107

Fukui, Y. 2005, in Astronomical Society of the Pacific Conference Series, Vol. 344, The Cool Universe: Observing Cosmic Dawn, ed. C. Lidman & D. Alloin, 155

Fukui, Y., & Kawamura, A. 2010, ARA&A, 48, 547

Fukui, Y., Mizuno, N., Yamaguchi, R., Mizuno, A., & Onishi, T. 2001, PASJ, 53, L41

Fukui, Y., et al. 1999, PASJ, 51, 745

—. 2008, ApJS, 178, 56

Garcia-Burillo, S., Combes, F., & Gerin, M. 1993a, A&A, 274, 148

Garcia-Burillo, S., Guelin, M., & Cernicharo, J. 1993b, A&A, 274, 123

Garcia-Burillo, S., Guelin, M., Cernicharo, J., & Dahlem, M. 1992, A&A, 266, 21

Glover, S. C. O., & Clark, P. C. 2012, MNRAS, 426, 377

Goad, J. W., de Veny, J. B., & Goad, L. E. 1979, ApJS, 39, 439

Goldreich, P., & Lynden-Bell, D. 1965, MNRAS, 130, 125

Goldsmith, P. F., Heyer, M., Narayanan, G., Snell, R., Li, D., & Brunt, C. 2008, ApJ, 680, 428

Gratier, P., et al. 2012, A&A, 542, A108

Grenier, I. A., Casandjian, J.-M., & Terrier, R. 2005, Science, 307, 1292

Guelin, M., Zylka, R., Mezger, P. G., Haslam, C. G. T., & Kreysa, E. 1995, A&A, 298, L29

Hagiwara, Y. 2007, AJ, 133, 1176

Hagiwara, Y., Henkel, C., Menten, K. M., & Nakai, N. 2001, ApJ, 560, L37

Heitsch, F., Slyz, A. D., Devriendt, J. E. G., Hartmann, L. W., & Burkert, A. 2006, ApJ, 648, 1052

Heitsch, F., Stone, J. M., & Hartmann, L. W. 2009, ApJ, 695, 248

Helfer, T. T., Thornley, M. D., Regan, M. W., Wong, T., Sheth, K., Vogel, S. N., Blitz, L., & Bock, D. C.-J. 2003, ApJS, 145, 259

Hennebelle, P., Audit, E., & Miville-Deschênes, M.-A. 2007, A&A, 465, 445

Hennebelle, P., & Chabrier, G. 2008, ApJ, 684, 395

Henry, A. L., Quillen, A. C., & Gutermuth, R. 2003, AJ, 126, 2831

Heyer, M., Krawczyk, C., Duval, J., & Jackson, J. M. 2009, ApJ, 699, 1092

Heyer, M. H., & Brunt, C. M. 2004, ApJ, 615, L45

Heyer, M. H., Carpenter, J. M., & Snell, R. L. 2001a, ApJ, 551, 852

—. 2001b, ApJ, 551, 852

Heyer, M. H., & Terebey, S. 1998, ApJ, 502, 265

Hirota, A., Kuno, N., Sato, N., Nakanishi, H., Tosaki, T., & Sorai, K. 2011, ApJ, 737, 40

Hitschfeld, M., Kramer, C., Schuster, K. F., Garcia-Burillo, S., & Stutzki, J. 2009, A&A, 495, 795

Hollenbach, D. J., & Tielens, A. G. G. M. 1999, Reviews of Modern Physics, 71, 173

Hopkins, P. F. 2012, MNRAS, 423, 2016

Hoyle, F. 1953, ApJ, 118, 513

Hu, T., Shao, Z., & Peng, Q. 2013, ApJ, 762, L27

Hughes, A., et al. 2010, MNRAS, 406, 2065

—. 2013, ArXiv e-prints

Israel, F. P. 1997, A&A, 328, 471

Israel, F. P., & Baas, F. 2002, A&A, 383, 82

Israel, F. P., Tilanus, R. P. J., & Baas, F. 2006, A&A, 445, 907

Jog, C. J. 2013, MNRAS, 434, L56

Julian, W. H., & Toomre, A. 1966, ApJ, 146, 810

Kainulainen, J., Beuther, H., Henning, T., & Plume, R. 2009, A&A, 508, L35

Kalnajs, A. J. 1973, Proceedings of the Astronomical Society of Australia, 2, 174

Kawamura, A., et al. 2009, ApJS, 184, 1

Kennicutt, Jr., R. C. 1981, AJ, 86, 1847

Kennicutt, Jr., R. C., et al. 2003, PASP, 115, 928

Kim, C.-G., Kim, W.-T., & Ostriker, E. C. 2006, ApJ, 649, L13

Kim, J., Ryu, D., & Jones, T. W. 2001, ApJ, 557, 464

Klessen, R. S., Heitsch, F., & Mac Low, M.-M. 2000, ApJ, 535, 887

Koda, J. 2013, ArXiv e-prints

Koda, J., et al. 2009, ApJ, 700, L132

—. 2011, ApJS, 193, 19

—. 2012, ApJ, 761, 41

Kormendy, J., & Norman, C. A. 1979, ApJ, 233, 539

Koyama, H., & Inutsuka, S.-I. 2000, ApJ, 532, 980

Koyama, H., & Ostriker, E. C. 2009a, ApJ, 693, 1346

—. 2009b, ApJ, 693, 1346

Kramer, C., Mookerjea, B., Bayet, E., Garcia-Burillo, S., Gerin, M., Israel, F. P., Stutzki, J., & Wouterloot, J. G. A. 2005, A&A, 441, 961

Kramer, C., Stutzki, J., Rohrig, R., & Corneliussen, U. 1998, A&A, 329, 249

Kritsuk, A. G., & Norman, M. L. 2011, ArXiv e-prints

Krumholz, M. R., & Matzner, C. D. 2009, ApJ, 703, 1352

Kuno, N., & Nakai, N. 1997, PASJ, 49, 279

Kuno, N., Nakai, N., Handa, T., & Sofue, Y. 1995, PASJ, 47, 745

Kwan, J. 1979, ApJ, 229, 567

Kwan, J., & Valdes, F. 1983, ApJ, 271, 604

—. 1987, ApJ, 315, 92

La Vigne, M. A., Vogel, S. N., & Ostriker, E. C. 2006, ApJ, 650, 818

Larson, R. B. 1981, MNRAS, 194, 809

—. 1985, MNRAS, 214, 379

—. 1992, MNRAS, 256, 641

Lequeux, J. 2005, The Interstellar Medium

Leroy, A., Bolatto, A., Walter, F., & Blitz, L. 2006, ApJ, 643, 825

Leroy, A. K., Walter, F., Brinks, E., Bigiel, F., de Blok, W. J. G., Madore, B., & Thornley, M. D. 2008, AJ, 136, 2782

Leroy, A. K., et al. 2009, ApJ, 702, 352

—. 2013a, ApJ, 769, L12

—. 2013b, AJ, 146, 19

Li, Z.-Y., & Nakamura, F. 2006, ApJ, 640, L187

Lin, C. C., & Shu, F. H. 1964, ApJ, 140, 646

—. 1966, Proceedings of the National Academy of Science, 55, 229

Lindblad, B. 1963, Stockholms Observatoriums Annaler, 22, 5

Lo, K. Y., Ball, R., Masson, C. R., Phillips, T. G., Scott, S., & Woody, D. P. 1987, ApJ, 317, L63

Lord, S. D., & Young, J. S. 1990, ApJ, 356, 135

Louie, M., Koda, J., & Egusa, F. 2013, ApJ, 763, 94

Lowe, S. A., Roberts, W. W., Yang, J., Bertin, G., & Lin, C. C. 1994, ApJ, 427, 184

Mac Low, M.-M., & Klessen, R. S. 2004, Reviews of Modern Physics, 76, 125

Maddox, L. A., Cowan, J. J., Kilgard, R. E., Schinnerer, E., & Stockdale, C. J. 2007, AJ, 133, 2559

Masset, F., & Tagger, M. 1997, A&A, 322, 442

Matsushita, S., Muller, S., & Lim, J. 2007, A&A, 468, L49

Matzner, C. D. 2002, ApJ, 566, 302

McKee, C. F. 1999, in NATO ASIC Proc. 540: The Origin of Stars and Planetary Systems, ed. C. J. Lada & N. D. Kylafis, 29

McKee, C. F., & Ostriker, E. C. 2007, ARA&A, 45, 565

Meidt, S. E., Rand, R. J., Merrifield, M. R., Shetty, R., & Vogel, S. N. 2008, ApJ, 688, 224

Meidt, S. E., et al. 2012, ApJ, 744, 17

—. 2013, ArXiv e-prints

Menéndez-Delmestre, K., Sheth, K., Schinnerer, E., Jarrett, T. H., & Scoville, N. Z. 2007, ApJ, 657, 790

Mentuch Cooper, E., et al. 2012, ApJ, 755, 165

Minchev, I., Famaey, B., Quillen, A. C., Dehnen, W., Martig, M., & Siebert, A. 2012, A&A, 548, A127

Miura, R. E., et al. 2012, ApJ, 761, 37

Miyazaki, A., & Tsuboi, M. 2000, ApJ, 536, 357

Molinari, S., et al. 2010, PASP, 122, 314

Moustakas, J., Kennicutt, Jr., R. C., Tremonti, C. A., Dale, D. A., Smith, J.-D. T., & Calzetti, D. 2010, ApJS, 190, 233

Muñoz-Mateos, J. C., Boissier, S., Gil de Paz, A., Zamorano, J., Kennicutt, Jr., R. C., Moustakas, J., Prantzos, N., & Gallego, J. 2011, ApJ, 731, 10

Murray, N. 2011, ApJ, 729, 133

Myers, P. C. 2009, ApJ, 700, 1609

Nakai, N., Kuno, N., Handa, T., & Sofue, Y. 1994, PASJ, 46, 527

Nakamura, F., & Li, Z.-Y. 2007, ApJ, 662, 395

Oka, T., Hasegawa, T., Sato, F., Tsuboi, M., & Miyazaki, A. 1998, ApJS, 118, 455

Oka, T., Hasegawa, T., Sato, F., Tsuboi, M., Miyazaki, A., & Sugimoto, M. 2001, ApJ, 562, 348

Ossenkopf, V., & Mac Low, M.-M. 2002, A&A, 390, 307

Ostriker, E. C. 2011, in IAU Symposium, Vol. 270, Computational Star Formation, ed. J. Alves, B. G. Elmegreen, J. M. Girart, & V. Trimble, 467–474

Padoan, P., & Nordlund, Å. 2002, ApJ, 576, 870

Padoan, P., Nordlund, A., & Jones, B. J. T. 1997, MNRAS, 288, 145

Parker, E. N. 1966, ApJ, 145, 811

Pety, J. 2005, in SF2A-2005: Semaine de l'Astrophysique Francaise, ed. F. Casoli, T. Contini, J. M. Hameury, & L. Pagani, 721

Pety, J., et al. 2013, ArXiv e-prints

Pringle, J. E., Allen, R. J., & Lubow, S. H. 2001, MNRAS, 327, 663

Pudritz, R. E. 2002, Ap&SS, 281, 493

Putman, M. E., Peek, J. E. G., & Joung, M. R. 2012, ARA&A, 50, 491

Rand, R. J. 1993, ApJ, 404, 593

Rand, R. J., & Kulkarni, S. R. 1990, in NASA Conference Publication, Vol. 3084, NASA Conference Publication, ed. D. J. Hollenbach & H. A. Thronson, Jr., 293–295

Rautiainen, P., & Salo, H. 1999, A&A, 348, 737

Rebolledo, D., Wong, T., Leroy, A., Koda, J., & Donovan Meyer, J. 2012, ApJ, 757, 155

Regan, M. W., Thornley, M. D., Helfer, T. T., Sheth, K., Wong, T., Vogel, S. N., Blitz, L., & Bock, D. C.-J. 2001, ApJ, 561, 218

Rix, H.-W., & Rieke, M. J. 1993, ApJ, 418, 123

Roberts, Jr., W. W., & Stewart, G. R. 1987, ApJ, 314, 10

Rogstad, D. H., Lockhart, I. A., & Wright, M. C. H. 1974, ApJ, 193, 309

Rosolowsky, E. 2005, PASP, 117, 1403

—. 2007, ApJ, 654, 240

Rosolowsky, E., & Blitz, L. 2005, ApJ, 623, 826

Rosolowsky, E., & Leroy, A. 2006, PASP, 118, 590

Rosolowsky, E. W., Pineda, J. E., Kauffmann, J., & Goodman, A. A. 2008, ApJ, 679, 1338

Rots, A. H., Bosma, A., van der Hulst, J. M., Athanassoula, E., & Crane, P. C. 1990, AJ, 100, 387

Rubio, M. 2004, in Astronomical Society of the Pacific Conference Series, Vol. 322, The Formation and Evolution of Massive Young Star Clusters, ed. H. J. G. L. M. Lamers, L. J. Smith, &

A. Nota, 237

Rydbeck, G., Hjalmarson, A., & Rydbeck, O. E. H. 1985, A&A, 144, 282

Sakamoto, K., Okumura, S. K., Ishizuki, S., & Scoville, N. Z. 1999, ApJS, 124, 403

Salo, H., & Laurikainen, E. 2000, MNRAS, 319, 377

Sanders, D. B., Scoville, N. Z., & Solomon, P. M. 1985, ApJ, 289, 373

Sawada, T., Hasegawa, T., & Koda, J. 2012, ApJ, 759, L26

Schiminovich, D., et al. 2007, ApJS, 173, 315

Schinnerer, E., Weiß, A., Aalto, S., & Scoville, N. Z. 2010, ApJ, 719, 1588

Schinnerer, E., et al. 2013, ArXiv e-prints

Schneider, N., & Brooks, K. 2004, PASA, 21, 290

Schoenmakers, R. H. M., Franx, M., & de Zeeuw, P. T. 1997, MNRAS, 292, 349

Schruba, A., et al. 2011, AJ, 142, 37

Schuster, K. F., Kramer, C., Hitschfeld, M., Garcia-Burillo, S., & Mookerjea, B. 2007, A&A, 461, 143

Schuster, K.-F., et al. 2004, A&A, 423, 1171

Schwarz, M. P. 1984, MNRAS, 209, 93

Scoville, N., & Young, J. S. 1983, ApJ, 265, 148

Scoville, N. Z., & Hersh, K. 1979, ApJ, 229, 578

Scoville, N. Z., & Solomon, P. M. 1975, in Lecture Notes in Physics, Berlin Springer Verlag, Vol. 42, H II regions and related topics, ed. T. L. Wilson & D. Downes, 272

Scoville, N. Z., Yun, M. S., Armus, L., & Ford, H. 1998, ApJ, 493, L63

Sellwood, J. A., & Binney, J. J. 2002, MNRAS, 336, 785

Sellwood, J. A., & Sparke, L. S. 1988, MNRAS, 231, 25P

Sheth, K., Vogel, S. N., Teuben, P. J., Harris, A. I., Regan, M. W., Thornley, M. D., & Helfer, T. T. 2002, in Astronomical Society of the Pacific Conference Series, Vol. 275, Disks of Galaxies: Kinematics, Dynamics and Peturbations, ed. E. Athanassoula, A. Bosma, & R. Mujica, 267

Sheth, K., Vogel, S. N., Wilson, C. D., & Dame, T. M. 2000, in Proceedings 232. WE-Heraeus Seminar, ed. E. M. Berkhuijsen, R. Beck, & R. A. M. Walterbos, 37–40

Shetty, R., Beaumont, C. N., Burton, M. G., Kelly, B. C., & Klessen, R. S. 2012, MNRAS, 425, 720

Shetty, R., & Ostriker, E. C. 2006, ApJ, 647, 997

Shetty, R., Vogel, S. N., Ostriker, E. C., & Teuben, P. J. 2007, ApJ, 665, 1138

Simon, R., Jackson, J. M., Clemens, D. P., Bania, T. M., & Heyer, M. H. 2001, ApJ, 551, 747

Solomon, P. M., & Rivolo, A. R. 1989, ApJ, 339, 919

Solomon, P. M., Rivolo, A. R., Barrett, J., & Yahil, A. 1987, ApJ, 319, 730

Solomon, P. M., & Sanders, D. B. 1980, in Giant Molecular Clouds in the Galaxy, ed. P. M. Solomon & M. G. Edmunds, 41–73

Solomon, P. M., Sanders, D. B., & Rivolo, A. R. 1985, ApJ, 292, L19

Solomon, P. M., Sanders, D. B., & Scoville, N. Z. 1979, ApJ, 232, L89

Stark, A. A., & Lee, Y. 2006, ApJ, 641, L113

Steinicke, W. 2012, Journal of Astronomical History and Heritage, 15, 19

Stutzki, J., & Guesten, R. 1990, ApJ, 356, 513

Tamburro, D., Rix, H.-W., Leroy, A. K., Mac Low, M.-M., Walter, F., Kennicutt, R. C., Brinks, E., & de Blok, W. J. G. 2009, AJ, 137, 4424

Tan, Q.-H., Gao, Y., Zhang, Z.-Y., & Xia, X.-Y. 2011, Research in Astronomy and Astrophysics, 11, 787

Tasker, E. J., & Tan, J. C. 2009, ApJ, 700, 358

Tasker, E. J., & Tan, J. C. 2011, in IAU Symposium, Vol. 270, Computational Star Formation, ed. J. Alves, B. G. Elmegreen, J. M. Girart, & V. Trimble, 377–380

Tomisaka, K. 1986, PASJ, 38, 95

Toomre, A. 1981, in Structure and Evolution of Normal Galaxies, ed. S. M. Fall & D. Lynden-Bell, 111–136

Toomre, A., & Toomre, J. 1972, in Bulletin of the American Astronomical Society, Vol. 4, Bulletin of the American Astronomical Society, 214

Tosaki, T., Kawabe, R., Ishiguro, M., Okumura, S. K., Morita, K.-I., Kasuga, T., & Ishizuki, S. 1991, in IAU Symposium, Vol. 146, Dynamics of Galaxies and Their Molecular Cloud Distributions, ed. F. Combes & F. Casoli, 79

Trachternach, C., de Blok, W. J. G., Walter, F., Brinks, E., & Kennicutt, Jr., R. C. 2008, AJ, 136, 2720

Troland, T. H., Crutcher, R. M., Goodman, A. A., Heiles, C., Kazes, I., & Myers, P. C. 1996, ApJ, 471, 302

Tukey, J. W. 1977, Exploratory data analysis

Tully, R. B. 1974a, ApJS, 27, 437

—. 1974b, ApJS, 27, 449

Turner, J. L., & Ho, P. T. P. 1994, ApJ, 421, 122

van de Ven, G., & Fathi, K. 2010, ApJ, 723, 767

van der Kruit, P. C., & Shostak, G. S. 1982, A&A, 105, 351

van Dishoeck, E. F., & Black, J. H. 1988, ApJ, 334, 771

Vazquez-Semadeni, E., Passot, T., & Pouquet, A. 1995, in Revista Mexicana de Astronomia y Astrofisica, vol. 27, Vol. 3, Revista Mexicana de Astronomia y Astrofisica Conference Series, ed. M. Pena & S. Kurtz, 61

Vázquez-Semadeni, E., Ryu, D., Passot, T., González, R. F., & Gazol, A. 2006, ApJ, 643, 245

Véron-Cetty, M.-P., & Véron, P. 2006, A&A, 455, 773

Verschuur, G. L. 1995a, ApJ, 451, 624

—. 1995b, ApJ, 451, 645

Visser, H. C. D. 1975, in La Dynamique des galaxies spirales, ed. L. Weliachew, 211

Vlahakis, C., van der Werf, P., Israel, F. P., & Tilanus, R. P. J. 2013, MNRAS, 433, 1837

Vogel, S. N., Kulkarni, S. R., Scoville, N. Z., & Hester, J. 1988, in Lecture Notes in Physics, Berlin Springer Verlag, Vol. 315, Molecular Clouds, Milky-Way and External Galaxies, ed. R. L. Dickman, R. L. Snell, & J. S. Young, 437

Vogel, S. N., Rand, R. J., Gruendl, R. A., & Teuben, P. J. 1993, PASP, 105, 666

Walter, F., Brinks, E., de Blok, W. J. G., Bigiel, F., Kennicutt, Jr., R. C., Thornley, M. D., & Leroy, A. 2008, AJ, 136, 2563

Whitmore, B. C., et al. 2011, ApJ, 729, 78

Williams, J. P., Blitz, L., & McKee, C. F. 2000, Protostars and Planets IV, 97

Williams, J. P., de Geus, E. J., & Blitz, L. 1994, ApJ, 428, 693

Williams, J. P., & McKee, C. F. 1997, ApJ, 476, 166

Wong, T., & Blitz, L. 2002, ApJ, 569, 157

Wong, T., Blitz, L., & Bosma, A. 2004, ApJ, 605, 183

Wong, T., et al. 2011, ApJS, 197, 16

Yorke, H. W. 1989, in Reviews in Modern Astronomy, Vol. 2, Reviews in Modern Astronomy, ed. G. Klare, 283–305

Zaritsky, D., Rix, H.-W., & Rieke, M. 1993, Nature, 364, 313

Zhang, X., & Buta, R. J. 2012, ArXiv e-prints